

Journal of **Geophysics** Zeitschrift für **Geophysik**

Volume 60 1986

Managing Editors

W. Dieminger, G. Müller, J. Untiedt

Editorial Board

K.M. Creer Edinburgh, Scotland
W. Dieminger Lindau, F.R.G.
C. Kisslinger Boulder, Colorado
Th. Krey Hannover, F.R.G.
G. Müller Frankfurt, F.R.G.
G.C. Reid Boulder, Colorado
U. Untiedt Münster, F.R.G.
S. Uyeda Tokyo, Japan

Advisory Board

G. Angenheister , München	St. Müller , Zürich
A.A. Ashour , Cairo	F. Neubauer , Köln
H.-J. Burkhardt , Berlin	H. Neugebauer , Clausthal-Zellerfeld
K. Fuchs , Karlsruhe	F. Rummel , Bochum
N. Fukushima , Tokyo	S. Saxov , Aarhus
H. Gebrande , München	U. Schmucker , Göttingen
V. Haak , Berlin	M. Siebert , Göttingen
W. Jacoby , Mainz	H. Soffel , München
T. Kirsten , Heidelberg	H. Stiller , Potsdam
I.P. Kosminskaja , Moskwa	P. Weidelt , Braunschweig
G. Kremser , Katlenburg-Lindau	J. Zschau , Kiel
W. Lowrie , Zürich	



Springer International

Journal of Geophysics – Zeitschrift für Geophysik

This journal was founded by the Deutsche Geophysikalische Gesellschaft on the initiative of L. Mintrop in 1924 as the Zeitschrift für Geophysik and edited by G. Angenheister from Vol. 1–18 (1944). It reappeared in 1954 edited by B. Brockamp from Vol. 19–26 (1960), and edited by W. Dieminger from Vol. 27–33 (1961), and from Vol. 34 (1968) edited by W. Dieminger and J. Untiedt. After Vol. 40 (1970) the title was changed to Journal of Geophysics – Zeitschrift für Geophysik.

Published: Vols. 19–39 by Physica-Verlag, Würzburg, from Vol. 40 by Springer Berlin, Heidelberg, New York, Tokyo.

Copyright

Submission of a manuscript implies that the work described has not been published before (except in the form of an abstract or as part of a published lecture, review or thesis), that it is not under consideration for publication elsewhere, that its publication has been approved by all the authors and by the responsible authorities – tacitly or explicitly – in the laboratories where the work was carried out and that, if accepted, it will not be published elsewhere in the same form, in either the same or another language, without the consent of the copyright holders. By submitting a manuscript, the authors agree that the copyright for their article is transferred to the publisher if and when the article is accepted for publication. The copyright covers the exclusive rights to reproduce and distribute the article, including reprints, photographic reproductions, microform, electronic data-base, video-disks, or any other reproductions of similar nature, and translations.

Photographic reproduction, microform, electronic data-base, video-disks, or any other reproduction of text, figures, or tables from this journal is prohibited without permission obtained from the publisher.

The use of general descriptive names, trade names, trade marks, etc., in this publication, even if the former are not specifically identified, is not to be interpreted as exempt from the relevant protective laws and regulations and may accordingly be used freely by anyone.

Special Regulations for the USA

The Article Fee Code on the first page of an article in this journal indicates the copyright owner's consent that in the USA copies may be made for personal or internal use, provided the stated fee for copying beyond that permitted by Section 107 or 108 of the United States Copyright Law is paid through the Copyright Clearance Center, Inc., 21 Congress Street, Salem, Mass. 01970, USA.

If a code does not appear, copies of the article may be made without charge, provided permission is obtained from the publisher.

The copyright owner's consent does not extend to copying for general distribution, for promotion, for creating new works, or for resale. Specific written permission must be obtained from the publisher for such copying.

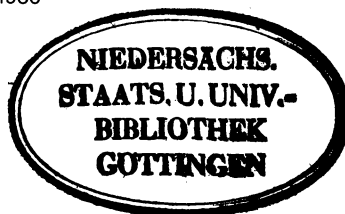
Other Regulations

Authors of this journal can benefit from library and photocopy fees collected by VG WORT if certain conditions are met. Authors of German nationality and those resident in the Federal Republic of Germany or Berlin (West), as well as citizens of Austria, Switzerland and member countries of the European Community, may apply to Verwertungsgesellschaft WORT, Abteilung Wissenschaft, Goethestraße 49, D-8000 München 2, for detailed information.

Springer-Verlag Berlin Heidelberg New York Tokyo

Printed in Germany by Universitätsdruckerei H. Stürtz AG Würzburg

© Deutsche Geophysikalische Gesellschaft. München 1986



Z 1988. 4137

Author Index

Babuška, V. 139	Hoffmann, V. 41	Pellinen, R.J. 186	Stauning, P. 186
Basham, P.W. 120	Jessner, A. 33	Plomerová, J. 139	
Baumjohann, W. 186	Jones, A.G. 56		Temme, P. 19
Bloch, W. 129		Qiyuan, L. 149	
Bösinger, T. 175, 186	Kind, R. 120, 139	Scherbaum, F. 157	Verö, J. 106
Bücker, C. 129	Kundt, W. 33	Schlittenhardt, J. 1	Wassif, N.A. 47
Correig, A.M. 167	Lana, X. 167	Schmidt, T. 199	Wendler, J. 157
Faber, S. 139	Lui, A.T.Y. 175, 186	Schult, A. 129	Wolf, D. 28
Fraser, B.J. 71	Matthews, J.P. 63	Sergeev, V. 175	
Guerreiro, S.D.C. 129	Müller, G. 19, 199	Sergeev, V.A. 186	Yumoto, K. 79
		Soffel, H.C. 41	

Subject Index

Crust – mantle boundary

Lateral variations of the structure of the crust-mantle boundary from conversions of teleseismic *P* waves (Qiyuan, L., Kind, R.) 149

Deglacial uplift

A method of calculating lithosphere thickness from observations of deglacial land uplift and tilt (Wolf, D.) 28

Earthquakes

Volcanoes, fountains, earthquakes, and continental motion – What causes them? (Kundt, W., Jessner, A.) 33

GRF broad-band array analysis of the 1982 Miramichi, New Brunswick earthquake sequence (Basham, P.W., Kind, R.) 120

Cross spectral analysis of Swabian Jura (SW Germany) three-component microearthquake recordings (Scherbaum, F., Wendler, J.) 157

Earth's mantle

Investigation of the velocity- and Q-structure of the lowermost mantle using *PcP/P* amplitude ratios from arrays at distances of 70°–84° (Schlittenhardt, J.) 1

Deep-seated lateral velocity variations beneath the GRF array inferred from mislocation patterns and *P* residuals (Faber, S., et al.) 139

Electromagnetic induction

On the use of line current analogues in geomagnetic depth sounding (Jones, A.G.) 56

Focal mechanism

The retrieval of the seismic moment tensor from first-order perturbation theory and generation of compatible models (Lana, X., Correig, A.M.) 167

Geomagnetic pulsations

Hydromagnetic waves at low latitudes a symposium review from the fifth IAGA assembly (Fraser, B.J.) 71

Generation and propagation mechanisms of low-latitude magnetic pulsations – A review (Yumoto, K.) 79

Experimental aspects of low-latitude pulsations – A review (Verö, J.) 106

Germany

Deep-seated lateral velocity variations beneath the GRF array inferred from mislocation patterns and *P* residuals (Faber, S., et al.) 139

Cross spectral analysis of Swabian Jura (SW Germany) three-component microearthquake recordings (Scherbaum, F., Wendler, J.) 157

Gräfenberg seismic array

Investigation of the velocity- and Q-structure of the lowermost mantle using *PcP/P* amplitude ratios from arrays at distances of 70°–84° (Schlittenhardt, J.) 1

GRF broad-band array analysis of the 1982 Miramichi, New Brunswick earthquake sequence (Basham, P.W., Kind, R.) 120

Deep-seated lateral velocity variations beneath the GRF array inferred from mislocation patterns and *P* residuals (Faber, S., et al.) 139

Lateral variations of the structure of the crust-mantle boundary from conversions of teleseismic *P* waves (Qiyuan, L., Kind, R.) 149

Hydromagnetic waves

Hydromagnetic waves at low latitudes: a symposium review from the fifth IAGA assembly (Fraser, B.J.) 71

Generation and propagation mechanisms of low-latitude magnetic pulsations – A review (Yumoto, K.) 79

Experimental aspects of low-latitude pulsations – A review (Verö, J.) 106

Inverse problems

A method of calculating lithosphere thickness from observations of deglacial land uplift and tilt (Wolf, D.) 28

Deep-seated lateral velocity variations beneath the GRF array inferred from mislocation patterns and *P* residuals (Faber, S. et al.) 139

Isostasy

A method of calculating lithosphere thickness from observations of deglacial land uplift and tilt (Wolf, D.) 28

Line currents

On the use of line current analogues in geomagnetic depth sounding (Jones, A.G.) 56

Lithosphere

A method of calculating lithosphere thickness from observations of deglacial land uplift and tilt (Wolf, D.) 28

Low latitude phenomena

Hydromagnetic waves at low latitudes: a symposium review from the fifth IAGA assembly (Fraser, B.J.) 71

Generation and propagation mechanisms of low-latitude magnetic pulsations – A review (Yumoto, K.) 79

Experimental aspects of low-latitude pulsations – A review (Verö, J.) 106

Magnetospheric physics

Hydromagnetic waves at low latitudes: a symposium review from the fifth IAGA assembly (Fraser, B.J.) 71

Generation and propagation mechanisms of low-latitude magnetic pulsations – A review (Yumoto, K.) 79

- Experimental aspects of low-latitude pulsations – A review (Verö, J.) 106
- Impulsive processes in the magnetotail during substorm expansion (Sergeev, V., Böisinger, T., Lui, A.T.Y.) 175
- Spatial and temporal characteristics of impulsive structure of magnetospheric substorm (Sergeev, V.A. et al.) 186
- NORSAR seismic array*
- Investigation of the velocity- and Q-structure of the lowermost mantle using *PcP/P* amplitude ratios from arrays at distances of 70°–84° (Schlittenhardt, J.) 1
- Olivine*
- Magnetic properties and oxidation experiments with synthetic olivines ($\text{Fe}_x\text{Mg}_{1-x}\text{SiO}_4$, $0 \leq x \leq 1$) (Hoffmann, V., Soffel, H.C.) 41
- Paleomagnetism*
- Rockmagnetism and palaeomagnetism of an Early Cretaceous/Late Jurassic dike swarm in Rio Grande do Norte, Brazil (Bücker, C., et al.) 129
- Plate tectonics*
- Volcanoes, fountains, earthquakes, and continental motion – What causes them? (Kundt, W., Jessner, A.) 33
- Q**
- Investigation of the velocity- and Q-structure of the lowermost mantle using *PcP/P* amplitude ratios from arrays at distances of 70°–84° (Schlittenhardt, J.) 1
- Seismic signal velocity in absorbing media (Schmidt, T., Müller, G.) 199
- Reflection seismics*
- Fast plane-wave and single-shot migration by Fourier transform (Temme, P., Müller, G.) 19
- Rock magnetism*
- Magnetic properties and oxidation experiments with synthetic olivines ($\text{Fe}_x\text{Mg}_{1-x}\text{SiO}_4$, $0 \leq x \leq 1$) (Hoffmann, V., Soffel, H.C.) 41
- Magnetic mineralogy of basalts from El-Bahnasa and Tahna, Egypt (Wassif, N.A.) 47
- Rockmagnetism and palaeomagnetism of an Early Cretaceous/Late Jurassic dike swarm in Rio Grande do Norte, Brazil (Bücker, C., et al.) 129
- Seismic migration*
- Fast plane-wave and single-shot migration by Fourier transform (Temme, P., Müller, G.) 19
- Seismic moment tensor*
- The retrieval of the seismic moment tensor from first-order perturbation theory and generation of compatible models (Lana, X., Correig, A.M.) 167
- Seismic wave absorption*
- Investigation of the velocity- and Q-structure of the lowermost mantle using *PcP/P* amplitude ratios from arrays at distances of 70°–84° (Schlittenhardt, J.) 1
- Seismic signal velocity in absorbing media (Schmidt, T., Müller, G.) 199
- Seismic wave velocity*
- Seismic signal velocity in absorbing media (Schmidt, T., Müller, G.) 199
- Seismology*
- Investigation of the velocity- and Q-structure of the lowermost mantle using *PcP/P* amplitude ratios from arrays at distances of 70°–84° (Schlittenhardt, J.) 1
- Deep-seated lateral velocity variations beneath the GRF array inferred from mislocation patterns and *P* residuals (Faber, S., et al.) 139
- Lateral variations of the structure of the crust-mantle boundary from conversions of teleseismic *P* waves (Qiyuan, L., Kind, R.) 149
- Cross spectral analysis of Swabian Jura (SW Germany) three-component microearthquake recordings (Scherbaum, F., Wendler, J.) 157
- The retrieval of the seismic moment tensor from first-order perturbation theory and generation of compatible models (Lana, X., Correig, A.M.) 167
- South America*
- Rockmagnetism and palaeomagnetism of an Early Cretaceous/Late Jurassic dike swarm in Rio Grande do Norte, Brazil (Bücker, C., et al.) 129
- Substorms*
- Impulsive processes in the magnetotail during substorm expansion (Sergeev, V.A., et al.) 175
- Spatial and temporal characteristics of impulsive structure of magnetospheric substorm (Sergeev, V.A.) 186
- Theoretical seismograms*
- GRF broad-band array analysis of the 1982 Miramichi, New Brunswick earthquake sequence (Basham, P.W., Kind, R.) 120
- Lateral variations of the structure of the crust-mantle boundary from conversions of teleseismic *P* waves (Qiyuan, L., Kind, R.) 149
- VLF waves*
- Observations of the VLF quiet band phenomenon (Matthews, J.P.) 63
- Volcanism*
- Volcanoes, fountains, earthquakes, and continental motion – What causes them? (Kundt, W., Jessner, A.) 33
- Book reviews* 69, 137, 207
- Conference* 136
- In memoriam* 68, 204

Journal of Geophysics Zeitschrift für Geophysik

28. Okt. 1986

Niedersächsische Staats- u.
Universitätsbibliothek
Göttingen

Volume 60⁻⁶² Number 1 1986^{-87/88}

Original investigations

J. Schlittenhardt

Investigation of the velocity- and Q-structure of the lowermost mantle using P_c/P amplitude ratios from arrays at distances of 70° – 84° 1

P. Temme, G. Müller

Fast plane-wave and single-shot migration by Fourier transform 19

D. Wolf

A method of calculating lithosphere thickness from observations of deglacial land uplift and tilt 28

W. Kundt, A. Jessner

Volcanoes, fountains, earthquakes, and continental motion – What causes them? 33

V. Hoffmann, H.C. Soffel

Magnetic properties and oxidation experiments with synthetic olivines $(\text{Fe}_x\text{Mg}_{1-x})_2\text{SiO}_4$, $0 \leq x \leq 1$ 41

N.A. Wassif

Magnetic mineralogy of basalts from El-Bahnasa and Tahna, Egypt 47

A.G. Jones

On the use of line current analogues in geomagnetic depth sounding 56

J.P. Matthews

Observations of the VLF quiet band phenomenon 63

In memoriam 68

Book reviews 69

Indexed in *Current Contents*

Evaluated and abstracted for *PHYS* on *STN*

1-3, T. 1

X, 501

8 Z Nat. 2148

Z 1988 4137

64



Springer International

Journal of Geophysics – Zeitschrift für Geophysik

Edited for the Deutsche Geophysikalische Gesellschaft by W. Dieminger, G. Müller, and J. Untiedt

This journal was founded by the Deutsche Geophysikalische Gesellschaft on the initiative of L. Mintrop in 1924 as the *Zeitschrift für Geophysik* and edited by G. Angenheister from Vols. 1–18 (1944). It reappeared in 1954, edited by B. Brockamp from Vols. 19–26 (1960), by W. Dieminger from Vols. 27–33 (1961), by W. Dieminger and J. Untiedt from Vols. 34 (1968), and edited by W. Dieminger, J. Untiedt and G. Müller from Vol. 45 (1979). After Vol. 40 (1970) the title was changed to *Journal of Geophysics – Zeitschrift für Geophysik*.

Published: Vols. 19–39 by Physica-Verlag, Würzburg, from Vol. 40 by Springer-Verlag GmbH & Co. KG Berlin, Heidelberg, New York, Tokyo.

Manuscripts may be addressed to any of the Editors. For addresses see last cover page. Manuscripts should conform with the journal's accepted practice as described in the Instructions to Authors.

The Journal accepts

- Review articles (invited by the editors)
- Original papers
- Short communications
- Letters to the editors
- Book reviews

In the field of Geophysics and Space Physics.

Copyright

Submission of a manuscript implies: that the work described has not been published before (except in the form of an abstract or as part of a published lecture, review, or thesis); that it is not under consideration for publication elsewhere; that its publication has been approved by all coauthors, if any, as well as by the responsible authorities at the institute where the work has been carried out; that, if and when the manuscript is accepted for publication, the authors agree to automatic transfer of the copyright to the society; and that the manuscript will not be published elsewhere in any language without the consent of the copyright holders. All articles published in this journal are protected by copyright, which covers the exclusive rights to reproduce and distribute the article (e.g., as offprints), as well as all translation rights. No material published in this journal may be reproduced photographically or stored on microfilm, in electronic data bases, video disks, etc., without first obtaining written permission from the publisher.

The use of general descriptive names, trade names, trademarks, etc., in this publication, even if not specifically identified, does not imply that these names are not protected by the relevant laws and regulations.

While the advice and information in this journal is believed to be true and accurate at the date of its going to press, neither the authors, the editors, nor the publisher can accept any legal responsibility for any errors or omissions that may be made. The publisher makes no warranty, express or implied, with respect to the material contained herein.

Special regulations for photocopies in the USA:

Photocopies may be made for personal or in-house use beyond the limitations stipulated under Section 107 or 108 of U.S. Copyright Law, provided a fee is paid. This fee is US \$ 0.20 per page, or a minimum of US \$ 1.00 if an article contains fewer than five pages. All fees should be paid to the Copyright Clearance Center, Inc., 21 Congress Street, Salem, MA 01970, USA, stating the ISSN 0340-062X, the volume, and the first and last page numbers of each article copied. The copyright owner's consent does not include copying for general distribution, promotion, new works, or resale. In these cases, specific written permission must first be obtained from the publisher.

Other regulations: Authors publishing in this journal can, under certain conditions, benefit from library and photocopy fees collected by VG WORT. Authors of German nationality and those resident in the Federal Republic of Germany or Berlin (West), as well as citizens of Austria, Switzerland and member countries of the European Community, may apply to Verwertungsgesellschaft WORT, Abteilung Wissenschaft, Goethestrasse 49, D-8000 München 2, FRG, for detailed information.

Subscription information

Volumes 59–60 (3 issues each) will appear in 1986.

Members. Members of the Deutsche Geophysikalische Gesellschaft are entitled to purchase the Journal for their own use at a privilege price of DM 98.00, plus carriage charges, payable with the Membership dues. Orders should be sent to the Society's office at the following address:
Deutsche Geophysikalische Gesellschaft e.V., Dr. A. Berktold, Theresienstrasse 41/IV, D-8000 München 2, FRG.

North America. Annual subscription rate: Approx. US \$ 166.00 (single issue price: Approx. US \$ 32.00), including carriage charges. Subscriptions are entered with prepayment only. Orders should be addressed to:

Springer-Verlag New York Inc.
Service Center Secaucus
44 Hartz Way
Secaucus, NJ 07094, USA
Tel. (2 01) 3 48-40 33, Telex 0 23-125 994.

All other countries. Annual subscription rate: DM 432.00 plus carriage charges. Airmail delivery on request only. Volume price: DM 216.00, single issue price: DM 86.40, plus carriage charges. Carriage charges for SAL (Surface Airmail Lifted) to Japan, India, Australia and New Zealand are available on request. Orders can either be placed with your bookdealer or sent directly to:
Springer-Verlag
Heidelberger Platz 3
1000 Berlin 33
Tel. (0)30/82 07-1, Telex 1-83 319.

Changes of address: Allow six weeks for all changes to become effective. All communications should include both old and new addresses (with Postal Codes) and should be accompanied by a mailing label from a recent issue.

Back volumes: Prices are available on request.

Microform: Microform editions are available from:
University Microfilms International
300 N. Zeeb Road
Ann Arbor, MI 48106, USA

Production

Springer-Verlag
Journal Production Department II
Postfach 10 52 80
D-6900 Heidelberg 1
Federal Republic of Germany
Tel. (0)62 21/4 87-3 42, Telex 4-61 690.

Responsible for advertisements

Springer-Verlag
E. Lückermann
Heidelberger Platz 3
1000 Berlin 33
Tel. (0)30/8 20 71, Telex 1-85 411.

Printers

Universitätsdruckerei H. Stürtz AG Würzburg
© the Deutsche Geophysikalische Gesellschaft, München, 1986
Springer-Verlag GmbH & Co. KG
1000 Berlin 33
Printed in Germany



Springer International

*Original investigations***Investigation of the velocity- and Q-structure of the lowermost mantle using *PcP/P* amplitude ratios from arrays at distances of 70°–84°****J. Schlittenhardt***

Institute of Meteorology and Geophysics, University of Frankfurt, Feldbergstrasse 47, D-6000 Frankfurt, Federal Republic of Germany

Abstract. Investigations of the core reflection *PcP* at distances in the neighbourhood of the core shadow zone are especially appropriate for the study of isolated regions of *D'* because *PcP* for these distances has a large angle of incidence at the core-mantle boundary and is strongly influenced by the structure immediately above the core. A striking result of this investigation of *PcP* in the distance range 70°–84° is that *PcP* could be detected only in four cases (from a total of 16 earthquakes and 29 nuclear explosions) in the NORSAR- and GRF-array beams for *PcP*. This result is found although the *P*-wave-coda noise levels in the *PcP* beams are very low, mostly below the amplitude level of *PcP* predicted by standard earth models. In the cases where *PcP* could not be identified, the *PcP/P* amplitude ratio, which is estimated from the beams with the aid of a cross-correlation procedure, must be regarded as an upper limit for the actual *PcP/P* ratio. The interpretation of the *PcP/P* amplitude ratios with *one* radially symmetric, elastic model proved to be impossible. The generally small *PcP/P* ratios can be explained by lateral variations in seismic wave absorption within *D'*. Q_a values for short-period *P* waves in *D'*, between 800 (below Usbekistan) and 100 (below the northern Hudson Bay and Central Siberia), were found.

Several recent seismological investigations of the *P*- and *S*-wave velocity of the lowermost mantle have suggested velocity models with first-order discontinuities (with velocity increases of the order of 1.5%–3.0%) 150–300 km above the core-mantle boundary. Through the calculation of synthetic short-period seismograms and comparison with the array data compiled for the main part of this study, it is shown that such models are very unlikely to be a global feature if the *P* velocity jump is of the order of 2.5%–3.0%. Even models with reduced *P* velocity jumps of 1.3% produce clear onsets in short-period seismograms. They are not observed for *P* waves with ray paths bottoming beneath Central Siberia.

Key words: Lower mantle structure – *D'* region – *PcP/P* amplitude ratios – Array data – Vespagrams – Matched filtering – Lower mantle discontinuities – Wave absorption

* Present address: Bundesanstalt für Geowissenschaften und Rohstoffe, Postfach 5101 53, D-3000 Hannover 51, Federal Republic of Germany

Introduction

The exact knowledge of the seismic wave velocities and Q-structure of the lowermost 100–200 km of the earth's mantle is of great importance for the understanding of the thermal and dynamical state of the earth's mantle as a whole. The simple conditions of chemical homogeneity and adiabaticity, which hold largely for the main part of the lower mantle and the outer core where the seismic wave velocities increase smoothly with depth, are possibly not valid within an approximately 200-km-thick zone directly above the core-mantle boundary [Bullen's (1950) zone *D'*] where the gradients of the wave velocities are possibly reduced or even negative. The physical significance of reduced or vanishing velocity gradients in this zone were first recognized by Bullen, who concluded from a hypothesis on the relation of compressibility and pressure (Bullen, 1949) that the density gradients within *D'* are approximately three times greater than in a homogeneous medium. However, reduced or vanishing velocity gradients may also be explained by superadiabatic temperature gradients in chemical homogeneous material where thermal boundary layers develop. Within such boundary layers with increased temperature gradients [temperature differences of 1,000 K across *D'* are discussed (Elsasser et al., 1979; Jeanloz and Richter, 1979)], the heat from the core is transferred by pure conduction and contributes to mantle-wide convection in the overlying mantle material (Jones, 1977; Peltier and Jarvis, 1982). Before being commonly accepted, however, these ideas about the state of the lowermost mantle should reflect, and find support in, the results of seismological work.

The methods which are applied to study the structure of the lowermost mantle with seismic body waves measure several different quantities of the waves interacting with the structure. Among these methods are measurements of the ray parameters of short- and long-period diffracted *P* and *S* waves (Gutenberg and Richter, 1936; Sacks, 1967; Cleary, 1969; Hales and Roberts, 1970; Bolt, 1970; Okal and Geller, 1979; Mula and Müller, 1980), determination of the decay constants of long-period diffracted *P* and *S* waves (Alexander and Phinney, 1966; Phinney and Alexander, 1966; Mondt, 1977; Doornbos and Mondt, 1979a, b; Mula, 1981; Doornbos, 1983), observation and interpretation of short-period precursors to *PKIKP* (Doornbos and

Husebye, 1972; King et al., 1974; Haddon and Cleary, 1974; Doornbos, 1978; Haddon, 1982) and of amplitude ratios PcP/P and ScS/S (Kanamori, 1967; Buchbinder, 1968; Ibrahim, 1971, 1973; Berzon et al., 1972; Buchbinder and Poupinet, 1973; Chowdhury and Frasier, 1973; Mitchell and Helmberger, 1973; Frasier and Chowdhury, 1974; Müller et al., 1977; Lay and Helmberger, 1983b). All these different investigations did not result in globally representative velocities at the base of the earth's mantle, and the question, of whether a zone with negative velocity gradient (velocity decrease with increasing depth) directly above the core-mantle boundary (CMB) exists or not, is still open. The only common result of these investigations is that the behaviour of body waves which sample the lowermost part of the mantle cannot be explained by simple extrapolation of the velocity gradients from the main part of the lower mantle (Cormier, 1985). Only recently, the partly spectacular results of seismic tomography of the earth's mantle (Dziewonski, 1984) established the D'' region as the region of the lower mantle with the greatest per cent lateral fluctuations of the seismic wave velocities. If such significant lateral variations exist, the question of the globally representative vertical velocity gradient loses some of its importance.

Matters are complicated even more by Lay and Helmberger's (1983a) proposal that a world-wide discontinuity in shear wave velocity exists about 280 km above the CMB. Their model, which has been derived by modelling the amplitudes and travel times of onsets between mantle S and ScS in transverse-component seismograms at distances from 70° to 80° , predicts pronounced pulse-form changes of long-period SH waves in the epicentral distance range 95° – 120° . Similar pulse-form changes are expected in P -wave seismograms, under the reasonable assumption of a similar increase in the P velocity. Schlittenhardt et al. (1985) compared nine long-period seismogram sections of SH and P waves from deep-focus earthquakes with synthetic seismograms for the PREM model (Dziewonski and Anderson, 1981) and the SLHO model of Lay and Helmberger and found practically no indication of the complications expected for the distance range 95° – 120° .

The purpose of this paper is, therefore, two-fold. First, a new data set of short-period PcP/P amplitude ratios, derived from observations of the GRF array (Fed. Rep. Germany) and the NORSAR array (Norway) in the distance range 70° – 84° , and the interpretation of these data with respect to the velocity gradients and Q structure at the base of the mantle, is presented. Secondly, short-period synthetic seismograms for P waves at distances from 70° to 100° that show pronounced differences between SLHO and PREM (which is of course expected) will be presented and compared to the short-period array data compiled for this study. It will be shown that, under the assumption of equal velocity jumps for the P and S velocity at the discontinuity of SLHO (we assumed 2.6% for both the S - and P -velocity jump), the existence of a world-wide discontinuity at the top of D'' can be disproved, in accordance with the findings from long-period data of Schlittenhardt et al. (1985). Values of the P -velocity increase of 1.3% and lower (keeping all other parameters in SLHO unchanged) can only be disproved by short-period data, as will be shown through comparison of synthetic seismograms with two selected observations.

Investigations of the core reflection PcP at distances in the neighbourhood of the core shadow zone are especially

appropriate for the study of the velocity gradients at the base of the mantle. For these observation distances, PcP has a large angle of incidence at the CMB and is influenced strongly by the structure immediately above the core. PcP has been studied in the literature several times for epicentral distances up to 60° , mostly with the disappointing result of strong scatter in the observed PcP/P ratios. The reason for this scatter is probably the different P and PcP ray paths through the inhomogeneous (near-surface) regions of the earth with strongly different phase velocities (Frasier and Chowdhury, 1974). By utilizing the wavenumber characteristics of the NORSAR and GRF arrays and through the restriction to an observation range where the ray paths of P and PcP are nearly identical especially for their near-surface parts, effects which influence the amplitude behaviour of P and PcP in a *different manner* can be practically excluded. It is a reasonable assumption that the differences still remaining between observed PcP/P amplitude ratios and theoretical amplitude ratios for standard earth models like PREM must then be caused by structure in the lowermost mantle.

PcP/P amplitude ratios from array data in the distance range 70° – 84°

For the distance range 70° – 84° , the turning points of the mantle P wave lie in the depth range 1,900–2,500 km, a part of the lower mantle which is characterized by a smooth and uncomplicated distribution of material parameters. The difference in the take-off angle for P and PcP in that distance range decreases from 8.5° to 3° . It can be assumed therefore that inhomogeneities in the upper parts of the earth, where the ray paths of P and PcP are close, influence the amplitude behaviour of P and PcP in practically the same way and that the effects of such inhomogeneities cancel in the amplitude ratios. This qualitative argument can be quantified by ray-tracing calculations for spherical earth models: at an epicentral distance of 70° , the horizontal distance between a P and PcP ray at a depth of 670 km is 100 km (Spies, 1985). For a depth of 220 km (lithosphere), this distance decreases to approximately 20 km, which is already of the order of the wavelength of short-period P waves. Hence, at smaller depths the ray paths of P and PcP agree within one dominant wavelength. The essence of the amplitude-ratio method of this paper is therefore to model observed PcP/P amplitude ratios through variation of the elastic parameters and Q in the *lowermost* mantle. The amplitude modelling is done through the calculation of theoretical seismograms with the reflectivity method for vertically inhomogeneous media with arbitrary depth dependence of the specific dissipation Q .

As the difference travel time $PcP-P$ is only approximately 7 s for an observation distance of 80° , events (earthquakes and nuclear explosions) with short and simple source pulses had to be selected. Besides this criterion, earthquakes selected for this study must have hypocentres deep enough that the surface reflection pP arrives after PcP and the focal mechanism must be orientated in such a way that P and PcP are radiated approximately with equal strength. Nine earthquakes with $m_b \geq 5.6$ recorded at GRF in the period 1976–1981 fulfilled these criteria (Table 1). For the time period of the full size of the NORSAR array (1971–1976), seven appropriate recordings from earthquakes with $m_b \geq 5.6$ could be selected (Table 1). Addition-

Table 1. List of earthquakes used for this study

No.	Region	Date	Origin time	Epicentre	Depth (km)	m_b	Δ (°)	$P_c/P/P$	R_{cor}	Fault plane solution from	Number of traces (sub-arrays)	Back-azimuth (°)	Azimuth (°)
Earthquakes observed at GRF													
1	S. of Okhotsk	10.07.76	11:37:14.0	47.31 N 145.75 E	402	5.8	75.7	0.10	1.09	+	3	30	331
2	Kuriles Is.	14.08.78	18:46:23.4	49.83 N 156.32 E	80	5.7	76.4	0.05	-	+	6	22	338
3	Fox Is.	01.09.79	05:27:17.6	53.98 N 165.20 W	69	5.8	76.7	0.07	1.36	+	5	2	358
4	Rat Is.	18.10.79	03:35:26.9	51.86 N 177.13 E	62	6.0	78.1	0.17	1.17	+	10	9	351
5	Kuriles Is.	04.10.78	03:54:15.2	46.25 N 151.80 E	86	5.6	78.5	0.09	0.88	+	5	27	335
6	Kuriles Is.	22.09.76	00:16:06.6	44.78 N 149.21 E	58	6.1	79.0	0.10	-	+	2	29	334
7	Kuriles Is.	19.03.77	10:56:22.0	44.20 N 148.20 E	70	6.0	79.3	0.07	0.99	+	3	30	333
8	Kuriles Is.	03.09.81	05:35:44.8	43.62 N 147.03 E	45	6.6	79.4	0.07	0.89	+	13	31	333
9	Honshu, Jap.	24.09.80	17:54:24.1	35.45 N 139.96 E	73	6.0	83.9	0.06	0.95	+	13	40	329
Earthquakes observed at NORSAR													
10	Sea of Jap.	10.06.71	19:59:53.3	41.10 N 138.52 E	233	5.6	69.9	0.09	1.44	+	22	40	336
11	Ryukyu Is.	26.10.72	17:05:05.6	27.48 N 128.57 E	63	6.0	78.6	0.05	0.98	+	22	53	334
12	N. of Taiwan	11.09.73	23:18:50.4	25.65 N 124.58 E	137	5.7	78.6	0.09	-	+	12	57	333
13	S. of Honshu	04.03.71	00:28:38.3	30.41 N 138.44 E	449	5.6	79.6	0.07	1.00	+	21	44	337
14	Nicobar Is.	05.08.76	13:37:14.7	7.00 N 94.31 E	87	5.7	80.8	0.13	0.63	+	20	92	330
15	Nicobar Is.	17.07.71	05:32:43.4	6.98 N 94.65 E	144	5.6	80.9	0.12	0.83	+	22	92	330
16	Bonin Is.	13.11.72	08:11:49.3	27.93 N 140.14 E	374	5.6	82.5	0.05	1.00	+	22	44	338

+ , Fault-plane solution based on polarity readings of the ISC;

+ + , Fault-plane solution based on own polarity readings of WWSSN-LP seismograms;

+ + + , Fault-plane solution by Needham (based on polarity readings), as published in the 'Monthly Listings, PDE' of the USGS

For explanation of the other parameters see text. Sources: ISC and USGS

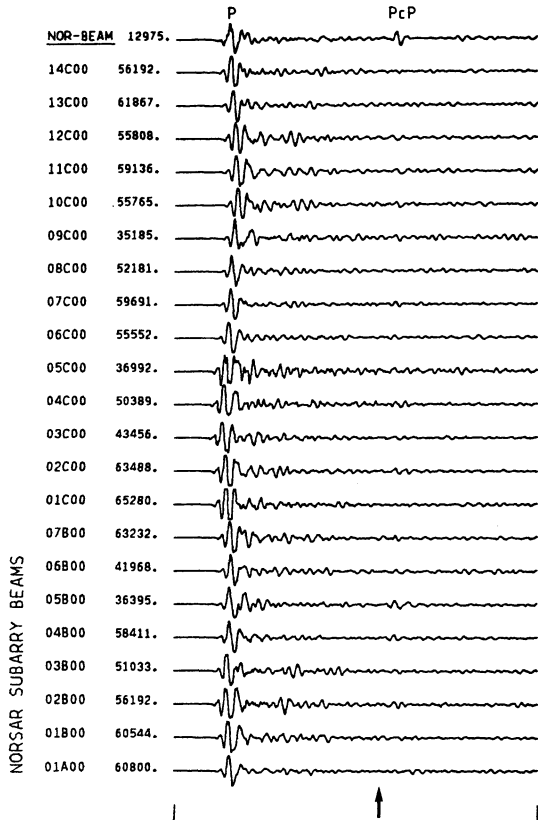


Fig. 1. NORARS subarray beams and array beam (*uppermost trace*) for *PcP* for earthquake No. 10 from Table 1. To the left of the seismograms, subarray codes and the maximum peak-to-peak amplitudes, respectively, are given. *The arrow* indicates the Herrin arrival time for *PcP*. The duration of the time window is 45 s

ally, from this period, recordings of 28 nuclear explosions at the Nevada Test Site, USA and of one explosion in Colorado, USA (No. 6 in Table 2) could be found. The geographical position of the epicentres of these events is shown in Fig. 11.

Estimation of the PcP/P amplitude ratio from correlograms of P and PcP array beams

Following e.g. Harjes and Henger (1973) or Kelly (1967), the array response function for monochromatic plane waves of the GRF and NORARS array has been calculated (Schlittenhardt, 1984) to determine how much P -wave energy can be suppressed in the PcP beam when the arrays are tuned to the slowness of PcP . It turned out that for all earthquakes and nuclear explosions recorded at the NORARS array (except No. 16 in Table 1) the wavenumber difference of P and PcP (assuming a dominant signal frequency of 1 Hz) is greater or equal to the minimum wavenumber difference k_{\min} which is necessary to reach the rejection band of the array response function. This means that the amplitude reduction of P waves in the NORARS PcP beams is -13 dB. For the GRF array, the situation is not as favourable because most of the events analysed are from times before the full configuration of the array had been completed.

The theoretical expectations concerning the P -wave amplitude reduction in the PcP beams could be verified in the course of our data analysis. This is illustrated in Fig. 1 where the NORARS-subarray beams and the PcP array

beam are shown for event No. 10 from Table 1. The reduction of the P -wave and P -wave-coda amplitudes in the PcP beam by a factor of approximately 0.22 (-13 dB) leads to a significant noise reduction at the arrival time of PcP and makes possible the emergence of the PcP signal. This is especially obvious when one compares the noise levels of the subarray beams and the array beam.

The data example has demonstrated the necessity and usefulness of simple beam-forming to detect the rather weak PcP signal in the coda of P . Therefore, for the investigation of the 44 events selected for this study, the P and PcP beams were calculated and plotted with equal amplitude scale to determine the PcP/P amplitude ratio by measuring the peak-to-peak amplitude. In the course of this analysis it turned out that PcP is characterized by very small amplitudes and that PcP could be detected reliably in only four cases, although the noise level at the arrival time of PcP is well below the expected amplitude level of PcP , e.g. for the PREM model. In all other cases one has to solve the problem of measuring the amplitude of a signal which is hidden in a time series with superimposed noise. In our special case here however, the problem reduces to the measurement of the amplitude of a signal with known *shape* which is hidden in noise: from the evidence of observations of short-period PcP waves (at smaller epicentral distances) one generally expects a no more complicated wave-form for the core reflection than for the direct P wave (Kanamori, 1967). The best existing data, namely the LASA-array beams for P and PcP (Chowdhury and Frasier, 1973; Frasier and Chowdhury, 1974; Engdahl and Johnson, 1974), show a reproduction of the pulse-form of P for PcP . To solve this kind of problem in digital signal processing (e.g. Lüke, 1979; Kanasewich, 1975), the correlation-filter or matched-filter technique is successfully applied. This method will be used throughout this study to estimate the PcP/P amplitude ratio.

Matched filtering of PcP beams. The matched filtering of PcP beams is performed through the calculation of the cross-correlation function $\Phi_{sx}(t)$ (filter output) of the time series $x(t)$ (here the PcP beam) and the signal $s(t)$ (here the P pulse with duration T defined in the P beam):

$$\Phi_{sx}(t) = \int_{-\infty}^{\infty} s(\tau) x(\tau + t) d\tau. \quad (1)$$

Assuming for the PcP beam $x(t)$:

$$x(t) = a s(t - t_0) + n(t), \quad (2)$$

where $a s(t - t_0)$ is the PcP signal with arrival time t_0 and $n(t)$ is the noise. Inserting Eq. (2) into Eq. (1) yields

$$\begin{aligned} \Phi_{sx}(t) &= \int_{-\infty}^{\infty} [a s(\tau) s(\tau - t_0 + t) + s(\tau) n(\tau + t)] d\tau \\ &= a \Phi_{ss}(t - t_0) + \Phi_{sn}(t). \end{aligned} \quad (3)$$

$\Phi_{ss}(t - t_0)$ is the auto-correlation function Φ_{ss} shifted by the time t_0 . The auto-correlation function $\Phi_{ss}(t - t_0)$ has its maximum at time $t = t_0$, the arrival time of PcP . Now we normalize Eq. (3) to the maximum of the auto-correlation function

$$\begin{aligned} \Phi_{ss}(0) &= \int_0^T s^2(\tau) d\tau \\ \Phi_{sx}^{\text{nor}} &= a \left[\frac{\Phi_{ss}(t - t_0)}{\Phi_{ss}(0)} \right] + \frac{\Phi_{sn}(t)}{\Phi_{ss}(0)}. \end{aligned} \quad (4)$$

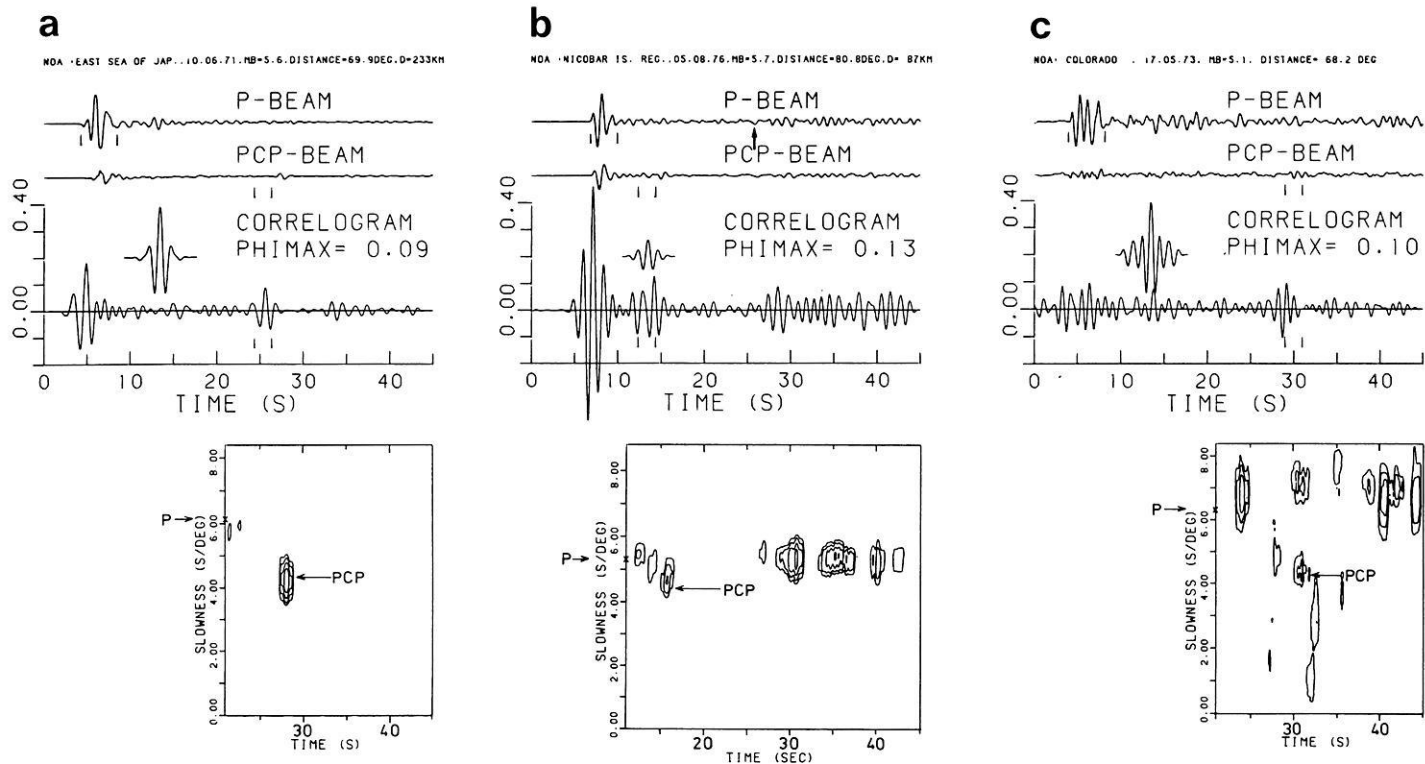


Fig. 2. **a** P , PcP beam, correlogram (upper part) and vespagram (lower part) for earthquake No. 10 from Table 1. The contour interval for the isolines in the vespagram is -3 dB. The arrows mark the slowness for P and PcP , respectively, after the Herrin tables. **b** The same as in Fig. 2a for earthquake No. 14 from Table 1. The arrow in the P beam marks the theoretical arrival time of the surface reflection pP . **c** The same as in Fig. 2a for the nuclear explosion in Colorado (No. 6 in Table 2)

The first term in the sum in Eq. (4), at time $t=t_0$, yields the desired amplitude ratio a . The second term in Eq. (4) corresponds to the normalized cross-correlation function of $s(t)$ and the noise $n(t)$. Taking into account that the noise mostly represents P -coda waves which are suppressed in the PcP beam, it can be assumed that $\Phi_{sn}(t) \approx 0$. Then Φ_{sx}^{nor} in Eq. (4) yields, at time $t=t_0$, the desired amplitude ratio a . This procedure for matched filtering of P and PcP array beams is illustrated in Fig. 2a for the Sea of Japan earthquake (No. 10 in Table 1). The upper part of this figure shows the P and PcP beam (plotted with equal amplitude scale) and the corresponding correlogram Φ_{sx}^{nor} according to Eq. (4). In the left part of the correlogram, the auto-correlation $\Phi_{ss}(t)$ for the signal $s(t)$ defined in the P beam is plotted for purposes of comparison. In the lower part of this figure, a vespagram for the last 25 s of the data window is shown. The P signal $s(t)$ is defined in the P beam by a pair of vertical bars. The pairs of vertical bars in the PcP beam and correlogram correspond to the minimum- and maximum-difference travel-time PcP - P , derived for two models with extremely positive and negative velocity gradients at the base of the mantle (P190 and N190 in Fig. 8). Additionally, for all events studied, these individually calculated minimum and maximum theoretical travel times were decreased and increased, respectively, by 1 s to take into account the finite width of the auto-correlation function for a signal with a dominant frequency of 1 Hz. The wanted PcP/P amplitude ratio a from Eq. (4) (denoted PHIMAX in Fig. 2a) is determined as the maximum of the correlogram Φ_{sx}^{nor} in the PcP arrival-time window. Our theoretical minimum and maximum travel times thus define a PcP arrival-time window whose limits are given by the

maximum possible range of variability for the PcP - P difference travel time for currently discussed gradient models. In Fig. 2a, the form of the auto-correlation function is in good agreement with the form of the correlogram in the arrival-time window for PcP , as expected of course. The peak of the correlation signal corresponds to the arrival time of PcP and lies within the predicted arrival-time window, as does the onset of the PcP signal in the PcP beam. The main peak and trough of the PcP signal (compare with the form of the P signal in the P beam) can be recognized shortly after the maximum arrival time for PcP . In the vespagram in the lower part of Fig. 2a, PcP causes a sharp maximum in the slowness-versus-time plane; this confirms again that it is possible to identify the rather weak PcP signals in the range 70° – 84° .

Earthquake data

Despite the rather small difference in take-off angles of P and PcP , a bias of the PcP/P amplitude ratios because of unequal radiation at the source is possible. Therefore, we tried to construct fault-plane solutions for all investigated earthquakes. For most of the earthquakes the first-motion data as published in the ISC bulletin were used (Table 1). There are inconsistencies in the polarity distributions derived from these data, but for all earthquakes investigated it is possible to make a decision as to whether the generally very small PcP/P amplitude ratios determined in this paper are caused by nodal radiation of PcP or not. The fault-plane solutions and polarity distributions for all earthquakes investigated are shown in Fig. 3. For those earthquakes for which a reliable determination of the fault-

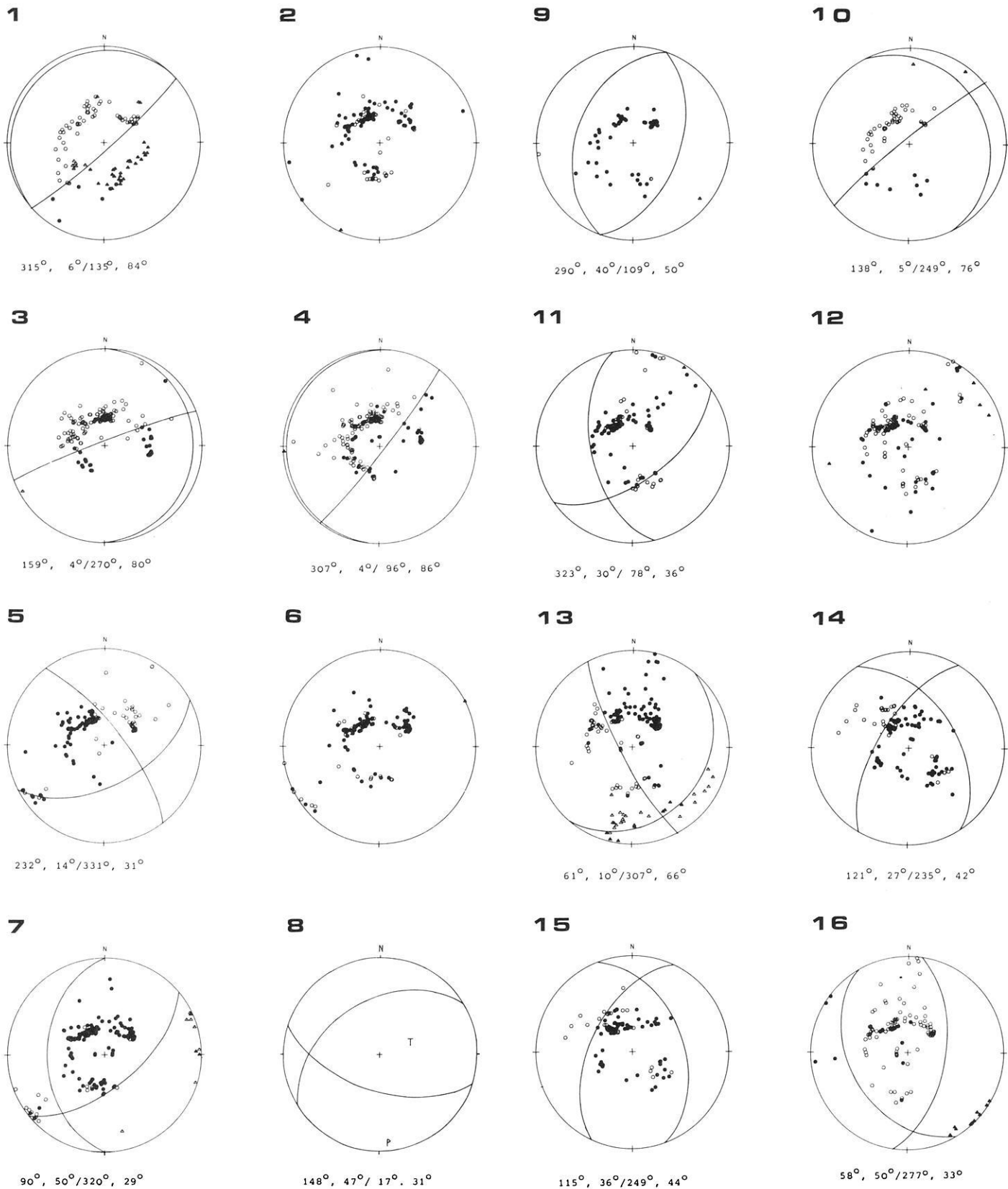


Fig. 3. Fault-plane solutions for the earthquakes listed in Table 1, shown as equal-area projections of the lower focal hemisphere. *Open (solid) symbols* indicate dilatation (compression). No attempt was made to draw the nodal planes for events 2 and 6. For event 8, a graphical representation of the fault-plane solution by Needham from the 'Monthly Listings, PDE' of the USGS is shown. The numbers below the fault-plane solutions indicate the trend and plunge of the poles of the P nodal planes

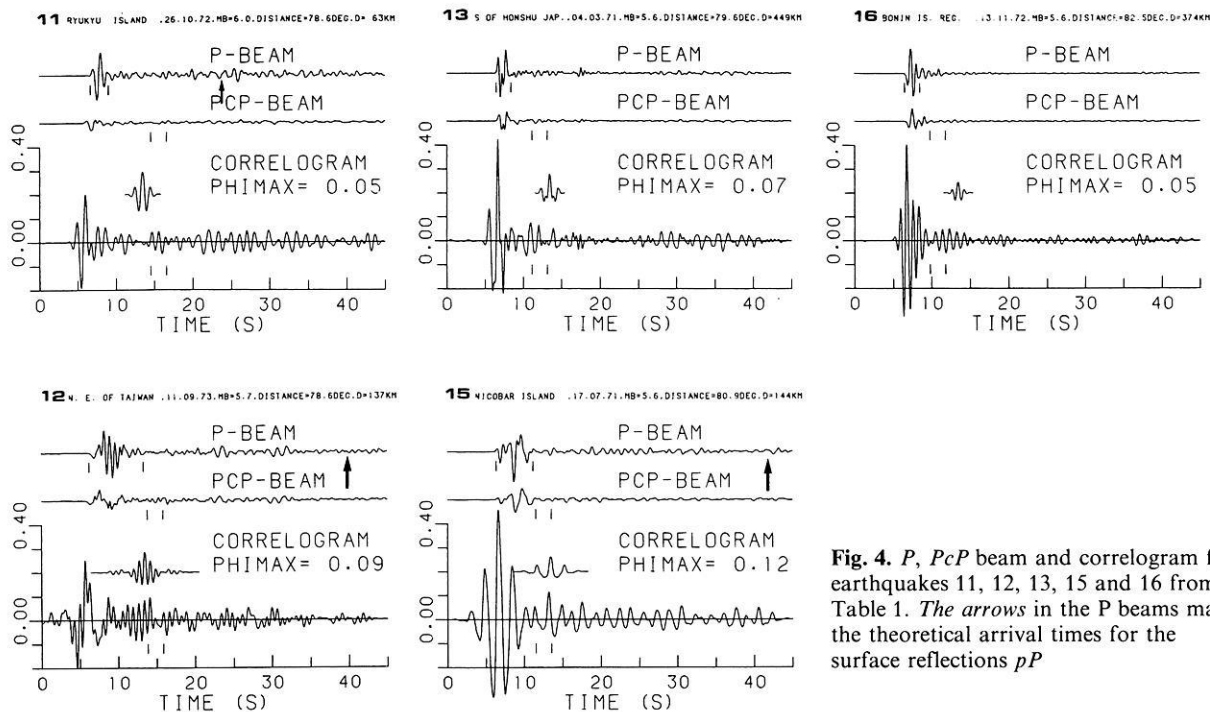


Fig. 4. *P*, *PcP* beam and correlogram for earthquakes 11, 12, 13, 15 and 16 from Table 1. The arrows in the *P* beams mark the theoretical arrival times for the surface reflections *pP*

plane solution was possible, a correction factor $R_{\text{cor}} = A_P / A_{PcP}$ for isotropic source radiation was calculated (Table 1), where A_P and A_{PcP} are the relative far-field radiations for *P* and *PcP* for the respective double-couple point source (Aki and Richards, 1980).

Recordings from NORSAR. The recordings from earthquakes recorded at the NORSAR array (Nos. 10–16 in Table 1) were processed as was illustrated for the Sea of Japan earthquake; they are presented in Figs. 2b and 4. For earthquake No. 14, the second one with identifiable *PcP* signal, a velocity-spectral analysis was made in addition to the matched-filtering: as in the case of the Sea of Japan earthquake the main minimum and maximum of the *PcP* signal can be identified in the *PcP* beam shortly after the maximum *PcP* arrival time, and the forms of the auto-correlation function and the correlogram in the corresponding arrival-time window are in good agreement (Fig. 2b). In the slowness-versus-time plane, *PcP* causes an isolated peak (lower part of Fig. 2b). For all other earthquakes in Fig. 4, despite the significant reduction of *P*-coda noise in the *PcP* beam, *PcP* could not be detected reliably, although at least in some cases (e.g. No. 16 in Fig. 4) the forms of the auto-correlation function of the *P* signal and the correlogram in the corresponding arrival-time window are relatively similar.

Recordings from GRF. The recordings from the nine earthquakes recorded at the GRF array (Nos. 1–9 in Table 1) are presented in Fig. 5. Because wavenumber difference increases with increasing frequency (at a given slowness difference for *P* and *PcP*) and because of the corresponding improvement in wavenumber filter capability of an array, it is appropriate to use short-period seismograms of the originally broadband GRF data. In this paper we work with short-period simulations of the broadband GRF data, according to the transfer function of a WWSSN-SP station

(Seidl, 1980). The treatment of the GRF data in Fig. 5 is analogous to that for the NORSAR data except that the plot of the auto-correlation of the *P* signal has been omitted. The reason for this is that the amplitude reduction of *P*-wave energy in the *PcP* beam is not very strong for most of the earthquakes, because they are form the time period before the full-size operation of the array. For those events with only a small reduction of *P*-wave energy in the *PcP* beam (e.g. No. 1 in Fig. 5), one obtains a function in the correlograms at the *P* arrival time which is very similar to the actual auto-correlation function and which can be compared with the form of the correlogram in the predicted arrival-time window for *PcP*. *PcP* can be detected in none of the recordings in Fig. 5, neither in the beam-trace at the predicted arrival-time window nor in the correlogram through comparison with the quasi auto-correlation function. PHIMAX in Fig. 5 is again the maximum of the correlogram [Eq. (4)] in the time window marked by a pair of vertical bars.

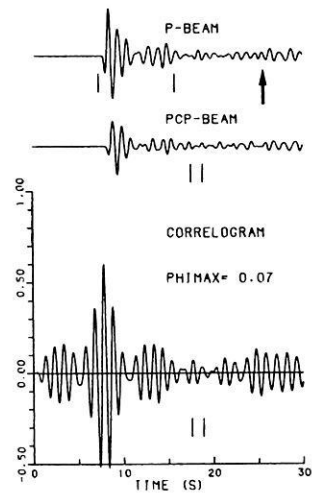
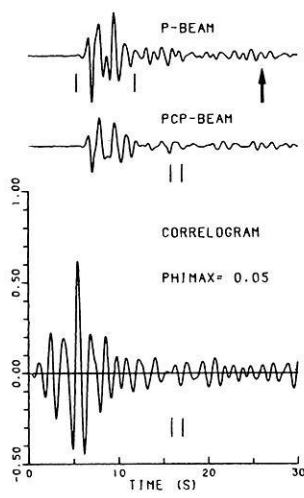
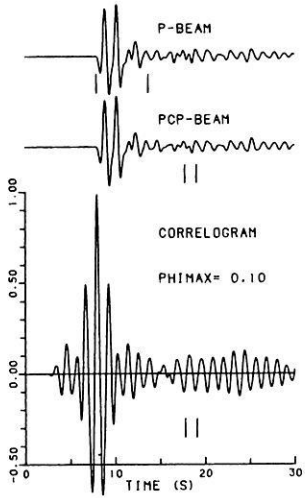
Explosion data

The source parameters of the 29 nuclear explosions recorded at the NORSAR array are given in Table 2. Besides one explosion in Colorado (No. 6) all other explosions were detonated at the Nevada Test Site (NTS). The majority of the recordings are presented in Fig. 6, with the plot of the auto-correlation function inserted in the correlogram. The remaining recordings from NTS explosions (presented in Schlittenhardt, 1984) have essentially the same information content (with regard to this study) and are not reproduced here. The mean distance from the NTS explosions to NORSAR is 73.2°. The record of the Colorado explosion is presented in Fig. 2c. This event at a distance of 68.2° from NORSAR is, besides the Sea of Japan and Nicobar Island earthquakes (Nos. 10 and 14 in Table 1), the third

GRF: S.o. Okhotsk, 10.07.76

GRF: Kuriles Is., 14.08.78

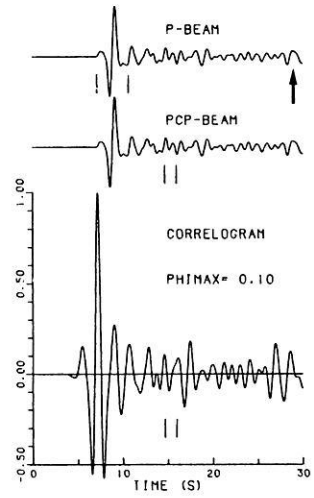
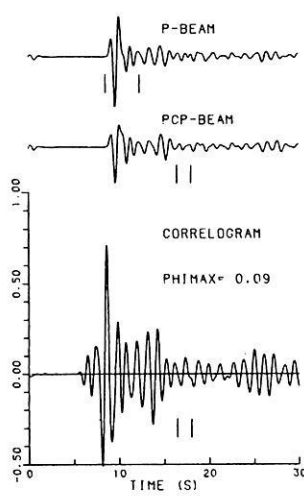
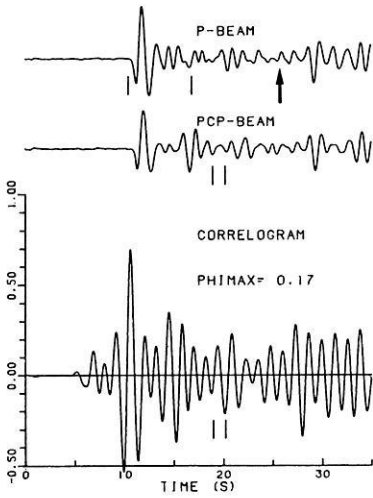
GRF: Fox. Isl., 01.09.79



GRF: Rat. Isl., 18.10.79

GRF: Kuriles Is., 04.10.78

GRF: Kuriles Is., 22.09.76



GRF: Kuriles Is., 19.03.77

GRF: Kuriles Is., 03.09.81

GRF: Honshu, Jap., 24.09.80

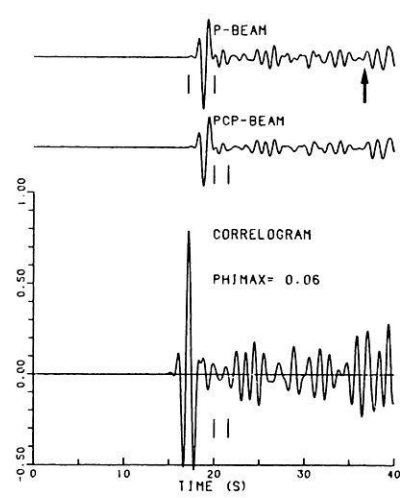
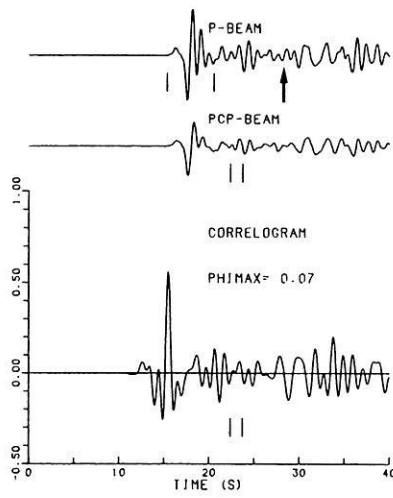
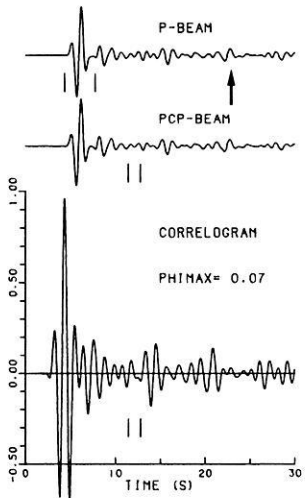


Fig. 5. *P*, *PcP* beam and correlogram for earthquakes 1–9 (from left to right) from Table 1. All seismograms are simulations of the original GRF broadband data according to the transfer function of a short-period WWSSN seismometer. The arrows in the *P* beams mark the theoretical arrival times of the surface reflection *pP*

Table 2. Source parameters and other parameters for the 28 explosions at the Nevada Test Site (NTS) and the nuclear explosion in Colorado (No. 6), recorded at NORSAR. The mean distance to the NTS events is 73.2°. The explosion in Colorado was at a distance of 68.2° from NORSAR. Source: ISC

No.	Date	Origin time	Epicentre	m_b	PcP/P	Number of subarrays
01	08.07.71	14:00:00.1	37.11 N 116.05 W	5.5	0.05	21
02	18.08.71	13:59:59.3	36.99 N 116.06 W	5.3	0.02	19
03	21.09.72	15:30:00.2	37.08 N 116.04 W	5.6	0.03	20
04	08.03.73	16:10:00.2	37.10 N 116.03 W	5.3	0.02	22
05	26.04.73	17:15:00.2	37.12 N 116.06 W	5.6	0.06	22
06	17.05.73	16:00:00	39.79 N 108.37 W	5.1	0.10	22
07	05.06.73	17:00:00.2	37.18 N 116.21 W	5.0	0.06	22
08	06.06.73	13:00:00.1	37.25 N 116.35 W	6.1	0.03	19
09	27.02.74	17:00:00.1	37.10 N 116.05 W	5.6	0.05	21
10	10.07.74	16:00:00.1	37.07 N 116.03 W	5.7	0.03	19
11	30.08.74	15:00:00.2	37.15 N 116.08 W	5.6	0.02	22
12	26.09.74	15:05:00.2	37.13 N 116.07 W	5.5	0.05	21
13	28.02.75	15:15:00.1	37.11 N 116.06 W	5.6	0.03	22
14	07.03.75	15:00:00.2	37.13 N 116.08 W	5.4	0.05	22
15	14.05.75	14:00:00.4	37.22 N 116.47 W	5.9	0.07	20
16	03.06.75	14:20:00.2	37.33 N 116.52 W	5.8	0.10	20
17	03.06.75	14:40:00.1	37.09 N 116.03 W	5.6	0.03	20
18	19.06.75	13:00:00.1	37.35 N 116.32 W	5.9	0.03	19
19	28.10.75	14:30:00.2	37.28 N 116.41 W	6.2	0.04	21
20	20.11.75	15:00:00.1	37.22 N 116.37 W	5.9	0.04	20
21	20.12.75	20:00:00.2	37.12 N 116.06 W	5.6	0.04	21
22	03.01.76	19:15:00.2	37.30 N 116.33 W	6.2	0.04	21
23	12.02.76	14:45:00.2	37.27 N 116.49 W	6.1	0.06	21
24	14.02.76	11:30:00.2	37.24 N 116.42 W	5.8	0.03	21
25	09.03.76	14:00:00.1	37.31 N 116.36 W	5.8	0.05	21
26	14.03.76	12:30:00.2	37.31 N 116.47 W	6.2	0.07	21
27	17.03.76	14:15:00.1	37.26 N 116.31 W	6.0	0.05	21
28	17.03.76	14:45:00.1	37.11 N 116.05 W	5.8	0.01	21
29	26.08.76	14:30:00.2	37.13 N 116.08 W	5.3	0.06	21

event with an identifiable PcP signal. PcP can be detected in the PcP beam as well as in the correlogram and in the vespagram within the predicted arrival-time window. The P -wave and P -wave-coda amplitude reduction in the PcP beams of Fig. 6 is so strong that the PcP beams nearly become straight lines. At the same time, in none of the beam traces can a clear indication for the emergence of a PcP signal in the predicted arrival-time window be found. However, at least in some of the correlograms in Fig. 6 (e.g. for the events 1, 5, 9 and 13) the form of the correlogram in the PcP arrival-time window is relatively similar to the form of the corresponding auto-correlation function of the P signal. This suggests that PcP begins to stand out from the noise at PHIMAX values between 0.03 and 0.06 (Fig. 6). The mean value of all PHIMAX values for the explosions at the Nevada Test Site is 0.045, with a standard deviation of 0.018. This mean value is close to the PHIMAX values of those events for which the emergence of PcP is suggested through comparison of the correlation functions and is therefore interpreted to represent a close estimate for the actual PcP/P amplitude ratio for the observation geometry NTS-NORSAR.

Amplitude ratios PcP/P

To summarize, it can be stated that for the 16 investigated earthquakes with simple and short source pulses, PcP can

be detected reliably in only two cases. Taking into account that practically no indication for the appearance of a PcP signal can be detected for the other events studied, neither in the PcP beams nor in the correlograms of Figs. 2a and b, 4 and 5, the uniformly determined PHIMAX values must be regarded as an upper limit for the actual, very small PcP/P amplitude ratio. In the presentation of the results in Fig. 7 these values are plotted as heavy dots on vertical bars to indicate that the true PcP/P amplitude ratios lies somewhere between the abscissa and the heavy dot. The values for the two events with identifiable PcP signal are plotted as encircled dots ('Jap' and 'Nicobar Is.'), for the NTS explosions the mean value and standard deviation of all PHIMAX values from the NTS explosions in Table 2 are plotted ('NTS'), and the amplitude ratio for the nuclear explosion in Colorado is given ('Co'). To comment on the reliability of this result of generally very small PcP/P amplitude ratios, it can be said that a systematic source or receiver effect, that leads to an underestimation of the PcP/P ratio for *all* events, can be practically excluded because of the different source regions and ray paths of the events studied. That nodal radiation of PcP is the cause of the non-observability of PcP can be excluded because of the fault-plane solutions for the earthquakes studied: the correction factor for isotropic radiation (R_{cor} in Table 1) is close to one or smaller for most of the earthquakes studied.

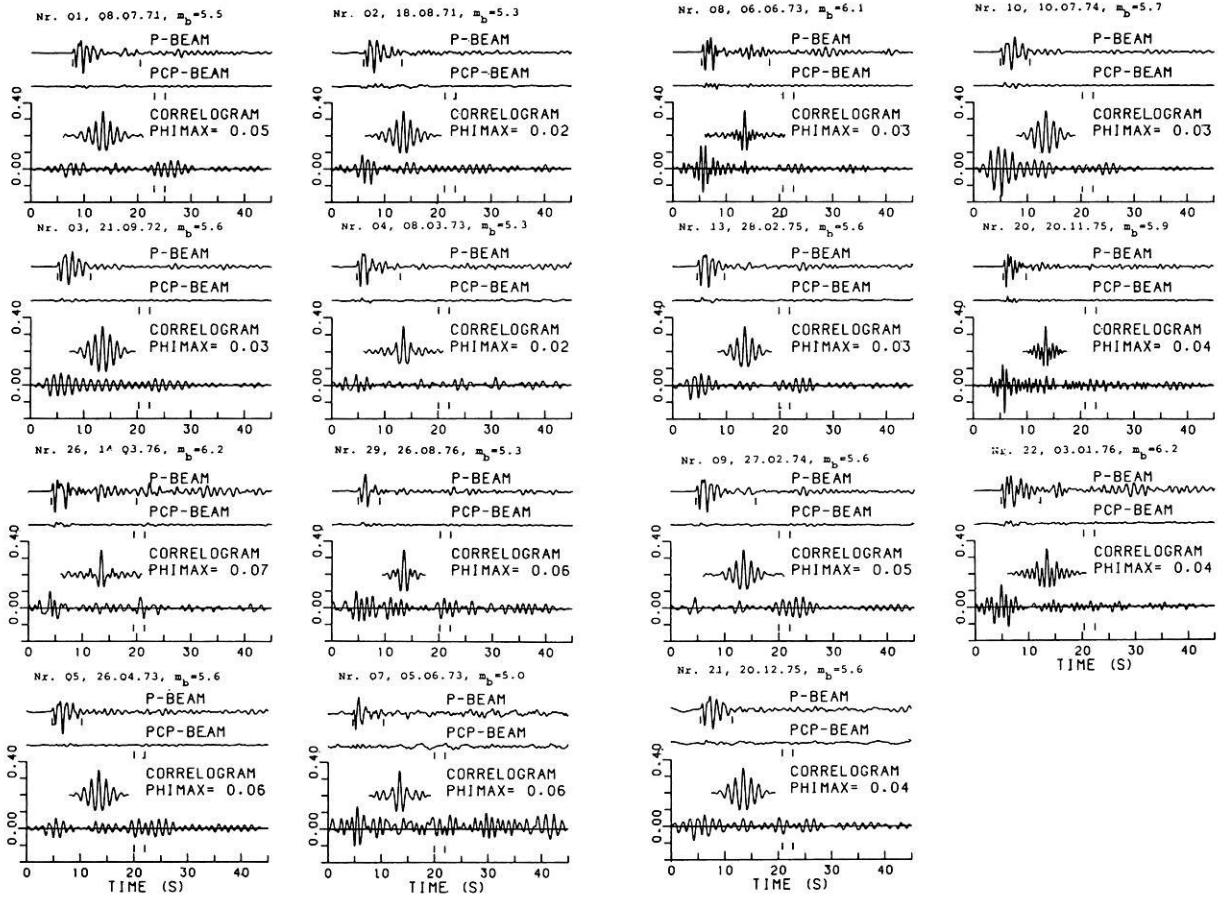


Fig. 6. *P*, *PcP* beam and correlogram for nuclear explosions from the Nevada Test Site (numbering according to Table 2)

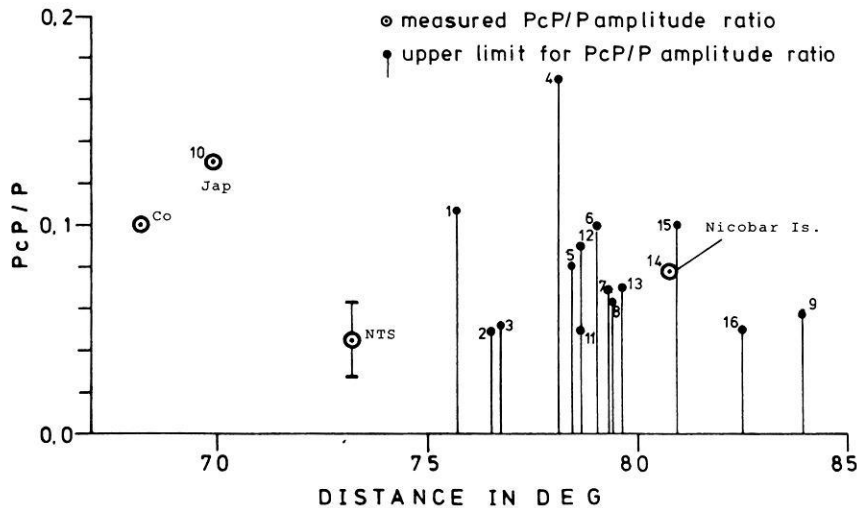


Fig. 7. *PcP/P* amplitude ratios for events with identifiable *PcP* signal (\circ) and upper limit for the *PcP/P* amplitude ratio for events without identifiable *PcP* signal (\bullet) for the earthquakes from Table 1 (with corresponding numbering) and for the nuclear explosions from Table 2. The value marked 'NTS' corresponds to the mean value (with bars indicating standard deviations) of all PHIMAX values from the nuclear explosions from the Nevada Test Site. 'Co' corresponds to the value for the nuclear explosion in Colorado (No. 6 in Table 2). All earthquake data have been corrected for isotropic source radiation

Amplitude behaviour of *PcP* for changes in the elastic parameters on both sides of the CMB and for increased absorption in D''

The models

The starting point for the theoretical investigation of the amplitude behaviour of *P* and *PcP* was the isotropic (1 Hz) PREM model of Dziewonski and Anderson (1981). Fig-

ure 8 shows the *P*- and *S*-wave velocity of this model for the lowermost 300 km of the mantle. In this model, the lowermost mantle is characterized by a second-order discontinuity 150 km above the core-mantle boundary. Starting at a depth of 2,700 km, three further models (P190, M190, N190) marked with an open square, circle and triangle are plotted. The dashed line in Fig. 8 defines a model with an extreme, positive velocity gradient in a 190-km-thick zone. Additionally, two models (P75 and N75) with

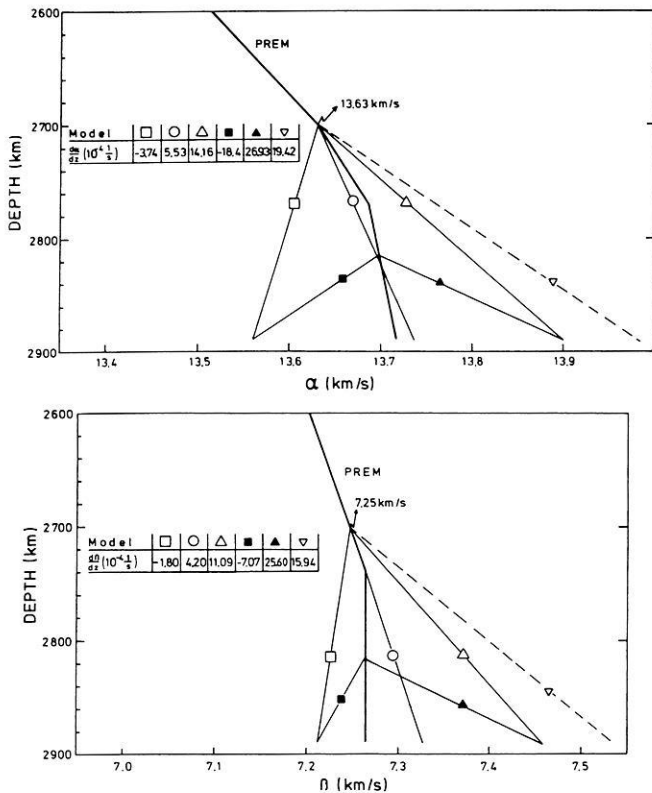


Fig. 8. P (above) and S velocity-depth function (below) for the low-velocity zone of the Earth's mantle with corresponding P - and S -velocity gradients $\frac{d\alpha}{dz}$ and $\frac{d\beta}{dz}$. The heavy line corresponds to the PREM model of Dziewonski and Anderson (1981). The other models are named in the text as follows: \square : N190, \circ : M190, \triangle : P190, \blacksquare : N75, \blacktriangle : P75, ∇ : extreme, positive velocity gradient

increased positive and negative velocity gradients in thin zones of 75 km thickness are marked with a full square and triangle. The three models which vary in 190-km-thick zones above the CMB correspond to the mean value (M190) and standard deviations (P190 and N190) of ray-parameter measurements of long-period P_{diff} and S_{diff} for a great number of earthquakes studied by Mula and Müller (1980). They can be regarded as limiting the model space for linear gradient models in zones of 190 km thickness. All models presented in Fig. 8 have Poisson's ratios near 0.3 at the CMB.

For these models, synthetic seismogram sections for P and PcP were calculated with an extended reflectivity method (Müller, 1985). In these calculations the elastic model structure is the same as for PREM at depths less than 2,700 km and the Q structure is identical with that of PREM for the whole mantle and the outer core. A constant- Q law which preserves causality was assumed in the calculations. Theoretical PcP/P amplitude ratios were determined from the record sections by measuring the peak-to-peak amplitudes of P and PcP . The resulting PcP/P amplitude ratios for the models M190, P190 and N190 are plotted in Fig. 9 as the uppermost dotted band of three amplitude-ratio distance curves. The denotation $Q_\alpha=826$ (PREM value for D'') in Fig. 10 indicates the Q_α value in a zone of 190 km thickness directly above the CMB. The theoretical PcP/P amplitude-ratio distance curves for models P75

and N75 cannot be distinguished from those for models P190 and N190 if the Q structure of PREM is assumed for all models and if one calculates for a purely elastic structure, respectively. Corresponding theoretical amplitude-ratio distance curves are therefore omitted in Fig. 10 and in the following. From Fig. 10 it can be clearly seen especially that the small observed amplitude ratios for the explosions from the Nevada Test Site and the upper limit values for observation distances around 79° cannot be explained by the model curves denoted with $Q_\alpha=826$. Therefore, the question arises of changing which parameter or combination of parameters can the small amplitude ratios required by the data be obtained.

Amplitudes of PcP due to changes in the elastic parameters on both sides of the CMB

The question of the behaviour of the reflection amplitude to changes of the elastic parameters (P and S velocities and densities) on both sides of the CMB can be answered with sufficient accuracy by calculating partial derivatives of the plane-wave reflection coefficient R_{PP} of the CMB of model PREM. A small relative change of R_{PP} is a linear combination of small relative changes of the velocities and densities on both sides of the CMB (Müller et al., 1977)

$$\frac{\Delta R_{PP}}{R_{PP}} = c_1 \frac{\Delta \alpha_m}{\alpha_m} + c_2 \frac{\Delta \rho_m}{\rho_m} + c_3 \frac{\Delta \beta_m}{\beta_m} + c_4 \frac{\Delta \alpha_c}{\alpha_c} + c_5 \frac{\Delta \rho_c}{\rho_c} + c_6 \frac{\Delta \beta_c}{\beta_c}, \quad (5)$$

where subscript m refers to parameters above, and subscript c to parameters below the CMB. Changes in β_c are normalized by α_c (Eq. 5) because $\beta_c=0$ for model PREM. The coefficients c_1, \dots, c_6 are given in Table 3 for three different angles of incidence at the CMB and, hence, epicentral distances of PcP . The coefficients are a measure of the influence of the corresponding parameter on the amount of R_{PP} , and some important properties of the CMB reflection coefficient can be derived from Table 3. The greatest change in the reflection amplitude (in the sense of a reduction) is caused by positive changes (i.e. by an increase) of the P -waves velocity α_m in the mantle and the S -wave velocity β_c in the core. Changes in the densities on both sides of the CMB and of the P -wave velocity α_c in the core have minor influence and can be neglected in our discussion. The reduction of the reflection amplitude caused by an increase of the velocity α_m is nearly compensated by an increase of the S velocity β_m . This means that the reflection amplitude cannot be reduced arbitrarily by increased P -velocity gradients in the lowermost mantle, when the S -velocity gradients are increased at the same time to obtain still reasonable Poisson's ratios. The dashed velocity-depth model of Fig. 8 is an attempt to explain the small observed PcP/P amplitude ratios by increased positive velocity gradients. The resulting theoretical PcP/P amplitude-ratio curve is presented in Fig. 10 for the distance range $70^\circ-75^\circ$. Obviously, the small amplitude ratios required by the data cannot be explained through increased velocity gradients in a physically reasonable frame. The greatest reduction of the reflection amplitude (Table 3) can be achieved through the introduction of a non-zero S -wave velocity in

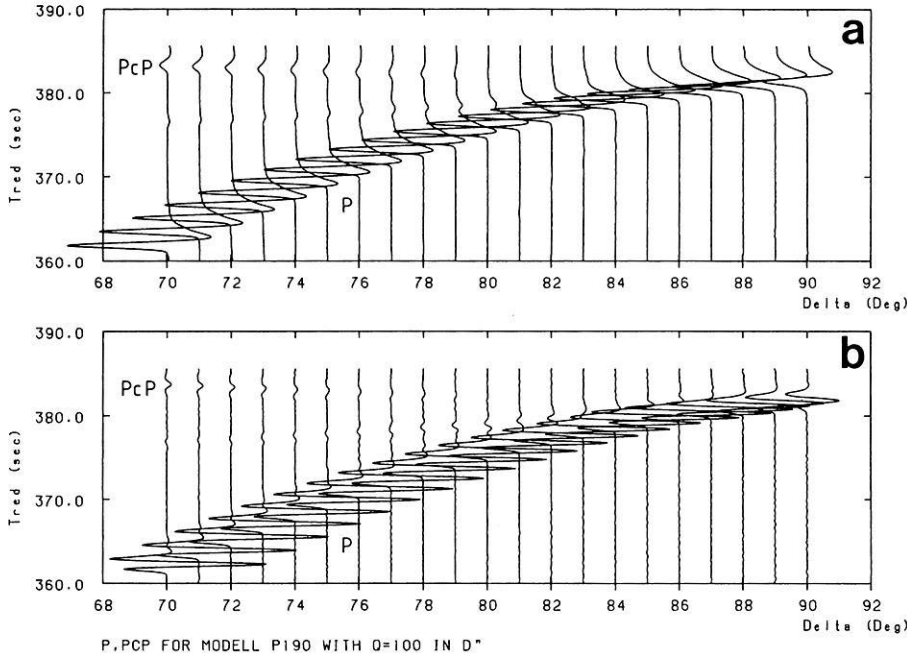


Fig. 9. **a** Theoretical record section (vertical component of particle velocity) for model P190 with $Q_\alpha = 100$ in D'' . The focal mechanism is of thrust type with the T -axis vertical and the profile is perpendicular to the strike of the P nodal planes. The dominant period of the source pulse (i.e. the rise time of the moment function) is 1 s. **b** Simulation of the seismograms from **a** according to the transfer function of a short-period WSSN seismometer

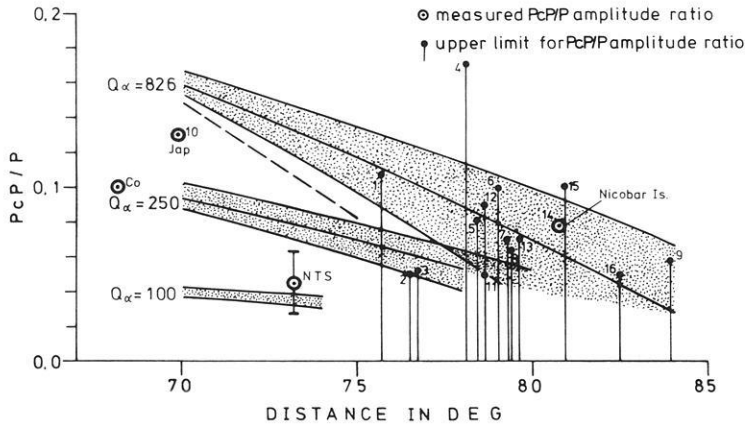


Fig. 10. The same as Fig. 7 with theoretical PcP/P amplitude-ratio distance curves superimposed. The *uppermost stippled band* (denoted $Q_\alpha = 826$) with three amplitude-ratio distance curves has been calculated (from above to below) for models N190, M190, P190 with the Q_α value of 826 in a D'' zone of 190 km thickness. The *dashed curve* corresponds to the model with the extreme, positive velocity gradient in Fig. 8. The two stippled bands denoted $Q_\alpha = 250$ and $Q_\alpha = 100$ are again calculated for the models (from above to below) N190, M190 (missing in the lowermost stippled band) and P190, but with Q_α values in D'' as indicated on the left. All theoretical curves correspond to isotropic radiation

Table 3. The plane-wave reflection coefficient R_{PP} of the CMB of model PREM and the coefficients c_1, \dots, c_6 in Eq. (5)

	R_{PP}	$c_1(\alpha_m)$	$c_2(\rho_m)$	$c_3(\beta_m)$	$c_4(\alpha_c)$	$c_5(\rho_c)$	$c_6(\beta_c)$
$\varphi = 72.5^\circ$ $\Delta = 70^\circ$	0.369	- 6.98	-1.02	5.69	1.15	0.81	- 8.31
$\varphi = 75.5^\circ$ $\Delta = 75^\circ$	0.321	- 8.41	-0.94	7.40	1.56	1.13	-10.60
$\varphi = 78.5^\circ$ $\Delta = 80^\circ$	0.247	-12.15	-1.52	10.22	2.02	1.26	-15.82

φ , angle of incidence at the core-mantle boundary; Δ , epicentral distance of PcP (focal depth 80 km)

the core. This more theoretical possibility for reducing the PcP/P amplitude ratio will not be considered further because it is in contrast to the results of independent seismological investigations by Müller et al. (1977) and Doornbos and Mondt (1979a). From this numerical investigation of

the reflection coefficient of the CMB it can be concluded that physically meaningful variations of the elastic parameters on both sides of the CMB fail to reduce the theoretical PcP/P amplitude ratios to the level of the majority of the observed amplitude ratios.

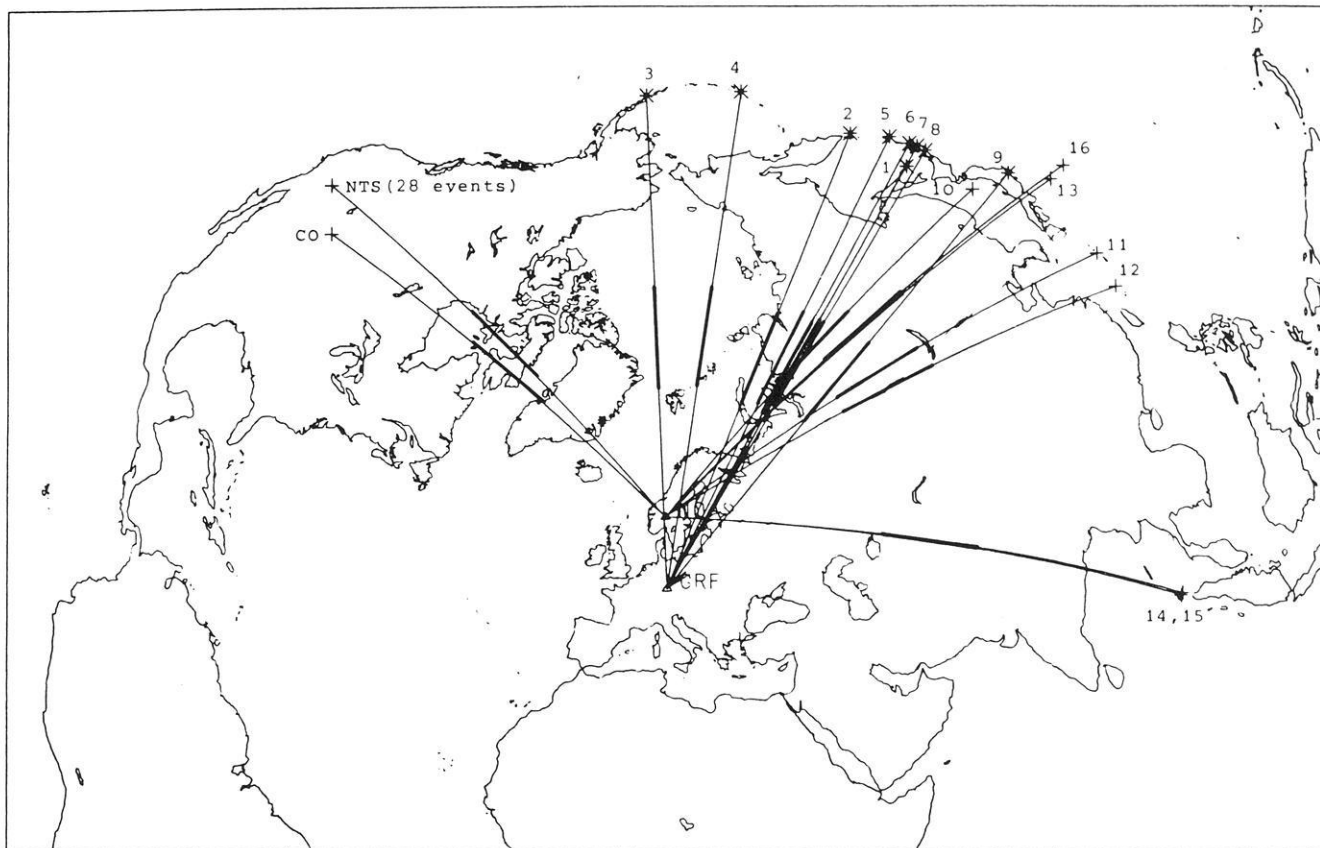


Fig. 11. Geographical distribution of events studied and great circle paths from the sources (* and +) to the receivers (GRF and NOA). Numbering of earthquake epicentres (Nos. 1–16) is according to Table 1. ‘NTS’ and ‘Co’ correspond to the epicentres of the nuclear explosions at the Nevada Test Site and Colorado, respectively. The lateral extent of that part of the ray path that PcP spends in a 190-km-thick D'' zone has been calculated and is marked with a *thick line*. The projection used is azimuthal equidistant with GRF as a projection pole

Increased absorption in D''

Another means to reduce the PcP/P amplitude ratio is the introduction of zones of reduced Q below the turning point of the mantle P wave. This leads to a relative increase of the dissipation time t_{PcP}^* of PcP compared to the dissipation time t_p^* of P . The resulting stronger damping of the reflection amplitude then gives the reduced PcP/P amplitude ratio. To evaluate this effect quantitatively we have calculated theoretical record sections for the models N190, M190 and P190 with Q_α values of 250 and 100 in a 190-km-thick D'' zone at the base of the mantle. The result is shown in Fig. 9a for the model P190 with $Q_\alpha = 100$. The dominant period of the source-time function for this and all other calculations was 1 s. Because of the low-pass effect of anelastic damping, the original 1-s dominant period of the double-couple source is broadened to an ‘observed’ dominant period of approximately 5 s in the particle-velocity seismogram (Fig. 9a). However, to enable a realistic comparison of observed and theoretical amplitude ratios it is important that the dominant periods in observed and theoretical seismograms are identical. This is especially important in our cases where the dissipation times of P and PcP are different and one obtains, therefore, different PcP/P amplitude ratios for different dominant periods. Figure 9b shows short-period simulations of the original seismograms from Fig. 9a according to the transfer characteristic of a WWSSN-SP

system. To guarantee the condition of equal frequency content in observed and theoretical seismograms, the theoretical amplitude ratios (Fig. 10) were determined by measuring peak-to-peak amplitudes from such filtered synthetic seismograms. As can be seen from the narrow width of the stippled band of curves for $Q_\alpha = 100$ in Fig. 10, a discrimination between different velocity gradients becomes impossible under the regime of such low Q_α values. Moreover, it can be concluded from Fig. 10 that observed PcP/P amplitude ratios which are smaller than those predicted for nearly elastic models (e.g. those for $Q_\alpha = 826$) cannot be interpreted uniquely with respect to the velocity structure, because the amplitude-ratio distance curve for the elastic models can be shifted to lower or higher values through combination with lower or higher Q_α values within D'' . On the other hand, the estimation of Q from the observed small amplitude ratios is possible with some reliability if one accepts models P190 and N190 as limiting the globally valid range for gradient models, as suggested by several investigations (Doornbos and Mondt, 1979; Mula and Müller, 1980; Mula, 1981; Doornbos, 1983).

Interpretation

The main result of the comparison of observed and theoretical PcP/P amplitude ratios in Fig. 10 is that a unique interpretation of the complete data set with one radially symmet-

ric model cannot be given. In Fig. 11 the ray-paths of all events used in this study are marked on a map of the northern hemisphere. The lateral extent of the ray path that PcP passes through D'' has been calculated (approximately 1,500 km at the surface) and is marked with a thick line in Fig. 11. We begin the interpretation of the data in Fig. 10 with those four data points for which PcP could reliably be identified. Among them are the amplitude ratios for the NTS and Colorado nuclear explosions, which are in close azimuthal neighbourhood. The mean PcP/P amplitude ratio for the observation geometry NTS-NORSAR is explained by Q_α values around 100 in D'' . According to Fig. 11 this value and the Q_α value of 250 for the Colorado explosion is representative for the region on the CMB below the northern Hudson Bay. The earthquake in the Sea of Japan (No. 10) lies within the bulk of events with reflection points on the CMB below Central Siberia. The Nicobar Island earthquake (No. 14) has its PcP reflection point on the CMB below Uzbekistan. It is the only event whose amplitude ratio falls within the range of theoretical amplitude ratios for models with a nearly elastic structure at the base of the mantle (Fig. 10). It is best explained by models M190 or N190 with a Q structure in D'' similar to that of PREM. The relatively small PcP/P amplitude ratio for the Sea of Japan earthquake (No. 10) cannot be explained with a nearly elastic structure at the base of the mantle. Q_α values of approximately 450 would lower the medium curve (model M190) of the uppermost stippled band in Fig. 10 to the observed amplitude ratio.

The events without identifiable PcP signal have their reflection points mainly below Central Siberia, except for events 3 and 4 which have their reflection points below the Arctic (Fig. 11). Despite the detailed investigation of the PcP beams and correlograms, practically no evidence for the existence of a PcP signal for these events could be found in the predicted arrival-time window. The corresponding data points in Fig. 10 are therefore interpreted as an upper limit for the true PcP/P amplitude ratio. On this background, the upper-limit estimates for the events with reflection points mainly below Central Siberia are interpreted by reduced Q_α values around 100, similar to the values found for the region below the northern Hudson Bay. For the region below the Arctic, only one upper limit value (no. 3 in Figs. 10 and 11) can be evaluated. The value for earthquake No. 4 cannot be interpreted because the P -wave-coda noise level in the arrival-time window for PcP is still high for this event (Fig. 5), so that the PHIMAX value exceeds the PcP/P amplitude ratio for all discussed models. A reliable interpretation for the region below the Arctic is impossible. However, Q_α values in D'' around 800 as in PREM, in connection with gradient models P190, M190 or N190, are unlikely.

It should be mentioned here that another mechanism besides anelastic absorption may be important for the low observed PcP/P amplitude ratios. Scattering of wide-angle PcP by the core-mantle boundary might distort the wave-form of PcP so that matched filtering is no longer adequate. So far no quantitative calculations for this problem are known and one can argue against this only by observational evidence. The observations of P and PcP by several authors (e.g. Kanamori, 1967; Chowdhury and Frasier, 1973; Engdahl and Johnson, 1974) in general show an exact reproduction of P and PcP signal wave-forms, but these data examples stem mainly from the steep-angle range. However, the

seismogram examples presented by Frasier and Chowdhury (Fig. 3, 1974) are an exception with respect to distance: they demonstrate impressively that the duplicity of P and PcP wave-forms holds up to distances of more than 70° . For the cases where PcP could be identified (Fig. 2) in this paper, the wave-forms of P and PcP are also very similar. This demonstrates that undulations on, or inhomogeneities near, the core-mantle boundary (if they exist for the sampled regions) have little influence on the wave-form of PcP even in the wide-angle range.

Evidence against discontinuities in the lowermost mantle from observations of short-period P

Several recent seismological investigations of the P - and S -wave velocity of the lowermost 200–300 km of the mantle have suggested velocity models with first-order discontinuities some hundred kilometres above the core-mantle boundary. The per cent velocity increase at such first-order discontinuities ranges from approximately 1.5% (Wright and Lyons, 1981) to 2.5%–3.0% (Wright et al., 1985) for the P -wave velocity (170 km above the core) and from 2.5%–3.0% (Lay and Helmberger, 1983a, b) for the S -wave velocity (280 km above the core). The P -velocity results, which hold for P waves recorded at the Yellowknife array (bottoming beneath the Caribbean) and for P waves recorded at a temporary network in Australia (bottoming beneath southeast Asia), were derived using special array data-processing methods (Wright and Lyons, 1981; Wright et al., 1985). The S -velocity results, which hold for three separate regions of D'' (beneath Alaska, northern Eurasia and the Caribbean) were derived by modelling the amplitudes and travel times of onsets between mantle S and ScS in transverse-component seismograms at distances from 70° to 80° (Lay and Helmberger, 1983a).

High-quality short-period P -wave data offer another means to study the reality of discontinuities in the lowermost mantle. Lay and Young (1986) argue that the S -wave velocity discontinuity in SLHO may be accompanied by a relatively smaller P -velocity increase. This possibility, which holds only to the extent that the change in bulk modulus is significantly less than the change in rigidity [cf. formula (1) in Schlittenhardt et al., (1985)], can be tested with the array data compiled for this study. No special array data-processing methods are needed, simple beam-forming is sufficient to demonstrate the effects.

The model SLHO of Lay and Helmberger (1983a) is shown in Fig. 12 together with the corresponding P travel-time curve for an earthquake at 80 km depth. The jumps in S and P velocity at the discontinuity are both 2.6%. For this model and a model with a reduced P -velocity jump of 1.3% (keeping all other parameters unchanged), we have computed short-period theoretical seismogram sections for P waves (Fig. 13). As expected from the travel-time curve in Fig. 12, the record sections in Fig. 13 show pronounced differences between SLHO and models with smooth velocity-depth functions in the lowermost mantle. Near the shadow boundary (at $\Delta \approx 95^\circ$), SLHO predicts three onsets with approximately equal magnitudes, whose arrival-time differences are great enough to be resolvable with a standard short-period instrument. The first of the three onsets (Figs. 12 and 13) is the diffraction P_{diff} along the CMB. It is followed by the phase labelled $PPDDP$, which is reflected once at the underside of the discontinuity. This phase is

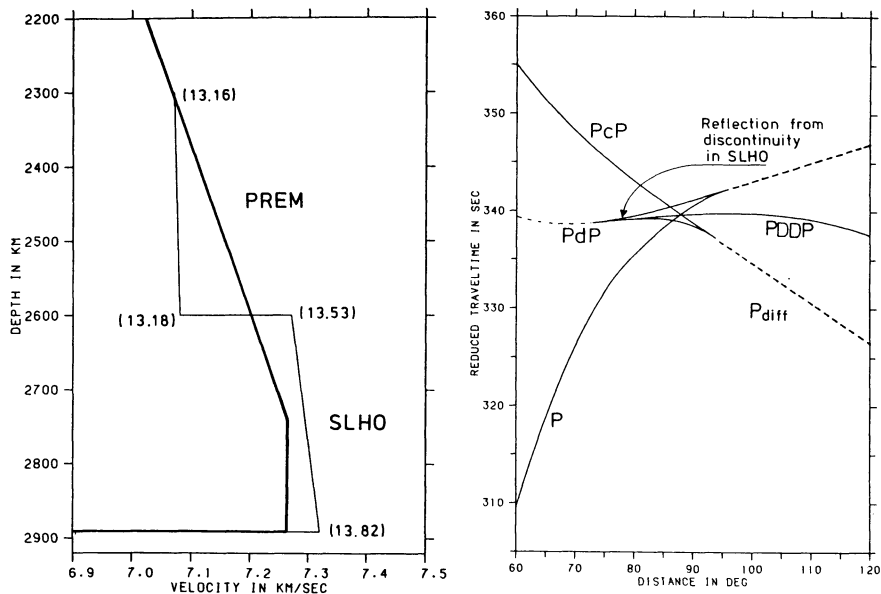


Fig. 12. Left: *S*-wave velocity distribution in the lowermost mantle for the models SLHO of Lay and Helmberger (1983a) and PREM (Dziewonski and Anderson, 1981). Velocity values in parentheses are assumed SLHOP-wave velocities. The jumps in *S* and *P* velocity at the discontinuity of SLHO are both 2.6%. Elsewhere in the earth, SLHO and PREM agree. Right: *P*-wave travel times for SLHO and a focal depth of 80 km (reduced with 4.8 s/deg). For explanation of the phases, see text

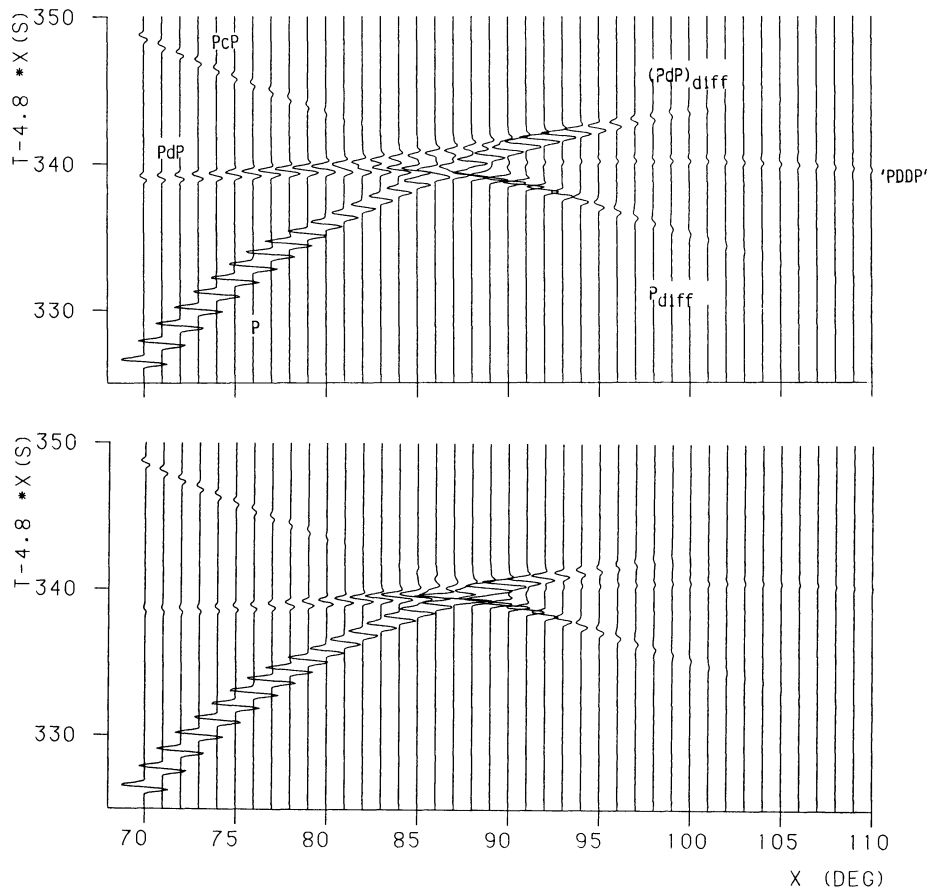


Fig. 13. Theoretical record sections for the SLHO model from Fig. 12 with jumps in *S* and *P* velocity both of 2.6% (above) and a reduced *P*-velocity jump of 1.3% (below), with all other parameters kept unchanged. The theoretical seismograms were computed with the reflectivity method and correspond to a focal depth of 80 km, the focal mechanism is of normal-fault type with the *P*-axis vertical and the profile is perpendicular to the strike of the *P* nodal planes. Times are reduced with 4.8 s/deg. The phases *PdP*, $(PdP)_{diff}$ and *PDDP* are caused by the discontinuity in SLHO (see text)

analogous to the phases *PKKP* or *SKKS* which are reflected once at the underside of the CMB. Note that at distances beyond $\Delta \approx 100^\circ$ the amplitudes of *PDDP* are greater than those of *Pdiff* in both sections of Fig. 13. The third onset is the diffraction $(PdP)_{diff}$ along the discontinuity (the letters *d* and *D* represent the depth of the discontinuity in SLHO). From Figs. 12 and 13 it is obvious that a test of SLHO with short-period *P*-wave data can be performed for the distance range near the core shadow zone. It appears

that even the model with the 1.3% velocity increase at the discontinuity, in such an investigation, will prove to be inconsistent with short-period *P*-wave data available for arrays. In the following we will concentrate, however, on the distance range 70° – 85° . The amplitude of the reflection from the discontinuity in SLHO (*PdP* in Figs. 12 and 13) increases from about 15% to over 90% of the amplitude of *P* in that distance range.

Events which are appropriate for a test of model SLHO

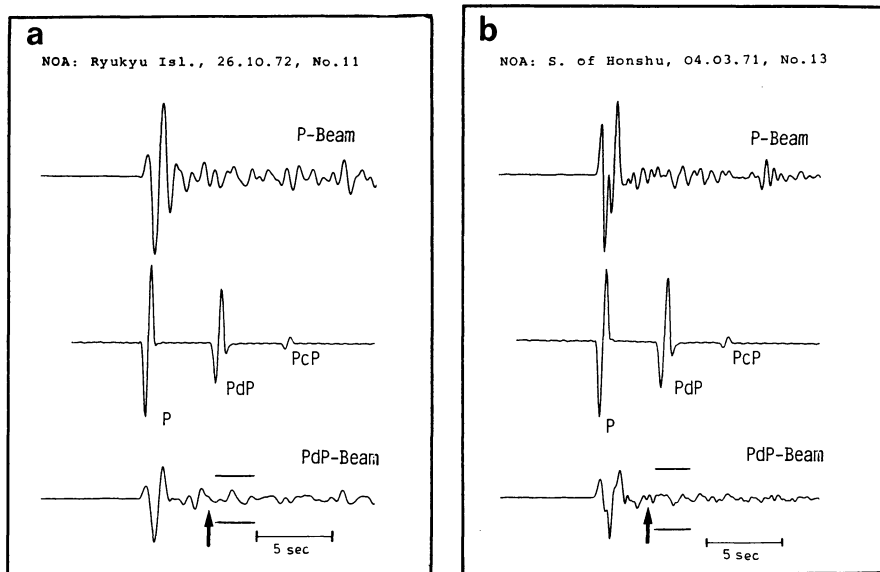


Fig. 14. **a** *P* beam (uppermost trace) and *PdP* beam (lowermost trace) for the Ryukyu earthquake (No. 11) at $\Delta=78.6^\circ$ and theoretical seismogram (middle trace) for the SLHO model of Lay and Helmberger (1983a) with jumps in *S* and *P* velocity both of 2.6%. *P* and *PdP* beam are plotted with equal amplitude scale. The peak-to-peak amplitude of the *P* signal in the theoretical seismogram in the middle is chosen to be identical with the maximum peak-to-peak amplitude of the *P* signal in the *P* beam. Hence, the amplitude of the theoretical *PdP* signal can be directly compared to the amplitudes in the *PdP* beam at the corresponding time interval. The pair of horizontal bars in the *PdP* beam indicates the peak-to-peak amplitude of *PdP*, predicted by a SLHO model with a reduced *P*-velocity increase of 1.3%. The phase *PdP*, predicted by model SLHO, is not observed, independently of whether the *S*-velocity jump of 2.6% is accompanied by a *P*-velocity jump of equal or half the size of that in the *S* velocity. **b** The same as in Fig. 14a for the earthquake south of Honshu at $\Delta=79.6^\circ$

must have, as in the investigation of *PcP*, a short source pulse compared to the difference travel time *PdP*-*P*. Simple and, compared to the *PdP*-*P* time, short *P* pulses are found for the NORSAR events 11 and 13. As the slownesses of *PdP* and *P* are different, *P*-coda amplitudes at the arrival time of *PdP* can be suppressed by *PdP* beam-forming. Although practically all events of this study, for distances from approximately 79° to 85° , can be used to disprove models with *P*-velocity jumps of 2.6% (e.g. compare the seismograms for events 7 and 14 in Figs. 2b and 5), in the following we will concentrate on the two events mentioned. From the travel-time curve in Fig. 12 we have derived the slowness-versus-distance curve for model SLHO (Schlittenhardt, 1984) to compute the NORSAR array beam for the phase *PdP* for events 11 and 13. Figure 14a and b shows a comparison of the *P*, *PdP* beam and the theoretical seismograms for model SLHO with a velocity increase of 2.6% for both the *S* and *P* velocity for the observation distances of 78.6° and 79.6° . The *P* and *PdP* beams are plotted with the same amplitude scale. The *P* amplitude in the *PdP* beams is reduced to approximately 50% of its value. The pair of horizontal bars in the *PdP* beams of Fig. 14 indicates the peak-to-peak amplitude of *PdP* predicted by the SLHO model with a reduced *P* velocity increase of 1.3%. Figure 14 demonstrates clearly that the complications expected for SLHO-type models are not observed for *P* waves bottoming beneath Central Siberia, irrespective of the *S*-velocity jump being accompanied by a *P*-velocity jump of equal or half the size of that in the *S* velocity.

Summary and conclusions

In this study the amplitude ratio *PcP*/*P* in the distance range 70° – 84° has been investigated for several regions on

the core-mantle boundary. For stations in this distance range, *PcP* spends about 900 km in a 190-km-thick *D''* zone. A main result of this investigation is that one radially symmetric model cannot simultaneously explain observations from different geographical regions. Hence, lateral heterogeneity must exist in the lowermost mantle. It turns out that this lateral heterogeneity in *D''* cannot only be restricted to the velocity structure [as was found e.g. by Dziewonski (1984) by inversion of a great amount of catalogued *P*-wave travel times], but that significant lateral variations in wave absorption within *D''* must exist. This follows from the fact that most of the observed, very small *PcP*/*P* amplitude ratios cannot be explained by physically reasonable variations of the elastic parameters on both sides of the CMB. The results, in detail, are as follows. Values of Q_α of about 100 were found for *D''* for the region below the northern Hudson Bay (NTS-NORSAR profile) with lateral variations to Q_α values around 250 (Colorado-NORSAR profile). Comparable low Q_α values around 100 were found for a more wide-spread region below Central Siberia (Sea of Okhotsk-GRF, Kuriles-GRF and Japan-NORSAR profiles) with lateral variations to $Q_\alpha \approx 450$ (Sea of Japan-NORSAR profile). The only region with normal wave absorption (in the sense of the PREM model which has Q_α around 800 in *D''*) is the region below Usbekistan, USSR (Nicobar Island-NORSAR profile). Only for this region, with nearly elastic conditions at the base of the mantle, is a statement about the *Q* and velocity structure possible. Compared to the velocity gradients in the main part of the lower mantle, slightly reduced velocity gradients were found for this region, whose values are limited by the values for the models M190 and N190 (Fig. 8).

The comparison of short-period synthetic seismograms for models with first-order discontinuities near the top of

D'' (e.g. as suggested by Wright and Lyons, 1981; Lay and Helmberger, 1983a, b; Wright et al. 1985; Lay and Young, 1986) with the short-period array data compiled for this study leads to a clear refutation of such models if the P -velocity jump at the discontinuity is of the order of 2.5%–3.0%, as was already concluded from a study of long-period diffracted P waves (Schlittenhardt et al., 1985). Such models are very unlikely to be a global feature. Even if the P -velocity jump is halved, to 1.3%, data examples which do not show the predicted effects can be found. These seismogram examples correspond to ray paths bottoming beneath Central Siberia.

Acknowledgements. I am grateful to Gerhard Müller for suggesting this study and for his support in the course of this work. I thank Peter Hubral for reading the manuscript and Rainer Kind for valuable comments. The staff of the NTFN/NORSAR Data Processing Center and the Seismologisches Zentralobservatorium Gräfenberg offered helpful support. This research was supported by a grant from the Deutsche Forschungsgemeinschaft. All this is gratefully acknowledged.

References

- Aki, K., Richards, P.G.: Quantitative seismology, theory and methods. Vol. I and II, Freeman and Co., 1980
- Alexander, S.S., Phinney, R.A.: A study of the core-mantle boundary using P waves diffracted by the earth's core. *J. Geophys. Res.* **71**, 5943–5958, 1966
- Berzon, I.S., Kogan, S.P., Pasechnik, I.P.: The character of the mantle-core boundary from observations of PcP waves. *Earth Planet. Sci. Lett.* **16**, 166–170, 1972
- Bolt, B.A.: PdP and PKiKP waves and diffracted PcP waves. *Geophys. J. R. Astron. Soc.* **20**, 367–382, 1970
- Buchbinder, G.G.R.: Properties of the core-mantle boundary and observations of PcP. *J. Geophys. Res.* **73**, 5901–5923, 1968
- Buchbinder, G.G.R., Poupinet, G.: Problems related to PcP and the core-mantle boundary illustrated by the two nuclear events. *Bull. Seismol. Soc. Am.* **63**, 2047–2070, 1973
- Bullen, K.E.: Compressibility-pressure hypothesis and the earth's interior. *Month. Not. R. Astron. Soc. Geophys. Suppl.* **5**, 355–368, 1949
- Bullen, K.E.: An earth model based on a compressibility-pressure hypothesis. *Month. Not. R. Astr. Soc. Geophys. Suppl.* **6**, 50–59, 1950
- Chowdhury, D.K., Frasier, C.W.: Observations of PcP and P at Lasa at distances from 26° to 40°. *J. Geophys. Res.* **78**, 6021–6027, 1973
- Cleary, J.R.: The S velocity at the core-mantle boundary from observations of diffracted S. *Bull. Seismol. Soc. Am.* **59**, 1399–1405, 1969
- Cormier, V.F.: Some problems with S, SKS and ScS observations and implications for the structure at the base of the mantle and the outer core. *J. Geophys.* **57**, 14–22, 1985
- Doornbos, D.J.: On seismic wave scattering by a rough core-mantle boundary. *Geophys. J. R. Astron. Soc.* **53**, 643–662, 1978
- Doornbos, D.J.: Present seismic evidence for a boundary layer at the base of the mantle. *J. Geophys. Res.* **88**, 3498–3505, 1983
- Doornbos, D.J., Husebye, E.S.: Array analysis of PKP phases and their precursors. *Phys. Earth Planet. Inter.* **5**, 387–399, 1972
- Doornbos, D.J., Mondt, J.C.: Attenuation of P and S waves diffracted around the core. *Geophys. J. R. Astron. Soc.* **57**, 353–379, 1979a
- Doornbos, D.J., Mondt, J.C.: P and S waves diffracted around the core and the velocity structure at the base of the mantle. *Geophys. J. R. Astron. Soc.* **57**, 381–395, 1979b
- Dziewonski, A.M.: Mapping the lower mantle: determination of lateral heterogeneity in P velocity up to degree and order 6. *J. Geophys. Res.* **89**, 5929–5952, 1984
- Dziewonski, A.M., Anderson, D.L.: Preliminary reference earth model. *Phys. Earth Planet. Inter.* **25**, 297–356, 1981
- Elsasser, W.M., Olson, P., Marsh, B.D.: The depth of mantle convection. *J. Geophys. Res.* **84**, 147–155, 1979
- Engdahl, E.R., Johnson, L.E.: Differential PcP travel times and the radius of the core. *Geophys. J. R. Astron. Soc.* **39**, 435–456, 1974
- Frasier, C.W., Chowdhury, D.: Effect of scattering on PcP/P amplitude ratios at Lasa from 40° to 84° distance. *J. Geophys. Res.* **79**, 5469–5477, 1974
- Gutenberg, B., Richter, C.F.: On seismic waves. *Gerlands Beitr. Geophys.* **43**, 56–133, 1936
- Haddon, R.A.W.: Evidence for inhomogeneities near the core-mantle boundary. *Phil. Trans. Roy. Soc. Lond.* **A306**, 61–70, 1982
- Haddon, R.A.W., Cleary, J.R.: Evidence for scattering of seismic PKP waves near the mantle-core boundary. *Phys. Earth Planet. Inter.* **8**, 211–234, 1974
- Hales, A.L., Roberts, J.L.: The travel times of S and SKS. *Bull. Seismol. Soc. Am.* **60**, 461–489, 1970
- Harjes, H.-P., Henger, M.: Array seismology. *J. Geophys.* **39**, 865–905, 1973
- Ibrahim, A.K.: The amplitude ratio PcP/P and the core-mantle boundary. *Pageoph.* **91**, 114–133, 1971
- Ibrahim, A.K.: Evidence for a low velocity core-mantle transition. *Phys. Earth Planet. Inter.* **7**, 187–198, 1973
- Jeanloz, R., Richter, F.M.: Convection, composition and the thermal state of the lower mantle. *J. Geophys. Res.* **84**, 5497–5504, 1979
- Jones, G.M.: Thermal interaction of the core and the mantle and long-term behaviour of the geomagnetic field. *J. Geophys. Res.* **82**, 1703–1709, 1977
- Kanamori, H.: Spectrum of P and PcP in relation to the mantle-core boundary and attenuation in the mantle. *J. Geophys. Res.* **72**, 559–571, 1967
- Kanasewich, E.R.: Time sequence analysis in geophysics. University of Alberta Press, 1975
- Kelly, E.J.: Response of seismic arrays to wide-band signals. *Linc. Lab. Techn. Note* 30, 1967
- King, D.W., Haddon, R.A.W., Cleary, J.R.: Array analysis of precursors to PKiKP in the distance range 128° to 142°. *Geophys. J. R. Astron. Soc.* **37**, 157–173, 1984
- Lay, T., Helmberger, D.V.: A lower mantle S-wave triplication and the shear velocity structure of D'' . *Geophys. J. R. Astron. Soc.* **75**, 799–837, 1983a
- Lay, T., Helmberger, D.V.: The shear velocity gradient at the base of the mantle. *J. Geophys. Res.* **88**, 8160–8170, 1983b
- Lay, T., Young, C.J.: The effect of SKS scattering on models of the shear velocity structure of the D'' region. *J. Geophys.* **59**, 11–15, 1986
- Lüke, H.D.: Signalübertragung, Heidelberg: Springer-Verlag 1979
- Mitchell, B.J., Helmberger, D.V.: Shear velocities at the base of the mantle from observations of S and ScS. *J. Geophys. Res.* **78**, 6009–6027, 1973
- Mondt, J.L.: SH-waves: theory and observations for epicentral distances greater than 90 degrees. *Phys. Earth Planet. Inter.* **15**, 46–59, 1977
- Müller, G., Mula, A.H., Gregersen, S.: Amplitudes of long-period PcP and the core-mantle boundary. *Phys. Earth Planet. Inter.* **14**, 30–40, 1977
- Müller, G.: The reflectivity method: a tutorial. *J. Geophys.* **58**, 153–174, 1985
- Mula, A.H.: Amplitudes of diffracted long-period P and S waves and the velocities and Q-structure at the base of the mantle. *J. Geophys. Res.* **86**, 4999–5011, 1981
- Mula, A.H., Müller, G.: Ray parameters of diffracted long-period P and S waves and the velocities at the base of the mantle. *Pageoph.* **118**, 1270–1290, 1980
- Okal, E.A., Geller, R.J.: Shear wave velocity at the base of the mantle from profiles of diffracted SH-waves. *Bull. Seismol. Soc. Am.* **69**, 1039–1053, 1979

- Peltier, W.R., Jarvis, G.T.: Whole mantle convection and the thermal evolution of the earth. *Phys. Earth Planet Inter.* **29**, 281–304, 1982
- Phinney, R.A., Alexander, S.S.: P wave diffraction theory and the structure of the core-mantle boundary. *J. Geophys. Res.* **71**, 5959–5975, 1966
- Sacks, I.S.: Diffracted P wave studies of the earth's core, 2. lower mantle velocity, core size, lower mantle structure. *J. Geophys. Res.* **72**, 2589–2594, 1967
- Schlittenhardt, J.: Array-Untersuchungen von reflektierten und diffraktierten Kernphasen. PhD thesis. University of Frankfurt, 1984
- Schlittenhardt, J., Schweitzer, J., Müller, G.: Evidence against a discontinuity at the top of D''. *Geophys. J. R. Astron. Soc.* **81**, 295–306, 1985
- Seidl, D.: The simulation problem for broad-band seismograms. *J. Geophys.* **48**, 84–93, 1980
- Spies, T.: Untersuchung der seismischen Geschwindigkeiten an der Basis des Mantels mit Amplituden und Laufzeiten der Kernreflexion PcP. Diploma Thesis. University of Frankfurt, 1985
- Wright, C., Lyons, J.A.: Further evidence for radial velocity anomalies in the lower mantle. *Pageoph.* **119**, 137–162, 1981
- Wright, C., Muirhead, K.J., Dixon, A.E.: The P wave velocity structure near the base of the mantle. *J. Geophys. Res.* **90**, 623–634, 1985

Received January 24, 1986; revised version May 20, 1986

Accepted May 23, 1986

Fast plane-wave and single-shot migration by Fourier transform

Paul Temme^{1*} and Gerhard Müller²

¹ Department of Geology and Geophysics, University of Utah, Salt Lake City, UT 84112, USA

² Institute of Meteorology and Geophysics, Feldbergstrasse 47, D-6000 Frankfurt/M., Federal Republic of Germany

Abstract. A method is presented by which plane-wave and single-shot migration can be performed very fast through Fourier transformation. The technique is similar to Stolt's (1978) migration procedure for CMP data; however, it is based on plane-wave and single-shot sections as input data. For the reconstruction of the subsurface structure, the appropriate imaging conditions are used (Temme, 1984), and the velocity is assumed to be constant. Plane-wave migration can be performed exactly, single-shot migration is exact only along a ray leaving the shot with a specified direction and close to it. The theory is tested on synthetic seismograms for a synclinal structure and a set of horizontal reflector elements separated by gaps. The proposed method requires mapping of the frequency-wavenumber spectrum corresponding to the observations, on to the two-dimensional wavenumber spectrum corresponding to the migrated section. The latter spectrum has to be sampled with sufficient detail, otherwise pronounced aliasing effects will appear in the migrated section. A time-saving alternative is to apply a smoothing phase-shift operation to the frequency-wavenumber spectrum and to remove the phase shift from the spectrum of the migrated section.

Key words: Prestack frequency-wavenumber migration – Directional migration – Computational aspects

Introduction

Modern migration techniques employ the scalar wave equation in order to reconstruct the subsurface structure from seismic wave fields measured at the earth's surface. Usually, common midpoint sections (CMP sections) are used as input data in standard migration. The exploding reflector model is employed (Loewenthal et al., 1976), i.e. the CMP wave field is downward continued in a first step to different depth levels by solving the wave equation using half the material velocity. In a second step, the migrated depth section $M(x, z)$ is constructed by taking the downward-contin-

ued wave field $U(x, z, t)$ for each depth level z at the imaging time $t_I=0$:

$$M(x, z) = U(x, z, t_I=0).$$

Instead of using a CMP section as input, plane-wave sections and single-shot sections can be used for the reconstruction of subsurface structures. A plane-wave section is the plane-wave response of an arbitrarily shaped structure due to an incident plane wave with a fixed angle of propagation. A single-shot section represents the reflected wave field at the earth's surface for point- or line-source excitation. In common seismic surveys, several single-shot sections are recorded by shifting the shotpoint-geophone configuration across the structure being investigated. These single-shot wave fields represent the data base for standard CMP stacking (Mayne, 1962). On the other hand, single-shot sections can also be used for synthesizing plane-wave sections by slant stacking (Schultz and Claerbout, 1978; Treitel et al., 1982). Plane-wave and single-shot sections represent physical wave fields that can be measured in a realistic physical experiment. Therefore, one can expect to be able to determine the reflection coefficients of the structure. This is more difficult in the case of CMP migration, which starts from a manipulated (and, in that sense, nonphysical) wave field (Temme, 1984).

The role plane-wave and single-shot migration could play in the reconstruction of subsurface structures is currently restricted to the detailed investigation of selected reflecting elements. Because of the finite geophone spread that is used to record the reflections, only segments of the structure can be seen. In order to obtain the total subsurface structure, as in the case of CMP migration, many single-shot sections with different shotpoint locations or many plane-wave sections with different angles of incidence have to be migrated. From a practical point of view this is only attractive if rapid algorithms performing single-shot and plane-wave migration are available.

The fastest migration algorithms have been formulated in the frequency-wavenumber domain. Gazdag (1978) presented the phase-shift method for CMP sections, where the Fourier-transformed wave field at the surface is downward continued to each desired depth level z using an appropriate z -dependent phase-shift operator. The migrated section results from subsequently evaluating the downward-continued wave field at time $t=0$. At each depth level the inverse

* New address: Institute of Planetology, University of Münster, Corrensstraße 24, D-4400 Münster, Federal Republic of Germany

Fourier transform from frequency to time is a simple summation of all frequency components. Finally, one depth level of the migrated section is obtained by a one-dimensional inverse Fourier transform over the horizontal wavenumber k_x . Stolt (1978) presented another fast algorithm of frequency-wavenumber migration. In his method the total depth structure $M(x, z)$ is calculated from the Fourier-transformed CMP section in one step. The frequency-wavenumber integral is transformed to a Fourier integral over k_x and the vertical wavenumber k_z using the substitution $k_z = \left(\frac{\omega^2}{c^2} - k_x^2\right)^{\frac{1}{2}}$, where c is half the wave velocity. The downward-continued wave field is only evaluated at time $t=0$. This Fourier integral can be calculated by an inverse two-dimensional Fast Fourier Transform (FFT) and results in the total migrated depth section.

Frequency-wavenumber migration deals with velocity variation only in an approximate way. Gazdag's phase-shift method allows for depth-dependent velocity only. For laterally varying velocity, Gazdag and Squazzero (1984) proposed an interpolation method. Stolt's method has the disadvantage of not allowing any velocity variation. In order to alleviate this difficulty he proposed a stretching of the time axis of each zero-offset seismogram, incorporating the root mean square velocity (Stolt, 1978: Eq. 75; Claerbout, 1985: p. 276). The transformed wave field looks more like it had come from a constant velocity structure. In spite of the weakness in dealing with varying velocity, the frequency-wavenumber migration is widely used in industrial practice.

In this paper a migration algorithm, which is similar to Stolt's method but formulated for plane-wave and single-shot sections will be presented. In order to deal with non-CMP input data, modified imaging conditions for the construction of the migrated section have to be used. The imaging conditions for plane-wave and single-shot sections have been described by Temme (1984). They are based on the principle that reflectors exist at those points (x, z) within the structure where the reflected wave is time coincident with the downgoing wave. If we assume the velocity to be constant, the imaging conditions can be expressed analytically. In the plane-wave case we use

$$M(x, z) = U\left(x, z, t_I = \frac{x}{v} \sin \phi + \frac{z}{v} \cos \phi\right). \quad (1)$$

For single-shot sections we use

$$M(x, z) = U\left(x, z, t_I = \frac{(x^2 + z^2)^{\frac{1}{2}}}{v}\right). \quad (2)$$

$M(x, z)$ represents the migrated depth section, U is the downward-continued reflected wave field at depth level z . t_I in Eq. (1) represents the arrival time of the downgoing plane wave measured from the surface point at $x=0$, where the plane wave passes at time $t=0$, to the reflection point at (x, z) . The angle ϕ is the propagation angle of the plane wave with respect to the z axis. t_I in Eq. (2) is the arrival time of the downgoing cylindrical wave (2D case), taken from the shotpoint location at $(x=0, z=0)$ to the reflector at (x, z) .

In the next section we will present the theory of plane-wave and single-shot migration in the Fourier domain. A discussion of computational aspects of the method and how aliasing can be avoided is included in a subsequent section.

Finally, the method is tested on synthetic seismograms for simple subsurface structures: a synclinal structure and a set of horizontal reflectors with gaps.

Theory

Plane-wave migration

$U(x, z=0, t)$ represents the reflected scalar wave field, which is known at the earth's surface; the depth coordinate is positive downwards. In order to calculate the reflected wave field at a deeper level z , we use the scalar wave equation. Its solution will be given in the frequency-wavenumber domain, where the wave equation reads

$$\frac{d^2 \bar{U}}{dz^2} + \left(\frac{\omega^2}{v^2} - k_x^2\right) \bar{U} = 0. \quad (3)$$

\bar{U} represents the Fourier-transformed reflected wave field; v is the constant material velocity. The following correspondences have been used:

$$\begin{aligned} \bar{U}(k_x, z, \omega) &= \int_{-\infty}^{\infty} \int_{-\infty}^{\infty} U(x, z, t) e^{-i(\omega t + k_x x)} dt dx \\ U(x, z, t) &= \frac{1}{4\pi^2} \int_{-\infty}^{\infty} \int_{-\infty}^{\infty} \bar{U}(k_x, z, \omega) e^{i(\omega t + k_x x)} d\omega dk_x. \end{aligned} \quad (4)$$

The general solution of Eq. (3) is

$$\bar{U}(k_x, z, \omega) = C e^{i\left(\frac{\omega^2}{v^2} - k_x^2\right)^{\frac{1}{2}} z} + D e^{-i\left(\frac{\omega^2}{v^2} - k_x^2\right)^{\frac{1}{2}} z}.$$

For reasons of simplicity, we are only dealing with positive frequencies ω . Thus, the arguments of the exponential functions have only one sign. The first term with coefficient C represents waves travelling upwards in the negative z direction. The second term with the coefficient D represents waves travelling downwards. We are only interested in the downward continuation of upgoing reflected waves. For this reason, we choose $D=0$. C can be determined from the boundary condition for $z=0$: $C = \bar{U}(k_x, 0, \omega)$. Finally, we obtain the downward-continued wave field at level z from Eq. (4):

$$\begin{aligned} U(x, z, t) &= \frac{1}{4\pi^2} \int_{-\infty}^{\infty} \int_{-\infty}^{\infty} \bar{U}(k_x, 0, \omega) \\ &\quad \cdot e^{i\left[\omega t + k_x x + \left(\frac{\omega^2}{v^2} - k_x^2\right)^{\frac{1}{2}} z\right]} d\omega dk_x. \end{aligned} \quad (5)$$

The migrated section $M(x, z)$ can be calculated by applying the imaging condition for plane waves, Eq. (1):

$$\begin{aligned} M(x, z) &= \frac{1}{4\pi^2} \int_{-\infty}^{\infty} \int_{-\infty}^{\infty} \bar{U}(k_x, 0, \omega) \\ &\quad \cdot e^{i\left\{\left(\frac{\omega}{v} \sin \phi + k_x\right)x + \left[\left(\frac{\omega^2}{v^2} - k_x^2\right)^{\frac{1}{2}} + \frac{\omega}{v} \cos \phi\right]z\right\}} d\omega dk_x. \end{aligned} \quad (6)$$

The calculation of the depth section $M(x, z)$ using Eq. (6) is cumbersome because the frequency-wavenumber integral has to be solved for each depth level z . The total depth section can be calculated more efficiently by rewriting Eq. (6) as a Fourier integral, which can be computed very fast by using the FFT. This is achieved by introducing new variables A and B into (6):

$$A(\omega, k_x) = \frac{\omega}{v} \sin \phi + k_x \quad (7)$$

$$B(\omega, k_x) = \frac{\omega}{v} \cos \phi + \left(\frac{\omega^2}{v^2} - k_x^2 \right)^{\frac{1}{2}}. \quad (8)$$

Equation (6) transforms into the Fourier integral

$$M(x, z) = \frac{1}{4\pi^2} \int_{-\infty}^{\infty} \int_{-\infty}^{\infty} \bar{U}[k_x(A, B), 0, \omega(A, B)] \cdot \left| \frac{\partial(\omega, k_x)}{\partial(A, B)} \right| e^{i(Ax + Bz)} dA dB, \quad (9)$$

from which we recognize A and B as new wavenumbers with respect to x and z . The Jacobian in Eq. (9) is

$$\frac{\partial(\omega, k_x)}{\partial(A, B)} = \frac{\partial \omega}{\partial A} \frac{\partial k_x}{\partial B} - \frac{\partial \omega}{\partial B} \frac{\partial k_x}{\partial A}.$$

Solving Eqs. (7) and (8) for k_x and ω , we obtain:

$$k_x(A, B) = \frac{(A^2 - B^2) \sin \phi + 2AB \cos \phi}{2(A \sin \phi + B \cos \phi)} \quad (10)$$

$$\omega(A, B) = \frac{v(A^2 + B^2)}{2(A \sin \phi + B \cos \phi)}. \quad (11)$$

Calculating the Jacobian from these expressions and inserting into Eq. (9), we have the migrated section

$$M(x, z) = \frac{1}{4\pi^2} \int_{-\infty}^{\infty} \int_{-\infty}^{\infty} \bar{M}(A, B) e^{i(Ax + Bz)} dA dB \quad (12)$$

with the Fourier transform

$$\bar{M}(A, B) = \bar{U}[k_x(A, B), 0, \omega(A, B)] \cdot \left| \frac{v(A^2 - B^2) \cos \phi - 2AB \sin \phi}{2(A \sin \phi + B \cos \phi)^2} \right|. \quad (13)$$

Equation (12), together with Eqs. (13), (10) and (11), is the final solution which can be used to calculate the migrated section in one step with the aid of the FFT. Before we discuss some computational aspects of Eqs. (12) and (13), we will first derive the migration algorithm of single-shot sections.

Single-shot migration

In the case of single-shot migration, the imaging condition Eq. (2) has to be applied to Eq. (5). A problem arises from the nonlinear dependence of $t_I = \frac{(x^2 + z^2)^{\frac{1}{2}}}{v}$ on x and z . t_I has to be approximated by a linear expression, which can be found by expansion into a Taylor series about (x_0, z_0) and neglecting higher-order terms:

$$\begin{aligned} t_I &\approx \frac{(x_0^2 + z_0^2)^{\frac{1}{2}}}{v} + \frac{1}{v(x_0^2 + z_0^2)^{\frac{1}{2}}} [x_0(x - x_0) + z_0(z - z_0)] \\ &= \frac{1}{v} \left(\frac{x_0}{R_0} x + \frac{z_0}{R_0} z \right) \\ t_I &\approx \frac{\sin \phi}{v} x + \frac{\cos \phi}{v} z. \end{aligned} \quad (14)$$

$R_0 = (x_0^2 + z_0^2)^{\frac{1}{2}}$ is the distance from the shotpoint at $(x = 0, z = 0)$ to the reflection point (x_0, z_0) , and ϕ is the angle

between the ray from shotpoint to reflection point and the z axis. From Eq. (14) we realize that the approximation of t_I does not depend on (x_0, z_0) , but only on the angle ϕ . The imaging condition (14) for single-shot migration is exact for all points on the ray leaving the shotpoint under the angle ϕ , but errors are introduced away from this ray. Hence, single-shot migration with Eq. (14) can be considered as *directional sounding* of the subsurface: reconstruction will be correct for the direction ϕ and directions close to it, but deviations will develop for directions significantly different from ϕ .

The single-shot imaging condition (14) has the same form as the plane-wave imaging condition Eq. (1). Therefore, the same program coding as in the case of plane-wave migration can be used.

Computational aspects

In this section a few computational aspects of solving Eqs. (12) and (13) will be discussed. Figure 1 shows the transformation of $\bar{U}(k_x, 0, \omega)$ from the $\omega - k_x$ domain to the newly introduced $A - B$ wavenumber domain. Homogeneous waves, which we will consider here only, correspond to the

shaded triangles shown in the left panel where $\left| \frac{\omega}{v} \right| \geq |k_x|$.

Elsewhere, $\bar{U}(k_x, 0, \omega)$ is equal to zero. By transforming the $\omega - k_x$ domain to the $A - B$ domain, lines of constant frequencies ω are imaged on to circles with centres located at $A = \frac{\omega}{v} \sin \phi$ and $B = \frac{\omega}{v} \cos \phi$. The horizontal and vertical Nyquist wavenumbers A_N and B_N have to meet the following conditions:

$$A_N = \frac{\pi}{\Delta x} \geq \frac{\omega_N}{v} (1 + \sin |\phi|), \quad (15a)$$

$$B_N = \frac{\pi}{\Delta z} \geq \frac{\omega_N}{v} (1 + \cos \phi). \quad (15b)$$

From these expressions follow the sampling intervals of the migrated section $M(x, z)$:

$$\Delta x \leq \frac{v \Delta t}{1 + \sin |\phi|}, \quad (16a)$$

$$\Delta z \leq \frac{v \Delta t}{1 + \cos \phi}. \quad (16b)$$

Here the circular Nyquist frequency $\omega_N = \frac{\pi}{\Delta t}$ has been used, where Δt is the time interval of the reflected wave field. The sampling intervals in the $A - B$ domain are

$$\Delta A = \frac{2\pi}{X}, \quad \Delta B = \frac{2\pi}{Z}, \quad (17)$$

where X is the length and Z the depth of the migrated section. X is usually assumed to be identical with the length L of the geophone array measuring the reflected wave field at $z=0$; this implies that $\Delta A = \Delta k_x$. For Z , a reasonable estimate has to be made. A possible choice is $Z = vT$, where T is the duration of the seismograms, representing the reflected wave field. The number of grid points in the $A - B$ domain (and in the $x - z$ domain) is determined by the in-

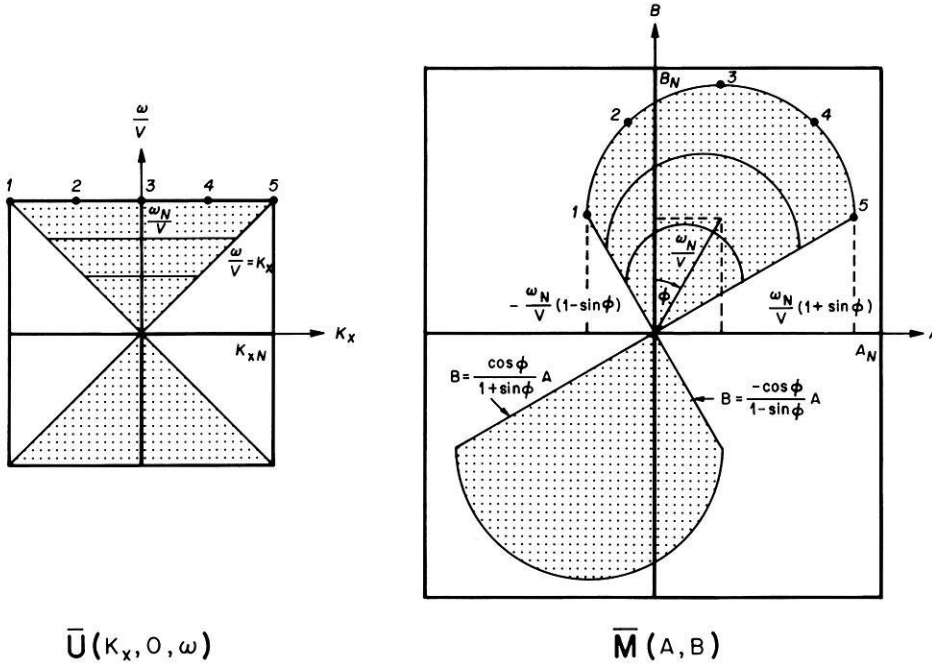


Fig. 1. Transformation of the Fourier-transformed reflected wave field $\bar{U}(k_x, 0, \omega)$ from the $k_x-\omega$ domain to the $A-B$ wavenumber domain. $\bar{M}(A, B)$ is the Fourier-transformed migrated section. Lines of constant frequency are mapped on to circles with centres at $A = \frac{\omega}{v} \sin \phi$ and $B = \frac{\omega}{v} \cos \phi$. A_N is the horizontal and B_N is the vertical Nyquist wavenumber. k_{xN} is the original horizontal Nyquist wavenumber and ω_N the temporal Nyquist frequency

tegers

$$LA = \frac{X}{\Delta x}, \quad LB = \frac{Z}{\Delta z}. \quad (18)$$

With Eqs. (15)–(18) the grid on which the Fourier transform $\bar{M}(A, B)$ of the migrated section, Eq. (13), has to be calculated is known. $\bar{M}(A, B)$ is nonzero only in the shaded area of the right panel of Fig. 1, and the computation can be restricted to $B \geq 0$. Inverse Fourier transformation of $\bar{M}(A, B)$ [and also calculation of $\bar{U}(k_x, 0, \omega)$] in the examples of this paper was performed with a FFT program written by Terefe (1985).

The computation of $\bar{M}(A, B)$ requires interpolation of $\bar{U}(k_x, 0, \omega)$, since the points in the $k_x-\omega$ domain, corresponding to the equidistant gridpoints in the $A-B$ domain according to Eqs. (10) and (11), will usually not fall on the gridpoints in which $\bar{U}(k_x, 0, \omega)$ is known. The two-dimensional sinc interpolation is used:

$$\begin{aligned} \bar{U}[(k_x(A, B), 0, \omega(A, B))] = & \frac{4\pi^2}{\Delta\omega \Delta k_x} \sum_m \sum_n \bar{U}(n\Delta k_x, 0, m\Delta\omega) \\ & \frac{\sin\left(\frac{k_x - n\Delta k_x}{\Delta k_x}\right) \sin\left(\frac{\omega - m\Delta\omega}{\Delta\omega}\right)}{\frac{k_x - n\Delta k_x}{\Delta k_x} \cdot \frac{\omega - m\Delta\omega}{\Delta\omega}}. \end{aligned} \quad (19)$$

In the examples discussed later, five grid lines, with both variable m and variable n and closest to the point (k_x, ω) , are included in the evaluation of Eq. (19).

The quality of the migrated result depends critically on the sampling intervals ΔA and ΔB , i.e. on the estimates of the length and the depth of the migrated section in Eq. (17). We assume $\bar{U}(k_x, 0, \omega)$ is sampled sufficiently finely by $\Delta k_x = \frac{2\pi}{L}$ and $\Delta\omega = \frac{2\pi}{T}$, such that Eq. (19) is accurate enough for points between the grid points. The nonequally spaced (k_x, ω) points, which contribute to $\bar{M}(A, B)$, may

represent a grid which is coarser than the original grid of $\bar{U}(k_x, 0, \omega)$, such that essential features in this spectrum may be lost, and in particular if $\bar{U}(k_x, 0, \omega)$ is a rapidly oscillating function. Then it may happen that pronounced spatial aliasing is produced in the migrated section $M(x, z)$. In such cases, ΔA and ΔB have to be reduced, i.e. X and Z have to be enlarged by increasing LA and LB in Eq. (18). Common practice, however, is to reduce $\Delta\omega$ and Δk_x , i.e. T and L will be increased; because of the assumed relations $X=L$ and $Z=vT$, the result is the same. Increasing T and L is equivalent to adding zeros at the end of the seismograms and zero traces at the end of the geophone array (Stolt, 1978). The disadvantage, however, is that zero traces unnecessarily have to be Fourier transformed from the $x-t$ domain to the $k_x-\omega$ domain, leading to an increase in computing time which may be substantial. The increase in computing time can be reduced or even avoided through multiplication of the spectrum $\bar{U}(k_x, 0, \omega)$ by the phase-shift operator $e^{i(\omega t_0 + k_x x_0)}$. This corresponds to the introduction of a new origin (x_0, t_0) in the $x-t$ domain. If this origin is placed at about the centre of the wave field $U(x, 0, t)$, the resulting spectrum $\bar{U}(k_x, 0, \omega)$ is considerably smoother than before and thus larger sampling intervals ΔA and ΔB can be used. After interpolation, the inverse phase shift is applied, such that the old origin is valid again. This method follows a suggestion of Claerbout (1985) and is similar to the spectral smoothing by the use of reduced travel times which is familiar from the theory of synthetic seismograms for layered media.

Applications

Fast plane-wave migration

The plane-wave migration will be tested on the synclinal model shown in Fig. 2. The model consists of two layers with different velocities v and densities ρ , which are separated by a curved interface having a maximum dip of 35° . A seismic line source S_i is located at the surface and gener-

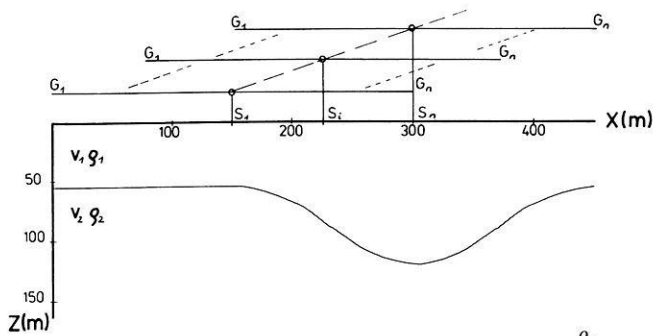


Fig. 2. Synclinal model: $v_1=1,500$ m/s, $v_2=1,000$ m/s, $\frac{\rho_2}{\rho_1}=0.5$. $S_1 \dots S_n$ denote shotpoints. $G_1 \dots G_n$ is the geophone spread. The shotpoint-receiver configuration is shifted across the structure in the x direction in order to simulate the field survey

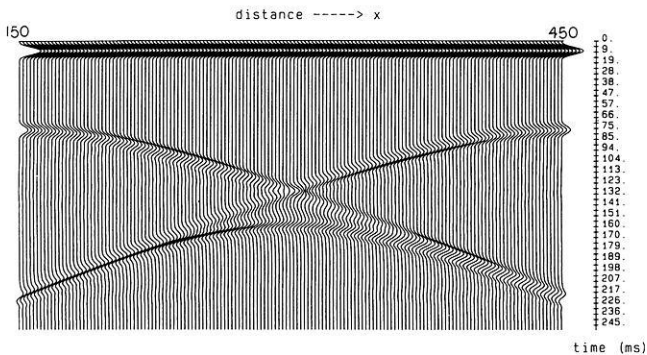


Fig. 3. Plane-wave response of the synclinal model for a plane wave propagating vertically ($\phi=0$). The direct plane wave starts at time $t=0$. The reflection is visible between 70 ms and 226 ms

ates cylindrical SH waves with a dominant frequency of 50 Hz. The reflection from the syncline is calculated along the finite geophone array $G_1 \dots G_n$ using a finite-difference technique (Korn and Stöckl, 1982). Reflections coming from the boundaries of the rectangular model are suppressed by using absorbing boundary conditions (Clayton and Engquist, 1980). In order to simulate the field survey, the single-shot experiment is repeated for different shots $S_1 \dots S_n$ at the surface, shifting the shotpoint-geophone configuration across the structure. The single-shot sections calculated in this way represent the data base for the plane-wave sections which can be synthesized from the single-shot sections by applying the slant-stack technique. The plane-wave sections we will show here have already been used as input data to a finite-difference migration technique (Temme, 1984).

Figure 3 shows the plane-wave response for a plane wave propagating vertically ($\phi=0$). The geophone array extends from 150 m to 450 m; the section contains 150 seismograms. The sampling interval in time is $\Delta t=1.89$ ms. For the frequency-wavenumber migration, 106 zero traces have been added on the right side. The number of time samples in each seismogram is $LT=128$. LA in Eq. (18), i.e. the number of samples along the horizontal wavenumber axis A , has been chosen equal to the number of seismograms $LX=256$. LB in Eq. (18) has been chosen equal to the number of time samples $LT=128$. The depth increment $\Delta z=1.28$ m has been used, and the maximum depth Z of the migrated section is 164 m. The migration result, corresponding to these parameters (Fig. 4), is characterized by strong aliased events; only the upper part of the syncline

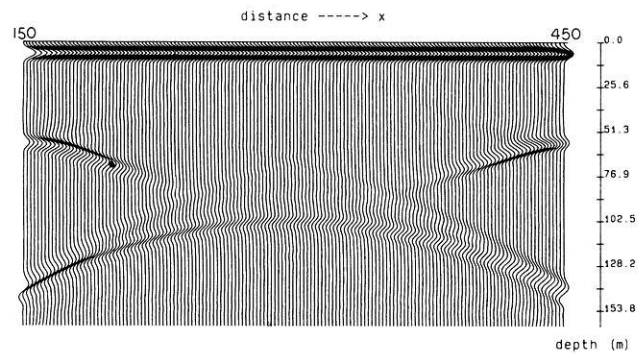


Fig. 4. Frequency-wavenumber migration of the plane-wave response of Fig. 3 without application of the phase-shift operation prior to interpolation. Strong aliased events are visible because of too coarse sampling of $\bar{U}(k_x, 0, \omega)$

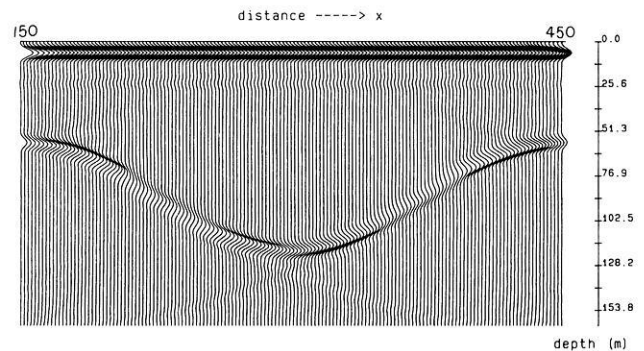


Fig. 5. Improved migrated section of the plane-wave response of Fig. 3, with the phase shift $e^{i(\omega t_0 + k_x x_0)}$ applied prior to interpolation: $t_0=113$ ms, $x_0=150$ m

to a depth of 50 m is migrated correctly. The reason for aliasing is too coarse sampling of $\bar{U}(k_x, 0, \omega)$ in ω . The migrated result can be improved without extra computing time if, prior to migration, a phase shift $e^{i(\omega t_0 + k_x x_0)}$ is applied to the plane-wave section. We have chosen $t_0=113$ ms and $x_0=150$ m, corresponding to a new origin at the centre of the record section in Fig. 3 (x_0 is measured from the x coordinate of the leftmost seismogram). After migration the phase shift is removed in order to get the true depth structure. The result is shown in Fig. 5. The complete syncline is migrated very well; there is good agreement with the results of the finite-difference migration of Temme (1984, Fig. 6). Segments of the structure lying horizontally, or having small dips, show large amplitudes because the plane wave is vertically incident.

The next example (Fig. 6) shows the slant-stacked section for a plane wave incident under the angle $\phi=-30^\circ$. The plane wave comes in from the right, travels to the left in the negative x direction, and hits upon the left flank of the syncline almost normally. The right side of the travel-time loop, carrying information about the left part of the syncline, is complete; whereas the left side shows a large gap. This is a consequence of the finite geophone spread used in the single-shot experiments. The geophone array again extends from 150 m to 450 m and the plane-wave section contains 150 seismograms. The sampling interval is $\Delta t=1.89$ ms. For migration, again 106 traces have been added on the right side, so that the total number of seismograms is $LX=256$. The number of time samples of each seismogram is $LT=256$ in this experiment. As in the first

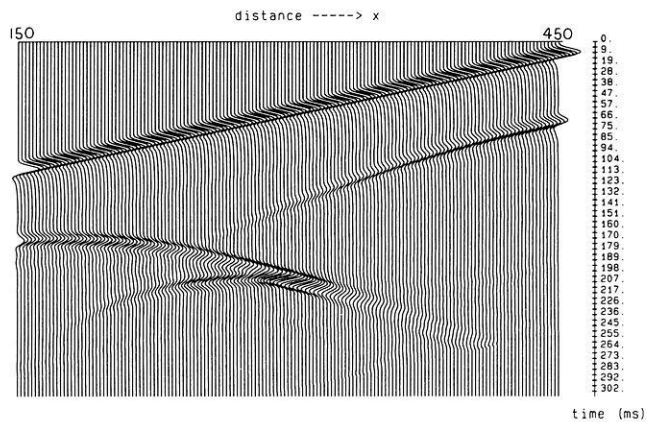


Fig. 6. Slant-stacked section for a plane wave with propagation angle $\phi = -30^\circ$. The plane wave is incident from the right and starts at $t=0$ at $x=450$ m; it travels to the left, in negative x direction. The reflection from the syncline is visible between 60 and 260 ms

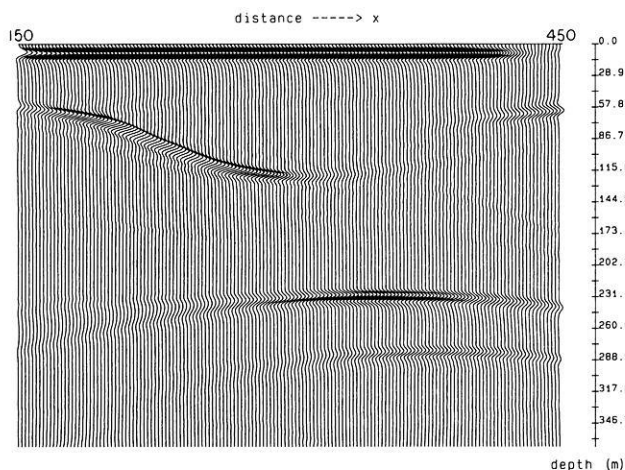


Fig. 7. Migration of the slant-stacked section of Fig. 6 without application of a phase shift. The left-hand part of the structure is successfully reconstructed. Strong aliased events occur at depths of 230–280 m

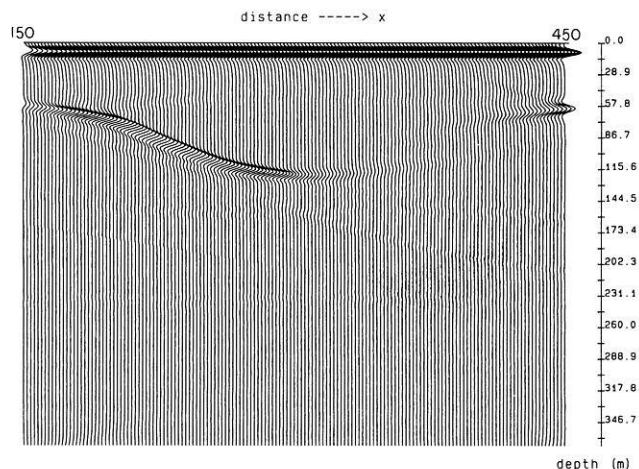


Fig. 8. Improved migrated section of the slant-stacked section of Fig. 6 with application of a phase shift: $t_0 = 132$ ms, $x_0 = 150$ m

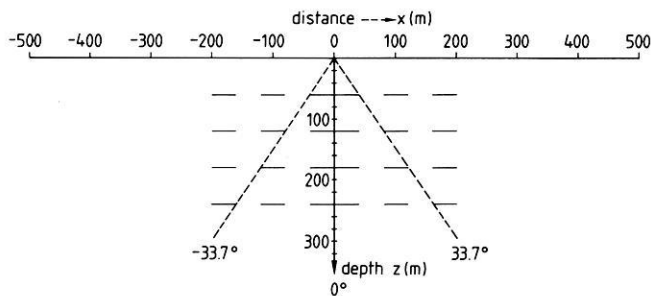


Fig. 9. Twenty horizontal reflectors embedded in a medium of constant velocity and density. For the calculation of *SH* reflections and diffractions, a reflection coefficient has been used which is characterized by a velocity contrast from $v_1 = 1,500$ m/s to $v_2 = 1,000$ m/s and a density contrast from $\rho_1 = 2$ g/cm³ to $\rho_2 = 1$ g/cm³. The line source is located at $(x=0, z=0)$

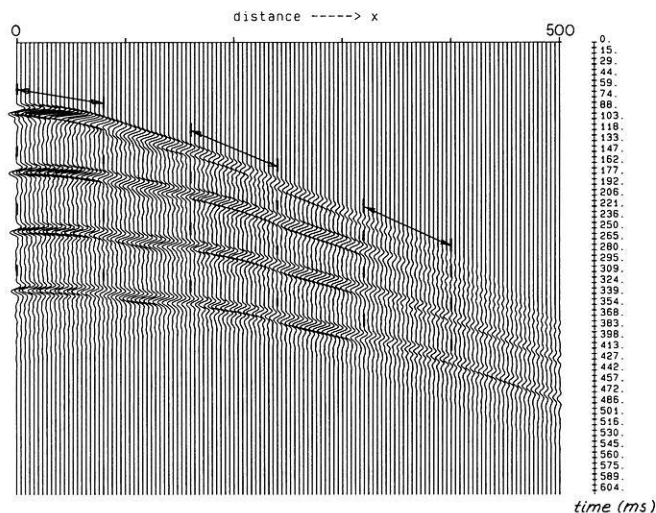


Fig. 10. Synthetic single-shot seismograms calculated along half the geophone array of Fig. 9 from $x=0$ to $x=500$ m. The position of each reflection is marked

plane-wave experiment, $LA=LX$ and $LB=LT$ has been chosen and $\Delta z = 1.44$ m has been used.

Figure 7 shows the migrated depth section without application of a phase shift. Again, strong aliased events are present at depths around 230–280 m. Using a phase shift with $t_0 = 132$ ms and $x_0 = 150$ m, we obtain the improved migrated result shown in Fig. 8. As expected, the largest amplitudes occur in the steep dip range of the syncline, where the plane wave comes in vertically. Again there is good agreement with the finite-difference migration results of Temme (1984, Fig. 7).

Fast single-shot migration

For the single-shot migration, the model shown in Fig. 9 was chosen. The structure consists of 20 horizontal reflector elements, which are separated from each other by roughly one wavelength. The shotpoint is located at $x=0$. The geophone array extends from $x = -500$ m to $x = +500$ m. The synthetic *SH* seismograms for this simple reflector model were calculated with a fast analytical technique (Fertig and Müller, 1979) which is comparable to the finite-difference technique as far as accuracy is concerned. The analytical formula is based on a generalization of the exact theory

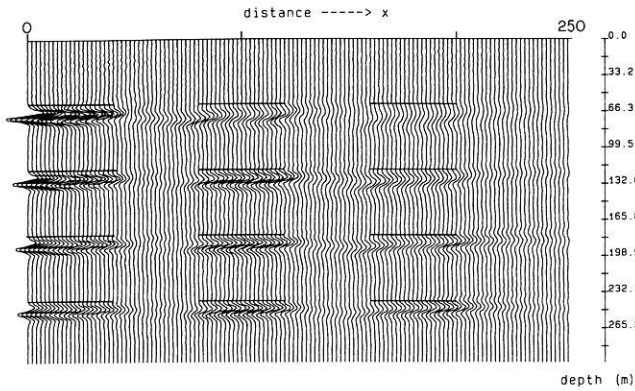


Fig. 11. 45° finite-difference migration of the single-shot section of Fig. 10. The true reflector positions are marked by *thin lines*

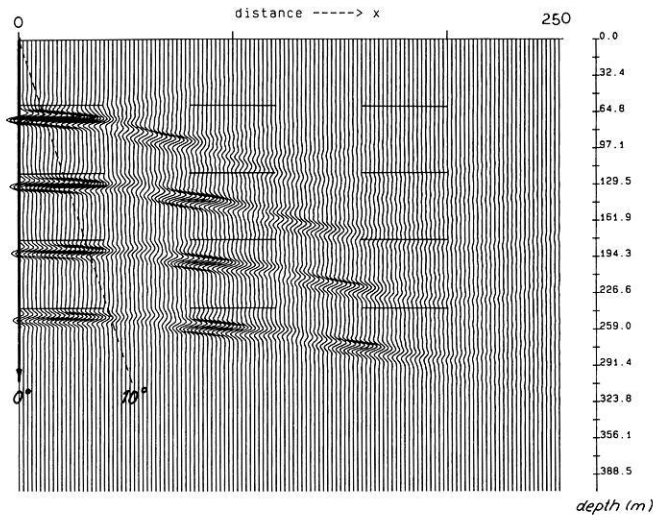


Fig. 12. Fast frequency-wavenumber migration of the single-shot section of Fig. 10 for the sounding direction $\phi=0^\circ$. The ray angle $\phi=10^\circ$ is shown for orientation. True reflector positions are marked by *thin lines*

for diffraction at an opaque half-plane. Interaction of the reflecting elements with each other cannot be taken into account with this forward modelling technique. The model in Fig. 9 was chosen to demonstrate the effects due to the approximate nature of the imaging condition Eq. (14). As was shown in the derivation of the theory of single-shot migration, the migrated result will be correct only along a specified ray. Here, three rays are investigated. The -33.7° and the $+33.7^\circ$ rays traverse the structure diagonally. We expect the diagonal elements to be migrated more or less correctly. The 0° sounding should give a good image of the elements below $x=0$.

Figure 10 shows the synthetic seismograms along half the geophone array from $x=0$ to $x=500$ m. The position of each reflection is marked along the four hyperbola-like events. Reflections at large x have small amplitudes due to cylindrical spreading and the angle-dependent reflection coefficient. Between the reflections, diffractions from the numerous reflector edges can be seen.

We first show in Fig. 11 the migrated section calculated with the 45° finite-difference technique. This method allows the application of the correct single-shot imaging condition

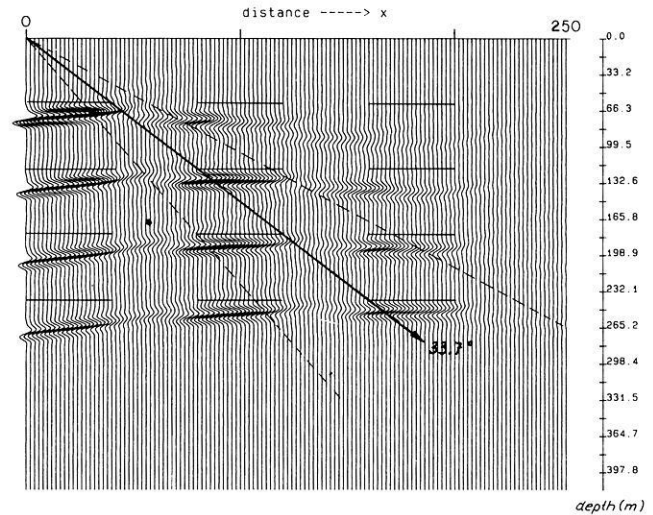


Fig. 13. Fast frequency-wavenumber migration of the single-shot section of the model of Fig. 9 for the sounding direction $\phi = +33.7^\circ$. Ray angles $\phi = 33.7^\circ \pm 10^\circ$ are shown for orientation

Eq. (2); the results serve as a reference for the following fast frequency-wavenumber migrations. We notice in Fig. 11 the good agreement of the reconstructed elements with the true positions indicated by thin lines. Reflections from the upper-right elements propagate with angles of 55° – 75° to the surface. For these angles, the 45° approximation of the wave equation becomes inaccurate. As a consequence we see distorted reflectors in the upper-right part of the reconstruction. Reflectors far from the shotpoint show small amplitudes due to cylindrical spreading. Additionally, amplitude variations can be seen along each element, which are caused by the angle-dependent reflection coefficient. Between the reflectors, diffracted energy is focussed to a range of approximately one wavelength.

Figure 12 shows the frequency-wavenumber migration for $\phi=0^\circ$. A phase shift of $t_0=300$ ms and $x_0=0$ has been applied. The imaging condition is exact along a ray pointing vertically downwards at $x=0$. We expect to migrate reflection points at $(x=0, z)$ correctly. From Fig. 12 we see that also segments within an aperture of 0° – 10° are also reconstructed very well. Reflecting elements beyond this range are mispositioned. They are too deep and are shifted towards smaller x values. Comparison of the reconstructed elements with the true reflector positions shows that the error is in the range 0–2 wavelengths.

The same data set was used to reconstruct elements along the sounding direction $\phi=33.7^\circ$. Figure 13 shows that in this experiment elements lining up diagonally can be reconstructed very well. Additionally, the ray angles $\phi=33.7^\circ \pm 10^\circ$ are marked for orientation. Reflectors outside this range, again, are mispositioned and show incompletely focussed diffractions.

The entire migrated section, now for the sounding direction $\phi = -33.7^\circ$, is shown in Fig. 14. The array of this example extends from $x = -500$ m to $x = +500$ m. Along the sounding ray the elements are reconstructed very well. We realize for positive x values, however, that the error increases. This is due to the slowness of the exact imaging hyperbola, Eq. (2), changing sign beyond $x=0$; whereas for the linear approximation, Eq. (14), the slowness remains constant over x .

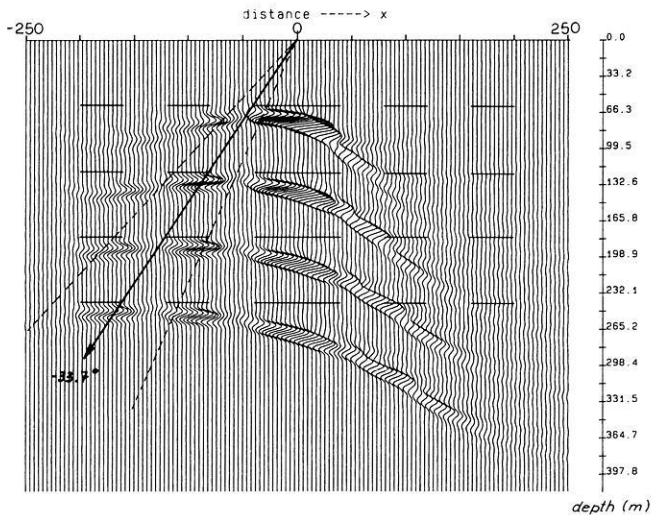


Fig. 14. Fast frequency-wavenumber migration of the entire single-shot section of the model of Fig. 9 for the sounding direction $\phi = -33.7^\circ$

The fast frequency-wavenumber technique needed a computing time for the section in Fig. 12 or 13, which was only 5% of the computing time of the finite-difference technique. Most of the CPU time was used to perform the two-dimensional FFT.

Discussion

Migration of plane-wave and single-shot sections can be performed very fast in the frequency-wavenumber domain. The steps included in this technique, outlined above in detail, are the following. First, the wave field which has been recorded at the earth's surface has to be transformed from the $t-x$ domain to the $\omega-k_x$ domain by using a two-dimensional FFT. In a second step, the spectrum $\bar{U}(k_x, 0, \omega)$ has to be mapped onto a new grid in the $A-B$ wavenumber domain. This is done by prescribing equidistant wavenumbers A, B within the shaded area of Fig. 1 (right panel) and solving Eqs. (10) and (11) for k_x and ω . Usually k_x and ω do not fall on gridpoints in the $\omega-k_x$ domain, and $\bar{U}[k_x(A, B), 0, \omega(A, B)]$ has to be interpolated. The examples shown in this paper have been calculated with a two-dimensional sinc interpolation of order 5, Eq. (19), which is sufficiently good. Tests with linear interpolation were not successful; this simpler interpolation generates background noise all over the migrated section. More critical than the interpolation is the choice of the sampling intervals ΔA and ΔB in Eq. (17). As Figs. 4 and 7 show, large ΔA and ΔB result in strong ghost events in the migrated section. The sampling intervals Δk_x and $\Delta \omega$ are sufficient for representation of the spectrum $\bar{U}(k_x, 0, \omega)$, but the sampling intervals resulting from Eqs. (10) and (11) may be too large, such that details of the spectrum may be lost in the $A-B$ domain. In such cases, a remedy is the phase-shift operation $e^{i(\omega t_0 + k_x x_0)}$ prior to interpolation which smooths the spectrum. The point $(x = x_0, t = t_0)$ is chosen at about the centre of the record section representing the reflected wave field $U(x, 0, t)$. After interpolation, the phase shift is removed through multiplication by $e^{-i(\omega t_0 + k_x x_0)}$ and the spectrum $\bar{M}(A, B)$ of the migrated section $M(x, z)$ follows from Eq. (13). The final step is an inverse two-dimensional FFT.

Plane-wave migration can be performed exactly with the imaging condition Eq. (1). Plane-wave sections for different angles of incidence, which can be synthesized from single-shot sections by slant stacking, can be used for the reconstruction of selected segments of the structure. An advantage of data stacking which forms part of the plane-wave migration procedure is noise reduction. A disadvantage is that a *complete* plane-wave response is only obtained if the single shots used have a sufficient spread length. Current recording techniques appear to allow the synthesis only for propagation directions close to vertical.

The reconstruction of the subsurface structure from single-shot sections can be performed with the algorithm that has been developed for plane-wave migration. However, a linear approximation of the exact imaging condition by Eq. (14) has to be used. As a consequence, the migrated result is only correct along a ray with direction ϕ with respect to the vertical axis. In Figs. 12–14 reconstruction is successful within an aperture of $\pm 10^\circ$ around this sounding direction; this aperture is frequency dependent and decreases with increasing frequency. As in plane-wave migration, single-shot sections can be used to reconstruct selected segments of the structure. No stacking is involved in single-shot migration, and the danger that noise is migrated is larger than in plane-wave migration. However, it is conceivable that stacking the migration results of closely neighboured shots, all being obtained for the same sounding direction, will produce noise reduction.

Conclusions

In this paper a fast frequency-wavenumber method for migration of single-shot and plane-wave sections was derived. It has been demonstrated that plane-wave migration can be performed exactly in constant-velocity media. The reconstruction of reflecting elements from single-shot sections can be done exactly only along preselected sounding directions. The direction selective features of plane-wave and single-shot migration can be used to reconstruct selected segments of the subsurface structure which are of special interest. It is conceivable that migrated single-shot sections, corresponding to several neighbouring sounding directions, can be combined into one section with extended validity.

As a technical result, it has been demonstrated that a two-dimensional phase shift in the frequency-wavenumber domain prior to migration can improve the migrated result without extra computing costs. The phase-shift operation is useful since it reduces zero padding of the reflected wave field and makes the proposed migration method even more economic.

The migration technique developed here is a straightforward extension of Stolt's (1978) technique for CMP or zero-offset wave fields. Stolt's method is frequently used in industrial practice, in spite of the limitations due to the constant-velocity assumption. We suggest that, in a similar way, the potential of fast plane-wave and, in particular, single-shot migration in the frequency-wavenumber domain be investigated with the abundant data volumes of the prospecting industry.

Since this paper has been completed, we have been able to generalize the fast frequency-wavenumber migration method for the case of depth-dependent velocity (Müller and Temme, in preparation). The focussing properties that were found here for single-shot migration then become more

pronounced: a migrated CMP or plane-wave section is correct only along a preselected horizontal line (and close to it), and a migrated single-shot section only at a preselected point (and close to it). The algorithm is basically the same as that used in this paper.

Acknowledgements. We profited considerably from Getahun Terefe's versions and improvements of two-dimensional FFT programs. The study was funded by a grant from the Deutsche Forschungsgemeinschaft Te 123/1-1. The computations were done at the computing center of the Department of Geology and Geophysics of the University of Utah in Salt Lake City.

References

- Claerbout, J.F.: Imaging the earth's interior. Palo Alto: Blackwell Scientific Publications 1985
- Clayton, R.W., Engquist, B.: Absorbing boundary conditions for wave-equation migration. *Geophysics* **45**, 895–904, 1980
- Fertig, J., Müller, G.: Approximate diffraction theory for transparent half planes with application to seismic wave diffraction at coal seams. *J. Geophys.* **46**, 349–367, 1979
- Gazdag, J.: Wave equation migration with the phase-shift method. *Geophysics* **43**, 1342–1351, 1978
- Gazdag, J., Squazzero, P.: Migration of seismic data by phase shift plus interpolation. *Geophysics* **49**, 124–131, 1984
- Korn, M., Stöckl, H.: Reflection and transmission of Love channel waves at coal seam discontinuities computed with a finite difference method. *J. Geophys.* **50**, 171–176, 1982
- Loewenthal, D., Lu, L., Roberson, R., Sherwood, J.: The wave equation applied to migration. *Geophys. Prosp.* **24**, 380–399, 1976
- Mayne, W.H.: Common reflection point horizontal data stacking techniques. *Geophysics* **27**, 927–938, 1962
- Schultz, P.S., Claerbout, J.F.: Velocity estimation and downward continuation by wavefront synthesis. *Geophysics* **43**, 691–714, 1978
- Stolt, R.: Migration by Fourier transform. *Geophysics* **43**, 23–48, 1978
- Temme, P.: A comparison of common-midpoint, single-shot, and plane-wave depth migration. *Geophysics* **49**, 1896–1907, 1984
- Terefe, G.: Tiefenmigration im Frequenz-Wellenzahl-Bereich. Diploma thesis, University of Frankfurt, 1985
- Treitel, S., Gutowski, P.R., Wagner, D.E.: Plane-wave decomposition of seismograms. *Geophysics* **47**, 1375–1401, 1982

Received March 25, 1986; revised June 24, 1986

Accepted June 25, 1986

A method of calculating lithosphere thickness from observations of deglacial land uplift and tilt

Detlef Wolf*

Department of Physics, University of Toronto, Toronto, Ontario, Canada, M5S 1A7

Abstract. The study proposes an inversion method applicable to observations of deglacial land uplift and tilt near the margin of a major Pleistocene ice-sheet. This information allows the determination of the cross-section of the ice-sheet and the calculation of the thickness of the lithosphere. The method is applied to the Pleistocene glaciations in Fennoscandia and Laurentia and yields similar lithosphere thicknesses of 110 ± 30 km and 130 ± 35 km, respectively. Since the method is based on a static theoretical model, the thicknesses must be interpreted as upper bounds.

Key words: Elastic plate – Ice-sheet – Inversion – Isostasy – Lithosphere

Introduction

The idea of using glacio-isostatic data to infer the elastic resistance of the earth's lithosphere is usually credited to McConnell (1968), McGinnis (1968), Brotchie and Silvester (1969). Walcott (1970a) and others, although these studies are predated by Niskanen's (1943, 1949) contributions to the subject.

Rather well known is the investigation of Walcott (1970a), who used the model of a thin elastic plate superimposed on an inviscid half-space and flexed by an external load of specified cross-section. Based on the tilted strandline of pro-glacial Lake Algonquin (Canada), Walcott inferred a flexural rigidity of the lithosphere of about 6×10^{24} N m, corresponding to a thickness of about 75 km.

Walcott's (1970a) model is characterized by several simplifications, viz. using (a) the plane half-space approximation and (b) the thin-plate approximation for the earth model and using (c) a two-dimensional approximation of the roughly axisymmetric ice-sheet for the load model. Simplifications (a), (b) and (c) were shown to be justified for predictions of surface displacement and slope close to the margins of loads of large radius (Comer, 1983; Wolf, 1984a, b, 1985a). Since the model is static, it also presupposes (d) that the earth's surface was in equilibrium with the Laurentide ice-sheet

during the existence of Lake Algonquin and (e) that it is in equilibrium at present. Clearly, assumptions (d) and (e) do not hold exactly, in which case the inferred lithosphere thickness must be interpreted as an upper bound (Walcott, 1970b).

In previous studies of glacio-isostatic adjustment in Fennoscandia, no use has yet been made of observations near the margin of the Pleistocene ice-sheet. In the present study, an upper bound on the thickness of the Fennoscandian lithosphere is obtained by *inverting* Walcott's (1970a) method using uplift *and* tilt data from the ice front. The inclusion of uplift data eliminates the dependence of the estimate on the cross-section of the load model, which is a limitation of Walcott's approach. The method shows the thickness of the Fennoscandian lithosphere to be less than 110 ± 30 km. The same method is applied to the uplift and tilt data associated with Lake Algonquin and yields an upper bound of 130 ± 35 km for the Laurentian lithosphere.

Theoretical model

The theoretical model considered is that of a thin elastic plate superimposed on an inviscid half-space and flexed by an external load. The analysis is confined to two dimensions, in which case the (symmetric) Green's function for downward displacement is (Gunn, 1943)

$$w_G(x) = \frac{a}{2\rho_2 g} \exp(-ax) [\sin(ax) + \cos(ax)], \quad x \geq 0, \quad (1)$$

where the load is at $x=0$. Parameter ρ_2 is the density of the inviscid half-space and $g=9.81 \text{ m s}^{-2}$ the gravitational acceleration. Parameter a^{-1} is the flexural scale-length defined by

$$a^{-1} = \left(\frac{4D}{\rho_2 g} \right)^{1/4}, \quad (2)$$

with

$$D = \frac{\mu_1 h_1^3}{6(1-\nu_1)} \quad (3)$$

the flexural rigidity. Parameters h_1 , μ_1 and ν_1 are the thickness, shear modulus and Poisson's ratio of the elastic plate, respectively.

* Present address: Division of Gravity, Geothermics and Geodynamics, Earth Physics Branch, Energy, Mines and Resources Canada, Ottawa, Ontario, Canada, K1A 0Y3

The pressure exerted by a load of exponential cross-section is

$$q(x) = \rho_0 g h_0 \begin{cases} 0, & x \leq 0 \\ 1 - \exp(-bx), & x > 0 \end{cases} \quad (4)$$

with h_0 the maximum load thickness, ρ_0 the load density and b the load steepness. The displacement caused by q is calculated by convolution with the Green's function, Eq. (1), yielding

$$w(x) = \frac{\rho_0 h_0}{2\rho_2} \frac{b \exp(ax)}{(b+a)^2 + a^2} \cdot [a \sin(ax) + (b+a) \cos(ax)], \quad x \leq 0, \quad (5a)$$

$$w(x) = \frac{\rho_0 h_0}{2\rho_2} \left\{ 2 - \frac{8a^4 \exp(-bx)}{b^4 + 4a^4} - \frac{b \exp(-ax)}{(b-a)^2 + a^2} \cdot [a \sin(ax) + (b-a) \cos(ax)] \right\}, \quad x > 0. \quad (5b)$$

If $b \rightarrow \infty$, the solution degenerates to that of a load of rectangular cross-section (e.g. Jeffreys, 1976, pp. 270–272). The mathematically convenient (but physically unfounded) case $a=b$ was discussed previously (Walcott, 1970a).

At the load margin, $x=0$, the displacement and slope are

$$w = \frac{\rho_0 h_0}{2\rho_2} \frac{b(b+a)}{(b+a)^2 + a^2} \quad (6)$$

and

$$w' = \frac{\rho_0 h_0 a}{2\rho_2} \frac{(b+a)^2 - a^2}{(b+a)^2 + a^2}. \quad (7)$$

Solving Eqs. (6) and (7) for b yields

$$b = a \frac{w_r - 2w}{2(w_r - w)} \left[\left(1 + \frac{8w}{w_r - 2w} \frac{w_r - w}{w_r - 2w} \right)^{1/2} - 1 \right] \quad (8)$$

and

$$b = a \left[\left(\frac{w'_r + w'}{w'_r - w'} \right)^{1/2} - 1 \right], \quad (9)$$

respectively, where $w_r = \lim_{b \rightarrow \infty} w = \rho_0 h_0 / (2\rho_2)$ and $w'_r = \lim_{b \rightarrow \infty} w' = \rho_0 h_0 a / (2\rho_2)$. Parameter b may be eliminated from Eqs. (8) and (9), yielding

$$a = w' \frac{2w - 3w_r - S^{1/2}}{2(w_r - 2w)(w_r - w) - w_r(w_r + S^{1/2})}, \quad (10)$$

where $S = (w_r - 2w)^2 + 8w(w_r - w)$. If w and w' are known at the load margin and h_0 and ρ_2 are assumed, Eq. (10) has a unique solution which, by Eqs. (2) and (3), may be converted into an estimate of h_1 .

Data analysis

To estimate an upper bound on lithosphere thickness in Fennoscandia, data from the Helsinki region (Finland) are used. During the Late Weichselian (10–12 ka

Table 1. Parameters of earth model

Layer l	h_l [km]	ρ_l [kg m ⁻³]	μ_l [N m ⁻²]	ν_l	η_l [Pa s]
1	h_1	0	0.67×10^{11}	ν_1	∞
2	∞	3380	0	0.5	0

Table 2. Results of inversion for Fennoscandia ($w=100$ m, $w'=0.70 \times 10^{-3}$, $\rho_0=910$ kg m⁻³ and $\nu_1=0.272$)

h_0 [km]	h_1 [km]	b^{-1} [km]
2.0	107	242
2.2	110	280
2.4	112	319
2.6	115	357
2.8	117	396
3.0	118	434

b.p.), this region was close to the ice front, which deposited the Salpausselkä terminal moraines in southern Finland (cf. Eronen, 1983). Niskanen's (1939) compilation of emergence data shows that Helsinki has emerged by at least 67 m since deglaciation. The land uplift w is obtained after corrections for eustatic sea-level rise (e.g. Andrews, 1970, pp. 22–24) have been applied and is estimated to be 100 ± 10 m. The oldest strandline near Helsinki is associated with an early stage of the Baltic Ice Lake, which formed at about 10.6 ka b.p. The strandline is only mapped over a short distance; its tilt w' can be inferred from strandline diagrams (e.g. Donner, 1980; Eronen, 1983) and is estimated to be $0.70 \pm 0.10 \times 10^{-3}$.

In Fig. 1, $b^{-1} = f(h_1, w)$ and $b^{-1} = g(h_1, w')$ for $w = 100$ m and $w' = 0.70 \times 10^{-3}$ are shown. The results apply to $h_0 = 2.45$ km and the parameter values listed in Table 1. Clearly, if either w or w' is given, the solution is non-unique. In agreement with Eqs. (2) and (3), incompressibility reduces the lithosphere thicknesses slightly; similarly small variations would result from uncertainties in μ_1 or ρ_2 . If, however, both $w = 100 \pm 10$ m and $w' = 0.70 \pm 0.10 \times 10^{-3}$ are assumed, a unique solution, $h_1 = 110 \pm 30$ km and $b^{-1} = 330 \pm 50$ km, is obtained (Appendix). Table 2 shows that the value inferred for h_1 is nearly insensitive to the value assumed for h_0 . This suggests 110 ± 30 km as an upper bound on the Fennoscandian lithosphere thickness.

In previous studies, estimates of the Laurentian lithosphere thickness from strandlines of pro-glacial lakes were based on strandline tilt alone (Walcott, 1970a, b; Wolf, 1985b). The present study supplements that by taking uplift into account. Land uplift and tilt can be estimated from Fig. 2, which is adapted from Chapman's (1954) strandline diagram for Lake Algonquin. The diagram assumes that no vertical movement has occurred in the "region of horizontality" of the strandline at $s < -300$ km since its formation at 10–12 ka b.p. (Farrand, 1962; Broecker, 1966). Then, from the portion of the strandline near $s = -75$ km, $w = 160 \pm 15$ m and $w' = 1.00 \pm 0.15 \times 10^{-3}$ are estimated.

In Fig. 3, $b^{-1} = f(h_1, w)$ and $b^{-1} = g(h_1, w')$ for w

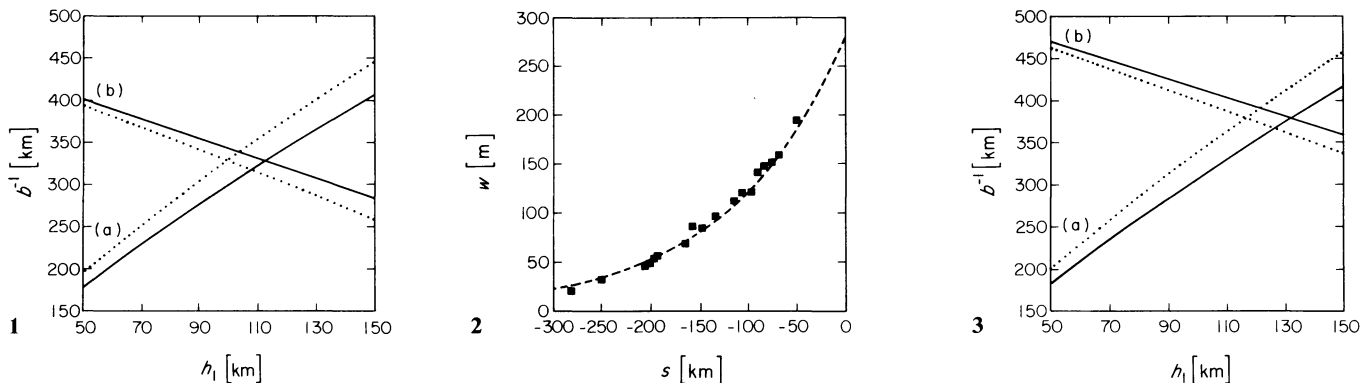


Fig. 1. Inverse steepness b^{-1} as function of lithosphere thickness h_1 for (a) $w=100$ m or (b) $w'=0.70 \times 10^{-3}$; inversion applies to $h_0=2.45$ km, $\rho_0=910$ kg m $^{-3}$ and earth model of Table 1 with $v_1=0.272$ (solid) or $v_1=0.5$ (dotted)

Fig. 2. Observed land uplift (squares) and exponential approximation (dashed) as functions of horizontal distance s from location of ice front at time of existence of Lake Algonquin (adapted from Chapman, 1954; Broecker, 1966)

Fig. 3. Inverse steepness b^{-1} as function of lithosphere thickness h_1 for (a) $w=160$ m or (b) $w'=1.00 \times 10^{-3}$; inversion applies to $h_0=4.00$ km, $\rho_0=910$ kg m $^{-3}$ and earth model of Table 1 with $v_1=0.272$ (solid) or $v_1=0.5$ (dotted)

Table 3. Results of inversion for Laurentia ($h_0=4.0$ km, $\rho_0=910$ kg m $^{-3}$ and $v_1=0.272$)

s [km]	w [m]	w' [10^{-3}]	h_1 [km]	b^{-1} [km]
-50	185	1.54	87	230
-100	122	1.01	96	411
-150	80	0.67	103	686
-200	53	0.44	108	1,102
-250	35	0.29	112	1,733
-300	23	0.19	115	2,691

$w=160$ m and $w'=1.00 \times 10^{-3}$ are shown. The results apply to $h_0=4.0$ km and the parameter values listed in Table 1. Again, with $w=160 \pm 15$ m and $w'=1.00 \pm 0.15 \times 10^{-3}$, a unique solution, $h_1=130 \pm 35$ km and $b^{-1}=380 \pm 60$ km, results (Appendix).

A possible problem with the proposed inversion method is that displacement and slope must be known at the location of the equilibrium load margin, $x=0$, which, for isostatic disequilibrium, is not necessarily identical with the assumed location of the actual load margin, $s=0$, at the time of strandline formation. The location of the equilibrium margin can be estimated from the second derivative of Eq. (5b), which shows that the inflection point of the displacement curve is always below the equilibrium load. Since the data do not suggest a sign change of the curvature (Fig. 2), any point s may, in principle, coincide with $x=0$.

Table 3 shows the sensitivity of the estimate of h_1 to the location of the equilibrium load margin assumed. The Lake Algonquin strandline has been approximated by the function

$$w = w_0 \exp(cs), \quad -300 \text{ km} \leq s \leq 0, \quad (11)$$

where $w_0=280$ m and $c^{-1}=120$ km (Fig. 2). Although the sensitivity of h_1 to s is obvious, $h_1 < 130$ km always holds, which suggests 130 ± 35 km as an upper bound on the Laurentian lithosphere thickness.

Discussion and conclusion

Some idea of possible limitations of the inversion method may be gained from a discussion of the results obtained for the cross-sections of the ice-sheets. Nye's (1952) theoretical analysis shows that the cross-section of an (axisymmetric) ice-sheet of radius R is approximately given by the parabola

$$h(x) = h_0 \left(\frac{x}{R} \right)^{1/2}, \quad 0 \leq x \leq R. \quad (12)$$

This can be replaced by the (two-dimensional) exponential cross-section

$$h(x) = h_0 [1 - \exp(-bx)], \quad 0 \leq x < \infty \quad (13)$$

provided that

$$\int_0^R [1 - \exp(-bx)] dx = \int_0^R \left(\frac{x}{R} \right)^{1/2} dx. \quad (14)$$

Usually $\exp(-bR) \ll 1$, which reduces Eq. (14) to the condition

$$R = 3b^{-1}. \quad (15)$$

The abscissa b^{-1} of the intersection point in Fig. 1 is about 330 km. Equation (15) therefore suggests $R \cong 1,000$ km, which is close to the radius of the Fennoscandian ice-sheet at glacial maximum. Similarly, from Fig. 3, $b^{-1} \cong 380$ km and therefore $R \cong 1,150$ km; a closer estimate of R for the Laurentide ice-sheet at equilibrium would be 1,600 km.

Orowan (1949) and Nye (1952) showed that maximum ice thickness h_0 and basal shear stress τ are related by

$$h_0^2 = \frac{2\tau R}{\rho_0 g}. \quad (16)$$

Substituting for R from Eq. (15) and solving for τ yields

$$\tau = \frac{\rho_0 g h_0^2}{6b^{-1}}. \quad (17)$$

For the Fennoscandian ice-sheet, $h_0=2.45$ km has been used and $\tau=0.27 \times 10^5$ N m⁻² therefore results. For the Laurentide ice-sheet, $h_0=4.0$ km applies and $\tau=0.63 \times 10^5$ N m⁻² is obtained. Both estimates are similar to other estimates of τ for Pleistocene ice-sheets (cf. Paterson, 1981, pp. 162–164). However, if the inversion method is applied to the Lake Algonquin data for locations $s < -150$ km, b^{-1} becomes very large (Table 3) and Eqs. (15) and (17) no longer yield reasonable estimates of R and τ . The results for $s < -150$ km may therefore be disregarded.

A more important limitation of the proposed inversion method is that it only provides an *upper bound* on lithosphere thickness. The bound of 110 ± 30 km inferred from the Fennoscandian data is notable, however, because it is reasonably close to thickness estimates by McConnell (1968) and Cathles (1975). McConnell's thickness value was based on the short-wavelength part of an estimate of the relaxation-time spectrum of the Fennoscandian uplift. However, that part of the spectrum is controlled by kinks of the strandlines, most of which appear to be spurious (cf. Hyvärinen and Eronen, 1979; Walcott, 1980). Cathles, on the other hand, proposed that the strength of the lithosphere is insufficient to modify glacio-isostatic uplift in central Fennoscandia and therefore merely *adopted* a conventional thickness value.

In fact, the strength of the lithosphere may be such that the sensitivity of uplift to this feature is marked in central Fennoscandia. A similar sensitivity is, however, indicated to the presence of a low-viscosity layer below the lithosphere, which prevents a unique inference of lithosphere thickness from the observed central uplift. This was discussed recently (Wolf, 1985c, 1986a), where it was suggested that data from the ice front may help resolve the non-uniqueness of interpretations of uplift in central Fennoscandia. The present study serves as a first step and suggests that solutions $h_1 \geq 110 \pm 30$ km can be eliminated. One of the objectives of future studies should be to improve this heuristic estimate using a dynamic earth model and a more accurate load model.

For the Laurentian lithosphere the study has suggested $h_1 \leq 130 \pm 35$ km. Considering the geological and tectonic similarities between Fennoscandia and Laurentia, the closeness of the two bounds is encouraging. The Laurentian estimate also overlaps with previous results obtained using a dynamic earth model and a more accurate load model (Wolf, 1985b, 1986b). It thus reinforces the conclusion that the Lake Algonquin data are incompatible with thicknesses significantly larger than the value proposed. The present study, therefore, does not support Peltier's (1984) interpretation of relative-sea-level data from the North American east coast, which led him to suggest that the North American lithosphere is about 200 km in thickness. The conflict with Peltier's interpretation was discussed previously (Wolf 1985b).

Appendix

Sensitivity of estimates to uncertainties in observations

To estimate the sensitivity of h_1 to the uncertainties in w and w' , D is eliminated from Eqs. (2) and (3) and Eq. (10) is substituted for a , yielding

$$h_1 = \left(\frac{w'}{w} \right)^{-4/3} F(w). \quad (18)$$

Substituting in Eq. (9) for a from Eq. (10) yields

$$b^{-1} = \frac{G(w)}{w' F(w)}. \quad (19)$$

Functions $F(w)$ and $G(w)$ are readily calculated and found to be only weakly sensitive to w for the values of interest. With $dF/dw = dG/dw = 0$,

$$\Delta h_1 = [(\Delta_w h_1)^2 + (\Delta_{w'} h_1)^2]^{1/2} \quad (20)$$

and

$$\Delta b^{-1} = \Delta_{w'} b^{-1} \quad (21)$$

obtains, where

$$\Delta_w h_1 = \frac{4}{3} h_1 \frac{\Delta w}{w}, \quad (22)$$

$$\Delta_{w'} h_1 = \frac{4}{3} h_1 \frac{\Delta w'}{w'} \quad (23)$$

and

$$\Delta_{w'} b^{-1} = b^{-1} \frac{\Delta w'}{w'}. \quad (24)$$

To estimate the uncertainties Δw and $\Delta w'$, random and systematic errors must be taken into account. Random errors in w are mainly caused by erroneous correlations of diachronous beach levels and appear as local kinks in strandline diagrams. Systematic errors are caused by (a) the uncertainty of the eustatic correction (Fennoscandia) or of the assumed zero-uplift level (Laurentia) and (b) the neglect of geoid perturbations.

Uncertainty (a) affects only w and, for Fennoscandia, can be estimated by comparing different eustatic corrections (e.g. Andrews, 1970, pp. 22–24); an estimate of uncertainty (b) can be obtained by calculating the deglaciation-induced geoid perturbation (e.g. Wolf, 1986b). In the present study, $\Delta w/w = 10\%$ and $\Delta w'/w' = 15\%$ are assumed, yielding $\Delta h_1/h_1 = 27\%$ and $\Delta b^{-1}/b^{-1} = 15\%$.

Acknowledgements. This investigation was financially supported by a Natural Sciences and Engineering Research Council of Canada Postdoctoral Fellowship and a Canadian Government Laboratory Visiting Fellowship. The contributions by M. Eronen, who provided copies of several older Scandinavian publications, and by A. Lambert, who carefully read the manuscript, are gratefully acknowledged.

References

- Andrews, J.T.: A geomorphological study of post-glacial uplift with particular reference to Arctic Canada. London: Institute of British Geographers 1970
- Broecker, W.S.: Glacial rebound and the deformation of the shorelines of proglacial lakes. *J. Geophys. Res.* **71**, 4777–4783, 1966
- Brochie, J.F., Silvester, R.: On crustal flexure. *J. Geophys. Res.* **74**, 5240–5252, 1969
- Cathles, L.M.: The viscosity of the earth's mantle. Princeton: Princeton University Press 1975
- Chapman, L.J.: An outlet of Lake Algonquin at Fossmill, Ontario. *Proc. Geol. Assoc. Can.* **6**, 61–68, 1954
- Comer, R.P.: Thick plate flexure. *Geophys. J.R. Astron. Soc.* **72**, 101–113, 1983

- Donner, J.: The determination and dating of synchronous Late Quaternary shorelines in Fennoscandia. In: *Earth rheology, isostasy, and eustasy*, N.-A. Mörner, ed.: pp. 285-293. Chichester: John Wiley 1980
- Eronen, M.: Late Weichselian and Holocene shore displacement in Finland. In: *Shorelines and isostasy*, D.E. Smith, A.G. Dawson, eds.: pp. 183-207. New York: Academic Press 1983
- Farrand, W.R.: Postglacial uplift in North America. *Am. J. Sci.* **260**, 181-199, 1962
- Gunn, R.: A quantitative evaluation of the influence of the lithosphere on the anomalies of gravity. *J. Franklin Inst.* **236**, 47-65, 1943
- Hyvärinen, H., Eronen, M.: The Quaternary history of the Baltic, the northern part. *Acta Univ. Ups. Symp. Univ. Ups. Ann. Quing. Cel.* **1**, 7-27, 1979
- Jeffreys, H.: *The earth, its origin, history and physical constitution*, 6th edn. Cambridge: Cambridge University Press 1976
- McConnell, R.K., Jr.: Viscosity of the mantle from relaxation time spectra of isostatic adjustment. *J. Geophys. Res.* **73**, 7089-7105, 1968
- McGinnis, L.D.: Glacial crustal bending. *Bull. Geol. Soc. Am.* **79**, 769-775, 1968
- Niskanen, E.: On the upheaval of land in Fennoscandia. *Ann. Acad. Sci. Fenn. Ser. A* **53**, 1-30, 1939
- Niskanen, E.: On the deformation of the earth's crust under the weight of a glacial ice-load and related phenomena. *Ann. Acad. Sci. Fenn. Ser. A3* **7**, 1-59, 1943
- Niskanen, E.: On the elastic resistance of the earth's crust. *Ann. Acad. Sci. Fenn. Ser. A3* **21**, 1-23, 1949
- Nye, J.F.: A method of calculating the thickness of the ice-sheets. *Nature* **169**, 529-530, 1952
- Orowan, E.: Contribution to discussion at joint meeting of the British Glaciological Society, the Rheologists' Club and the Institute of Metals. *J. Glaciol.* **1**, 231-236, 1949
- Paterson, W.S.B.: *The physics of glaciers*, 2nd edn. Oxford: Pergamon Press 1981
- Peltier, W.R.: The thickness of the continental lithosphere. *J. Geophys. Res.* **89**, 11303-11316, 1984
- Walcott, R.I.: Isostatic response to loading of the crust in Canada. *Can. J. Earth Sci.* **7**, 716-727, 1970a
- Walcott, R.I.: Flexural rigidity, thickness, and viscosity of the lithosphere. *J. Geophys. Res.* **75**, 3941-3954, 1970b
- Walcott, R.I.: Rheological models and observational data of glacio-isostatic rebound. In: *Earth rheology, isostasy, and eustasy*, N.-A. Mörner, ed.: pp. 3-10. Chichester: John Wiley 1980
- Wolf, D.: On the relation between two-dimensional and axisymmetric loads in plate flexure problems. *J. Geophys. Res.* **54**, 232-235, 1949a
- Wolf, D.: The relaxation of spherical and flat Maxwell earth models and effects due to the presence of the lithosphere. *J. Geophys. Res.* **56**, 24-33, 1949b
- Wolf, D.: Thick-plate flexure re-examined. *Geophys. J. R. Astron. Soc.* **80**, 265-273, 1985a
- Wolf, D.: An improved estimate of lithospheric thickness based on a reinterpretation of tilt data from Pleistocene Lake Algonquin. *Can. J. Earth Sci.* **22**, 768-773, 1985b
- Wolf, D.: The normal modes of a layered, incompressible Maxwell half-space. *J. Geophys. Res.* **57**, 106-117, 1985c
- Wolf, D.: Glacio-isostatic adjustment in Fennoscandia revisited. *J. Geophys. Res.* **59**, 42-48, 1986a
- Wolf, D.: On deglaciation-induced perturbations of the geoid. *Can. J. Earth Sci.* **23**, 269-272, 1986b

Received November 12, 1985; revised version April 10, 1986

Accepted April 17, 1986

Volcanoes, fountains, earthquakes, and continental motion – What causes them?

Wolfgang Kundt and Axel Jessner

Institut für Astrophysik der Universität Bonn, Auf dem Hügel 71, D-5300 Bonn 1, Federal Republic of Germany

Abstract. As a common mechanism for the various volcanic phenomena on Earth we point out a severe disobedience of Poincaré's (von Zeipel's) theorem: hot, gas-rich, high-pressure "fingers" (diatremes) can grow out of the boundary layer above a molten domain and thrust their way up from the asthenosphere toward the surface. The isobars of a planet or moon can look like the surface of a bed of nails. Linear arrays of high-pressure diatremes can drive continental motion. Moreover, we hold the tidal torque responsible for magnetic dynamo action.

Key words: Volcanism – Continental motion – Plate tectonics – Earthquakes – Outgassing – Diatremes – Magnetic dynamo

Introduction

During the past 20 years Wegener's conviction of moving continents has been corroborated by a large body of geophysical evidence (Baumann, 1984; Bonatti and Crane, 1984; Burchfiel, 1983; Closs et al., 1984; Francheteau, 1983; Jordan, 1984; McKenzie, 1983; Moorbath, 1984; Toksöz, 1984; Wilson, 1984; Worsley et al., 1984; Runcorn, 1980; Loper, 1985). At the same time, volcanism and its driving forces have been thoroughly studied and have been related to plate tectonics, continental growth, earthquakes, and mineral deposits (Williams and McBirney, 1979; Dawson, 1980; Huppert and Sparks, 1984; also Tryggvason et al., 1983; Wilson and Head, 1983; Baumann, 1984; Burbank and Reynolds, 1984). Studies of the ocean basins have revealed submarine rifting, seafloor spreading, transform faulting, hot fountains (black smokers), and bizarre ecosystems feeding on H_2S (Sclater and Tapscott, 1984; Bonatti and Crane, 1984; Macdonald and Luyendyk, 1984; Edmond and von Damm, 1984). Moreover, there are the phenomena of mud volcanoes created by escaping gases, predominantly methane and water vapor (Gold and Soter, 1980), of peatlands (Foster et al., 1983), and of combustible gas eruptions during earthquakes most of which are thought to be of biogenic origin but whose mass rates are so high and whose correlations with plate boundaries are so strong that an explanation via outgassing of the Earth's mantle may well be indicated (Gold, 1979; Gold and Soter, 1982; Giardini and Melton, 1983). Note that volcanic gases are predomi-

nantly composed of water vapor plus CO_2 , H_2S , SO_2 , and HCl , whereby these gases dominate at exhalation temperatures increasing from below 100 K (CO_2) up to 900 K (HCl), respectively. Instead, the Earth's interior may be in a more reduced state, with dominating contributions of CH_4 , H_2 , and atomic carbon – as is evidenced by occasional gas inclusions in diamonds and in quartz, by the existence of mud volcanoes, and by measurements on minerals from mafic rocks that cool at high pressures (Mathez, 1984; Freund, 1980), and as is expected in view of the composition of the carbonaceous chondrites which were probably major building blocks of the Earth, at least during late stages of its formation.

In spite of all this detailed knowledge on the geometrical, thermal, and chemical structure of volcanism, fountains, earthquakes, outgassing, and plate tectonics, there does not seem to be a complete understanding of their driving forces and causal connections such that unique predictions for other planets (Mars, Venus) and satellites (Moon, Io) could be made. For instance, it is not clear whether the huge volcanoes and valleys on Mars were formed by lava or by glaciers (cf. Wilson and Head, 1983; Gold, 1978), and the sulfuric volcanoes on Io were a surprising discovery. Furthermore, what is the connection between spin and magnetism? Parker (1983) points out that magnetic dynamos depend on circulation patterns with nonzero helicity (cyclonic convection), but that the almost synchronous planet Mercury ($P_{spin} = 2/3 P_{orbit}$) has a polar field strength of $3.5 \cdot 10^{-7}$ T, whereas the fast-spinning planet Mars has not revealed a magnetic field of its own.

In this paper we point out a disobedience of Poincaré's (von Zeipel's) theorem which states that in a gravitating, rigidly rotating fluid body (of simple chemistry), the level surfaces ($p = \text{const}$, $\rho = \text{const}$, $T = \text{const}$) are all identical and agree with the surfaces of constant geopotential. (Small deviations – the Eddington-Vogt meridional circulation – are caused by a non-conserved cooling flow; they are negligible for cool, slowly spinning planets like Earth. We also ignore long-time-scale rearrangements between highly viscous fluids). Instead, the boundary layer between a fluid domain and a solid crust is unstable to the growth of hot (light, vertical), gas-rich fingers (or channels, pipes, chimneys, diatremes, conduits) which allow low-lying isobars to almost touch the surface, in the shape of a fakir's bed of nails (see Fig. 1). When these fingers end in (porous) sand or clay deposits near the surface with a thickness of at least a few 10^2 m, they may create a mud volcano; when they

end below solid rock, they will blow or melt their way out in the form of an ordinary volcano or kimberlite; and when they pierce a subsurface porous layer, they will pump it up like an air cushion until fissures open and allow a sudden discharge in the form of a shallow earthquake.

The overpressure exerted by a linear array of hot fingers – an “isobaric fence” – is argued to be strong enough to cause continental motion (plate tectonics).

We shall discuss isolated diatremes in Sect. 1, chains of diatremes in Sect. 2, and their various geophysical consequences in Sect. 4. Section 3 is devoted to tidal forces and their possible importance for the magnetic dynamo.

1. Isobars of a Geoid

In a heavy fluid body, the equations of static equilibrium imply that the surfaces of constant pressure and mass density coincide with those of constant potential; in a rigidly rotating body, the potential has to include that of the centrifugal forces.

A different situation arises when solid crust, or lithosphere, overlies a warmer partially molten asthenosphere. As soon as the fluid/solid boundary layer develops small deviations from a planar (spherical) geometry, the domes of this surface tend to be nearer to the melting point than the lower parts because the convective thermal gradient (of the fluid) is smaller than the conductive gradient (of the solid). Moreover, if this liquid contains dissolved gases like CH_4 , H_2 , etc. and dissolved light salts (due to their large ionic radii) like those of the radioactive elements U, Th, and K, these light ingredients will tend to concentrate near the domes.

All three properties, convection, reacting gases, and concentration of radioactive elements, tend to partially melt the ceiling of a dome, thereby enhancing the non-planar geometry: a hot finger (diatreme) starts growing upward. This is clear for the first property because a decreasing pressure (at fixed temperature) tends to induce melting. It is equally clear for radioactive heating. Concerning hydrogen-rich gases, we assume that they are stable in the high-pressure, hot mantle whereas they convert to CO_2 and H_2O near the surface (cf. Gold and Soter, 1982, Fig. 1). Le Chatelier's principle (of the yielding to changes of an intensive thermodynamic variable) then implies that heat is stored in the virtual reaction in which the gases are formed by heating and compression. By conservation of energy, the inverse reaction must be exothermic.

When a dome grows a hot vertical finger, this finger is lighter than its environment because it is hotter and contains more light ingredients. The pressure at the top (ceiling) of the finger is therefore higher than that of its environment. This local overpressure must tear the ceiling, and light gases (or fluids) of low viscosity can enter the fissures, thereby causing overhead stoping (hydraulic fracturing: large chunks of solid rock will sink down the chimney while fresh, hot magma from the mantle rises and replaces them). The longer the finger, the larger the overpressure near its ceiling and the larger the thermal and pressure contrast (see Fig. 1).

Note that our suggested instability of the lithosphere to the growth of hot fingers is different from the ordinary well-studied Rayleigh-Taylor instability of viscous fluids which can give rise to the formation of thermo-chemical plumes in the mantle (Christensen, 1984), or to the forma-

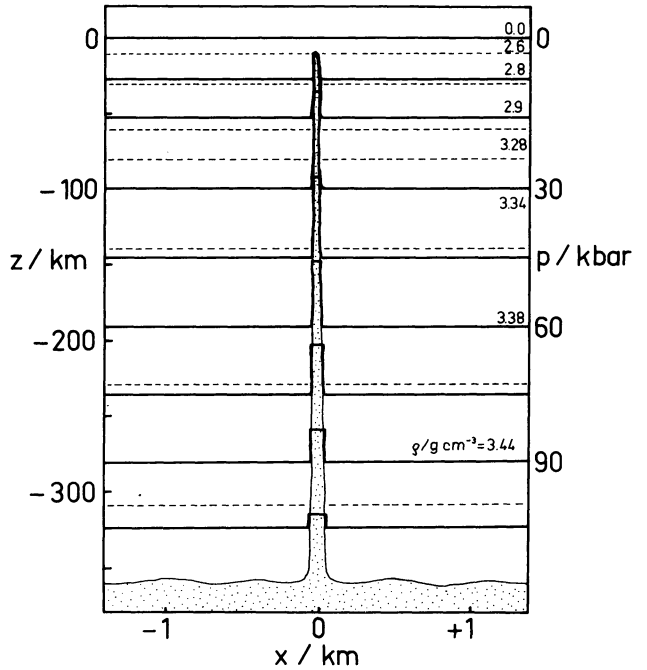


Fig. 1. Schematic isobars (heavy) and density discontinuities (thin and dashed) in the vicinity of a hot finger (diatreme). The horizontal distance scale has been enlarged by a factor of 10^2 . The magma has been assumed to have an average density of $\rho = 2.7 \text{ g cm}^{-3}$. Note that in extreme cases, isobars can jump by more than 50 km in height at the edge of the magma conduit

tion of salt domes in sedimentary strata (Woigt, 1978). Hot fingers grow via overhead stoping through solid rock on the time scale of days to years, whereas plumes grow hydrodynamically on the time scale of My or longer.

Why do we expect the growth of a finger to be stable, i.e., to continue up to the vicinity of the surface? Several conditions have to be satisfied. To begin with, cooling of the finger at its ceiling and along its walls must be compensated. Without exothermic reactions, heat losses per volume q at the ceiling can be overcome by convective replacements (at typical speed v) if the vertical growth rate \dot{z} satisfies

$$\dot{z}/v \leq \zeta c \Delta T / q \quad \text{and} \quad \dot{z}/v \ll 1, \quad (1)$$

where c is the specific heat per volume of the rising magma, ΔT is the temperature contrast between bottom and top of the chimney, and $\zeta \leq 0.5$ measures the degree to which ΔT is used for heating the ceiling. We estimate $\dot{z}/v \lesssim 10^{-1}$ because $q \lesssim c T_{\text{melt}}$ for heating and partial melting.

Secondly, heat losses $2\pi R \Delta z S$ through the wall can be overcome by convective supply $\pi R^2 c \Delta T v$ through a sufficiently large cross section of the chimney (of radius R); the condition reads (for $S = c D \Delta T \approx c D \delta T / R$, D = thermal diffusion coefficient)

$$R \gtrsim 2 [(\Delta z D / v) (\delta T / \Delta T)]^{1/2} \approx 10 \text{ m} (\Delta z_5 / v_{-2})^{1/2}, \quad (2)$$

where Δz_5 stands for $\Delta z / 10^5 \text{ m}$, $v_{-2} := v / 10^{-2} \text{ m s}^{-1}$, and where we have inserted $D = 10^{-6} \text{ m}^2 \text{ s}^{-1}$, $\delta T / \Delta T \approx 3$. Quite likely, convective velocities v can be 10 to 10^2 times larger than inserted, so that heat losses through the walls are unimportant for diameters in excess of a few meters.

A third condition to be met concerns convective instability. For this to be satisfied, the adiabatic temperature gradient $(\nabla T)_{\text{ad}} = (dT/dp)_{\text{ad}} |dp/dz| = \rho g \alpha / c_p$ with ρ = mass den-

sity, g = gravity acceleration, and $\alpha := |\partial \ln \rho / \partial \ln T|_p$ (Lang, 1974, 3–297) must not exceed the structural gradient $|dT/dz| \approx \Delta T / \Delta z$, whence

$$\Delta T / T \gtrsim \rho g \Delta z \alpha / c_p, T = \Delta p \alpha / c_p, T \approx 10^{-2} \Delta z_5 \quad (3)$$

for a chimney height of $\Delta z = 10^5$ m, temperature of $T \gtrsim 10^3$ K, $\alpha \approx 10^{-2}$, and a typical specific heat per volume $c_p = 10^{6.3}$ J/m³ K ~ 0.2 cal/g K. In the absence of friction, a temperature drop of a few K per 10 km in the chimney is therefore well sufficient to maintain convective overturn.

As a fourth condition, wall friction limits the convective velocities v . Clearly, buoyancy forces $\pi R^2 \rho k \Delta T / \langle m \rangle$ in the chimney (with k = Boltzmann's constant, ΔT = structural minus adiabatic temperature difference, and $\langle m \rangle$ = mean atomic weight) must be larger than viscous shear forces $2\pi R \Delta z \eta \nabla v \gtrsim 2\pi \Delta z \eta v$ so that v is bounded by

$$v < R^2 k \Delta T / 2v \Delta z \langle m \rangle = 10^{-1} \text{ m s}^{-1} R_{0.5}^2 \Delta T_2 / \Delta z_5 \quad (4)$$

with $R_{0.5} := R/3$ m, $\Delta T_2 := \Delta T / 10^2$ K, and where we have used $v = \eta / \rho \lesssim 30 \text{ m}^2 \text{ s}^{-1}$ for the kinematic viscosity coefficient v (of silicic magma). Apparently, convective velocities $v \gtrsim 10^{-1} \text{ m s}^{-1}$ are permitted for chimneys of diameters in excess of several meters and driving temperature drops in excess of 1 K/km (cf. Wilson and Head, 1983). Considerably higher surging velocities ($R^2 \Delta T / \Delta z \gg 10^{-2} \text{ K m}$) are needed to explain the formation and survival of xenoliths (Dawson, 1980).

A fifth condition for convective overturn is Rayleigh's criterion, which wants convective heat transport to be fast compared with conductive transport. For vertical pipes, the Rayleigh number

$$Ra := \alpha g \cdot \nabla \ln T R^4 / \nu D = 10^{1.5} (\Delta T / T \Delta z)_{-6} R_1^4 / \nu_{1.5} \quad (5)$$

must be larger than 67 (Landau and Lifshitz, 1966, § 56, exercise 6), where $D \gtrsim 10^{-6} \text{ m}^2 \text{ s}^{-1}$ is the thermal diffusivity of the magma (= thermal conductivity per specific heat), and ν has been inserted for silicic magmas. This criterion is easily satisfied both for deep pipes of mafic magma ($\nu_{1.5} \approx 10^{-4}$) with $R \gtrsim 3$ m and for shorter pipes of silicic magma ($\nu_{1.5} \approx 1$).

Sixthly, we have to argue that the walls of a diatreme can take the enormous overpressures implied by their height and weight contrast (cf. Fig. 1). Drilling experience teaches that hydraulic fracture sets in at overpressures exceeding several 10^2 bar (Williams and Birney, 1979, p. 57). However in our case, the rising magma heats the walls to almost melting temperature so that the rocks tend to expand and flow (rather than tear, like cold rock). Moreover, silicic magma is some 10^8 times more viscous than the aqueous fluids used for hydraulic fracture so that it cannot easily penetrate thin fissures. We therefore expect the walls not to fracture or yield (on the time scale of years) even for pressure differences δp exceeding 10 kbar.

Note that pressure differences δp of this magnitude are needed to throw rock over distances of $d = 10$ km, as has been recorded for volcanic eruptions. The energy $Mv^2/2 = (Mgd/4)(\text{tg } \vartheta + \text{ctg } \vartheta) = Mgd/2\varepsilon$ (with ϑ = elevation angle, $\varepsilon \leq 1$; $\varepsilon = 1$ for $\vartheta = 45^\circ$, $h = d/4$) needed to throw a body of mass M in the Earth's gravitational field over a distance d (with peak height h of the ballistic orbit) must be supplied by a pressure difference δp between bottom and top of the body acting over a distance δx . Here we have ignored air friction. This leads to $\delta p A \delta x \geq Mgd/2\varepsilon$ where A is the

cross-sectional area. Now for $d \approx 10$ km, v must be on the order of the speed of sound in air. Such a high speed can be acquired inside a gun but not inside a diatreme. Consequently, the driving pressure δp can only act near the outlet, where the pipe widens conically, and must quickly drop to zero. We write $\xi := A \delta x / V$, where $V := M/\rho$ is the volume of the body, and estimate $\xi \lesssim 0.5$. This leads to

$$\delta p \geq \rho g d / 2 \xi \varepsilon = 3 \text{ kbar } (d_4 / 2 \xi \varepsilon). \quad (6)$$

Very likely, $2\xi\varepsilon \ll 1$ holds so that pressure differences (in the released and expanding gases) on the order of 10 kbar at the outlet of a diatreme are needed to throw rock over a distance of 10 km.

On top of meeting these elementary constraints, a hot finger cannot grow quasi-cylindrical unless the conditions at its ceiling are highly inhomogeneous, favoring a tearing and melting near the highest point; it would otherwise open up in the shape of an inverted cone. Most likely, an excess of light (and combustible) gases near the highest point helps to keep a hot finger thin.

Naively one might think that convection establishes an ordered circulation pattern with fresh, hot magma rising near the axis and colder material falling near the walls. The necessary horizontal temperature gradient would imply a horizontal density gradient (for homogeneous chemistry) which in turn would imply higher pressures near the axis than near the walls (for a uniform pressure at the bottom of the finger). The resulting horizontal pressure gradient would cause the light, hot component to move toward the walls, and the colder, descending component toward the central region, thereby wiping out the horizontal temperature gradient. Consequently, there cannot be horizontal gradients inside a chimney. Rather, the colder component is expected to sink in the form of chunks or drops through the rising, warmer component. The pattern may be stabilized by the fact that the necessary horizontal gradients near the walls will send cooler (heavier) material toward the axis, thereby preventing freezing from the sides.

The real structure of a hot finger will be further complicated by the presence of double-diffusive convection which can drive vertical mass exchange and establish compositional gradients. Huppert and Sparks (1984) speak of "convective fractionation" when they discuss the consequences of density changes during partial crystallization (see also Spera et al., 1984). In particular, thin laminar boundary-layer flows can form. Of course, the growth of a finger will not only depend on its own chemistry but also on the inhomogeneous structure of the lithosphere and crust through which it pushes its way up and on the conditions which it meets near the planetary surface. We shall discuss a number of such possibilities in the last section.

2. Plate tectonics

The lithospheric plates move with respect to each other at speeds reaching and exceeding 10^{-1} m/y. Along their divergence zones (spreading axes), hot magma surges and replenishes the crust, while at the opposite end the pushed, cooled plate is forced underneath an adjacent plate in the form of a subduction zone because plate area is conserved (see Fig. 2). What drives this motion?

It is often believed that convective motions inside the (upper) mantle are responsible for the motion of the continents so that the driving power is convective cooling of

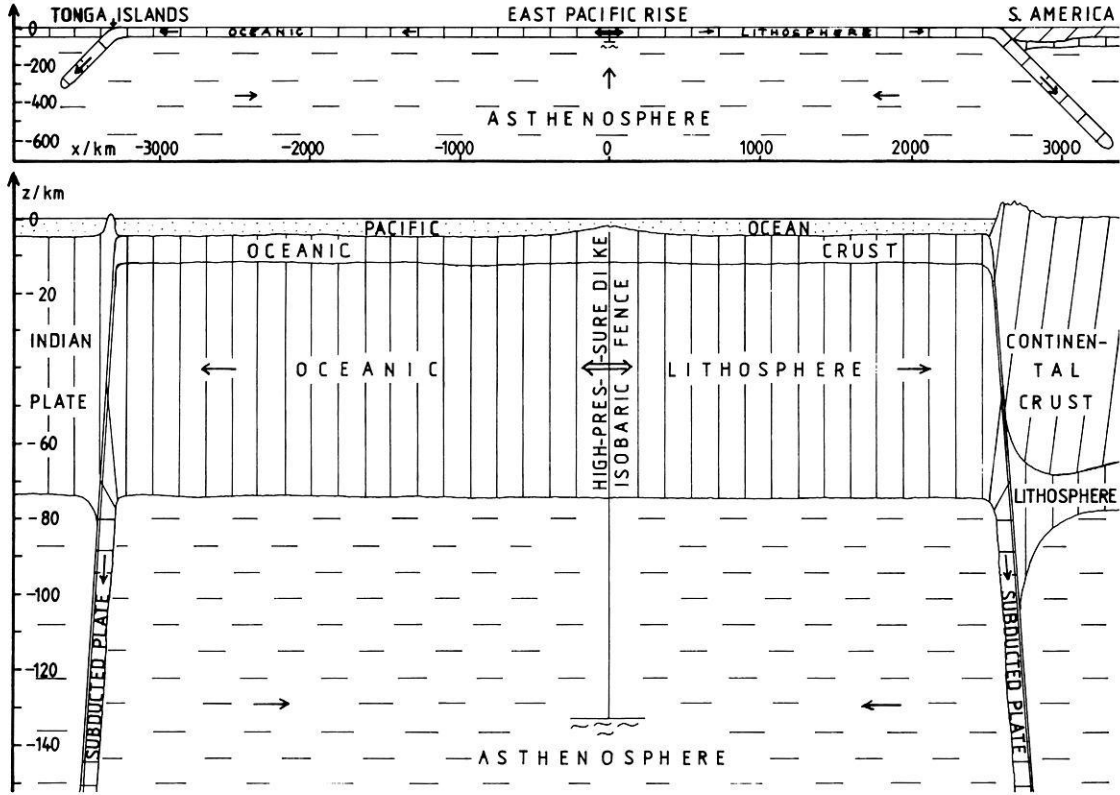


Fig. 2. Cross section through the lithosphere underneath the South Pacific ocean; upper drawing to scale, lower drawing the same with vertical scale enlarged 20-fold. Oceanic crust and lithosphere (total thickness of 70 km) move apart along the East Pacific Rise at a speed of some 15 cm/y and are subducted at the Tonga trench in the west and below the Andes in the east where they descend at an angle of $\approx 45^\circ$. Note how thin a layer is moving. We hold a deep-rooted, high-pressure dike responsible for propelling this global circulation; the dike pushes the two plates apart with an overpressure on the order of unity

the Earth's interior (e.g., Runcorn, 1980; Loper, 1985). But why are such motions preferentially oriented east-west, whereas surface temperature gradients are oriented north-south, and why are there only some six large plates instead of thousands of small ones?

Along a divergence zone hot magma rises to the seafloor in the form of a chain of small volcanoes (hot fingers) or a sheet (dike) of rising magma. In such a hot dike, overpressures must build up intermittently which are comparable to the ones evaluated in the last section: the nailboard of isobars degrades into an "isobaric fence." Such an isobaric fence must have the same effect as an array of wooden wedges which can split stone when watered or as a number of high-pressure concrete injections into the ground that can lift a building. The fence pushes adjacent plates apart. Essentially this same mechanism has been reviewed by Jacoby (1980) and credited to Lliboutry (1972).

In order to see quantitatively that a chain of high-pressure vertical pipes can push two plates apart, we estimate the shear modulus μ of solid rock by

$$\mu \lesssim p \approx \rho g h = 10^9 \text{ Jm}^{-3} h_{4.5}, \quad (7)$$

where h is the height of an oceanic plate, on the order of 30 km. Somewhat more reliable would be the molecular estimate

$$\mu \lesssim e^2 (2a)^{-4} (m_e/m_p)^{1/2} = 4 \cdot 10^{10} \text{ Jm}^{-3} \quad (8)$$

for the shear modulus μ of "crud" (Press and Lightman, 1983; a = Bohr's radius) which agrees with the values deter-

mined both from the propagation of shear waves ($\mu = \rho v_s^2$) and with the reaction of the mantle to tidal forces (Jeffreys, 1970) but which tends to overestimate the long-term yield strength of realistic crust material by a factor on the order of 10^2 . We shall prefer Eq. (7) because of its simplicity, yet keep in mind that it must not be applied to very shallow or very deep layers. Note that in a fluid mantle, shear forces would be due to viscosity, with $\mu = \eta |\nabla v|$, where η is the dynamic viscosity, on the order of $\lesssim 10^6$ poise ($= 10^5 \text{ Ns/m}^2$) for silicic (acid) magmas (near the surface) and on the order of 10^2 poise for (deeper) mafic (alkalic) magmas (e.g., Huppert and Sparks, 1984). An equality of solid shear stresses with viscous shear stresses would therefore ask for shear velocity gradients $|\nabla v| = v/h$ on the order of

$$v \lesssim \rho g h^2 / \eta = 10^{8.5} \text{ m s}^{-1} (h_{4.5}^2 / \eta_5), \quad (9)$$

which correspond to relative velocities near that of light. We infer that fluid viscosity is negligible compared with that of a solid.

Let us then equate the force $\delta p h l$ – exerted by a temporary overpressure fence of height h (between 50 and 10^2 km) onto the face of a square-shaped lithospheric plate of length l ($\approx 10^3$ km) – with the shear force $\mu l b$ needed to push the plate across an effective area $l b$ of solid resistance (the path length b is expected to be on the order of the penetration depth of the plate into the subduction zone). We find that

$$\delta p / p \lesssim b / h; \quad (10)$$

i.e., the needed overpressure $\delta p/p$ is on the order of unity. This estimate is uncertain because it is not clear whether the plate rides on a convection cell of the upper mantle, and whether its diving front end can locally crumble or melt the rock into which it submerges. Additionally, the effective shear modulus μ may be smaller than ρgh when the rock has structural flaws. However, the estimate suggests that temporary overpressures on the order of unity can push two plates apart under favorable circumstances. A glance at Fig. 1 shows that such temporary overpressures can be provided by a dense chain of rising hot fingers, each of which acts as a spreading center.

The literature often declares buoyancy forces to be responsible for causing plate motion (e.g., Loper, 1985). "Buoyancy forces" are understood as vertical forces exerted by a fluid medium on immersed objects; such forces per area are on the order of $\delta\rho gh$, where $\delta\rho$ is the difference in mass density, and h is the vertical extent of an immersed object. In contrast, the pressures $\delta p \approx \rho gh$ exerted by a deep-rooted isobaric fence can be some $\rho/\delta\rho \approx 10^2$ times higher and, moreover, act as a horizontal thrust, not a vertical pull (cf. Fig. 2).

The overpressure δp exerted by a hot finger discharges when the finger reaches the surface (seafloor). During a lava ejection, the pressure relaxes and the finger cools. An isobaric fence is therefore not static: it behaves like a collection of relaxation oscillators. Its overpressure builds up in a quasi-periodic fashion. It derives its power from thermal convection in the mantle during which hot magma rises in a divergence zone and cooler material sinks at the other end of the plate in the subduction zone.

We can therefore estimate the T -gradient of seafloor spreading from the condition that the buoyant energy gain per time, $P_{\text{therm}} \approx l b v n (f/2) k \Delta T$, in the rising column of a global convection cell balance the dissipative losses $P_{\text{diss}} \approx \mu l b v$ (mainly at the other end of the cell (subduction zone)). Here it is assumed that the plate floats on the convection cell so that the speed v of its horizontal motion equals the average convective speed of the rising magma, and that the width b of the rising column is comparable with the width of the resistive zone. ΔT is the driving temperature difference between bottom and top of the cell, $n = \rho / \langle m \rangle =$ atomic number density, $f =$ number of thermal degrees of freedom ≈ 3 , and $k =$ Boltzmann's constant. From the condition $1 \lesssim P_{\text{therm}}/P_{\text{diss}}$ with $\mu \lesssim \rho gh$ we thus find

$$1 \approx f k \Delta T / 2 \langle m \rangle g h \approx (\Delta T)_3 / h_5 \quad (11)$$

for $\Delta T \approx 10^3$ K and a plate height h of 10^2 km, in remarkable agreement with the observations. This estimate shows that convection cells can power plate motion once they are set up.

There is, however, the yet open question of stability: How did the large-scale convection cells come into existence, i.e., why did Pangea break up some $2 \cdot 10^8$ y ago and why does continental motion persist? The (present) heat-energy content of the $3 \cdot 10^3$ -K Earth is some $10 k T / \langle m \rangle R^2 \Omega^2 \approx 10^2$ times larger than its (present) rotational energy, and some $k T R / \langle m \rangle g (\Delta h)^2 = 10^6 (\Delta h)_3^{-2}$ times larger than the energy $\rho g A (\Delta h)^2 / 2$ of gravity anomalies due to changing surface loads (such as the melting of ice). We therefore consider volcanism (convective cooling) the only viable powerhouse for driving continental motion. Isobars in the shape of an oscillating bed of nails are likely to make the

shells move wherever the former cluster in linear arrays, i.e., wherever they form fences.

At this point, smaller energy reservoirs may enter the scene in controlling the initial location of the volcanic diatremes, thereby enforcing the observed large-scale plate morphology. Such causes for large-scale order are (1) continental insulation (causing a heat accumulation and melting under central parts of a continent), (2) a (minor) shrinking of the cooling Earth (causing the thin lithosphere to wrinkle), (3) a wandering of positive gravity anomalies toward the equator (thereby changing the curvature of a continental shell; Anderson, 1984), (4) localized tidal dissipation (causing the upper mantle to melt preferentially in inelastic regions of the equatorial belt); and (5) cratering by impact: their circular edges are natural sites for subduction zones. Either one or a combination of these processes is likely to have caused an inhomogeneous shape of the initial "isobaric nailboard," with high-pressure volcanic fences being preferentially arranged in strips aligned with meridional circles, predominantly so along an equatorial belt.

Once the lithosphere starts tearing along a few fissures filled with hot (light) magma, a convective circulation pattern in the mantle can be started that has local (≥ 10 km) negative gravity anomalies above the rising columns (=spreading axes; Macdonald and Luyendyk, 1984) and extended (≥ 300 km) positive gravity anomalies above the sinking columns (=subduction zones; Toksöz, 1984). The likewise observed extended (≥ 300 km) positive gravity anomalies around spreading axes (Dixon and Parke, 1983) can be understood as the result of horizontal thrusting: the pushed plate bulges up. Enhanced cooling of an aging oceanic plate guarantees that sinking columns of a convection cell are kept cooler than rising ones, thereby keeping the heat engine at work. The idealized pattern of hot, upwelling magma closing the gaps between diverging plates whose cool opposite ends sink and fuse with the upper mantle appears to be dynamically stable when one accepts the presence of high-pressure volcanic conducts which push the plates apart. Note that in the absence of such quasi-permanent over-pressure along the spreading axes, the moving plates are likely to be arrested by friction forces and the fissures likely to freeze. Continental shell motion owes its existence to a drastic violation of Poincaré's law.

3. Tidal torque and the magnetic dynamo

The present spin of Earth is controlled by tidal forces; let us compare them with the forces controlling plate tectonics. The tidal torque T exerted by one body of a celestial binary system onto its companion is given by (cf. Goldreich and Peale, 1968)

$$T = (3k/2)(GM_*^2 R^5/a^6) \sin 2\delta. \quad (12)$$

Here, M_* is the mass of the disturbing body, R is the radius of the disturbed body, a is their separation, $k := (3/2)(1 + 19\mu/2g\rho R)^{-1}$ is the "tidal Love number," and δ is the (small) phase lag angle of the tidal bulge. δ is related to the Q factor of the tidal oscillations by $\tan 2\delta = Q^{-1}$, where Q for the Earth's mantle is probably of order 10^3 (Lambeck, 1980).

However, oceanic tides achieve much stronger dissipation, corresponding to a (present) effective $Q = 12$ or $\sin 2\delta = 0.08$. Together with an empirical $k = 0.3$, one thus obtains for the present tidal torque exerted on Earth

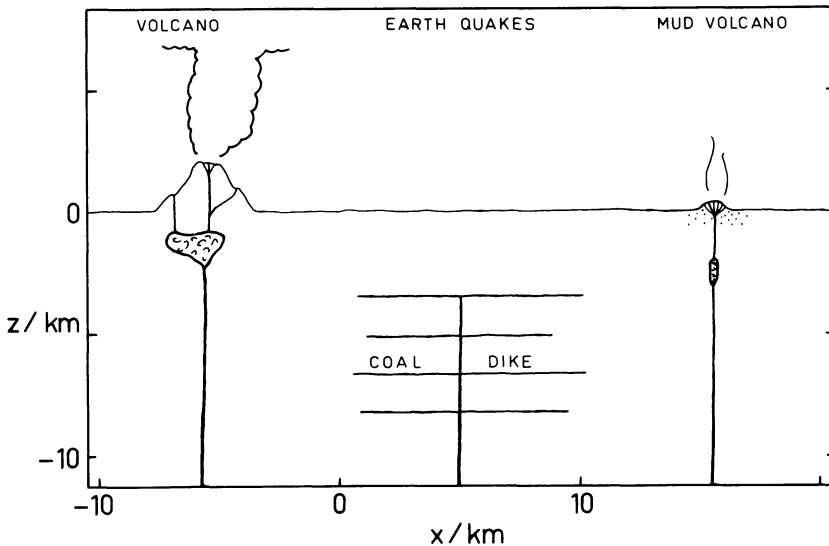


Fig. 3. Sketch of the different expected surging modes of a hot finger (diatreme) depending on the ground structure near the surface. A cap rock gives rise to volcano formation, a sand layer to the formation of a mud volcano, and a porous subsurface layer (of biogenic origin) can lead to (shallow) earthquakes and to the formation of coal seams

$$T_{\oplus} = 5.3 \cdot 10^{16} \text{ N m}, \quad (13)$$

in which the Sun has a share of 21%. For a moment of inertia $I \approx MR^2/3 = 0.8 \cdot 10^{38} \text{ kg m}^2$, this torque corresponds to the observed present average growth rate of $2 \cdot 10^{-5} \text{ s/y}$ of the length of the day. Note that this rate would be some 10^2 times smaller if the effective Q were $\approx 10^3$, i.e., if there were no oceans on Earth.

The tidal forces are much smaller on the average than the volcanic forces which are thought to push the continental plates: the volcanic forces acting east-west across one midoceanic ridge exert a partial torque $phlR \lesssim \rho gh^2 lR \approx 10^{27.5} \text{ N m h}_5^2$ which is some 10^{11} times stronger than the tidal torque. Nevertheless, tidal forces may not be negligible for three reasons: (1) they can be much stronger locally when oceans are excited not too far from resonance, (2) their dissipated energy is an inhomogeneous heat source for the Earth's crust (as noted above), and (3) their net torque does not vanish so that they brake the spin motion.

If essentially the whole tidal torque on Earth is exerted through its oceans, the interior of the planet must be decelerated through internal shear forces rather than through smooth gravitational (body) forces. The implied average shear modulus $\langle \mu \rangle$ is given by

$$\langle \mu \rangle = T/2\pi R^3 = 3 \cdot 10^{-5} \text{ N m}^{-2}. \quad (14)$$

When compared with Eqs. (7) and (8), this needed shear modulus is some 10^{13} times smaller than that of solid rock. A layer of mafic magma, on the other hand, would need a (large!) shear-velocity gradient of $|\nabla v| \geq 3 \cdot 10^{-6} \text{ s}^{-1}$ in order to transfer the torque, which corresponds to a velocity profile of 1 mm s^{-1} across 300 m. We conclude that a solid Earth would rotate rigidly whereas the existence of a fluid layer implies differential rotation.

Now it is known from the propagation of shear waves, the weak response of Earth to tidal forces, and its near-rigid free precession that the mantle behaves almost like a solid body with a (large) effective viscosity $\eta = \mu\tau$ in excess of several 10^{20} poise (cf. Jeffreys, 1970, p. 345). On the other hand, the closeness of the mantle to isostatic equilibrium and the feasibility of continental motion set a rough upper limit of $\eta \lesssim 10^{23}$ poise, because Maxwell's relaxation time scale τ (for plastic flow of the asthenosphere) is on the order

of $\tau = 10^{5.5 \pm 1} \text{ y}$ (see also Vetter et al., 1980). However, it is equally known that the outer core is fluid. Consequently, we expect the Earth's core to be less decelerated than the mantle, i.e., to spin faster. Instead, magnetic anomalies are known to drift westward during the past (at least) 300 y at an equatorial speed of 0.64 mm s^{-1} (Lambeck, 1980; Morrison, 1985; Bloxham and Gubbins, 1985).

If we interpret the westward drift of the magnetic anomalies as a relative rotation between the flux-generating core and the mantle, we are forced to conclude that the spin of the core oscillates, coupled to the mantle by the magnetic field. According to Eq. (14), the necessary toroidal magnetic field component B_{ϕ} amounts to

$$B_{\phi} = 8\pi \langle \mu \rangle / B = 10^{-6} \text{ T} \quad (15)$$

for a total field B of 1 Gauß ($= 10^{-4} \text{ T}$). Its oscillation period P would be given by

$$P = 2\pi [I_{\text{core}} / (dT/d\theta)]^{1/2} = 2 \cdot 10^3 \text{ y} (d \ln T/d\theta)^{-1/2}, \quad (16)$$

where $I_{\text{core}} \approx 5 \cdot 10^{36} \text{ kg m}^2$ is the estimated moment of inertia of the core, and $dT/d\theta$ is the change in the torque per change in the torsion angle between core and mantle (= torsion constant). $d \ln T/d\theta$ would be on the order of 10^2 if the magnetic fields were also anchored in the (decelerated) mantle, but may well be $\lesssim 10$ due to the poor electrical conductivity of the latter. We thus arrive at the prediction that the magnetic anomalies fluctuate with a period on the order of 10^3 y .

This interpretation of a magnetic coupling between core and mantle of a spun-down planet suggests that the tidal torque may be driving the magnetic dynamo. It is supported by the fact that the magnetic dipole moments of Mercury, Venus, Earth, Moon, and Mars do not scale as their angular velocities but rather as their tidal decelerations (cf. Parker, 1983).

4. Volcanic activities

The surfaces of several planets and satellites are controlled by volcanism. This is already indicated by the fact that the highest mountains tend to be as high as they can be given the finite yield strength of the underlying lithosphere

(cf. Weisskopf, 1975) and despite efficient erosive processes. On the present Earth, crustal volume is newly created at a rate of $\dot{V} \lesssim 10^{2.5} \text{ m}^3 \text{ s}^{-1}$ by seafloor spreading along the oceanic ridges. The ejection by one volcano like Tambora (1815) every 10^2 y would amount to $\dot{V} \approx 10^2 \text{ m}^3 \text{ s}^{-1}$ (Stothers, 1984), and the remaining ≥ 600 active volcanoes together do not fall behind by a large factor (cf. Williams and McBirney, 1979; LaMarche and Hirschboeck, 1984). The erosive volume rate is (independently) estimated as $\dot{V} \approx 10^2 \text{ m}^3 \text{ s}^{-1}$, or $\dot{M} = 10^{5.5} \text{ kg s}^{-1}$, as is to be expected for a steady state.

The Earth has a volume V of 10^{21} m^3 . A present volcanic volume rate of $\dot{V} \lesssim 10^{2.5} \text{ m}^3 \text{ s}^{-1}$ therefore means that $\lesssim 0.05 V$ has been turned over throughout its history, ignoring a likely higher rate at earlier times. If only the upper mantle (with a volume of $\lesssim 0.3 V$) has participated in this overturn, its average overturn probability exceeds 10%. These numbers illustrate the importance of volcanism for the surface structure of our planet. What are the causes for such an activity?

We propose that the ejection of mantle material to the surface is brought about by the formation of hot fingers, due to the instability of a liquid/solid boundary layer. Clearly, such volcanic activity culminates in divergence zones. Note that there are no mass ejections along transform faults even though crustal rocks have slid past each other: without a local overpressure, torn crust is welded again and no ejection occurs. On the other hand, volcanoes can form in the middle of a plate in a static region through the action of a hot spot which we interpret as a large (old) hot finger (cf. McKenzie, 1983; Anderson, 1984). Given our above estimates, such fingers very likely cannot pierce a lithosphere of arbitrary thickness, nor could they have pierced the present lithosphere of Earth without the help of dissolved gases and/or radioactive elements. It is not clear to us whether past measurements have been able to discriminate between radioactive heating of the crust and heating by nonemerged hot fingers (cf. O'Nions and Oxburgh, 1983).

At this point, it is time to discuss the different ways in which a hot finger can make its appearance at the surface. The most spectacular form of volcanism is encountered when the rising magma does not intersect a loose or porous layer so that it conserves its enormous overpressure until very near the surface (≥ 300 m). It can then lift the ground, blow off the top of a mountain, and eject material at velocities of $\lesssim \text{km s}^{-1}$ to heights in excess of 30 km. Kimberlites are another form of remnant of such pyroclastic events. How much material is ejected will depend on the geometry of the diatreme (hot finger), i.e., on its diameter, length, and in particular on the existence of large high-pressure magma chambers which can form on encounter with an easily melting zone. Another necessary condition for explosive ejection is a (silicic, acid) magma of high viscosity ($\eta \lesssim 10^6$ poise) so that the dissolved gases (H_2O , CO_2 , etc.) cannot escape beforehand through thin fissures. Note that during the explosion, their volume increases by a factor of $\lesssim 10^3$. If such a discharge happens under the surface of the ocean, a tsunami will result.

In the case of (mafic, alkalic) magmas of low viscosity ($\eta \approx 10^2$ poise), on the other hand, the formerly dissolved gases will largely escape before outburst, thereby releasing the enormous overpressure and giving rise to fire fountains and/or magma flows. Near the surface of a volcano, a hot finger can branch into several and give rise to independent

outbursts. A stagnating side branch may thereby freeze and lock itself off from the main conduct.

A rising, mafic magma finger may also grow into a porous surface layer, with a thickness of several 10^2 m, through which the gases can easily escape. Its first outburst may be violent, but subsequent outbursts need no longer supply hot, burnt gases. We get a cool mud volcano, inside of which a substantial fraction of the dissolved H_2O vapor has condensed out (whence the mud).

When a mafic magma finger pierces a subsurface porous layer (of biogenic origin) its partially dissolved gases will penetrate this layer and pump it up like an air cushion. This process may take several years and extend horizontally over several 10^2 km. When a critical thickness of the cushion is reached, the gas will eventually find a way out, i.e., we get an earthquake. Another possibility is peaceful, steady outgassing observed particularly in lakes and valleys. In all these cases, however, we think that the escaping gases made most of their way up through one of those diatremes in the form of channelled surging which is much faster than any diffusive process. There may be many more diatremes than volcanoes.

If this scheme is correct, it implies that an earthquake which is unrelated to a moving plate boundary marks the momentary end of an episode during which a layer of biogenic origin is exposed to high-pressure gases of hydrocarbonic composition. The regularity, thickness, large extent, and carbon enrichment of coal seems may thus find a natural explanation (cf. Fig. 3).

Another corollary of our thesis is that crystals which only form under high pressure, like diamonds, need not have formed at a depth h given by $h = p/\rho g$: they may well have formed nearer to the surface in a high-pressure diatreme and may have been convected upward and ejected during one of the subsequent eruptions. The isobars of a partially solid planet or moon can grossly deviate from equipotentials.

Acknowledgements. Our interest in these problems has been raised by Tom Gold during his stay at Bonn in 1982. Thereafter, a number of scientists have been very helpful in confronting us with geophysical facts and literature, among them Franz Görlich, Wolfgang Priester, Karl-Friedrich Seifert, Agemar Siehl, Klaus Vieten, Karl Fuchs, Larry McKenna, and two anonymous referees. We thank all of them for their patience. We also acknowledge conversations with Marko Robnik.

References

- Anderson, D.L.: The Earth as a planet: paradigms and paradoxes. *Science* **223**, 347–355, 1984
- Baumann, L.: Die Zyklicität in der Plattentektonik und in den zugehörigen metallogenetischen Prozessen. *Z. geol. Wiss. Berlin* **12**, 141–173, 1984
- Bloxham, J., Gubbins, D.: The secular variation of Earth's magnetic field. *Nature* **317**, 777–781, 1985
- Bonatti, E., Crane, K.: Oceanic fracture zones. *Sci. Amer.*, May, 36–47, 1984
- Burbank, D.W., Reynolds, R.G.H.: Sequential late Cenozoic structural disruption of the northern Himalayan foredeep. *Nature* **311**, 114–118, 1984
- Burchfiel, B.C.: The continental crust. *Sci. Amer.*, September, 86–97, 1983
- Christensen, U.: Instability of a hot boundary layer and initiation of thermochemical plumes. *Annales Geophysicae* **2**, 311–320, 1984

- Closs, H., Giese, P., Jacobshagen, V.: Alfred Wegeners Kontinentalverschiebung aus heutiger Sicht. In: *Ozeane und Kontinente, Spektrum der Wissenschaft*, Heidelberg, pp. 40–53, 1984
- Dawson, J.B.: *Kimberlites and their Xenoliths*. Berlin, Heidelberg, New York: Springer 1980
- Dixon, T.H., Parke, M.E.: Bathymetry estimates in the southern oceans from Seasat altimetry. *Nature* **304**, 406–411, 1983
- Edmond, J.M., von Damm, K.: Heiße Quellen am Grund der Ozeane. In: *Ozeane und Kontinente, Spektrum der Wissenschaft*, Heidelberg, pp. 216–229, 1984
- Foster, D.R., King, G.A., Glaser, P.H., Wright, H.E. jr.: Origin of string patterns in boreal peatlands. *Nature* **306**, 256–258, 1983
- Francheteau, J.: The oceanic crust. *Sci. Amer.*, September, 68–83, 1983
- Freund, F.: Atomic carbon in magnesium oxide. *Mat. Res. Bull.* **15**, 1767–1772, 1980
- Giardini, A.A., Melton, Ch.E.: A scientific explanation for the origin and location of petroleum accumulations. *J. Petroleum Geology* **6**, 117–138, 1983
- Gold, T.: Mars, the icy planet. *COSPAR proceedings*, Innsbruck, May 1978
- Gold, T.: Terrestrial sources of carbon and earthquake outgassing. *J. Petroleum Geology* **1**, 3–19, 1979
- Gold, T., Soter, St.: The deep-earth-gas hypothesis. *Sci. Amer.*, June, 130–137, 1980
- Gold, T., Soter, St.: Abiogenic methane and the origin of petroleum. *Energy Exploration & Exploitation* **1**, 89–103, 1982
- Goldreich, P., Peale, S.J.: The dynamics of planetary rotations. *Ann. Rev. Astron. Astrophys.* **6**, 287–320, 1968
- Huppert, H.E., Sparks, R.S.J.: Double-diffusive convection due to crystallization in magmas. *Ann. Rev. Earth Planet. Sci.* **12**, 11–37, 1984
- Jacoby, W.R.: Plate sliding and sinking in mantle convection and the driving mechanism. In: *Mechanisms of continental drift and plate tectonics*, P.A. Davies, S.K. Runcorn (eds.), pp. 159–172. London: Academic Press 1980
- Jeffreys, H.: *The Earth, its origin, history, and constitution*, 5th edn. London: Cambridge University Press 1970
- Jordan, T.H.: Die Tiefenstruktur der Kontinente. In: *Ozeane und Kontinente, Spektrum der Wissenschaft*, Heidelberg, pp. 94–105, 1984
- LaMarche, V.C. jr., Hirschboeck, K.K.: Frost rings in trees as records of major volcanic eruptions. *Nature* **307**, 121–126, 1984
- Lambeck, K.: *The Earth's variable rotation: Geophysical causes and consequences*. London: Cambridge University Press 1980
- Landau, L.D., Lifshitz, E.M.: *Theoretische Physik VI, Hydrodynamik*, Akademie-Verlag, Berlin, 1966
- Lang, K.R.: *Astrophysical Formulae*. Berlin, Heidelberg, New York: Springer 1974
- Lliboutry, L.: The driving mechanism, its source of energy, and its evolution studied with a three-layer model. *J. Geophys. Res.* **77**, 3759–3770, 1972
- Loper, D.E.: A simple model of whole-mantle convection. *J. Geophys. Res.* **90** B2, 1809–1836, 1985
- Macdonald, K.C., Luyendyk, B.P.: Tauchexpedition zur ostpazifischen Schwelle. In: *Ozeane und Kontinente, Spektrum der Wissenschaft*, Heidelberg, pp. 200–215, 1984
- Mathez, E.A.: Influence of degassing on oxidation states of basaltic magmas. *Nature* **310**, 371–375, 1984
- McKenzie, D.P.: The Earth's Mantle. *Sci. Amer.* September, 51–62, 1983
- Moorbath, St.: Die ältesten Gesteine. In: *Ozeane und Kontinente, Spektrum der Wissenschaft*, Heidelberg, pp. 80–93, 1984
- Morrison, L.: The day time stands still. *New Scientist* 27 June, 20–21, 1985
- O'Nions, R.K., Oxburgh, E.R.: Heat and helium in the Earth. *Nature* **306**, 429–431, 1983
- Parker, E.N.: Magnetic fields in the Cosmos. *Sci. Amer.*, August, 36–46, 1983
- Press, W.H., Lightman, A.P.: Dependence of macrophysical phenomena on the values of the fundamental constants. *Philos. Trans. R. Soc. London* **A310**, 323–336, 1983
- Runcorn, S.K.: Some comments on the mechanism of continental drift. In: *Mechanisms of continental drift and plate tectonics*, P.A. Davies, S.K. Runcorn eds.: pp. 193–198. London: Academic Press 1980
- Sclater, J.G., Tapscott, Ch.: Die Geschichte des Atlantik. In: *Ozeane und Kontinente, Spektrum der Wissenschaft*, Heidelberg, pp. 118–130, 1984
- Spera, F.J., Yuen, D.A., Kemp, D.V.: Mass transfer rates along vertical walls in magma chambers and marginal upwelling. *Nature* **310**, 764–767, 1984
- Stothers, R.B.: The Great Tambora eruption in 1815 and its aftermath. *Science* **224**, 1191–1197, 1984
- Toksöz, M.N.: Die Subduktion der Lithosphäre. In: *Ozeane und Kontinente, Spektrum der Wissenschaft*, Heidelberg, pp. 106–116, 1984
- Tryggvason, K., Husebye, E.S., Stefansson, R.: Seismic image of the hypothesized icelandic hot spot. *Tectonophysics* **100**, 97–118, 1983
- Vetter, U.R., Strehlau, J.F., Meissner, R.O.: Viscosity estimates of the lithosphere and asthenosphere. In: *Mechanisms of continental drift and plate tectonics*, P.A. Davies, S.K. Runcorn eds.: pp. 295–303. London: Academic Press 1980
- Weisskopf, V.F.: Of atoms, mountains, and stars: a study in qualitative physics. *Science* **187**, 605–612, and **188**, 783, 1975
- Williams, H., McBirney, A.R.: *Volcanology*. San Francisco: Freeman, Cooper & Co, 1979
- Wilson, J.T.: Kontinentaldrift. In: *Ozeane und Kontinente, Spektrum der Wissenschaft*, Heidelberg, pp. 10–25, 1984
- Wilson, L., Head, J.W. III.: A comparison of volcanic eruption processes on Earth, Moon, Mars, Io and Venus. *Nature* **302**, 663–669, 1983
- Woidt, W.-D.: Finite element calculations applied to salt dome analysis. *Tectonophysics* **50**, 369–386, 1978
- Worsley, T.R., Nance, D., Moody, J.B.: Global tectonics and eustasy for the past 2 billion years. *Marine Geology* **58**, 373–400, 1984

Received October 31, 1985;
revised version January 17 and July 3, 1986
Accepted July 8, 1986

Magnetic properties and oxidation experiments with synthetic olivines $(\text{Fe}_x\text{Mg}_{1-x})_2\text{SiO}_4$, $0 \leq x \leq 1$

V. Hoffmann and H.C. Soffel

Institut für Allgemeine und Angewandte Geophysik der Universität,
Theresienstrasse 41, D-8000 München 2, Federal Republic of Germany

Abstract. Olivines with the composition of $(\text{Fe}_x\text{Mg}_{1-x})_2\text{SiO}_4$ with $x=0.1, 0.3, 0.5, 0.7, 0.9$, and 1.0 have been synthesized using a modification of the method by Hoye and O'Reilly (1972). The structural and magnetic properties of the olivines have been tested with X-ray powder pattern studies and the measurement of the magnetic susceptibility and its variation with temperature. The specific susceptibility X_g at room temperature, the Curie constant C_g and the asymptotic Curie temperature θ_a , the Néel temperature T_N , and the transition temperature T_i were found to vary systematically with x thus confirming and extending the results obtained by Hoye and O'Reilly (1972). The oxidation experiments were done in air at various temperatures up to 700°C and heating times up to 70 h. The resulting ferrimagnetic phases in the olivines have been identified with magnetic measurements and X-ray studies.

Key words: Rock magnetism – Olivine – Oxidation – Magnesianoferrite – Paleomagnetism

Introduction

Many natural silicates contain inclusions of ferrimagnetic minerals which alter their magnetic properties from paramagnetism to antiferromagnetism or even weak ferrimagnetism. Due to these ferrimagnetic inclusions a remanent magnetization can be produced in these rocks which is often related to a metamorphic event. If the generation of the ferrimagnetic inclusions occurred at appreciably lower temperatures than the blocking temperatures, the thus formed remanence is generally called a chemical remanent magnetization (CRM). In cases where higher temperatures are involved, a partial thermoremanent magnetization (PTRM) or even a thermoremanent magnetization (TRM) may result. Due to the often extremely small size of the ferrimagnetic phases they can generally not be observed with reflected-light microscopes and often not by X-ray powder diffraction methods as well. Electron microscope studies, Mössbauer spectroscopy, and magnetic measurements are reliable methods to identify these phases.

An essential prerequisite for the generation of ferrimagnetic inclusions in silicates by oxidation processes is the presence of iron, either as a principle constituent in the minerals or as an accessory cation. Therefore, such fre-

quently occurring minerals like pyroxenes (Evans et al., 1968; Evans and Wayman, 1970), biotite (Wu et al., 1974), hornblende (Wu et al., 1974), and even some feldspars (Hargraves and Young, 1969; Murthy et al., 1971; Wu et al., 1974) have been reported to carry stable remanent magnetization components due to ferrimagnetic inclusions of sub-microscopic size.

The olivines are generally described as a solid solution between the two end members forsterite (Mg_2SiO_4) and fayalite (Fe_2SiO_4). In natural olivines the composition is generally close to the forsterite side, and natural olivines with compositions close to the fayalite are rarely found. Furthermore, other naturally occurring cations in olivines like chromium, manganese, and others could eventually lead to complicated ferrimagnetic exsolution products. It was therefore decided to make synthetic olivines for our oxidation experiments with given compositions to avoid problems of uncertain chemistry and to get representative compositions along the forsterite-fayalite line.

Synthesis and structural control of the olivines

The olivines of our study have been sintered using a modification of the method by Hoye and O'Reilly (1972). It consists of a solid-state reaction in a self-buffered system to generate the appropriate oxygen partial pressure. The constituents which have been used for the synthesis are: MgO (99.99%), Fe_2O_3 (99.99%), Fe (99.9%), and SiO_2 (99.999%). The SiO_2 powder was heated at $1,000^\circ\text{C}$ for 48 h to remove all water. The mixture of the constituents for 5 g of olivine was milled for 30 min in acetone for homogenization and reduction of the grain size, sealed into quartz tubes, heated for 120 h at $1,000^\circ\text{C}$ and quenched to room temperature. After the first run the X-ray powder patterns still showed lines of enstatite, cristobalite, magnetite, or wuestite. After a second run under the same conditions homogeneous olivines of white or light-olive color were able to be obtained. The sintering time of 10 h (after Hoye and O'Reilly, 1972) turned out to be insufficient for the production of homogeneous phases.

The exact composition of the olivines and the quality of the specimens were tested by X-ray powder diffraction using the $d(130)$ line which depends on the fayalite content x . Schwab and Küstner (1977) have set up a calibration curve, where x is given by the nonlinear equation:

$$x = 7.522 - 14.9071 * (3.0199 - d(130))^{0.5}.$$

According to this calibration curve the fayalite content x of our specimens was always slightly smaller (up to 3 mol%) than the theoretical value. This is explained by a diffusion of some Fe into the quartz tubes.

The $\text{Fe}^{3+}/\text{Fe}^{2+}$ ratio was determined by wet chemical analyses. The ratio never exceeded 3%, which is also observed for natural olivines (Schwab, 1967).

The paramagnetic specific susceptibility X_g at room temperature can also be used to test the purity of the synthetic olivines. Eventually occurring exsolutions of ferrimagnetic phases (mainly magnetite) can be detected because of the very large specific susceptibility of magnetite ($0.1\text{--}1.0\text{ cm}^3\text{ g}^{-1}$). However, as will be discussed in detail in the next section, the values of X_g were always on the order of $10^{-5}\text{--}10^{-4}\text{ cm}^3\text{ g}^{-1}$, which is in good agreement with the expected values for purely paramagnetic substances and the olivines specifically (Hoye and O'Reilly, 1972).

Magnetic properties of the synthetic olivines

Hoye and O'Reilly (1972) have determined some magnetic properties of the olivines at room temperature for the solid-solution series between forsterite and fayalite. Forsterite (Mg_2SiO_4) is diamagnetic because it contains no paramagnetic cations. Its specific diamagnetic susceptibility is $X_g = -0.31 \cdot 10^{-6}\text{ cm}^3\text{ g}^{-1}$. With increasing fayalite (Fe_2SiO_4) content the paramagnetic specific susceptibility X_g increases according to Fig. 1. The dashed line gives the values determined by Hoye and O'Reilly (1972), crosses are data from this paper. The value for a natural olivine is shown by a circle. The data set can be approximated by the following curve of second degree:

$$X_g = 2.6 + 161.4x - 71.6x^2 \quad \text{for } 0.1 \leq x \leq 1.0.$$

The olivines are not paramagnetic in the strictest sense. A plot of the reciprocal specific susceptibility, $1/X_g$ versus the absolute temperature, T , shows in fact a weak antiferromagnetic interaction with a straight line intersecting the temperature axis at negative values (asymptotic Curie temperature, θ_a). This is shown in Fig. 2 for an olivine of the composition $\text{Fa}_{30}\text{Fo}_{70}$. θ_a varies linearly with the fayalite content x , as shown in Fig. 3. The data can be approximated by the following relationship:

$$\theta_a = -0.45 - 102.4x \quad \text{for } 0.1 \leq x \leq 1.0.$$

In the theory of antiferromagnetism (Néel, 1948) the slope of the $1/X_g$ vs T curve determines the Curie constant C_g according to the following equation:

$$1/X_g = (T - \theta_a)/C_g.$$

C_g varies with the fayalite content x as shown in Fig. 4. The data can be approximated by the following nonlinear relationship:

$$C_g = 5.1x - 1.51x^2 \quad \text{for } 0 \leq x \leq 1.$$

Because of technical reasons it was not possible to observe the $1/X_g$ vs T curves down to temperature close to $t=0$ and to determine the Néel temperature T_N , above which the antiferromagnetic ordering disappears, and the temperature T_i , below which spin canting occurs instead

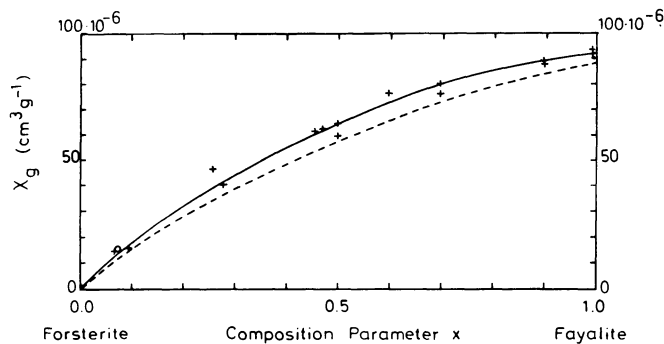


Fig. 1. Dependency of the specific susceptibility X_g of olivines on the fayalite content x . Dashed curve, values from Hoye and O'Reilly (1972); crosses, our data; circle, a natural olivine. The solid line is a best fit of a polynomial of the second degree

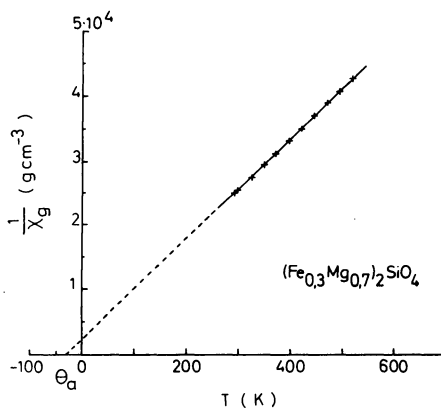


Fig. 2. Plot of the reciprocal specific susceptibility $1/X_g$ versus the absolute temperature T for a synthetic olivine of the composition Fa_{30} and the definition of the asymptotic Curie temperature θ_a

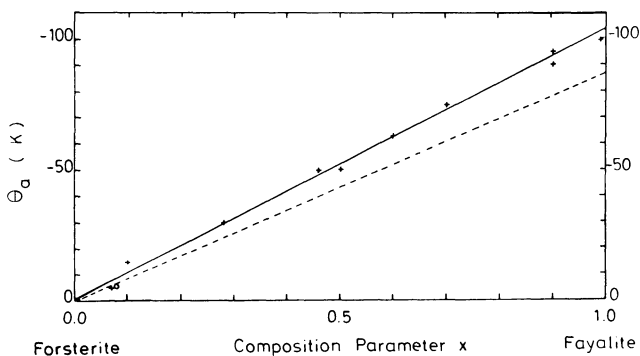


Fig. 3. Dependency of the asymptotic Curie temperature θ_a on the fayalite content x in olivines. For symbols see legend of Fig. 1. The line is a linear least square fit

of a collinear spin arrangement (Fuess et al., 1983). Santoro et al. (1966) determined simple relationships between θ_a , T_N and T_i which are given by:

$$T_N/\theta_a = 0.68; \quad T_i/T_N = 0.29.$$

The relationships between θ_a , T_N , T_i , and the fayalite content x are shown in Fig. 5 (dashed lines, data from Hoye and O'Reilly, 1972; solid lines, calculation of this paper). According to Hoye and O'Reilly (1972) any magnetic order-

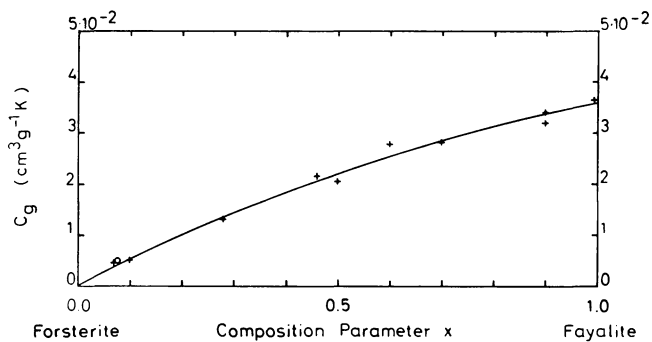


Fig. 4. Dependency of the Curie constant C_g of olivines on the fayalite content x . Crosses, our data; circle, a natural olivine. The line is a best fit by a polynomial of the second degree

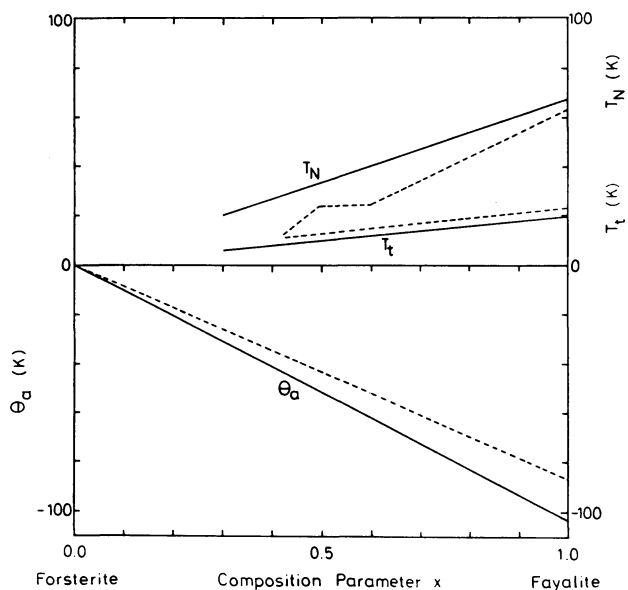


Fig. 5. Variation of the asymptotic Curie temperature θ_a , the Néel temperature T_N , and the transition temperature T_t on the fayalite content x of olivines. Dashed lines, after Hoyer and O'Reilly (1972); solid lines, own data for θ_a and own calculations for T_N and T_t

ing should disappear when the fayalite content becomes less than 30% ($x \leq 0.3$). T_N and T_t have therefore not been plotted in Fig. 5 for values $x \leq 0.3$.

Oxidation experiments with synthetic olivines

The synthetic olivine specimens were first milled in acetone to a grain size of 0.5 μm and then heated in air in a sintered Al_2O_3 crucible within a quartz tube furnace at temperatures up to 700° C between 10 and 4,200 min (70 h) and quenched to room temperature within a few minutes. The upper temperature limit was chosen to simulate oxidation conditions occurring in nature during weathering, hydrothermal, and deuteric alteration. The color of the olivines gives a first indication for the onset of oxidation. According to Koltermann (1962) the following colors are indicative for the oxidation state:

- white to light olive unoxidized (depending on Fa content)
- olive to dark olive partial oxidation of Fe^{2+} to Fe^{3+}

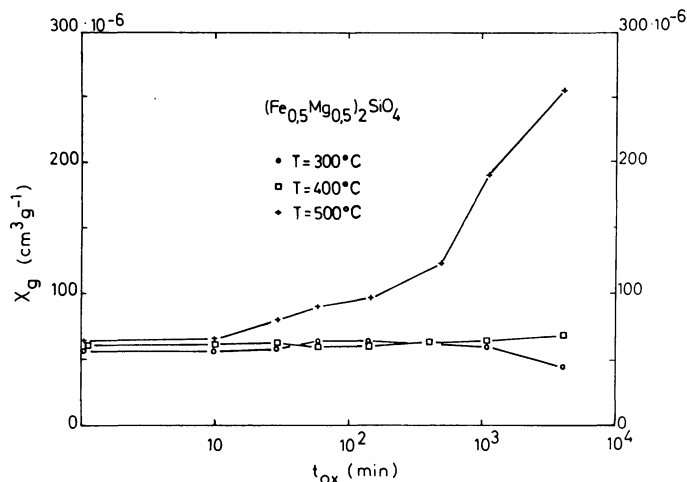


Fig. 6. Oxidation experiment with Fa_{50} heated at 300°, 400°, and 500° C. A drastic change of the specific susceptibility X_g with the logarithm of the heating time t in minutes occurs at the heating temperature of 500° C indicating the formation of a ferrimagnetic phase in the olivine

Table 1. Chemical, structural, and some magnetic properties of the synthetic olivines. d, composition determined with X-ray powder diffraction methods; c, composition determined by wet chemical analysis

Sintering products		Color	$d(130)$ in Å	Susceptibility in $10^{-6} \text{ cm}^3 \text{ g}^{-1}$
Theoretical composition	Real composition			
$\text{Fa}_{10}\text{Fo}_{90}$	d, $\text{Fa}_{10}\text{Fo}_{90}$ c, $\text{Fa}_{09}\text{Fo}_{91}$	white	2.7719	20.2
$\text{Fa}_{30}\text{Fo}_{70}$	d, $\text{Fa}_{28}\text{Fo}_{72}$ c, $\text{Fa}_{28}\text{Fo}_{72}$	white	2.7835	40.7
$\text{Fa}_{50}\text{Fo}_{50}$	d, $\text{Fa}_{47}\text{Fo}_{53}$ c, $\text{Fa}_{49}\text{Fo}_{51}$	light olive	2.7964	60.6
$\text{Fa}_{70}\text{Fo}_{30}$	d, $\text{Fa}_{70}\text{Fo}_{30}$ c, $\text{Fa}_{68}\text{Fo}_{32}$	light olive	2.8101	76.5
$\text{Fa}_{90}\text{Fo}_{10}$	d, $\text{Fa}_{90}\text{Fo}_{10}$ c, $\text{Fa}_{88}\text{Fo}_{12}$	light olive	2.8241	88.2
Fayalite	d, $\text{Fa}_{100}\text{Fo}_0$ c, $\text{Fa}_{100}\text{Fo}_0$	light olive	2.8263	94.0

- dark olive to dark grey and black almost complete oxidation of Fe^{2+} to Fe^{3+} , generation of hematite or spinel phases
- reddish brown complete oxidation, decomposition of the olivine, generation of hematite

Besides this qualitative scale the following quantitative methods have been used for the identification and quantification of the oxidation products:

- specific magnetic susceptibility,
- X-ray powder diffraction, $d(130)$ line, and
- saturation magnetization J_s vs temperature T , Curie temperature.

Because of the limited quantities of synthetic olivines only 50–100 mg of material was used for the oxidation experiments.

Table 2. Oxidation experiments with synthetic olivines Fa₁₀, Fa₃₀, Fa₅₀ (two runs for 500° C), Fa₇₀, and Fa₁₀₀. *T*(°C), heating temperature; unox, unoxidized specimen; *t*(min), heating time in minutes; color, color of the olivine after the heating experiment (w, white; lo, light olive; o, olive; do, dark olive; lb, light brown; b, brown; dark brown; gb, grey brown; dg, dark grey; bk, black); *X_g* specific susceptibility in 10⁻⁶ cm³ g⁻¹; *d*(130), *d*(130) line in Å; X-ray, composition of the olivine and other phases after heating determined from powder pattern analysis; *T_C*, Curie temperature of exsolved ferrimagnetic phases; no *T_C*, no ferrimagnetic phases detectable in *J_s*(*T*) curves; He, hematite present; Mt, magnetite present; S, spinel phase present; Fa, fayalite; Fo, forsterite

Table 2a. Experiments with Fa₁₀

<i>T</i> (°C)	<i>t</i> (min)	Color	<i>X_g</i>	<i>d</i> (130)	X-ray	<i>T_C</i> (°C)
unox.	0	w	20.2	2.7719	Fa ₁₀	
200	4,320	w	19.8	2.7719	Fa ₁₀	no <i>T_C</i>
unox.	0	w	18.1	2.7719	Fa ₁₀	
300	10	w	15.7			
300	30	w	15.6			
300	60	w	15.0	2.7719		
300	150	w	23.3			
300	1,080	w	19.5			
300	4,200	w	18.5	2.7719	Fa ₁₀	
unox.	0	w	20.2	2.7719	Fa ₁₀	
400	10	w	14.6			
400	30	w	14.4			
400	60	w	14.7			
400	150	lo	17.8			
400	420	lo	25.5			
400	1,080	lo	21.0			
400	4,200	lo	26.6	2.7705	Fa ₀₇	550°
unox.	0	w	18.1	2.7700	Fa ₀₇	
500	10	lo	24.4			
500	30	lo	30.3			
500	60	lo	32.1			
500	150	lo	39.8			
500	480	lo	40.5			
500	1,080	lo	42.7			500°(?)
500	4,200	lo	43.1	2.7656	Fo	500°
unox.	0	w	20.2	2.7719	Fa ₁₀	
600	4,200	lb	244.4	2.7655	Fo	360°, 570°

Table 2b. Experiments with Fa₃₀

<i>T</i> (°C)	<i>t</i> (min)	Color	<i>X_g</i>	<i>d</i> (130)	X-ray	<i>T_C</i> (°C)
unox.	0	w	40.7	2.7835	Fa ₂₈	
200	4,320	w	41.2	2.7824	Fa ₂₆	no <i>T_C</i>
unox.	0	w	40.7	2.7835	Fa ₂₈	
300	10	w	39.2			
300	30	w	40.0			
300	60	lo	38.1			
300	150	lo	40.2			
300	420	lo	43.3			
300	1,080	lo	43.5			
300	4,200	lo	42.3	2.7814	Fa ₂₄	
unox.	0	w	40.7	2.7835	Fa ₂₈	
400	10	lo	40.6			
400	30	lo	43.6			
400	60	lo	39.9			
400	150	lo	38.3			
400	420	o	43.1			
400	1,080	o	36.2			
400	4,200	o	38.4	2.7782	Fa ₁₉	no <i>T_C</i>
unox.	0	w	40.7	2.7835	Fa ₂₈	
500	10	lo	40.3			
500	30	o	39.3			
500	60	o	37.9			
500	150	o	40.7	2.7814	Fa ₂₄	
500	420	o	48.3			
500	1,080	o	57.4			
500	4,200	o	103.4	2.7719	Fa ₁₀	360°
unox.	0	w	40.7	2.7835	Fa ₂₈	
600	4,200	b	337.0	2.7657	Fo, S	360°

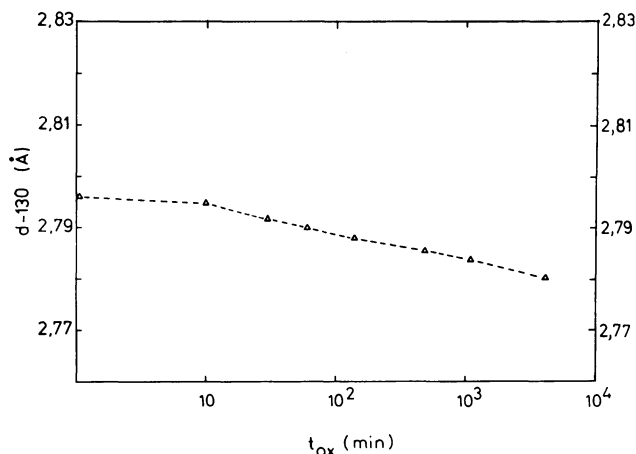


Fig. 7. Example for an oxidation experiment with Fa₅₀ heated at 500° C. Change of the *d*(130) line with the logarithm of the heating time *t* indicating the variation of the composition of the olivine toward a phase less rich in Fe

Similar to the experiments by Hoye and Evans (1975) we used the following oxidation times: 10, 30, 60, 150, 420, (480), 1080, 4200, and (4,320) min. The specimens were put in a ceramic crucible and placed into the preheated furnace. According to Hoye and Evans (1975) they reach their maxi-

um temperature within less than 3 min. This heating time was included in the total heating time. After the heating experiment the powder was quickly filled into a quartz tube and cooled under running water within 2–3 min to room temperature to avoid further oxidation. Olivines of the composition Fa₁₀, Fa₃₀, and Fa₅₀ were studied in more detail than the other compositions due to their more frequent occurrence in nature. Special attention was also given to pure fayalite, Fa₁₀₀, because it contains no magnesium. Table 2 describes the results of the heating experiments, while Table 3 gives a description of the ferrimagnetic exsolution products in the olivines.

Ferrimagnetic phases as a result of the oxidation

It is interesting to see from Table 3 that the heat treatment of up to 4,320 min was not able to produce ferrimagnetic phases in the olivines with a fayalite content of less than Fa₇₀ at temperatures lower than 300° C. The main effects occur at temperatures higher than 400° C. In fayalite the ferrimagnetic phase is predominantly hematite; magnetite is also formed to a lesser degree. During the heating experiment amorphous quartz is also formed but cannot be identified by X-ray methods. In all Mg-rich olivines a Mg–Fe spinel has been identified, mainly from the Curie temperature measurements. According to Nagata (1961) the Curie

Table 2c. Experiments with Fa₅₀

<i>T</i> (°C)	<i>t</i> (min)	Color	<i>X</i> _g	<i>d</i> (130)	X-ray	<i>T</i> _c (°C)
unox.	0	lo	62.4	2.7951	Fa ₄₆	
200	4,320	lo	61.9	2.7951	Fa ₄₆	no <i>T</i> _c
unox.	0	lo	62.8	2.7959	Fa ₄₇	
300	10	lo	61.0			
300	30	lo	60.5			
300	60	lo	61.7			
300	150	o	60.1			
300	1,080	o	60.9			
300	4,200	o	44.2	2.7951		no <i>T</i> _c
unox.	0	lo	62.4	2.7940	Fa ₄₄	
400	10	o	63.5			
400	30	o	61.6			
400	60	o	60.1			
400	150	o	60.2			
400	420	o	63.4			
400	1,080	o	63.6			
400	4,200	do	67.5	2.7930	Fa ₄₂	no <i>T</i> _c
unox.	0	lo	62.8	2.7959	Fa ₄₇	
500	10	lo	65.2	2.7947	Fa ₄₅	
500	30	o	80.5	2.7915	Fa ₄₀	
500	60	do	90.9	2.7898	Fa ₃₇	
500	150	do	97.8	2.7877	Fa ₃₄	
500	480	do	122.8	2.7853	Fa ₃₀	360°
500	1,080	do	189.2	2.7835	Fa ₂₇	
500	4,200	do	253.9	2.7803	Fa ₂₂ , S	360°
unox.	0	lo	60.6	2.7964	Fa ₅₀	
500	30	o	79.2	2.7932	Fa ₄₂	
500	60	o	85.0	2.7913	Fa ₃₉	
500	150	do	90.8	2.7888	Fa ₃₅	
500	420	do	116.5	2.7870	Fa ₃₃	360°
500	1,080	do	132.2	2.7858	Fa ₃₂	360°
500	4,200	do	160.6	2.7803	Fa ₂₁ , S	360°
unox.	0	lo	62.8	2.7959	Fa ₄₇	
600	4,200	db	489.0	2.7655	Fo, S	360°

temperatures of the solid-solution series Mg-Fe spinel (MFS) to magnetite (Mt) vary between around 320° C for MFS and 570° C for Mt. curie temperatures around 360° C are normally attributed to titanomagnetites in the Curie temperature analysis of basaltic rocks. The absence of any titanium in the synthetic olivines demands another interpretation. As the lattice parameters of the observed Mg-Fe spinel are not very different from those of pure magnetite (ASTM Charts, 1969), the actual composition of this spinel may have been misinterpreted by previous authors because most investigators speak of magnetite exsolution in olivines during oxidation experiments (Koltermann, 1962).

Table 2 shows that the growth of the ferrimagnetic phases reduces the nominal fayalite content of the remaining olivine phase. This is revealed by a shift in the *d*(130) line toward compositions which are less rich in Fe. Table 2c (500° C) gives a good example of this effect.

Kinetics of the oxidation process

One of the aims of this study has been the determination of the kinetics of the oxidation of olivines. The results for the heat treatment are listed in detail in Table 2 and in Figs. 6 and 7.

Figure 6 shows the variation of the specific susceptibility *X*_g with the logarithm of heating time *t*. There is a more

Table 2d. Experiments with Fa₇₀

<i>T</i> (°C)	<i>t</i> (min)	Color	<i>X</i> _g	<i>d</i> (130)	X-ray	<i>T</i> _c (°C)
unox.	0	lo	76.5	2.8101	Fa ₇₀	
500	10	db	182.4	2.8047	Fa ₆₁	360°
500	30	dg	197.0			
500	60	dg	198.3			
500	150	bk	189.8			360°
500	420	bk	203.2	2.7824	Fa ₂₆ , S	
500	1,080	bk	253.0			360°
500	4,200	bk	241.0	2.7782	Fa ₁₉ , S	360°

Table 2e. Experiments with Fa₁₀₀ fayalite

<i>T</i> (°C)	<i>t</i> (min)	Color	<i>X</i> _g	<i>d</i> (130)	X-ray	<i>T</i> _c (°C)
unox.	0	lo	93.9	2.8263	Fa ₁₀₀	
300	10	b	91.7			
300	30	b	91.5			
300	60	b	92.0			
300	150	b	91.3			
300	1,080	gb	91.9	2.8252		
300	4,200	gb	86.6	2.8242		680°
unox.	0	lo	93.9	2.8263	Fa ₁₀₀	
500	10	dg	85.6			
500	30	dg	76.4			
500	60	bk	71.3	2.8112	Fa ₇₁ , He	680°
500	150	bk	71.3			
500	480	bk	58.6			
500	1,080	bk	54.7	2.7856	Fa ₃₁ , He	
500	4,200	bk	45.6	2.7761	Fa ₁₆ , He	680°
unox.	0	lo	93.9	2.8263	Fa ₁₀₀	
700	10	bk	51.1	2.8176	Fa, He	680°
700	30	bk	84.8			
700	60	bk	82.1	2.8292	Fa, He, Mt	
700	150	bk	328.9			
700	1,080	bk	621.5		He, Mt	570°, 680°

Table 3. Ferrimagnetic exsolutions in synthetic olivines after heat treatment in air for 4,200 min. Maximum heating temperature in °C. Curie temperatures are also given in °C. He, hematite; Mt, magnetite; MFS, Mg-Fe spinel; n.ex., no exsolution could be observed under the above-mentioned conditions; n.m., not measured

<i>T</i> (°C)	Fa ₁₀	Fa ₃₀	Fa ₅₀	Fa ₇₀	Fa ₁₀₀
200°	n.ex.	n.ex.	n.ex.	n.m.	n.m.
300°	n.ex.	n.ex.	n.ex.	MFS, 360°	He, 680°
400°	MFS, 550°	n.ex.	n.ex.	n.m.	n.m.
500°	MFS, 500°	MFS, 360°	MFS, 360°	MFS, 360°	He, 680°
600°	MFS, 360° Mt, 570°	MFS, 360°	MFS, 360°	n.m.	n.m.
700°	n.m.	n.m.	n.m.	n.m.	Mt, 570° He, 680°

or less linear increase in *X*_g with log *t*, which can of course not be extrapolated to geological times because the process comes to an end when all the Fe in the olivines has been consumed for the formation of first a Mg-Fe spinel and later for hematite when the oxidation goes on. Similarly,

the composition of the remaining olivine phase changes due to the concentration of part of the Fe in the iron oxides. This is revealed by the shift in the $d(130)$ line toward compositions less rich in Fe. This shift follows also a log/normal law as shown in Fig. 7.

Conclusions

Our results confirm to a large degree those of Hoye and O'Reilly (1973). Heating temperatures around 300° C are necessary to start the oxidation process under laboratory conditions. Depending on the availability of magnesium either Mg-poor or Mg-rich Mg-Fe spinels are formed. While Hoye and O'Reilly (1973) report also the generation of pure magnetite under these conditions - Champness (1970) reports even the formation of hematite - we only found Mg-Fe spinels. Only at oxidation temperatures above 600° C did we discover magnetite as a ferrimagnetic phase. The situation is completely different for the fayalite, which contains no Mg. Here, hematite is formed already at low heating temperatures, and magnetite appears at temperatures above 700° C.

The ferrimagnetic ore grains were found to be submicroscopic. They are presumably in the size range between superparamagnetism and the single-domain state. This is revealed by a strong magnetic viscosity of the material. With increasing oxidation time there seems to be a tendency for further crystal growth of the ferrimagnetic inclusions leading to first more single-domain and later even multidomain grains. The identification of Mg-Fe spinels in the olivines indicates that at least part of the remanent magnetization of altered mafic and ultramafic rocks may be carried by this not so intensively studied magnetic mineral.

Acknowledgements. We thank Prof. Dr. G. Huckenholz, Dr. T. Fehr, Dipl. Min. R. Hochleitner, and Dipl. Chem. T. Dorfner from the Mineralogical Institute of our university for their help in the preparation of the synthetic olivines and for the possibility to use their equipment. Thanks are also due to Priv. Doz. Dr. E. Schmidbauer for many helpful discussions.

References

- ASTM Charts. Powder Diffraction File, Amer. Soc. for Testing and Materials, Philadelphia, USA, 1969
- Champness, P.E.: Nucleation and growth of iron oxides in olivines, $(\text{Mg, Fe})_2\text{SiO}_4$. *Mineral. Mag.*, **37**, 790-800, 1970
- Evans, M.E., Wayman, M.L.: An investigation of small magnetic particles by means of electron microscopy. *Earth Planet. Sci. Letters*, **9**, 365-370, 1970
- Evans, M.E., McElhinny, M.W., Gifford, A.C.: Single domain magnetite and high coercivities in a gabbroic intrusion. *Earth Planet. Sci. Letters*, **4**, 142-146, 1968
- Fuess, H., Lottermoser, W., Müller, R.: Magnetische Eigenschaften der synthetischen Olivine Tephroit und Fayalit. *Fortschr. Min.* **61**, Beiheft **1**, 134-136, 1983
- Hargraves, R.B., Young, W.M.: Source of stable remanent magnetism in Lambertville diabase. *Amer. J. Sci.*, **267**, 1161-1177, 1969
- Hoye, G.S., Evans, M.: Remanent Magnetisations in Oxidized Olivine. *Geophys. J.*, **41**, 139-151, 1975
- Hoye, G.S., O'Reilly, W.: A magnetic study of ferromagnesian olivines, $(\text{Fe}_x\text{Mg}_{1-x})_2\text{SiO}_4$, $0 \leq x \leq 1$. *J. Phys. Chem. Solids*, **33**, 1827-1834, 1972
- Hoye, G.S., O'Reilly, W.: Low-temperature oxidation of ferromagnesian olivines - a gravimetric and a magnetic study. *Geophys. J.*, **33**, 81-92, 1973
- Koltermann, M.: Der thermische Zerfall fayalithaltiger Olivine bei hohen Temperaturen. *N. Jb. f. Mineral., Monatshefte*, 181-192, 1962
- Murthy, G.S., Evans, M.E., Gough D.I.: Evidence of single-domain magnetite in the Michikamau anorthosite. *Can. J. Earth Sci.*, **8**, 361-370, 1971
- Nagata, T.: *Rock Magnetism*. Maruzen Comp. Ltd. Tokyo, Japan, 1961
- Néel, L.: Magnetic properties of ferrites: ferrimagnetism and antiferromagnetism. *Ann. Phys.*, **3**, 137-198, 1948
- Santoro, R.P., Newnham, R.E., Nomura, S.: Magnetic properties of Mn_2SiO_4 and Fe_2SiO_4 . *J. Phys. Chem. Solids*, **27**, 655-666, 1966
- Schwab, R.: Die Bedeutung und die experimentelle Beherrschung des Sauerstoffpartialdruckes bei der Synthese und Untersuchung Fe^{2+} -haltiger Silikate. *N. Jb. Mineral. Monatsh.*, 244-254, 1967
- Schwab, R., Küstner, D.: Präzisionsgitterkonstantenbestimmung zur Festlegung röntgenographischer Bestimmungskurven für synthetische Olivine der Mischkristallreihe Forsterit-Fayalit. *N. Jb. Mineral. Monatsh.*, 205-215, 1977
- Wu, Y.T., Fuller, M., Schmidt, V.A.: Microanalysis of N.R.M. in a granodiorite intrusion. *Earth Planet. Sci. Letters*, **23**, 275-285, 1974

Received January 31, 1986; revised version June 13, 1986

Accepted July 8, 1986

Magnetic mineralogy of basalts from El-Bahnasa and Tahna, Egypt

Nadia A. Wassif

Department of Geophysics, National Research Centre, Cairo, Egypt

Abstract. The present work gives the magnetic characteristics and opaque mineralogy of 30 porphyritic olivine basalt samples from El-Bahnasa and Tahna (Egypt). Ore microscopic studies, Curie temperature and X-ray diffraction analysis suggest primary titanomagnetites to be the major magnetic mineral present. The Q values and the maximum peak values of Rayleigh loops are largely controlled by magnetic mineralogy, oxidation state and the grain size of the magnetic minerals within the rock sample.

Key words: Rock magnetism – Basalts-Titanomagnetite – Q value

Introduction

Systematic rock magnetic, palaeomagnetic and opaque mineralogical studies were carried out on numerous lava flows in the northern part, especially, of Egypt (Fig. 1). They show close similarity to each other, being characterized by reversed magnetization. The opaque mineralogy of these occurrences indicates: (a) presence of magnetite and ilmenite as subhedral coarse grains indicating slow rate of cooling, (b) the predominance of ilmenite over magnetite, (c) the frequent association of ilmenite and magnetite in intimate intergrowths in the same grain (mainly exsolution, sandwich and granule intergrowths) and also in composite grain and (d) the common alteration of magnetite to martite, the complete oxidation of ulvöspinel to ilmenite and the alteration of ilmenite to rutile-hematite aggregates (El-Rashidi, 1964; El-Sheikh, 1968; Refai and Wassif, 1970; El-Shazly and Krs, 1971; Fahim and Gouda, 1976; Basta et al., 1981).

To the south of the Nile valley, an outcrop of lava flows appears in the neighbourhood of Tahna (Fig. 1). On the opposite side of the Nile, near El-Bahnasa, there are also flows that extend through isolated outcrops from Qaret El-soda near Manfalout of the south-west to Baharia. Ball and Beadnell (1903) reported to similarity of volcanic rocks on the Feshn-Baharyia Desert Road to those occurring west of El-Bahnasa. The volcanic rocks in this area intruded into Eocene limestones, and were described as "hard andesitic basalt". The fluvio-marine series is absent at El-Bahnasa and Tahna. Based on field observations, the basalt flows are considered of Lower Oligocene age.

The primary Fe-Ti oxides which crystallize from basaltic magma above 1000° C are members of magnetite-ulvöspinel

and ilmenite-hematite solid solution series. These minerals dominate the bulk magnetic properties (natural remanence, initial susceptibility, Curie point ... etc.) regardless of the subsolidus petrological history. These accessory oxides of both El-Bahnasa and Tahna flows will be described and their magnetic properties will be compared with those of other localities in the northern part of Egypt (Fig. 1). Thirty basaltic samples were collected from three hillocks at El-Bahnasa (sites 700 and 800) and Tahna (site 1,000). The natural remanent magnetization (NRM) and initial susceptibility (χ) were measured by an inductometer. The magnetic mineralogy was investigated by reflected-light microscopy, Curie temperature and X-ray analysis.

Microscopic investigations

Petrographically, the rocks are porphyritic olivine basalts consisting of plagioclase, pyroxenes and olivine phenocrysts (25%–30%) embedded in a ground mass of opaque minerals, pyroxenes, plagioclase and exhibit ophitic and sub-

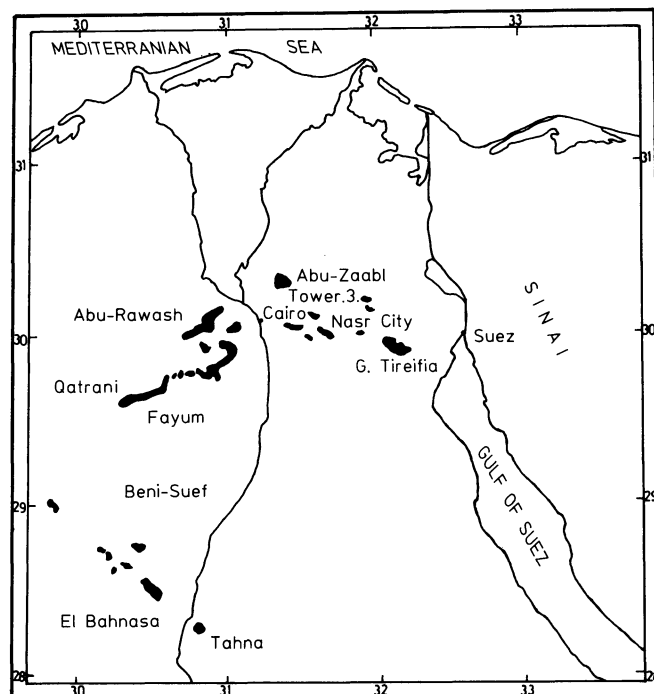


Fig. 1. Key map of the northern and southern basaltic occurrences

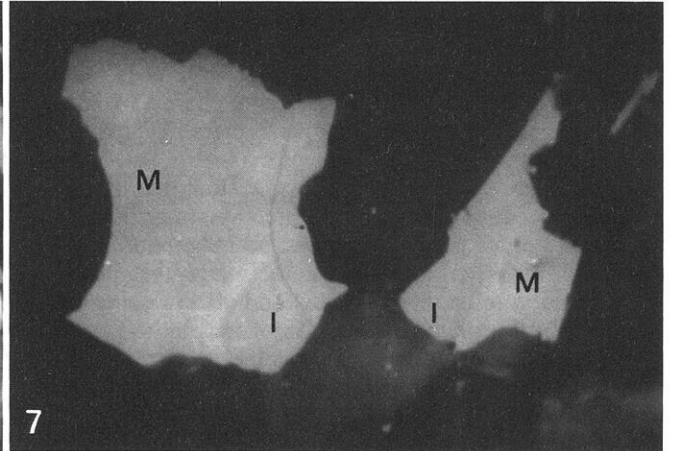
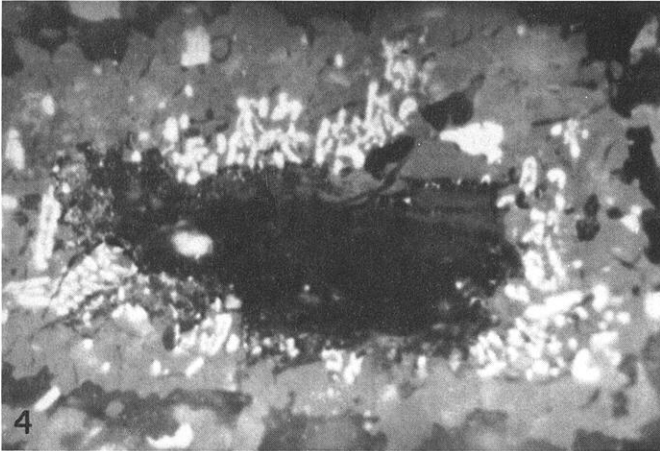
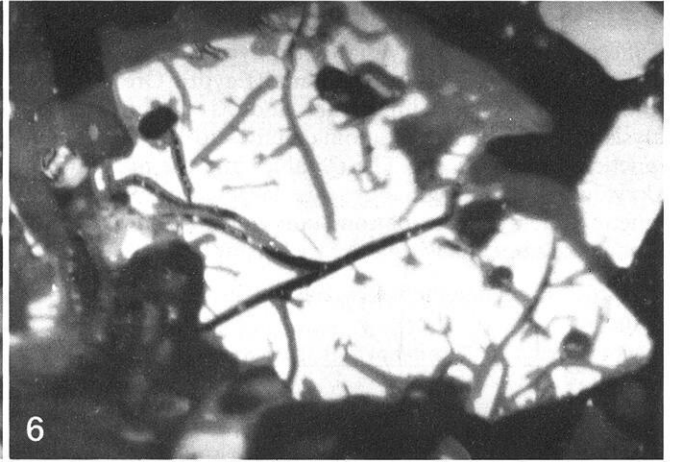
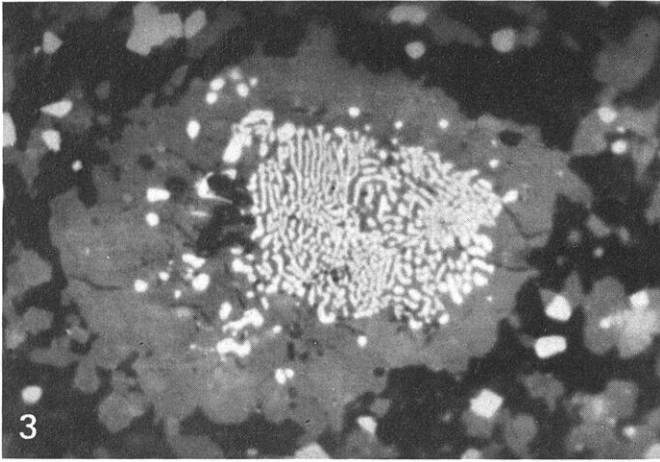
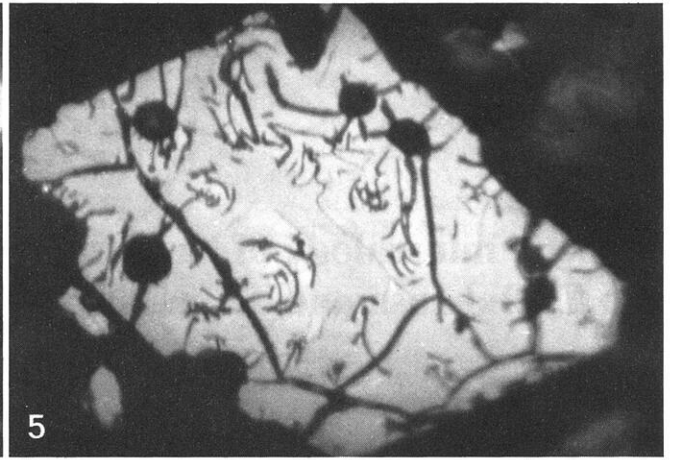
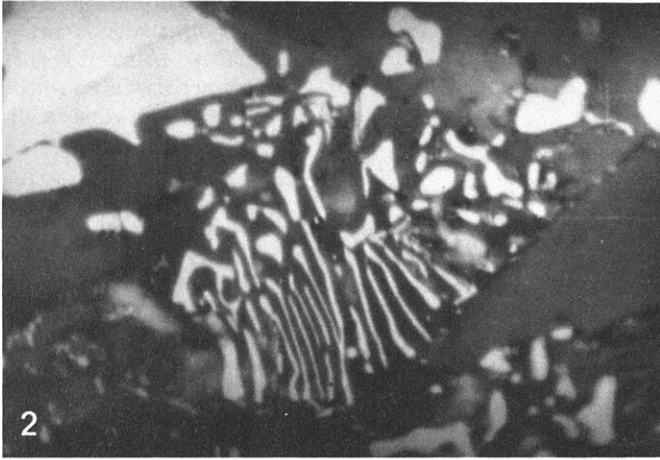


Fig. 2. Myrmikitic intergrowth of secondary magnetite with secondary amphiboles, site 800. Reflected light, oil immersion, $\times 1,000$

Fig. 3. Graphic intergrowth of magnetite in the core of a pyroxene grain, site 700. Reflected light, oil immersion, $\times 1,000$

Fig. 4. Keliphitic rim of magnetite around a pyroxene grain, site 1,000. Reflected light, oil immersion, $\times 500$

Fig. 5. Intensely cracked titanomagnetite (microscopically homogeneous to a magnification $\times 1,000$) with colour heterogeneity around fine cracks where bluish grey patches of maghemite appear, site 700. Reflected light, oil immersion, $\times 1,000$

Fig. 6. Maghemitized magnetite grain with pronounced cracks which are filled by silicates, site 700. Reflected light, oil immersion, $\times 1,000$

Fig. 7. Ilmenite-magnetite sandwich grain embayed and dissected by the silicates (*black*); notice that ilmenite on both sides has the same colour indicating optical continuity, site 800. Reflected light, oil immersion, $\times 1,000$

Table 1. Summary of ore microscopical results

Site	Opaque minerals % by volume	Magnetite			Ilmenite
		Grain size and texture	Type and intergrowths	Alteration	
700 and 1000	80–100 magnetite 0–20 ilmenite	Few porphyritic grains (400–600 μm) in a very fine ground mass (up to 20 μm)	Mainly titanomagnetite ^a	Partially or severely to maghemite with the development of irregular fine and thick cracks	Minute discrete laths
800	60–70 magnetite 30–40 ilmenite	Fine to medium grains (20–40 μm) with octahedral faces, skeletal crystals and myrmikites (Fig. 2)	Ti-poor ^a magnetite and titanomagnetite in equal amounts. Intergrowths of sandwich (Fig. 7) and granules	Partially to martite and maghemite	Discrete plates (100–150) (10–30) μm

^a The differentiation between titanomagnetite and Ti-poor magnetite is based on the optical properties as shown under the microscope (particularly colour, reflectivity and presence of weak anomalous anisotropism of titanomagnetite)

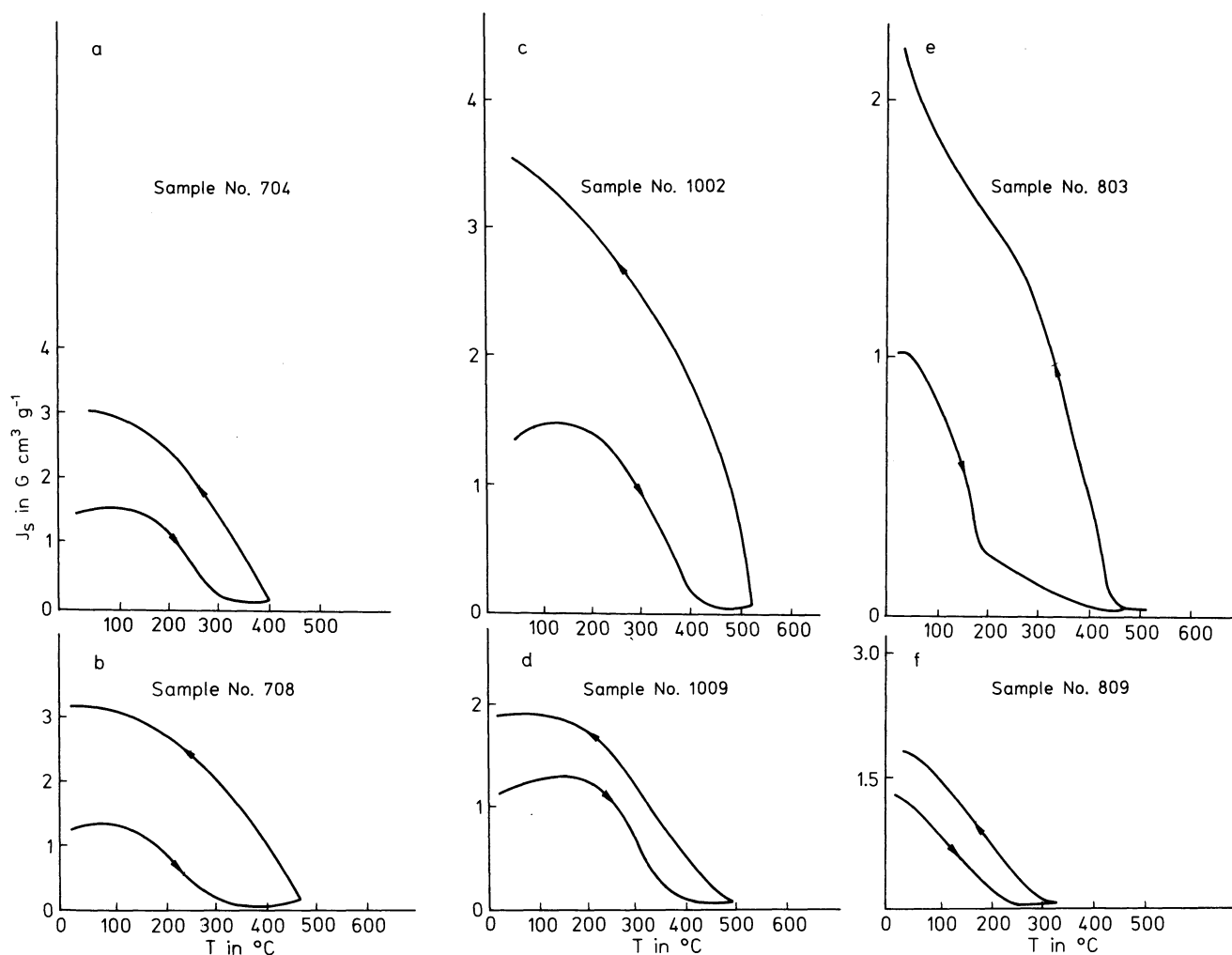


Fig. 8a-f. Representative J_s - T curves for samples from each site. Both heating and cooling cycles are shown and indicated by arrows. Note that saturation magnetizations are given in $\text{G cm}^3 \text{g}^{-1}$ ($= \text{Am}^2 \text{kg}^{-1}$)

phitic textures. Although no significant mineral variations among the three sites are observed, the ground mass of sites 700 and 1,000 is finer grained than that of site 800 and contains some glass.

In reflected light, the opaque minerals are abundant,

forming about 25% of the total rock; their form testifying to fairly rapid cooling after emplacement at shallow depth. They include magnetite and homogeneous ilmenite, the magnetite being the predominant mineral. It should be emphasized that the terminology used to describe opaque min-

erals and their intergrowths is that given by Basta (1970). The term titanomagnetite indicates a homogeneous single-phased magnetite containing Ti in solid solution, while titaniferous magnetite is used for magnetite containing at least one exsolved phase of Ti-minerals (ilmenite and/or ulvöspinel).

The reflectivity and colour of magnetite suggest the presence of two homogeneous main types; titanomagnetite and a Ti-poor magnetite free of exsolutions. Titaniferous magnetite which contains ilmenite lamellae is completely absent. The titanomagnetite has been formed by very rapid cooling of the parent magma that did not allow the unmixing of its ilmenite or ulvöspinel solid solution. The Ti-poor magnetite is found to be less abundant and occasionally being associated with titanomagnetite. In some instances the titanomagnetite shows some colour variation, possibly due to a variable Ti content or beginning low-temperature oxidation.

Secondary magnetite is sometimes present in the form of myrmikitic intergrowths with secondary amphibole (Fig. 2), graphic intergrowth in the core of pyroxene grain (Fig. 3) and keliphitic rims which are mainly due to deuteric alteration (Fig. 4).

The alteration of magnetite is represented by maghemitization along fine and thick cracks (Figs. 5 and 6) and martitization along grain peripheries. The origin of these alterations is attributed to oxidation, where the titanomagnetite is preferentially altered to maghemite and Ti-free magnetite is usually martitized; late martitization due to weathering is also possible. The transformation of magnetite into maghemite has been considered to be characteristic of low-temperature oxidation (Ozima and Ozima, 1971; Lowrie, 1974; Haggerty, 1976), being more common in submarine basalts (Cockerham and Hall, 1976; Johnson and Hall, 1978). The development of cracks resulted from the defect structure of maghemite. Similar observations were described by Wassif (1983) from the Hefhuf basalts of the Bahariya Oases.

The results of optical examination of sites 700 and 1,000 and site 800 are summarized in Table 1.

Thermomagnetic measurements

For the Curie-point determination, small chips from a basalt sample were ground to a coarse powder and were heated in air in applied magnetic fields of about $3,100 \text{ Oe}^1$ using a horizontal automatic magnetic balance. At least three J_s - T determinations were performed on samples from each site and the results are summarized in the following.

All J_s - T curves are essentially irreversible during heating and cooling. They show a single Curie temperature upon heating around $300^\circ\text{--}350^\circ\text{C}$ for site 700 and around $400^\circ\text{--}450^\circ\text{C}$ for site 1,000 (Fig. 8a-d). The irreversible behaviour is caused by continual oxidation and/or unmixing of titanomagnetite-maghemite during heating (Ozima and Ozima, 1971). The unstable Curie temperatures and the increase in J_s after heating support the validity of this interpretation. Ore microscopy confirms the presence of titanomagnetite with maghemite-lined cracks (Figs. 5 and 6). The shape of the J_s - T curves and the low Curie temperatures ($200^\circ\text{--}250^\circ\text{C}$) at site 800 (Fig. 8e, f) reveal that the magnetic mineral present is an almost unoxidized form of

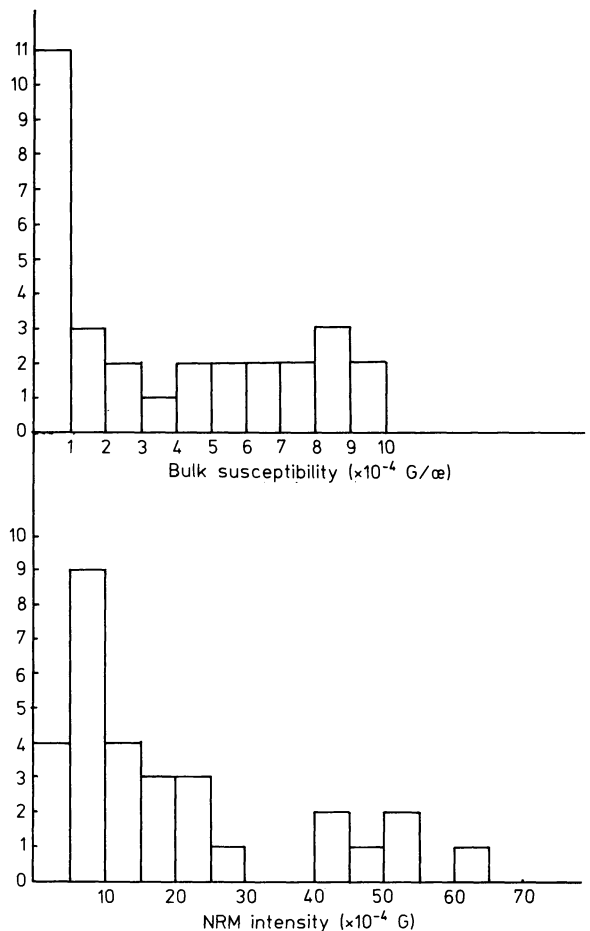


Fig. 9. Histograms of NRM intensities and bulk susceptibilities of 30 basaltic samples

an ulvöspinel-rich (40%–50%) titanomagnetite (Ozima and Larson, 1970). Ore microscopy also supports this interpretation. One sample from this site (Fig. 8e) shows two distinct Curie temperatures, one around 200°C and one around $400^\circ\text{--}450^\circ\text{C}$. This sample, with low initial Curie point, also gave an irreversible thermomagnetic curve with a substantial increase in magnetization but with an increased Curie point higher than 450°C after thermal cycling. This thermomagnetic behaviour can be accounted for by the initial presence of a titanomagnetite or titanomaghemite which separates upon heating to a titanium-rich phase and a titanium-poor phase near to magnetite in composition. On cooling from high temperature, the stronger magnetization of this magnetite appears at a high Curie temperature and increases to its room temperature value (Kent et al., 1978). The subsequent microscopic examination of this sample confirmed the presence of both Ti-poor magnetite and titanomagnetite. Previous studies of unaltered submarine basalts from the Mid-Atlantic Ridge show Curie temperatures of 120°C to 150°C for the original titanomagnetite and Curie points up to a maximum of 400°C for the completely oxidized titanomaghemite (Schaeffer and Schwarz, 1970; Johnson and Atwater, 1977). Although martite was sometimes observed in a microscopic examination of samples from site 800, a thermomagnetic expression was not apparent, presumably due to small amounts of the more weakly magnetic hematite in the presence of mag-

¹ $1 \text{ Oe} \approx 80 \text{ Am}^{-1}$

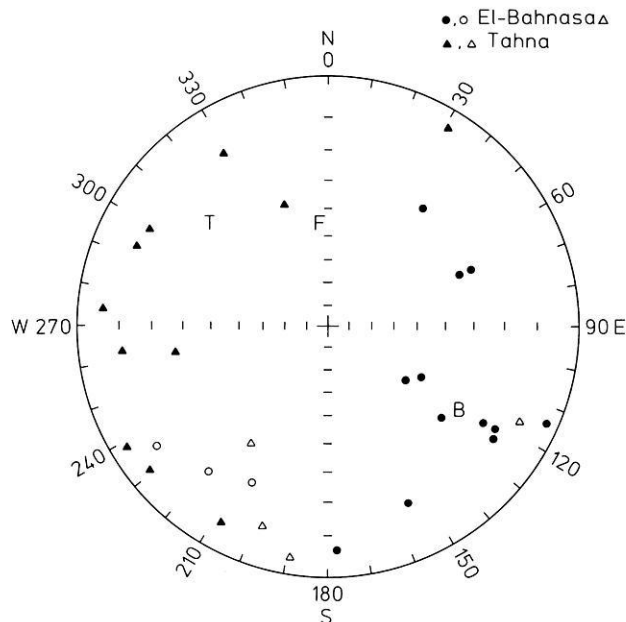


Fig. 10. Stereo plot showing the NRM directions for all samples. Full (open) symbols = positive (negative) inclinations. *F*: present field direction and *B(T)* are site mean directions for El-Bahnasa (Tahna) areas

netite which was volumetrically and magnetically dominant in most samples.

X-ray diffraction analysis (XRD)

XRD data for magnetically separated opaques confirmed the microscopic determinations, where the patterns of titanomagnetite and maghemite in site 800 are present together with a strong pattern of ilmenite. In sites 700 and 1,000, the titanomagnetite and maghemite patterns are more distinct, while ilmenite is absent or very weak.

NRM and susceptibility

The remanent magnetization vectors and low field susceptibilities were measured by an inductometer (Thellier, 1938). Histograms of natural remanent magnetization (NRM) intensities J_{NRM} and bulk susceptibilities χ for all the 30 samples are shown in Fig. 9. The remanence intensities vary between 1.21×10^{-4} G and 65.01×10^{-4} G², while the initial susceptibilities range from 0.18×10^{-4} G/Oe to 10.01×10^{-4} G/Oe³. The Koenigsberger ratio Q_n is a measure of the relative contribution of remanent to induced magnetization in a sample and is calculated as $Q_n = J_{\text{NRM}}/\chi \cdot F$ where F is the geomagnetic field intensity at the studied area ($F = 0.42$ Oe). The calculated Koenigsberger values of all samples are much greater than unity (from 2 to 136). Therefore, remanent magnetization dominates the total magnetization of all these basalts in the Earth's magnetic field.

It is clear from the results that a large variation in magnetization (NRM and susceptibility) as well as opaque mineralogy content is observed in specimens taken from a single

Table 2. NRM mean directions from the three sites, with precision parameters

Site	<i>N</i>	<i>D</i> (°)	<i>I</i> (°)	α_{05} (°)	<i>R</i>	<i>K</i>	<i>R</i> ₀
700	8	148	+24	16	7.452	12.77	4.48
800	7	149	+32	38	5.265	8.16	4.18
El-Bahnasa	2	148	+28	25	1.990	100	
Tahna (1000)	15	313	+24	39	7.748	2.24	6.19

N, number of samples; *D*, *I*, declination, inclination; α_{05} , *R*, *K* and *R*₀, precision parameters (Fisher, 1953) and (Watson, 1956)

sample. Similar fluctuations were noted by Kent et al. (1978) and Johnson and Hall (1978). They suggest that the rocks are not very homogeneously magnetized even on a hand-sample scale, as a result of different local concentrations of magnetic minerals.

Because viscous components of remanent magnetization affect the measurements, the collection was measured again after 1 month in order to obtain a rough qualitative estimate of the stability of magnetization. Samples from El-Bahnasa yielded more stable NRM directions, while those from Tahna showed varying consistency between measurements. NRM directions are widely scattered (Fig. 10). Mean directions of each site, together with statistical parameters, are reported in Table 2. Occasionally, samples collected from one and the same spot (from Tahna area) yield totally different directions. Strong viscous components of magnetization varying rapidly with time made the measurements unreliable and those samples were discarded as unreliable for further palaeomagnetic studies.

The ratio between the magnetic moment per unit mass (otherwise termed magnetization) and the applied field has been used successfully to obtain a representative set of loops. Long uniform cylindrical polished samples were prepared and by using Gough's method (1889) the changes in susceptibility with applied field (up to 25 Oe) were measured. The rocks under investigation did not saturate because of the limitation on the peak magnetic field obtainable. The results of 12 representative samples (Table 3) clearly showed Rayleigh loops (1887) that could be classified into two groups. The first group (Fig. 11a–d) has high peak susceptibility values (*K*) between 14×10^{-3} and 25×10^{-3} G/Oe and clearly shows irreversible behaviour. The Rayleigh loops of the second group are nearly reversible (Fig. 11e and f) and characterized by a lower peak at the same applied field.

Discussion and conclusions

Correlation between magnetic data and opaque mineralogy

Table 3 shows that, for opaque minerals (frequency, species and intergrowths), the maximum peak values *K* and *Q* values of sites 700 and 1,000 are very similar, while site 800 shows different opaque constituents being characterized by lower *K* and *Q* values. These data may possibly be interpreted by the following: (a) coarser grain size of site 800, despite the presence of few porphyritic crystals in samples from sites 700 and 1,000 (see Table 1); (b) the composition and alteration of magnetite at site 800 is characterized by

² 1 G = 10^3 Am⁻¹

³ 1 G/Oe = 4π SI units (m³ m⁻³)

Table 3. Correlation between magnetic data and ore microscopical results

Site	Sample no.	Opaque minerals % by volume	Textures and mode of occurrence of ore minerals	Magnetite		Degree of martitization	Degree of magnetization	Composite grains sandwich, mass and juxta position inter-growths	Ilmenite	Max. peak values of K (10^{-3} G/Oe)	$Q_n = J/\chi \cdot F$	Curie Temp. ($^{\circ}$ C)	J_s (G/g)
				Ti-free magnetite	Titano-magnetite								
Site 700	701	<20	Porphyritic, intensely cracked	-	XXXX	-	XXXX	-	-	25.91	104.23	-	-
	704(a)	<20	Porphyritic, slightly cracked	-	XXXX	-	XX	-	-	15.20	116.48	325	1.4-3
	705	>20	Fine to medium grains	XX	X	XX	X	X	XX	5.05	36.25	-	-
	708(b)	<20	Porphyritic-myrmikitic	X	XX	X	X	-	-	16.90	134.50	325	1.2-3.2
Site 1000	1002(c)	<20	Porphyritic-fine cracks	-	XXXX	-	XX	-	-	25.95	82.47	425	1.3-3.5
	1005	>20	Porphyritic-fine cracks	-	XXX	-	XX	-	-	10.42	97.28	-	-
	1007	<20	Porphyritic-keliphetic rims	-	XXXX	-	XXX	-	-	15.02	136.73	-	-
	1009(d)	<20	Porphyritic-fine cracks	-	XXX	-	XX	-	X	20.59	96.28	400	1.25-2
	1012	<20	Porphyritic-thick cracks	X	XXX	XX	XX	-	X	14.10	45.87	-	-
Site 800	803(e)	15-20	Fine to medium grains, skeletal crystals	XXX	XX	XX	X	XXX	XXX	6.93	36.03	200	1-2.2
	805	15-20	Fine to medium grains, very initial skeletal	XX	XX	XX	X	XX	XXX	3.66	21.52	425	-
	809(f)	15-20	Fine to medium grains	XX	XX	X	X	XX	XX	8.24	16.01	250	1.4-1.6

--absent; X = rare; XX = fairly common; XXX = common; XXXX = predominant

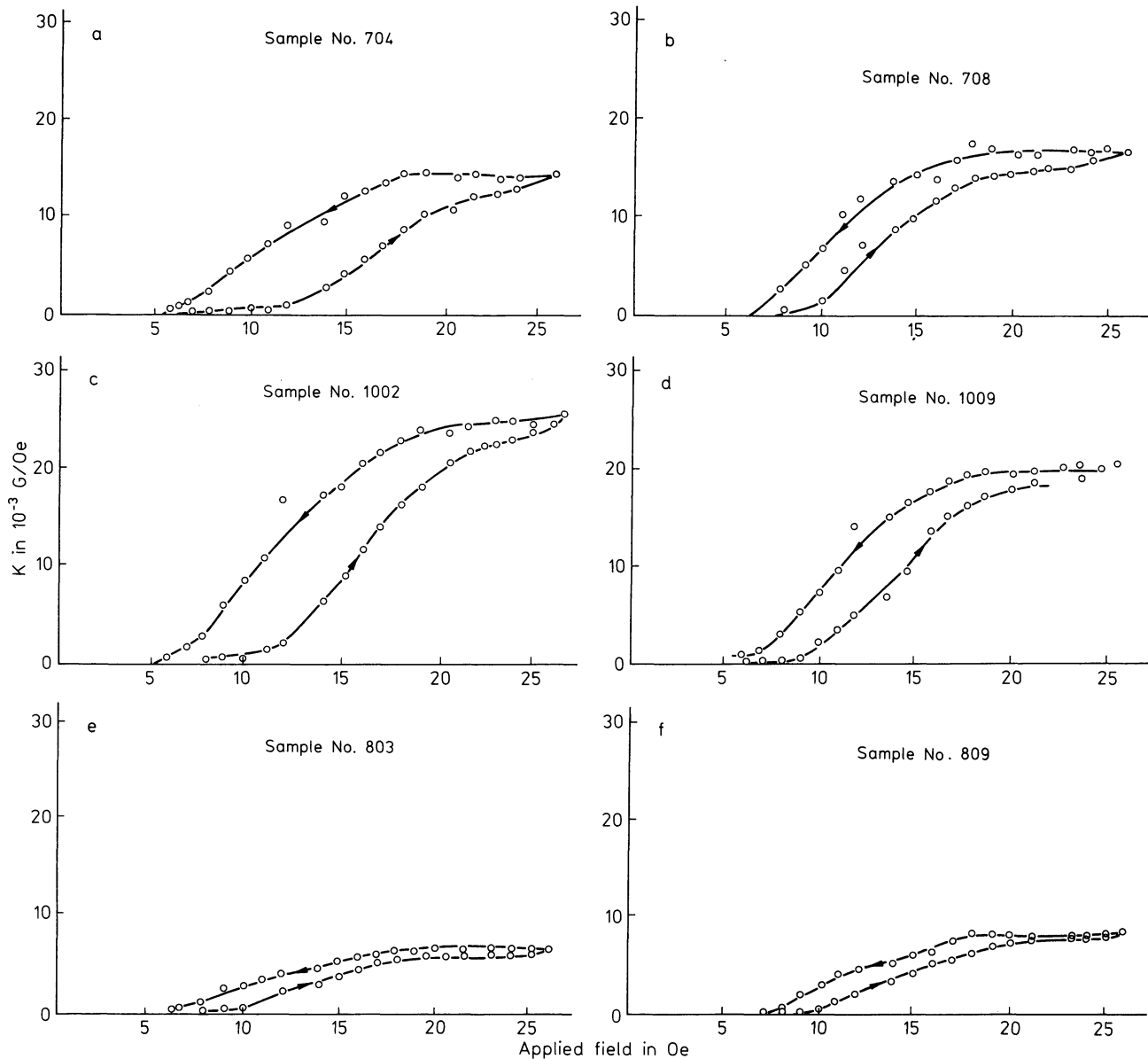


Fig. 11 a-f. The dependence of susceptibility on the applied magnetic field. The upper parts **a-d** refer to high $K(\text{G}/\alpha)$ peak values with irreversible behaviour, while **e** and **f** are characterized by lower peak values

the presence of almost equal amounts of Ti-poor and Ti-rich varieties which are altered into martite and maghemite (as for sites 700 and 1,000, titanomagnetite predominates, being altered to maghemite); (c) common presence of ilmenite-magnetite sandwich and granule intergrowths as well as discrete ilmenite at site 800.

The magnetic and mineralogical properties studied here have been found in rocks carrying normal as well as reversed remanent magnetization directions. These properties have no bearing on the polarity of the natural magnetization of the rocks.

Comparison with results from northern egypt

Table 4 reveals that the directions of magnetization of the northern volcanic rocks (Fig. 1) are reversed, i.e. the inclinations are always negative. The declinations were also found to be quite consistent, pointing to SSW. The direc-

tions of El-Bahnasa and Tahna are grossly different, with low positive inclinations. Semiangle circles of confidence (α_{95}) are very large. The initial susceptibility values for both the northern and southern volcanics indicate that they range from very low values to rather high values. But the magnetic intensities for El-Bahnasa and Tahna are about three times higher than the northern localities and the Q_n values are ten times those of the northern sites.

The magnetic properties of the completely oxidized Fe-Ti oxides are distinctly different from the unoxidized or little oxidized. Hematite has a weak ferromagnetism with a saturation magnetization about 200 times less than that of magnetite and a Curie temperature of 670°C , while rutile and pseudobrookite are dia- or paramagnetic at room temperature. Therefore, the highly oxidized lava flows (northern lavas) are characterized by low intensity of magnetization on the one hand and high stability of remanence on the other hand (see Table 4) since hematite is able to carry

Table 4. Magnetic and mineralogical results from the northern and southern lava flows

Locality	<i>N</i>	<i>D_m</i> (°)	<i>I_m</i> (°)	α_{95} (°)	<i>R</i>	<i>K</i>	Mean values			Mineralogical results
							<i>J_{NRM}</i> (10 ⁻⁴ G)	χ (10 ⁻⁴ G/Oe)	<i>Q_n</i>	
<i>Abu Rawash</i> (Refai and Wassif, 1970)	20	193	-57	3	19.80	190	6.40	2.66	5.68	Total opaque % by volume (6-12) coarse grained, highly oxidized Fe-Ti oxides
<i>Abu Zaabal</i> (El-Rashidi, 1964)	33	208	-58	4	31.92	29	3.90	2.77	3.30	
<i>Cairo-Zuec Road (T 3)</i> (Fahim et al., 1971)	9	210	-59	5	8.93	114	3.63	1.63	3.10	
<i>East of Cairo (Nasr City)</i> (El-Sheikh, 1968)	9	200	-59	4	8.96	197	2.39	1.47	3.70	
<i>Qatrani-Fayum</i> (Basta et al., 1981)	22	191	-55	3	21.83	123	4.5	3.21	3.04	Total opaque % by volume (20-25). Fine grain unoxidized or little oxidized Fe-Ti oxides
	21	195	-63	3	20.84	129				
	9	204	-57	5	8.89	76				
<i>El-Bahnasa</i> Present work	8	148	+24	16	7.45	13	16.25	3.65	40	
	7	149	+32	38	5.26	8				
<i>Tahna</i> Present work	15	313	+24	39	7.74	2	18.5	4.15	48.53	

**Fig. 12.** Some pillowed basalts from Tahna area

a very stable remanent magnetization. The slow rate of cooling is the most important controlling factor in the determination of grain size. This would again encourage exsolution lamellae of ilmenite (northern lava) to divide the more magnetic fraction, essentially magnetite, into very small portions of the order of 0.01 μm of linear dimensions. It is very likely that some of these subdivisions (0.01 μm) reach single-domain particle dimension and are probably the source of a hard component of magnetization (Stott, 1971).

In a magma body which behaves as a closed system, and cools very rapidly, the composition of the primary ore minerals is frozen in (Hargraves and Petersen 1971). Rocks originating in such an environment are extremely vulnerable to oxidation by air or water, leading to substantial changes in mineralogy and magnetic properties. If the oxidation of the primary Fe-Ti oxides has not been completed at high temperatures but goes on at temperatures below 600°C, a metastable cation-deficient spinel phase titanomaghemite may be formed. It seems that the subaqueous environment

which is rich in water appears to favour the particular oxidation into maghemite or low-temperature oxidation (Ozima and Ozima, 1971). As a result of rapid cooling, the size of ore grains is relatively small, from submicroscopic to a few tens of microns (southern lavas); they therefore possess high coercivities and low Curie points. This is reflected in the high values of their Q_n factors as reported, for example, by Ade-Hall (1965), Stacey (1967) as well as Hargraves and Petersen (1971).

The mechanism of Tertiary volcanicity in Egypt has been discussed by Rittman (1954). He raised the question of whether the eruptions happened on land or beneath a shallow sea. He stated that this will be difficult to decide because the characteristic surface features of the Tertiary volcanics of Egypt were removed by erosion during Pliocene and Pleistocene times. The absence of pillow lavas presents an argument in favour of subaerial origin of the flows; an argument which, however, is not absolutely cogent. According to Abdel Maksoud (1968), the eruptions of Tahna and El-Bahnasa were certainly partly erupted beneath shallow waters. The data presented in the foregoing, together with the occasional presence of pillowed basalts in a matrix of clays and carbonates (Fig. 12) in Tahna, might suggest that at least a portion of these basalts were formed in a subaqueous environment (e.g. lakes). However, quantitative correlations of the cooling history and accurate age determinations are still lacking.

Finally, it is concluded that the ore microscopic observations can help a great deal towards the understanding of the magnetic data. Titanomagnetite was found to be the major opaque mineral in all the basalts, a feature that is corroborated by the J_s - T curves. Although titanomagnetite is the dominant phase, variations in the magnetic characteristics were observed. Such differences are attributed to variation in grain size, amount of magnetic minerals, degree and type of magnetite alteration and frequency of ilmenite present as a coexisting phase. This is clear when comparing

the magnetic and opaque characteristics of the three investigated sites. Furthermore, the directions of magnetization at the two sites of El-Bahnasa are almost similar. However, the above-mentioned mineralogical differences are behind the variation in the other magnetic properties.

Acknowledgements. I am grateful to Professor Dr. Maher A. Takla for valuable discussions and critically reading the manuscript. Also, I am thankful to Professor Dr. Bahga H. Mawaid for generous help in various stages of the work and Professor Dr. Gamel S. Saleeb for providing facilities during collection of the oriented sample.

References

- Abdel Maksoud, M.A.: Petrographical, geochemical and physical properties of Egyptian basaltic rocks with special references to Abu-Zaabal. M.Sc. Thesis, Cairo University, 1968
- Ade-Hall, J.M.: The magnetic properties of some submarine oceanic lavas. *J. Geophys.* **9**, 85–94, 1965
- Ball, J., Beadnell, H.J.L.: Baharia oasis, its topography and geology. *Egypt Survey Dept.*, Cairo, 84, 1903
- Basta, E.Z.: Different types of ilmenite-magnetite intergrowths and their origin. *Bull. Fac. Sci.*, Cairo University, **44**, 195–212, 1970
- Basta, E.Z., Refai, E., Wassif, N.A.: Correlation between magnetic and mineralogical properties of some Tertiary basaltic rocks from Qatrani-Fayum Area, Egypt. *Pageoph.* **119**, 357–372, 1981
- Cockerham, R.S., Hall, J.W.: Magnetic properties and paleomagnetism of some DSDP, Leg. 33, basalts and sediment and their tectonic implications. *J. Geophys. Res.* **81**, 4207–4222, 1976
- El-Rashidi, Y.M.: Study of the magnetic properties of some Egyptian rocks and their relation to the Earth's magnetic field. M.Sc. Thesis, Cairo University, 1964
- El-Shazly, E.M., Krs, M.: Magnetism and paleomagnetism of oligocene basalts from Abu-Zaabal and Qatrani, Northern Egypt. *Travaux Inst. Geophys. Acad. Tchecosl. Sci.* No. 356, *Geofysikalni Sbomnik*, 1971
- El-Sheikh, M.E.: Magnetic survey in the area East of Cairo. M.Sc. Thesis, Cairo University, 1968
- Fahim, M., Gouda, H.: Magnetization and paleomagnetism of Abu-Zaabal and Abu-Rawash basalts. Egypt, Helwan Institute of Astronomy and Geophysics, *Bull.* No. 134, 1976
- Fahim, M., Basta, E.Z., El-Rashidi, Y.M.: A paleomagnetic study on some Tertiary basalts from Egypt. IAGA, XV IUGG, General Assembly, Moscow, 1971
- Fisher, R.A.: Dispersion on a sphere. *Proc. R. Soc. London*, A **217**, 295–305, 1953
- Gough, L.G.: *Compt. Rend.* **109**, 935, 1889
- Haggerty, S.E.: Opaque mineral oxides in terrestrial igneous rocks. In: *Oxide minerals*, Rumble, D. (ed.) Mineralogical Society of America short course notes, 3: pp 101–140. Blackburg, Virginia, USA: Southern Printing Company, 1976
- Hargraves, R.B., Petersen, N.: Notes on the correlation between petrology and magnetic properties of basaltic rocks. *Z. Geophys.* **37**, 367–382, 1971
- Johnson, H.P., Atwater, T.: A magnetic study of the basalts from the Mid-Atlantic Ridge at 37°N. *Bull. Geol. Soc. Am.* **88**, 637–647, 1977
- Johnson, H.P., Hall, J.M.: A detailed rock magnetic and opaque mineralogy study of the basalts from the Nazca Plate. *Geophys. J.R. Astron. Soc.* **52**, 45–64, 1978
- Kent, D.V., Honnorez, B.M., Opdyke, N.D., Fox, P.J.: Magnetic properties of dredged oceanic gabbros and the source of marine magnetic anomalies. *Geophys. J.R. Astron. Soc.* **55**, 513–537, 1978
- Lowrie, W.: Oceanic basalt magnetic properties and the Vine and Matthews hypothesis. *J. Geophys.* **40**, 513–536, 1974
- Ozima, M., Larson, E.E.: Low- and high-temperature oxidation of titanomagnetite in relation to irreversible changes in the magnetic properties of submarine basalts. *J. Geophys. Res.* **75**, 1003–1018, 1970
- Ozima, M., Ozima, M.: Characteristic thermomagnetic curve in submarine basalts. *J. Geophys. Res.* **76**, 2051–2056, 1971
- Rayleigh, L.: Notes on electricity and magnetism. III-on the behaviour of iron and steel under the operation of feeble magnetic forces. *Phil. Mag.* **23**, 225, 1887
- Refai, E., Wassif, N.A.: Studies on the magnetism of Abu-Rawash basalts. *Bull. Fac. Sci.*, Cairo University, **44**, 219–230, 1970
- Rittman, A.: Remarks on the eruptive mechanism of the Tertiary volcanoes in Egypt. *Bull. Volcanologique*, **XV**, 109, 1954
- Schaeffer, R.M., Schwarz, E.J.: The Mid-Atlantic Ridge near 45°N. IX. Thermomagnetism of dredged samples of igneous rocks. *Can. J. Earth Sci.* **7**, 268–273, 1970
- Stacey, F.D.: The Koenigsberger ratio and the nature of thermoremanence in igneous rocks. *Earth Planet. Sci. Lett.* **2**, 67–68, 1967
- Stott, P.M.: The stability of magnetization in basic igneous rocks. *BMR Bull.* **129**, Australia, 1971
- Thellier, E.: Sur l'aimantation de terres cuites et ses application en géophysique. Thèse, Paris, 1938
- Wassif, N.A.: Opaque mineralogy and magnetic investigation of basaltic rocks from the Bahariya area, Egypt. *J. Univ. Kuwait (Sci)* **10**, 111–123, 1983
- Watson, G.S.: Analysis of dispersion on a sphere. *Roy. Astron. Soc. Geophys. Suppl.* **7**, 153, 1956

Received October 18, 1984;

revised versions December 23, 1985, and June 2, 1986

Accepted June 12, 1986

On the use of line current analogues in geomagnetic depth sounding*

Alan G. Jones

Lithospheric Geophysics, Geological Survey of Canada, 1 Observatory Crescent, Ottawa, Ontario, Canada, K1A 0Y3

Abstract. Various workers have appealed to Biot-Savart's law for interpreting their anomalous geomagnetic response functions as an aid to describing the electromagnetic induction process. This approach, of using such a line current analogue, is shown herein to be erroneous if the conductivity of the lower half-space is not taken into consideration. A numerical solution, using an FFT, is derived from the kernels of the electromagnetic field components involved, and is compared with the simplistic solution offered by Biot-Savart's static field approximation. It is shown that within a close proximity of the surface position of the buried line current, Biot-Savart's law is reasonable. However, outwith this distance the *anomalous* magnetic field components, and accordingly their ratio, cannot be described by Biot-Savart's law, but closely resemble induction, at the inductive limit, in an isolated well-conducting inhomogeneity.

Uses of a line current in a conducting half-space as a suitable analogue of the true induction processes are illustrated with comparison to three anomalies – a conducting block, Alert, and the Great Glen fault.

Key words: Line current analogue – Electromagnetic induction – Alert – Great Glen fault

Introduction

In the field of electromagnetic induction studies of the Earth, many workers have found cause to interpret their observations in terms of a line (or sheet or box) current flowing beneath their recording locations as a convenient analogue for the actual induction processes that are taking place. Recently this approach has been used by Niblett et al. (1974), Wilhelm and Friis-Christensen (1974), Alabi et al. (1975), Jankowski et al. (1977), Lilley and Woods (1978), Lienert (1979), Woods and Lilley (1980), DeLaurier et al. (1981), Lilley et al. (1981), Praus et al. (1981), Kirkwood et al. (1981), Ingham and Hutton (1982), Ingham et al. (1983) and Bingham et al. (1985). However, all of these authors considered that their line current was flowing in free space and used the static-field approximation which leads to Biot-Savart's law. The effect due to the conductivity of the lower half-space was neglected. In this work, this parameter is

treated in full and it is shown that the electromagnetic field components may be derived by Fourier transforming their respective kernels in the *wavenumber-frequency* domain.

The erroneous conclusions that result from treating the lower half-space as having zero conductivity are detailed and three examples are considered to illustrate the advantages of using a line current in a conducting half-space as an analogue for the true electromagnetic induction processes involved.

Theory

As shown, for example, in Patra and Mallick (1980, pp. 85–87), for an infinite line source oriented along the x direction at location $y=0$ and depth d in the lower half-space (denoted as region 1, of conductivity σ_1 , permeability μ_1 , and permittivity ϵ_1) of a two-media problem (Fig. 1) in which the discontinuity between the media is along the $z=0$ plane (the upper half-space, region 2, has appropriate parameters σ_2 , μ_2 and ϵ_2 , respectively), only the $\Pi_x(\omega)$ electric Hertz vector potential exists. This vector potential satisfies the Helmholtz equation

$$\frac{\partial^2}{\partial z^2} \Pi_x(y, z, \omega) + \frac{\partial^2}{\partial y^2} \Pi_x(y, z, \omega) - k_n^2 \Pi_x(y, z, \omega) = 0 \quad (1)$$

where k_n is the electromagnetic wave propagation constant for the medium of interest, given by

$$k_n^2 = \omega \mu_n (i\sigma_n - \omega \epsilon_n). \quad (2)$$

The vector potential in the lower half-space is given by

$$\Pi_x^1 = \Pi_0 + \int_{-\infty}^{\infty} A e^{-\eta_1 z} e^{-i\nu y} d\nu \quad (3a)$$

where Π_0 is the source term (see Patra and Mallick, 1980, p. 86), and in the upper half-space by

$$\Pi_x^2 = \int_{-\infty}^{\infty} B e^{\eta_2 z} e^{-i\nu y} d\nu, \quad (3b)$$

where $\eta_i^2 = \nu^2 + k_i^2$ (the usual root chosen for η_i such that the solutions for A and B lead to physical fields) and ν is the wavenumber. From the electric vector potential, the electromagnetic field components that exist, namely E_x , H_y , and H_z , can be derived by

* Geological Survey of Canada Publication 14186

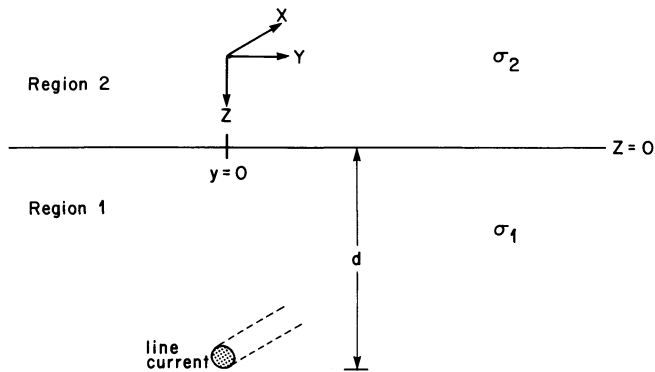


Fig. 1. The mathematical model to be considered. A line current, infinite in the x -direction, at y, z co-ordinates $(0, d)$ in the lower half-space (region 1) of a two half-space problem

$$E_x = -k^2 \Pi_x, \quad (4a)$$

$$H_y = \frac{k^2}{i\omega\mu} \frac{\partial \Pi_x}{\partial z} = \frac{-1}{i\omega\mu} \frac{\partial E_x}{\partial z}, \quad (4b)$$

$$H_z = -\frac{k^2}{i\omega\mu} \frac{\partial \Pi_x}{\partial y} = \frac{1}{i\omega\mu} \frac{\partial E_x}{\partial y}. \quad (4c)$$

The boundary conditions require that the tangential electric and magnetic field components are continuous across the $z=0$ boundary. Hence, at $z=0$

$$k_1^2 \Pi_x^1 = k_2^2 \Pi_x^2 \quad (5a)$$

from the continuity of E_x , and

$$k_1^2 \frac{\partial \Pi_x^1}{\partial z} = k_2^2 \frac{\partial \Pi_x^2}{\partial z} \quad (5b)$$

from H_y (assuming $\mu_1 = \mu_2$, and neither σ_1 nor σ_2 are infinite). Applying these boundary conditions at the interface $z=0$ to Eq. (3b) leads to a solution for B such that the vector potential in the upper half-space is given by

$$\Pi_x^2(y, z, \omega) = I \frac{1}{2} \int_{-\infty}^{\infty} \left[\frac{i\omega\mu e^{-\eta_1 d}}{\pi k_2^2 (\eta_1 + \eta_2)} \right] e^{\eta_2 z} e^{-i\eta_1 y} d\eta_1 \quad (6)$$

(see Patra and Mallick, 1980, pp. 86–87) where I is the current flowing in the wire.

Just above the boundary $z=0$, the three components of the electromagnetic fields present are given by Eq. (4),

$$E_x(y, 0, \omega) = I \frac{1}{2} \int_{-\infty}^{\infty} \left[\frac{-i\omega\mu}{\pi(\eta_1 + \eta_2)} e^{-\eta_1 d} \right] e^{-i\eta_1 y} d\eta_1, \quad (7a)$$

$$H_y(y, 0, \omega) = I \frac{1}{2} \int_{-\infty}^{\infty} \left[\frac{-\eta_2}{\pi(\eta_1 + \eta_2)} e^{-\eta_1 d} \right] e^{-i\eta_1 y} d\eta_1, \quad (7b)$$

$$H_z(y, 0, \omega) = I \frac{1}{2} \int_{-\infty}^{\infty} \left[\frac{i\eta_1}{\pi(\eta_1 + \eta_2)} e^{-\eta_1 d} \right] e^{-i\eta_1 y} d\eta_1. \quad (7c)$$

Note that these integrals can be recognised as Fourier transformations from the wavenumber domain (η) into the space domain (y) of three kernel functions K_{E_x} , K_{H_y} and K_{H_z} given by

$$K_{E_x}(\eta) = \frac{-i\omega\mu}{\pi(\eta_1 + \eta_2)} e^{-\eta_1 d}, \quad (8a)$$

$$K_{H_y}(\eta) = \frac{-\eta_2}{\pi(\eta_1 + \eta_2)} e^{-\eta_1 d}, \quad (8b)$$

$$K_{H_z}(\eta) = \frac{i\eta_1}{\pi(\eta_1 + \eta_2)} e^{-\eta_1 d}. \quad (8c)$$

These kernels are such that $K_{E_x}(\eta)$ and $K_{H_y}(\eta)$ are symmetric, and $K_{H_z}(\eta)$ anti-symmetric, about $\eta=0$.

The authors cited in the introduction all considered that their line currents were flowing in free space of zero conductivity. Accordingly, we may derive the electromagnetic field components observable by taking the appropriate values for their respective physical parameters for both region 1 and region 2, i.e. $\sigma_1 = \sigma_2 = 0$, $\epsilon_1 = \epsilon_2 = \epsilon_0$, $\eta_1 = \eta_2 = \eta_0 = \sqrt{v^2 + k_0^2}$, $k_1 = k_2 = k_0 = \sqrt{(-\omega^2 \mu_0 \epsilon_0)}$. The fields can be expressed as modified Bessel functions, with certain limiting forms,

$$E_x(y, 0, \omega) = I \frac{1}{2} \int_{-\infty}^{\infty} \left[\frac{-i\omega\mu_0 e^{-\eta_0 d}}{2\pi\eta_0} \right] e^{-i\eta_0 y} d\eta_0 \quad (9a)$$

$$= I \frac{-i\omega\mu_0}{2\pi} K_0(k_0 \sqrt{y^2 + d^2}) \quad (9b)$$

$$\approx I \frac{i\omega\mu_0}{2\pi} \ln(k_0 \sqrt{y^2 + d^2}) \quad (9c)$$

where the approximation is valid for $|k_0 \sqrt{y^2 + d^2}| \ll 1$ (Abramowitz and Stegun, 1970, 9.6.8),

$$H_y(y, 0, \omega) = I \frac{1}{2} \int_{-\infty}^{\infty} \left[\frac{-e^{-\eta_0 d}}{2\pi} \right] e^{-i\eta_0 y} d\eta_0 \quad (10a)$$

$$= \frac{I}{2\pi} \frac{k_0 d}{\sqrt{y^2 + d^2}} K_1(k_0 \sqrt{y^2 + d^2}) \quad (10b)$$

$$\approx \frac{I}{2\pi} \frac{d}{y^2 + d^2} \quad (10c)$$

and

$$H_z(y, 0, \omega) = I \frac{1}{2} \int_{-\infty}^{\infty} \left[\frac{i\eta_0 e^{-\eta_0 d}}{2\pi\eta_0} \right] e^{-i\eta_0 y} d\eta_0 \quad (11a)$$

$$= \frac{I}{2\pi} \frac{k_0 y}{\sqrt{y^2 + d^2}} K_1(k_0 \sqrt{y^2 + d^2}) \quad (11b)$$

$$\approx \frac{I}{2\pi} \frac{y}{y^2 + d^2} \quad (11c)$$

where approximations (10c) and (11c) are valid for $|k_0 \sqrt{y^2 + d^2}| \ll 1$ (Abramowitz and Stegun, 1970, 9.6.9). Noting that the correct value of k_0 in free space is $k_0 = \sqrt{\omega\mu(i\sigma_0 - \omega\epsilon_0)}$, and for values of ω of interest in electromagnetic induction studies ($< 10^5 \text{ s}^{-1}$) neglecting σ_0 (valid for $\omega\epsilon_0 \gg \sigma_0$, and $\sigma_0 \approx 10^{-13} \text{ S/m}$, Dolezalek, 1984) $k_0 \approx i\omega/c$, then this condition becomes $\omega \sqrt{y^2 + d^2} \ll c$. The static-field approximations given by Eqs. (10c) and (11c) can be recognised as Biot-Savart's law.

The forms (10c) and (11c) are those that have been utilised by the authors cited at the beginning of this note. Obviously, the ratio of the vertical magnetic field to the horizontal magnetic field, where both are due to a line current, is given by dividing Eq. (10b) by (11b)

$$\frac{H_z(y, 0, \omega)}{H_y(y, 0, \omega)} = \frac{y}{d}$$

when both regions 1 and 2 are considered to be free space. Also of significance is that the phase lead of E_x over H_y is $\pi/2$, i.e. they are totally out-of-phase, and the phase between H_z and H_y is 0, i.e. they are totally in phase.

However, for $\sigma_1 \neq 0$ and $\sigma_2 = 0$, as is the case for an infinite-length line current flowing at some depth d within a homogeneous half-space, then solutions to Eq. (7) must be sought. Closed-form solutions of these integrals do not appear to exist, and accordingly solutions must be sought resorting to numerical techniques taking advantage of the Fourier transform property of the three field-component kernels [Eq. (8)].

Discussion

To determine the validity of assuming that the line current is flowing in free space rather than within the lower half-space, it is of interest to examine the kernels [Eq. (8)] of the integrals. With medium 2 being free space, then $|\eta_2| = \sqrt{|v|^2 + k_2^2} \approx \sqrt{v^2 - \omega^2/c^2} \approx |v|$ for $|v| \gg \omega/c$. Accordingly, for $|v| \gg \omega/c$, the kernels become

$$K_{E_x}(v) = \frac{-i\omega\mu}{\pi(\eta_1 + |v|)} e^{-\eta_1 d}, \quad (12a)$$

$$K_{H_y}(v) = \frac{-|v|}{\pi(\eta_1 + |v|)} e^{-\eta_1 d}, \quad (12b)$$

$$K_{H_z}(v) = \frac{iv}{\pi(\eta_1 + |v|)} e^{-\eta_1 d}. \quad (12c)$$

Note the interesting feature that the magnetic-field-component kernels given by Eq. (12b, c) are related by $K_{H_z}(v) = -i \operatorname{sgn}(v) K_{H_y}(v)$, which implies that $-H_z(y, 0, \omega)$ and $H_y(y, 0, \omega)$ form a Hilbert transform pair. Thus, for a dataset consisting of a profile of stations over a body whose response can be approximated by a line current analogue, the surface perpendicular-to-strike horizontal magnetic and vertical magnetic fields are related to each other by the Hilbert transform. This Hilbert transform relationship of internal anomalous fields has already been noted by Kertz (1954) (see also Berdichevsky and Zhdanov, 1984, pp. 200–201).

Obviously, the kernels given by Eq. (7) are only significantly different from the free space ones [Eqs. (9a), (10a), (11a)] when $|\eta_1| = \sqrt{|v|^2 + k_1^2} \gg |v|$, which is true for $|k_1|^2 = |\omega\mu(i\sigma_1 - \omega\varepsilon_1)| \gg |v|^2$. Assuming that the displacement-current term may be neglected in the conducting lower half-space, then this condition becomes $\omega\mu\sigma_1 \gg |v|^2$, i.e. for small values of wavenumber compared to the wave propagation constant in the conducting half-space. Note also that the free space kernels have dramatically different values at both zero and ω/c wavenumbers to those expressed by Eq. (12). For $v=0$, then obviously $|\exp(-\eta_1 d)| \rightarrow 1$. For free space, $K_{E_x}(0) = -60 \Omega$, $K_{H_y}(0) = -1/2\pi$ and $K_{H_z}(0) = 0$. However, for $\sigma_1 \neq 0$, then

$$K_{E_x}(0) \approx -i\omega\mu/\pi \sqrt{i\omega\mu\sigma_1} = -(1+i) \sqrt{\omega\mu/2\sigma_1}/\pi,$$

$$K_{H_y}(0) \approx -(1+i) \sqrt{\omega\mu\sigma_1}/\pi c \quad \text{and} \quad K_{H_z}(0) = 0.$$

For $|v| = |k_0| = \omega/c$, then $\eta_0 = 0$, and in free space $K_{E_x}(|k_0|)$

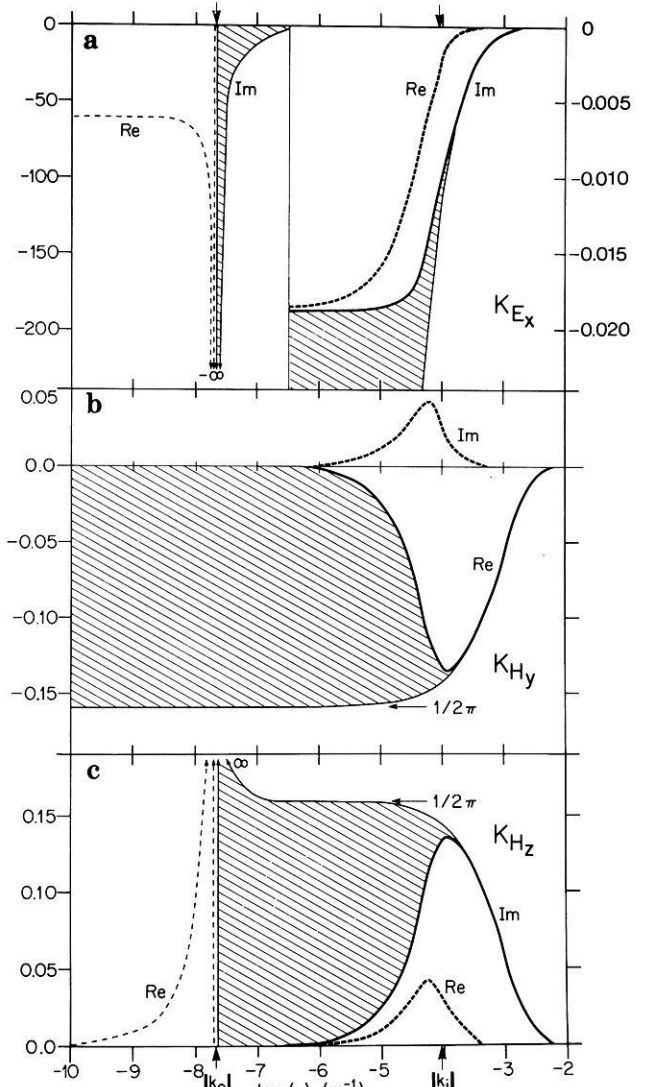


Fig. 2a–c. The bold lines illustrate the kernels for a line current at a depth of 1 km in a half-space of $1,000 \Omega\text{m}$ excited at a frequency of 1 Hz, whereas the light lines are those for a line current in free space. The shaded regions are those areas included in the integral when the line current is considered to be in free space. **a** $K_{E_x}(v)$, (Im in full lines, Re in dashed) – note the dramatic change in ordinate scale at $v = 10|k_0|$, **b** $K_{H_y}(v)$, (Re in full lines, Im in dashed), **c** $K_{H_z}(v)$, (Im in full lines, Re in dashed)

$= -(\infty + i\infty)$, $K_{H_y}(|k_0|) = 1/2\pi$ and $K_{H_z}(|k_0|) = (\infty + i\infty)$; whereas for a conducting lower half-space

$$K_{E_x}(|k_0|) \approx -(1+i) \sqrt{\omega\mu/2\sigma_1}/\pi,$$

$$K_{H_y}(|k_0|) = 0 \quad \text{and} \quad K_{H_z}(|k_0|) = (1+i) \sqrt{\omega/2\mu\sigma_1}/\pi c.$$

As an example, consider a half-space of $\sigma_1 = 10^{-3} \text{ S/m}$ with a source line current at a depth of 1,000 m radiating with a frequency of 1 Hz. The kernels for such a configuration are illustrated in Fig. 2a–c. The contributions to the electromagnetic field components due to the conducting lower half-space are important for wavenumbers smaller than $\approx 10^{-6} \text{ m}^{-1}$. Note the dramatic difference at very small wavenumbers for K_{E_x} [there is a change of scale at $\log(v) = -6.5$] in Fig. 2a. The shaded areas of the three figures indicate those parts of the integrals that are included

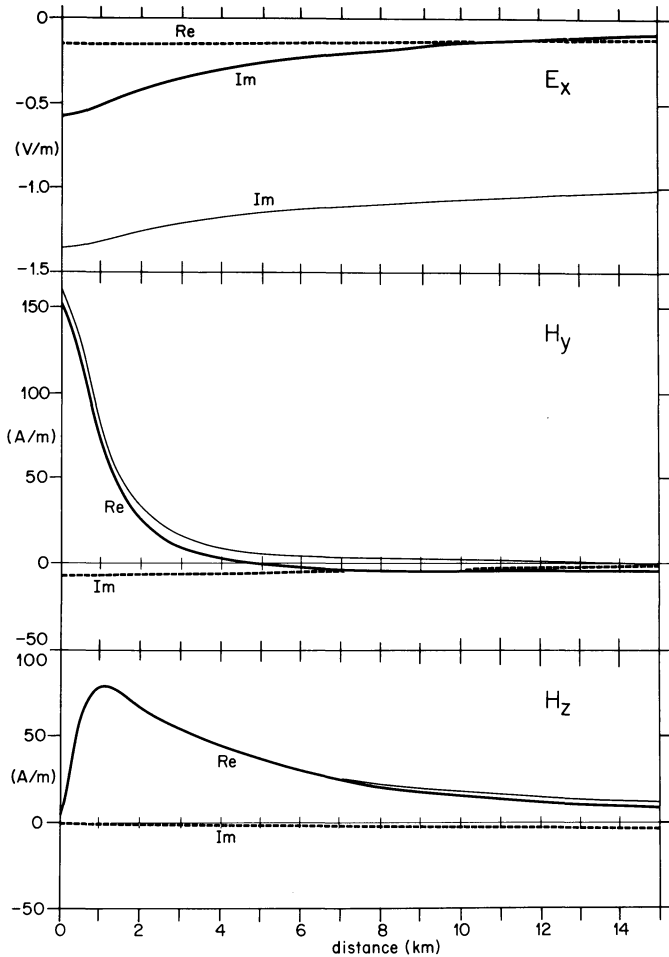


Fig. 3. The surface electromagnetic fields $E_x(y)$, $H_y(y)$, $H_z(y)$ given by a line current at a depth of 1 km in a half-space of $1,000 \Omega\text{m}$ excited at a frequency of 1 Hz. The *light* lines are for the fields observed in a free space

when the conductivity of the lower half-space is not taken into consideration. Obviously,

$$\eta_1 = \sqrt{v^2 + k_1^2} = v[1 + (k_1/v)^2]^{1/2} \approx v[1 + (k_1/v)^2/2]$$

for $v \gg |k_1|$, and thus $\exp(-\eta_1 d) \approx \exp(-vd)(1 - k_1^2 d/2v)$ for large v . At $v = 10|k_1|$, then

$$K_{H_y} = -|v|/2\pi(\eta_1 + v) \exp(-\eta_1 d) \\ \approx (-1/2\pi) \exp(-vd)(1 - k_1 d/20).$$

For our example, $|k_1|d \approx 0.1$, and accordingly the free space kernel given by Eq. (10a) equals the conducting half-space kernel to within 0.5% at $v = 10|k_1|$.

In Fig. 3 are illustrated the three fields for a source current of 10^6 A derived by Fast Fourier Transforms of the three kernels in the range $v = [-81.92|k_1|, 81.92|k_1|]$ ($= [-7.28, 7.28] \times 10^{-2} \text{ m}^{-1}$) with $\Delta v = |k_1|/100$ ($= 8.88 \times 10^{-6} \text{ m}^{-1}$), i.e. each series of 16,384 complex points. Also shown in the figure are the fields that would be observed for a line current in free space, i.e. determined from Eq. (9c), (10c) and (11c). Ignoring the fact that the imaginary components of the magnetic fields cannot be computed for the free space formalism, $H_z(y, 0, \omega)$ is well-approximated by Biot-Savart's law out to a distance of

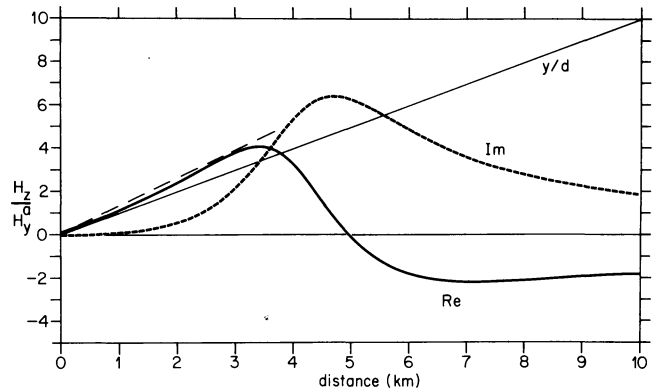


Fig. 4. The ratio of the vertical magnetic field component to the horizontal magnetic field component for a line current at a depth of 1 km in a half-space of $1,000 \Omega\text{m}$ excited at a frequency of 1 Hz. $\text{Re}(H_z/H_y)$ denoted by *full* line, $\text{Im}(H_z/H_y)$ as *dashed* line. The function y/d illustrates the response if the line current were considered to be in free space

≈ 7 km. For $H_y(y, 0, \omega)$, the relative difference becomes significantly large at distances greater than ≈ 1 km, and indeed $\text{Re}(H_y)$ changes sign at ≈ 5 km. This infers that the return currents are flowing beyond 5 km, whereas they flow at infinity for a line current in free space. It is apparent from the figure that $E_x(y, 0, \omega)$ is most affected by having a non-zero conductivity for the lower half-space. This is to be expected considering the greater attenuation of the electric field in a medium of non-zero conductivity. Accordingly, the anomalous electric field due to a line current source at depth within a conducting half-space is much smaller, for the same equivalent anomalous magnetic component magnitudes, than would arise if the current source were in free space. This feature implies that investigation of the possible effects on the computed magnetotelluric ratio of E_x^t/H_y^t (where superscript t denotes *total* fields) due to a line current source of the form carried out by, for example, Ingham and Hutton (1982), is of little practical use unless the conductivity of the host rock is taken into consideration. Ingham and Hutton quote an electric field magnitude due to a line current source of 3.5 mV/km ; whereas in a half-space of $75 \Omega\text{m}$, a current of 127 A of 300 s periodicity at a depth of 50 km yields an electric field directly above the line of magnitude $\approx 0.1 \text{ mV/km}$. Note that in accordance with the requirement that $H_x(y)$ and $-H_z(y)$ form a Hilbert transform pair, $\text{Re}(H_z)$ maximises approximately at the distance where $\text{Re}(H_y)$ shows maximum gradient.

In induction studies, often the magnetic field components themselves are not as important as their ratios. The ratio H_z/H_y for free space is given simply by y/d . For the example described above, for which the fields are shown in Fig. 3, the ratio H_z/H_y is as illustrated in Fig. 4. As could be expected from the discussion above, y/d is a reasonable approximation out to ≈ 1 km. Accordingly, for stations within a "short" distance from the surface expression of the line current, where "short" here is obviously a function of the frequency of interest, the conductivity of the half-space and the depth of the line current, then the line current can be considered to be in free space. Beyond this distance, and out to ≈ 3 km, then a line current in free space at a depth of 750 m is a reasonable approximation to $\text{Re}(H_z/H_y)$ (shown by the dashed line in Fig. 4). At distances greater than 3 km, then the response function cannot be

described by a line current in free space analogue. This is especially true at distances where the return currents flow, i.e. greater than 5 km, beyond which $\text{Re}(H_y)$ has changed sign and accordingly $\text{Re}(H_z/H_y)$ must change sign.

For a profile of *residual* magnetic observations, $H'_y(y, 0, \omega)$ and $H'_z(y, 0, \omega)$, i.e. observations of H_z and H_y that have had the effects of source fields, ocean effect, etc. removed, that are believed to originate from a channelled current that can be reasonably approximated by a line current, the most effective approach for modelling the data is to inverse Fourier transform the observations into the wavenumber-frequency domain, to give $H'_y(v, 0, \omega)$ and $H'_z(v, 0, \omega)$, and then find the best-fitting parameters I , σ_1 and d such that

$$H'_y(v, 0, \omega) = IK_{H_y}(v)$$

and

$$H'_z(v, 0, \omega) = IK_{H_z}(v)$$

are satisfied over all available frequencies ω . Interpretation in the wavenumber domain requires two Fourier transform operations (after suitable interpolating and extrapolating), and linear inverse theory can be applied directly to solve for the unknown parameters. In comparison, interpretation in the space domain requires two Fourier transform operations every time one (or more) of the parameters are changed.

Examples

In this section, I wish to consider three specific examples for which a line current in a conducting half-space provides a useful concept to describe the electromagnetic induction process.

Block

To compare the example chosen in the previous section to a model in which induction occurs, consider a square block of infinite length in the x -direction with sides 250 m long at a depth of 1 km in a host half-space of 1,000 Ωm (Fig. 5). The ratios of the vertical magnetic field to the *total* horizontal magnetic field (H_z/H'_y) at 1 Hz for four different values of anomaly resistivity (1 = 10 Ωm ; 2 = 1 Ωm ; 3 = 0.1 Ωm ; 4 = 0.01 Ωm) are as illustrated in Fig. 6. By fitting a straight line to the initial rise of $\text{Re}(H_z/H'_y)$, one would conclude that the maximum depth of the anomaly, from y/d arguments, was at a depth of 20 km, 3.3 km, 1.67 km and 1.67 km for the four resistivities of the anomaly, respectively. Therefore, especially for anomalies of moderate resistivity contrast compared with the host rock, misleadingly deep maximum depths would be interpreted. However, if one considers the ratio of the vertical magnetic field component to the *anomalous* horizontal magnetic field component (H_z/H_y^a) – as illustrated in Fig. 7 – the initial rise of $\text{Re}(H_z/H_y^a)$ would imply a maximum depth of ≈ 1.4 km (light dashed line in Fig. 7). Summers (1981) and Jones (1983) have previously suggested that H_z/H_y^a is a more useful response function to interpret for anomalous structure than is H_z/H'_y . Jones (1983) defined “anomalous induction vectors” from the transfer functions relating $H_z(\omega)$ to $[H_x^a(\omega), H_y^a(\omega)]$. As is evident from Fig. 7, once the contrast in resistivity between the host rock and the anomaly reaches approximately three orders of magnitude (curve 2), then induc-

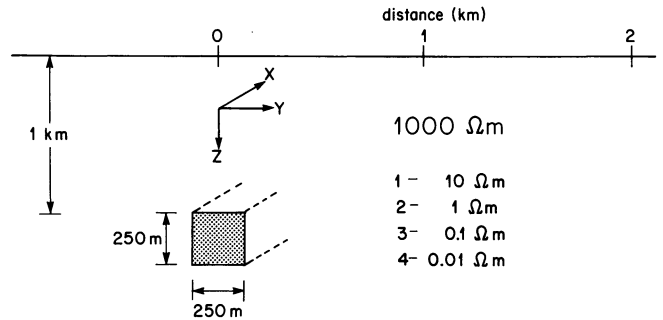


Fig. 5. The block model discussed in the text

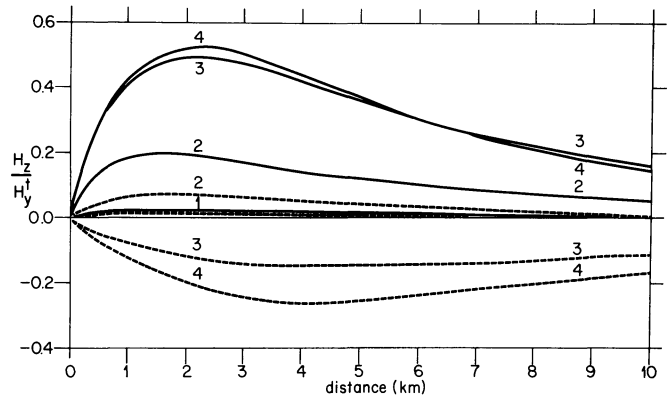


Fig. 6. The ratio of the vertical magnetic field to the *total* horizontal magnetic field, for the model illustrated in Fig. 5 at a frequency of 1 Hz for the four different block resistivities. $\text{Re}[H_z(y)/H'_y(y)]$ in full line, $\text{Im}[H_z(y)/H'_y(y)]$ dashed line

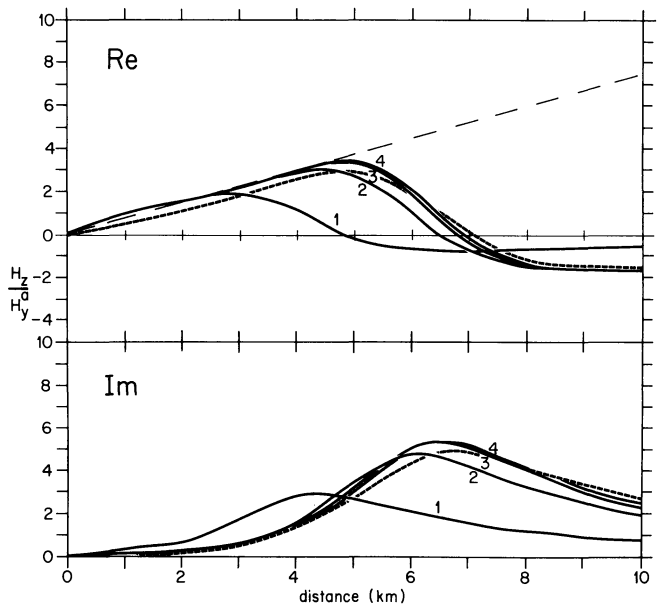


Fig. 7a, b. The ratio of the vertical magnetic field to the *anomalous* horizontal magnetic field, for the model illustrated in Fig. 5 at a frequency of 1 Hz for the four different block resistivities. **a** $\text{Re}[H_z(y)/H_y^a(y)]$, **b** $\text{Im}[H_z(y)/H_y^a(y)]$. The light dashed line in **a** is the y/d response for a line current in free space at a depth of 1.4 km and the heavy dashed lines in both **a** and **b** are the responses for a line current in a conducting half-space (of 1,000 Ωm) at a depth of 2 km

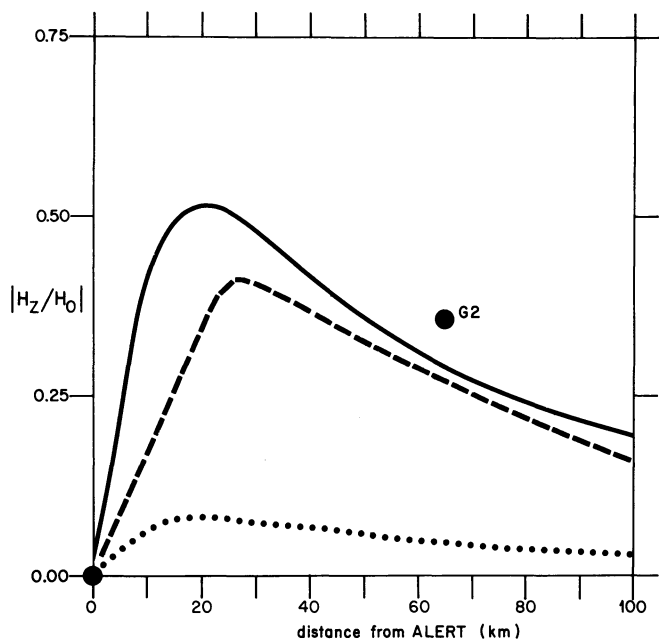


Fig. 8. The two *solid dots* indicate the ratio of $|H_z/H_0|$ observed at Alert and at station G2. The *dashed line* is the analogue response derived by Dyck and Garland for an embedded anomaly with its top at a depth of 25 km. The *dotted line* is the response for a line current in free space at 25 km, whilst the *full line* is the response for a line current in a half-space of $1,000 \Omega\text{m}$ at a period of 2,000 s

tion in the anomaly is at the inductive limit and the ratio of H_z/H_y^a does not change for greater contrast. However, the ratio of H_y^a/H_x^a varies with conductivity contrast and, accordingly, so does H_z/H_y^a (Fig. 6). Obviously, a line current in free space at a depth of 1.4 km (*light dashed line* in Fig. 7a) would well approximate $\text{Re}(H_z/H_y^a)$ at distances out to $\approx 4\text{--}5$ km, but not beyond that. However, a line current at a depth of 2 km in a conductive half-space of $1,000 \Omega\text{m}$, excited at 1 Hz (*heavy dashed lines* in Fig. 7a, b) is an excellent approximation to the response for both $\text{Re}(H_z/H_y^a)$ and $\text{Im}(H_z/H_y^a)$ over the whole distance range.

Alert

The Alert anomaly on Ellesmere Island in northern Canada was one of the first geological structures in the crust whose geomagnetic response was ascribed to current channelling rather than local induction. Figure 8 displays two of the $|H_z/H_0|$ ratios – where H_0 is the “normal” horizontal magnetic field as observed at a station some 120 km from Alert (Law et al., 1963) – for the Alert anomaly and for station G2 as published by Dyck and Garland (1969) and taken from Whitham (1964). The analogue response of an embedded anomaly with dimensional scaling such that it is equivalent to an anomaly 20 km deep, 30 km width and 15 km vertical extent with a conductivity contrast to the host rock of 7×10^4 at a period of 2,000 s was determined by Dyck and Garland and is shown here in Fig. 8 (*dashed line*). Also shown in the figure are the $|H_z/H_0|$ ratios for a line current in free space at 25 km depth (*dotted line*, note that this response is not simply y/d because we are normalizing H_z by the horizontal magnetic field at $y=120$ km, and not by the local H_y) and a line current in a half-space of $10^4 \Omega\text{m}$ at a depth of 25 km radiating at 2,000 s (*solid line*). It is

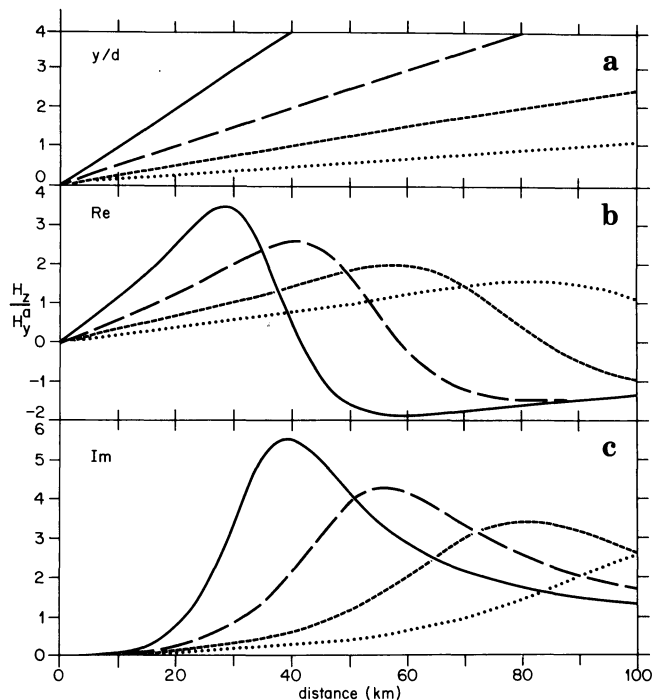


Fig. 9a–c. Modelling the Great Glen fault using line currents. **a** The responses H_z/H_y^a to a line current in free space at depths of 10 km (*solid line*), 20 km (*long dashed line*), 40 km (*short dashed line*) and 80 km (*dotted line*). **b** and **c** are the responses when the line current is in a half-space of $100 \Omega\text{m}$ for a period of 8 min

obvious that whereas the free space line current is not a good simplification, the line current in a conducting half-space is.

Great Glen fault

The geomagnetic anomaly associated with the Great Glen fault in northern Scotland was studied using a line current in free space analogue by Kirkwood et al. (1981). Figure 9a shows the H_z/H_y^a ratio as y/d for a line current in free space at 10 km (*solid line*), 20 km (*long dashed line*), 40 km (*short dashed line*) and 80 km (*dotted line*). Figure 9b and c display $\text{Re}(H_z/H_y^a)$ and $\text{Im}(H_z/H_y^a)$, respectively, for a line current in a half-space of resistivity $100 \Omega\text{m}$ at the four depths given above. It is obvious that the initial rise of $\text{Re}(H_z/H_y^a)$ is well-approximated by a line current in free space, i.e. out to distances of 25, 40, 60 and 85 km for depths of 10, 20, 40 and 80 km, although the depth estimates would be in error. However, beyond these distances, the full solution must be used for $\text{Re}(H_z/H_y^a)$.

Conclusions

It has been shown unequivocally that when one is attempting to interpret observed responses due to induction in an anomaly by using a line current analogue, it is not sufficient to ignore the conductivity of the half-space in which the current is flowing. This is especially true at distances where the return currents are flowing.

Three examples have been chosen to illustrate that induction in a body may be described by a line current in a conducting half-space provided that the induction is at the “inductive limit”. Also, the necessity for considering

the transfer function H_z/H_y^a , rather than H_z/H_y^i , has been stressed.

The Fast Fourier Transform calculations used herein are not particularly "fast" when compared to numerical modelling – only a factor of three increase in speed is realized – however, that was not the thrust of this work. For practical application of a fast line current approximation solution, then either linear filter methods can be used (Johansen and Sorensen, 1979) or Logarithmic Fourier Transforms (Talman, 1978).

Acknowledgements. Part of this work was presented orally to the participants of the Sixth Workshop on Electromagnetic Induction in the Earth and Moon held at Victoria, B.C., Canada, during September, 1982, but was not published in Jones (1983). During that period, the author was at the University of Toronto and received financial support from Professor G.D. Garland (NSERCC A2115) and Professors R.N. Edwards and G.F. West (NSERCC G0501), for which he wishes to acknowledge his gratitude.

The author is also grateful to Gerry Haines and Ron Kurtz for their thoughtful reading of the preliminary version of this manuscript, and Marianne Mareschal and Peter Weidelt for their constructive criticisms of the submitted version.

References

- Abramowitz, M., Stegun, I.A.: Handbook of Mathematical Functions. Dover, New York, 1970
- Alabi, A.O., Camfield, P.A., Gough, D.I.: The North American Central Plains anomaly. *Geophys. J.R. Astron. Soc.* **43**, 815–834, 1975
- Berdichevsky, M.N., Zhdanov, M.S.: Advanced theory of deep geomagnetic sounding. Elsevier, ISBN 0-444-41690-0, 1984
- Bingham, D.K., Gough, D.I., Ingham, M.R.: Conductive structures under the Canadian Rocky Mountains. *Can. J. Earth Sci.* **22**, 384–398, 1985
- DeLaurier, J.M., Plet, F.C., Drury, M.J.: A geomagnetic depth sounding profile across the northern Yukon and the Mackenzie Delta region, Canada. *Can. J. Earth Sci.* **18**, 1092–1100, 1981
- Dolezalek, H.: Atmospheric electricity. In: CRC Handbook of chemistry and physics, 65th Edition, R.C. Weast, ed.: pp. F-158–F-160. Boca Raton, Florida: CRC Press Inc., 1984
- Dyck, A.V., Garland, G.D.: A conductivity model of certain features of the Alert anomaly in geomagnetic variations. *Can. J. Earth Sci.* **6**, 513–516, 1969
- Ingham, M.R., Bingham, D.K., Gough, D.I.: A magnetovariational study of a geothermal anomaly. *Geophys. J.R. Astron. Soc.* **72**, 597–618, 1983
- Ingham, M.R., Hutton, V.R.S.: Crustal and upper mantle electrical conductivity structure in southern Scotland. *Geophys. J.R. Astron. Soc.* **68**, 579–594, 1982
- Jankowski, J., Szymanski, A., Pec, K.: Electromagnetic studies of the Carpathian conduction anomaly. *Acta Geodaet. Geophys. et Montanist. Acad. Sci. Hung.* **12**, 99–109, 1977
- Johansen, H.K., Sorensen, K.: Fast Hankel Transforms. *Geophys. Prospect.* **27**, 876–901, 1979
- Jones, A.G.: The problem of "current channelling": a critical review. *Geophys. Surv.* **6**, 79–122, 1983
- Kertz, W.: Modelle für erdmagnetischen induzierte elektrische Ströme in Untergrund. *Nachr. Akad. Wiss. Göttingen, Math.-Phys. Kl.* **11A**, 101–110, 1954
- Kirkwood, S.C., Hutton, V.R.S., Sik, J.: A geomagnetic study of the Great Glen fault. *Geophys. J.R. Astron. Soc.* **66**, 481–490, 1981
- Law, L.K., DeLaurier, J., Andersen, F., Whitham, K.: Investigations during 1962 of the Alert anomaly in geomagnetic variations. *Can. J. Phys.* **41**, 1868–1882, 1963
- Lienert, B.R.: Crustal electrical conductivities along the eastern flank of the Sierra Nevadas. *Geophysics* **44**, 1830–1845, 1979
- Lilley, F.E.M., Singh, B.P., Arora, B.R., Srivastava, B.J., Prasad, S.N., Sloane, M.N.: A magnetometer array study in northwest India. *Phys. Earth Planet. Inter.* **25**, 232–240, 1981
- Lilley, F.E.M., Woods, D.V.: The channelling of natural electric currents by orebodies. *Bull. Aust. Soc. Explor. Geophys.* **9**, 62–63, 1978
- Niblett, E.R., DeLaurier, J.M., Law, L.K., Plet, F.C.: Geomagnetic variation anomalies in the Canadian Arctic. I. Ellesmere island and Lincoln Sea. *J. Geomagn. Geoelectr.* **26**, 203–221, 1974
- Patra, H.P., Mallick, K.: Geosounding principles, 2. Time-varying geoelectric soundings. Amsterdam: Elsevier, 1980
- Praus, O., Pecova, J., Petr, V., Pec, K., Hvozdar, M., Cerv, V., Pek, J., Lastovickova, M.: Electromagnetic induction and electrical conductivity in the Earth's body. In: Geophysical synthesis in Czechoslovakia, A. Zatopek, ed.: pp. 297–315, Bratislava: Veda, 1981
- Summers, D.M.: Interpreting the magnetic fields associated with two-dimensional induction anomalies. *Geophys. J.R. Astron. Soc.* **65**, 535–552, 1981
- Talman, J.D.: Numerical Fourier and Bessel transforms in logarithmic variables. *J. Comput. Phys.* **29**, 35–48, 1978
- Whitham, K.: Anomalies in geomagnetic variations in the Arctic Archipelago of Canada. *J. Geomagn. Geoelectr.* **15**, 227–240, 1964
- Wilhelm, J., Friis-Christensen, E.: The Igdlorssuit geomagnetic variation anomaly in the rift-fault zone of northern west Greenland. *J. Geomagn. Geoelectr.* **26**, 173–189, 1974
- Woods, D.V., Lilley, F.E.M.: Anomalous geomagnetic variations and the concentration of telluric currents in south-west Queensland, Australia. *Geophys. J.R. Astron. Soc.* **62**, 675–689, 1980

Received January 29, 1986; revised version June 16, 1986

Accepted June 20, 1986

Observations of the VLF quiet band phenomenon

J.P. Matthews*

Radio Atmospheric Science Center, Kyoto University, Uji, Kyoto, Japan

Abstract. In 1979, VLF receivers were operated near Roberval, Canada, by a team from the Japanese Institute of Space and Astronautical Science. Data obtained from this experiment on July 23 near 12.16 UT show one hop signals at just below 3 kHz, originating from the VLF transmitter located at Siple Station, Antarctica. On the low-frequency side of the Siple signals, a “quiet band” of background noise suppression is visible, ~ 95 Hz in width. The time taken for the effect to develop is between 5 and 10 s and the recovery time of the noise is ≥ 20 s. The level of suppression is ~ 3 dB. The important aspect of these data is that, although growth is enhanced above the frequency of the Siple signals, on the lower border of the quiet band little or no enhancement is observed, in contrast to some theoretical models. These data are not of sufficient duration or simplicity to provide a decisive test of recent quiet band theories.

Key words: VLF waves – Quiet band – Siple transmitter – Wave-particle interaction

Introduction

The quiet band phenomenon is observed below the frequency of VLF transmitter signals propagating in the magnetosphere and develops as a band of noise suppression that can be up to 200 Hz in width [Raghuram et al., 1977, henceforth (1)]. The unexpected discovery of the quiet band reported in (1) was made during VLF wave injection experiments conducted along the Siple/Roberval meridian (Helliwell and Katsufurakis, 1974). In these experiments signals from the VLF transmitter located at Siple Station, Antarctica, may enter the magnetosphere and be guided to the northern hemisphere in ducts of enhanced ionisation which are aligned parallel to the geomagnetic field. This guidance sometimes produces detectable ‘one hop’ Siple signals in the conjugate region near Roberval, Canada. An additional magnetospheric response in the form of wave growth or suppression is often observed, along with the transmitter signal itself (Helliwell and Katsufurakis, 1974).

The results described in (1) and in the report by Raghuram (1977) demonstrate that the type of noise suppressed within the frequency range of the quiet band is broadband

midlatitude hiss (Dowden, 1971) and that the level of suppression can be as much as 6 dB for transmitter frequencies near 5 kHz. The quiet bands were rarely observed and required conditions of good whistler-mode echoing between hemispheres. The suppression took between 5 and 25 s to develop and could last up to 1 min after the end of transmissions. Above the transmitter frequency, rapidly developing enhancements were detected due to the triggering of rising tones by the transmitter signal. On the low-frequency border of the quiet band, noise enhancements were observed to develop over a long period (~ 20 min) and seemed to be part of the hiss band itself. Secondary quiet bands could be produced below the enhanced lower border.

The quiet band events reported in (1) occurred during deep quietening in magnetic activity over a time interval of a few hours. The level of noise suppression tended to a limiting value as the amplitude of the source signal increased, whereas the frequency width of the quiet band increased roughly linearly with the source amplitude.

Earlier theoretical work (e.g. Helliwell, 1967; Das, 1978; Ashour-Abdalla, 1972; Bud’ko et al., 1972; Roux and Pellat, 1976) investigated the interaction between monochromatic VLF signals and the energetic electron distribution within the magnetosphere, mainly with a view to explaining the triggered emission phenomenon (Helliwell, 1965). Little emphasis was placed on the investigation of suppression effects. A review of some of these works, which proposes, in particular, that the quasilinear approach is inadequate for a description of the quiet band phenomenon, can be found in Cornilleau-Wehrin and Gendrin (1979).

The discovery of the VLF quiet band phenomenon stimulated several more recent theoretical studies. Raghuram (1977) presented numerical simulation results which demonstrated that monochromatic VLF signals of large enough amplitude could alter the distribution function of energetic magnetospheric electrons, and so be responsible for the suppression below the transmitter frequency. Cornilleau-Wehrin and Gendrin (1979) used the formalism of Roux and Pellat (1976) to present a detailed theoretical model of the phenomenon. They considered the competition between the phase trapping effects of the wave and the detrapping effects caused by the inhomogeneity of the geomagnetic field. Basically, their model relies on the reduction in particle number (caused by wave trapping) within a small range of equatorial parallel velocities corresponding to frequencies below that of the transmitter. This depletion leads to reduced growth rates. The predicted quiet band width

*Present address: Department of Oceanography, Marine Science Laboratories, Menai Bridge, Gwynedd, LL59 5EY, United Kingdom

should increase with frequency and depend on B_w^2 , where B_w is the coherent wave amplitude. A strong noise enhancement was predicted at the low-frequency edge of the quiet band, but no enhancement above the transmitter frequency.

Matthews et al. (1984) used a different analytical approach. Their work was an attempt to explain computer simulation results which showed how the electron distribution becomes distorted in the presence of a coherent VLF signal. The nature and size of the distortion was found to be critically dependent on gradients in the electron distribution function with respect to parallel velocity. Matthews et al. (1984) showed that in their case the trapping-induced reduction in the number of electrons near the resonant velocity was small. They showed that changes in gradient in the electron distribution with respect to parallel velocity might account for quiet band generation. In their model a weak noise enhancement was predicted on the low-frequency edge of the quiet band, and a strong enhancement at frequencies just above the transmitter frequency. The quiet band width was predicted to vary as the square root of B_w .

In order to help resolve some of these conflicting theoretical predictions it is useful to study the experimental data in more detail. As the total number of quiet band events detected so far is small, it is important to make full use of the available data. In the present work, new observations of the quiet band are presented which basically confirm the properties reported by Raghuram et al. (1977), although, as we shall see, several factors prevent a straightforward comparison. Here we study the initial development of the quiet band in some detail. We concentrate, in particular, on how the distribution of wave energy with frequency is influenced by the arrival of the coherent signal in the interaction region. These changes can be clearly determined from the data and serve as a basis for comparison with theoretical predictions.

Observations

Between July 10 and August 10, 1979, a team from the Institute of Space and Astronautical Science in Tokyo, Japan, conducted a campaign to obtain a contour map of the field intensity of Siple transmitter signals received in the conjugate region in the northern hemisphere (Tsuruda et al., 1982). Twelve identical crossed loop VLF receivers were operated at quiet locations in the Roberval region.

Data from the low-latitude station 'G' (Tsuruda et al., 1982; Machida and Tsuruda, 1984) at $L=4.15$ are presented here.

On 23 July 1979, between 1216.00 UT and 1217.00 UT, quiet bands were observed at station G below three groups of one hop Siple pulses, each of total duration 10 s. The first of these groups is labelled 'a' in Fig. 1. The transmitted format of these signals is not obvious from the spectrogram, but consists of four 2-s pulses at the central frequency of 2,710 Hz, each of which is followed by two shorter pulses having progressively longer duration as the transmission proceeds. These shorter pulses are offset from the central frequency by +300 Hz and -300 Hz respectively. Initially they are 100 ms in duration, but reach 400 ms by the end of the transmission block. Hence the total duration of each transmitted group is 10 s. (D. Carpenter, personal communication). The other two groups are clearly visible at later times in the record, centred on the same frequency. Intense enhancements in noise are visible above the central frequency - that above the second signal group is labelled 'b' in Fig. 1. The enhancements are made up of some discrete tones near the central frequency and a diffuse component of some several hundred Hz bandwidth. Discrete structure was also observed on the upper-frequency side in the events described in (1), although the presence of a diffuse component was not reported. The intense vertical lines in Fig. 1 are caused by local spheric activity.

Quiet bands are visible below each of the signal groups starting from 'a', but the effect is best defined after the termination of the third group. This quiet band is labelled 'c'. The time taken for the suppression to develop is difficult to see in the spectrograms, but detailed spectral analysis shows that it probably lies between 5 s and 10 s. The noise recovery time is ≈ 20 s. In (1), at transmitter frequencies near 5.5 kHz, recovery times for the noise were ~ 30 s, with faster recovery at lower frequencies. This seems consistent with our results. Assuming comparable conditions and extrapolating the quiet band development times given in (1) for transmitter signals near 3 kHz leads to an expected development time which is much longer than the 5-10 s observed here. Two main factors could account for this difference. At the time of observation there was evidence of magnetospheric line radiation activity and of remnant echoes from preceding transmissions (D. Carpenter, personal communication), both of which could influence the onset time.

The transmitter pulses of 1 s duration give rise to con-

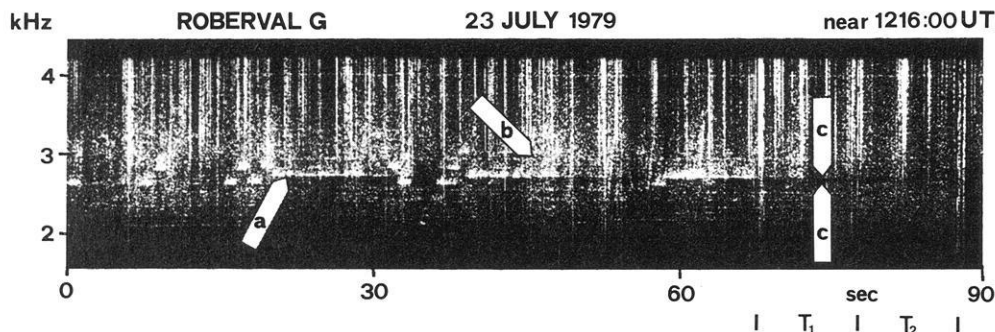


Fig. 1. The dynamic spectrograms of the three Siple VLF transmitter signal groups considered are shown, with received signals in white. The central frequency of the first group is labelled 'a'. Noise enhancement appear above the central frequency of each group, with that for the second group labelled 'b'. Quiet band type suppression develops below the central frequencies, and 'c' marks the quiet band associated with the third group. The intense vertical lines are caused by spheric activity. Periods T_1 and T_2 are analysed in Fig. 2

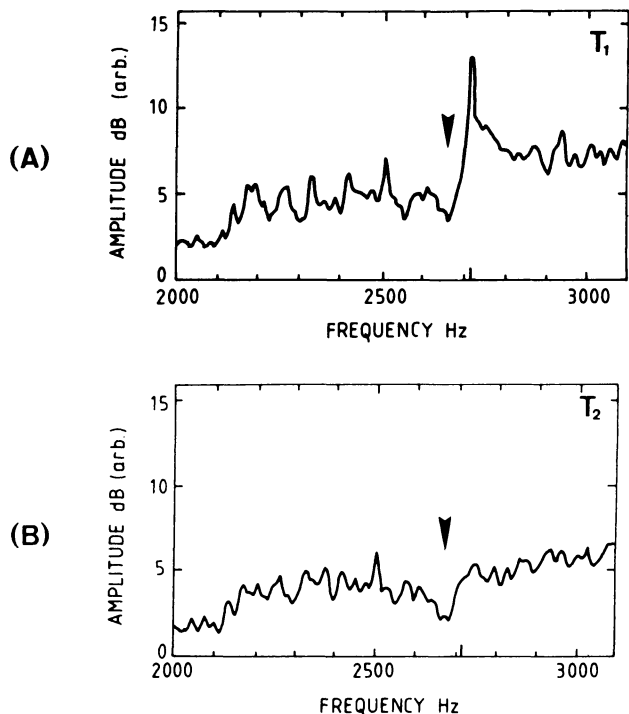


Fig. 2A, B. Amplitude/frequency plots of the 10-s data periods T_1 and T_2 shown in Fig. 1. In **A** the intense peak corresponds to the central Siple transmitter frequency. Below this peak a quiet band of noise suppression has formed (marked by an arrow). In **B** the quiet band is still visible, although no one-hop transmitter signal is present

siderable diffuse and discrete wave growth on their upper-frequency sides, but no quiet bands. This effect is clearly visible just before the long group 'a'. Such growth stimulation is almost coincident with the arrival of the one hop signal, whereas the quiet bands take 5–10 s develop. Some discussion of the nature of the noise enhancement on the upper-frequency side is given by Raghuram (1977). In addition, a study of diffuse noise generation by coherent signals propagating in stable (i.e. noise-free) plasmas has been made by the author (Matthews, 1985). The details of this work are relevant to the present data, but here a bandwidth limit for the triggered hiss cannot be calculated since the plasma is already unstable. Rather, changes in the shape of the electron distribution function could act to limit the emission width.

Two time periods (labelled T_1 and T_2 in Fig. 1) have been analysed in greater detail. In Fig. 2A, an amplitude/frequency plot of the period T_1 is presented. Here the wave amplitude is averaged over the 10 s following the termination of the last central Siple pulse. The large peak occurs at the central transmitter frequency of 2,710 Hz. Some contribution from the one hop transmitter signal (and previous echoes) is probably present here since it is difficult to determine the exact termination time. On the low-frequency edge of the central transmitter frequency the quiet band of suppression is visible (marked with an arrow) and extends down to a frequency of 2,615 Hz, giving a quiet band width of ~ 95 Hz. The short 400 ms pulses transmitted at the end of the format blocks lie well outside this frequency band. These short-duration signals do not seem to play an important role in determining the properties of the quiet bands.

On the low-frequency border of the quiet band, the noise level is close to the unperturbed amplitude and there is no pronounced noise enhancement. Below the lower border the noise level is again depressed. In (1) this effect was described as a 'secondary quiet band'. It may lead to the generation of magnetospheric line arrays such as power line harmonic radiation (Helliwell et al., 1975; Matthews and Yearby, 1981).

Above the central transmitter frequency the overall level of wave activity is intensified, especially immediately above this frequency. In the discussion of Fig. 1 this was identified as being due to discrete rising tones and to an intensification of the general hiss level which is lower prior to the arrival of the transmitted signals.

In Fig. 2B, the amplitude/frequency plot represents an average over the 10-s period marked as T_2 in Fig. 1. The intense peak corresponding to the central transmitter frequency (2,710 Hz) which was visible in Fig. 2A is now absent. A quiet band of suppression is still present (marked with an arrow) – its width is 95 Hz and the level of suppression is 3 dB. Both of these values are comparable with the observations reported in (1).

On the low-frequency border of the quiet band shown in Fig. 2b the noise is near the background level as in Fig. 2a. Here too, a strong noise enhancement is not observed on the lower border. The secondary quiet band is barely visible in this plot. Above the central transmitter frequency the noise level is comparable to the pre-transmission values.

Discussion

The limited amount of data presented in this paper confirm, in a general way, the results reported in (1) and by Raghuram (1977). In particular, in the initial stages of quiet band formation studied here, intense enhancement at the lower border of the quiet band were not observed. This agrees with the detailed observations presented by Raghuram (1977) which show that the lower border enhancement develops slowly (i.e. over a period of some 20 min). On the other hand, growth enhancements above the transmitter frequency developed rapidly in both these data and in those of (1). Quiet band widths and levels of suppression are similar in both studies. One additional feature reported here is the enhancement in diffuse noise level (in addition to discrete emissions) above the transmitter frequency. Because of the possible influence of magnetospheric line radiation, previous transmitter echoes and a complex transmitter format, the comparison between these observations and those of (1) is not a direct one.

Theories of the coherent whistler-mode wave/energetic electron interaction can be applied, with various degrees of success, to explain the data presented here. For example, the quasilinear theory of Welty et al. (1973) predicts absorption above and below the transmitter frequency. This is clearly at odds with the present data and with those reported in (1). However, the model of Das (1968) comes quite close to the situation observed here, except that a large growth rate is predicted both above and below the transmitter frequency (rather than a weak or zero enhancement below the transmitter frequency). The reason for this is probably that Das (1968) did not consider the effect of trapping at points away from the equator.

In Ashour-Abdalla (1972), a scheme for computing

pitch angle diffusion coefficients was derived to study the effect of narrow band VLF signals on the electron distribution function. Trapping of particles by the waves was not considered. In the long time limit, a strong peak in growth above, and offset from, the transmitted pulse was predicted. On the low-frequency side the model gave a region of suppressed growth bordered by a weak enhancement. These predictions are similar to the observations reported here. In particular, the width in frequency covered by the suppression was about 96 Hz, although this value was obtained for a 10-pT wave amplitude, a wave frequency of 16 kHz and L value of 3 (rather different parameters to those relevant here). The lower border enhancement was shown to develop at later times ($t \sim 500$ s), which fits the observed behaviour. In the long time limit, Ashour-Abdalla's work seems to show a suppressed band with a frequency width independent of wave amplitude, which is at odds with Raghuram's data. However, the data reported here do not indicate a strong dependence of the time averaged Δf on B (see later). In addition, a gradual shift in the peak growth to higher frequencies is predicted – this is not observed in connection with the present data, and is more relevant to the situation of discrete triggered emission generation. Further, Ashour-Abdalla's theory requires a long time ($t \sim 500$ s) for the growth of wave energy above the transmitted frequency to develop. As described in this report, growth enhancements on the upper-frequency side develop more rapidly than this.

Cornilleau-Wehrin and Gendrin (1979) predicted a strong noise enhancement at the lower border of the quiet band but no enhancement above the transmitter frequency. As far as the lower border enhancement is concerned, this model could possibly describe the situation in which a long transmitter pulse (e.g. of length 10 min) produces quiet bands. This is because the lower border enhancement is established slowly. However, it does not seem appropriate to the early stages of quiet band development studied here. Matthews et al. (1984) predicted a relatively weak lower border enhancement and a strong enhancement just above the transmitter frequency. In their results (see Fig. 8b of Matthews et al. 1984), a secondary quiet band effect may also be visible. This model fits the present observations well.

The important question of whether the quiet band width varies with the coherent wave amplitude (B_w) as B_w^2 (Cornilleau-Wehrin and Gendrin, 1979) or as the square root of B_w (Matthews et al., 1984) cannot really be investigated with these limited data. However, for the three quiet bands, averaged widths over the duration of the suppression are 100 Hz, 100 Hz and 120 Hz, respectively, and the corresponding amplitudes are 7.7, 5.2 and 9.3 in arbitrary units. There is, therefore, a broader range of relative variation in amplitude than there is in frequency, which militates against a B_w^2 type of dependence. This result is not decisive since signal amplitudes could vary with the mixing of returning two hop transmitter echoes.

For theories employing the concept of particle trapping by the coherent signal it is important to consider what happens when the transmitted wave is switched off and the wave-induced phase-ordering of particles is consequently terminated. The quiet band might, on first reflection, be assumed to rapidly decay, rather than to fade slowly over a time scale of $\gtrsim 20$ s. However, if wave growth is to pick up again within the frequency range previously occupied

by the quiet band, the distribution function must be restored to something like its pre-transmission configuration, and the randomization introduced by the phase mixing process and wave-induced pitch angle diffusion overcome. One way for this to take place is for fresh particles to be provided by the process of pitch angle diffusion, as suggested by Cornilleau-Wehrin and Gendrin. The strong hiss band, which is always present on the lower-frequency side in the data of Fig. 1, should lead to a smoothing of the wave-induced perturbation by pitch angle diffusion on an approximate time scale (Matthews, 1985)

$$\Delta t \sim \frac{1}{2\Omega} \left(\frac{V_s B}{V_\perp B_h} \right)^2$$

where $V_s = 2\omega_i/k$ and $\omega_i = \sqrt{k v_\perp e B_w/m}$. A value of v_\perp can be obtained by using the whistler-mode dispersion relation together with the gyroresonance relation, and assuming $v_\perp = v_\parallel$. This gives $v_\perp = 4 \times 10^7$ m s⁻¹ at $L=4$ and a wave frequency of 3 kHz. Estimating $B_w \sim 5$ pT and, from Fig. 2a a corresponding value of $B_h \sim 1$ pT for the r.m.s. hiss wave field, we obtain $\Delta t = 73$ s, which is reasonable. Other source mechanisms, such as azimuthal particle drift or radial diffusion would restore the distribution function over much longer time scales.

Acknowledgements. I would like to thank K. Tsuruda and S. Machida and the staff of the Institute of Space and Astronautical Science, Tokyo, Japan, for their kind assistance. I also thank I. Kimura, H. Matsumoto and Y. Omura of Kyoto University, Japan, for their help and friendship while I was a Japan Society for the Promotion of Science research fellow. Thanks are also due to A.J. Smith for useful discussion and assistance in the preparation of figures, and to I.A. Ward and colleagues at Sheffield University, U.K. for data analysis. Correspondence with D. Carpenter provided vital information on the Siple transmissions, and suggestions for data interpretation. I thank the field engineers at Siple Station, Antarctica, for their work during the period analysed here. This work was completed while I was a research fellow of the European Space Agency.

References

- Ashour-Abdalla, M.: Amplification of whistler waves in the magnetosphere. *Planet. Space Sci.* **20**, 639–662, 1972
- Bud'ko, N.I., Karpman, V.O., Pikhotelov, O.A.: Nonlinear theory of the monochromatic circularly polarized VLF and ULF waves in the magnetosphere. *Cosmic Electrodynamics* **3**, 147–164, 1972
- Cornilleau-Wehrin, N., Gendrin, R.: VLF transmitter-induced quiet bands: a quantitative interpretation. *J. Geophys. Res.* **84**, 882–890, 1979
- Das, A.C.: A mechanism for VLF emissions. *J. Geophys. Res.* **73**, 7457–7471, 1968
- Dowden, R.L.: Distinctions between midlatitude VLF hiss and discrete emissions. *Planet. Space Sci.* **19**, 374–376, 1971
- Helliwell, R.A.: Whistlers and related ionospheric phenomena. Stanford: Stanford University Press, 1965
- Helliwell, R.A.: A theory of discrete VLF emissions in the magnetosphere. *J. Geophys. Res.* **72**, 4773–4790, 1967
- Helliwell, R.A., Katsufurakis, J.P.: VLF wave injection into the magnetosphere from Siple Station, Antarctica. *J. Geophys. Res.* **79**, 2511–2518, 1974
- Helliwell, R.A., Katsufurakis, J.P., Bell, T.F., Raghuram, R.: VLF line radiation in the earth's magnetosphere and its association with power system radiation. *J. Geophys. Res.* **80**, 4249–4258, 1975
- Machida, S., Tsuruda, K.: Intensity and polarization characteris-

- tics of whistlers deduced from multi-station observations. *J. Geophys. Res.* **89**, 1675–1682, 1984
- Matthews, J.P.: A theory of emission bursts triggered by coherent VLF signals propagating parallel to the geomagnetic field. *J. Geophys. Res.* **90**, 2910–2914, 1985
- Matthews, J.P., Yearby, K.: Magnetospheric line radiation observed at Halley, Antarctica. *Planet. Space Sci.* **29**, 97–106, 1981
- Matthews, J.P., Omura, Y., Matsumoto, H.: A study of particle trapping by whistler mode waves in the geomagnetic field: the early development of the VLF quiet band. *J. Geophys. Res.* **89**, 2275–2287, 1984
- Raghuram, R.: Suppression effects associated with VLF transmitter signals injected into the magnetosphere. Tech. Rep. 3456-3, Stanford University, Stanford, California, 1977
- Raghuram, R., Bell, T.F., Helliwell, R.A., Katsufurakis, J.P.: A quiet band produced by VLF transmitter signals in the magnetosphere. *Geophys. Res. Lett.* **4**, 199–202, 1977
- Roux, A., Pellat, R.: A study of triggered emissions. In: *Magnetospheric particles and fields*, B. McCormac, ed.: pp. 209–222, Dordrecht: D. Reidel, 1976
- Tsuruda, K., Machida, S., Terasawa, T., Nishida, A., Maezawa, K.: High spatial attenuation of the Siple transmitter signal and natural VLF chorus observed at ground-based chain stations near Roberval, Quebec. *J. Geophys. Res.* **87**, 742–750, 1982
- Welti, R., Pellat, R., Roux, A.: Contribution a l'étude des interactions entre ondes monochromatiques et particules en milieu inhomogene. *Ann. Géophys.* **29**, 263–271, 1973

Received September 27, 1984;
 revised versions received August 9, 1985, and March 17, 1986
 Accepted May 27, 1986

*In memoriam***Gustav Adolf Schulze (1911–1986)**

On February 28, 1986, Gustav Adolf Schulze, long-standing director of the geophysical division of Gewerkschaft Briggitta (today BEB Erdgas und Erdöl GmbH), died at the age of 75. Those who knew him during his last years must admire him for the courageous way in which he endured his illness. G.A. Schulze is survived by his wife Gertrud (maiden name Engel) and two sons. All his life he was proud of his hometown, Hannover, where he was born on January 10, 1911, and where he died. Here, he went to school at the tradition-rich "Ratsgymnasium" and afterward in 1931 began his studies in the natural sciences at Göttingen. In addition to physics and mathematics, he quickly went into geophysics and received his Ph.D. in 1935 from Gustav Angenheister with his thesis on the dispersion of seismic waves. Today this could be described as an early application of the Vibroseis method, by which the changing frequencies, which were generated in the ground by the unbalanced wheel of a machine at the railway workshop

and were correlated and interpreted as seismic refraction measurements.

Dr. Schulze remained at the Göttingen Geophysical Institute as a scientific assistant, interrupted once by military service. Here he wrote papers on various aspects of acoustic wave propagation, seismic disturbance measurements, air waves, and microseismics.

He made significant contributions to the seismic-reflection recording and interpretation of the internationally important Helgoland shooting (1947). As is well known, with these measurements it was shown for the first time that blasting can be observed and interpreted over very great distances. This was the beginning of the seismic-reflection study of the earth's crust using blasting, a method which has yielded many fruitful results.

All this predestined him for his subsequent occupation, which he began in 1948 as a geophysicist and chief of the seismic field crew for the former Gewerkschaft Briggitta. Soon afterward, he became director of the geophysical division and developed the seismic crews and interpretation groups into an effective instrument for researching the subsurface for useful hydrocarbon deposits. Under his direction, the division outgrew the age of working with analog paper seismograms and of interpreting and analyzing with traditional systems of levers and screws, and advanced into the age of digital field recording and data processing with modern computers. His former colleagues and co-workers knew of his continual interest in new developments in his field and of the enthusiasm with which he promoted the use of such developments in his area. His work at BEB dealt with questions of seismic interpretation.

After retiring from active service, he stayed in contact with geophysics through various activities, i.e., in the European Community, as a consultant in Egypt, and in research projects of the German oil industry in cooperation with universities.

We all mourn the death of Gustav Adolf Schulze, a committed colleague and long-standing member of the German Geophysical Society.

Horst Dürschner

Book reviews

Bakun-Czubarow, N., Guterch, A., Leliwa-Kopystynski, J., Maj, S., Teisseyre, R.: Constitution of the Earth's Interior. Leliwa-Kopystynski, J., Teisseyre, R. (eds.). Elsevier, Amsterdam, Oxford, New York, PWN-Polish Scientific Publishers, Warszawa, 368 p., DM 200, – approx., 1984.

This is the first volume of a series of books on “Physics and Evolution of the Earth's Interior”, edited by R. Teisseyre. In this volume the basic physical laws are presented which govern the state and the properties of matter under the conditions of the earth's interior. Their application to data of geophysical fields leads to models on the physical and chemical constitution of the earth currently under discussion. It was probably a good idea of the editors to invite several of their colleagues to contribute with rather comprehensive, critically and mostly excellently written reviews on particular aspects of the broad field covered by this book. In the eight chapters of this well-organized book the following topics are treated: thermodynamic equations of state based on continuum and quantum physics and geophysical equations of state related to seismic wave velocities; density models of the earth's interior with a brief account also of models of the interior of moon and planets; basic formulations of viscous material behaviour and description of the classical mechanisms of steady-state creep; effective viscosities of the earth's mantle as derived from isostatic uplift; quality factor Q and a frequency-independent Q model of the earth; heat flow, heat production, the mechanisms of heat conductivity and of electric conductivity in the earth; estimates of the temperature-depth distribution based on various kinds of evidence; general features of the physical and petrological structure of the earth's crust and upper mantle mainly based on deep seismic sounding; thermodynamics and kinetics of phase transformations and phase transition boundaries in the presence of large-scale motion in the mantle. This particularly interesting chapter contains many original contributions by the author Leliwa-Kopystynski; mineralogical-petrological considerations on possible and hypothetical phase transformations within the earth's mantle. The book closes with an overview on models of the chemical and mineralogical composition of the mantle.

This book is the first comprehensive modern presentation of the physics of the earth's interior and will certainly be welcomed not only by geophysicists but also by petrologists interested in physical aspects. Depending on author and subject, it has in some chapters almost the character of a textbook for advanced students and in others more the character of a critical compilation of relevant information. It is certainly of a particular advantage that the authors are acquainted both with the western and the eastern literature. Publications up to the end of the 1970s have been evaluated in this book. This puts some limit to the actuality of the otherwise very valuable and informative work.

H. Berckhemer

Schove, D.J. (ed.): Sunspot Cycles. Hutchinson Ross Publishing Company, Stroudsburg, PA, 397 p., 1983.

The book does not deal with the nature of sunspots nor with their presumed causes. It is devoted exclusively to the well-known feature that their numbers and some accompanying phenomena are waxing and waning in a period of about 11 years, the sunspot cycle. The book, as a matter of fact, is a collection of 40 articles or extracts of articles written by 21 authors of the present and the past century. After a general introduction by the editor the papers are combined in seven parts, each preceded by comments by the editor to the individual articles.

In the introduction, sources of data of past sunspot cycles are summarized: notably telescope observations, auroral displays, radio carbon content, tree rings, barometric pressure and temperature indices. In Part I: Early sunspots, pretelescopic records of sunspots are quoted going back as far as some centuries B.C. in China and to 1600 A.D. in Europe. In Part II: The eleven-year cycle, the discovery of the sunspot cycle is illustrated by quoting classical papers. Tables of observations by Schwabe, by Wolf and the famous Maunder diagram are reproduced together with excerpts from the original papers. In Part III: Early aurorae, observations of aurorae going back as far as 500 B.C. in China and to 400 A.D. in north-west Europe are compiled. Needless to say, the observations are scattered and in many events the interpretation is difficult. A graphical presentation at the end of the chapter summarizes the observations between 701 B.C. and 2000 A.D. In Part IV: Synthesis, an attempt is made to establish a full series of sunspot cycles combining all available observations of sunspots as well as aurorae. The prolonged sunspot minimum 1645–1715 (Maunder Minimum) and its implications are presented at length. The variation of the period of the individual cycles, the mean value and the deviations are discussed as well as the reliability of the predictions. The hazards of an unreliable forecast are demonstrated by the demise of Skylab in July 1979.

Part V: Longer cycles, deals with the 22-year, 80-year and 200-year cycle. The 22-year cycle shows up very distinctly in the reversal of the magnetic polarity of the preceding spot in bipolar groups. The existence of a 80-year and a 200-year cycle is still controversial. Part VI: Sunspots in history and their effect on climate, is devoted to problems which are rather controversial among experts as well as in common life, the correlation of economical and meteorological cycles with those of sunspots. A period of 10.3 years may be detected in the succession of commercial crises during the 18th and 19th century connected perhaps with a similar variation of crops in tropical countries. Indications of periods in barometric pressure and climatic fluctuations are present in the weather records of some regions. The correlation between tree rings and meteorological parameters enables an extension of the series to times when no meteorological records are available. The well-established biennial oscillation (2.2 years) in meteorological phenomena

is about one-fifth of the sunspot cycle. Also, a period of 22 years and of 80 years (Hale period) in climate has allegedly been found. All these investigations suffer apparently from the scarcity of reliable, long-time observations. In Part VII: Varve and geological cycles, the results of efforts to derive climatic variations from varves back to 14000 B.C. are presented.

The editor summarizes the content of the book as follows: "Sunspot cycles averaging 11.1 years have been dated through the last 2000 years and we have learned something of the way in which they and several longer cycles affect our climate. We have found that within certain limits we can predict both sunspot activity and its climatological consequences", and later on ... "The papers selected explain the how but not the why of sunspot cycles – their cause remains an enigma".

The feelings in reading the book may be somewhat controversial: well-established correlations as well as rather vague presumptions are presented together. In any case, the book serves its purpose: to collect information which is scattered widely in time and space. The author citation index contains about 600 names. Reiterations are unavoidable in that kind of documentation and the differences in nomenclature are sometimes annoying. Needless to say, the centre of gravity of the book lies in the speciality of the editor: sunspot cycles, tree-rings, weather history and chronology. The referee has successfully consulted the book in many instances.

W. Dieminger

Fitch, A.A. (ed.): Developments in Geophysical Exploration Methods – 6. Elsevier Applied Science Publishers, pp. 264, 120 illust., hardbound, 1985.

The 6th volume from the series on *Developments in Geophysical Exploration Methods* published over the last several years by A.A. Fitch has just been released. This series is aimed at presenting recent developments in applied geophysics in clear, yet challenging individual contributions. Correspondingly, each volume deals with a spectrum of different subjects, as is the case with the 6th volume.

The first chapter on spike recovery deconvolution concentrates on the restoration of the reflectivity function as a series of ideal spikes in contrast to the usual deconvolution process, where an

inverse wavelet (which is estimated from the trace without considering the change of the wavelet along the trace) is convolved with the trace.

During usual seismic stacking processing arise, as is generally known, stacking errors in the case of dipping strata (there is no longer a common reflection point, and the apex of the NMO hyperbola no longer lies at zero offset). This leads to reduced quality for inclined reflection elements in the stacked section. In the second chapter of the book ("Normal moveout correction, offset continuation, and prestack partial migration compared as prestack processes"), an algorithm dip moveout, DMO, is introduced to correct these errors in connection with usual NMO correction.

The determination of seismic wave absorption from vertical seismic profiles (VSP) is the subject of the third contribution. The problems of determination of seismic attenuation and how to overcome the distorting influences (mainly short time interferences) are demonstrated by using case histories: (1) From the reflectivity function, deduced from sonic log, a log of the apparent absorption, including all multiples, is computed using the measured input wavelet. This apparent absorption is then subtracted from the computed spectral ratio, derived from the actual data and the inherent absorption will be left. (2) The spectral ratios may be averaged over a short depth interval, thus eliminating structural (apparent attenuation) effects.

A further chapter of the book deals with "The inverse scattering concept and its seismic application" followed by an article on V_p/V_s interpretation, i.e., on the application of shear wave seismics in estimating lithological (physical and facies) parameters. Numerous field examples of surprisingly high quality of the shear wave sections, as is not generally attained today, are presented.

"Stacking methods other than simple summation" is a further subject treated in the volume. Stacking with fixed or data-adaptive statistical weights, iterative and other methods are discussed. The book concludes with a contribution on electrical logging techniques ("Focused resistivity logs").

Like all of the previously published volumes of this series, this volume is a valuable enrichment for the practicing and researching applied geophysicist by its high scientific level presented in clear review contributions. It is of outstanding layout, including printing and the so often problematic reproduction of seismic sections.

L. Engelhard

*Review articles***Hydromagnetic waves at low latitudes:
a symposium review from the fifth IAGA assembly*****B.J. Fraser**¹

Institute of Geophysics and Planetary Physics, University of California, Los Angeles, CA 90024, USA

Abstract. The aim of the symposium was to bring together investigators with interests in low latitude hydromagnetic waves in order to review the present state of knowledge in this area of magnetospheric physics. Of particular importance is the means by which wave energy is transferred to low latitudes to produce geomagnetic pulsations on the ground. The group of contributed papers reviewed shows that definitive experiments are underway and new theories capable of providing resonant wave energy at low latitudes are being developed. Particular topics covered by the review include solar wind control, wave spectra, array studies of wave parameters, storm time waves, and global wave resonance theory involving the coupling of compressional and transverse waves in the magnetosphere.

Key words: Hydromagnetic waves – Geomagnetic pulsations – Magnetospheric physics – Low latitude phenomena

1. Introduction

Our understanding of hydromagnetic wave generation and propagation mechanisms in the magnetosphere and the ionosphere has greatly increased over the last few years (see for example the review by Hughes, 1982). This occurred largely because of the data accumulated during the International Magnetospheric Study (IMS) between 1976–1979, and the stimulation provided by the ULF Pulsation Working Group within Division III of the International Association of Geomagnetism and Aeronomy (IAGA) on Magnetospheric Phenomena. However, until recently research has concentrated on waves observed at high and middle latitudes. This is a natural consequence of the available spacecraft data and the location of ground recording stations and arrays at that time. Theoretical work has also been largely confined to high latitudes through the development of generation theories such as the Kelvin-Helmholtz instability (Southwood, 1974; Chen and Hasegawa, 1974) and the drift mirror and bounce resonance instabilities (Hasegawa, 1969; Southwood, 1973) which relate to the outer magnetospheric region beyond the plasmapause.

* The managing editor thanks L.S. Lanzerotti for handling the reviewing process of this paper and of the subsequent two papers by K. Yumoto and J. Verö

¹ *Permanent address:* Department of Physics, University of Newcastle, N.S.W. 2308, Australia

Despite this improved understanding of hydromagnetic wave phenomena, we still have not specifically identified the mechanisms which transfer wave energy to low and equatorial latitudes. Spacecraft measurements cannot be undertaken in these low altitude field line regions and we must look at groundbased observations to provide the experimental data required. In order to stimulate both theoretical and experiment research in this area, IAGA organized a half day symposium on hydromagnetic waves at low latitudes which was held at the Fifth General Assembly of IAGA in Prague on August 12, 1985. The symposium was convened by L.J. Lanzerotti and its aim was to assemble and present observational and theoretical results from low latitude wave studies in order to assess the present state of knowledge. This would then provide a basis on which to plan future research. This review attempts to summarize the more important results which came from the contributed papers presented at the symposium. It is written as an overview and it has not been possible to treat all papers equally. What is presented orally or by poster to stimulate discussion may not always be suitable for publication. Papers have been selected to fit an ordered set and those omitted may well be the more important ones. Two invited review papers summarizing previous experimental and theoretical work on low latitude hydromagnetic waves were also presented and they are included elsewhere in this issue (Vero, 1986; Yumoto, 1986).

The symposium, with only a one-half day duration, was short by IAGA standards. However it was well attended and a total of 21 contributed papers were presented. Of these, ten were oral presentations with the remainder displayed as poster papers. In what follows, papers are cited from two reference lists. The first contains references used in the review and are generally key papers in the development of the topic and provide a background to that topic. These references are cited in the normal way by author and year. The papers in the second list are cited by author name only and are those presented as contributed papers to the symposium.

2. Solar wind control

The energy source for hydromagnetic waves observed on the ground as geomagnetic pulsations may be either internal or external to the magnetosphere. Internal sources of energy include instabilities associated with the cyclotron, bounce and drift motion of particles whose distribution functions

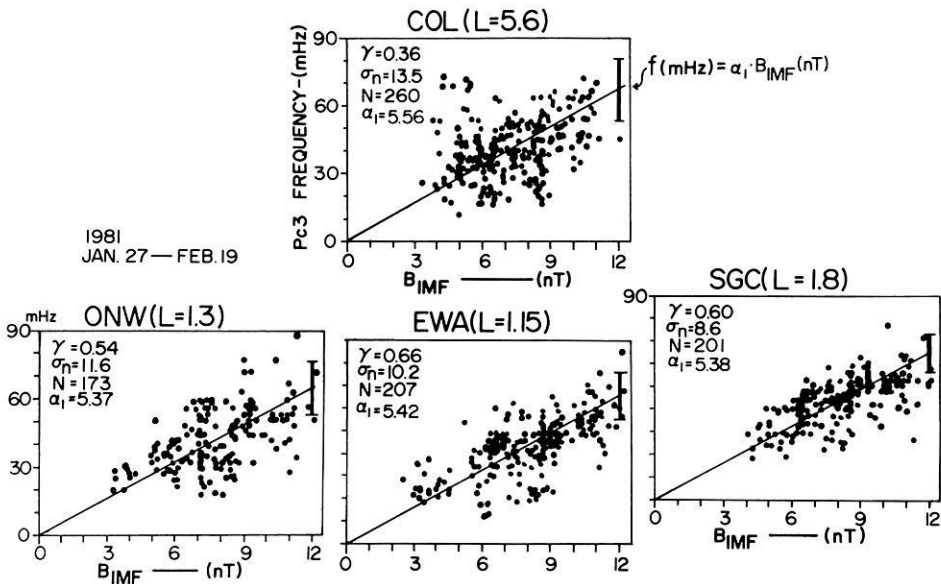


Fig. 1. Scatter plots of the daytime Pc 3-4 wave frequencies observed at four ground stations against the IMF magnitude observed by ISEE-3 for 23 days of data. The solid line indicates the regression line $f(\text{mHz}) = \alpha_1 \cdot B_{\text{IMF}}(\text{nT})$. The γ and σ_n are the linear correlation coefficient and the deviation about the regression respectively. [From Yumoto et al., 1985a]

are anisotropic. Free energy internal sources include pressure gradients, velocity shears, and rapid changes in magnetospheric geometry associated with substorms.

It is generally accepted that some of the dayside Pc 3-4 pulsation energy is associated with sources external to the magnetosphere (Odera, 1986). Statistical studies show that the period of these waves is strongly correlated with the magnitude of the interplanetary magnetic field (IMF) while the occurrence rate depends on the orientation of the IMF (see for example, Greenstadt et al., 1980). These effects are often seen most significantly at low latitudes (Russell et al., 1983). This topic is well covered in the accompanying reviews by Vero (1986) and Yumoto (1986).

The basis for the association of Pc 3-4 pulsation wave frequency (f) with the IMF magnitude (B_{sw}) has been the "Borok B-index" originally formulated by Troitskaya et al. (1971) in the form $f(\text{Hz}) \approx 0.006 B_{\text{sw}}(\text{nT})$. A number of contributed papers readdressed this relationship with respect to the variability of magnetospheric conditions. Using wave frequencies determined by spectral analysis, Best et al. investigated the seasonal and K_p variation in the $f-B_{\text{sw}}$ relationship for daytime Pc 4 pulsations recorded over four years at a $L=2.4$ station. A strong correlation was found to exist in summer afternoon data only, and took the empirical form

$$B_{\text{sw}} = 0.7 + 1.1 K_p + 150 f$$

over the range $0 \leq K_p \leq 4$. It is important to note that no dependence on K_p was found for Pc 3 pulsation data. A more extensive study of IMF relationships using three low latitude Pacific stations separated in longitude over $L=1.1-1.8$, and a high latitude station, College at $L=5.6$ was reported by Saito et al. and many of the results have since been published (Yumoto et al., 1985a). The Pc 3-4 wave frequencies were found to be well correlated with B_{sw} with the best correlation at low latitudes. This result is illustrated in Fig. 1. Furthermore, the daytime wave amplitudes at low latitudes correlated well with the IMF cone angle θ_{XB} . Changes in θ_{XB} on a short time scale (20-60 min) were found to be consistent with the microstructure of the daytime Pc 3 activity. This important result has been reported previously by Troitskaya (1984) and was also alluded to

in other symposium papers. The conclusion from the Saito et al. results was that high latitude Pc 3-4 pulsations are associated with both the surface waves at the magnetosphere and the upstream waves in the earth's foreshock, while low latitude Pc 3-4 pulsations are associated mainly with the magnetosonic upstream waves propagating into the inner magnetosphere.

In contrast to the results of Saito et al. just described, Playasova-Bakounina et al. found that IMF associated Pc 2-4 wave events with amplitudes up to 20 nT appeared predominantly near cusp latitudes. Using the $f=0.006 B_{\text{sw}}$ formula, these authors separated their data into two categories; waves of external origin and waves of internal origin. With both f and B_{sw} known, waves which satisfied the formula were classified to be of external origin while those which did not were considered to be of internal magnetospheric origin. The former group showed greatest amplitudes near the cusp while the latter group peaked at lower latitudes.

In accepting the results of Saito et al. and Playasova-Bakounina et al. derived from the $f-B_{\text{sw}}$ relationship, it appears that we have two irreconcilable conclusions. However, there are a number of points that must be considered. Firstly, the $f-B_{\text{sw}}$ relationship is an empirical non-linear function which also depends on other upstream magnetosonic wave parameters (Russell and Hoppe, 1981). In spite of this it relates f and B_{sw} with remarkably high correlation. Secondly, Pc 3-4 are the dominant daytime pulsations seen at low and middle latitudes. At high latitudes their signature is often contaminated by Pi 1 aurorally associated pulsations, a point noted by Yumoto et al. (1985a), and a lower correlation from the $f-B_{\text{sw}}$ relationship may not be unexpected.

Preliminary results from a Pc 3-4 pulsation study at cusp latitudes (Engebretson, private communication) indicates that the wave data satisfies the $f-B_{\text{sw}}$ relationship remarkably well and concludes that the source is in the upstream region. From these results we can conclude that there may be two paths for the entry of upstream Pc 3 wave energy into the inner magnetosphere, one directly through the subsolar region of the magnetosheath and another along high latitude field lines and into the cusp region. The importance

of these two propagation paths for the transmission of wave energy into the magnetosphere and their relative contribution to low latitude Pc 3 pulsations must await further research.

3. Wave spectra

Dynamic spectral analysis provides a convenient method for studying the wave characteristics of pulsations. This is particularly important nowadays with the availability of digital data and the use of modern digital analysis techniques. If wave results from station arrays are available, then the comparison of dynamic spectra provides a simple but effective means of observing interstation wave properties across ground or satellite networks or between ground stations and satellites.

These techniques were utilized in the studies reported by Miletits and Vero, and Hollo and Vero. In the first study, dynamic spectra from a subauroral station and a low latitude station were compared. An example is shown in Fig. 2 where it can be seen that the predominant wave periods near 20 s and 90 s are common to both latitudes and activity commences and ceases at the same time. This high degree of correlation in time and frequency was not always seen, although the dominant frequencies at the two stations were occasionally harmonically related. The common signals were interpreted as primary waves from the upstream source. In another study, using activity indices and spectra from the same low latitude station in association with ATS-6 synchronous spacecraft magnetometer data, Hollo and Vero found Pc 3-4 wave activity on the ground at low latitudes that was not evident at synchronous orbit. The presence of harmonic structure seen at synchronous orbit (see for example Takahashi and McPherron, 1982) did not appear to have a significant influence on the wave spectra seen on the ground. Simultaneous commencement and cessation of wave events at synchronous orbit and on the ground were significant only during the local morning and in the 20–25 s period range. Conclusions were that wave amplification in the inner magnetosphere below synchronous altitude is strongly modulated by the solar wind and creates sharp resonant spectral lines in the ground wave activity observations.

Boshoff and Sutcliffe reported observations from three stations at $L=1.76$ and spanning 35° in longitude. From comparisons of dynamic spectra they reported one day in which the high frequency Pc 3 spectral components present at two stations were absent at the third, more westerly, station situated on an island below the South Atlantic Magnetic Anomaly. It was speculated that the lower magnetic field intensity and the associated particle precipitation at the anomaly may deplete the plasmasphere thereby eliminating the resonances at the higher frequencies.

Over closer distances and using a network of four low latitude Pc 3 recording stations, Ansari and Fraser considered longitudinal and latitudinal variations in dynamic wave spectra. In general, wave spectra were similar over a longitudinal range of 17° at $L=1.8$ with a dominant frequency band at 40–45 mHz. The higher latitude station at $L=2.8$ also exhibited lower frequency Pc 4 bands (~ 10 mHz) on some days and higher frequency bands (60–80 mHz) on others. Sometimes completely different wave spectra were observed on the north-south and east-west components with the longitudinal stations showing

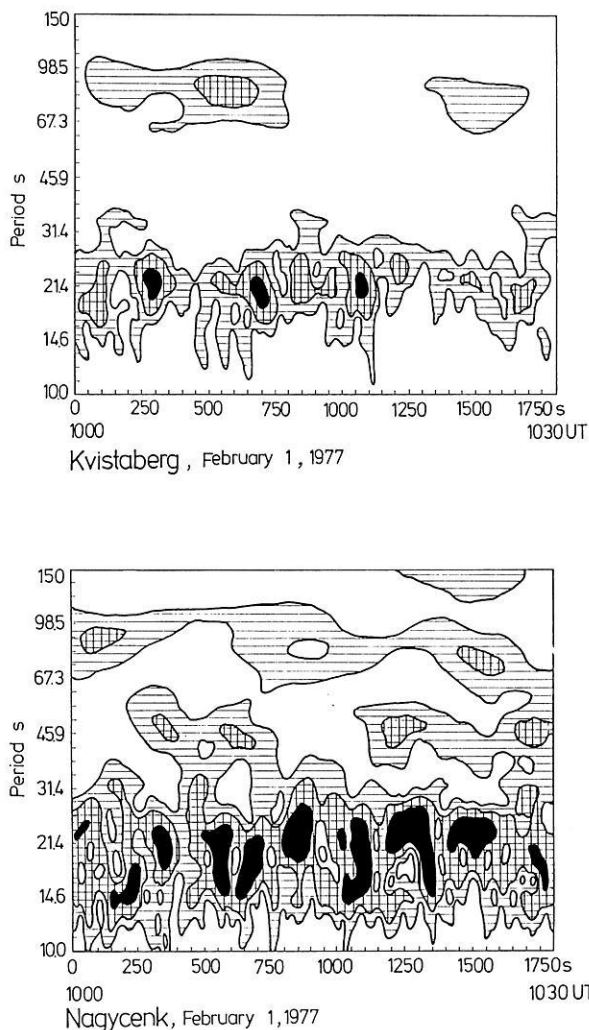


Fig. 2. Dynamic spectra of Pc 3-5 pulsations observed between 1,000–1,030 h LT, February 1, 1977 at Kvistaberg at subauroral latitudes and Nagyecenk at low latitudes. (From Miletits and Vero)

similar spectra on corresponding components. This could indicate decoupling between the radial and azimuthal wave components in the magnetosphere. Harmonic structure with $\Delta f \sim 10$ mHz was occasionally seen during local afternoon.

4. Array studies

In order to study the properties of resonant field line structures associated with Pc 3-5 pulsations it is necessary to employ latitudinal and/or longitudinal chains of stations. The importance of multipoint observations in pulsation research was established by Samson et al. (1971) who identified phase variations with latitude which were later interpreted in terms of the Kelvin-Helmholtz instability at the magnetopause, coupling to a transverse field line resonance within the magnetosphere (Southwood, 1974; Chen and Hasegawa, 1974). It is only recently that interstation studies have been undertaken at low latitude stations. For example, Saka and Kim (1985) and Ansari and Fraser (1986) often observed Pc 3 propagation azimuthally away from the noon meridian towards dusk and dawn with left-hand (LH) wave

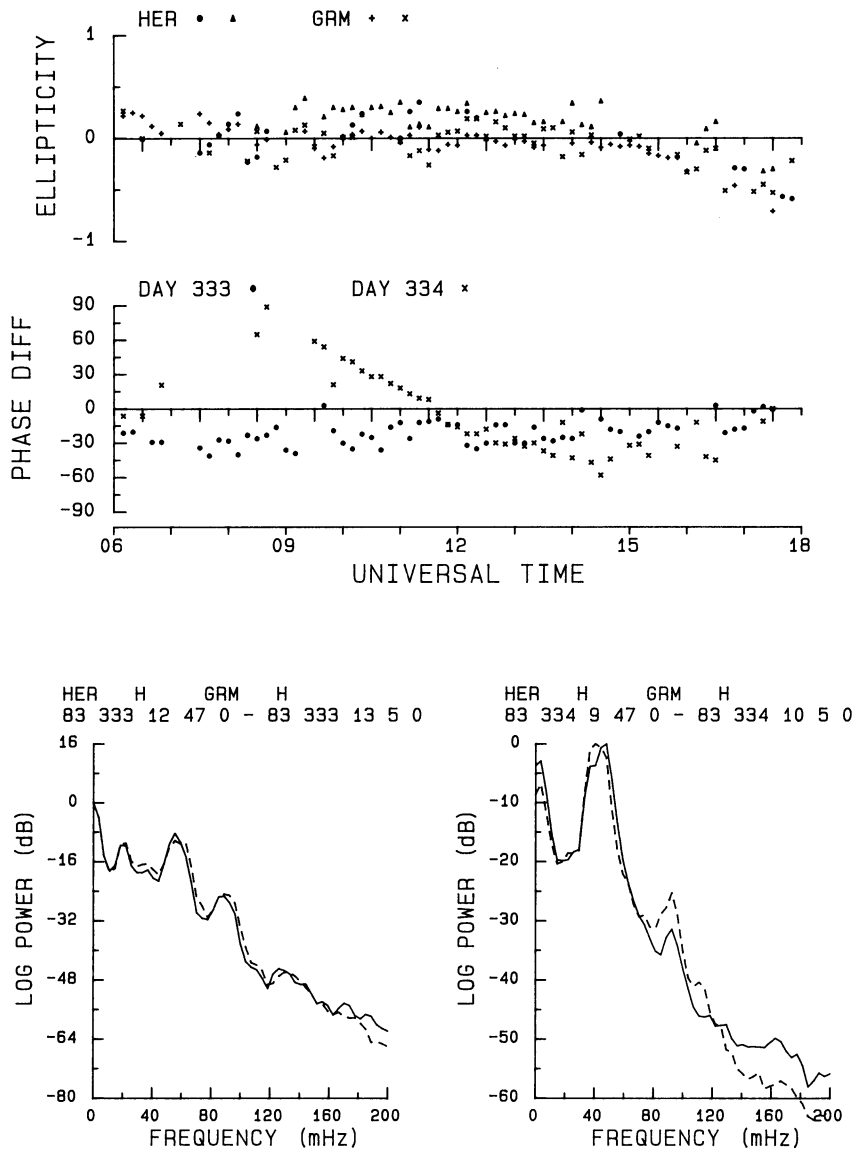


Fig. 3. *Top:* Polarization ellipticity of Pc 3 waves observed at Hermanus and Grahamstown ($L=1.85$) on November 29–30, 1983. LH polarization is positive and RH negative. *Centre:* Phase difference between signals observed at the two stations for the two days. Eastward propagation is positive and westward negative. *Bottom:* Wave spectra from two 63 min segments on November 29 and 30, 1983, respectively. The H components from both stations are plotted. (From Sutcliffe)

polarization before noon and right-hand (RH) after noon. Azimuthal wave numbers were generally low with $m < 10$.

The resonant field line model explains the latitudinal variation of wave amplitude and the associated reversal of wave polarization near the resonant field line latitude (Walker, 1980). Assuming this model, the apparent latitudinal propagation away from the equator (Saka and Kim, 1985; Ansari and Fraser, 1986) may be interpreted in terms of the latitudinal phase variation in the field line resonance structure and is consistent with a resonance region situated at a higher latitude. The diurnal azimuthal propagation and polarization patterns predicted by the Kelvin-Helmholtz instability at the magnetopause are also observed at low latitudes. However, these properties are not necessarily unique to the Kelvin-Helmholtz mechanism, a point discussed by Ansari and Fraser (1986).

The spatial and temporal structure of Pc 3 waves at two stations 7° apart in longitude at $L=1.85$ were considered by Sutcliffe. Using two days of data, it was found that wave polarization was LH almost all day with dominant RH appearing only after 15 h. Low wave numbers were observed ($m < 10$) and interstation phase differences

indicated westward propagation all day on one of the days. Eastward propagation is seen only before noon, which is contrary to earlier studies. These results are illustrated in Fig. 3. However, there is often a significant day to day variability in azimuthal propagation (Mier-Jedrzejowicz and Southwood, 1981) and these results are not unexpected. They may in fact, suggest a field line resonance source moving towards noon. Harmonic structure was also exhibited in the wave spectra (Fig. 3), with odd harmonics being identified on one day and even harmonics on the other.

The complex nature of individual Pc 3–5 wave packet structure was first noted at synchronous orbit by Mier-Jedrzejowicz and Hughes (1980) with observations of a gradual change in the relative phase between two spacecraft signals with time across a wave packet. The gradual phase drift ended with a sudden jump back into phase at the commencement of a new wave packet. Similar phase jumps were also observed in ground data from middle latitude stations. One possible explanation is that the phase drifts are a consequence of a free resonant shell oscillation in the absence of a driving force.

At low latitudes Lanzerotti et al. (1981) reported com-

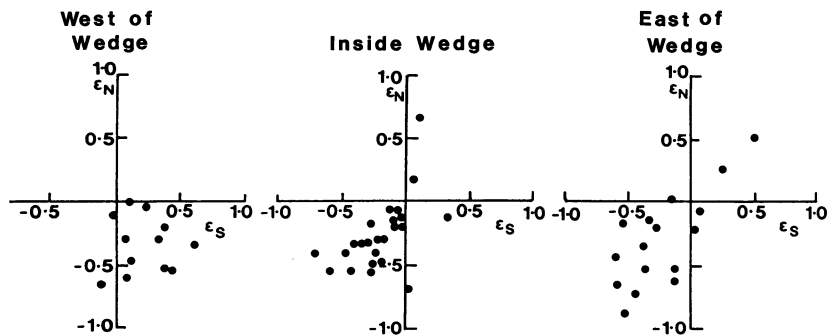


Fig. 4. Pi 2 polarization ellipticities (ϵ_s) at two low latitude stations ($L \sim 1.7$) plotted in current wedge centred coordinates against polarization ellipticities (ϵ_n) at higher latitude stations. (From Lester and Singer)

plicated phase jumps and polarization changes over intervals of a few minutes which were variable between signal components and stations. At the symposium Lanzerotti et al. extended their earlier results by noting that significantly different frequencies were often observed simultaneously with the polarization changes. The paper by Sutcliffe previously discussed also noted ellipticity changes over short time intervals, which were attributed to the mixing of LH and RH polarized wave packets.

Pc 3 phase structure observed at three longitudinally spaced stations ($L = 1.8$) by Ansari and Fraser did not show any systematic temporal or spatial patterns. Phase differences between corresponding signal components at different stations often showed a greater similarity than did the two components at a single station. Phase differences between pairs of stations were mostly variable and no consistent frequency changes or phase jumps were observed. None of the phase jump results considered above suggest a consistent phase pattern and are difficult to explain in terms of currently understood hydromagnetic wave theory in the magnetosphere. It may be necessary to look at nighttime impulsive Pi 2 pulsations in association with daytime Pc 3 waves or amplitude and phase variations resulting from low latitude ionospheric currents and irregularities in order to find an answer to the phase jump phenomenon.

A useful method for identifying hydromagnetic wave modes in the magnetosphere is to study conjugate wave characteristics. This was undertaken at $L \sim 1.5$ by Saito et al. using data from Australia and Japan. Comparison of conjugate polarization data indicated predominantly LH waves in the daylight morning hours with mixed and often opposite polarizations in the afternoon. No particular wave mode types were identified, but a primary source outside the magnetosphere was assumed. Following earlier arguments (Saka and Kim, 1985; Ansari and Fraser, 1986) it was speculated that these waves produce westward propagation in the morning and eastward propagation in the afternoon and can couple to various hydromagnetic resonances in the plasmasphere. Further details of this work are included in Yumoto et al. (1985b).

5. Statistical studies

In the past a great deal of knowledge on groundbased pulsations has been obtained using statistical data. At the symposium, two papers were presented using extensive data sets. Ansari and Fraser studied the diurnal seasonal and magnetic activity variations using four low latitude stations. Average frequencies at $L = 1.8$ were higher than those at $L = 2.7$ perhaps illustrating a frequency-latitude relationship. A single noon peak in wave occurrence was seen at all stations,

not a new result but a property which has important implications with regard to the identification of wave generation mechanisms. Wave occurrence was evenly distributed over the range of magnetic activity $K_p = 2-5$. In contrast to this, Yang and Chang found Pc 3 occurrence at Beijing peaked for local $K = 3$. Day-time wave frequencies were found to be higher than night-time frequencies, a result which is consistent with the field line resonance theory.

6. Storm associated waves

Three papers were presented on the low latitude observation of waves associated with substorms and magnetic storms. In the only paper presented at the symposium on Pc 1 ion cyclotron waves, Maltseva and Troitskaya studied the variation in IPDP wave frequency with latitude with the emphasis on low latitude signatures. IPDP events are a train of irregular amplitude pulsations normally seen at high latitudes and showing intervals of diminishing wave period with time. It was found that the frequency variation with latitude is such that $f_{O^+} < f_{IPDP} < f_{He^+}$ where f_{O^+} and f_{He^+} are the cyclotron frequencies of oxygen and helium ions in the magnetospheric plasma. Using this frequency variation with latitude it was suggested that IPDP may be capable of penetrating down to latitudes $L < 3$.

Pi 2 pulsations seen at the onset of a substorm are now used extensively to study the dynamics of substorms. Of importance is the relationship between the Pi 2 wave polarization characteristics and the location of a three dimensional current system, called the current wedge (McPherron et al., 1973) which develops at substorm onset. At midlatitudes ($L \sim 3$) Pi 2 polarization is anticlockwise west of the wedge, inside the wedge and also to the east of the wedge (Lester et al., 1984). However, at the symposium Lester and Singer reported that at low latitudes ($L \sim 1.7$) it is clockwise west of the wedge and anticlockwise inside and east of the wedge (Fig. 4). This suggests that a polarization reversal occurs somewhere between $L = 1.3$ and 3 west of the wedge, a result which has yet to be directly observed.

7. Ionosphere effects

Interesting measurements of vertical ionospheric electron drift velocities at the equator by the Jicamarca radar were reported by Patel and Lagos. They found quasiperiodic fluctuations with 90–120 s periods over an altitude range of 200–935 km. These vertical oscillations of the electrons resulted from an east-west electric field component. A number of suggestions were made as to the origin of these waves. They could be drift waves of internal ionospheric origin driven by plasma gradients, or alternatively, hydro-

magnetic modes of magnetospheric origin. Further details are discussed by Patel and Lagos (1985).

Wide ranging results on the ionospheric and magnetospheric signatures of a ground explosion at $L=1.5$ were the subject of a paper by Alperovich et al. This is an example of coupling between earth, ionospheric and magnetospheric processes resulting in the generation of a nonlinear mixture of RH and LH polarized ion-acoustic impulsive waves. The signatures were observed by the low altitude Aureol 3 satellite in the conjugate hemisphere. Several inter-hemispheric bounces of the wave energy packet were seen and an interpretation was made in terms of large amplitude solitary waves.

8. Hydromagnetic wave theory

In the preceding sections many papers have reported the existence of significant Pc 3-4 wave energy in discrete bands at low latitudes ($L < 3$). Furthermore it was shown that these waves may or may not be associated with similar activity at middle and high latitudes. It is generally considered that the probable source of the low latitude pulsations is the field line resonance mechanism. If the wave energy source is external to the magnetosphere, in the upstream waves region, then it is necessary to transfer significant energy to middle and low latitude field lines in order to excite these resonances. The Kelvin-Helmholtz instability is incapable of doing this, and furthermore it will not produce the single noon maximum observed in Pc 3 wave occurrence. Also, the coupling of compressional mode waves from this instability to the field line resonance is limited to waves with large azimuthal wave numbers. However, the coupling of global magnetospheric compressional modes, excited by impulses at the magnetopause, to field line resonances has recently been suggested as a possible source of waves (Kivelson and Southwood, 1985; Allan et al., 1985). The two modes exhibit strong coupling and relate to low azimuthal wave numbers, which are now known to predominate (Sect. 4). Kivelson and Zhu explained that this mechanism can excite waves at any latitude within the bounds of the chosen magnetosphere-plasma-sphere system. The global compressional wave has a finite amplitude over a large radial scale and a discrete frequency spectrum will be seen, determined by the radial boundary conditions. The dominant transverse component may be either toroidal or poloidal. The toroidal oscillations are confined to L-shells whose resonant frequency matches the frequency of the global mode. There is a transfer of energy from the global mode to the field line resonance resulting in the damping of the global mode. Further details of this work are included in Kivelson and Southwood (1986) and Allan et al. (1986).

Although we have known for a long time that the field line resonance mechanism is the origin of many discrete wave phenomena seen on the ground it was not until the observations of the STARE radar at high latitudes became available that the spatial amplitude and phase structure of the resonance was seen (Walker, 1980). Because of ionospheric screening and spatial integration it is difficult to identify unambiguously the resonance using ground magnetometer arrays. The application of a novel method developed by Baransky et al. (1985) was described by Feygin et al. using low latitude data. It is assumed that each field line has its own discrete frequency of oscillation as shown

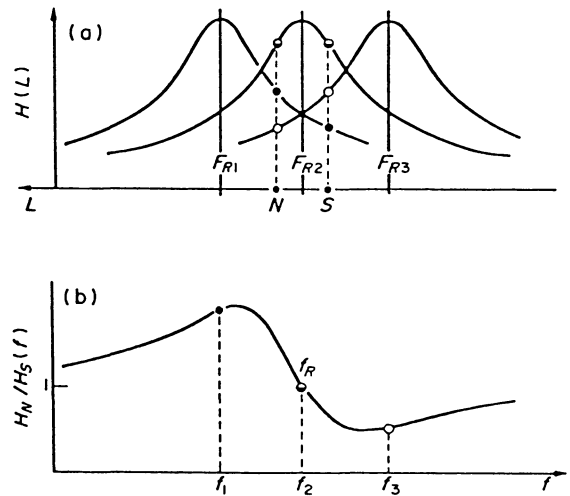


Fig. 5. **a** Schematic of the meridional distributions of wave amplitude $H(L)$ for three spectral components $f_1 < f_2 < f_3$ of geomagnetic pulsations. Each component experiences the local resonance amplification at the foot of the field line with resonance frequency $F_i = f$. **b** Ratio of spectral amplitudes $H_N/H_S(f)$ of pulsations recorded simultaneously at points N and S. The frequency f_R determined from the conditions $H_N/H_S(f) = 1$ and $\partial(H_N/H_S)/\partial f < 0$, should be the resonant frequency of the field line intersecting the meridian at the midpoint of NS ($f_R = F_{R2}$) [From Baransky et al., 1985]

in Fig. 5a. Using north-south and east-west magnetometer data from two stations (N and S) spaced 100 km apart, it was shown that the frequency at which the amplitude ratio of the north-south components from the two stations passes through unity indicates the field line resonance frequency for the field line midway between the two stations (Fig. 5b). Feygin et al. described results from pairs of stations spaced 100 km apart at Sogra ($L=3.6$). A resonance was found at 33 mHz which was interpreted as the second harmonic of the $L=3.6$ field line. A "gradient-time analysis" method based on the numerical comparison of digital dynamic spectra was also described. Over 34 min, the resonant frequency varied from 26 to 38 mHz. The phase characteristics of the resonance signatures observed on the ground were also discussed and it was concluded that the plasmasphere may be a more favorable region for the field line resonance than the plasmapause. This is a potentially powerful method for locating the latitude of the field line resonance and may be capable of determining the range of latitude over which the field line resonance mechanism operates and the associated frequency variation with latitude.

9. Conclusions

The symposium on low latitude hydromagnetic waves provided an opportunity for the assessment of present knowledge and a forum to plan for the future. Current understanding of the source and properties of long period hydromagnetic waves at low latitudes are summarized below. The summary is certainly not complete, but concentrates on the results reported at the symposium and reinforced to some extent by recent results reported in the open literature.

The energy sources for waves observed on the ground may be internal or external. Overwhelming evidence presented at the symposium supported upstream waves as an

external source of Pc 3-4 waves at low latitudes. This included the solar wind/IMF parameter correlations with pulsation frequency and amplitude and the simultaneous switch-on and switch-off of wave activity over short intervals of time and a wide range of latitude. In contrast to this, Pi 2 and Pc 1/Pi 1 waves result from internal free energy processes directly or indirectly associated with magnetospheric substorms.

At low latitudes, ground magnetometer arrays provide the primary data for spatial and temporal studies of wave properties. Pc 3-4 wave properties of importance for identifying generation and propagation mechanisms that have been determined from array studies include:

1. The relationships between solar wind/IMF and Pc 3 wave parameters;
2. A predominance of LH polarized waves before noon and RH waves after noon on particular days. This pattern is not always seen and must be clarified.
3. Low azimuthal wave numbers ($m < 10$).
4. On many occasions, a propagation pattern is seen in which waves propagate away from noon towards the dawn and dusk terminators. Again, this pattern is not always seen.
5. Harmonic wave structure, known to exist at synchronous orbit and at high latitudes, has been tentatively observed at low latitudes, but further studies are needed.
6. High and low latitude dynamic wave spectra often show similar characteristics.
7. Pc 3 wave amplitudes and occurrences peak near local noon.

Recently suggested wave theories involving the coupling of global compressional wave eigenmodes to the field line resonance appear to be capable of explaining many of the properties listed above. However, these models are still in their infancy and have yet to be applied to a fully realistic magnetosphere.

From the experience of this symposium a number of directions for future research in low latitude hydromagnetic waves are obvious. Firstly, observations should be undertaken to check the predictions of the global compressional wave theory. These include observations of compressional waves and resonance structures in the magnetosphere and plasmasphere using radial satellite paths, and the association of these wave properties with upstream waves and pulsations on the ground. Observations of the latitudinal structure of Pc 3-4 pulsations at low latitudes must be undertaken using ground arrays in order to identify field line resonance regions. The confused results on the spatial structure of Pc 3 phase jumps and associated polarization and frequency changes over short intervals of time must also be explained. For substorm associated waves, particularly the Pi 2 and IPDP pulsations, it is important to understand the low latitude signatures in detail before we can determine the mechanisms by which the waves are propagated to these latitudes.

Hopefully, much of this work can be accomplished within the next year or two. This would seem appropriate since a symposium on hydromagnetic waves in the polar cusp region is scheduled to be held at the next IUGG General Assembly in Vancouver in August 1987. By this time we may understand the sources of low latitude hydromagnetic waves and be capable of relating them to the higher latitude observations.

Acknowledgements. This paper was written while the author was on study leave at UCLA. He wishes to thank R.L. McPherron for his support during this time. At the University of Newcastle N.S.W. Australia support was provided by the University and the Australian Research Grants Committee and at UCLA by grants from the National Science Foundation (ATM83-18200), the Office of Naval Research (N00014-84-C-0158) and the National Aeronautics and Space Administration (NGL-05-007-004).

References

- Allan, W., White, S.P., Poulter, E.M.: Magnetospheric coupling of hydromagnetic waves – initial results. *Geophys. Res. Lett.* **12**, 287–290, 1985
- Allan, W., White, S.P., Poulter, E.M.: Impulse excited hydromagnetic cavity and field line resonances in the magnetosphere. *Planet. Space Sci.* **34**, 1986
- Ansari, I.A., Fraser, B.J.: A multistation study of low latitude Pc 3 geomagnetic pulsations. *Planet. Space Sci.* **34**, 1986
- Baransky, L.N., Bororkov, J.E., Gokhberg, M.B., Krylov, S.M., Troitskaya, V.A.: High resolution method of direct measurement of the magnetic field lines' eigen frequencies. *Planet. Space Sci.* **33**, 1369–1374, 1985
- Chen, L., Hasegawa, A.: A theory of long period magnetic pulsations. 1, Steady state excitation of field line resonance. *J. Geophys. Res.* **79**, 1024–1032, 1974
- Greenstadt, E.W., McPherron, R.L., Takahashi, K.: Solar wind control of daytime mid-period geomagnetic pulsations. *J. Geomagn. Geoelectr.* **32**, Suppl. II, 89–110, 1980
- Hasegawa, A.: Drift mirror instability in the magnetosphere. *Phys. Fluids* **12**, 2642–2650, 1969
- Hughes, W.J.: Pulsation research during the IMS. *Rev. Geophys. Space Phys.* **20**, 641–652, 1982
- Kivelson, M.G., Southwood, D.J.: Resonant ULF waves: A new interpretation. *Geophys. Res. Lett.* **12**, 49–52, 1985
- Kivelson, M.G., Southwood, D.J.: Coupling of global magnetospheric MHD eigenmodes to fieldline resonances. *J. Geophys. Res.* **91**, 1986
- Lanzerotti, L.J., Medford, M.V., MacLennan, C.G., Hasegawa, T., Acuna, M.H., Dolce, S.R.: Polarization characteristics of hydromagnetic waves at low geomagnetic latitudes. *J. Geophys. Res.* **86**, 5500–5506, 1981
- Lester, M., Hughes, W.J., Singer, H.J.: Longitudinal structure in Pi 2 pulsations and the substorm current wedge. *J. Geophys. Res.* **89**, 5489–5494, 1984
- McPherron, R.L., Russell, C.T., Aubry, M.P.: Satellite studies of magnetospheric substorms on August 15, 1968. 9, Phenomenological model for substorms. *J. Geophys. Res.* **78**, 3131–3149, 1973
- Mier-Jedrzejowicz, W.A.C., Hughes, W.J.: Phase skipping and packet structure in geomagnetic pulsation signals. *J. Geophys. Res.* **85**, 6888–6892, 1980
- Mier-Jedrzejowicz, W.A.C., Southwood, D.J.: Comparison of Pc 3 and Pc 4 pulsation characteristics on an east-west mid-latitude chain of magnetometers. *J. Atmos. Terr. Phys.* **43**, 911–917, 1981
- Odera, T.J.: Solar wind controlled pulsations. *Rev. Geophys.* **24**, 55–74, 1986
- Patel, V.L., Lagos, P.: Low frequency fluctuations of the electric field in the equatorial ionosphere. *Nature* **313**, 559–560, 1985
- Russell, C.T., Hoppe, M.M.: The dependence of upstream wave periods on the interplanetary magnetic field strength. *Geophys. Res. Lett.* **8**, 615–617, 1981
- Russell, C.T., Luhmann, J.G., Odera, T.J., Stuart, W.F.: The rate of occurrence of dayside Pc 3-4 pulsations: The L value dependence of the IMF cone angle effect. *Geophys. Res. Lett.* **10**, 663–666, 1983
- Saka, O., Kim, J.S.: Spatial phase structure of low latitude Pc 3-4 pulsations. *Planet. Space Sci.* **33**, 1073–1080, 1985
- Samson, J.C., Jacobs, J.A., Rostoker, G.: Latitude-dependent

- characteristics of long period geomagnetic micropulsations. *J. Geophys. Res.* **76**, 3675–3683, 1971
- Southwood, D.J.: The behavior of ULF waves and particles in the magnetosphere. *Planet. Space Sci.* **21**, 53–65, 1973
- Southwood, D.J.: Some features of field line resonances in the magnetosphere. *Planet. Space Sci.* **22**, 639–642, 1984
- Troitskaya, V.A.: Results of ULF wave investigations in the USSR. *Proc. Conf. Achievements of the IMS, ESA, SP-217*, 639–642, 1984
- Troitskaya, V.A., Plyasova-Bakounina, T.A., Gulelmi, A.V.: Relationship between Pc 2-4 pulsations and the interplanetary magnetic field. *Dokl. Akad. Nauk. SSSR*, **197**, 1312, 1971
- Vero, J.: Experimental aspects of low latitude pulsations – a review. *J. Geophys.* **58**, 1986
- Walker, A.D.M.: Modelling of Pc 5 pulsation structure in the magnetosphere. *Planet. Space Sci.* **28**, 213–223, 1980
- Yumoto, K.: Theoretical considerations on low latitude magnetic pulsations. *J. Geophys.* **58**, 1986
- Yumoto, K., Saito, T., Akasofu, S.-I., Tsurutani, B.T., Smith, E.J.: Propagation mechanism of daytime Pc 3-4 pulsations observed at synchronous orbit and multiple ground-based stations. *J. Geophys. Res.* **90**, 6439–6450, 1985a
- Yumoto, K., Saito, T., Tanaka, Y.: Low latitude Pc 3 magnetic pulsations observed at conjugate stations ($L \sim 1.5$). *J. Geophys. Res.*, **90**, 12201–12207, 1985b
- Papers presented at the symposium**
- Alperovich, L.S., Y.I. Galperin, M.B. Gokhberg, O.A. Pokhotelov, R.Z. Sagdeev: Solitary Alfvén wave in the low-latitude magnetosphere.
- Ansari, I.A., B.J. Fraser: Spectral characteristics of low-latitude Pc 3 geomagnetic pulsations in South East Australia.
- Ansari, I.A., B.J. Fraser: Wave packet structure and phase jumps in low-latitude Pc 3 geomagnetic pulsations.
- Ansari, I.A., B.J. Fraser: A statistical study of low latitude Pc 3 geomagnetic pulsations.
- Best, A., I. Best, and J.J. Linth: Spectral characteristics of Pc 3 and Pc 4 pulsations in middle latitudes.
- Boshoff, H.F.V., and P.R. Sutcliffe: Local time and longitudinal variations of Pc 3 pulsation frequency.
- Feygin, F.Z., Yu. N. Kurchashov, Ya. S. Nikomarov, V.A. Pilenko, and A. Best: Preliminary results of U.S.S.R.-G.D.R. experiment for the synchronous registration of geomagnetic pulsations at two low-latitude meridional profiles.
- Fraser, B.J.: A review of contributed papers.
- Hollo, L., and J. Vero: One year comparison of ATS and ground pulsation spectra.
- Ivanova, P.K., and N.G. Kleimenova: Long-period pulsations at $L < 3$ during great magnetic disturbances.
- Kivelson, M.G., and X.M. Zhu: Pc 3-4 pulsations at low latitudes and generation of parallel currents.
- Lanzerotti, L.J., L.V. Medford, and A. Wolfe: Variations in hydro-magnetic wave frequencies at low geomagnetic latitudes.
- Lester, M., H.J. Singer: Pi 2 pulsations and the substorm current wedge-polarization characteristics at low latitudes ($L < 3$)
- Maltseva, N., V. Troitskaya: On movement of IPDP generation sources in the region $L < 3$.
- Menk, F.W., C. Ziesolleck, B.J. Fraser, R.L. McPherron, and P.W. McNabb: Propagation of Pc3-4 pulsations across a low-latitude array.
- Miletits, J.Cz., and J. Vero: Dynamic spectra of pulsation events at $L = 2$ and 3.
- Patel, V.L., and P. Lagos: Low-frequency fluctuations of the electric field in the equatorial ionosphere.
- Plyasova-Bakounina, T.A., V.A. Troitskaya, J.W. Munch, H.F. Gauler: A new maximum of Pc 2-4 intensity.
- Saito, T., K. Yumoto, K.D. Cole, J. Ward, J. Soegijjo, A.J. Chen, and Y. Tanaka: Wave characteristics of Pc 3-4 pulsations observed at low latitude conjugate stations ($L < 2.1$).
- Saito, T., K. Yumoto, B.T. Tsurutani, E.J. Smith, S.-I. Akasofu: IMF controls of low-latitude Pc 3-4 pulsations at longitudinally separated ground stations.
- Sutcliffe, P.R.: The spatial and temporal structure of low-latitude Pc 3 pulsation fields.
- Vero, J.: Experimental aspects of low-latitude pulsations – A review.
- Yang, S.-F., and J.-X. Chang: The correlation between Pc 3 geomagnetic pulsation and K-index in Beijing.
- Yumoto, K.: Theoretical considerations on low-latitude magnetic pulsations.

Received March 11, 1986; revised May 16, 1986

Accepted July 18, 1986

Generation and propagation mechanisms of low-latitude magnetic pulsations – A review

Kiyohumi Yumoto

Onagawa Magnetic Observatory and Geophysical Institute, Tohoku University, Sendai 980, Japan

Contents

1. Introduction
2. Low-latitude Pc 3 magnetic pulsations
 - 2.1 Introduction
 - 2.2 Upstream waves as a source of low-latitude Pc 3
 - 2.3 Transmission of upstream waves through the bow shock and the magnetopause
 - 2.4 Propagation mechanism of Pc 3 source waves into the deep magnetosphere
 - 2.5 Transmitted Pc 3 source waves in the magnetosphere
 - 2.6 Characteristic frequencies of various Pc 3 oscillations in the magnetosphere
 - 2.7 Wave characteristics of low-latitude Pc 3
 - 2.8 Pc 2–3 at very low latitudes ($\Phi < 22^\circ$)
3. Low-latitude Pi 2 magnetic pulsations
 - 3.1 Introduction
 - 3.2 Unresolved characteristics of Pi 2 pulsations
 - 3.3 Wave and current fluctuation models for Pi 2 generation
 - 3.4 Model of instantaneous transmission from the polar electric field to the equator
 - 3.5 A possible model for daytime Pi 2
4. Summary and conclusions

Key words: Geomagnetic pulsations – Pc 3 pulsations – Pi 2 pulsations – Low-latitude phenomena – Hydromagnetic Waves – Magnetosphere

1. Introduction

It is more than thirty years since J.W. Dungey first suggested that sinusoidal oscillations in the earth's magnetic field, recorded almost a hundred years before by B. Stewart and known as geomagnetic pulsations, were due to hydromagnetic waves in the magnetosphere. In recent years there has been an amazing increase in both the quantity and quality of data due to new techniques of measurement such as the availability of extensive magnetometer chains, multi-satellite observations, and auroral radars, in addition to the many advances in our theoretical understanding of the phenomena (see review of Hughes, 1983).

Magnetic pulsations can be basically classified into two groups. One is "exogenic" pulsations which are continuously driven by the solar wind. The other is "endogenic" pulsations which are excited mainly by transient and abrupt changes of the ambient magnetized plasma and/or the free

energy stored in the earth's magnetosphere. The present review deals mainly with low-latitude Pc 3 ($T=10\text{--}45$ s) and Pi 2 (40–150 s) magnetic pulsations, which can be categorized as "exogenic" and "endogenic" pulsations, respectively. A significant part of the "exogenic" Pc 3 pulsations observed in daytime is in some way a function of the state of the solar wind (cf. Verö, 1985). It has been recently demonstrated that daytime Pc 3 magnetic pulsations assume an important role in the transmissions of the solar wind energy into the inner magnetosphere, which is of vital importance in understanding the physics of important aspects of the solar wind-magnetosphere interaction (Wolfe et al., 1985; Yumoto et al., 1985a). On the other hand, "endogenic" Pi 2 pulsations have been considered as transient hydromagnetic signals associated with substorm expansion onsets or intensifications (see Baumjohann and Glassmeir, 1984). Therefore, Pi 2 magnetic pulsations are generally believed to play an important role in the dynamic coupling of the magnetosphere and the ionosphere during substorm expansion onset (e.g., Nishida, 1979; Lysak and Dum, 1983; Sun and Kan, 1985). Undoubtedly it seems worthwhile now to review both our knowledge and our ignorance and to clarify how low-latitude Pc 3 and Pi 2 magnetic pulsations assume important roles in the dayside solar-terrestrial relationships and in the magnetosphere-ionosphere couplings, respectively.

In Sect. 2, we will review the generation and propagation mechanisms of hydromagnetic energies in the Pc 3 frequency range in the solar wind into the inner magnetosphere ($L \sim 1.5$). Wave characteristics of Pc 3 pulsation at $L \lesssim 3.0$ will be theoretically and observationally investigated. The generation mechanism of very low latitude Pc 2–3 ($\Phi < 22^\circ$) will be also theoretically discussed. In Sect. 3, selected wave characteristics of Pi 2 pulsations will be summarized with an emphasis on the unresolved generation and propagation mechanisms of low-latitude Pi 2. After theoretical models of Pi 2 pulsations have been reviewed, we propose a possible Pi 2 model. In the final section, conclusions and remaining future studies on the generation and propagation mechanisms of low-latitude magnetic pulsations will be summarized.

2. Low-latitude Pc 3 magnetic pulsations

2.1 Introduction

Low-latitude Pc 3 magnetic pulsations have been recently studied by many scientists (Verö, 1980, 1981; Lanzerotti

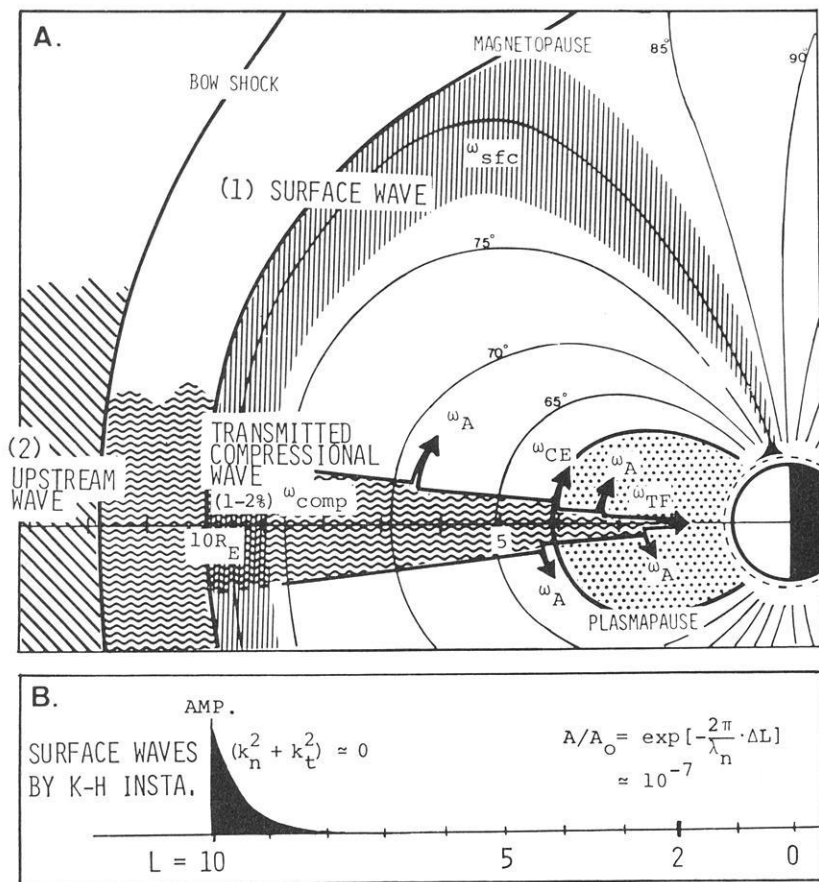


Fig. 1 A and B. Two possible generation mechanisms for daytime Pc 3 (after Yumoto et al., 1985a). **A** Surface waves in the Pc 3 range excited by the Kelvin-Helmholtz-type instabilities in the dayside high-latitude boundary layer can transmit only into the high-latitude ionosphere. Magnetic upstream waves in the earth's foreshock can propagate into the magnetosphere, can couple with various HM oscillations (ω_A^n , ω_{CE} , ω_{TF}) in the inner magnetosphere, and then can be a source of low-latitude Pc 3 magnetic pulsations. **B** Damping rate (A/A_0) of typical Pc 3 surface waves in the radial direction. The Pc 3 amplitude at $L = 2.0$ is seven orders of magnitude below that at the magnetopause for wavelength $\lambda \sim 3 R_E$.

et al., 1981; Kunaratnam, 1981; Yumoto and Saito, 1982, 1983; Green et al., 1983; Russell et al., 1983; Saito et al., 1984; Sutcliffe and Poole, 1984; Yumoto et al., 1984, 1985a; Fraser and Ansari, 1985; Odera and Stuart, 1985; Saka and Kim, 1985). It is generally accepted that there are two candidates of main exogenic sources for daytime Pc 3–4 pulsations as shown in Fig. 1a. One is surface waves excited by the shear flow (Kelvin-Helmholtz-type) instability driven by the solar wind at the dayside high-latitude magnetospheric boundary (Miura, 1984; Yumoto, 1984; Yumoto et al., 1985a). The other is the bow-shock-associated wave phenomena associated with particle reflected and/or accelerated by the bow shock (Fairfield, 1969; Russell et al., 1971; Greenstadt, 1976; Russell and Hoppe, 1983; Yumoto et al., 1984).

However, the existence of Pc 3 pulsations at very low latitudes on the ground is difficult to explain if they are related to the surface waves at the dayside high-latitude magnetopause because of the high damping rate of the evanescent wave in the Pc 3 frequency range in the radial direction as shown in Fig. 1b (cf. Lanzerotti et al., 1981; Yumoto et al., 1984). The damping rate [A/A_0] of typical Pc 3 surface waves in the radial direction produces an amplitude reduction of seven orders of magnitude from the magnetopause to $L=2.0$ for a typical Pc 3 wavelength of $\lambda=3 R_E$. The Pc 3 surface waves can only penetrate into the high-latitude ionosphere and then could be observed as high-latitude Pc 3 magnetic pulsations (see Sect. 2.4). Lanzerotti et al. (1981) proposed a possible way to obtain low-latitude waves without excessive damping for excitation by disturbances produced in the magnetospheric cusp, and

suggested that these cusp disturbances would propagate to lower latitudes via the ionosphere. Some authors had also studied the transmission process of HM waves in the ionosphere from high latitudes to the equator, as reviewed in Sect. 3.4. However, it has not yet been theoretically examined how low-latitude Pc 3 standing oscillations observed at $L \sim 1.5$ (see Sect. 2.7) could be excited by the transmitted Pc 3 disturbance in the ionosphere. Moreover, morphological relationships between high-latitude Pc 3 and low-latitude Pc 3 are still not conclusively clarified. Further theoretical and observational studies are needed to investigate quantitatively the transmission of Pc 3 pulsations in the ionosphere.

On the other hand, studies of the solar-wind-controlled mid- and low-latitude Pc 3–4 pulsations have been highlighted (see Greenstadt et al., 1980; Wolfe et al., 1980; Odera, 1986). The fact that magnetosonic upstream waves with 15–100 mHz range, excited by the reflected ion beams in the earth's foreshock (cf. Tsurutani and Rodriguez, 1981; Russell and Hoppe, 1983), transmit into the magnetosphere without significant changes in spectra recently appears to be accepted (Yumoto and Saito, 1983; Greenstadt et al., 1983; Yumoto et al., 1984; Yumoto, 1985). The transmitted compressional Pc 3–4 waves are believed to be a main source of low-latitude Pc 3–4 pulsations (Wolfe et al., 1985; Yumoto et al., 1985a).

The purpose of this section is to review the generation and propagation mechanisms of Pc 3 magnetic pulsations observed at low latitudes ($L \lesssim 3.0$). The generation mechanism of upstream waves in the Pc 3–4 frequency range in the earth's foreshock will be summarized in Sect. 2.2. Trans-

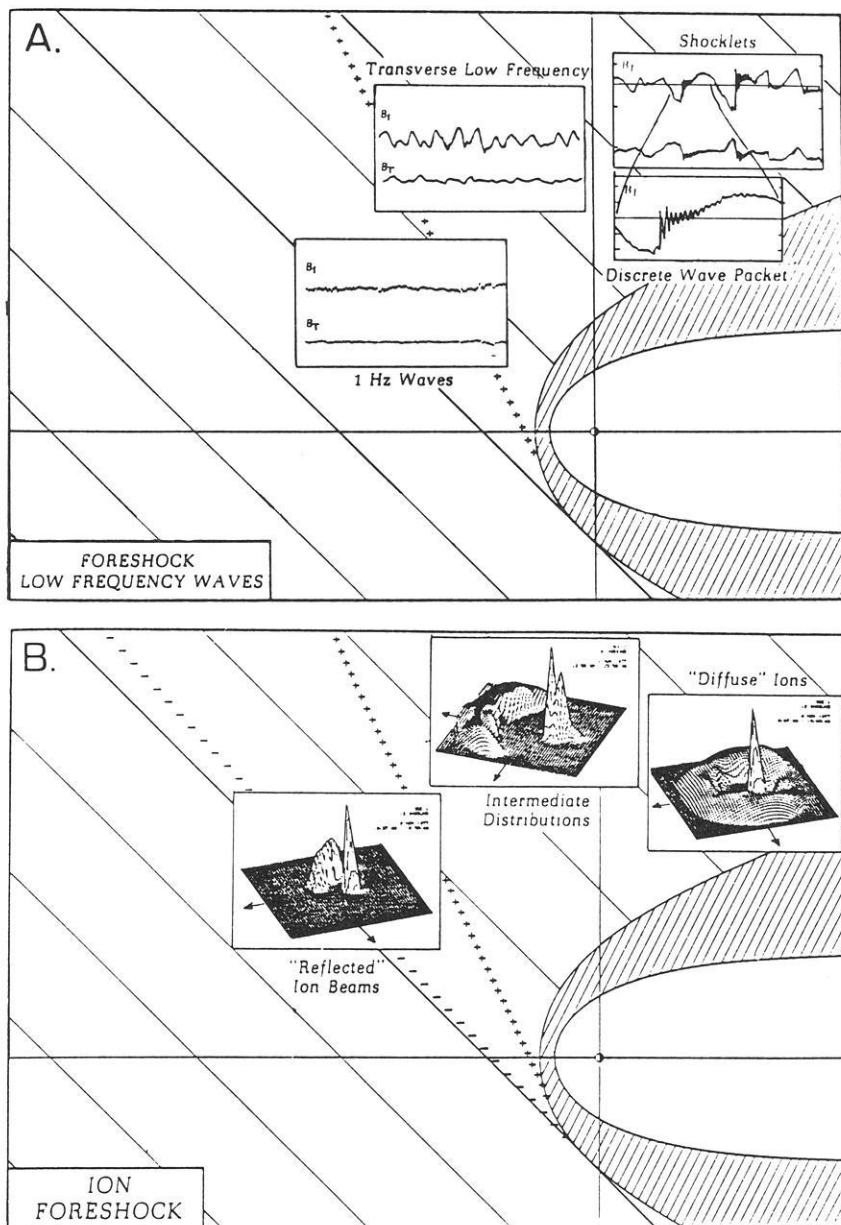


Fig. 2A and B. Upstream waves and particles (after Russell and Hoppe, 1983). **A** Low frequency upstream waves, i.e., the transverse low-frequency and shocklet waves, are associated with ion distributions of the earth's foreshock. The 1-Hz waves are associated with electron anisotropies and are observed both upstream and downstream of the ion foreshock boundary. **B** Ion distributions of the earth's foreshock. The high narrow peak in each distribution is the solar wind. The foreshock ions appear as a narrow "reflected" beam, as the kidney-bean-shaped intermediate ions, and the more nearly isotropic "diffuse" distributions. The upstream boundaries of foreshock electrons (-) and ions (+) are sketched

missions of the Pc 3-4 upstream waves through the bow shock and the magnetopause into the outer magnetosphere will be described in Sect. 2.3. In Sects. 2.4 and 2.5, propagation mechanisms (i.e., coupling mechanisms) of Pc 3-4 source waves from the outer to the inner magnetosphere will be discussed. Characteristic frequencies of various Pc 3-4 oscillations coupled with the source waves will be theoretically summarized in Sect. 2.6. Wave characteristics of low-latitude Pc 3 pulsations observed at conjugate stations will be demonstrated in Sect. 2.7. Finally, a generation mechanism of Pc 2-3 observed at very low latitudes ($L < 1.2$) and unresolved problems will be discussed in Sect. 2.8.

2.2 Upstream waves as a source of low-latitude Pc 3

A major early discovery was the existence of large-amplitude low-frequency waves that fill most of the upstream region that is connected to the bow shock by the interplanetary magnetic field (IMF) (Greenstadt et al., 1968; Fair-

field, 1969). The upstream waves are considered to be generated by reflected protons coming from the earth's foreshock (Fairfield, 1969; Barnes, 1970; Fredricks, 1975; Kovner et al., 1976; Gray et al., 1981; Lee, 1982; Watanabe and Terasawa, 1984; Hada et al., 1986). Using magnetic field data from the dual ISEE 1 and 2 spacecraft, Hoppe and Russell (1983) have determined the plasma rest-frame frequencies of the large-amplitude, low-frequency upstream waves as shown in Fig. 2a. The monochromatic sinusoidal waves associated with "intermediate" ion fluxes (Fig. 2b) were concluded to be magnetosonic waves with rest-frame frequency ~ 0.05 - 0.2 times the ion cyclotron frequency (Ω_i) and wavelength $\sim 1 R_E$ in the earth's foreshock. They also identified these as magnetosonic right-handed mode signals from the rest-frame polarizations.

On the other hand, Gosling et al. (1978) reported the presence of two distinct and mutually exclusive populations of low-energy ions (≈ 40 KeV) in the upstream solar wind, so-called "reflected" and "diffuse" components. Pasch-

mann et al. (1981) indicated the distinction among three types of upstream ion populations on the basis of pronounced differences in their distribution functions, i.e., “reflected” ion beam, “intermediate,” and “diffuse” ion distribution (Fig. 2b). Although the low-frequency magnetosonic waves with larger amplitude were demonstrated to be associated mostly with the intermediate and diffuse ion distributions (Paschmann et al., 1980, 1981; Sentman et al., 1981; Hoppe et al., 1981; Tsurutani and Rodriguez, 1981; Russell and Hoppe, 1983), it is generally considered that instability of the reflected ion beams generates waves; the waves pitch angle scatter the beams into intermediate and diffuse distributions and then all are convected back toward the shock (Gray et al., 1981; Bavassano-Cattaneo et al., 1983; Hoppe and Russell, 1983). Recently, Hada et al. (1986) theoretically studied the relations between the ion distributions and large-amplitude upstream waves and excitations of compressional waves in the earth’s foreshock in detail.

Paschmann et al. (1981) showed the large velocity variation of reflected ions from 650 km/s to 1,150 km/s in the solar wind frame, i.e., in the rest frame. If the low-frequency magnetosonic waves with $(\omega/\Omega_i) = 0.05\text{--}0.2$ in the earth’s foreshock (Hoppe and Russell, 1983) are assumed to be a magnetosonic right-handed wave excited by the well-established cyclotron resonance mechanism driven by narrow reflected ion beams (Stix, 1962; Kennel and Petschek, 1966), the proton resonant velocity (V_{\parallel}) in the solar wind frame can be expected to be $(V_{\parallel}/V_A) \sim 8\text{--}20$ with respect to the resonance condition (Yumoto et al., 1984). The local Alfvén velocity (V_A) in the upstream region is typically ~ 50 km/s, so that the proton resonant velocity (V_{\parallel}) exciting the magnetosonic right-handed waves with $(\omega/\Omega_i) = 0.05\text{--}0.2$ in the rest frame is inferred to be 400–1,000 km/s. This inference is in agreement with the range of the observed velocities of reflected ion beams in the solar wind frame (Paschman et al., 1981). When the cone angle θ_{XB} of the IMF is small, the subsolar foreshock is occupied by complex, compressional waves. Although the relationship between the IMF magnitude and the frequencies of the complex, compressional foreshock waves have not been published, the low-frequency magnetosonic waves with large amplitude in the earth’s foreshock could be associated with the magnetosonic right-handed waves excited by the anomalous Doppler-shifted ion cyclotron resonance with the narrow reflected ion beams.

2.3 Transmission of upstream waves through the bow shock and the magnetopause

Many authors have theoretically studied the transmitted magnetohydrodynamic waves in the magnetosheath resulting from the incidence of an upstream wave on the bow shock (Westphal and McKenzie, 1969; Barnes, 1970; Fairfield and Ness, 1970; McKenzie and Bornatici, 1974; Hassam, 1978; Zhuang and Russell, 1982). They tried to explain the higher level of fluctuations in the magnetosheath than in the upstream solar wind on the basis of Snell’s law, i.e., the continuity of the frequency and the tangential component of the wave vector. Zhuang and Russell (1982) concluded that the fast mode of upstream waves whose incident angle is less than the critical angle ($\sim 20^\circ$) can enter through and be amplified by the bow shock. The amplified waves are believed to account for the low-frequency turbulence-

like structure observed downstream of the quasi-parallel shock (McKenzie and Westphal, 1970; McKenzie, 1970).

Using a convection pattern model of the shocked solar wind flow around the Venus obstacle, Luhmann et al. (1983) recently demonstrated that the period and polarization of ULF magnetic fluctuations observed by Pioneer Venus in the magnetosheath are similar to those observed upstream of the quasi-parallel bow shock. Russell et al. (1983) have found the L value dependence of the IMF cone angle effect, i.e., when θ_{XB} is 15° or less, the normalized rate of occurrence of daytime Pc 3–4 pulsations of $L = 2.4\text{--}4.3$ is much higher near zero θ_{XB} at low latitudes than at high latitudes. The L value dependence of the IMF cone angle effect was examined quantitatively by using a simple approximation to the magnetosheath flow field for a variety of angles between the IMF and shock normal, θ_{BN} as shown in Fig. 3. When $\theta_{XB} = 0^\circ$, upstream waves which are most intense near the streamline that passes through the shock at θ_{BN} of 0° are believed to propagate radially inward and be convected to the magnetopause. When θ_{XB} becomes larger, upstream waves generated away from the subsolar region of the shock have access to the magnetopause by propagating across streamlines until far downstream in the magnetosheath, but these do not seem to penetrate deeply into the magnetosphere. They concluded that the sharp dependence on θ_{XB} at low L values probably reflects the dependence of upstream wave amplitude at the nose of the shock on θ_{XB} , whereas the weaker θ_{XB} dependence at higher L values is indicative of cross streamline propagation and wave coupling over a range of a local times.

The mechanism of MHD wave transmission in the Pc 3 frequency range through the tangential discontinuity at the earth’s magnetopause was theoretically demonstrated to be important for magnetosonic fast waves with a nearly normal incident angle (McKenzie, 1970; Verzariu, 1973; Wolfe and Kaufmann, 1975). The transmission coefficient averaged over a hemispherical distribution of incident fast waves was found to be 1%–2%. The daily averaged magnitude of energy flux deposited into the magnetosphere over a hemispherical distribution of waves having amplitudes of say 2–3 nT, has been estimated to be on the order 10^{22} erg. Therefore, the energy input of MHD waves can contribute significantly to the energy budget of the magnetosphere (Verzariu, 1973).

For the magnetopause of a rotational discontinuity, Kwok and Lee (1984) demonstrated that five types of incident waves (Alfvén, fast and slow magnetosonic, convected slow and entropy waves) from upstream (magnetosheath) can exist and transmissions occur over a wide range of incident angle. The fast magnetosonic wave reflected from the magnetopause at a rotational discontinuity was also suggested to contribute to the cause of magnetosheath turbulence. The integral power of the Alfvén-wave transfer was found to be proportional to the total open magnetic flux in the magnetosphere and is typically $\sim 1\%$ of the electromagnetic energy transfer rate across the open magnetopause (Lee, 1982). The numerical results for wave transmission at a rotational discontinuity indicated a strong dependence of the transmitted wave amplitudes on the B_n/B_t ratio (the normal to the tangential component of the ambient magnetic field), which can also be dependent on the solar wind velocity and the rotation angle of the magnetic field (see Figs. of Kwok and Lee, 1984). This theoretical result supports the control of the solar wind velocity on

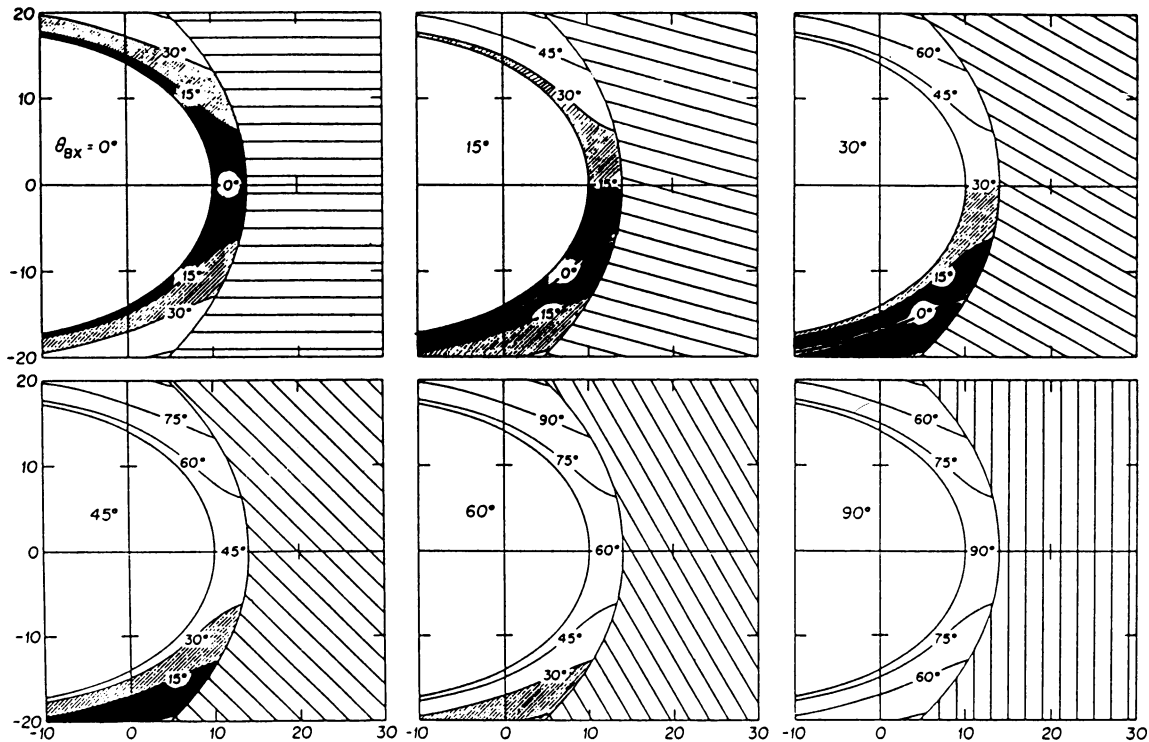


Fig. 3. Relation between the IMF cone angle (θ_{Bx}) and Pc 3–4 waves in the magnetosheath (after Russell et al., 1983). Pc 3–4 waves are assumed to be generated at the shock only for the angles $\theta_{BN} = \langle \mathbf{B}_{IMF}, \mathbf{n}_{shock} \rangle \lesssim 15^\circ$ and then to be convected back without propagating across stream lines. Stream lines in the $B-V$ plane in the magnetosheath are labelled and shaded according to the θ_{BN} angles at the point the streamline crosses the shock

the Pc 3–4 activity in daily averages, especially when the Kelvin-Helmholtz mechanism is expected not to be effective (Wolfe et al., 1980).

Wolfe et al. (1985) recently demonstrated that the correlation between the low-latitude geomagnetic power in the Pc 3 frequency range (15–30 s) and the interplanetary conditions is slightly better for the case of negative B_z of the IMF than for the case of the unconstrained north/south direction. This evidence is believed to suggest that power of Pc 3 source waves is transmitted more readily across an open magnetopause, i.e., across interconnected field lines, or rotational discontinuities. However, component-by-component details of the transfer process, the global picture describing where the most effective transfer takes places, and the pathways whereby broadband energy in the magnetosheath is recorded as monochromatic pulsations in the magnetosphere remain to be clarified.

2.4 Propagation mechanism of Pc 3 source waves into the deep magnetosphere

From the comparison of power spectra of magnetic field data from ISEE 1 and 2 recorded simultaneously on both sides of the magnetopause, Greenstadt et al. (1983) observationally demonstrated that the same frequencies were enhanced on the two sides of the boundary. Ratios of the magnetic power in the magnetosphere to that in the magnetosheath in the $0.01 < f < 0.1$ -Hz range were found to be from about 0.001 to 0.08. Such low ratios across the magnetopause are consistent with those of transferred powers predicted theoretically by Verzariu (1973) for tan-

genial discontinuities and by Lee (1982) for rotational discontinuities, and demonstrated observationally in single-satellite crossing by Wolfe and Kaufmann (1975). These results support the theory of external wave origin, i.e., the transfer of a small fraction of magnetosheath wave power which is possibly derived from quasi-parallel shock structure (Greenstadt, 1972; Kovner et al., 1976) and/or magnetosonic upstream waves originating in the earth's foreshock (see Sect. 2.2), across a stable magnetopause into the magnetosphere to appear as waves in the Pc 3–4 range.

On the other hand, another candidate for an exogenic source of daytime Pc 3–4 pulsations is generally believed to be surface waves excited by Kelvin-Helmholtz type instability at the dayside high-latitude magnetopause (see Yumoto, 1984). However, the existence of Pc 3 pulsations at very low latitudes is difficult to explain by the surface waves at the magnetopause because of the higher damping rate of the evanescent waves in the radial direction as shown in Fig. 1 b (cf. Lanzerotti et al., 1981; Yumoto et al., 1984). The damping rate $[A/A_0 = \exp(ik_n \Delta L)]$ of typical Pc 3 evanescent waves is of the order 10^{-3} for $\lambda_{\parallel} \sim (V_t/f) \sim 500 \text{ km s}^{-1}/60 \text{ mHz} \sim 1 R_E$ at the penetrating distance of $\Delta L = 1 R_E$ from the magnetopause in the radial direction, where A , k_n , λ_{\parallel} , V_t , and f indicate the amplitude, wave number in the normal direction, characteristic Pc 3 wave length parallel to the magnetopause, phase velocity, and frequency of the surface waves with $k_n^2 + k_{\parallel}^2 = k_n^2 + (2\pi/\lambda_{\parallel})^2 \sim 0$, respectively. The Kelvin-Helmholtz instabilities occurring mostly at the flank-side magnetopause (Southwood, 1968, 1979; Yumoto and Saito, 1980) are not a likely process to account for daytime Pc 3–4 pulsations observed predominantly near local noon.

Uberoi (1983) described the compressional surface wave at the magnetopause, penetrating into the inner magnetosphere by the following approximate dispersion relation:

$$\omega_{\text{comp}}^{\text{surf}} \sim V_A(k_{\perp}/\tan \theta) (2\rho_{o1}/\rho_{o2})^{1/2} \quad (1)$$

where $\omega_{\text{comp}}^{\text{surf}}$, V_A , k_{\perp} , θ , and ρ_{o1}/ρ_{o2} stand for the angular frequency, Alfvén velocity, mean wave number normal to the ambient field, wave propagation angle from the ambient magnetic field ($\theta > 60^\circ$), and ratio of plasma density in the outer magnetosphere to the magnetosheath, respectively. The compressional propagating wave (i.e., fast magnetosonic mode) was approximately expressed by $\omega_{\text{comp}} \sim V_A k_{\perp}$ (see Yumoto and Saito, 1983). If $k_{\perp} = (k_R^2 + k_A^2)^{1/2} \sim (m/LR_E)$ and $\rho_{o2}/\rho_{o1} \sim 20$, azimuthal wave numbers m_{surf} of the compressional surface wave and m_{prop} of the propagating compressional wave can be expressed as follows:

$$m_{\text{surf}} \sim (\omega_{\text{comp}}^{\text{surf}}/V_A) LR_E \tan \theta / 10 \quad (2.1)$$

and

$$m_{\text{prop}} \sim (\omega_{\text{comp}}/V_A) LR_E. \quad (2.2)$$

For $\omega_{\text{comp}}^{\text{surf}} \sim \omega_{\text{comp}} \sim 2\pi/T = 2\pi/20$ s, $\theta \sim 72^\circ$, and $V_A \sim 1,500$ km/s at $L \sim 2$, we have $m_{\text{surf}} \sim 26$ and $m_{\text{prop}} \sim 3$. On the other hand, Ansari and Fraser (1985), Fraser and Ansari (1985), and Sutcliffe (1985) recently observationally demonstrated that azimuthal wave numbers of low-latitude Pc 3 are typically $\lesssim 6$ at $L \lesssim 2.0$. The low-latitude Pc 3 having smaller $m \lesssim 6$ cannot be explained by the linear resonance theory of surface waves excited by the Kelvin-Helmholtz-type instabilities at the magnetopause (Southwood, 1974; Chen and Hasegawa, 1974a; Uberoi, 1983). Low-latitude Pc 3 pulsations with $m \sim 3-6$ are believed to couple directly with the compressional Pc 3 waves propagating in the magnetosphere (cf. Yumoto et al., 1985a; Sect. 2.5).

From the theoretical considerations and observational facts, it is concluded that a main source of low-latitude Pc 3 pulsations is the magnetosonic upstream waves, being transmitted from outside the magnetosphere and propagating across the ambient magnetic field into the inner magnetosphere.

2.5 Transmitted Pc 3 source waves in the magnetosphere

In this section, we will summarize observational evidence that wave characteristics of Pc 3 waves in the magnetosphere are related to the solar wind parameters and thus support the transmission of the magnetosonic upstream waves into the magnetosphere.

On the basis of data analysis of Pc 3 band waves at geosynchronous orbit, Arthur and McPherron (1977) first reported that no relationship was found between the interplanetary magnetic field (IMF) magnitude and the frequency of both transverse and compressional magnetic pulsations, but that there was a clear, although weak, relationship between the cone angle of the IMF and the amplitude of the pulsations. Takahashi et al. (1984) also demonstrated that pulsation events exhibiting the harmonic structure (i.e., high-harmonic standing waves) at geostationary orbit, show a weak negative correlation between pulsation frequencies and the IMF magnitude. The above results of the dependence of Pc 3 frequencies at the synchronous orbit on the IMF magnitude can be explained by considering the existence of both standing Alfvén waves with larger ampli-

tudes on local field lines and compressional waves with smaller amplitudes propagating from outside the magnetosphere; these waves at synchronous orbit (GOES 2) were observationally confirmed and theoretically discussed by Yumoto and Saito (1983) and Yumoto et al. (1984, 1985a). Figure 4a shows an example of GOES 2 magnetic pulsation data in the (*HP*, *HE*, *HN*) coordinates. The *HP* axis is taken parallel to the spin axis of the satellite, which is approximately perpendicular to the solar-ecliptic plane. The *HE* axis is taken radially inward toward the center of the earth through the satellite. The *HN* is defined by $\mathbf{HN} = \mathbf{HP} \times \mathbf{HE}$. Therefore, the *HP*, *HE*, and *HN* components approximately give the total, radial, and azimuthally westward components of magnetic pulsations near the magnetic equator, respectively. Both compressional in the *HP* component (δB_{\parallel}) and transverse magnetic pulsations in the *HE* and *HN* components (δB_{\perp}) with broad frequency spectrum exist simultaneously in the dayside magnetosphere. The amplitude of the compressional Pc 3-4 waves in the *HP* component at $L=6.67$ is smaller than that of the transverse Pc 4-5 oscillations in the *HE* and *HN* component, but it is generally larger than that of low-latitude Pc 3-4 pulsations observed simultaneously at SGC ($L = 1.8$) near the satellite's meridian (Yumoto and Saito, 1983). Figure 4b indicates scatter plots of the amplitude of compressional Pc 3-4 waves against the IMF cone angle. Pc 3-4 events from 1100 to 1400 LT (near the occurrence peak) are illustrated in the figure. The weak negative correlation of the compressional Pc 3-4 activity detected at GOES 2 is in agreement with those of low-latitude Pc 3-4 pulsations observed at separated ground stations (cf. Fig. 3, Yumoto et al., 1985a). The correlation between the frequency of the transverse oscillations in the *HE* and *HN* directions at GOES 2 and the IMF intensity could not be recognized, whereas scatter plots of the dominant frequency of compressional waves in the daytime (0800-1700 LT from Jan. 27, to Feb. 16, 1981) was found to be related to the IMF magnitude. The distribution in the bottom right panel shows a range limited by the two lines of $f = 4.5 B_{\text{IMF}}$ and $f(\text{mHz}) = 7.5 B_{\text{IMF}}(\text{nT})$.

Yumoto et al. (1984) recently inferred the spacecraft-frame frequency (f_{sc}) of magnetosonic upstream waves. The phase velocity of the waves is $V_{\text{ph}}^2 \sim V_A^2 (1 + f_o/f_{\text{ci}}) \sim V_A^2$, where f_o is the plasma frame frequency, $f_{\text{ci}} = eB_{\text{IMF}}/m_i c$ is the local ion cyclotron frequency, and V_A is the Alfvén speed. The waves are excited by an anomalous Doppler-shifted ion cyclotron resonance of reflected ion beams in the earth's foreshock. The resonance condition is

$$(f_{\text{sc}}/f_{\text{ci}}) \sim V_{\text{sw}} |\cos \theta_{\text{KV}}| / V_{\parallel}, \quad (3)$$

where V_{sw} , θ_{KV} , and V_{\parallel} are the solar wind speed, angle between \mathbf{V}_{sw} and the wave vector \mathbf{k} , and proton resonant velocity of reflected ion beams in the solar wind frame, respectively (for further details see Tsurutani et al., 1983). Thus, it is reasonable to assume a regression line in the form of $f = \alpha_1 B_{\text{IMF}}$ to represent the data points in Fig. 4b, where $\alpha_1 \sim (V_{\text{sw}} |\cos \theta_{\text{KV}}| / V_{\parallel}) e/m_i c$. From observations of ion beam velocity of 650-1,150 km/s (cf. Paschmann et al., 1981; Yumoto et al., 1984), the frequency of the magnetosonic right-handed waves in the spacecraft frame is estimated to be on the order of 0.3-0.5 times the local proton cyclotron frequency (f_{ci}) in the earth's foreshock for $V_{\text{sw}} |\cos \theta_{\text{KV}}| \sim 350$ km/s. The averaged angle θ_{KV} determined by the minimum variance analysis was suggested to be $\cos \theta_{\text{KV}} = -0.8$

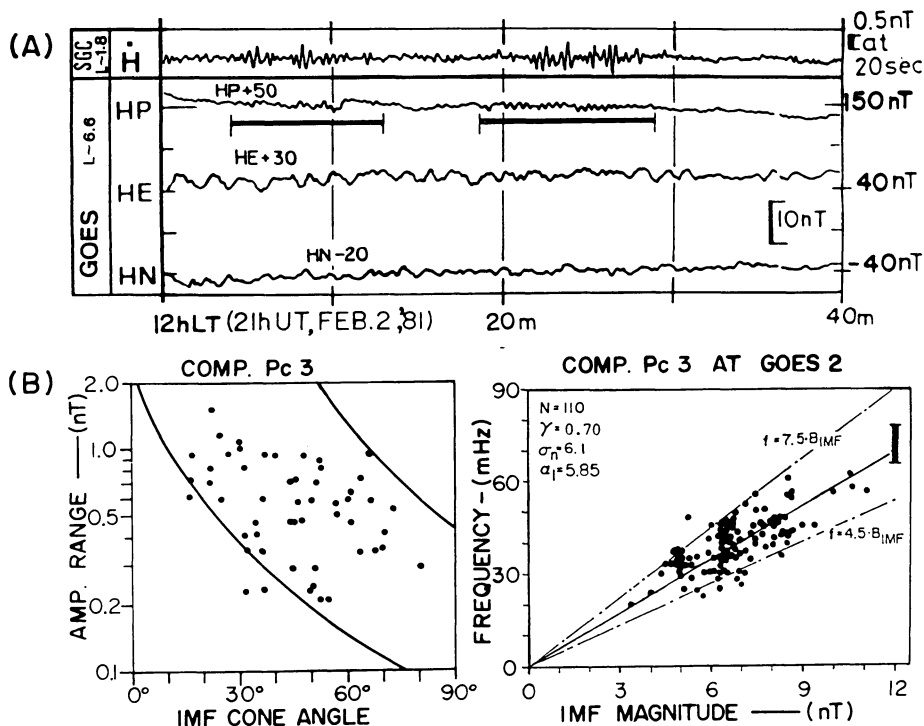


Fig. 4 A and B. Compressional Pc 3 waves in the magnetosphere (after Yumoto et al., 1985a). **A** An example of simultaneous records of daytime magnetic pulsations at GOES 2 ($L = 6.67$) and SGC ground station near the satellite meridian. **B** IMF controls of the amplitude (*left*) and dominant frequency (*right*) of compressional Pc 3 waves in the HP component at the synchronous orbit from January 27 to February 16, 1981

by Hoppe and Russell (1982). It is interesting to note that the range ($f_{sc}/f_{ci} = 0.3-0.5$) of the inferred frequency of the magnetosonic right-handed waves in the earth's foreshock is in excellent agreement with the range of data distribution bounded by $f = 4.5 B_{IMF}$ and $f = 7.5 B_{IMF}$ (Fig. 4b). This observation supports the idea that the magnetosonic right-handed waves in the earth's foreshock are convected across the magnetosheath to the magnetopause, and transmitted into the magnetosphere without significant changes in spectra, and that they are observed as the compressional Pc 3-4 waves at the synchronous orbit.

Yumoto and Saito (1983) and Yumoto et al. (1984, 1985a) observationally clarified the occurrence probability, the correlation coefficient and the standard deviation of frequency of Pc 3-4 pulsations observed at globally separated low-latitude stations ($L < 2.0$) against the compressional Pc 3-4 waves at synchronous orbit. The low-latitude Pc 3-4 pulsations observed at the ground near the GOES 2 longitude were found to have a higher occurrence probability and a smaller standard deviation than those at stations well separated from the longitude. Hence, the compressional Pc 3-4 waves were concluded to propagate mainly in the radial direction toward the earth's center (Yumoto et al., 1985a). The larger frequency deviations at the separated stations were explained by a finite longitudinal region ($\Delta\lambda \sim \pm 10^\circ$) where the compressional wave propagates, and suggest the existence of various resonant HM oscillations coupled with the compressional source waves in the plasmasphere. From the satellite-ground comparisons for pulsation data, Holló and Verő (1985) also concluded that the low-latitude pulsation activity is more evident than that at $L = 6.6$ in the magnetosphere and there are differences in the pulsation spectra between ground and space, and that it should be due to different propagation and/or excitation mechanism in the inner magnetosphere.

From the theoretical and observational facts, we can construct a scenario in which the daytime-propagating com-

pressional Pc 3, originating in the earth's foreshock, has an important role in the transmission of the solar wind energy into the deep magnetosphere as shown in Fig. 1a (cf., Yumoto and Saito, 1983; Yumoto et al., 1984 and 1985a). Compressional upstream waves in the earth's foreshock propagate and/or are convected through the bow shock, the magnetosheath and the magnetopause, and penetrate into the deep magnetosphere. Transmitted compressional waves (ω_{comp}) with a finite Pc 3 bandwidth from outside the magnetopause can excite high-harmonic standing oscillations (ω_A) of local field lines in the outer magnetosphere and a fundamental standing oscillation (ω_A) just outside the plasmopause, i.e., in the plasma trough. The ω_{comp} waves can further propagate into the inner magnetosphere and couple with various HM oscillations as discussed in the next section.

2.6 Characteristic frequencies of various Pc 3 oscillations in the plasmasphere

Compressional Pc 3 waves (i.e., fast magnetosonic wave) can propagate across the ambient field into the plasmasphere and can couple with surface waves at the plasmopause, trapped oscillations, and/or eigen oscillations of local field lines at low latitudes in the plasmasphere (Yumoto and Saito, 1983).

Transverse magnetic pulsations in the Pc 3 frequency range near the plasmopause are theoretically expected to consist of the standing field-line oscillations in the plasma trough and the collective eigen mode of surface waves on the plasmopause (e.g., Lanzerotti et al., 1973; Fukunishi and Lanzerotti, 1974a, b). The frequency of the surface eigen mode is given approximately by

$$\omega_{CE} = \sqrt{2} k_{\parallel} V_A^{\parallel} \quad (4)$$

where V_A^{\parallel} is the Alfvén velocity just inside the plasmopause (Chen and Hasegawa, 1974b; Lanzerotti et al., 1974). The

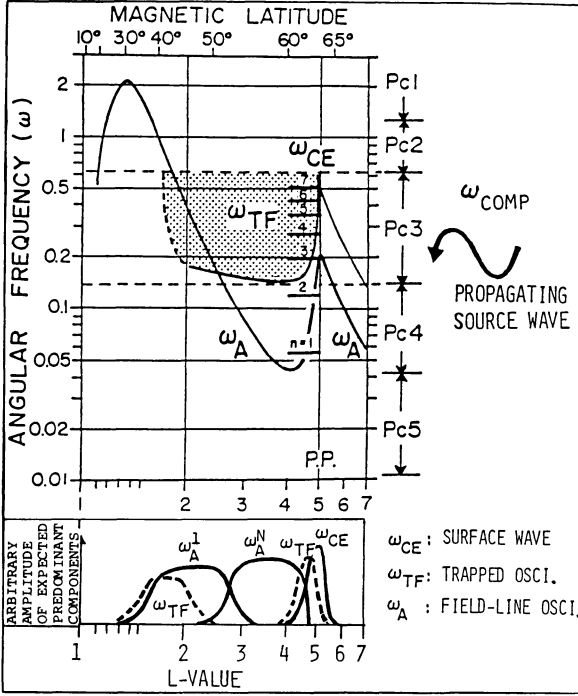


Fig. 5. Characteristic frequencies of coupled HM resonance oscillations in the plasmasphere (after Yumoto and Saito, 1983). Compressional Pc 3 waves, propagating from the earth's foreshock, (ω_{comp}) can couple with the collective surface wave (ω_{CE}) on the plasmopause, trapped oscillation (ω_{TF}) of fast magnetosonic wave in the Alfvén trough, and fundamental and high-harmonic standing field-line oscillations (ω_{A}^n) in the plasmasphere

value of k_{\parallel} is decided by the length of local field line (l), i.e., $k_{\parallel} = n\pi/l$ with $n \gtrsim 1$. If $V_{\text{A}}^{\parallel} = 800$ km/s at $L = 4$, the frequency of fundamental collective mode is ~ 10 mHz as shown in Fig. 5. Therefore, Pc 3 pulsations excited by the propagating compressional source waves on the plasmopause are expected to be a high harmonic of the collective eigen mode of the surface waves. The propagating compressional waves, which have a larger normal wave number and a finite bandwidth in the Pc 3 frequency range in the outer magnetosphere, can also couple with the fundamental collective eigen oscillation on the plasmopause by means of the nonlinear resonance mechanism (Yumoto and Saito, 1982). The condition of the nonlinear resonance is expressed by

$$\omega_{\text{comp}} = \omega_r + \omega_2^{\text{fs}}, \quad (5)$$

where ω_{comp} , ω_2^{fs} , and ω_r are frequencies of the propagating compressional wave in the outer magnetosphere, one component of HM noise near the plasmopause, and the collective eigen oscillation (ω_{CE}), respectively. In another possible case for the nonlinear resonance excitation of magnetic pulsations inside the plasmopause, ω_{comp} , ω_2^{fs} , and ω_r can be frequencies of the propagating compressional wave from the outer magnetosphere, a trapped oscillation of fast magnetosonic wave, and a standing oscillation of local field lines in the plasmasphere, respectively.

Inside the plasmopause, part of the propagating compressional waves can be trapped within the Alfvén speed trough from the plasmopause to a near $1.7 L$ value. Discrete frequency spectra (ω_{TF}) of the trapped oscillations are determined mainly by the radial distance of the Alfvén trough.

The period of trapped oscillations of the fast magnetosonic wave, which propagates nearly in the equatorial plane in the Alfvén trough region (Doobov and Mainstone, 1973; Tamao, 1978), is given approximately by

$$T_{\text{trapped}} \lesssim (2\Delta L/V_{g\perp}) \sim 2\Delta L[V_{\text{A}}^2(k_{\parallel}^2 + k_{\perp}^2)/k_{\perp}^2]^{-1/2} \lesssim 2\Delta L/V_{\text{A}}, \quad (6)$$

where ΔL is a distance between the two peaks of Alfvén velocity and $V_{g\perp}$ stands for the group velocity of a fast magnetosonic wave normal to the ambient magnetic field in the plasmasphere. The estimated periods of trapped oscillations are indicated in Fig. 5. If $\Delta L = L_{\text{pp}} - 1.7 = 2.5 R_E$ and $V_g \sim V_{\text{A}} \sim 800$ km/s, the period of trapped oscillation becomes $\lesssim 40$ s. These trapped oscillations are recently theoretically discussed to couple into standing field-line oscillation by Kivelson and Southwood (1985). They suggested that coupled field-line resonance oscillations occur on the magnetic shell where the transverse mode dispersion relation is satisfied, but the spectrum is dominated by the eigen frequencies of trapped oscillations.

In the plasmasphere, the compressional Pc 3 source waves which have predominantly a \mathbf{k} vector normal to the ambient magnetic field, can also couple directly with standing oscillations of local field lines (see references of Yumoto, 1985b). The linear coupled oscillations can occur only when the resulting dispersion laws satisfy the following equations:

$$(\omega_{\text{comp}}^2 - \omega_{\text{eigen}}^2) = [V_{\text{A}}^2(k_{\parallel}^2 + k_{\perp}^2) - (2\pi/T_{\text{eigen}}^n)^2] = 0, \quad (7)$$

where k_{\parallel} and k_{\perp} are parallel and normal components of the source's wave vector to the ambient magnetic field and T_{eigen}^n is a n -th "harmonic" eigen period of the standing field-line oscillation. Figure 5 illustrates eigen frequencies (ω_{A}) of the guided toroidal mode against L value for the gyro-frequency plasma model in the daytime magnetosphere, which were numerically obtained by Yumoto et al. (1983a). The eigen period of a local field line at very low latitude is expected to be ~ 20 s for an equatorial cold hydrogen plasma density $n_i \sim 2000$ cm $^{-3}$ at $L \sim 2$ (Orr and Matthew, 1971). Low- and mid-latitude pulsations in the Pc 3 frequency range are concluded to appear mainly as a fundamental at $L = 1.7$ – 2.6 and a higher harmonic standing oscillation at $L = 2.0$ – L_{pp} , respectively (see Fig. 5).

Orr and Hanson (1981) and Gough and Orr (1984) also considered a simplified model of forced field-line oscillations in the magnetosphere of $L = 2$ – 12 , which indicates the latitudinal variation of pulsation phase on the ground. In their model, each individual flux tube responds independently to the driving force of a fast mode HM wave, and then brings about forced damped transverse oscillations. They concluded the latitudinal extent of a mid-latitude Pc 3–4 resonance region being $\lesssim 3^\circ$ for typical value of the damping factor in the daytime ionosphere.

On the other hand, Poulter et al. (1984) suggested that since the low-latitude geomagnetic field is not expected to be significantly distorted by the solar wind, the observed diurnal period variations in the Pc 3 range should be determined by changes in the ambient plasma density. They had applied a physically realistic plasmaspheric model (Fig. 6b) along the $L = 2.3$ flux tube to the determination of eigen periods of standing field-line oscillation over a 24-h interval. The resulting model-pulsation periods are largest during the day with minimum and maximum values at 0500 and 1800 LT, respectively, as shown in Fig. 6a. The model predicts a general increase in the eigen periods during the re-

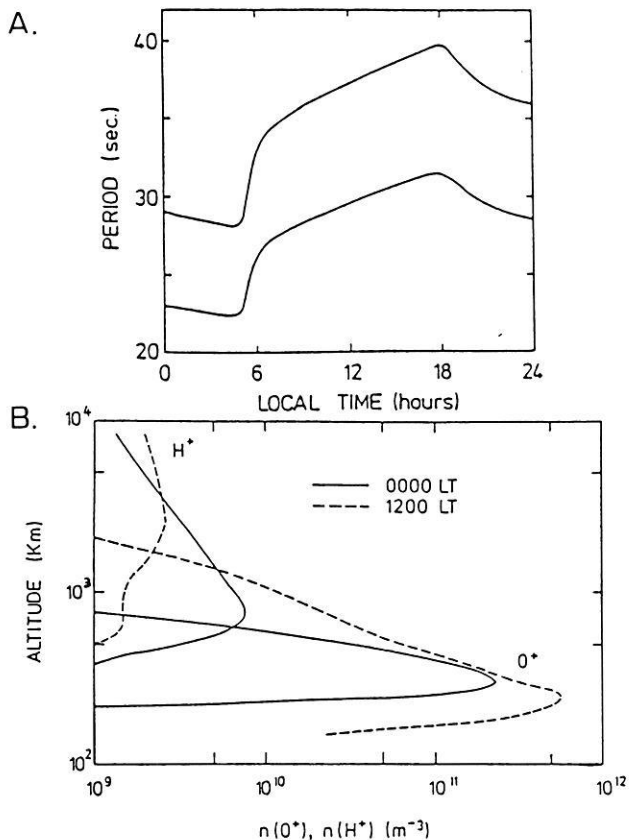


Fig. 6A and B. Diurnal period variation of low-latitude pulsations (after Poulter et al., 1984). **A** Diurnal eigen period variation of the guided poloidal- (*upper curve*) and toroidal-mode (*lower curve*) fundamental standing oscillations at $L = 2.3$. **B** Realistic plasma-spheric O^+ - and H^+ -number density models along the $L = 2.3$ flux tube at 0000 LT and 1200 LT

plenishment of the protonosphere after a period of geomagnetic activity.

In the lower panel of Fig. 5, arbitrary amplitude of expected predominant components of the excited oscillations (ω_{CE} , ω_{TF} , ω_A^n) are summarized as a function of the L value. Low-latitude Pc 3 pulsations observed at $1.2 < L \lesssim 3.0$ on the ground are believed to be a superposition of these coupled resonance oscillations in the plasmasphere. We are now analyzing pulsation data at low-latitude conjugate stations in order to examine which components of the oscillations dominate on the ground, i.e., to clarify whether the observed low-latitude Pc 3 pulsations are just the propagating compressional Pc 3 waves originating in the outer magnetosphere or the coupled resonance oscillations between the compressional source waves and the trapped, fast magnetosonic waves and/or fundamental and higher harmonic eigen oscillations of local field lines in the plasmasphere. In the next section, we will show preliminary works on wave characteristics of low-latitude Pc 3 magnetic pulsations observed at conjugate stations.

2.7 Wave characteristics of low-latitude Pc 3

From polarization analysis of magnetic pulsations observed simultaneously at northern and southern conjugate sta-

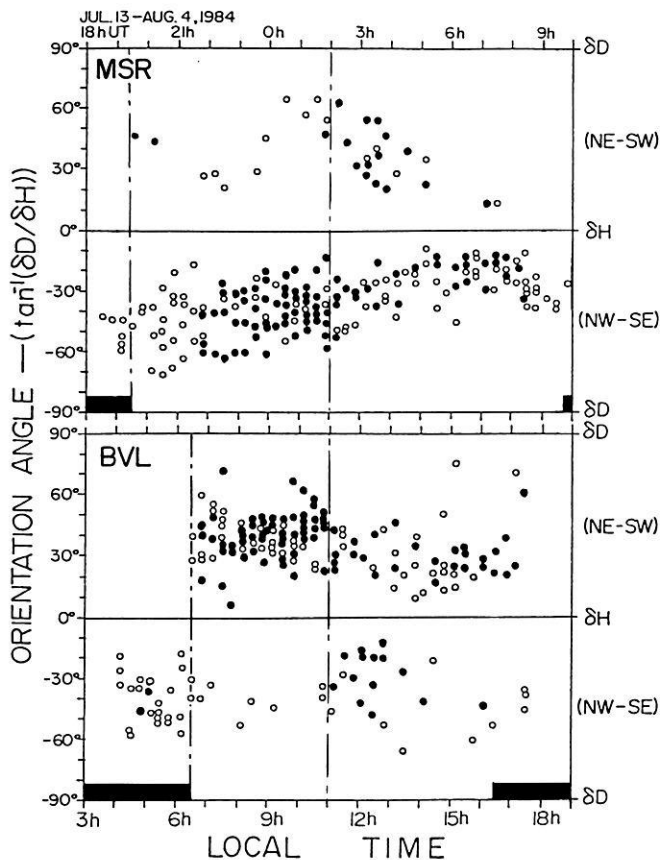


Fig. 7. Diurnal variation of the major axis orientation of low-latitude Pc 3 polarization ellipses in the H-D plane detected at low-latitude conjugate stations ($L \sim 1.5$) (after Yumoto et al., 1985b). *Solid thick lines* indicate the nighttime ionosphere. The orientation angle of the major axis from the H axis toward NE-SW (NW-SE) quadrant is represented as positive (negative). *Solid dots* imply an orientation reversal of the major axis between the northern and southern conjugate stations

tions, we can examine whether the observed pulsations are odd and even modes of standing field-line oscillations (Sugiura and Wilson, 1964) or not resonant field-line oscillations. Although diurnal variations of the conjugate magnetic polarizations are related to the ionospheric conductivity condition in both hemispheres (cf. Yumoto et al., 1985b), propagation characteristics in the azimuthal direction can also be inferred statistically.

In order to clarify wave characteristics of low-latitude Pc 3 magnetic pulsations, Yumoto et al. (1985b) recently statistically analyzed pulsation data of rulfmeters (ring-core-type ULF fluxgate magnetometer) at conjugate stations, i.e., Moshiri in Japan and Birdsville in Australia ($L \sim 1.5$). Amplitude variations of 20 min–1 h duration of the low-latitude Pc 3 were found to occur simultaneously at the conjugate stations. The global behavior in activity of the low-latitude Pc 3 pulsations must be controlled by the cone angle of the IMF (see Verö, 1985). Diurnal amplitude variations of the low-latitude Pc 3 which appears primarily in the morning hours were demonstrated to be related to the shaded and sunlit ionospheres.

Figure 7 shows the diurnal variation of low-latitude Pc 3 polarizations in the H-D plane at the conjugate stations with a L value of 1.5. Top and bottom panels indicate major axis orientations at the northern and southern conju-

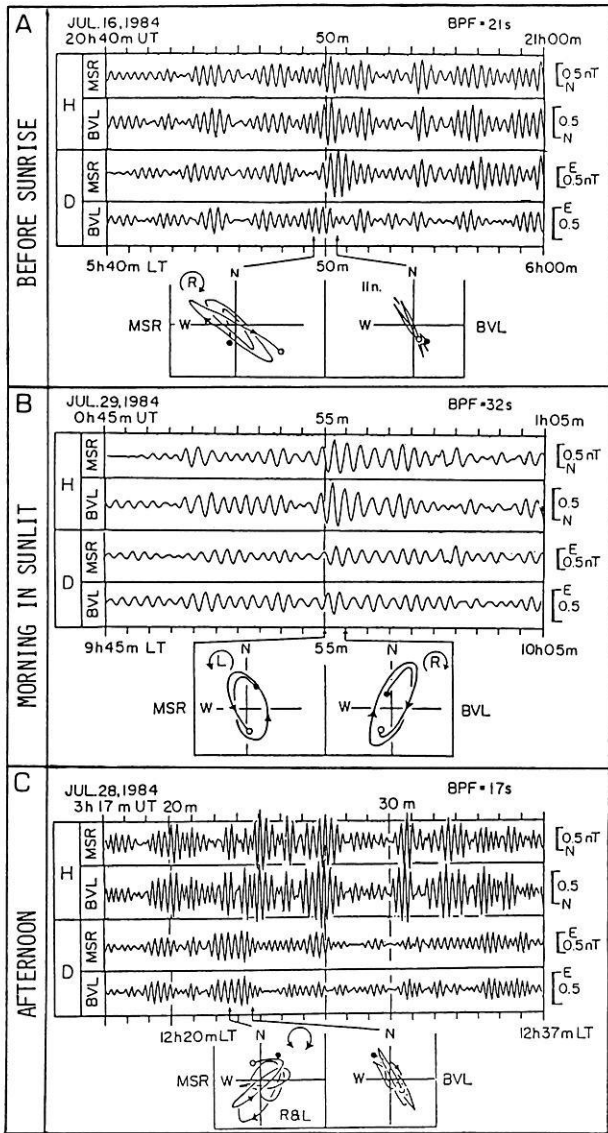


Fig. 8A-C. Typical examples of simultaneous amplitude-time records of low-latitude Pc 3 at conjugate stations ($L \sim 1.5$) (after Yumoto et al., 1985b). Hodograms in the H-D plane at Moshiri and Birdsville are illustrated in the lower panels; **A** before sunrise, **B** "mirror" polarization in the sunlit morning, and **C** in the afternoon

gate stations, respectively. The solid thick line in the figure stands for the nighttime ionosphere determined by the ionospheric f_oE data near the stations. Two transitions for Pc 3 polarizations can be seen. Before sunrise, when the southern ionosphere is still dark, the major axis is in the same northwest-southeast quadrant in both hemispheres. After sunrise, when both the conjugate ionospheres are in sunlit, the major axes are predominantly oppositely directed at the conjugate stations. Moreover, the sense of Pc 3 polarizations at the conjugate stations tends to be reversed.

Typical examples of simultaneous amplitude-time records and Pc 3 polarizations at Moshiri and Birdsville before sunrise, in the sunlit morning, and in the afternoon are illustrated in Fig. 8a, b, and c, respectively. The polarization relation in the sunlit morning is mirrorlike and is consistent with the expected polarization of odd-mode standing field-line oscillations near a L value of 2.0 (see

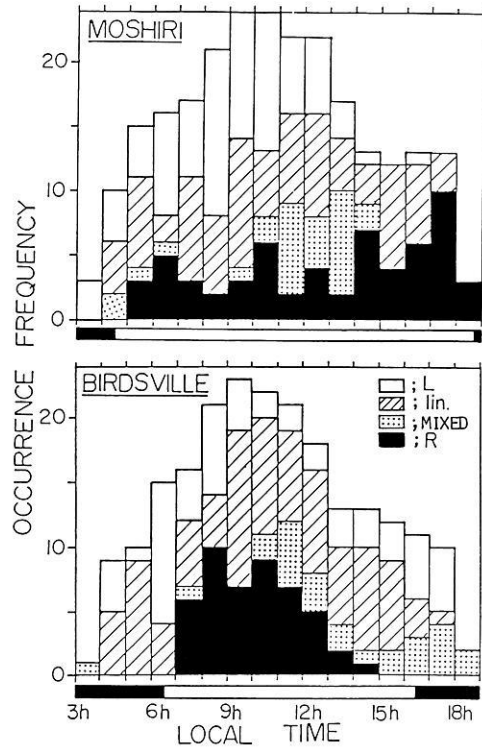


Fig. 9. Diurnal variation of low-latitude Pc 3 polarization senses in the H-D plane detected simultaneously at the conjugate stations ($L \sim 1.5$) (after Yumoto et al., 1985b). Open, shaded, dotted, and solid areas indicate left-hand, linear, mixed, and right-hand polarizations from a view looking down onto the earth in each hemisphere, respectively

Sect. 2.6). After 0630 LT, Pc 3 waves which would have a smaller normal wave number than a parallel one (i.e., $k_{\perp} < k_{\parallel}$), are believed to be effectively reflected at both ionospheres; standing oscillations of local field lines then occur predominantly near $L=1.7-2.6$ (cf. Yumoto and Saito, 1983; Poulter et al., 1984). Dominant periods of standing oscillations at $L=1.5$ were predicted to be in the Pc 1-2 range as shown in Fig. 5. The observed Alfvén-type Pc 3 pulsations at $L \sim 1.5$ are believed to be associated with the standing field-line oscillations at $L=1.7-2.6$.

Saka et al. (1980) showed that the increase of D/H ratio (amplitude ratio of D- to H-component) of low-latitude Pc 4 pulsations at $L=1.16$ appears to coincide with the E-layer ionization enhancement associated with sunrise. However, Yumoto et al. (1985b) could not find the increase of D/H ratio of low-latitude Pc 3 at the conjugate stations of $L \sim 1.5$. It is believed that the E-layer ionization enhancement is responsible only for the abrupt changes of observed Pc 3 polarization senses and major axes at sunrise at the conjugate stations.

The other transition between polarization types is found to appear near local noon. The low-latitude Pc 3 polarizations at the conjugate stations ($L \sim 1.5$) change from predominantly left-handed (right-handed) in the NW-SE (NE-SW) quadrant to predominantly right-handed (left-handed) in no specific quadrant at ~ 1100 LT near local noon in the northern (southern) hemisphere (see Figs. 7, 8, and 9). Lanzerotti et al. (1981) and Fraser and Ansari (1985) also pointed out that the polarization reversal of low-latitude Pc 3 at $L \sim 2.0$ occurs near local noon and the orientation

of major axis of polarization ellipses changes from a predominantly NW-SE direction in the local morning to a mixed NW-SE/NE-SW direction in the afternoon. Since the ionospheric conductivity changes smoothly near local noon (see Fig. 4 of Takeda and Maeda (1980)), the transition cannot be explained by the ionospheric variation. This transition may be associated with either the propagation or the generation mechanism of Pc source waves in and/or outside the magnetosphere. The lack of a simple pattern of diurnal variation of low-latitude Pc 3 polarizations as shown in Fig. 9 indicates the existence of multiple propagation and/or coupling mechanisms of Pc source waves with various HM oscillations in the inner magnetosphere (see Sect. 2.6.).

By using AFGL- and southeast Australia-network pulsation data, Saka and Kim (1985) and Ansari and Fraser (1985) recently examined azimuthal wave numbers of Pc 3 pulsations at $L=3.0$ and $L=1.8-2.7$, respectively. Figure 10 shows statistical diurnal variation of the azimuthal wave number at $L\sim 3.0$. We can see that the longitudinal phase propagation changes from westward in the morning to eastward in the afternoon sector. Thus, Pc 3 source waves in the magnetosphere are believed to propagate statistically in the opposite directions. Magnitudes of the azimuthal wave number at $L\sim 3.0$ are comparable in the morning and afternoon sector (Fig. 10). However, Saito et al. (1984) recently demonstrated that in the afternoon sector incoherent wave packets of Pc 3 are predominantly simultaneously observed at longitudinally separated stations at $L\leq 2.0$ within $\sim 10^\circ$ in longitude, implying larger azimuthal wave numbers ($m\gtrsim 35$). Hughes et al. (1978) also showed that the sign of azimuthal wave numbers of magnetic pulsations observed simultaneously on the three geostationary satellites changes near noon, and that strong pulsations in the afternoon are detected with low coherence, implying large azimuthal wave numbers. These Pc 3 pulsations of large azimuthal wave numbers (i.e., $k_\perp > k_\parallel$) in the afternoon and evening would be less reflected along the field line in both the northern and southern ionospheres and then would show incoherent wavepackets on the ground as shown in Fig. 8c. The pre- and postnoon asymmetry of azimuthal wave number of Pc 3 pulsations may be associated with the reason why an evening effect similar to the sunrise effect as shown in Fig. 7 could not be found in the low-latitude Pc 3 polarizations at the conjugate stations at $L\sim 1.5$.

However, we cannot yet explain why the azimuthal wave number of Pc 3 source waves is larger in the afternoon than in the morning sector. The morning-afternoon asymmetry of Pc 3 characteristics may be associated with the dawn-dusk asymmetry of Pc 5 pulsations observed in the outer magnetosphere, i.e., azimuthally transverse and radially compressional modes appear predominantly in the dawnside and duskside magnetospheres, respectively (Kokubun, 1981, 1985; Yumoto et al., 1983b). Further theoretical and observational studies are needed to clarify the cause of the dawn-dusk polarization asymmetry of low-latitude Pc 3 magnetic pulsations.

On the basis of these observational and theoretical results, we could construct a possible propagation mechanism for exciting Pc 3 pulsations at $L=1.5-L_{pp}$ as shown in Fig. 11. Magnetosonic upstream waves in the earth's foreshock can penetrate into the inner magnetosphere and be observed as compressional Pc 3 waves at synchronous orbit.

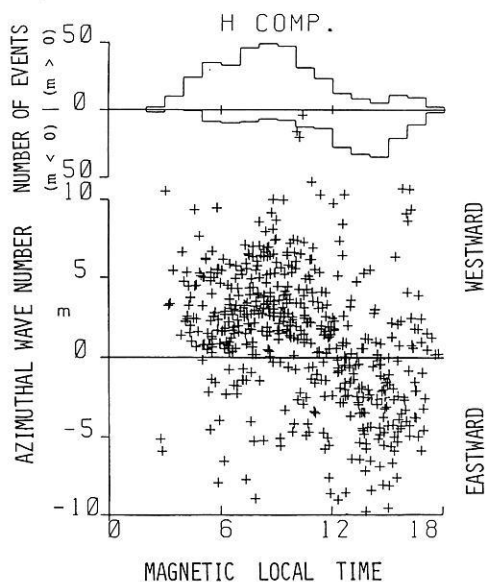


Fig. 10. Azimuthal wave number of Pc 3 pulsations detected at the AFGL network stations of $L\sim 3.0$ (after Saka and Kim, 1985). Number of events (upper panel) and azimuthal wave number [m] (lower panel) are illustrated as a function of magnetic local time. Positive and negative m values indicate westward and eastward longitudinal propagation, respectively

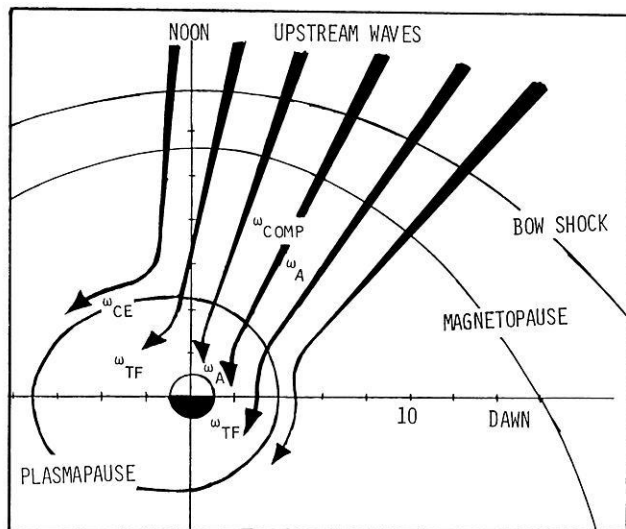


Fig. 11. A probable propagation mechanism for exciting low-latitude Pc 3 at $L\sim 1.5-L_{pp}$. Magnetosonic upstream waves (ω_{comp}) can penetrate, can propagate westward in the morning and eastward in the afternoon, and can couple with high-harmonic standing field-line oscillation (ω_A) in the outer magnetosphere, collective surface waves (ω_{CE}) on the plasmopause, trapped oscillation (ω_{TF}) of fast magnetosonic wave in the Alfvén speed trough, and fundamental and high-harmonic standing field-line oscillations (ω_A) in the plasmasphere

These transmitted Pc 3 source waves could further propagate predominantly westward in the morning and eastward in the afternoon sector, and then could couple into surface waves on the plasmopause, trapped oscillations in the plasmasphere, and standing field-line oscillations at low latitudes. Pc 3 pulsations observed on the ground at $L=1.5-L_{pp}$ would be a superposition of these hydromagnetic reso-

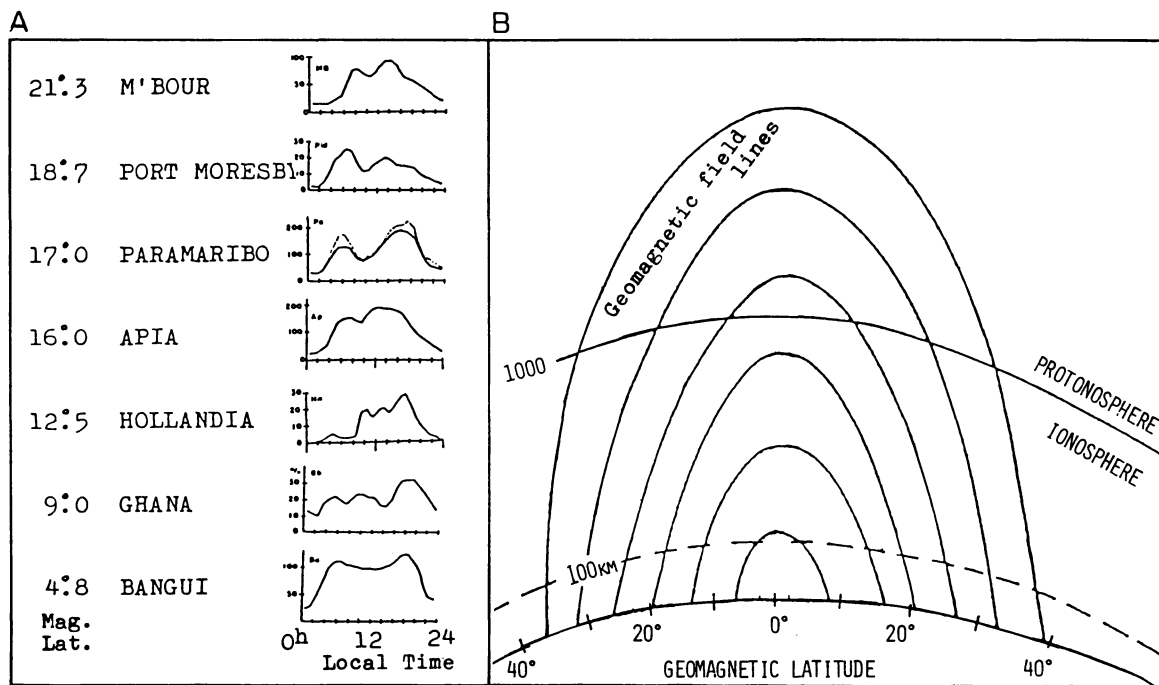


Fig. 12A and B. Pc 2-3 pulsations observed at very low latitudes ($\Phi \lesssim 22^\circ$, $L < 1.2$). **A** Diurnal variation of Pc 2-3 activity at latitudes lower than 22° , summarized by Saito (1983). **B** Magnetic field lines of force illustrated as a function of magnetic latitudes. In the ionosphere ion-neutral particle collisions dominate and thus HM field-line oscillations are believed to be effectively damped (Prince and Bostick, 1964)

nance oscillations in the plasmasphere as shown in Fig. 5; however, further coordinated observations of low-latitude Pc 3 are needed to clarify which modes of various HM waves dominate in the plasmasphere.

2.8 Pc 2-3 at very low latitudes ($\Phi < 22^\circ$)

In the preceding, we reviewed mainly the low-latitude Pc 3 magnetic pulsations which are associated with HM resonance oscillations at $L=1.5-3.0$. On the other hand, Pc 2-3 pulsations detected at very low latitudes ($\Phi < 22^\circ$) are not yet sufficiently clarified either observationally or theoretically. Saito (1983) compared diurnal variations of Pc 2-3 occurrences at many stations in the different periods (cf. Románá and Cardús, 1962; Románá, 1962; Hutton, 1960). The evening maximum of Pc 3 activities is a peculiar feature noted only in the subtropical region of approximately $5^\circ-20^\circ$ in geomagnetic latitude as shown in Fig. 12a. The evening maximum of very low latitude Pc 3 at $\Phi < 20^\circ$ is inconsistent with the local-noon maximum of Pc 3 pulsations which are believed to originate predominantly from the upstream waves in the earth's foreshock at $L = 1.5-3.0$ (cf. Figs. 9, 10). Therefore, Saito (1983) proposed a candidate of endogenic Pc 2-3 source in the equatorial ionosphere.

Pc 2-3 pulsations at $L < 1.2$ may be caused by endogenic ionospheric currents and/or exogenic compressional waves filtered out through the low-latitude ionosphere (Jacobs and Watanabe, 1962; Prince and Bostick, 1964; Greifinger and Greifinger, 1965). Geomagnetic field lines at lower latitudes are illustrated as a function of geomagnetic latitude in the right panel of Fig. 12. The boundary between the magnetosphere and the ionosphere was estimated to be about 1,000 km above the ground (cf. Prince and Bos-

tick, 1964; Saka, 1985). It is noteworthy that the magnetic field lines anchoring below 22° in magnetic latitude are almost entirely in the ionosphere, and thus not easy to oscillate like a standing field-line oscillation in the magnetosphere. Therefore, we can conclude that low-latitude Pc 3 pulsations observed at $\Phi < 22^\circ$ in magnetic latitude are not associated predominantly with a HM resonance oscillation in the plasmasphere. Kuwashima et al. (1979) pointed out that the diurnal variation of very low latitude Pc 3 polarizations at Chichijima ($\Phi = 17.1^\circ$, $A = 208.9^\circ$) is different from that of low-latitude Pc 3 observed simultaneously at Memambetsu (34.0° , 208.4°), where Pc 3 polarization changes from predominant left-handed in the morning to predominant right-handed in the afternoon (consistent with low-latitude Pc 3 polarization at the conjugate station, Moshiri at $L \sim 1.5$; see Fig. 9). Yumoto (1986a) and Saito et al. (1986) recently demonstrated that diurnal variations of Pc 3 polarization senses at northern and southern low-latitude stations ($|\Phi| \sim 10^\circ-20^\circ$) are opposite to those at the conjugate low-latitude stations ($\Phi \sim \pm 35^\circ$; cf. Fig. 9) in the sunlit hemisphere. They suggested the possibility that the low-latitude Pc 3 polarization can be explained by the azimuthally propagating, ionospheric, Pedersen eddy currents induced by inductive electric field of compressional Pc 3 waves at very low latitudes (cf. Yumoto, 1986a; Yumoto et al., 1986).

As one possible exogenic candidate for the generation of very low latitude Pc 2-3, a filtering action of the region between topside and bottomside ionosphere for transversely propagating compressional waves was proposed by Jacobs and Watanabe (1962). By using the filtering mechanism, Prince and Bostick (1964) predicted frequency-power spectra of Pc 2-3 pulsations at very low latitudes. The structure between the topside and bottomside ionosphere and the

particle parameters, e.g., integrated ion-neutral particle collisions, were demonstrated to control directly and effectively the attenuation and phase velocity of the transmitted compressional waves. On the other hand, diurnal variation of f_oF_2 , which indicate mostly the feature of total electron content (T.E.C.) in the ionosphere, at very low latitudes shows the “noon bite-out” in ionization (cf. Anderson, 1973; Rajaram, 1977). This “noon bite-out” feature is very similar to the occurrence pattern of the very low latitude Pc 2–3 as shown in Fig. 12a (cf. Saito, 1983). Recently, Chao (personal communication, 1985) also demonstrated that the postnoon peak of Pc 3 occurrence at Chung-Li ($\Phi = 13.8^\circ$) during the declining phase of sunspot number is consistent with that of the T.E.C. obtained by satellite differential Doppler measurements, although Pc 3 activities at mid latitudes bear an anticorrelation to increase in F2-region electron concentrations (Verö and Menk, 1986). The T.E.C. is generally considered to be proportional to ionization. If the T.E.C. would be inversely proportional to ion-neutral particle collisions, the good correlation between the postnoon peaks of Pc 3 occurrence and the T.E.C. at Chung-Li can be explained by the filtering action for transversely propagating compressional Pc 3 waves through the very low latitude ionosphere (cf. Prince and Bostick, 1964).

However, the ionospheric parameters at very low latitudes show magnetic activity, diurnal, latitudinal, seasonal, and solar cycle dependences (cf. Rajaram, 1977). Further theoretical studies and simultaneous conjugate observations of Pc 2–3 pulsations and ionospheric variations at very low latitudes ($\Phi < 22^\circ$, i.e., $L < 1.2$) are needed to clarify the existence of endogenic and/or exogenic source waves near the equator, and then to understand completely the propagation and generation mechanisms of low-latitude Pc 3 magnetic pulsations.

3. Low-latitude Pi 2 magnetic pulsations

3.1 Introduction

Pi 2 magnetic pulsations (damped pulsations with 40–150-s periods) associated with substorm expansion onsets or intensifications have been widely researched by a number of scientists. The main morphological characteristics were established in the 1960s and 1970s (see Saito, 1969; Jacobs, 1970; Orr, 1973; Lanzerotti and Fukunishi, 1974; Southwood and Stuart, 1980; McPherron, 1980). However, by using extensive magnetometer chains and multisatellite data, considerable attention has been recently refocused on completely understanding the global feature of Pi 2 pulsations (see Hughes, 1983; Samson and Rostoker, 1983; Baumjohann and Glassmeier, 1984; Verö, 1985). Pi 2 pulsations are generally interpreted as a transient hydromagnetic signal associated with a sudden change in the physical state of the magnetosphere at substorm expansion onset. The sudden change is caused by a short-circuiting of the cross-tail current to the auroral oval via field-aligned currents, i.e., by the formation of a substorm current wedge (McPherron et al., 1973; Mallinckrodt and Carlson, 1978; Sakurai and McPherron, 1983). The Pi 2 transient HM signal associated with the sudden formation of field-aligned currents in the magnetotail is believed to play an important role in the dynamic coupling between the magnetosphere and the ionosphere.

However, occurrence and wave characteristics of Pi 2 on a global scale, especially concerning low-latitude Pi 2, have not yet been sufficiently studied and thus are not completely understood. Here, we would like to restrict our considerations to the unresolved problems associated with the generation and propagation mechanisms of low-latitude Pi 2 pulsations. The associated characteristics will be described in Sect. 3.2, and recent theoretical models for generation and propagation mechanisms of Pi 2 pulsations will be reviewed in Sects. 3.3 and 3.4. On the basis of the morphological and theoretical results, a possible model for daytime Pi 2 will be proposed in the final Sect. 3.5.

3.2 Unresolved characteristics of Pi 2 pulsations

Firstly, we summarize only important characteristics which give a clue to the unresolved generation and propagation mechanisms of low-latitude Pi 2, i.e., (1) Pi 2 polarization distribution as a function of local time and magnetic latitude, (2) latitudinal and longitudinal dependences of azimuthal wave numbers, (3) simultaneous occurrence of daytime Pi pulsations, and (4) equatorial enhancement of daytime Pi 2 pulsations.

1. Pi 2 polarization. The morphology of Pi 2 polarization is not quite so simple as shown in Fig. 13 (cf. Saito, 1969). High-latitude Pi 2 pulsations have mostly right-handed polarization toward the pole and left-handed toward the equator of the Pi 2 maximum in the premidnight sector (Samson and Rostoker, 1983; Lester et al., 1985), and vice versa in the postmidnight sector (Kuwashima, 1978; Kuwashima and Saito, 1981; Samson and Harrold, 1983). At midlatitudes from $\sim 56^\circ$ to $\sim 43^\circ\text{N}$ geomagnetic latitude, i.e., $L \sim 3.2$ – 1.9 , the polarization of Pi 2 is predominantly left-handed, independent of local time (Rostoker, 1967; Lanzerotti et al., 1974; Fukunishi, 1975; Mier-Jedrzejowicz and Southwood, 1979; Baranskiy et al., 1980; Novikov et al., 1980; Samson and Harrold, 1983; Lanzerotti and Medford, 1984; Lester et al., 1984). The predominant left-handed polarization of mid- and low-latitude Pi at all longitudes was believed to be associated with westward propagation from the nighttime source region (Green and Stuart, 1979; Mier-Jedrzejowicz and Southwood, 1979; Lester et al., 1983). Samson (1985) proposed that the midlatitude left-handed polarization could be explained as a direct result of high-latitude, field-aligned current propagating westward. On the other hand, Lanzerotti and Medford (1984) suggested that the low-latitude Pi 2 observation is difficult to interpret straight-forwardly in the context of hydromagnetic wave resonance theory where the plasmopause responds to only one of the source frequencies. Southwood and Hughes (1985) recently proposed that superposition of two waves with different amplitude, travelling in opposite direction is required to produce the polarization characteristic of midlatitude Pi 2.

At very low latitude ($L \lesssim 1.5$), Kato et al. (1956), Sakurai (1970), and Sutcliffe (1981) reported that low-latitude Pi 2 has right-handed and left-handed polarizations prior to and after local midnight, respectively. These observations are also difficult to interpret by using the existing theories, which were constructed to explain mainly high- and mid-latitude Pi 2 pulsations, e.g., the substorm current wedge model (Lester et al., 1983). Further coordinated simultaneous observations at separated stations of 70° – 0° in mag-

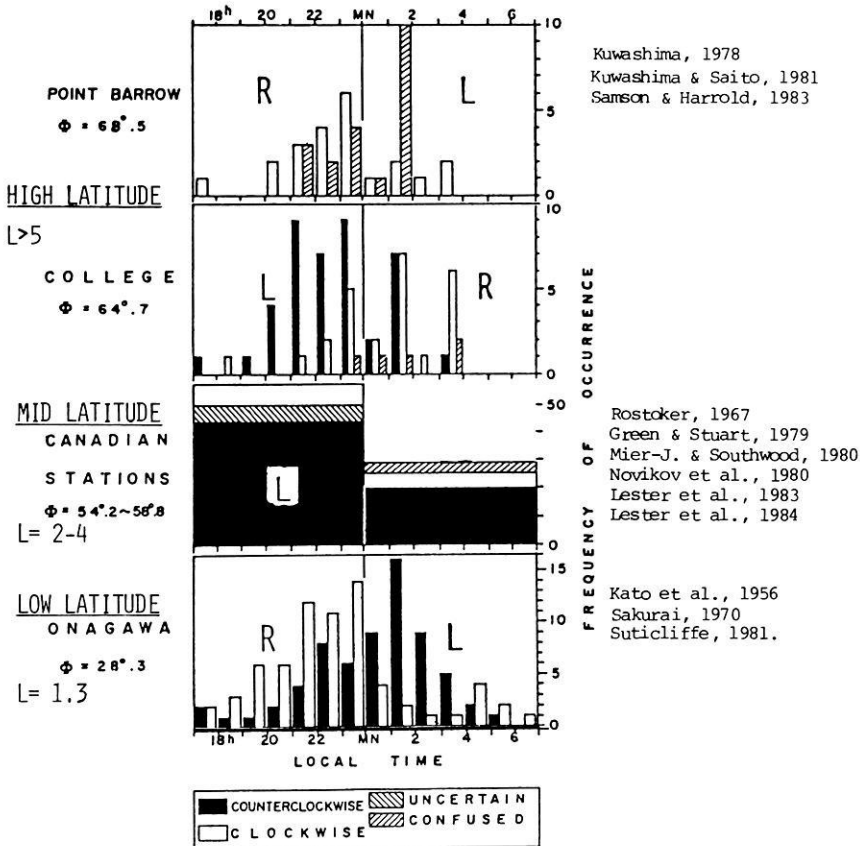


Fig. 13. Latitudinal and longitudinal dependences of nighttime Pi 2 polarizations, obtained by adding the results of many workers to the original figure of Sakurai (1970). Open, shaded, and solid areas indicate right-handed, mixed, and left-handed polarizations in the H-D plane from a view looking down onto the earth, respectively

netic latitude are needed at all local times to clarify the unresolved problem.

2. Azimuthal wave number of Pi 2. Samson and Harrold (1983) suggested that elliptical polarizations at high latitudes were caused by azimuthal expansion of the oscillating field-aligned current associated with Pi 2. The spatial motion of substorm electrojets and the region of Pi 2 localization is as much as 1,000–2,000 km westward in 10 min, i.e., 1.5–3.0 km/s, implying large apparent azimuthal wave number (e.g., $|m| \sim 20$ –40 for a Pi 2 period of 150 s). However, Samson and Harrold (1985) recently reported that the phase velocities of high-latitude Pi 2 from the University of Alberta are eastward to the east of the region of the onset of the field-aligned currents, and westward to the west of the region of the onset. They estimated that the westward velocities are extremely high, approximately 20–50 km/s (i.e., $|m| \sim 2.4$ –7.2 for 100–150-s periods), which are likely not correlated with motion of the westward surge.

Lester et al. (1985) also demonstrated that apparent azimuthal wave number of high-latitude Pi 2 near the eastward electrojet at $\Phi = 60^\circ$ – 70° is $|m| \sim 8$, which is larger than the average wave number ($|m| \sim 2$ –4) at midlatitudes ($\Phi \sim 40^\circ$ – 55°) (see Green and Stuart, 1979; Mier-Jedrzejowicz and Southwood, 1979; Lester et al., 1983, 1984). The phase propagation of Pi 2 observed at SMA and AFGL network stations was reported to be westward at all geographic latitudes of 28° – 71° , and was generally believed to be associated with the westward movement or expansion of the equivalent ionospheric current vortex (Pashin et al., 1982) and an oscillating field-aligned current system (Samson and

Rostoker, 1983) after the breakup. However, Lester et al. (1984) recently found that from estimates of signal phase differences between station pairs, westward propagation of midlatitude Pi 2 dominates west of and within the field-aligned current meridians but eastward propagation dominates east of the current system.

At very low latitudes ($L \lesssim 1.5$), east-west phase variations have not yet been examined sufficiently in the east-west chain system. The top panel in Fig. 14 shows an example of simultaneous records of low-latitude Pi 2 magnetic pulsations obtained at Onagawa ($\lambda = 141.5^\circ\text{E}$, $L = 1.30$), Ewa Beach ($\lambda = 202.0^\circ\text{E}$, $L = 1.15$), and San Gabriel Canyon ($\lambda = 242.0^\circ\text{E}$, $L = 1.83$). Time lags of the first impulse in the H component between the two low-latitude stations, i.e., ONW-EWA and SGC-EWA, are illustrated with the local times of the stations in the bottom panels. Broken lines indicate the least squares fitting a straight line in the data. The result suggests that low-latitude Pi 2 pulsations observed near midnight would propagate westward during premidnight and eastward during postmidnight. Apparent propagating velocities in the longitudinal direction can be estimated to be $\sim 5.3^\circ/\text{s}$ (~ 530 km/s) and $\sim 4.5^\circ/\text{s}$ (~ 450 km/s) at the low-latitude ground stations ($L = 1.15$ – 1.83). These faster longitudinal velocities correspond to smaller azimuthal wave numbers of $m = 360^\circ \cdot \Delta T / (\Delta \Phi \cdot T) \sim 0.4$ – 2 for wave period of $T = 40$ – 150 s, where ΔT is time lag and $\Delta \Phi$ ($= 40^\circ$ – 60°) is longitudinal distance between two stations. The apparent opposite propagation of low-latitude Pi 2 pulsations may be associated with the polarization reversal across the midnight as shown in Fig. 13. On the other hand, low-latitude (and/or equatorial) Pi 2 pulsations appear even during the daytime on many

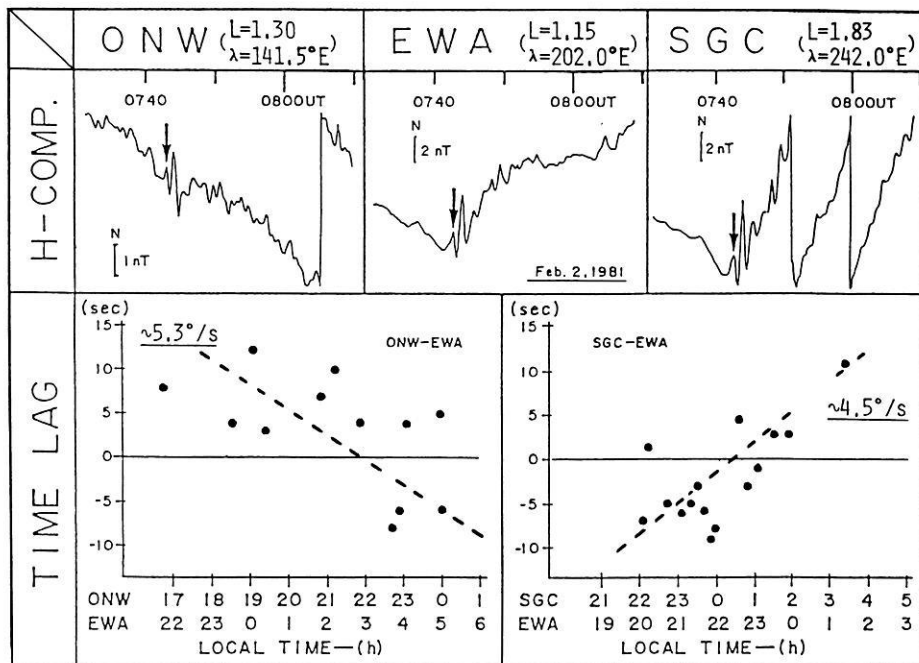


Fig. 14. Phase relations of low-latitude Pi 2 pulsations observed simultaneously at longitudinally separated stations, Onagawa (ONW, $\lambda = 141.5^\circ\text{E}$), Ewa Beach (EWA, 202.0°E), and San Gabriel Canyon (SGC, 242.0°E). Upper and lower panels show an example of simultaneous amplitude-time records of low-latitude Pi 2 pulsations and phase lags of the first impulse of Pi 2 detected simultaneously at ONW and EWA and at SGC and EWA, respectively (after Saito et al., 1981)

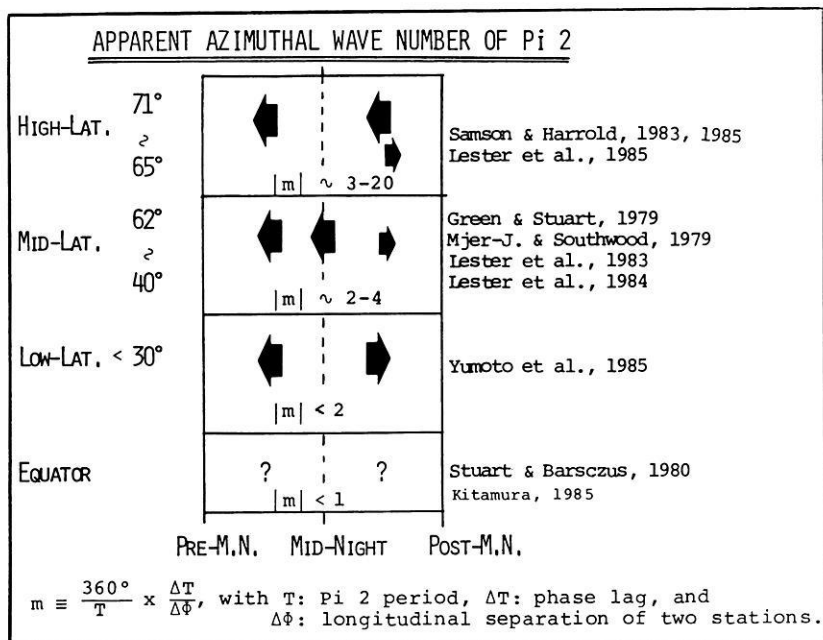


Fig. 15. Summary of apparent azimuthal wave numbers of Pi 2 pulsations obtained at high, middle, low and equatorial latitudes by many workers. Solid arrows indicate apparent longitudinal propagation direction

occasions in simultaneity, within the accuracy of comparison (± 30 s), with the onset of magnetospheric substorms in the night hemisphere (Grenet et al., 1954; Yanagihara and Shimizu, 1966; Saito et al., 1976b; Sakurai and Saito, 1976; Stuart and Barszczus, 1980; Sastry et al., 1983), implying small apparent azimuthal wave number ($|m| < 1$). Kitamura (personal communication, 1985) recently suggested that since no phase lag between daytime and nighttime Pi 2 pulsations could be detected at Fukuoka, Japan, and Maroa, Cameroun, near equatorial latitude, the azimuthal wave number of Pi 2 pulsations near the equator would be zero.

It is noteworthy that the apparent azimuthal wave numbers of Pi 2 have a latitudinal dependence, i.e., $|m|$

$\sim 3-20$ at high latitudes, $|m| \sim 2-4$ at mid and low latitudes, and $|m| < 1$ at very low latitudes as summarized in Fig. 15. Further theoretical studies are needed to explain why the azimuthal wave number of Pi 2 depends on magnetic latitudes.

3. Simultaneous occurrence of daytime Pi pulsations. There are very few reports showing evidence of the possibility of Pi 2 observed during the daytime (cf. Table 3b of Kato et al., 1960, 1961). Yanagihara and Shimizu (1966) examined the simultaneous occurrence of daytime Pi 2 at equatorial latitude by using rapid-run magnetograms from Koror and Guam in the daylit hemisphere and Fredericksburg in the night hemisphere. They found that of 112 Pi 2's

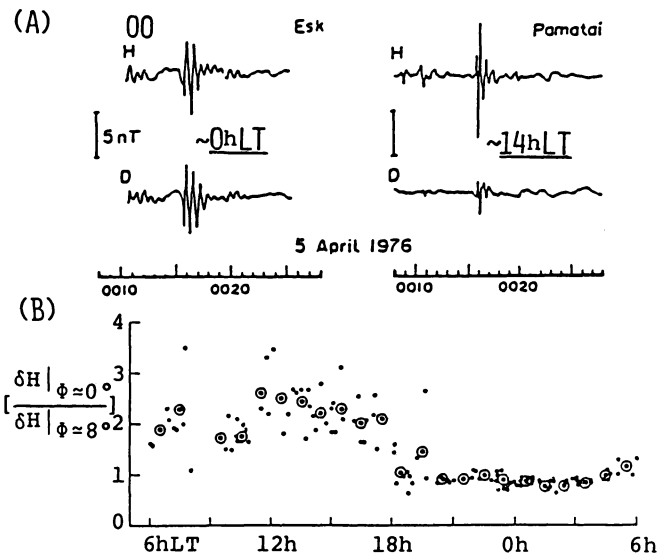


Fig. 16 A and B. Daytime Pi pulsations. **A** An example of Pi pulsation observed simultaneously at ~ 0015 UT on April 5, 1976, at Pamatai ($\lambda = 149.5^\circ\text{W}$) and at Eskdalemuir (3.2°W) (after Stuart and Barszczus, 1980). **B** Local time variation of Pi amplitude at equatorial latitude ($\phi \sim 0^\circ$) normalized by that at off-equatorial latitude ($\phi \sim 8^\circ$) (after Sastry et al., 1984)

observed during the night, 74 could be identified at the daytime equatorial station. Within the accuracy of comparison (± 30 s), daytime Pi's occur simultaneously with their nighttime counterparts (Fig. 16a; Stuart and Barszczus, 1980). The dominant spectral component is generally at a shorter period than the current nighttime Pi 2, which is in agreement with a selective response of the low-latitude field lines to a transient, as described by field-line resonance theory. Yumoto et al. (1980) also demonstrated that about 40% of Pi 2 pulsations observed at the midlatitude Fredericksburg station in the night sector correspond with Pi pulsations identified at the low-latitude Onagawa station in the daylit hemisphere.

The lack of large and systematic differences of the arrival time over the globe suggests that a transient change occurs simultaneously all through the magnetosphere, and that the differences in character of the Pi 2 pulsations are associated with local regions of critical response to the change in magnetospheric condition.

4. Equatorial enhancement of daytime Pi 2. Yanagihara and Simizu (1966) showed that when Pi's are observed during the daytime their amplitudes near the dip equator are enhanced by a factor of between 2 and 5 relative to those at Kakioka, on the same longitude but at 26°N . The appearance of Pi on the dayside of the earth was reported to be limited to a narrow latitude band around the geomagnetic equator (Stuart and Barszczus, 1980). Sastry et al. (1983) demonstrated that Pi 2 does appear even during the daytime on many occasions at equatorial latitudes in simultaneity with the onset of magnetospheric substorms at AE stations located in the night hemisphere. They also showed the daytime enhancement of observed Pi amplitudes in H at the dip equator. The local time variation in the ratio of H amplitudes at the equator of $\Phi = -0.6^\circ$ to those at the off-equator of $\Phi = 7.5^\circ$ during daytime appears to indicate the possible influence of equatorial electrojet

on the Pi signals (Fig. 16b). In view of this, the enhancement of daytime Pi could be described by the enhanced ionospheric conductivity in the equatorial electrojet region.

Although it is almost certain that Pi 2 originates in association with auroral zone current systems (or transient changes in them), there is considerable uncertainty about how its effects are transmitted across field lines both latitudinally and longitudinally into the nighttime and daytime equators. In the following sections, recently proposed Pi 2 models for generation and propagation mechanisms, related to the above-mentioned four characteristics, will be reviewed.

3.3 Wave and current fluctuation models for Pi 2 generation

Theories of the generation mechanism of Pi 2 magnetic pulsations have been categorized physically, basically into two groups: one group primarily concerns with the wave resonance theory, and the other group concerns with the current fluctuation theory. Although no one still knows conclusively which groups of Pi 2 pulsations really predominate in the magnetosphere, recently proposed Pi 2 models can be reviewed as follows:

1. Transient-response wave model. Transient-response mechanisms are considered to interpret the observed Pi 2 pulsation as large-amplitude Alfvén wave, i.e., odd mode standing oscillation of auroral field lines, launched by a sudden change in the magnetospheric convection and/or configuration (Stuart, 1974; Maltsev et al., 1977; Saito et al., 1976a; Olson and Rostoker, 1977; Kuwashima and Saito, 1981). The launched Alfvén wave is believed to be subsequently damped by the ionosphere during reflection (Newton et al., 1978; Gough and Orr, 1984; Glassmeier et al., 1984; Kan and Sun, 1985). The transient response in the magnetosphere-ionosphere coupling has been studied by many researchers.

Nishida (1979) showed that a constant current source in the plasma sheet can produce a transient response in the ionospheric electric field, resembling the Pi 2 signature. Kan et al. (1982) suggested that the transient response to a step function voltage source in the magnetosphere can also produce an overshoot damped oscillation at the nonuniform ionospheric conductivity. Two-dimensional models of the magnetosphere-ionosphere coupling were analyzed by Lysak and Dum (1983) for the temporal development of the current and voltage sources. Expected electric and magnetic field variations on the ground are illustrated for both current and voltage generators in Fig. 17 (cf. Baumjohann and Glassmeier, 1984). Sun and Kan (1985) represented a two-dimensional model of the transient response in which the ionosphere electric field and current are calculated from the successive reflections of Alfvén waves launched in opposite directions toward both the ionospheres by enhanced convection in the plasma sheet. By matching the field-aligned current density of the incident and reflected Alfvén waves to the field-aligned current density due to the divergence of the ionospheric current driven by the electric field of the waves (Kan et al., 1982; Glassmeier, 1983; Ellis and Southwood, 1983), they have shown that the damped oscillatory nature of Pi 2 pulsations observed on the ground can be produced by the transient ionospheric response to an enhancement of the convection in the plasma sheet.

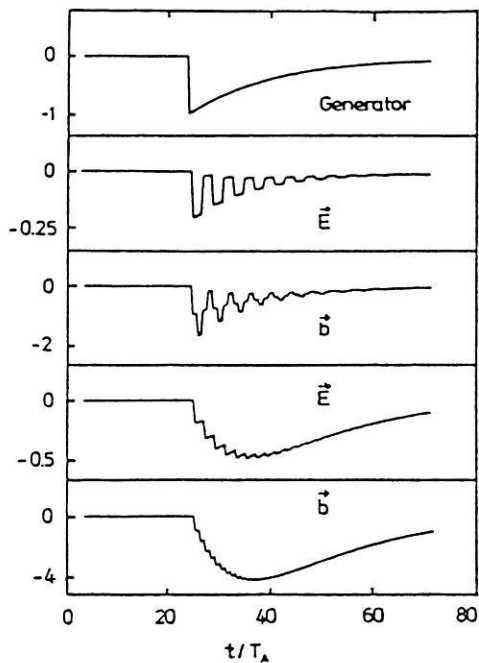


Fig. 17. Development of the magnetic field in the magnetosphere and the electric field in the ionosphere after a current (voltage) generator is switched on in the magnetotail (cf. Baumjohann and Glassmeir, 1984). The upper time series represents the generator function; the following two traces show the electric and the magnetic field if a current generator is switched on; the lower two traces show electric and magnetic field for a voltage generator. T_A is the travel time of the impulse between the equatorial plane and the ionosphere. The amplitudes of the fields are normalized to the value of the generator field just after it has been switched on

Gough and Orr (1984) analyzed individual field-line oscillations of the magnetosphere responding independently to a monochromatic driving fast mode force, i.e., a kind of the transient response mechanism. Assuming the variation of nighttime ionospheric conductivity with latitude of 46° – 72° and the appropriate damping factors, they successfully demonstrated the latitudinal profile of amplitude and phase changes of the forced damped oscillations in the magnetosphere. The results of the high-latitude resonance and lower-latitude near-resonance conditions near the plasmapause are illustrated in Fig. 18.

Lester et al. (1984) recently reported that although the sense of horizontal polarization of midlatitude Pi 2 is predominantly left-handed at all longitudes, the westward propagation dominates west of and within the substorm-associated, field-aligned current meridians, but the eastward propagation dominates east of the substorm current system. These observed polarizations at midlatitude cannot all be explained by either a purely westward wave or a purely standing wave. In order to interpret the polarization characteristics of midlatitude Pi 2, Southwood and Hughes (1985) recently proposed a superposition of two circularly polarized waves propagating azimuthally in opposite directions with different amplitudes (Fig. 19). The two waves are polarized in the opposite sense. The large-amplitude, left-handed wave is assumed to propagate westward. The eastward wave has a smaller amplitude than the westward propagating one, but the same value of $|k|$. Such a pattern could be set up by a partially reflecting boundary which

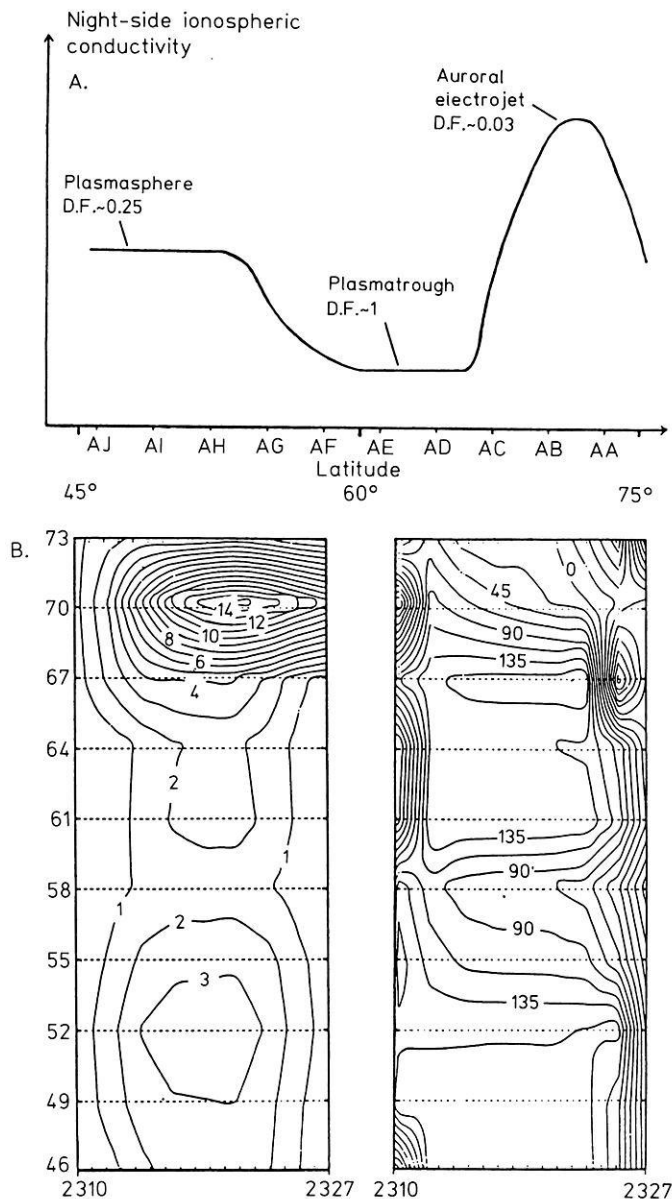


Fig. 18 A and B. Individual field-line oscillations driven by forced damped simple harmonic motion in the magnetosphere (Gough and Orr, 1984). **A** The assumed variation of nighttime ionospheric conductivity and the appropriate damping factors (D.F.) versus latitude. **B** Amplitude (left) and phase contours (right) of the forced oscillations for nighttime condition are illustrated as a function of latitude

reflects some of the originally westward travelling incident signal. The resultant wave was demonstrated to be left-handed elliptically polarized and to have a net westward phase motion, which is very similar to Pi 2 polarizations observed at midlatitudes (see Fig. 4 of Lester et al. (1984)).

These theoretical considerations and the complex Pi 2 polarization patterns as shown in Fig. 13 suggest that Pi 2 pulsations observed at high, mid, and low latitudes on the ground should consist of various HM resonance (or forced) oscillations at different locations in the magnetosphere. Wave characteristics of the various oscillations depend on local plasma parameters and the magnetospheric structure (cf. Yumoto and Saito, 1983). In order to establish the global transient Pi 2 response in the magnetosphere,

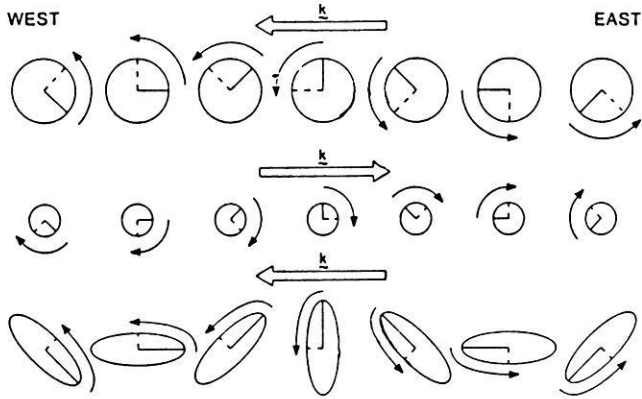


Fig. 19. Southwood and Hughes's (1985) model for midlatitude Pi 2 polarizations. A superposition of two waves, i.e., a left-handed circularly polarized westward wave and a right-handed circularly polarized eastward wave with amplitude half of the westward wave, is similar to Pi 2 polarization patterns at midlatitudes

coordinate simultaneous observations are needed from high latitudes to the equator in both the daytime and nighttime hemispheres.

2. *Pi 2 models associated with the substorm current wedge.* After substorm expansion onset magnetic energy in the magnetotail is believed to be suddenly released by short-circuiting the enhanced cross-tail current, which is still not conclusively understood (cf. Akasofu, 1977; Nishida, 1978; McPherron, 1979). The geometry of the substorm current wedge in the magnetosphere was proposed by Clauer and McPherron (1974). During substorm expansion onset associated with the sudden disappearance of part of the dawn-dusk-directed cross-tail current, the ionospheric conductivities are believed to be greatly enhanced in the localized breakup region. The inhomogeneously enhanced conductivity causes a southward polarization electric field, which drives a strong westward ionospheric current in the breakup region (cf. Coronitti and Kennel, 1972). The westward ionospheric current is considered to be closed via localized upward field-aligned currents at western edge and wider weaker downward field-aligned currents in the eastside active region.

Sakurai and McPherron (1983) recently examined the relation between the substorm current wedge and Pi 2 polarizations observed at synchronous orbit. They demonstrated that the initial perturbation in the azimuthal component of a Pi 2 event is in the same sense as the perturbations caused by the substorm-associated, field-aligned currents, i.e., positive (eastward) in premidnight and negative (westward) in postmidnight as shown in Fig. 20, and suggested that there may be a very close association between their causative mechanisms. Saito (1986) recently discussed the close association.

In order to understand high- and midlatitude Pi 2 characteristics on the ground, many workers recently tried to apply the substorm current wedge model to transient Pi 2 magnetic pulsations. From detailed observations of Pi 2 characteristics in the auroral zone, Rostoker and Samson (1981) and Pashin et al. (1982) discussed relations among the observed Pi 2 polarizations, oscillating localized field-aligned currents of the westward travelling surge, and equivalent ionospheric currents. Assuming that the periodic

Pi2 INITIAL DEFLECTION — DC SHIFT DUE TO FIELD-ALIGNED CURRENTS IN THE EAST-WEST COMPONENT

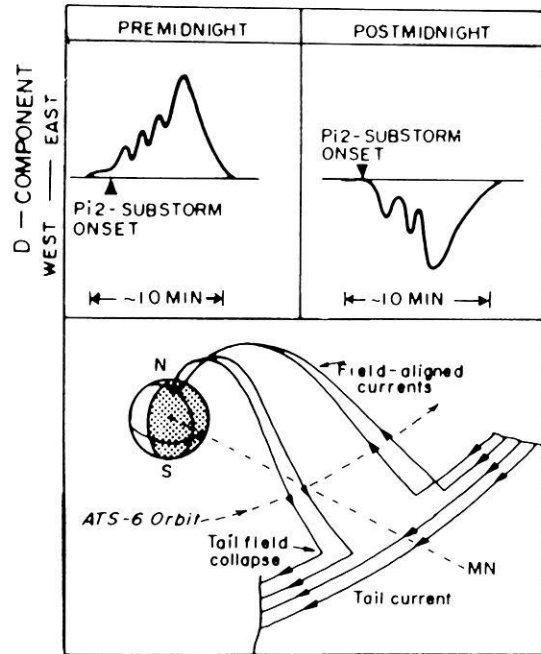


Fig. 20. Schematic representation of initial deflection of Pi 2 wave and dc shift (*top panel*) is interpreted as an effect of the substorm field-aligned currents (*bottom panel*) (after Sakurai and McPherron, 1983)

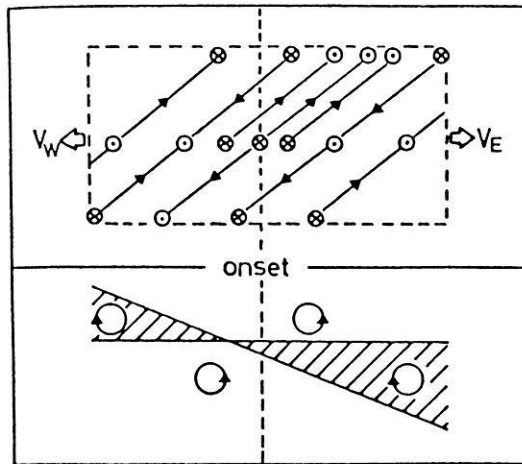


Fig. 21. Samson and Rostoker's (1983) model for the time-dependent currents associated with high-latitude Pi 2 (*top panel*). Different sense of polarizations is produced when the oscillating current system in the top panel expands eastward and westward (*bottom panel*)

fluctuations of particle precipitation in the oscillating upward field-aligned current can generate a periodic change in the ionospheric conductivity distribution with gradients in radial direction only and then also generate a radial electric field, the equivalent Pi 2 current system observable at the ground is expected to be due to the ionospheric Hall current (Pashin et al., 1982). On the other hand, Tamao (1985) and Tamao et al. (1985) evaluated a direct contribution from the horizontal component of oblique field-aligned currents to surface magnetic variations in the auroral re-

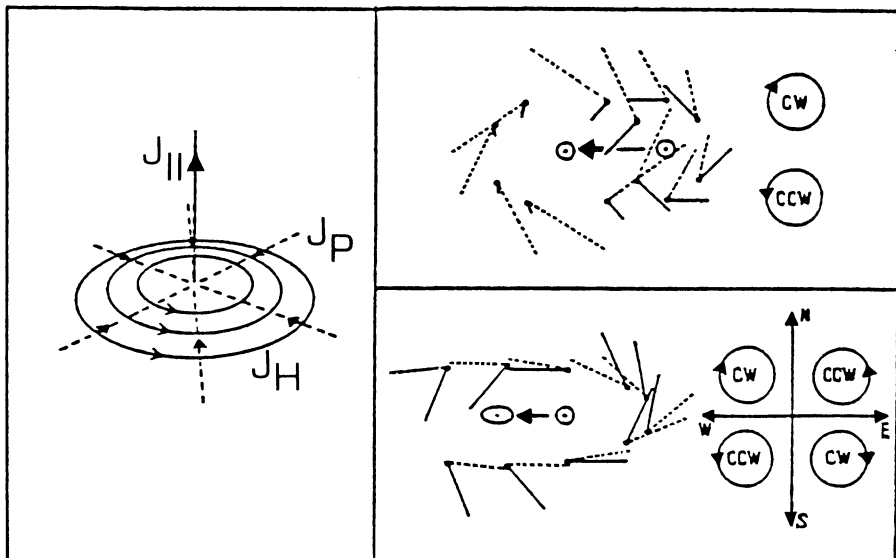


Fig. 22. Pashin et al.'s (1982) model for the ionospheric circular current system associated with high-latitude Pi 2. Schematic representation of Hall (J_H) and Pedersen currents (J_P) associated with localized upward field-aligned current ($J_{||}$) in an ionosphere with uniform conductivity distribution (*left panel*). Two cases of circular and elliptic current distributions separated in space and time producing different polarization features (*right panel*). Current vectors at the earlier and later time are shown by solid and dashed lines, respectively. The right part shows schematically the polarization pattern around the center line if during the westward movement the current strength changes periodically with time

gion, in comparison with that of the ionospheric eddy current associated with a localized electric potential distribution on the horizontal plane. For the localized perturbation with an isotropic horizontal structure at 60° geomagnetic latitude, they demonstrated that the direct contribution attains up to about 80% of the magnetic contribution of the ionospheric Hall current.

Samson and Rostoker (1983) have considered a system of oscillating field-aligned currents expanding eastward and westward as shown in Fig. 21 to explain the high-latitude Pi 2 polarization. The oscillating field-aligned current and the ionospheric Hall electrojet contribute largely to the D- and H-component, respectively. The expected polarization pattern is also illustrated in the figure. On the other hand, due to the westward movement of the region of intense upward vertical field-aligned current and the Pi 2-associated equivalent ionospheric current system of circular shape, a different sense of magnetic polarizations was inferred by Pashin et al. (1982) as shown in Fig. 22. When a circular streamline of the equivalent current at the beginning of the Pi 2 pulsation moves to the west and the streamline changes its form to be an elliptical shape, four quadrants with a different sense of polarization were predicted to appear. This is in good agreement with the more complicated polarization patterns of high-latitude Pi 2 pulsations (Kuwashima, 1978; Samson and Harrold, 1983; see Fig. 13). Pashin et al. (1982) concluded that high-latitude Pi 2 polarizations will strongly depend on the shape, direction, and velocity of the movement of the actual ionospheric current pattern. However, real configuration of current systems in the auroral zone during substorm is more complicated. It is still not clarified which of these Pashin et al.'s and Samson and Rostoker's models are more effective and realistic. The high-latitude Pi 2 polarizations will be able to be interpreted by using both the more sophisticated oscillating field-aligned current and the equivalent Pi 2 ionospheric current in the near future.

Polarization characteristics of midlatitude Pi 2 pulsations were compared with those predicted from the current wedge model by Lester et al. (1983, 1984) (Fig. 23), where the substorm-associated, field-aligned current was assumed to oscillate with Pi 2 period. They demonstrated a good

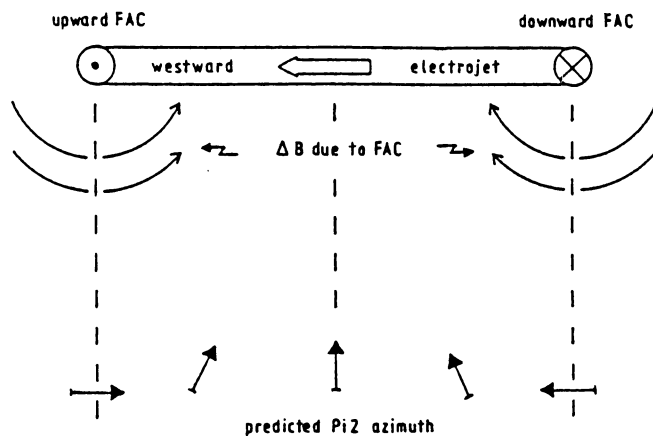


Fig. 23. Lester et al.'s (1983) model for the substorm current wedge associated with mid- and low-latitude Pi 2. A schematic view of the ionospheric and field-aligned portions of the substorm current wedge and the predicted Pi 2 polarization azimuths within the two extreme meridians of the current system are illustrated if the Pi 2 is a result of the oscillation of such a current system

agreement between the observed and the predicted Pi 2 azimuths of horizontal polarization ellipses at midlatitudes. From the comparison between the substorm center determined from the midlatitude Pi 2 azimuth and that determined from the midlatitude bay disturbance associated with the substorm current wedge, they also showed that substorm and Pi 2 current systems are not always collocated. On the other hand, low-latitude Pi 2 polarization reversal near local midnight as shown in Fig. 13 can not yet be conclusively understood by using the present theoretical models. The above-mentioned models of Figs. 21, 22, and 23 have to be modified to explain the low-latitude Pi 2 characteristics.

Magnetic field variations on the ground are believed to be due to the fluctuations of the oblique field-aligned current, oscillating in the Pi 2 frequency range (cf. Tamao, 1985), the coexisting ionospheric eddy currents (cf. Pashin et al., 1982) in the auroral zone, and the ionospheric eddy current induced by Pi 2 wave fields (cf. Tamao, 1984; Glass-

meier, 1984). Future theoretical studies are needed to quantitatively examine which contributions from the current fluctuations appear more effective in the magnetic field variations at mid and low latitudes on the ground.

3.4 Model of instantaneous transmission from the polar electric field to the equator

In order to interpret the simultaneous occurrence of daytime Pi and the equatorial enhancement of daytime Pi 2 (cf. Sect. 3.2), we would like to review the propagation mechanisms of Pi 2 pulsations and then introduce a possible candidate in this section.

Magnetic variations of long period ($T \gtrsim 10$ s) without equatorial enhancement, e.g., a positive magnetic impulse (PPI) of SSC at low latitudes, have been recently theoretically considered to be a compressional HM wave transversely propagating from the magnetosphere to low and equatorial latitudes (Kikuchi, 1986), while variations with equatorial enhancement, e.g., main impulse of SSC, are associated with the polar electric field transmitting almost simultaneously to the equator in the vacuum wave guide bounded by the ionosphere and the earth's surface (see Kikuchi and Araki, 1985). On the basis of the existence of daytime Pi's corresponding with nighttime Pi 2's and the equatorial enhancement of daytime Pi's, many authors had suggested that an instantaneous transmission process would occur from high latitudes to the daytime equator as follows: (1) Any hydromagnetic process in the magnetosphere for the transmission of Pi 2, thought to originate at high latitudes in the midnight sector, to the dayside needs a relatively large travel time (~ 100 s or more). The propagation velocity and transmitted energy in the Pi 2 frequency range are limited by the HM conditions of the medium (cf. Kikuchi and Araki, 1979a, b). (2) Jacobs et al. (1965) and Rostoker (1965) considered that the electric field or ionospheric current was transmitted one-dimensionally in the uniform E region in explaining the east-west spread of the equivalent current of Pi 2 pulsations. However, the time required for observing an appreciable intensity at the equator is more than 1 h, since the time scale of field variation is proportional to the square of propagation distance (see Kikuchi and Araki, 1979a). The attenuation of transmitted electric field in the ionosphere was also estimated to be about 100 dB/1000 km for a harmonic wave with a period of 100 s (Prince and Bostick, 1964). (3) Almost instantaneous transmissions were considered to be possible in the ionospheric wave guide centered in the F_2 ionization peak; however, the lower cutoff frequency of the wave guide is about 1 Hz (Greifinger and Greifinger, 1968). Therefore, the electric field transmission of our concern is not likely to occur in the F region. (4) Assuming the earth-ionosphere wave guide model as shown in Fig. 24, Kikuchi and Araki (1979b) demonstrated that the TM mode can transmit the polar electric field instantaneously to low latitudes. When the source field has a finite scale in the east-west direction, the transmitted field spreads in the plane of the ionosphere and simultaneously suffers from geometrical attenuation (Fig. 24b). Nevertheless, they concluded that sufficient currents can flow along the daytime dip equator, because the electrical conductivity is anomalously enhanced there (Kikuchi et al., 1978). Models (1), (2), and (3) are impossible to explain the simultaneous occurrence of daytime Pi 2's with equato-

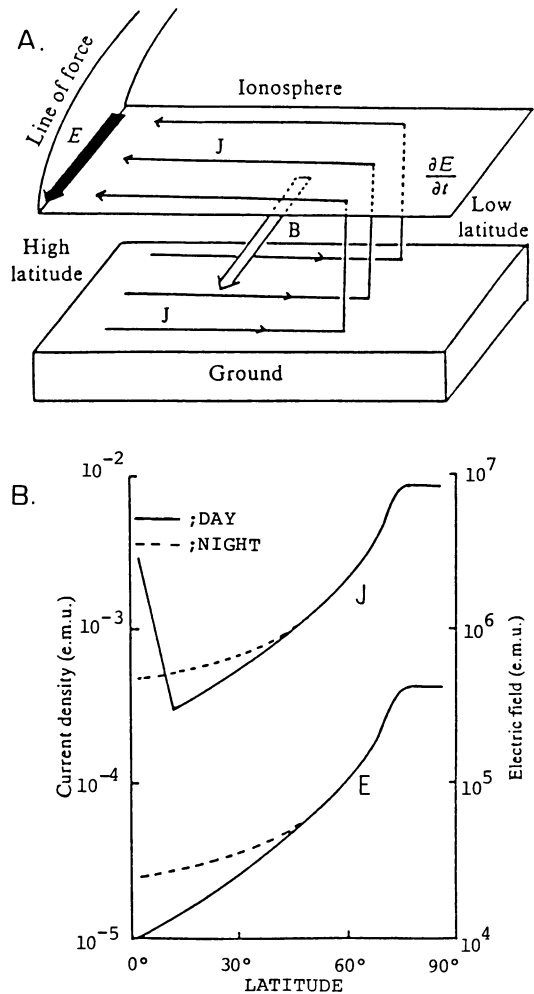


Fig. 24A and B. Model of instantaneous transmission from the polar electric field to the equator (cf. Kikuchi et al., 1978). **A** Horizontal propagation of electric fields impressed on the high-latitude ionosphere through the wave guide between the ionosphere and the earth's surface. **B** Latitudinal variations of electric field, E , and currents, J , at noon (solid line) and midnight (dashed line). The ionospheric conductivity is assumed to be isotropic and uniform at all latitudes at nighttime and at latitudes greater than 10° at daytime. In the daytime equatorial region, it varies sinusoidally with local time and is maximum at the noon equator

rial enhancement, whereas model (4) is probable for excitation of daytime Pi 2's near the equator.

Daytime Pc 3 magnetic pulsations having unclear equatorial enhancements (see Kannangara, 1972) are believed to be associated with the compressional waves, propagating across the magnetosphere and filtered out through the low-latitude ionosphere (cf. Sect. 2.8). We concluded that low-latitude Pi 2 pulsations having the equatorial enhancement during the day (Sastry et al., 1983) can be explained by using model (4) of the equatorial ionospheric current system driven by the instantaneously transmitted polar electric field during substorm expansion onset. In order to establish the daytime Pi 2 transmission model through the ionosphere-earth's surface wave guide, simultaneous magnetic and electric fields observations are needed by using latitudinal and longitudinal chain stations with new techniques of measurement from high latitudes to the equator.

3.5 A possible model for daytime Pi 2

Theoretical scenario on the generation and propagation mechanisms of low-latitude Pi 2 pulsations at $L \lesssim 3$ is not yet constructed, because morphological characteristics of low-latitude Pi 2 have not been established (see Sect. 3.2). The simultaneous occurrence of daytime Pi 2 and the apparent smaller azimuthal wave number of $|m| < 1$ at very low latitudes can not be interpreted by either longitudinal movements (or expansions) of the oscillating field-aligned current (Fig. 21) and the equivalent ionospheric current (Fig. 22) systems in the auroral zone or propagations of HM compressional Pi 2 waves across the magnetospheric field. The apparent longitudinal phase velocity of low-latitude Pi 2 projected on the auroral latitude (i.e., $V_{ph} \sim \pi R_E/mT \sim 200$ km/s for $m=1$ $T=100$ s at $\Phi=60^\circ$) is much higher than the expansion velocity of westward surges (i.e., $\sim 1-3$ km/s; see Akasofu, 1977). The HM propagation process in the magnetosphere also needs a relatively larger travel time ($\gtrsim 100$ s). More realistic Pi 2 model has to be constructed.

Figure 25 shows an example of the simultaneous occurrence of daytime and nighttime Pi 2 pulsation observed at mid and low latitudes (cf. Yumoto, 1986b). This is one of the CDAW-6 events studied by Hughes and Singer (1985). The top panel of the figure illustrates ordinary magnetograms at Halley (HY) and the AFGL network stations (TPA, SUB, MCL, CDS, RPC) in the nighttime, and Japanese stations (MMB, KAK, KNY) and Guam in the daytime. The middle panel indicates induction magnetograms at Onagawa ($\Phi = 28.55^\circ$, $A = 208.14^\circ$) in the afternoon sector. The bottom panel shows how Pi 2 polarization hodograms relate to the ionospheric currents computed by Kamide et al. (1983). The daytime Pi 2 hodogram at ONW and nighttime Pi 2 hodograms at the AFGL stations are superimposed on maps of the ionospheric current vector as a function of the station locations. Although the significant westward electrojet on the postnoon sector is not consistent with the usual DP 2 currents caused by the magnetospheric convection enhancements, it is noteworthy that the major axes at ONW and the AFGL stations approximately point toward the centers of substorm-associated ionospheric currents near 1500 LT and 0100 LT, respectively. The daytime and nighttime low-latitude bay disturbances also agree with magnetic variations caused by the current wedges formed near 1500 LT and 0100 LT, respectively (cf. Lester et al., 1983, 1984; Yumoto, 1986b). Therefore, daytime Pi 2 pulsations are believed to appear with the substorm-associated current wedge formed in the daytime sector.

In order to interpret the result in Fig. 25 and the unresolved problems in Sect. 3.2, i.e., (3) the simultaneous occurrence of daytime Pi 2 and (4) the equatorial enhancement of daytime Pi 2, Yumoto (1986b) proposed a possible daytime Pi 2 model (Fig. 26) as follows: Before and/or during substorm expansion onset, a conventional DP 2 eastward current (or another substorm-associated westward current as shown in Fig. 25c) governed by electric field enhancements, e.g., the magnetospheric convection enhancements, and a substorm DP 1 current caused by a strong conductivity increase appear concurrently in the postnoon-evening and in the midnight sectors, respectively. Nighttime Pi 2 pulsations are generally believed to be excited at the moment when part of the dawn-dusk directed cross-tail current

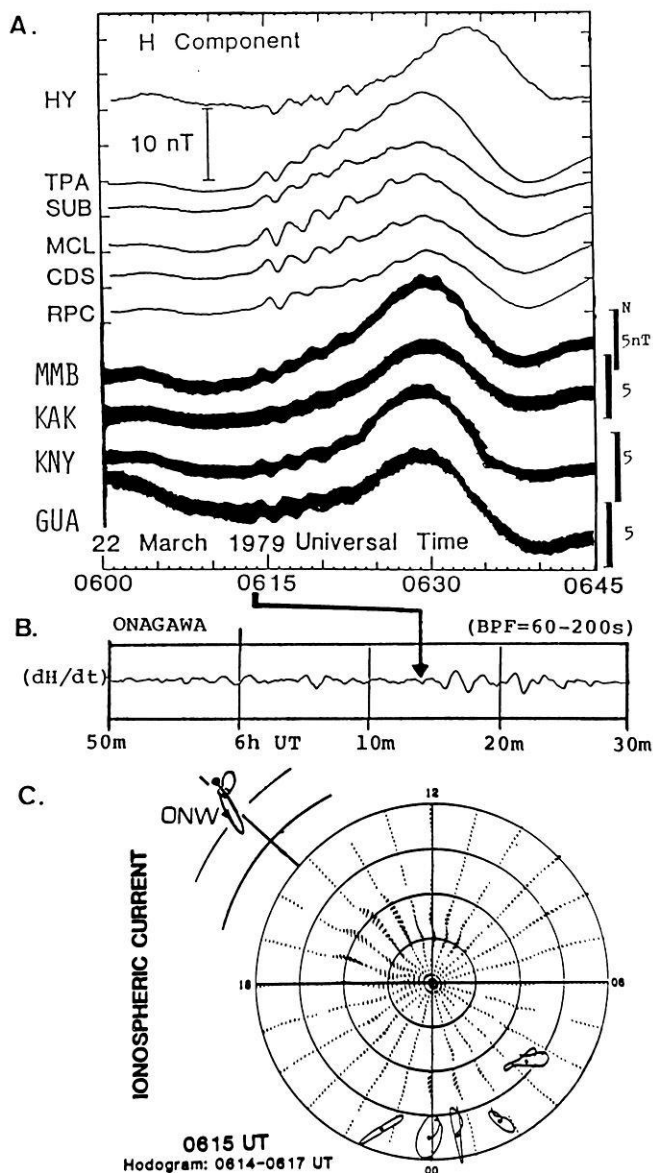


Fig. 25A–C. Relations among daytime and nighttime Pi 2 pulsations, magnetic bay variations, and ionospheric currents. **A** Magnetometer data from Halley (HY) and five of the AFGL network stations in the midnight sector (Hughes and Singer, 1985) and from Japanese and Guam stations in the daytime sector showing the magnetic bay and Pi 2 pulsation signatures of a substorm onset at 0614 UT. **B** Amplitude-time record of daytime Pi pulsation in the induction magnetogram at Onagawa during the CDAW-6 event. **C** Pi hodograms at ONW and the AFGL stations are superimposed on maps of the total ionospheric current vectors (cf. Hughes and Singer, 1985). The maps are in corrected geomagnetic coordinates; circles mark 10° increments of latitude from the pole. Westward electrojets grow in the 0000–0200-LT and 1400–1700-LT sectors which correspond approximately to the centers of the nighttime Pi 2 and the daytime Pi polarization patterns, respectively

suddenly disappears and after which the substorm current wedge is set up (see Fig. 20). If the sudden change of the cross-tail current could be transferred instantaneously through the three-dimensional current system to the ionospheric current enhanced in the postnoon-evening sector, and thus into a partial ring current in the outer magnetosphere ($L \gtrsim 8$), another transient response could be ex-

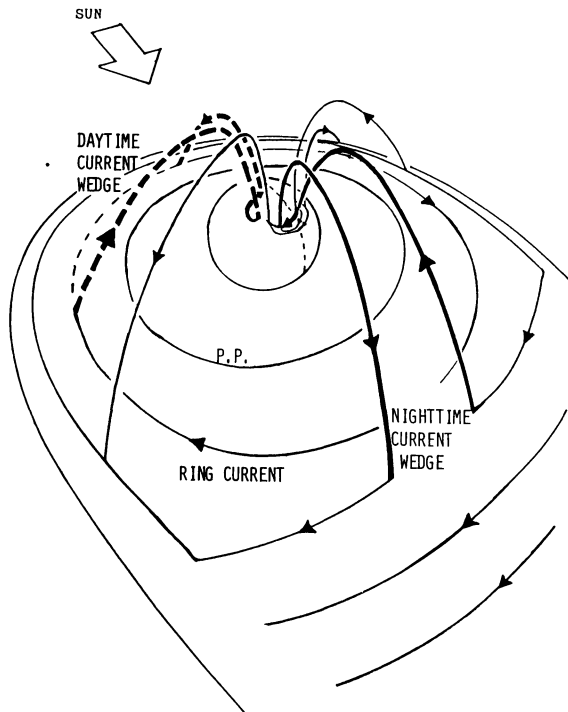


Fig. 26. A possible generation and propagation mechanism of daytime Pi pulsation on the basis of the present observational results and theoretical models. Before and/or during the substorm onset, if an enhanced electric field or currents in the dayside high-latitude ionosphere could become a current wedge system (*dashed lines*) similar to the nightside substorm current wedge (*solid thick lines*), the equatorial enhancement of Pi 2 and the simultaneous occurrence of daytime Pi pulsations can be explained by the combination of the substorm current wedge model (Sect. 3.3) and the instantaneous transmission model of polar electric field (Sect. 3.4)

pected to occur in the daytime sector as illustrated by dotted lines in Fig. 26. The dayside transient response can appear as another substorm-associated current wedge, and as an ionosphere-magnetosphere coupling oscillation in the Pi 2 frequency range at high latitudes (see Fig. 17 in Sect. 3.3). At the same time, if the oscillating electric field enhanced in the postnoon auroral zone could be instantaneously transmitted to the equator, it could produce the equatorial enhancement of daytime Pi 2. This model can explain the two unresolved problems (3) and (4) in Sect. 3.2. However, further simultaneous observations at globally distributed chains of stations are needed to clarify how the dayside substorm current wedge can be set up, and then associated with daytime Pi 2 pulsations.

The unresolved problems (1) and (2) of low-latitude nighttime Pi 2 pulsations have not been yet theoretically studied in the present paper. Pi 2 magnetic pulsations observed at low-latitudes on the ground are believed to be contributed from ionospheric currents, flowing overhead, induced by the electric field transmitted from the polar region through the ionosphere-earth's surface wave guide (cf. Kikuchi et al., 1976b), ionospheric eddy currents induced by Pi 2 wave field in the magnetosphere (e.g., Lysak and Dum, 1983; Gough and Orr, 1984; Southwood and Hughes, 1985) and by the compressional Pi 2 waves filtered out through the low-latitude ionosphere (Prince and Bos-tick, 1964), and the oscillating field-aligned currents in the

auroral zone (cf. Pashin et al., 1982; Tamao, 1985; Samson, 1985). In order to understand the generation mechanism of low-latitude Pi 2 in the nighttime, we must first theoretically and/or observationally clarify which components of the various contributions dominate at low latitudes on the ground.

4. Summary and conclusions

Low-latitude Pc 3 and Pi 2 magnetic pulsations play important roles in the solar wind-magnetosphere interaction and the dynamic coupling of the magnetosphere and the ionosphere. Therefore, investigations of the generation and propagation mechanisms of low-latitude Pc 3 and Pi 2 pulsations are concluded to be indisputable and indispensable in understanding the essential aspects of the solar-terrestrial relationships. The resolved generation and propagation mechanisms and future studies to establish the mechanisms and to clarify unresolved problems can be summarized as follows:

1. *Low-latitude Pc 3.* Magnetosonic upstream waves excited by the reflected ion beams in the earth's foreshock are convected through the bow shock and the magnetosheath to the magnetopause, transmitting into the magnetosphere, and can be the most probable source of low-latitude Pc 3 pulsations (see Sects. 2.2, 2.3, and 2.5). The propagating compressional Pc 3 source waves can couple with various hydromagnetic oscillations in the inner magnetosphere (Sects. 2.4 and 2.6). At low latitudes of $L \sim 1.5-3.0$, Pc 3 pulsations are theoretically believed to be a superposition of the propagating compressional source waves and the various HM resonance oscillations, e.g., fundamental and high-harmonic standing field-line oscillations and trapped oscillations in the Alfvén trough. The predominant modes of observed Pc 3 at low-latitude conjugate stations ($L \sim 1.5$) were found to depend on both the ionospheric conditions and the propagation characteristics of the source waves (see Sect. 2.7). A possible candidate of Pc 3 pulsations at very low latitudes ($\Phi \lesssim 22^\circ$, i.e., $L < 1.2$) was suggested in Sect. 2.8 to be the filtered-out compressional waves propagating from the outer magnetosphere through the very low latitude ionosphere.

In order to observationally establish the generation and propagation mechanisms of low-latitude Pc 3, simultaneous observations are needed by means of both multiple conjugate stations from high to low latitudes on the ground and multiple satellites in the solar wind near the magnetopause and in the magnetosphere. Simultaneous observations of magnetic and ionospheric variations at longitudinally separated low-latitude stations are also needed to examine the propagation characteristics and predominant modes and to clarify how the ionospheric parameters control the occurrence and wave characteristics of low-latitude Pc 3 pulsations.

2. *Low-latitude Pi 2.* Although the generation and propagation mechanisms of low-latitude Pi 2 have not yet been clarified, four characteristics, having a clue to the unresolved problems, were pointed out in Sect. 3.2 as follows: (1) Pi 2 polarization distribution as a function of local time and magnetic latitudes, (2) latitudinal and longitudinal dependences of apparent azimuthal wave numbers, (3) simultaneous occurrence of daytime Pi pulsations, and (4) equa-

torial enhancement of daytime Pi 2. The complex Pi 2 polarization and azimuthal wave number distributions of (1) and (2) imply that observed Pi 2 pulsations consist of multiple magnetic variations, whose characteristics reflect propagation and coupling (or resonance) mechanisms and thus depend on local plasma parameters in the magnetosphere. With respect to the recently published theoretical models (Sects. 3.3 and 3.4), a possible daytime Pi 2 model was proposed to explain the unresolved problems (3) and (4) in Sect. 3.5. The simultaneous formation of a dayside current wedge (see Fig. 26) by the enhanced polar electric field in the postnoon sector before and/or during substorm expansion onset is believed to be a more reasonable explanation for the simultaneous occurrence of daytime Pi and the equatorial enhancement of daytime Pi 2 pulsations.

In order to clarify the unresolved problems and to establish the generation and propagation mechanisms of Pi 2, we also have to carry out an international coordinated simultaneous observation by means both of longitudinally and latitudinally, i.e., worldwide, separated stations and multiple satellites in space.

Acknowledgments. I am grateful to everyone who helped me prepare this paper by sending me preprints and reprints of their recent works. Special thanks are due to L.J. Lanzerotti for organizing the publication of the reviews of hydromagnetic waves at low latitudes ($L \lesssim 3.0$). I received advice and encouragement from Y. Kato (M.J.A.) for making this work possible. Useful comments of various aspects of these problems were given by T. Saito, J. Veró, T. Sakurai, M. Kuwashima, A. Wolfe, O. Saka, T. Kikuchi, T. Araki, Y. Kamide, J.K. Chao, B.J. Fraser, T. Tamao, T. Kitamura, S. Kokubun, T. Hirasawa, and H. Oya. I would like to thank A. Nishida for reading the initial manuscript. The travel expenses to present this paper at the fifth IAGA meeting in Prague on August 12, 1985, were partially supported by the Division III of IAGA, A. Nishida, and the Yamada Science Foundation, Japan.

References

- Akasofu, S.-I.: *Physics of Magnetospheric Substorms*. Reidel, Dordrecht, 1977
- Anderson, D.N.: A theoretical study of the ionospheric F region equatorial anomaly-II. Results in the American and Asian sectors. *Planet. Space Sci.*, **21**, 421–442, 1973
- Ansari, I.A., Fraser, B.J.: Multistation observations of low latitude Pc 3 geomagnetic pulsations. *Indian J. Phys.*, **598**, 239–266, 1985
- Arthur, C.W., McPherron, R.L.: Interplanetary magnetic field conditions associated with synchronous orbit observations of Pc 3 magnetic pulsations. *J. Geophys. Res.*, **82**, 5138–5142, 1977
- Baranskiy, L.N., Vinogradov, P.A., Raspopov, O.M.: Polarization of geomagnetic pulsations of the Pi 2 type. *Geomagn. Aeron.*, **10**, 743, 1980
- Barnes, A.: Theory of generation of bow-shock-associated hydromagnetic waves in the upstream interplanetary medium. *Cosmic Electrodyn.*, **1**, 90, 1970
- Baumjohann, W., Glaßmeier, K.-H.: The transient response mechanism and Pi 2 pulsations at substorm onset – review and outlook. *Planet. Space Sci.* **32**: 1361–1370, 1984
- Bavassano-Cattaneo, M.B., Bonifazi, C., Dobrowolny, M., Moreno, G., Russell, C.T.: Distribution of MHD wave activity in the foreshock region and properties of backstreaming protons. *J. Geophys. Res.* **88**, 9280–9286, 1983
- Chen, L., Hasegawa, A.: A theory of long-period magnetic pulsations, 2, steady state excitation of field line resonance. *J. Geophys. Res.* **79**, 1024–1032, 1974a
- Chen, L., Hasegawa, A.: A unified theory of long period magnetic pulsations, 2, Impulse excitation of surface eigenmode. *J. Geophys. Res.* **79**, 1033–1037, 1974b
- Clauer, C.R., McPherron, R.L.: Mapping the local time-universal time development of magnetospheric substorms using mid-latitude magnetic observations. *J. Geophys. Res.* **79**, 2811–2820, 1974
- Coroniti, F.V., Kennel, C.F.: Polarization of the auroral electrojet. *J. Geophys. Res.* **77**, 2835, 1972
- Doobov, A.L., Mainstone, J.S.: Investigations of Pi 2 micropulsations, 2. Relevance of observations to generation theories. *Planet. Space Sci.* **21**, 731–740, 1973
- Ellis, P., Southwood, D.J.: Reflection of Alfvén waves by nonuniform ionosphere. *Planet. Space Sci.* **31**, 107
- Fairfield, D.H.: Bow shock associated waves observed in the far upstream interplanetary medium. *J. Geophys. Res.* **74**, 3541, 1969
- Fairfield, D.H., Ness, N.F.: Magnetic field fluctuations in the earth's magnetosheath. *J. Geophys. Res.* **75**, 6050–6060, 1970
- Fraser, B.J., Ansari, I.A.: The spatial characteristic of low latitude Pc 3 geomagnetic pulsations. *Mem. Natl. Inst. Polar Res. Spec. Issue*, **36**, 1–14, 1985
- Fredricks, R.W.: A model for generation of bow-shock-associated upstream waves. *J. Geophys. Res.* **80**, 7, 1975
- Fukunishi, H., Lanzerotti, L.J.: ULF pulsation evidence of the plasmopause, 1. Spectral studies of Pc 3 and Pc 4 pulsations near $L = 4$. *J. Geophys. Res.* **79**, 142–158, 1974a
- Fukunishi, H., Lanzerotti, L.J.: ULF pulsation evidence of the plasmopause, 2. Polarization studies of Pc 3 and Pc 4 pulsations near $L = 4$ and at a latitude network in the conjugate region. *J. Geophys. Res.* **79**, 4632–4647, 1974b
- Fukunishi, H.: Polarization changes of geomagnetic Pi 2 pulsations associated with the plasmopause. *J. Geophys. Res.* **80**, 98–110, 1975
- Glassmeier, K.-H.: Comment on “A transient response model of Pi 2 pulsations.” by J.R. Kan, D.U. Longenecker, and J.V. Olson. *J. Geophys. Res.* **88**, 7261, 1983
- Glassmeier, K.-H.: On the influence of ionospheres with nonuniform conductivity distribution on hydromagnetic waves. *J. Geophys. Res.* **54**, 125, 1984
- Glassmeier, K.-H., Volpers, H., Baumjohann, W.: Ionospheric joule dissipation as a damping mechanism for high latitude ULF pulsations: Observational evidence. *Planet. Space Sci.* **32**, 1463–1466, 1984
- Gosling, J.T., Asbridge, J.R., Bame, S.J., Paschman, G., Sckopke, N.: Observations of two distinct populations of bow shock ions. *Geophys. Res. Lett.* **5**, 957–960, 1978
- Gough, H., Orr, D.: The effect of damping on geomagnetic pulsation amplitude and phase at ground observations. *Planet. Space Sci.* **32**, 619–628, 1984
- Gray, S.P., Gosling, J.T., Forslund, D.W.: The electromagnetic ion beam instability upstream of the Earth's bow shock. *J. Geophys. Res.* **86**, 6691–6696, 1981
- Green, C.A., Odera, T.J., Stuart, W.F.: The relationship between the strength of the IMF and the frequency of magnetic pulsations on the ground and in the solar wind. *Planet. Space Sci.* **31**, 559–567, 1983
- Green, C.A., Stuart, W.F.: Apparent phase velocities of Pi 2's, paper presented at IAGA General Assembly. Canberra, Australia, 1979
- Greenstadt, E.W.: Field-determined oscillations in the magnetosheath as possible source of medium-period, daytime micropulsations, in *Proceedings of Conference on Solar Terrestrial Relations*, 515, Univ. of Calgary, April 1972
- Greenstadt, E.W., Green, I.M., Inouye, G.T., Hundhausen, A.J., Bame, S.J., Strong, I.B.: Correlated magnetic field and plasma observations of the earth's bow shock. *J. Geophys. Res.* **73**, 51–60, 1968
- Greenstadt, E.W., Olson, T.V.: Pc 3, 4 activity and interplanetary field orientation. *J. Geophys. Res.* **81**, 5911–5920, 1976
- Greenstadt, E.W., McPherron, R.L., Takahashi, K.: Solar wind

- control of daytime, midperiod geomagnetic pulsations. *J. Geomag. Geoelec.* **32**, [supplement] 89–110, 1980
- Greenstadt, E.W., Mellott, M.M., McPherron, R.L., Russell, C.T., Singer, H.J., Knecht, D.J.: Transfer of pulsation-related wave activity across the magnetopause: Observations of corresponding spectra by ISEE 1 and ISEE 2. *Geophys. Res. Lett.* **10**, 659–662, 1983
- Greifinger, C., Greifinger, P.: Transmission of micropulsation through the lower ionosphere. *J. Geophys. Res.* **70**, 2217–2231, 1965
- Greifinger, C., Greifinger, P.: Theory of hydromagnetic propagation in the ionospheric wave guide. *J. Geophys. Res.* **73**, 7473–7490, 1968
- Grenet, G., Kato, Y., Oosaka, J., Okuda, M.: Pulsations in terrestrial magnetic field at time of day disturbance. *Sci. Rept. Tohoku Univ. Ser. 5, Geophys.* **6**, 1–10, 1954
- Hada, T., Kennel, C.F., Terasawa, T.: Excitation of compressional waves and the formation of shocks in the earth's foreshock. submitted to *J. Geophys. Res.*, 1986
- Hassam, A.B.: Transmission of Alfvén waves through the earth's bow shock: Theory and observation. *J. Geophys. Res.* **83**, 643–653, 1978
- Holló, L., Verő, J.: One year comparison of ATS and ground pulsation spectra. Paper presented at the IAGA Symposium, Prague, 1985
- Hoppe, M.M., Russell, C.T.: Particle acceleration at planetary bow shock waves. *Nature* **295**, 41–42, 1982
- Hoppe, M.M., Russell, C.T.: Plasma rest frame frequencies and polarizations of the low-frequency upstream waves: ISEE 1 and 2 observations. *J. Geophys. Res.* **88**, 2021–2028, 1983
- Hoppe, M.M., Russell, C.T., Frank, L.A., Eastman, T.E., Greenstadt, E.W.: Upstream hydromagnetic waves and their association with backstreaming ion populations: ISEE 1 and 2 observations. *J. Geophys. Res.* **86**, 4471–4492, 1981
- Hughes, W.J.: Hydromagnetic waves in the magnetosphere. *Rev. Geophys. Space Phys.* **21**, 508–520, 1983
- Hughes, W.J., Singer, H.J.: Mid-latitude Pi 2 pulsations, geosynchronous substorm onset signatures and auroral zone currents on March 22, 1979: CDAW 6, *J. Geophys. Res.* **90**, 1297–1304, 1985
- Hughes, W.J., McPherron, R.L., Barfield, J.N.: Geomagnetic pulsations observed simultaneously on the geostationary satellites. *J. Geophys. Res.* **83**, 1109–1116, 1978
- Hutton, R.: Regular micropulsations of the earth's field at the equator. *Nature* **4729**, 955–956
- Jacobs, J.A.: Geomagnetic micropulsations. In: *Physics and Chemistry in Space*, Vol. 1, J.G. Roederer (ed) Springer, New York, 1970
- Jacobs, J.A., Watanabe, T.: Propagation of hydromagnetic waves in the lower exosphere and the origin of short period geomagnetic micropulsations. *J. Atmos. Terr. Phys.* **24**, 413–434, 1962
- Jacobs, J., Rostoker, G., Watanabe, T.: World-wide propagation of impulsive micropulsation activity through the ionosphere. *Nature, Lond.* **205**, 61–62, 1965
- Kamide, Y., Kroehl, H.W., Hausman, B.A., McPherron, R.L., Akasofu, S.-I., Richmond, A.D., Reiff, P.H., Matsushita, S.: Numerical modeling of ionospheric parameters from global IMS magnetometer data for the CDAW 6 intervals, *Pep. UAG-88*, World Data Center A for Sol.-Terr. Phys., Boulder, Colo., 1983
- Kan, J.R., Sun, W.: Simulation of the westward traveling surge and Pi 2 pulsations during substorms. *J. Geophys. Res.* **90**, 10911–10922, 1985
- Kan, J.R., Longenecker, D.U., Olson, J.V.: A transient response model of Pi 2 pulsations. *J. Geophys. Res.* **87**, 7483–7488, 1982
- Kannangara, M.L.T.: Some polarization characteristics of Pc 3–5 micropulsations observed at Colomb, Ceylon. *J. Geophys. Res.* **31**, 6161–6167, 1972
- Kato, Y., Osaka, J., Okuda, M., Watanabe, T., Tamao T.: Investigation on the magnetic disturbance by the induction magnetograph, Part 5, On the rapid pulsation psc. *Sci. Rept. Tohoku Univ. Ser. 5, Geophys.* **7**, 136–146, 1956
- Kato, Y., Saito, T., Kondo, M.: Geomagnetic rapid variations observed at the Onagawa magnetic observatory during the International Geophysical Year. Part I, *Sci. Rept. Tohoku Univ. Ser. 5, Geophys.* **11**, [suppl.], 9–49, 1960
- Kato, Y., Saito, T., Kondo, M.: Geomagnetic rapid variations observed at the Onagawa magnetic observatory during the International Geophysical Year, Part II, *Sci. Rept. Tohoku Univ., Ser. 5, Geophys.* **12** [suppl.], 5–75, 1961
- Kennel, C.F., Petschek, H.E.: Limit on stably trapped particle fluxes. *J. Geophys. Res.* **71**, 1–28, 1966
- Kikuchi, T.: Evidence of transmission of polar electric fields to the low latitude at times of geomagnetic sudden commencements. *J. Geophys. Res.* **91**, 3101–3105, 1986
- Kikuchi, T., Araki, T.: Transient response of uniform ionosphere and preliminary reverse impulse of geomagnetic storm sudden commencement. *J. Atmos. Terr. Phys.* **41**, 917–925, 1979a
- Kikuchi, T., Araki, T.: Horizontal transmission of the polar electric field to the equator. *J. Atmos. Terr. Phys.* **41**, 927–936, 1979b
- Kikuchi, T., Araki, T.: Preliminary positive impulse of storm sudden commencement observed at dayside mid-latitude and equator, paper presented at the IAGA Symposium, Prague, 1985
- Kikuchi, T., Araki, T., Maeda, H.: Transmission of polar electric fields to the equator. *Nature* **273**, 650–651, June 22, 1978
- Kivelson, M.G., Southwood, D.J.: Resonant ULF waves: A new interpretation. *Geophys. Res. Lett.* **12**, 49–52, 1985
- Kokubun, S.: Observations of Pc pulsations in the magnetosphere: Satellite-ground correlation, ULF Pulsations in the Magnetosphere, ed. by D.J. Southwood, Center for Academic Pub. Japan/Tokyo, D. Reidel Pub. Comp./Dordrecht·Boston·London, 17–39, 1981
- Kokubun, S.: Statistical characteristics of Pc 5 waves at geostationary orbit. *J. Geomag. geoelectr.* **37**, 759–779, 1985
- Kovner, M.S., Lebedev, V.V., Plyasova-Bakunina, T.A., Troitskaya, V.A.: On the generation of low-frequency waves in the solar wind in the front of the bow shock. *Planet. Space Sci.* **24**, 261–267, 1976
- Kunaratnam, K.: Spatial dependence of day-time vertical polarization of Pc 3–5 magnetic pulsations in Sri Lanka. *J. Atmos. Terr. Phys.* **43**, 1289–1294, 1981
- Kuwashima, M.: Wave characteristics of magnetic Pi 2 pulsations in the auroral region, Spectral and polarization studies. *Mem. Nat. Inst. Polar Res., Series A*, **15**, 1978
- Kuwashima, M., Sano, Y., Kawamura, M.: On the geomagnetic pulsation Pc (Part III) – Spectral and polarization characteristics of middle- and low-latitude Pc 3 –, *Mem. of Kakioka Mag. Obs.* **18**, 1–28, 1979
- Kuwashima, M., Saito, T.: Spectral characteristics of magnetic Pi 2 pulsations in the auroral region and lower latitudes, *J. Geophys. Res.* **86**, 4686–4696, 1981
- Kwok, Y.C., Lee, L.C.: Transmission of magnetohydrodynamic waves through the rotational discontinuity at the earth's magnetopause. *J. Geophys. Res.* **89**, 10697–10708, 1984
- Lanzerotti, L.J., Medford, L.V.: Local night, impulsive (Pi 2-type) hydromagnetic wave polarization at low latitudes. *Planet. Space Sci.* **32**, 135–142, 1984
- Lanzerotti, L.J., Fukunishi, H., Chen, L.: ULF pulsation evidence of the plasmopause, 3. Interpretation of polarization and spectral amplitude studies of Pc 3 and Pc 4 pulsations near L=4. *J. Geophys. Res.* **74**, 4648–4653, 1974
- Lanzerotti, L.J., Fukunishi, H., Hasegawa, A., Chen, L.: Excitation of the plasmopause at ULF frequencies. *Phys. Rev. Lett.* **31**, 624, 1973
- Lanzerotti, L.J., Fukunishi, H.: Modes of magnetohydrodynamic waves in the magnetosphere. *Rev. Geophys. Space Phys.* **12**, 724–729, 1974
- Lanzerotti, L.J., Medford, L.V., MacLennan, C.G., Hasegawa, T., Acuna, M.H., Dolce, S.R.: Polarization characteristics of hy-

- dromagnetic waves at low geomagnetic latitudes. *J. Geophys. Res.* **86**, 5500–5506, 1981
- Lee, M.A.: Coupled hydromagnetic wave excitation and ion acceleration upstream of the earth's bow shock. *J. Geophys. Res.* **87**, 5063–5080, 1982
- Lester, M., Hughes, W.J., Singer, H.J.: Polarization patterns of Pi 2 magnetic pulsations and the substorm current wedge. *J. Geophys. Res.* **88**, 7958, 1983
- Lester, M., Hughes, W.J., Singer, H.J.: Longitudinal structure in Pi 2 pulsations and the substorm current wedge. *J. Geophys. Res.* **89**, 5489–5494, 1984
- Lester, M., Glaßmeier, K.-H., Behrens, J.: Pi 2 pulsations and the eastward electrojet: A case study. *Planet. Space Sci.* **33**, 351–364, 1985
- Luhmann, J.G., Tatrallaya, M., Russell, C.T., Winterhalter, D.: Magnetic field fluctuations in the Venus magnetosheath. *Geophys. Res. Lett.* **10**, 655–658, 1983
- Lysak, R.L., Dum, C.T.: Dynamics of magnetosphere-ionosphere coupling including turbulent transport. *J. Geophys. Res.* **88**, 365–380, 1983
- Mallinkrodt, A.J., Carlson, C.W.: Relations between transverse electric fields and the field-aligned current. *J. Geophys. Res.* **83**:1426–1432, 1978
- Maltsev, Yu.P., Lyatsky, W.B., Lyatskaya, A.M.: Currents over the auroral arc. *Planet. Space Sci.* **25**, 53, 1977
- McKenzie, J.F.: Hydromagnetic wave interaction with the magnetopause and the bow shock. *Planet. Space Sci.* **18**, 1, 1970
- McKenzie, J.F., Westphal, K.O.: Interaction of hydromagnetic waves with hydromagnetic shocks. *Phys. Fluids* **13**, 630, 1970
- McKenzie, J.F., Bornatici, M.: Effect of sound waves, Alfvén waves, and heat flow on interplanetary shock waves. *J. Geophys. Res.* **79**, 4589, 1974
- McPherron, R.L.: Magnetospheric substorms. *Rev. Geophys. Space Phys.* **17**, 657, 1979
- McPherron, R.L.: Substorm associated micropulsations at synchronous orbit. *J. Geomag. Geoelectr.* **32**, Suppl. II. SII 57–72, 1980
- McPherron, R.L., Russell, C.T., Aubry, M.P.: Satellite studies of magnetospheric substorms on August 15, 1968, 9. Phenomenological model for substorm. *J. Geophys. Res.* **78**, 3131–3149, 1973
- Miura, A.: Anomalous transport by magnetohydrodynamic Kelvin-Helmholtz instabilities in the solar wind-magnetosphere interaction. *J. Geophys. Res.* **89**, 801–818, 1984
- Mier-Jedrzejowicz, W.A.C., Southwood, D.J.: The East-West structure of mid-latitude geomagnetic pulsation in the 8–25 mHz band. *Planet. Space Sci.* **27**, 617–630, 1979
- Newton, R.S., Southwood, D.J., Hughes, W.J.: Damping of geomagnetic pulsations by the ionosphere. *Planet. Space Sci.* **26**, 201, 1978
- Nishida, A.: *Geomagnetic Diagnosis of the Magnetosphere*, Springer, Berlin, 1978
- Nishida, A.: Possible origin of transient dusk to dawn electric field in the nightside magnetosphere. *J. Geophys. Res.* **84**, 3409–3419, 1979
- Novikov, Yu.P., Kopytenko, Yu.A., Raspopov, O.M., Bosinger, T., Kangus, J., Ranta, H.: Simultaneous maxima of geomagnetic pulsations and riometer absorption on the afternoon side of the auroral zone. *J. Geophys. Res.* **85**, 116, 1980
- Odera, T.J.: Solar wind controlled pulsations: A review. *Rev. Geophys.* **24**, 55–74, 1986
- Odera, T.J., Stuart, W.F.: The relationship between the IMF magnitude and the frequency of Pc 3, 4 pulsations on the ground simultaneous events. *Planet. Space Sci.* **33**, 387–393, 1985
- Olson, J.V., Rostoker, G.: Latitude variation of the spectral components of auroral zone Pi 2. *Planet. Space Sci.* **25**, 663, 1977
- Orr, D.: Magnetic pulsations within the magnetosphere: A review. *J. Atmos. Terr. Phys.* **35**, 1–50, 1973
- Orr, D., Matthew, J.A.D.: The variation of geomagnetic micropulsation period with latitude and the plasmopause. *Planet. Space Sci.* **19**, 897–905, 1971
- Orr, D., Hanson, H.W.: Geomagnetic pulsation phase patterns over an extended latitudinal array. *J. Atmos. Terr. Phys.* **43**, 899–910, 1981
- Paschmann, G., Sckopke, N., Asbridge, J.R., Bame, S.J., Gosling, J.T.: Energization of solar wind ions by reflection from the Earth's bow shock. *J. Geophys. Res.* **85**, 4689–4693, 1980
- Paschmann, G., Sckopke, N., Papamastorakis, I., Asbridge, J.R., Bame, S.J., Gosling, J.T.: Characteristics of reflected and diffuse ions upstream from the Earth's bow shock. *J. Geophys. Res.* **86**, 4355–4364, 1981
- Pashin, A.B., Glaßmeier, K.-H., Baumjohann, W., Raspopov, O.M., Yahnin, A.G., Opgenoorth, H.J., Pellinen, R.J.: Pi 2 magnetic pulsations, auroral break-ups, and the substorm current wedge: A case study. *J. Geophys. Res.* **51**, 223–233, 1982
- Poulter, E.M., Allan, W., Bailey, G.J., Moffett, J.: On the diurnal period variation of mid-latitude ULF pulsations. *Planet. Space Sci.* **32**, 727–734, 1984
- Prince, C.E., Jr., Bostick, F.X., Jr.: Ionospheric transmission of transversely propagated plane wave at micropulsation frequencies and theoretical power spectrums. *J. Geophys. Res.* **69**, 3213–3234, 1964
- Rajaram, G.: Structure of the equatorial F-region topside and bottomside – a review. *J. Atmos. Terr. Phys.* **39**, 1125–1144, 1977
- Rao, B.C.N.: Some characteristic features of the equatorial ionosphere and the location of the F-region equator. *J. Geophys. Res.* **68**, 2541–2549, 1963
- Romaña, A.: Sobre algunas singularidades de las curvas de frecuencia de horas con pc en los observatorios de la zona ecuatorial. *Geomagnetica* **217–227**, 1962
- Romaña, A., Cardús, J.O., S.I.: Geomagnetic rapid variations during IGY and IGC, *J. Phys. Soc. Japan*, Vol. 17, Suppl. A–II, International Conf. Cosmic Ray and Earth Storm, Part II, 47–55, 1962
- Rostoker, G.: Propagation of Pi 2 micropulsations through the ionosphere. *J. Geophys. Res.* **70**, 4388–4390, 1965
- Rostoker, G.: The polarization characteristics of Pi 2 micropulsations and their relation to the determination of possible source mechanisms for the production of nighttime impulse micropulsation activity. *Can. J. Phys.* **45**, 1319, 1967
- Rostoker, G., Samson, J.G.: Polarization characteristics of Pi 2 pulsations and implications for their source mechanisms: Location of source regions with respect to auroral electrojet. *Planet. Space Sci.* **29**, 225, 1981
- Russell, C.T., Hoppe, M.M.: Upstream waves and particles. *Space Sci. Rev.* **34**, 155–172, 1983
- Russell, C.T., Childers, D.D., Coleman, P.J., Jr.: Ogo 5 observations of upstream waves in the interplanetary medium: Discrete wave packets. *J. Geophys. Res.* **76**, 845, 1971
- Russell, C.T., Luhmann, J.G., Odera, T.J., Stuart, W.F.: The rate of occurrence of dayside Pc 3, 4 pulsations: The L-value dependence of the IMF cone angle effect. *Geophys. Res. Lett.* **10**, 663–666, 1983
- Saito, T.: Mechanisms of geomagnetic continuous pulsations and physical states of the exosphere. *J. Geomag. Geoelectr.* **16**, 115–151, 1964
- Saito, T.: Geomagnetic pulsations. *Space. Sci. Rev.* **10**, 319–412, 1969
- Saito, T.: Resonance model on Pc 3 in subtropical region. *Contribuciones científicas para conmemorar el 75 aniversario del Observatorio del Ebro*. Cardús, J.O., Roquetes, S.I. (eds). 175–180, 1983
- Saito, T.: *Aurora, Comet, and Geomagnetic Storms*. Kyoritsu Publ. Comp. (in Japanese), 1986
- Saito, T., Sakurai, T., Koyama, Y.: Mechanism of association between Pi 2 pulsation and magnetospheric substorm. *J. Atmos. Terr. Phys.* **38**, 1265, 1976a
- Saito, T., Yumoto, K., Koyama, Y.: Magnetic pulsation Pi 2 as a sensitive indicator of magnetospheric substorm. *Planet. Space Sci.* **24**, 1025–1029, 1976b
- Saito, T., Yumoto, K., Seto, M., Akasofu, S.-I., Smith, E.J.: Substorm and Pi 2 observed simultaneously at circum-northern

- Pacific and Alaskan chain stations. Paper presented at the IAGA meeting, Edinburgh, 1981
- Saito, T., Yumoto, K., Seto, M., Cole, K.D., Dyson, P., Ward, J., Gibson-Wilde, B.: Low-latitude conjugate ULF observation by rulfmeters. *Mem. Natl. Inst. Polar Res. Tokyo, Special issue No. 31*, 52–62, 1984
- Saito, T., Yumoto, K., Chen, A.J., Chao, J.K., Soegijo, J., Paradede, M.: Pc 3 magnetic pulsations observed at very low latitudes ($|\Phi| < 20^\circ$). 1. Polarization characteristics. Submitted to *Mem. Natl. Inst. Polar Res.* 1986
- Saka, O., Kim, J.S.: Spatial phase structure of low-latitude Pc 3–4 pulsations. *Planet. Space Sci.* **33**, 1073–1079, 1985
- Saka, O.: Low latitude limit of field line resonance, Proc. of Symp. on Prospect and Retrospect in Studies of Geomagnetic Field Disturbances, *Geophys. Res. Lab. Univ. of Tokyo*, held on Jan. 25–26, 1985, pp. 141–145
- Saka, O., Iijima, T.-J., Kitamura, T.: Ionospheric control of low latitude geomagnetic micropulsations. *J. Atmos. Terr. Phys.* **42**, 517–520, 1980
- Sakurai, T.: Polarization characteristics of geomagnetic Pi 2 micropulsations. *Sci Rep. Tohoku Univ. Ser. 5, Geophys.* **20**, 107–117, 1970
- Sakurai, T., Saito, T.: Magnetic pulsation Pi 2 and substorm onset. *Planet. Space Sci.* **24**, 573–575, 1976
- Sakurai, T., McPherron, R.L.: Satellite observations of Pi 2 activity at synchronous orbit. *J. Geophys. Res.* **88**, 7015–7027, 1983
- Samson, J.C.: Large-scale studies of Pi 2's associated with auroral breakup. *J. Geophys. Res.* **56**, 133–145, 1985
- Samson, J.C., Harrold, B.G.: Maps of the polarizations of high latitude Pi 2's. *J. Geophys. Res.* **88**, 5736–5744, 1983
- Samson, J.C., Rostoker, G.: Polarization characteristics of Pi 2 pulsations and implications for their source mechanisms, 2. Influence of the westward travelling surge. *Planet. Space Sci.* **31**, 435, 1983
- Samson, J.C., Harrold, B.G.: Characteristic time constants and velocities of high-latitude Pi 2's. *J. Geophys. Res.* **90**, 12173–12181, 1985
- Sastry, T.S., Sarma, Y.S., Sarma, S.V.S., Sanker Narayan, P.V.: Day-time Pi pulsations at equatorial latitudes. *J. Atmos. Terr. Phys.* **45**, 733–741, 1983
- Sentman, D.D., Kennel, C.F., Frank, L.A.: Plasma rest frame distributions of suprathermal ions in the Earth's foreshock region. *J. Geophys. Res.* **86**, 4365–4373, 1981
- Southwood, D.J.: The hydromagnetic instability of the magnetospheric boundary. *Planet. Space Sci.* **16**, 587, 1968
- Southwood, D.J.: Some features of field line resonance in the magnetosphere. *Planet. Space Sci.* **22**, 483–491, 1974
- Southwood, D.J.: Magnetopause Kelvin-Helmholtz instability, *Proceeding of the Chapman Conference on Magnetospheric Boundary Layers. Eur. Space Agency Spec. Publ., ESA SP 148*, 357, 1979
- Southwood, D.J., Stuart, F.W.: Pulsations at the substorm onset, in *Dynamics of the Magnetosphere*, *Astr. Space Sci. Lib. Series* edited by S.-I. Akasofu, 341–355, 1980
- Southwood, D.J., Hughes, W.J.: Concerning the structure of Pi 2 pulsations, *J. Geophys. Res.* **90**, 386–392, 1985
- Stix, T.H.: *The Theory of Plasma Waves*. McGraw-Hill, New York, 1962
- Stuart, W.F.: A mechanism of selective enhancement of Pi 2's by the plasmasphere. *J. Atmos. Terr. Phys.* **36**, 851, 1974
- Stuart, W.F., Barszczus, H.G.: Pi's observed in the daylight hemisphere at low latitudes. *J. Atmos. Terr. Phys.* **42**, 487–497, 1980
- Sugiura, M., Wilson, C.: Oscillation of the geomagnetic field lines and associated magnetic perturbations at conjugate points. *J. Geophys. Res.* **69**, 1211–1216, 1964
- Sun, W., Kan, J.R.: A transient-response theory of Pi 2 pulsations. *J. Geophys. Res.* **90**, 4395–4397, 1985
- Sutcliffe, P.R.: Ellipticity variations in Pi 2 pulsations at low latitudes. *Geophys. Res. Lett.* **8**, 91–94, 1981
- Sutcliffe, P.R.: The spatial and temporal structure of low latitude Pc 3 pulsation fields, Paper presented at the IAGA meeting, Prague, 1985
- Sutcliffe, P.R., Poole, A.M.V.: Low latitude Pc 3 pulsations and associated ionospheric oscillations measured by a digital chirp ionosonde. *Geophys. Res. Lett.* **11**, 1172–1175, 1984
- Takahashi, K., McPherron, R.L., Terasawa, T.: Dependence of the spectrum of Pc 3–4 pulsations on the interplanetary magnetic field. *J. Geophys. Res.* **89**, 2770–2780, 1984
- Takeda, M., Maeda, H.: Three-dimensional structure of ionosphere currents, 1. Currents caused by diurnal tidal winds. *J. Geophys. Res.* **85**, 6895–6899, 1980
- Tamao, T.: Coupling modes of hydromagnetic oscillations in non-uniform, finite pressure plasma: Two-fluids model. *Planet. Space Sci.* **26**, 1141–1148, 1978
- Tamao, T.: Magnetosphere-ionosphere interaction through hydromagnetic waves, Proc. of Achievements of IMS, Graz, Austria ESA Pub. Branch, **SP-217**, 427–435, 1984
- Tamao, T., Taniguchi, H., Nambu, M., Miura, A.: Direct contribution of oblique field-aligned currents to magnetic field variations on the ground. *Mem. Natl. Inst. Polar Res., Special Issue No. 36*, 273–280, 1985
- Tamao, T.: Direct contribution of oblique field-aligned current to ground magnetic fields. *J. Geophys. Res.*, (in press), 1985
- Tsurutani, B.T., Rodriguez, P.: Upstream waves and particles: An overview of ISEE results. *J. Geophys. Res.* **86**, 4317, 1981
- Tsurutani, B.T., Smith, E.J., Jones, D.E.: Waves observed upstream of interplanetary shocks. *J. Geophys. Res.* **88**, 5645–5656, 1983
- Uberoi, C.: Comment on 'Nonlinear resonance theory of Pc 3 magnetic pulsation' by Kiyohumi Yumoto and Takao Saito. *J. Geophys. Res.* **88**, 4959, 1983
- Verö, J.: Geomagnetic pulsations and parameters of interplanetary medium. *J. Atmos. Terr. Phys.* **42**, 371–379, 1980
- Verö, J.: Changes of pulsation activity during two solar cycles. *J. Atmos. Terr. Phys.* **43**, 919–926, 1981
- Verö, J.: Experimental aspects of low latitude pulsations – A review. Paper presented at the IAGA meeting, Prague, 1985
- Verö, J., Holló, L.: A comparison of Pc magnetic pulsations on the ground and at synchronous orbit. *Acta Geodact. Geophys. Montanist. Hung.* **18**, 403–419, 1983
- Verö, J., Holló, L., Potapov, A.S., Polyushkina, T.N.: Analysis of the connections between solar wind parameters and day-side geomagnetic pulsations based on data from the observatories Nagyecenk (Hungary) and Uzur (USSR). *J. Atmos. Terr. Phys.* **47**, 557–565, 1985
- Verö, J., Menk, F.W.: Damping of geomagnetic Pc 3–4 pulsations at high F2-layer electron concentrations. *J. Atmos. Terr. Phys.* **48**, 231–243, 1986
- Verzariu, P.: Reflection and refraction of hydromagnetic waves at the magnetopause. *Planet. Space Sci.* **21**, 2213–2225, 1973
- Watanabe, Y., Terasawa, T.: On the excitation mechanism of the low frequency upstream waves. *J. Geophys. Res.* **89**, 6623–6630, 1984
- Westphal, K.O., McKenzie, J.F.: Interaction of magnetoacoustic and entropy waves with normal magnetohydrodynamic shock waves. *Phys. Fluids* **12**, 1228–1236, 1969
- Wolfe, A., Kaufmann, R.L.: MHD wave transmission and production near the magnetopause. *J. Geophys. Res.* **80**, 1764, 1975
- Wolfe, A., Lanzerotti, L.J., MacLennan, C.G.: Dependence of hydromagnetic energy spectra on solar wind velocity and interplanetary magnetic field direction. *J. Geophys. Res.* **85**, 114–118, 1980
- Wolfe, A., Meloni, A., Lanzerotti, L.J., MacLennan, C.G., Bamber, J., Venkatesen, D.: Dependence of hydromagnetic energy spectra near $L = 2$ and $L = 3$ on upstream solar wind parameters. *J. Geophys. Res.* **90**, 5117–5131, 1985
- Yanagihara, K., Shimizu, N.: Equatorial enhancement of micropulsation pi 2. *Mem. Kakioka Mag. Obs.* **12**, 57–63, 1966
- Yumoto, K.: Reply on Uberoi's comments. *J. Geophys. Res.* **88**, 4960, 1983
- Yumoto, K.: Long-period magnetic pulsations generated in the

- magnetospheric boundary layers. *Planet. Space Sci.* **32**, 1205–1218, 1984
- Yumoto, K.: Low-frequency upstream waves as a probable source of low-latitude Pc 3–4 magnetic pulsations. *Planet. Space Sci.* **33**, 239–249, 1985a
- Yumoto, K.: Characteristics of localized resonance coupling oscillations of the slow magnetosonic wave in a non-uniform plasma. *Planet. Space Sci.* **33**, 1029–1036, 1985b
- Yumoto, K.: Generation mechanism of Pc 3 magnetic pulsations at very low latitudes. *Planet. Space Sci.* (in press), 1986a
- Yumoto, K.: Characteristics of daytime bay and Pi 2 magnetic variations: A case study of a CDAW substorm on 22 March 1979. *Planet. Space Sci.* (in press), 1986b
- Yumoto, K., Saito, T.: Hydromagnetic waves driven by velocity shear instability in the magnetospheric boundary layer. *Planet. Space Sci.* **28**, 789–798, 1980
- Yumoto, K., Saito, T.: Nonlinear resonance theory of Pc 3 magnetic pulsation. *J. Geophys. Res.* **87**, 5159–5168, 1982
- Yumoto, K., Saito, T.: Relation of compressional HM waves at GOES 2 to low-latitude Pc 3 magnetic pulsations. *J. Geophys. Res.* **88**, 10041–10052, 1983
- Yumoto, K., Saito, T., Eitoku, A., Kamide, K.: A statistical study of low-latitude Pi 2's associated with magnetospheric substorm, Proc. Symp. on Magnetosphere and Ionosphere, held at ISAS, Tokyo Univ., on 27–28 Nov., 1980, pp. 139–145
- Yumoto, K., Eitoku, A., Saito, T.: Hydromagnetic eigen-oscillations in the dipolar field. *Mem. Nat. Inst. Polar Res.* [Spec. Issue] **26**, 61–80, 1983a
- Yumoto, K., Saito, T., Sakurai, T.: Local time asymmetry in the characteristics of Pc 5 magnetic pulsations. *Planet. Space Sci.* **31**, 459–471, 1983b
- Yumoto, K., Saito, T., Tsurutani, B.T., Smith, E.J., Akasofu, S.-I.: Relationship between the IMF magnitude and Pc 3 magnetic pulsations in the magnetosphere. *J. Geophys. Res.* **89**, 9731–9740, 1984
- Yumoto, K., Saito, T., Akasofu, S.-I., Tsurutani, B.T., Smith, E.J.: Propagation mechanism of daytime Pc 3–4 pulsations observed at synchronous orbit and multiple ground-based stations. *J. Geophys. Res.* **90**, 6439–6450, 1985a
- Yumoto, K., Saito, T., Tanaka, Y.: Low-latitude Pc 3 magnetic pulsations observed at conjugate stations ($L \sim 1.5$). *J. Geophys. Res.* **90**, 12201–12207, 1985b
- Yumoto, K., Saito, T., Tanaka, Y.: Pc 3 magnetic pulsations observed at low latitudes ($|\Phi| < 20^\circ$): 2. A possible model. Submitted to *Mem. Natl. Inst. Polar Res.* 1986
- Zhuang, H.-C., Russell, C.T.: Interaction of small-amplitude fluctuations with a strong magnetohydrodynamic shock. *Phys. Fluids* **25**, 748–758, 1982

Received January 2, 1986; revised June 11, 1986

Accepted July 18, 1986

Experimental aspects of low-latitude pulsations – A review

J. Veró

Geodetic and Geophysical Research Institute of the Hungarian Academy of Sciences, Sopron, Pf. 5, H-9401 Hungary

Abstract. This paper reviews results mainly from the past 3 years. In the first part the connection between interplanetary medium/solar wind and pulsation parameters is dealt with. The effects due to modification of the primary waves in the magnetosphere, i.e., propagation and field line resonances, are summarized in Sect. 3. A survey of a few specific questions (ionospheric effects, man-made pulsations, etc.) and of some recent results on low-latitude Pi 2 conclude the review.

Key words: Geomagnetic pulsations – Low-latitude phenomena – Solar wind-magnetosphere coupling – Hydro-magnetic waves – Magnetosphere – Pi 2 pulsations

1 Introduction

Within the more than one-century-long history of geomagnetic pulsations, there were several intervals of increased interest which stressed the clarification of some more or less essential problems. Over about the last 10 years there has been a rise in interest due to discoveries of the connections between pulsation parameters and parameters of the interplanetary medium. In recent years several investigations have been carried out at low-latitude (below the auroral zone, i.e. roughly below $L \sim 3$) ground stations and arrays because it was thought that they would carry clearer information than high-latitude or outer-magnetospheric ones (Yumoto, 1985a, b). One problem with the low-latitude pulsations is that corresponding satellite data cannot be obtained; therefore, ground-based data are of special importance.

2 Connections between Pc 3–4 pulsations and the solar wind

2.1 Connection between Pc 3–4 amplitudes and solar wind velocity

Since it was first suggested that the solar wind controls the pulsation amplitudes, this relationship has been nearly unanimously accepted. Many details remain, however, to be clarified. Odera (1984b) computed correlations between the amplitudes of about 100 Pc 3 and Pc 4 events and the solar wind velocity (V_{sw}) with the result that at $L \sim 2.8$ (Eskdalemuir) the correlation factor was 0.43 for Pc 3 and only 0.13 for Pc 4, and at $L \sim 2.4$ (Cambridge) both correlations were nearly zero. Wolfe et al. (1985) found correlation

coefficients of 0.08–0.50 for 9 low-latitude stations (hourly averages) with higher values in an open magnetosphere (with negative, southward B_z), but the main factor governing pulsation activity was B_x , and not V_{sw} . In the case of longer (daily) averages, the correlation is closer, e.g., Střešník (1984) found a value of 0.6 both for Pc 3 and Pc 4 at $L \sim 2.0$ (Fürstenfeldbruck).

Veró et al. (1985) found at $L \sim 1.9$ (Nagyecenk) that the exponent x in the function $A = c V_{sw}^x$ (A is the amplitude of the pulsation, c a constant) depended on the period of the pulsations studied (Fig. 1). For short periods the exponent is greater than 2; for periods around 60 sec it is less than 1 or even nearly zero. This corresponds to a shift

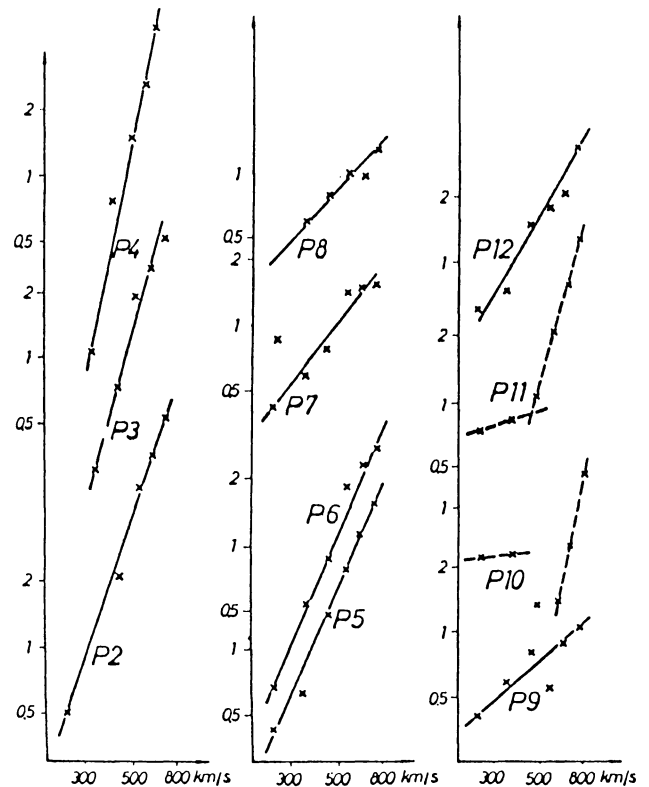


Fig. 1. Average amplitudes of the pulsations in 11 period bands (P2, 5–10 sec; P3, 10–15 sec; P4, 15–20 sec; P5, 20–25 sec; P6, 25–30 sec; P7, 30–40 sec; P8, 40–60 sec; P9, 60–90 sec; P10, 90–120 sec; P11, 2–5 min; P12, 5–10 min) as a function of solar wind velocity at $L \sim 1.9$ (Veró, 1980)

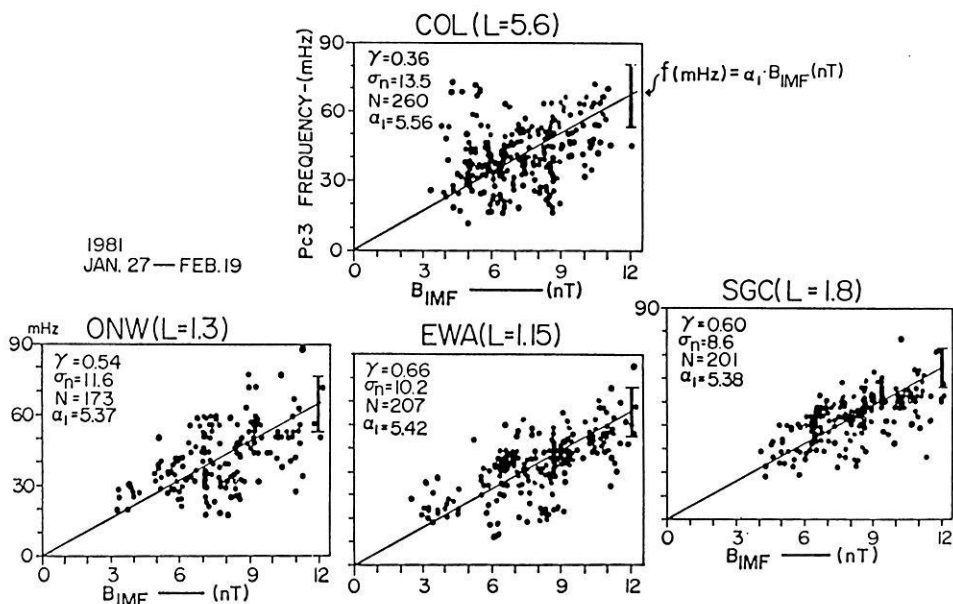


Fig. 2. Scatter plots of daytime Pc 3-4 frequencies at four globally coordinated stations against IMF magnitude from Jan. 27 to Feb. 19, 1981 (a very quiet interval). The solid lines indicate the function $f(\text{mHz}) = \alpha_1 B_{\text{IMF}}(\text{nT})$. γ and δ_n are the linear correlation coefficient and the standard deviation ($\pm \Delta f$ mHz) of the observed value from the computed one, respectively (Yumoto, 1985b)

in the pulsation periods toward shorter ones for high V_{sw} (see Sect. 2.2).

Plyasova-Bakounina (1985) found an asymmetry between morning and evening hours in the relationship between V_{sw} and the amplitude of solar-wind-controlled pulsations. Adopting a Kelvin-Helmholtz (KH) source she supposed that at a given V_{sw} the higher evening activities are due to the different directions of the magnetospheric convection at the dusk and dawn sides. This increases V_{sw} at the magnetopause in the evening and decreases it in the morning hours, i.e., the limit of the driving instability is attained more often at dusk.

The connection between pulsation amplitudes and V_{sw} changes little during the solar cycle (Veró, 1981; Polyushkina and Potapov, 1983); the deviations were found to be less than 10% of the values expected on the basis of the relationship between solar wind velocity and pulsation activity. The connection is, however, disturbed during the solar maximum by the winter minima of the pulsation activity due to ionospheric screening (see Sect. 4).

This stability is somewhat surprising as Troitskaya and Bolshakova (1984) found different pulsation types in different solar wind conditions. For instance, quiet, homogeneous, high-velocity solar wind generates regular Pc 3, and more variable solar wind, mixed Pc 3-4. The occurrence of these conditions does change quite strongly within the solar cycle.

The better correlations for averages from longer time intervals may be due to the elimination of IMF effects which change on a much shorter time scale than V_{sw} . In longer time intervals, the IMF effects are averaged out from the results, and therefore correlations become better.

2.2 Connection between interplanetary magnetic-field magnitude and pulsation periods

As clear as the connection between IMF magnitude and pulsation periods seemed to be at the time of its discovery, much controversy has developed around it. Because the time scale of IMF variations is shorter than those of V_{sw} , an hourly basis is often insufficient for correlation studies.

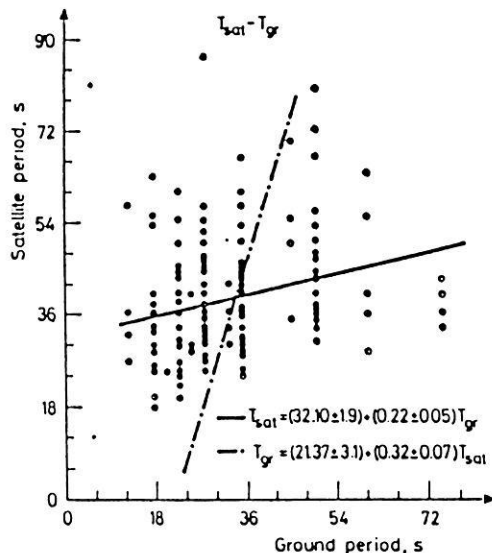


Fig. 3. Scatter plot of measured periods (T_{sat}) of waves in the solar wind on board the ISEE-2 satellite and measured periods (T_{gr}) on the ground at Nagycenk ($L \sim 1.9$) (Odera, 1984a)

If two or more spectral peaks are superimposed the “period” of a time series (pulsations) within an interval can be defined in several ways. Thus, the “period of pulsations” is an ambiguous notion if several spectral components appear simultaneously. Both these facts mean serious problems in investigations involving pulsation periods.

Based on a study including globally coordinated low-latitude stations ($L \sim 1.15-1.8$), a high-latitude station (College) and the GOES-2 satellite, Yumoto (1985a) found correlation coefficients of 0.54-0.66 between B and F (frequency of the pulsations) at low-latitude stations; in College it was 0.36, and for GOES, 0.70 (Fig. 2). He attributed the low-latitude increase in the correlation to a filtering effect during magnetospheric propagation, when localized waves in the high-latitude ionosphere and magnetosphere are effectively removed. Yumoto’s data refer to spectral peaks from 20-min-long periods of the records.

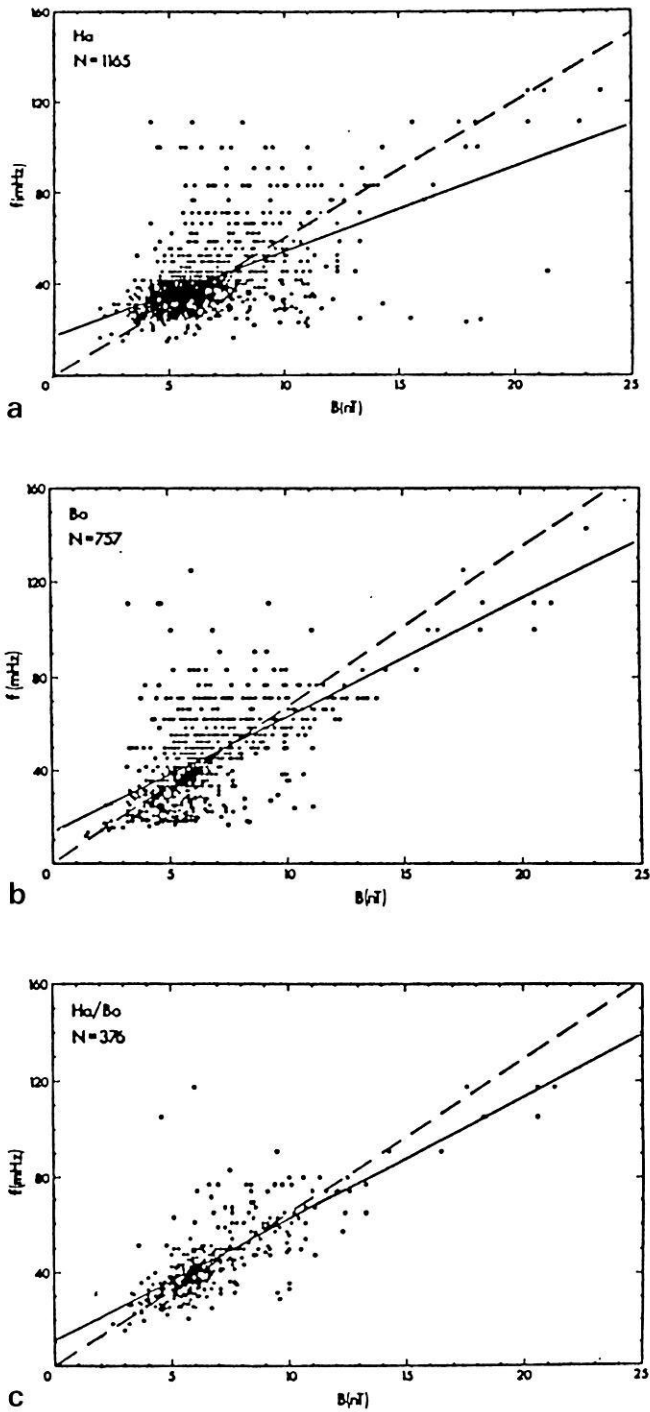


Fig. 4a–c. Scatter plots of ground pulsation frequencies against IMF magnitude. **a** Data from station Ha alone, **b** data from station Borok alone, **c** data when period at Hartland \approx period at Borok (dotted line, $F=6B$; full line, $F=c_1B+c_0$, with the free constants c_0 and c_1) (Green et al., 1983)

Odera (1984a) compared pulsation periods from Nagycenk ($L \sim 1.9$) with those onboard ISEE-2 and found rather low correlation (Fig. 3). He considered the differences only partly due to differences in response of the instruments.

From a wider data basis, Odera (1984b) found the best-fitting regression lines between $F=1/T$ (Pc 3) and B of the form $F=c_0+c_1B$, i.e., not forced through the origin. This idea is shared by Green et al. (1983; Fig. 4). As their statisti-

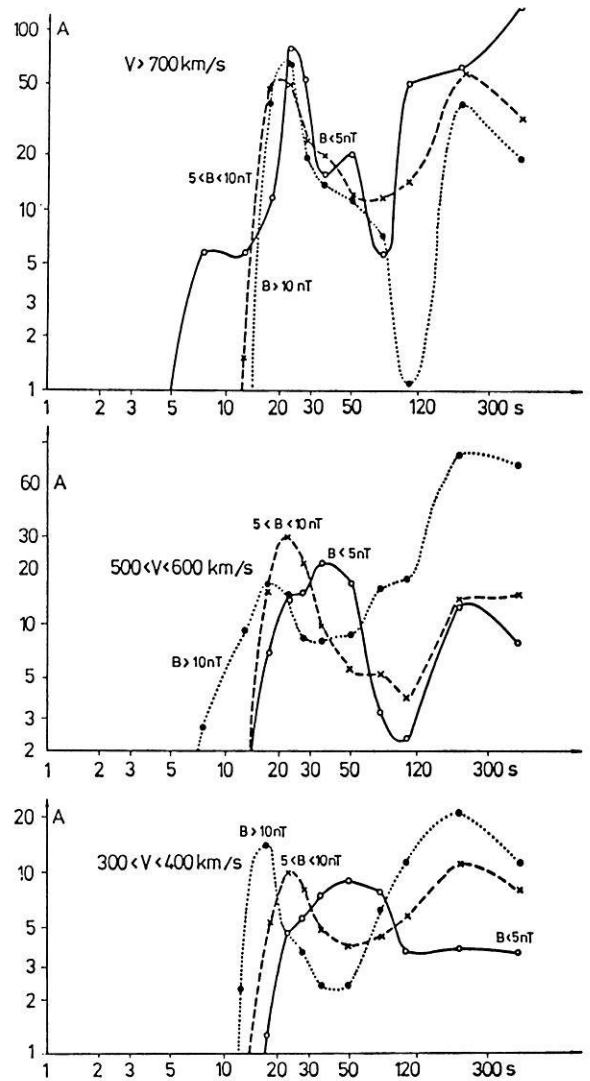


Fig. 5. Pulsation amplitudes at the observatory Nagycenk ($L \sim 1.9$) at different solar wind velocities and at different values of B . The three panels correspond to three discontinuous ranges of V_{sw} , increasing from bottom to top

cal treatment was very careful, the form given by Green et al. and Odera must be taken into account. We suppose that at least a part of the deviations from the $F=cB$ law is due to an effect of V_{sw} (or Kp). Figure 5 shows data from Nagycenk for selected ranges of the solar wind velocity as amplitudes vs B . At lower V_{sw} values, the $c \cdot B$ law is correct at least up to a B value of 10 nT, but with increasing V_{sw} , the change in T vs B becomes less and less evident (Fig. 6). In the limits, at a solar wind velocity below 300 km/s, the $F=cB$ law is correct in a rather wide range of B while at very high velocities (> 700 km/s) there is little or no dependence of F on B . If different values of V_{sw} occur in a sample, the correlation decreases, and depending on the amount of higher V_{sw} values, the regression line does not cross the origin. It is characteristic that Yumoto's (1985a) data are from a time interval of quiet and very quiet magnetic conditions with the exception of a single day.

An intriguing problem is how to select solar-wind-controlled pulsations. As supposed by Gul'elmi et al. (1973)

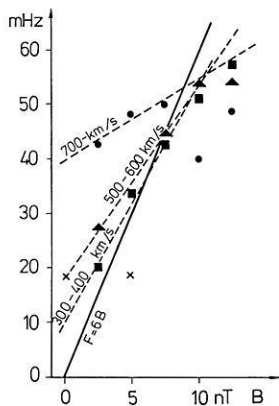


Fig. 6. Peaks in amplitude distribution of Fig. 5 against B at different solar wind velocities and the corresponding linear approximations

and Plyasova-Bakounina et al. (1982) and accepted by Odera and Stuart (1985), the correlation between B and F can be significantly improved if pulsations are used whose periods coincide at distant stations (of distances more than 20° in longitude, surpassing the supposed dimension of in-framagnetospheric pulsation sources). They used data from Borok ($L \sim 2.9$) and Hartland ($L \sim 2.4$) and then from Cambridge ($L \sim 2.5$) and Faroes ($L \sim 4.4$) with the result that the connection improved for pulsations with identical periods at both stations (Fig. 7).

This selection is very difficult to harmonize with Cz. Miletits's (1980) result that regular pulsations have a strong latitude dependence of periods corresponding to a field line resonant amplification of certain periods. Accepting the latitude dependence of periods, however, the criterion of the period identity would exclude a very essential part of the pulsations from the direct $F-B$ connection for which a reasonable fit with the predicted periods is evident. This problem will be discussed in Sect. 3.1.

2.3 Connection between the cone angle and Pc 3-4 amplitudes

The cone angle, $\theta = \cos^{-1}(B_x/|B|)$, was shown by Saito (1964) and Bolshakova and Troitskaya (1968) to control Pc 3-4 activity. After some initial discussion, the existence of such a control became generally accepted; nevertheless, there are many controversial points within this dependence.

As the two main factors controlling pulsation activity, the solar wind velocity V_{sw} , and the cone angle θ have very different time scales for the variations (typical value for V_{sw} , around one day; for θ , some tens of minutes to a few hours), the changes in the Pc 3-4 activity due to these two factors can be quite easily separated. Switches, i.e., sudden changes in the activity, are connected to changes in θ , while smooth changes, e.g., in daily averages, are mostly due to changes in V_{sw} . Thus, in addition to looking for correlations between θ and pulsation amplitudes, the immediate effect of switch-offs and switch-ons can be found, too.

Wolfe et al. (1985) found a decrease by about a factor of 3 between the cone angles of 30° and 90° (Fig. 8), and the correlation coefficients between pulsation power and θ were rather high, -0.4 to -0.8 .

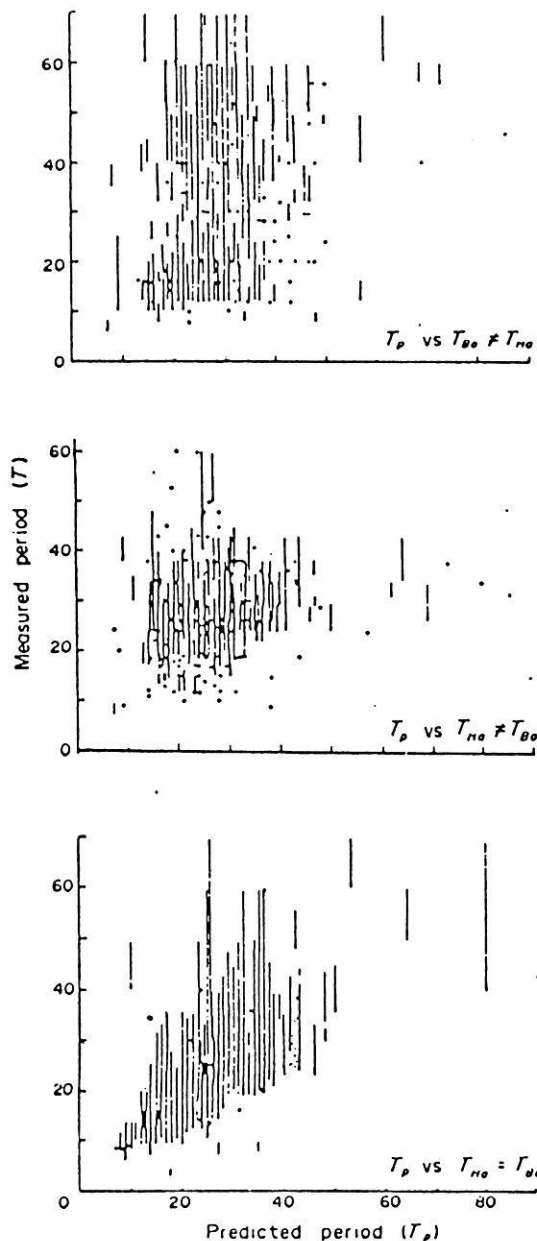


Fig. 7a-c. Scatter plot of measured periods (T) against predicted period (T_p) at Borok and Hartland using $160/B$ as a general model. **a** Borok data alone ($T_{Bo} \neq T_{Ha}$), **b** Hartland data alone ($T_{Ha} \neq T_{Bo}$), **c** Hartland and Borok data when the period range at both stations are the same within 10% error ($T_{Ha} = T_{Bo}$) (Odera and Stuart, 1985)

Odera (1984b) called attention to internal correlations between different parameters of the solar wind. θ depends both on V_{sw} and B . In his sample, θ increases from 35° to 55° for V_{sw} values of 300 and 600 km/sec, and from 45° to 55° for B values of 4 and 12 nT. The correlation between V_{sw} and θ may contribute to lower correlations in certain samples between V_{sw} and pulsation power if the cone angle effect is neglected. Moreover, Odera (1984b) found also correlations of -0.45 between Pc 3 power and θ and of -0.35 between Pc 4 power and θ , in accordance with the previously mentioned results. Without continuing the enumeration of correlation results, two effects should be mentioned which are of particular interest.

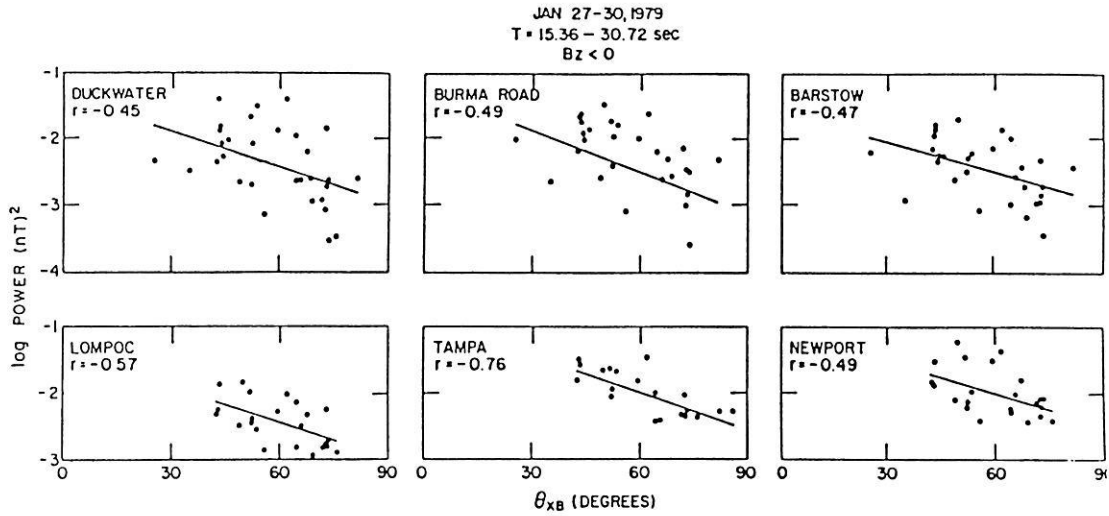


Fig. 8. Scatter plots of log power (15.36–30.72-sec band) vs cone angle θ_{XB} for all $L=2$ (and $L=3$ at Newport) dayside stations of the AT & T Bell Laboratories and AFGL networks. Correlation coefficients (r) are also indicated. (Wolfe et al., 1985)

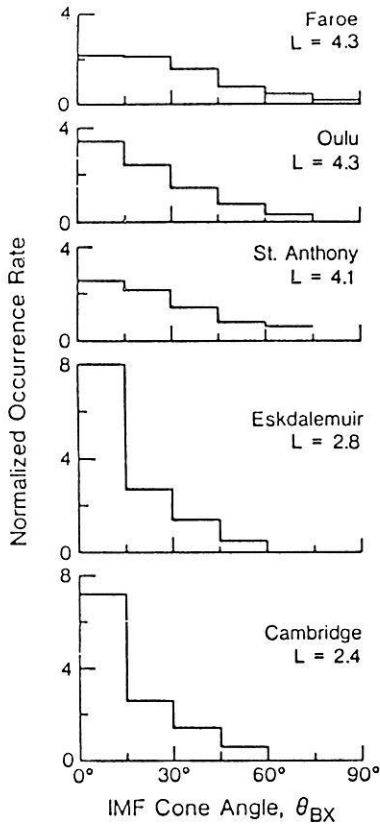


Fig. 9. The rate of occurrence of dayside Pc 3–4 pulsations at five IGS stations as a function of the cone angle. The rates have been normalized by the rate of occurrence of orientations of the IMF during the period of survey (Russell et al., 1983)

The first one is from Russell et al. (1983) who found a significant change in the cone angle effect with latitude in the sense that the effect was felt at larger θ at higher latitudes (Fig. 9). The sharp dependence at low L on θ reflects the dependence of upstream wave amplitudes at the nose of the magnetosphere on θ , while at high L the weak effect should be due to a shift of the stream lines

which convect the waves from the magnetopause and indicates cross-stream line propagation.

The other, controversial point is the cone angle optimum. Generally, an optimum at 0° is accepted, but the number of cases around $\theta=0^\circ$ is quite low; therefore, in smaller samples values around 0° are mostly lacking (see, e.g., Wolfe et al.'s and Odera's data). At Nagycken ($L \sim 1.9$), from the data of two years, a maximum in amplitude at 30° was found in the period of 15–30 sec, but a similar investigation at the Uzur observatory at similar latitude failed to confirm this result (Veró et al., 1985). The cause of this difference lies neither in a difference in the period ranges (which does not exist) nor in a difference in the processing method. The Nagycken values for cone angles of 0° – 20° are averages for about 200 hand-scaled amplitudes.

Switch-ons and switch-offs are conspicuous events; perhaps this is why a considerable amount of research has been concentrated on them. Anyway, in satellite and ground data both simultaneous and noncoinciding events can be found. A characteristic positive example is presented by Yumoto et al. (1984) and Yumoto (1985a) for three stations and several switches. Odera (1984a, b) presented on the contrary a few cases in which switches in the solar wind were absent in ground records (Fig. 10). His figure contains data from Cambridge (at $L \sim 2.5$) and ISEE-2. The switch-off and switch-on sequence around 0800 UT on December 3, 1977, was clearly present on ISEE-2 and much less evident and shorter at the ground station. Nagycken records, however, are more similar to the ISEE-2 spectra than to the Cambridge ones. Both frequency ranges and the switches are evident there as shown in Fig. 10 by dotted areas. The interruption of the activity at ~ 25 mHz lasts on ISEE-2 for about 90 min, at Cambridge for about 15 min, and at Nagycken for about 120 min.

Wolfe et al. (1985) discussed a time interval with evidence both of an association and lack of it between interplanetary conditions and ground-based hydromagnetic energy at low latitudes. They found two consecutive switch-on/switch-off sequences, identified at stations between $L \sim 2$ and $L \sim 4$. Both events were connected with the IMF. The first event occurred after a short deviation in the IMF direc-

tion; the second followed a change of the IMF direction (Figs. 11 and 12). The duration of the disturbance at the ground station was longer than in the solar wind within roughly identical period ranges.

Holló and Veró (1985a) selected events on an hourly basis from IMF data when θ changed from unfavorable

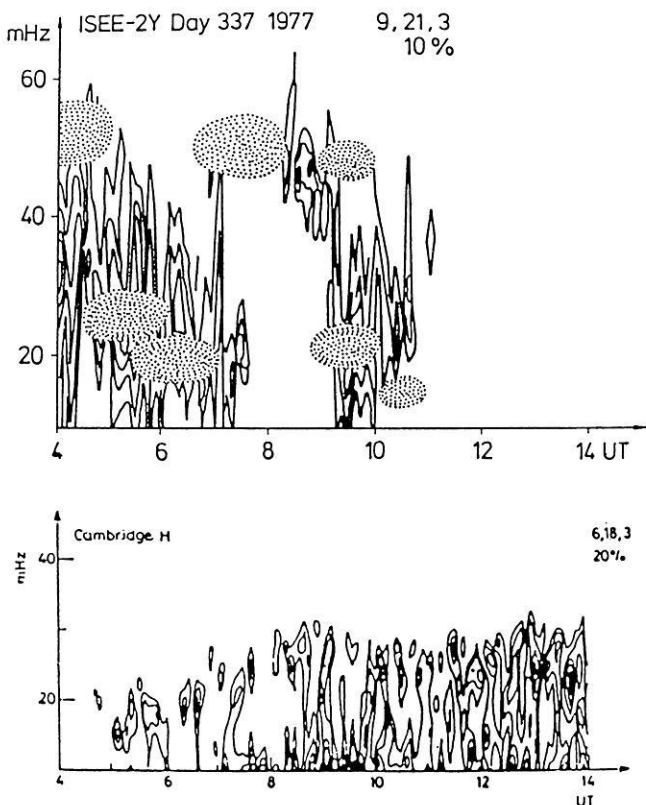


Fig. 10. Dynamic spectra of waves in the solar wind (*top panel*) and the simultaneous Pc 3-4 pulsations on the ground (*bottom panel*) for 0400-1400 UT on day 337 at Cambridge. The active pulsation periods in Nagycenk are shown by dotted areas for comparison (after Odera, 1984a)

to favorable and vice versa. The simultaneous changes in the activity of several period ranges are shown in Fig. 13. For Pc 3, the average changes are 30%-45% both for switch-offs and switch-ons, but the latter have a more uniform change in all period ranges studied. Two hours after the switch-on, amplitudes return to the previous level. In switch-offs, the amplitudes remain low for a longer time. This corresponds to Wolfe et al.'s (1985) result where the high activity events were of rather short duration (less than 1 h).

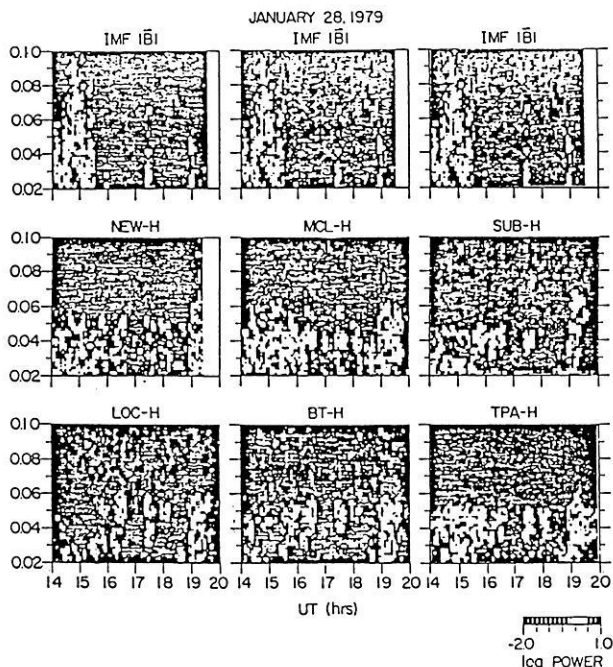


Fig. 12. Comparison of dynamic power spectra of magnetic field data measured in the interplanetary medium and at ground stations (*H* component) near $L \sim 2$ and $L \sim 3$ across the USA. Enhancements in ground-measured Pc 3 wave power occur simultaneously with enhancements for these same frequencies in the magnetic field power in interplanetary field at 1730 UT and 1900 UT (Wolfe et al., 1985)

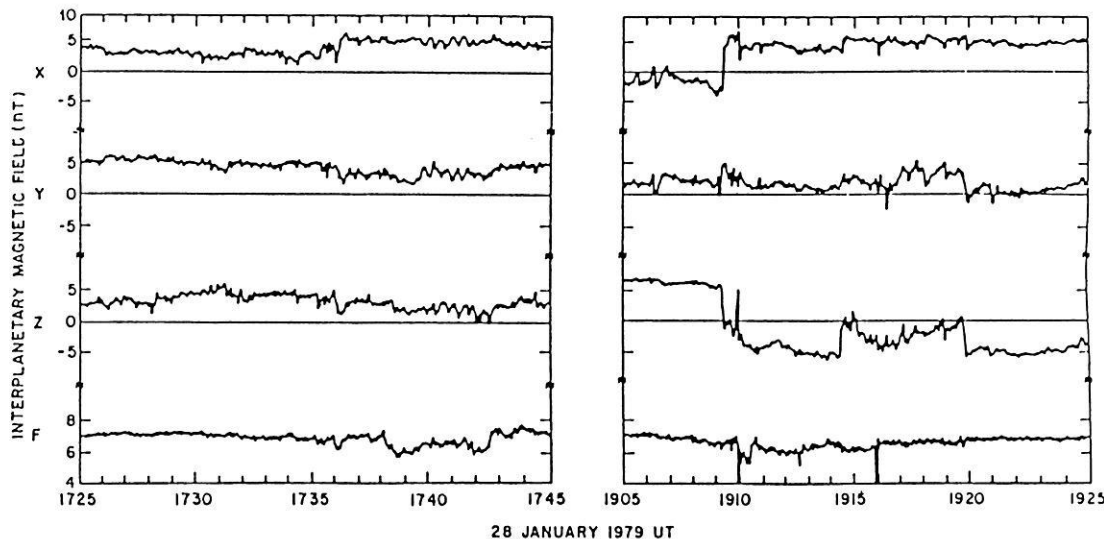


Fig. 11. Interplanetary magnetic field data in solar-magnetospheric coordinates and total field magnitude for two time intervals. *Left panel*, abrupt changes in the field occurred near 1735 UT; *Right panel*, changes in the field begin near 1910 UT (Wolfe et al., 1985)

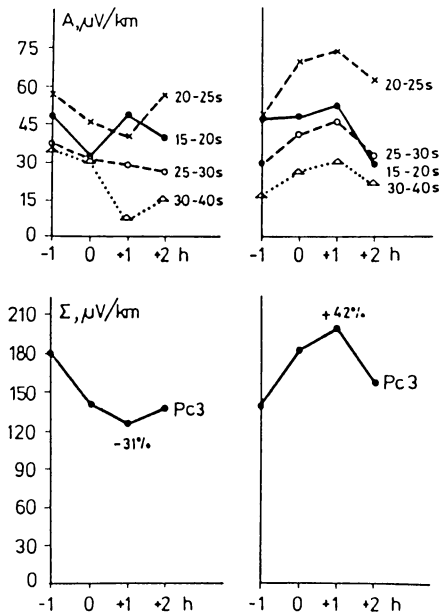


Fig. 13. Effect of switch-offs (*left*) and switch-ons (*right*) selected on the basis of IMF data (cone angle changes) at $L \sim 1.9$ in narrow period bands (*top*) and in the full range of Pc 3 (*bottom*) (Holló and Veró, 1985a)

If for synchronization similar switch-like events in ATS 6 records are used (Halló and Veró, 1985b), only those occurring between 0600–1200 UT (0700–1300 LT in Nagycenk, with the difference in LT between Nagycenk and ATS being 8 h) were present at the ground station. Afternoon events were poorly correlated; the events were synchronous mostly only at periods of 15–30 sec. It seems that the inward propagating upstream waves can be seen in favorable situations at a synchronous orbit, too.

Summarizing these observations, solar wind velocity and cone angle control at least a significant part of Pc 3–4 pulsations. The effects of V_{sw} on the activity are more important on longer time scales; on shorter ones the θ effects prevail. Both connections are, however, disturbed by other factors. Higher solar wind velocities promote the occurrence of shorter Pc 3 periods for which the θ control is stronger than for longer Pc 4 periods. The upper limit of favorable cone angles changes with the L value, i.e., it is less at lower L . Switches are sometimes very complicated events, and only a fraction of them can be identified in the solar wind, on synchronous-orbit and at ground-based stations.

Pulsation periods are controlled by B , but the exact form is not yet clear, and the solar wind velocity may also disturb this connection. At low V_{sw} , the $F = cB$ law may be valid, and the fit deteriorates at higher V_{sw} .

2.4 Comparison of observations with predictions for the upstream wave source

It should be mentioned first that there are evidently waves present in the low- L magnetosphere which do not follow the usual pattern of waves from the upstream source. To mention only a few, low-latitude Pc 4 exists irrespective of IMF (e.g., Gul'elmi, 1974), resonances of localized field lines may be excited also at very low B values with periods

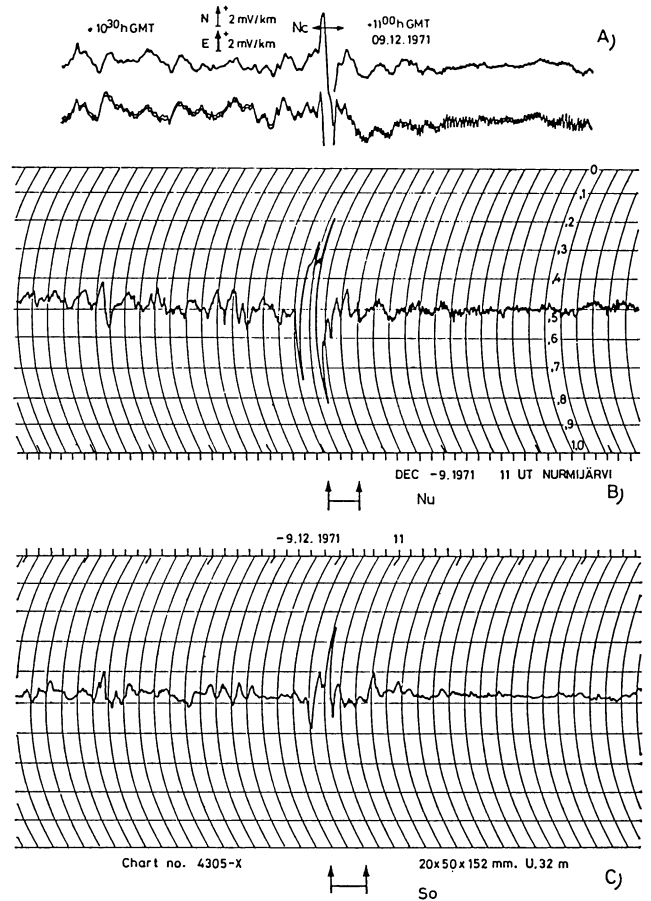


Fig. 14. Earth-current record from Nagycenk ($L \sim 1.9$) and induction records of Nurmijärvi ($L \sim 3.3$) and Sodankylä ($L \sim 5.0$) of a SI (1054 UT) followed after an interruption of pulsations by a change of the pulsation regime around 1102 UT (Tátrallyay and Veró, 1973; Veró, 1975)

of around 20 sec at $L \sim 2$ (Veró, 1980), and Pi-type pulsations excite Pc 3–4-type pulsations (Sect. 6). In spite of all this, low-latitude pulsations reflect better interplanetary conditions than high L pulsations do (Yumoto, 1985a, b).

Magnetosonic upstream waves excited by the anomalous Doppler-shifted, ion-cyclotron resonance with the narrowly reflected ion beam in the Earth's foreshock explain at least two of the three major connections between Pc 3–4 and interplanetary conditions, i.e., the period dependence on B and the θ effect on the amplitude (Yumoto, 1985b). As these connections are clearer at low latitudes, some waves having other properties than the upstream source (e.g., waves due to a KH instability) in the outer magnetosphere are filtered out during inward propagation. Solar wind velocity may also influence pulsation periods (Yumoto et al., 1984; Yumoto, 1985b; Sect. 2.2).

The most easily identifiable events at geostationary orbits ($L \sim 6.6$, GOES 2, ATS 6) and on the ground, namely switches, indicate that there is no general coincidence of pulsations at the two sites. Events may be observed at synchronous orbit without a counterpart on the ground when the corresponding wave is localized or filtered out during propagation, and only on the ground when the satellite does not see the corresponding low-amplitude wave which is amplified at lower L values.

In the context of the interplanetary medium, an earlier observation should be mentioned. Geomagnetic SI impulses indicate sudden changes in the interplanetary medium. The pulsation activity often ceases at such SI (Tátrallyay and Verő, 1973; Verő 1975). After a few minutes pulsations with other periods appear in a part of the events, corresponding to the new situation. The reappearance of the activity is, however, delayed by several minutes (Fig. 14), and the time interval without pulsations may correspond to the growth time of the upstream source in the new situation. This idea does not conflict with Hoppe et al.'s (1981) result that changes in the ion population and of the upstream waves are quite simultaneous. Here, the interval is between a change in the IMF and the corresponding change of ions and waves.

The solar wind control of the pulsation amplitudes is not included in the original upstream source theory. As this control is quite stable in the long run (Verő, 1981; Polyushkina and Potapov, 1983), in complete solar cycles any of the following mechanisms may contribute to it: an increase of hydromagnetic noise with V_{sw} initiating the beam cyclotron instability in high velocity streams; weaker attenuation of the waves in a narrower magnetosheath at higher V_{sw} ; a more transparent magnetosphere (Verő et al., 1985).

3 Propagation of upstream waves to low latitudes

In recent years, the number of in situ magnetospheric measurements of pulsations has increased rapidly, partly due to the discovery of the presence of several harmonics in the pulsation spectra at synchronous orbits (Takahashi et al., 1981). In the outer magnetosphere there is a wide variety of waves, including radially inward propagating, compressive waves and guided transverse waves, both of azimuthal and radial polarizations. Waves propagating from the magnetopause region excite field line resonances up to the sixth harmonic at $L \sim 6.6$. The compressive propagating waves reach lower L shells, and there they may excite surface waves on the plasmopause, and in the plasmasphere, trapped oscillations ($L = 1.7 L_{pp}$), fundamental ($L = 1.7 - 2.6$), and higher harmonic ($L = 2.0 L_{pp}$) standing oscillations (Yumoto, 1985b). ($L_{pp} = L$ value at the plasma pause.) Only a part of the waves observed at high L shells reach lower L . This fact explains the sometimes poor correlation between high- and low-latitude observations. The observational problems which need clarification include the identification of waves which can reach low latitudes, the low-latitude structure of pulsation periods which contributes to the selection of the mechanism being active there, the problem of the harmonic structure at low latitudes and its connection with the primary source and the harmonic structure at high L values, as well as polarization characteristics of the waves.

3.1 Dependence of Pc 3–4 parameters on latitude

The dependence of pulsation parameters on latitude is quite a delicate problem. Complications are due to the sometimes rapidly changing parameters which may be smoothed out by averaging over longer distances (or times). Anyway, closely spaced stations in the meridional direction are necessary for this problem, and the visual determination of “av-

erage” periods may be of equal value or even superior to power spectra. Dynamic spectra are best used for the detection of temporal variations.

It has been known for a long time that Pc 3–4 periods change sometimes rapidly with geomagnetic latitude or L value even at low latitudes (Voelker, 1962, 1963). Quite a great number of studies have been published but mostly were based on little data. The main effects found should be summarized, based mainly on a chain of stations in central Europe consisting of 6 stations between 43° and 64° geomagnetic latitudes (Cz. Miletits, 1980), in the following:

1. There are two groups of Pc 3–4 pulsations; the first one has periods rapidly changing with latitude (4%–10% change for one degree of latitude), the other has constant or nearly constant periods (less than 4% change for one degree of latitude).
2. The group with latitude-dependent periods has at $L \sim 2$ mostly periods of about 20–30 sec and regular waveforms (one sharp peak in the spectrum). The constant period group has a much wider period range (12–100 sec) and less regular waveforms.
3. Pc 4 occurrence frequency and amplitude decrease quickly toward lower latitudes around $L \sim 2$.
4. Pc 3 with regular waveform sometimes appears on the background of irregular Pc 4.
5. The change of the period with latitude is monotonic, but discontinuous; the period changes quickly within short distances, and then remains nearly constant.
6. The amplitude increases around $L \sim 2$ smoothly with the latitude to about $L \sim 2.5$ (50° – 55°) where in certain cases a maximum occurs. Plyasova-Bakounina et al. (1985) found that solar-wind-controlled pulsations have an amplitude maximum within the polar cap at about 74° – 77° (corresponding to a $K-H$ source) while those of magnetospheric origin have the amplitude peak at much lower latitudes. However, at low L the solar-wind-controlled pulsations prevail.

The fact that the most regular pulsations have the greatest latitude dependence sometimes leads to subjectively produced predominance of this group in selected samples. On the average there are more pulsations with constant rather than with latitude-dependent periods (the ratio is about 1:1.5 to 1:2 in occurrence frequency).

From the effects listed, Wolfe et al. (1985) confirm, for example, 3 and in part 6. The events presented by Lanzerotti et al. (1981) in their Fig. 7a and b have a latitude dependence at the 10% upper limit given in 1.

Accepting such a latitude dependence, the problem is that it should be reconciled with the dependence of the pulsation periods on B . In spite of the rather strong frequency decrease at higher latitudes, the coefficient c_1 in $F = c_1 B$ is not latitude dependent (Fig. 15). In Fig. 15b the two straight lines from Fig. 15a are redrawn in the form of $c_1 = f(L)$ to enable a comparison with experimental data.

Another observation difficult to understand with the latitude-dependent periods is why the $F-B$ relationship improves when events are considered with equal periods at two stations. Odera and Stuart (1985) used data at $L \sim 2.4$ (Hartland) and 2.9 (Borok), corresponding to a latitude difference of about 4° , and as Fig. 7 shows, the fit was much better when the periods were the same. As they accepted only those cases in which the periods differed by less than 10%, events with 4%–10% change in period for one degree of latitude are excluded from this comparison.

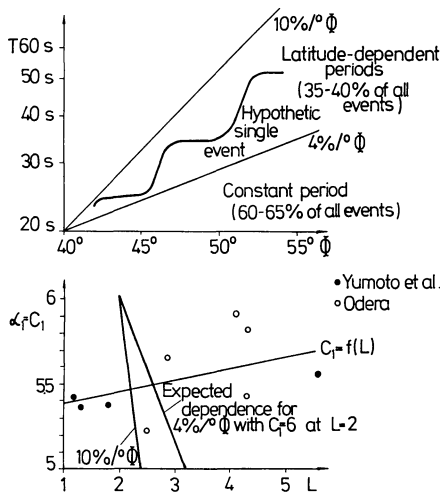


Fig. 15. Observed extrema of the period change vs. latitude in the group with latitude-dependent periods with indication of the real variation (top). Values of the c_1 factor in the equation $F = c_1 B$ at various L values from Yumoto et al. (1984) and Odera (1984b), and the limiting straight lines from Fig. 15 top transformed into a system of (L, c)

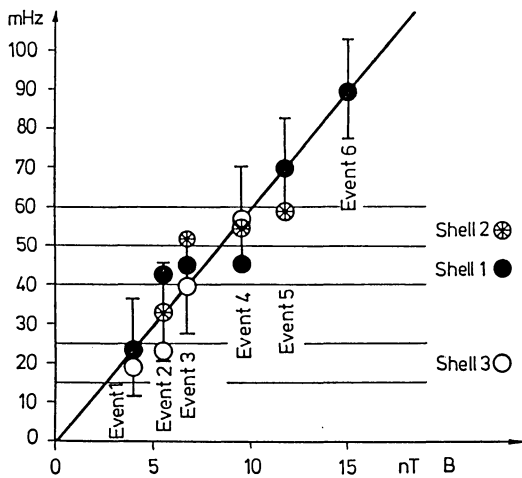


Fig. 16. Scheme of the shell resonances with conservation of the B dependence of the pulsation periods. It is supposed that stations with resonant periods outside the primary compressive wave spectrum see the original frequency, other stations see their own resonant period. Three shells and six events are indicated; the observed period for each shell is identified by the corresponding symbols

These seemingly contradictory facts can be partly understood within the following scheme.

The upstream source produces waves centered at a frequency corresponding to $F = 6B$, but in a wider range (Varga, 1980). Yumoto et al. (1985) found a range of frequencies active between $F = 4.5B$ and $F = 7.5B$. Individual shell resonances are possible within this range. Shells are not constant formations; they shift both in extent and position. Thus, there is some scatter in the periods observed, but the average for a certain L value is just $6.0B$.

Figure 16 summarizes the situation. Events 1–6 correspond to different B values as indicated on the ordinate axis. The straight line corresponds to $f_0 = 6B$; three shells are investigated which have resonant periods 40–50 mHz,

50–60 mHz and 15–25 mHz, respectively. The (constant) width of the source spectrum is supposed to be ± 12 mHz around the central frequency f_0 of each event. In case of, for example, event 3, $B = 6.7$ nT, $f_0 = 40$ mHz, and the range is 28–52 mHz. Shell 3 has a resonant period outside of this range, shell 1 is fully within the range 40 ± 12 mHz, and shell 2 is partly within. Therefore, the characteristic frequency of shell 3 (dots in Fig. 16) is equal to $f_0 = 40$ mHz, that of shell 1 is at say 45 mHz, and that of shell 2 at 51 mHz. In such a case all three shells have nearly the same frequency, and this corresponds to $f_0 = 6B$, as Odera and Stuart (1985) observed. In case of event 2, shells 1 and 3 are within the range of 35 ± 12 mHz, so they experience different periods (corresponding to the shell resonance) and cannot be fit to the $f_0 = 6B$ equation. Both the primary upstream waves and those from field line resonances should have the possibility to reach the ground, they correspond to the following two classes of pulsations. Regular, narrow-peaked pulsations with periods of about 20–30 sec at $L \sim 2$ are due to shell resonances. Longer period Pc 4 could propagate through the whole magnetosphere to the ground with the nearly unchanged original spectrum of the upstream waves. (Surface waves at the plasmopause cannot cause this Pc 4, as the close correlation with interplanetary parameters would be hardly possible.) In the case of sudden changes, field lines get excited even outside of the primary spectrum. The period changes more or less quickly at the boundary of neighboring shells, otherwise it remains nearly constant.

There are several possibilities to detect certain parameters of the shells. One of these possibilities is the phase (or polarization) change. Lanzerotti et al. (1981) quite often observed phase and polarization changes at closely spaced stations. Gough and Orr (1984) found similar changes, too, but they argued that due to damping of the waves, the phase changes are partially smoothed out at such boundaries, and there is no complete phase reversal (by 180°) when crossing the shells. Baransky et al. (1985) used $\text{grad}_M H$, the gradient of the H amplitudes in meridional direction to determine the frequency of the shell ($\text{grad}_M H$ changes its sign just at this frequency).

Yumoto et al. (1984) listed the possible waves from the upstream source at low latitudes. The main contribution should come from fundamental standing oscillations in the plasmasphere (regular waves with latitude-dependent periods) and directly from compressional waves (less regular waves without latitude dependence of periods). Higher harmonic waves in the plasmasphere will be considered in the next section. Waves originating at the plasmopause are probably of less importance at low latitudes, and for other modes no observational evidence is known.

3.2 Harmonic structure of pulsations at low and high latitudes

The harmonic structure of high L -pulsation spectra has been discovered by Takahashi et al. (1981) using ATS 6 data. There are also early indications for a low-latitude harmonic structure of Pc 3–4 pulsations (Stuart and Usher, 1966; Ádám et al. 1972). At the ground, equally spaced frequencies were found to be active at one station or at the stations of an array. The harmonic structure was, however, by no means unambiguous (see also Ansari and Fraser, 1985a).

A comparison of ground-based daily indices for differ-

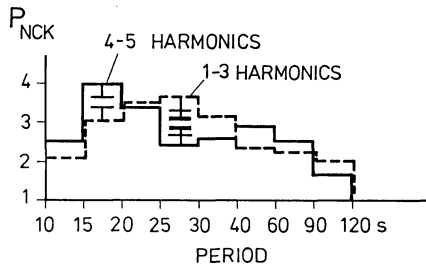


Fig. 17. Activity of some period bands in Nagycenk expressed by the daily indices P_{Nck} for each period range; if there are different numbers of harmonics present in ATS records, 90% and 99% confidence limits are indicated for two period bands (Holló and Verő, 1985b)

ent period ranges with the number of harmonics on ATS 6 (Holló and Verő, 1985b) has shown that if there are more than three harmonics in the ATS 6 spectra, then the ground-pulsation spectrum is broader, too (Fig. 17). (The number of harmonics can be quite easily counted for a full day as in such a case the absence of a harmonic, e.g., due to the position of the satellite at a node, can be detected.) In such a case the ground activity in the ranges of 10–20 sec and 40–90 sec is higher; if there are less harmonics, the activity is concentrated at the ground station into the 20–40-sec range. There are many features which differ in the two records, the most characteristic being the regular daily variation of the period lacking at the ground station. These results led to the conclusion that the harmonic structure on ATS 6 records is only correlated with ground data to the extent that it indicates the width of the primary spectrum.

3.3 Phase and polarization characteristics of low-latitude pulsation

It has been already mentioned that polarization changes may be used for the detection of resonant shells. Recently, several studies were devoted to the polarization characteristics of low-latitude pulsations to help clarify problems connected with the magnetospheric wave sources.

The polarization sense of the low-latitude pulsations has two rather characteristic changes during the day. The first one is at sunrise and may be connected to the ionospheric E layer. At this time the polarization changes from an “identical” to a “mirror” situation at conjugate stations (Yumoto, 1985b). This change is, however, rather difficult to study as it coincides with the rapid growth of Pc 3 amplitudes, and thus prior to it, mostly low-amplitude pulsations exist. The second change is around local noon, when the morning left-hand polarization changes to a right-hand or linear one on the northern hemisphere. This change should be understood as true in a statistical sense, as exceptions occur (more often in the afternoon) and even the time of the transition changes. Fraser and Ansari (1984) also found the same situation in the southern hemisphere (Fig. 18), while Yumoto et al. (1985) found opposite polarizations there. The noon reversal of the polarization is accompanied by a number of other changes, e.g., rotation of the polarization ellipse, characterized by low amplitudes in the H_y component in the afternoon, etc. These changes are not connected with the change of any ionospheric parameter, i.e., they should be characteristic for the pulsation source.

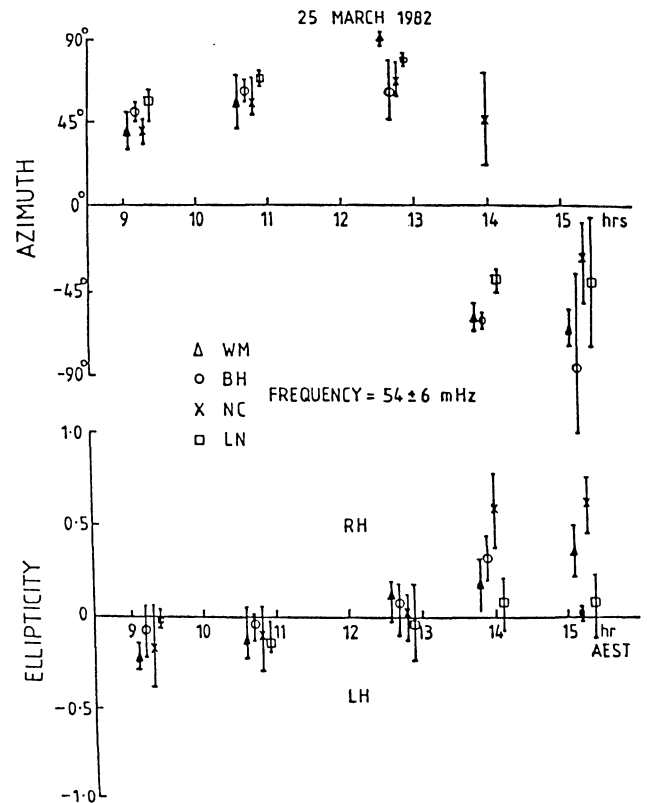


Fig. 18. Diurnal variation in polarization azimuth and ellipticity for March 25, 1982, at four Australian stations (NC, BH, WM at $L \sim 1.8$; LN at $L \sim 2.6$). AEST is within ± 1 h LT for all stations. Positive (negative) azimuth indicates a major axis in the NE (NW) quadrant. Error bars indicate the standard deviation (Fraser and Ansari, 1984)

Wave numbers deduced from phase differences of coherent waves at several separated stations were recently published by Fraser and Ansari (1984) and Sutcliffe (1985). The direction of propagation changes sign before local noon, between 0900 and 1100 LT. Azimuthal wave numbers are in the range of 3–6, at least in the morning hours. This value is in accordance with theoretical calculations for the upstream wave source (Yumoto, 1985b). Nevertheless, the results in this field are contradictory in several points, and some authors think that the observations can be better explained by a $K-H$ source (e.g., Southwood, 1983). This may be, at least partly, due to sudden jumps in the parameters of the pulsations over limited areas, as described by Sutcliffe and Boshoff (1985) for the frequency and by Ansari and Fraser (1985b) for phases. Such jumps indicate sudden changes in the resonant conditions over limited areas. The phase studies are also rendered more difficult by period changes with the latitude.

3.4 Types of HM waves observed at low-latitudes during the day

An essential part of Pc 3–4 events have periods which change rapidly, monotonically and discontinuously with the L value. In spite of magnetospheric modification, the pulsation periods are correlated to the B value of the IMF, and thus the source should be sought outside the magnetosphere. The width of the coherently excited shells lies at

a few to about 10° in latitude (some tenths of L). The monotonic increase indicates that waves of higher harmonic numbers occur seldom (or they are everywhere the same higher harmonic). Exceptions do exist, as Sutcliffe and Boshoff (1985) have shown. Thus, the $F=6B$ law remains valid in a rather wide range of frequencies (about 10–100 sec). This is in favor of a direct propagation of the upstream waves to the ground. Waves propagating compressionally in the magnetosphere and locally amplified waves by field line resonance would thus be the two main types present at low latitudes around $L\sim 2$. Other mechanisms have less importance there, but their share increases rapidly with latitude.

4 Ionospheric effects from/on pulsations

Most studies on the ionospheric modification/origin of pulsations, whether theoretical or experimental ones, refer to high latitudes. Several effects are expected due to ionospheric modification, but only a few are experimentally confirmed.

The best-known effect from the ionosphere is the rotation of the polarization ellipse by 90° , resulting in a mutual substitution of the components H and D .

Ionospheric damping, as a decrease in consecutive amplitudes was studied by Hughes and Southwood (1976a, b) and experimentally by Gough and Orr (1984). The latter compared computed waveforms with measured ones and concluded that in addition to Joule heating, another mechanism contributes to the damping which is therefore stronger than computed on the basis of the Joule heating. Such mechanisms may be coupling between adjacent flux tubes or energy loss to plasma populations in the magnetosphere. The damping is accompanied in the ionosphere by a "smearing" (Poulter and Allan, 1985) which means an averaging of spatially rapidly changing characteristics, e.g., latitudinal period changes.

The ionosphere may also screen pulsations when they propagate downward. There are many computations for the amplitude ratios above and below the ionosphere, but mostly for periods shorter than Pc 3–4. Veró (1981) and Veró and Menk (1986) were able to show that if a certain limit in f_0F2 is surpassed (10–11 MHz), pulsations are locally screened (amplitudes decrease by a factor of about 0.6). The screening does not originate in the outer magnetosphere as opposite hemispheres experience screening in respective local winter, also not from the ionosphere, as the screening does not follow the daily variation of f_0F2 . Thus, only a region of intermediate position, i.e., the upper ionosphere-lower plasmasphere where the shell resonances take place, can be the source region of this screening.

Disturbances and fields in the ionosphere associated with pulsations have been reported from the Chatanika incoherent radar (Doupnik et al., 1977) and from the Scandinavian STARE (Walker et al., 1979). Lathulliere et al. (1981) reported on Pc 3–4 waves in the incoherent scatter facility at Saint Santin in France and concluded that they had a very short horizontal wavelength. Menk et al. (1983) used a high-resolution, computer-controlled phase path ionosonde at $L\sim 2.1$ and detected changes by some tens of meters in the height of the reflection point which were correlated with Pc 3–4 bursts (Pi 2 had effects greater by one order of magnitude). Sutcliffe and Poole (1984) detected oscillations in the ionospheric Doppler velocity using the

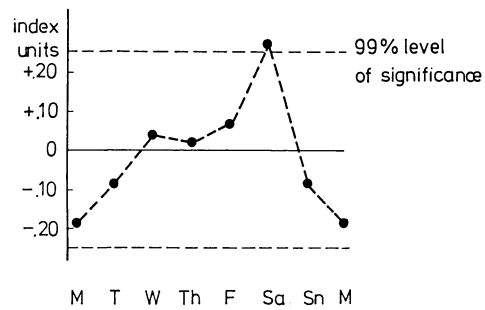


Fig. 19. Deviation of the pulsation activities on different days of the week at Nagycenk from the average of four years (1958, 1970, 1974, 1984). 99% confidence level of the deviations is indicated

Grahamstown chirp ionosonde in South Africa. To explain the results, both variations in the ionospheric refractive index due to the transient oscillating magnetic field and a vertical drift in the ionosphere as a whole due to $\mathbf{E} \times \mathbf{B}$ were necessary.

Lanzerotti et al. (1981) attributed the already mentioned frequent changes of the polarization pattern of Pc 3–4 at closely spaced stations to ionospheric effects. Such polarization jumps are at all times usual, e.g., magnetotelluric field work would be hardly possible without changing polarization.

5 Man-made pulsations

Without speaking about the artificial generation of pulsations by radio waves, an interesting observation by Tsirs and Loginov (1985), who found a Thursday minimum in Pc 1 and Pi 2 activities, is mentioned here. They referred to Fraser-Smith and Roxburgh (1969) when they pleaded for a human origin of this weekly variation. A survey of the Nagycenk daily pulsation indices from 4 years between 1958 and 1984 (this index characterizes the daily average amplitude of pulsations, see e.g., Veró, 1981) indicated a Saturday maximum in all years (Fig. 19), deviating somewhat from Tsirs and Loginov's result; the Saturday peak is, however, significant at a 2% level. As the effect was present in 1958, and it was strongest from the years studied just then, it cannot be due to satellite transmissions.

6 Some recent observations of Pi 2 at low latitudes

The current wedge model (McPherron et al., 1973) has been accepted at least as a working hypothesis for the basis of the organization of Pi 2 observations at subauroral latitudes. The primary process is essentially short-circuiting the enhanced cross-tail current by field-aligned currents (FAC) and currents in the auroral ionosphere. The model offers a natural system of coordinates centered at the center of the current wedge and the width of the wedge between the upward and downward FAC is characterized by the values of $\Delta H=0$. An other local and substorm-centered system of coordinates can be deduced from the polarization pattern of Pi 2; Lester et al. (1983, 1984) have shown that the two systems coincide if there is no preexistent current system which would shift the two systems with respect to each other. If Pi 2 on a quiet background is selected, there then is seldom any difference between the two systems. In case of such events, Lester et al. (1983, 1984) found polar-

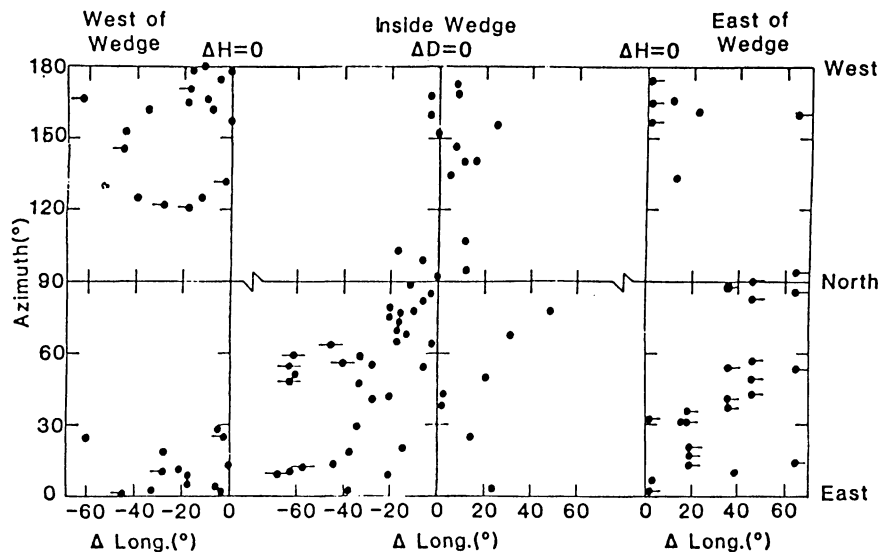


Fig. 20. Azimuth of the major axis of the horizontal polarization ellipse plotted against longitude for Pi 2. The left, center, and right panels correspond to points west, inside, and east of the wedge, respectively (Lester et al., 1983)

ization patterns and a number of other characteristics of Pi 2 which correspond to expectations on the basis of the current wedge model. Figure 20 is a summary of the results: it shows that the direction of the major axis of the polarization ellipse changes according to predictions within the wedge from E-W through the NE quadrant to N-S, then through the NW quadrant again to E-W, and the polarization is predominantly counterclockwise. This is confirmed by Lanzerotti and Medford (1984) who found constantly counterclockwise polarization at latitudinally spread stations. W of the wedge there are more cases in the NW quadrant, E of it in the NE quadrant, and the polarization is in the majority of cases counterclockwise here as well with more clockwise-polarized events than within the wedge. The angular azimuthal wave number indicated westward propagation with more exceptions occurring E of the wedge. Lester et al. (1984) interpreted the results as the consequence of the superposition of two circularly polarized waves propagating azimuthally in opposite directions with different amplitudes (Southwood and Hughes, 1985). These waves are generated by a partially reflecting boundary west of the model system. These surface waves would be responsible for the observed characteristics of Pi 2, e.g., the E-propagating wave (E of the wedge) is due to reflection from the western current. The eastern current causes less reflection as it is more distributed longitudinally.

Among the few features not explained by this model, the frequency changes in certain events are the most significant ones. They occur both inside and outside the wedge, and they can be explained by field line resonances or localized surface waves at the plasmapause.

As the sequence of events organized in the substorm-defined system of coordinates can be transferred into a local time-dependent system, even if the centers of substorms have rather great time spread, similar results are expected for the LT variations of the direction of the major axis of the polarization ellipse with the center of the substorm substituted by a LT around 23 h. This is in reality what was found by Lanzerotti and Medford (1984).

The westward travelling surge greatly modifies Pi-2 properties at auroral latitudes, but at lower latitudes less, as, for example, the counterclockwise polarization of Samson and Rostoker (1983) is shown to be in accordance with

the results of Lester et al. (1984). The former authors supposed a lower-latitude, second Pi 2 source region but they found only an increase in amplitudes toward the equator around 60° as no low-latitude stations were used. This increase leads sometimes to an amplitude maximum around 55° .

By comparing data from the AFGL network (the same, as used by Lester et al., 1983, 1984) with magnetospheric Pi 2, Singer et al. (1983) found that Pi 2 has much narrower occurrence in longitude (sometimes less than 30°) on synchronous orbit than on the ground (here up to 60°). They found a clear difference between low- and high-Kp situations, as in latter cases the events were quite often seen both at synchronous orbit and on the ground, while in quiet conditions only the ground stations experienced Pi 2. They supposed that the position of the source region (plasmashet) is responsible for this difference, and the inner edge is beyond synchronous orbit at low Kp. The difference in the longitudinal extent should be due to the transformation of low-amplitude compressional waves (below the detection limit) into resonant modes similarly to dayside Pc 3–4. Maltsev and Lyatsky (1984) computed a period of 100 sec for the surface wave on the plasmashet, corresponding to the typical period of Pi 2.

Sastry et al. (1983) identified daytime Pi 2 at Indian equatorial stations. The period of their cases, however, is shorter than normal Pi 2 periods, being around 30 sec.

The possibility that Pi 2 can trigger Pc 3–4 pulsations in the sunlit hemisphere has been suggested by Yanagahira and Shimazu (1966) and Holló and Veró (1970). Propagation is more likely toward the west, i.e., afternoon hours are more favorable for Pi 2-triggered Pc 3–4. These Pc 3–4 may be identical with Voelker's Pse (Pulsational single effects) (1962, 1963). Such "transformed" Pi 2 or Pse are amplified 1.5–3.5 times at equatorial latitudes relative to somewhat higher latitudes (Sastry et al., 1983).

The mentioned role of field line resonances in Pi 2 is also supported by the observation that noiselike, continuous Pi 2 may have smooth transitions both in morning and evening hours from/into Pc 3–4 (Veró, 1964).

As a conclusion, the problem of the generation of low-latitude pulsations seems to be near to a solution. There are, however, a number of problems which need further

experimental and theoretical work. Such problems are, for example, the conditions of the propagation of upstream waves through the magnetopause and the magnetosphere, the nature of low-latitude field line resonances and their changes, the form of the connection between frequency of pulsations and IMF B magnitude, the complex nature of ionospheric modification, and the postulated low-latitude additional source for Pi 2.

Acknowledgements. The author thanks all colleagues who helped him in writing this review by sending him recent papers in the form of manuscripts or preprints.

References

- Ádám, A., Cz.Miletits, J., Verő, J.: Das Mikropulsationsfeld in Osteuropa. *Acta Geod. Geoph. Mont. Hung.* **7**, 289–304, 1972
- Ansari, J.A., Fraser, B.J.: Spectral characteristics of low-latitude Pc 3 geomagnetic pulsation in South East Australia. IAGA Symposium, Prague, 1985a
- Ansari, J.A., Fraser, B.J.: Wave packet structure and phase jumps in low-latitude Pc 3 geomagnetic pulsations. IAGA Symposium, Prague, 1985b
- Baransky, L.N., Borovkov, J.E., Gokhberg, M.B., Krylov, S.M., Troitskaya, V.A.: High-resolution method of direct measurement of the magnetic field lines eigen frequencies. Manuscript. 1985
- Bolshakova, O.V., Troitskaya, V.A.: Connection of the IMF direction with the continuous pulsations (in Russian). *Dokl. AN SSSR* **180**, 343–346, 1968
- Cz.Miletits, J.: Microstructure of the latitude dependence of Pc-type pulsation periods. *J. Atm. Terr. Phys.* **42**, 563–567, 1980
- Doupnik, J.R., Brekke, A., Banks, P.M.: Incoherent scatter radar observations during three sudden commencements and a Pc 5 event on August 4, 1972. *J. Geophys. Res.* **82**, 499–514, 1977
- Fraser, B.J., Ansari, J.A.: The spatial characteristics of low-latitude Pc 3 geomagnetic pulsation. 7th Symp. on Coordinated Observations of the Ionosphere and the Magnetosphere in the Polar Regions, Tokyo, 1984
- Fraser-Smith, A.C., Roxburgh, K.B.: Triggering of hydromagnetic “whistlers” by sferics. *Planet. Space Sci.* **17**, 1310, 1969
- Gough, H., Orr, D.: The effect of damping on geomagnetic pulsation amplitude and phase at ground observatories. *Planet. Space Sci.* **32**, 619–628, 1984
- Green, G.A., Odera, T.J., Stuart, W.F.: The relationship between the strength of the IMF and the frequency of magnetic pulsations on the ground and in the solar wind. *Planet. Space Sci.* **31**, 559, 1983
- Gul’elmi, A.V.: Diagnostics of the magnetosphere and interplanetary medium by means of pulsations. *Space Sci. Rev.* **16**, 331, 1974
- Gul’elmi, A.V., Plyasova-Bakounina, T.A., Shchepetnov, R.V.: Relationship between period of geomagnetic pulsations Pc 3–4 and parameters of the interplanetary medium at the Earth’s orbit. *Geomagn. Aeron.* **13**, 331, 1973
- Holló, L., Verő, J.: Pi-triggered Pc pulsations. Fifteen Years Geodetical and Geophysical Research Laboratories of the Hungarian Academy of Sciences in Sopron, 53–63, 1970
- Holló, L., Verő, J.: On the immediate effect of cone angle changes on geomagnetic pulsations. *J. Atm. Terr. Phys.* **47**, 523–528, 1985a
- Holló, L., Verő, J.: One-year comparison of ATS and ground pulsation spectra. IAGA Symposium, Prague, 1985b
- Hoppe, M.M., Russell, C.T., Frank, L.A., Eastman, T.E., Greenstadt, E.W.: Upstream hydromagnetic waves and their association with backstreaming ion populations: ISEE-land 2 observations. *J. Geophys. Res.* **86**, 4471–4492, 1981
- Hughes, W.J., Southwood, D.J.: The screening of micropulsation signals by the atmosphere and ionosphere. *J. Geophys. Res.* **81**, 3234–3240, 1976a
- Hughes, W.J., Southwood, D.J.: An illustration of modification of geomagnetic pulsation structure by the ionosphere. *J. Geophys. Res.* **81**, 3241–3247, 1976b
- Janzerotti, L.J., Medford, L.V.: Local night, impulsive (Pi 2-type) hydromagnetic wave polarization at low latitudes. *Planet. Space Sci.* **32**, 135–142, 1984
- Janzerotti, L.J., Medford, L.V., MacLennan, C.C., Hasegawa, T., Acuna, M.H., Dolce, S.R.: Polarization characteristics of hydromagnetic waves at low geomagnetic latitudes. *J. Geophys. Res.* **86**, 5500–5506, 1981
- Lauthulliere, C., Glangaud, F., Lacoume, J.L., Lejeune, G.: Relationship between ionospheric electric field and ground magnetic pulsations in the Pc 3 domain at mid-latitude. *J. Geophys. Res.* **86**, 7669–7678, 1981
- Lester, M., Hughes, W.J., Singer, H.J.: Polarization patterns of Pi 2 magnetic pulsations and the substorm current wedge. *J. Geophys. Res.* **88**, 7958–7966, 1983
- Lester, M., Hughes, W.J., Singer, H.J.: Longitudinal structure in Pi 2 pulsations and the substorm current wedge. *J. Geophys. Res.* **89**, 5489–5494, 1984
- McPherron, R.L., Russell, C.T., Aubry, M.P.: Satellite studies of magnetospheric substorms on August 15, 1968. 9. Phenomenological model for substorms. *J. Geophys. Res.* **78**, 3131–3149, 1973
- Menk, F.W., Cole, K.D., Devlin, J.C.: Associated geomagnetic and ionospheric variations. *Planet. Space Sci.* **31**, 569–572, 1983
- Maltsev, Yu, P., Lyatsky, M.B.: Surface waves on the plasma sheet boundary. *Planet. Space Sci.* **32**, 1547–1549, 1984
- Odera, T.J.: Relationship between the period of ground pulsations and the period of pulsations in the solar wind. *Acta Geod. Geoph. Mont. Hung.* **19**, 297–304, 1984a
- Odera, T.J.: Control of the solar wind parameters on the ground Pc 3, 4 pulsations. *Acta Geod. Geoph. Mont. Hung.* **19**, 305–338, 1984b
- Odera, T.J., Stuart, W.F.: The relationship between the IMF magnitude and the frequency of Pc 3, 4 pulsations on the ground: simultaneous events. *Planet. Space Sci.* **33**, 387–393, 1985
- Plyasova-Bakounina, T.A.: Influence of magnetospheric convection upon the generation of pulsations. *Issled. po geomagn. aeron. i fiz. solntsa.* **70**, 144, 1985
- Plyasova-Bakounina, T.A., Troitskaya, V.A., Münch, J.W., Gauler, H.F.: Super-high-latitude maximum of Pc 2–4 intensity. *Acta Geod. Geoph. Mont. Hung.* **21**, 1985 (in press)
- Plyasova-Bakounina, T.A., Troitskaya, V.A., Stuart, W.F., Kharchenko, I.P.: Solar-wind-controlled Pc 3–4 micropulsations. *Issled. po geomagn. aeron. i fiz. solntsa.* **62**, 103, 1982
- Polyushkina, T.N., Potapov, A.S.: The relation of the amplitude of daytime geomagnetic pulsation to solar wind velocity over the scalar activity cycle. *Issled. po geomagn. aeron. i fiz. solntsa.* **66**, 54, 1983
- Poulter, E.M., Allan, W.: Transient ULF pulsation decay rates by ground based magnetometers: the contribution of spatial integration. *Planet. Space Sci.* **33**, 607–616, 1985
- Russell, C.T., Luhman, J.G., Odera, T.J., Stuart, W.F.: The role of occurrence of dayside Pc 3–4 pulsations: the L value dependence of the IMF cone angle effect. *Geophys. Res. Lett.* **10**, 663, 1983
- Saito, T.: Long-period geomagnetic oscillations in southern high latitudes. *Rept. Ionosph. Space Res. Japan* **18**, 173, 1964
- Samson, J.C., Rostoker, G.: Polarization characteristics of Pi 2 pulsations and implications for their source mechanisms: influence of the westward travelling surge. *Planet. Space Sci.* **31**, 435–458, 1983
- Sastry, T.S., Sarma, Y.S., Sarma, S.V.S., Sanker Narayan, P.V.: Day-time Pi pulsations at equatorial latitudes. *J. Atm. Terr. Phys.* **45**, 733–742, 1983
- Singer, H.J., Hughes, W.J., Fougere, P.F., Knecht, D.J.: The localization of Pi 2 pulsations. Ground-satellite observations. *J. Geophys. Res.* **88**, 7029–7036, 1983

- Southwood, D.J.: Wave generation in the terrestrial magnetosphere. *Space Sci. Rev.* **34**, 259–270, 1983
- Southwood, D.J., Hughes, W.J.: Concerning the structure of Pi 2 pulsations. *J. Geophys. Res.* **90**, 386–392, 1985
- Štřeštitk, J.: Connections between parameters of the interplanetary medium and geomagnetic activity. *Acta Geod. Geoph. Mont. Hung.* **19**, 415–420, 1984
- Stuart, W.F., Usher, M.J.: An investigation of micropulsations at middle latitudes. *Geophys. J.* **12**, 71, 1966
- Sutcliffe, P.R.: The spatial and temporal structure of low-latitude Pc 3 pulsation fields. IAGA Symposium, Prague, 1985
- Sutcliffe, P.R., Boshoff, B.F.V.: Local time and longitudinal variation of Pc 3 pulsation frequency. IAGA Symposium, Prague, 1985
- Sutcliffe, P.R., Poole, A.W.V.: Low-latitude Pc 3 pulsations and associated ionospheric oscillations measured by a digital chirp ionosonde. *Geophys. Res. Lett.* **11**, 1172–1175, 1984
- Takahashi, K., McPherron, L., Greenstadt, B.W., Neely, C.A.: Factors controlling the occurrence of Pc 3 magnetic pulsations at synchronous orbit. *J. Geophys. Res.* **86**, 5472–5484, 1981
- Takahashi, K., McPherron, R.L., Hughes, W.J.: Multispacecraft observations of the harmonic structure of Pc 3–4 magnetic pulsations. *J. Geophys. Res.* **89**, 6758–6774, 1984
- Tátrallyay, M., Verő, J.: Changes of geomagnetic micropulsations following sudden impulses. *J. Atmos. Terr. Phys.* **35**, 1507–1515, 1973
- Troitskaya, V.A., Bolshakova, O.V.: Hydromagnetic diagnosis of the non-homogeneous structure of the solar wind. *Acta Geod. Geoph. Mont. Hung.* **19**, 285–296, 1984
- Tsirs, G.P., Loginov, G.A.: Peculiarities of week variations of Pc 1 and Pi 2 geomagnetic pulsations. *Geomagn. i aeronom.* **25**, 165–166, 1985
- Varga, M.: A numerical study of the excitation of Pc 2–4 type pulsations. *J. Atmos. Terr. Phys.* **42**, 365–369, 1980
- Verő, J.: Geomagnetic pulsation. Dissertation, Sopron (in Hungarian), 1964
- Verő, J.: Geomagnetic pulsations around impulses. *Acta Geod. Geoph. Mong. Hung.* **10**, 247–253, 1975
- Verő, J.: Geomagnetic pulsations and parameters of the interplanetary medium. *J. Atmos. Terr. Phys.* **42**, 371–380, 1980
- Verő, J.: Changes of pulsation activity during two solar cycles. *J. Atmos. Terr. Phys.* **43**, 919–926, 1981
- Verő, J., Holló, L.: Connections between interplanetary magnetic field and geomagnetic pulsations. *J. Atmos. Terr. Phys.* **40**, 857–865, 1978
- Verő, J., Menk, F.W.: Damping of geomagnetic Pc 3–4 pulsations at high F2-layer electron concentrations. *J. Atmos. Terr. Phys.* **48**, 231–243, 1986
- Verő, J., Holló, L., Potapov, A.S., Polyushikina, T.N.: Analysis of the connections between solar wind parameters and dayside geomagnetic pulsations based on the data of the observatories Nagyecen (Hungary) and Uzur (USSR). *J. Atmos. Terr. Phys.* **47**, 557–565, 1985
- Voelker, H.: Zur Breitenabhängigkeit der Perioden erdmagnetischer Pulsationen. *Naturwissenschaften* **49**, 8, 1962
- Voelker, H.: Zur Breitenabhängigkeit erdmagnetischer Pulsationen. *Mitteilungen aus dem Max-Planck-Institut für Aeronomie*, 11, 1963
- Walker, A.D.M., Greenwald, R.A., Stuart, W.F., Green, C.A.: STARE auroral radar observations of Pc 5 geomagnetic pulsations. *J. Geophys. Res.* **84**, 3373–3388, 1979
- Wolfe, A., Meloni, A., Lanzerotti, L.J., MacLennan, C.G., Bamber, J., Venkatesan, D.: Dependence of hydromagnetic energy spectra near $L=2$ and $L=3$ on upstream solar wind parameters. *J. Geophys. Res.* **90**, 5117–5131, 1985
- Yanagahira, K., Shimazu, N.: Equatorial enhancement of micropulsation Pi 2. *Mem. Kakioka Magn. Obs.* **12**, 57–63, 1966
- Yumoto, K.: Low-frequency upstream wave as a probable source of low-latitude Pc 3–4 magnetic pulsations. *Planet. Space Sci.* **33**, 239–249, 1985a
- Yumoto, K.: Theoretical considerations on low-latitude magnetic pulsations. IAGA Symposium, Prague, 1985b
- Yumoto, K., Saito, T., Tsurutani, B.T., Smith, E.J., Akasofu, S.-I.: Relationship between the IMF magnitude and Pc 3 magnetic pulsations in the magnetosphere. *J. Geophys. Res.* **89**, 9731–9740, 1984
- Yumoto, K., Saito, T., Tanaka, Y.: Low-latitude Pc 3 magnetic pulsations observed at conjugate stations ($L \sim 1.5$). *J. Geophys. Res.* **90**, 12201–12208, 1985

Received November 22, 1985; revised March 28, 1986;
Accepted July 18, 1986

*Original investigations***GRF broad-band array analysis of the 1982 Miramichi, New Brunswick earthquake sequence***P.W. Basham¹ and R. Kind²¹ Geophysics Division, Geological Survey of Canada, 1 Observatory Cr., Ottawa, Canada K1A 0Y3² Seismologisches Zentralobservatorium Gräfenberg, Krankenhausstraße 1–3, 8520 Erlangen, Federal Republic of Germany

Abstract. Digital broad-band seismic data from the Gräfenberg array station (GRF) in southern Germany and reflectivity-method theoretical *P*-wave modelling place new constraints on focal depth and mechanism dip of the four principal 1982 Miramichi, New Brunswick, Canada, earthquakes. Relying on previous information for the choice between conjugate dip directions, the m_b 5.7 mainshock is confirmed to have occurred at a depth of 7 km with an average westward dip of about 60°. It was preceded by 0.9 s by a precursory rupture of about m_b 5.2. The first large aftershock (m_b 5.1) occurred at a depth of 6 km and average dip 55° in the region of the lower portion of the mainshock rupture. The largest aftershock (m_b 5.4), confined to the conjugate, east-dipping plane, ruptured from a depth of 6 km with an average dip of 50°. The third large aftershock (m_b 5.0) occurred in the shallow region of the mainshock with a depth of about 3.5 km and 50° dip. Broad-band array data prove very useful for even the smallest events in this sequence, and waveform modelling of such data provides close constraints on some source parameters. In the case of the Miramichi earthquakes there is good resolution on depth (± 1 km) and dip ($\pm 10^\circ$), but little resolution on rake and strike.

Key words: New Brunswick, Canada, earthquakes – Thrust faulting – Gräfenberg array – Reflectivity method – Theoretical seismograms

Introduction

The m_b 5.7 mainshock that occurred on 9 January 1982 at 12:53 in the Miramichi region of north-central New Brunswick, Canada (Fig. 1), was the largest historical earthquake in New Brunswick and the largest earthquake in eastern Canada since the Cornwall-Massena earthquake of 1944. The mainshock was followed by an extensive aftershock sequence with principal aftershocks on 9 January at 16:36 (m_b 5.1), 11 January at 21:41 (m_b 5.4) and 31 March at 21:02 (m_b 5.0). Wetmiller et al. (1984) have presented an extensive analysis of the earthquake sequence, based mainly on field recordings of aftershocks. Choy et al. (1983) have determined the source characteristics of the mainshock from recordings of the Global Digital Seismo-

graph Network. Basham and Adams (1984) have presented some speculations on the types of fault systems in the upper crust that may be responsible for the earthquakes in the presence of an east-west horizontal stress regime. Mueller and Cranswick (1985), Saikia and Herrmann (1985) and Cranswick et al. (1985) have presented analyses of some of the smaller aftershocks in the Miramichi sequence.

We will begin this analysis from the basis of the conceptual model of the four principal shocks (Fig. 2) developed by Wetmiller et al. and discussed further by Basham and Adams. Briefly, the hypothesis is as follows. The mainshock of m_b 5.7 was a thrust mechanism with rupture up-dip on a west-dipping plane from a depth of about 7 km. This was followed 3.5 h later by the m_b 5.1 aftershock, located somewhere on or near the lower portion of the mainshock rupture surface. The m_b 5.4 aftershock ruptured, probably up-dip, the conjugate east-dipping plane 2.5 days later. And finally, 2.5 months later, the m_b 5.0 aftershock occurred somewhere on or near the upper portion of the mainshock rupture surface.

As indicated by Wetmiller et al. (1984), not all aspects of this hypothesis are yet proven by available data. The general characteristics of the mainshock are not in doubt and there is convincing evidence that its rupture surface steepens as it approaches the surface. There is also a suggestion (Choy et al., 1983) that the main rupture was a double event with the crack growth momentarily interrupted by a fracture barrier. There is no good independent evidence for the location of the m_b 5.1 aftershock; its speculated location in the region of the lower portion of the main rupture is a convenience, given the shallow occurrence of the m_b 5.0 aftershock. The principal evidence for a conjugate rupture by the m_b 5.4 event came from the aftershock distribution in the early days of the field monitoring (following this event) which showed most of the smaller aftershocks scattered about this east-dipping plane. The location of the m_b 5.0 aftershock is inferred from a concentration of smaller aftershocks in the shallow, northeastern portion of the active zone established by field observations for a few days following this event.

It is this hypothesis of the characteristics of the four principal Miramichi earthquakes that we wish to assess using the broad-band Gräfenberg (GRF) array data and theoretical waveform modelling. In particular, we wish to establish the constraints that can be put on the focal depths and mechanism orientations of these closely spaced, moderate magnitude earthquakes using broad-band data from a teleseismic array and associated modelling.

* Geological Survey of Canada Contribution Number 19386

Offprint requests to: R. Kind

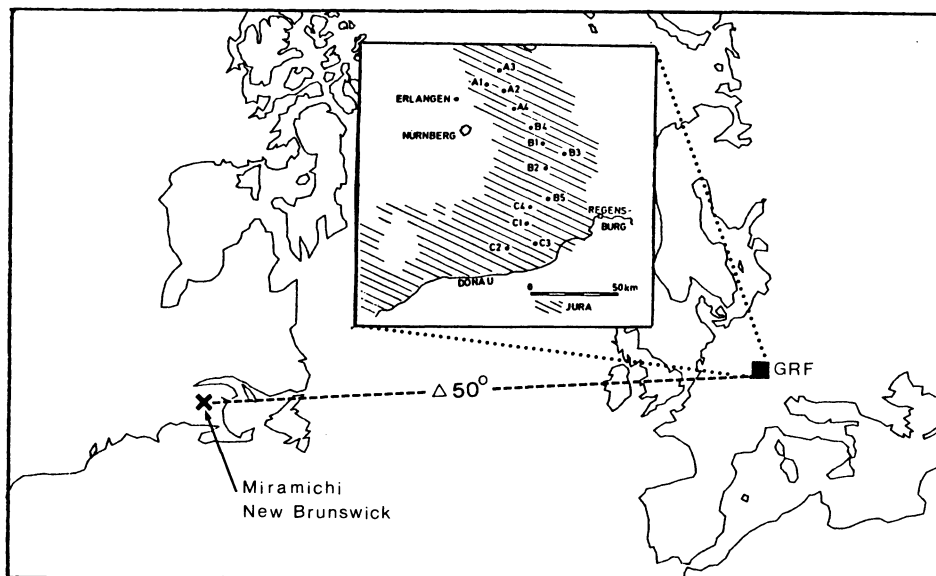


Fig. 1. Location map showing the epicentre of the Miramichi, New Brunswick, earthquakes in eastern Canada and the GRF array in southern Germany (epicentral distance 50°). The configuration of the GRF array is shown in the inset

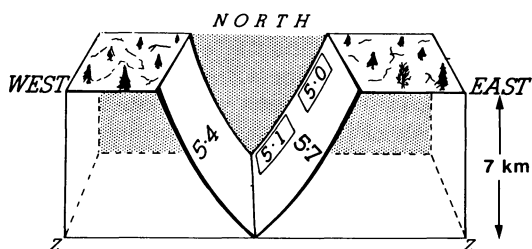


Fig. 2. Perspective view of the suggested orientations of the Miramichi mainshock (m_b 5.7) and its three main aftershocks. (After Basham and Adams, 1984.)

The GRF array and data processing

The 13-element broad-band GRF array in northern Bavaria, FRG, has an aperture of about $40 \times 100 \text{ km}^2$ (see inset in Fig. 1). The 13 elements have vertical, and 3 have horizontal, broad-band Wielandt seismometers with a flat velocity response between 20 s and 5 Hz. The dynamic range of the data acquisition system is 132 dB and the resolution is 66 dB. A complete description of the array is given by Harjes and Seidl (1978). Data from the array can be studied using simulations of different seismograph responses (broad-band displacement, SRO, WWSSN, LRSM, etc.) in order to enhance particular characteristics of waveforms (Seidl, 1980; Seidl and Stammer, 1984).

GRF data has been successfully applied in studies of: regional body waves and source properties (Kind, 1979a, 1981; Räckers and Müller, 1982; Seidl and Berckhemer, 1982; Zonno and Kind, 1984; Faber and Bonjer, 1985; Barbano et al., 1985), regional surface waves (Brüstle and Müller, 1983; Hanka, 1982) and teleseismic body waves (Upadhyay and Duda, 1980; Kind and Seidl, 1982; Brüstle, 1985; Engdahl and Kind, 1986). Many of these have been single array-station (GRF) studies of particular earthquakes and earthquake sequences.

GRF recordings of the Miramichi events

Figure 3 shows all available GRF vertical broad-band velocity recordings of the Miramichi mainshock. The SUM

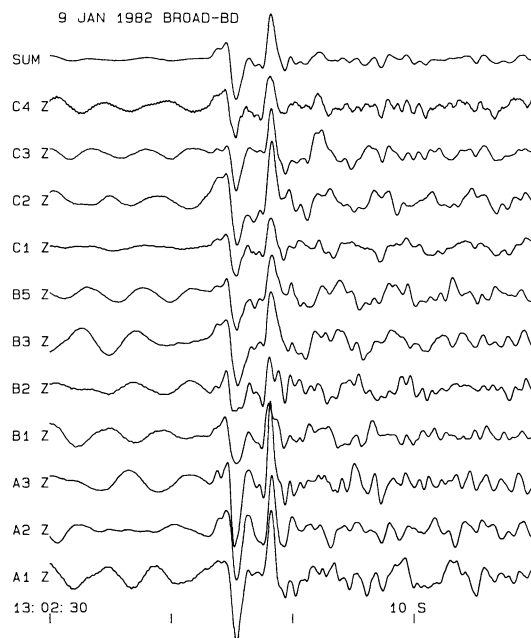


Fig. 3. Broad-band velocity recordings from the 11 available channels of the GRF array for the Miramichi mainshock P wave. The SUM trace at the top is produced by delay and sum of the 11 channels for an azimuth of 294° and a slowness of 7.3 s/deg. Tick marks on the time axis are every 10 s

trace shown at the top was produced by fitting a plane-wave arrival to picks of the first major through on the 11 channels. Considerable variations in amplitude, but not in general pulse characteristics, are seen across the array. Sub-array A generally records the largest amplitudes for this event; sub-arrays B and C are more variable in amplitude across the sub-arrays. Station B2 shows signal characteristics that differ most from "average" signal characteristics shown in the SUM trace. Nevertheless, the important characteristics seen in the SUM trace can be seen in each individual channel, confirming that these are produced by near-source effects and not by near-station effects.

Therefore, the Miramichi mainshock broad-band velocity recorded at GRF can be characterized by two large velo-

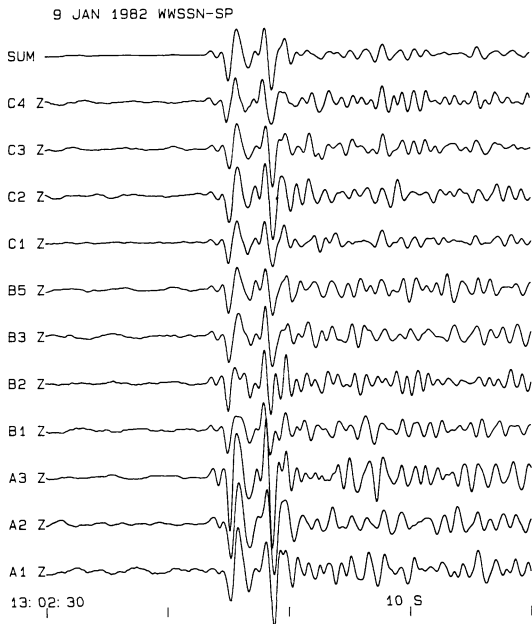


Fig. 4. As in Fig. 3 with a WWSSN-SP filter

city pulses of equal amplitude and opposite sign separated by about 3 s. Each of these pulses is preceded by a precursor pulse producing a flattening in the onsets of the main pulses. The second main pulse has been interpreted by Choy et al. (1983) as *sP*. (Choy et al. used the A3 record in their body-wave modelling.) They also interpreted the precursor as a momentary stopping of crack growth by a fracture barrier, which then failed producing the main rupture event. Both of these interpretations will be treated below as part of the theoretical modelling.

The simulated WWSSN-SP response to the mainshock is shown in Fig. 4. All important characteristics of the *P* wave are preserved with this narrower band filtering, indicating that the dominant energy falls within the WWSSN-SP passband. The two main pulses are very clear and the precursors to the main pulses are somewhat enhanced over what can be observed in the broad-band recordings.

SUM recordings of broad-band velocity and WWSSN-SP for the mainshock and three aftershocks are shown in Figs. 5 and 6, respectively. The 11 January aftershock,

smaller than the mainshock by 0.3 m_b units, has a lower signal-to-noise ratio on the broad-band SUM (Fig. 5). Nevertheless, it is clear that the *P*-wave group for this event differs significantly from that of the mainshock. It is a single velocity wavelet followed by higher frequency energy superimposed on a broader pulse. The broader secondary pulse may be source-generated, but may also be due to a partially coherent microseism cycle that is retained in the SUM. With the WWSSN-SP filter (Fig. 6), the secondary energy after the first pulse appears as ringing with a period of about 0.9 s. Explaining the difference between this aftershock, believed to be the principal rupture on the conjugate fault plane, and the mainshock is one of the principal tasks of the modelling described below.

The two smaller aftershocks (9 January, m_b 5.1, and 31 March, m_b 5.0) have poor long-period signal-to-noise ratio in the broad-band SUM (Fig. 5), although the SUM has significantly improved the signal-to-noise ratio over that available on a single channel. This illustrates the advantage of a broad-band array over a single station in studies of moderate magnitude earthquakes. The differences among the four events are seen most clearly with the WWSSN-SP filter. The signals in Fig. 6 are aligned on the first major trough, which is a common feature of the four *P* waves. The amplitudes of the three aftershocks relative to the mainshock have been scaled by the factors shown in the figure. The 9 January aftershock has a second strong velocity pulse, but it precedes the second pulse of the mainshock (the trough of which is shown by line segments) by about 0.8 s. The 31 March aftershock has no strong secondary pulse and little energy above the background noise level in this time period. These two aftershocks are speculated to be on the lower and upper portions, respectively, of the mainshock fracture surface. We also address this question with modelling below.

Theoretical seismograms

The reflectivity method for computing theoretical seismograms was developed by Fuchs (1968) and Fuchs and Müller (1971). Kind (1978, 1979b) developed a version of the method for the computation of complete earthquake seismograms, and extended the method to allow the computation of complete body waves for different source and re-

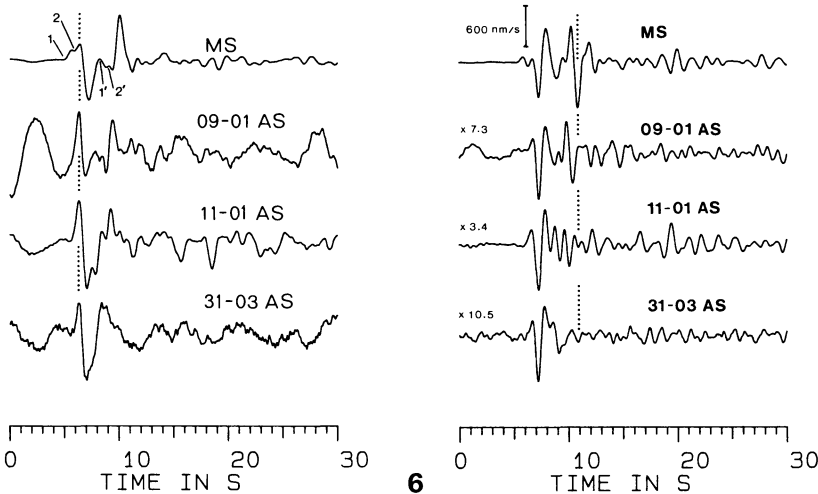


Fig. 5. Broad-band velocity SUM seismograms for the Miramichi mainshock (MS) and three aftershocks (AS). The signals have been aligned on the first major peak. The principal phases identified for the mainshock are: 1, *P* wave of precursor; 2, main *P* wave; 1', possible *sP* of precursor; 2', *sP*

Fig. 6. WWSSN-SP SUM seismograms for the mainshock (MS) and three aftershocks (AS). The signals have been aligned on the first major trough. Vertical line segments are shown at the time of the second major trough of the mainshock. Signals are plotted with equal maximum amplitudes. Vertical bar above first record shows amplitude scale. Plot scaling factors are shown for the subsequent events

ceiver structures (Kind, 1985). The latter version of the method is used here to model the Miramichi earthquake P waves.

The source is a dislocation double-couple point source whose orientation is defined by the three angles, strike (ϕ), dip (δ) and slip (or rake, λ). The source time function used is that of Brüstle and Müller (1983) in which the moment function describes a smooth increase to the final moment during the rise time T . The corresponding far-field displacement, the only function actually employed in the modelling described here, is a simple single-sided pulse with duration T . Brüstle and Müller have emphasized that in this representation T has nothing to do with the rise time of the dislocation on the rupture surface. Neither are we concerned with the absolute amplitude of the pulse, the final moment, as we do not attempt to model moment estimates for these earthquakes. In the principal modelling we will vary the three source orientation angles and focal depth to attempt to match observed signals.

The rise time, T , is varied in the initial modelling until a reasonable fit of the pulse width is achieved in a long-period component (e. g. broad-band displacement). Short-period seismograms are then checked to see if this value of T produces appropriate higher frequency energy. If not, the value of T is decreased, i. e. the equivalent corner frequency of the source spectrum is increased, until a reasonable short-period match is achieved. This does not give a high degree of resolution on T , but appropriate values were found to be 1.5 s for the mainshock and 1.0 s for the three aftershocks. These values have been used for the theoretical seismograms described below.

The Miramichi earthquakes occurred in a massive granite pluton. The source crust is modelled with a simple single-layer crust 36 km thick with a P -wave velocity of 6.2 km/s over an 8.2-km/s upper mantle. S -wave velocities are scaled from the P -wave velocities by dividing by the square root of 3. The artificial interface between the source region and the mantle (and between the receiver region and the mantle) required by the method (see Kind, 1985) is at a depth of 100 km. The Jeffreys-Bullen mantle model is used.

The receiver crust is a simplified model of the crust under GRF. It consists of a 30-km-thick layer with a P -wave velocity of 6 km/s over an 8-km/s upper mantle. The GRF array is underlain by Mesozoic sediments with a P -wave velocity of about 3.5 km/s whose thickness varies from about 300 m at stations in the south to about 2 km at stations in the north. The differences in sediment thickness and structure of the crust produce the different signal characteristics seen across the array (Figs. 3 and 4). For comparison with theoretical seismograms we will use the SUM signals, which in a gross manner average out the crustal differences across the array. Once a reasonable match to the mainshock signal was obtained with no surficial sediments in the GRF crust, experiments were undertaken to assess the influence on the theoretical seismograms of sediment thicknesses up to 2 km. It was found that up to 500 m of sediments produced no discernable difference in the theoretical seismograms: 1 km of sediments introduced additional high-frequency energy into the signals; and 2 km of sediments tended to attenuate the high-frequency energy. The 1-km sedimentary layer, which is a reasonable average for the sediment thickness across the array, produced the greatest improvement in the match with observed broad-band and WWSSN-SP filtered SUM signals.

Therefore, 1 km of 3.5-km/s sediments was added to the final GRF receiver crust.

Clearly, there is a trade-off between the energy content as a function of frequency introduced into the theoretical seismograms by the assumed source spectrum and by the model for the GRF crust (as well as by the attenuation over the whole travel path). The overall model is therefore not unique and we should not expect to model minor observed signal characteristics and attribute them to the source.

The method used here cannot give diagnostic information on the actual plane of rupture. For thrust faults, conjugate east- and west-dipping mechanisms have identical radiation patterns, and therefore produce identical theoretical seismograms, for complementary values of dip angle. The modelling cannot distinguish between, for example, a 60° east-dipping and a 30° west-dipping pure thrust for any values of strike. Therefore, the choice between the conjugate east- or west-dipping ruptures must be constrained by other information, and we will rely mainly on the earlier results of Wetmiller et al. (1984) and Choy et al. (1983) in choosing between conjugate mechanisms.

Results and discussion

Mainshock

The general characteristics of the mechanism of the mainshock established by Wetmiller et al. (1984) and Choy et al. (1983) were a west-dipping thrust with approximately north-south strike. The starting model for the theoretical seismograms was therefore a pure thrust ($\lambda = 90^\circ$) with south strike ($\phi = 180^\circ$) and dip of 45° to the west ($\delta = 45^\circ$). In addition to focal depth (h) governing the delay times of the depth phases pP and sP , initial modelling indicated that the relative amplitudes of pP and sP were sensitive to the dip angle and, once sP is established as the dominant depth phase, its amplitude relative to P is sensitive to rake and strike. It is apparent, however (Figs. 3 and 4), that the precursor is causing some destructive interference with the two main velocity pulses of the mainshock. This suggests that unless we attempt to account for the influence of the precursor, we cannot rely too heavily on the relative amplitudes of P and the depth phase. Therefore, again using a preliminary result for the mainshock, we undertook experiments to simulate the precursor.

If we accept the assumption that the precursor is the initial rupture momentarily stopped by a barrier, it will have a signal character similar to the main rupture but reduced in amplitude and advanced in time. This was simulated by taking the theoretical seismogram of the mainshock and adding to it the same seismogram reduced in amplitude and advanced in time, with a number of trial amplitude reductions and time shifts. This implicitly assumes that the precursor and main rupture occurred at the same hypocentre, which is physically unrealistic, but has no influence on producing a P -wave signal appropriate for the precursor. The results suggest an amplitude of 0.3 and a time advance of 0.9 s for the precursor. The amplitude ratio indicates that the precursory rupture is about 0.5 m_b units smaller than the main rupture. This simulated precursor has been added to all of the theoretical mainshock seismograms discussed below.

We present the modelling results (Fig. 7) with three of

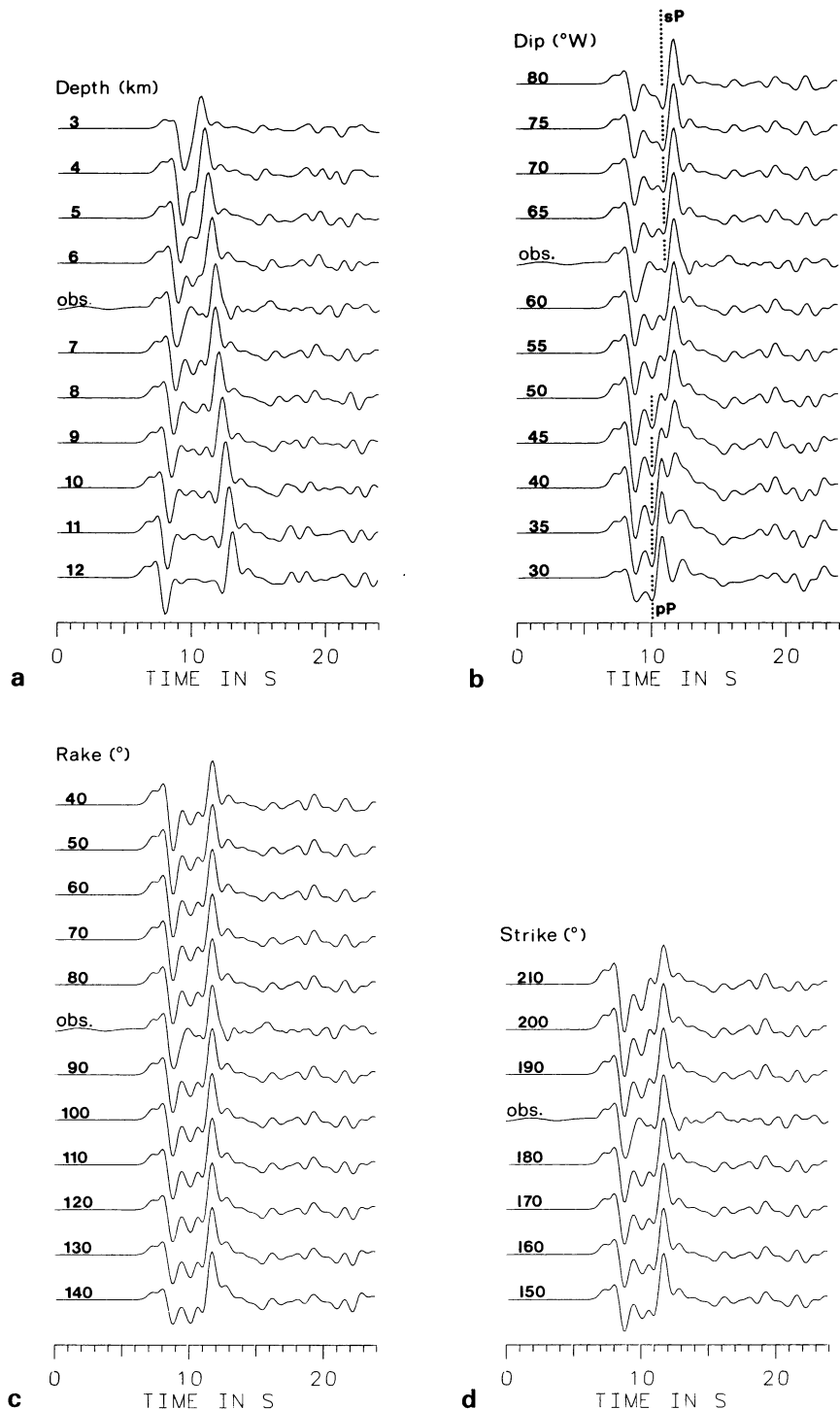


Fig. 7 a–d. Theoretical broad-band velocity seismograms for the mainshock, including the precursor with amplitude 0.3 of the main rupture and time advance of 0.9 s. Adopted parameters are $h = 7$ km, $\delta = 60^{\circ}$ west, $\lambda = 90^{\circ}$ and $\phi = 180^{\circ}$. The theoretical seismograms are shown with variable **a** depth, **b** dip, **c** rake and **d** strike with the other three parameters fixed at their adopted values. The observed seismogram (obs.) is superimposed above the theoretical seismogram with the appropriate value of the varying parameter

the four parameters (h , δ , λ , ϕ) fixed at their final values with the other varying over a fairly wide range to show its influence. Note that in each of the theoretical seismograms a precursor has been added as described above, assuming that in each model variation the precursor and the main rupture have the same model parameters.

In Fig. 7a, the effect of focal depth on the arrival time of *sP* is obvious. The time difference between the positive *P* and *sP* peaks in the observed seismogram matches exactly the time difference in the theoretical seismogram for a depth of 7 km. This time difference is about 0.5 s too small for

$h = 6$ and 0.5 s too large for $h = 8$. Therefore, we suggest the resolution of focal depth is better than 1 km. Although Wetmiller et al. (1984) estimated a mainshock depth of 7 km based on aftershock distribution and surface-wave analysis, Choy et al. (1983) established a depth of 9 km. We believe that Choy et al. have over-estimated the depth by measuring the time interval from the onset of the precursor (rather than the main pulse) to the onset of the main depth phase pulse; i. e. their *sP*-*P* and *pP*-*P* intervals are about 1 s too large. It is possible in these data (see mainshock in Fig. 5) to also identify what may be the precursor

to sP , which makes the correspondence between the principal P and sP pulses very clear.

Figure 7b shows that the amplitudes of pP and sP are significantly affected by the dip angle. The amplitudes of the two depth phases are approximately equal for $\delta=45^\circ$; pP dies out for steeper dips, sP for shallower dips. The simple double-pulse nature of the observed seismogram can best be matched by sP for dip in the range 50° – 70° . For dips less than 50° , the waveform match deteriorates because of the emergence of pP ; for dips greater than 70° , the theoretical sP pulse is too strong relative to P . A single pP depth phase would be produced with the appropriate time delay with greater focal depth and shallower dip, but the theoretical seismograms show that this would be near a node for P . We have adopted $\delta=60^\circ$, and suggest a resolution of about 10° on this angle.

From composite P -nodal solutions of small aftershocks, Wetmiller et al. showed that both the west- and east-dipping rupture surfaces steepen as they approach the surface. For the west-dipping surface the dip is about 50° at depth and about 77° near the surface. Choy et al. (1983) estimated a dip of 65° for the mainshock from analysis of relative amplitudes and polarities of direct P and surface reflections. Wetmiller et al. (1984) estimated a dip of 47° – 53° from P first motions. For an up-dip rupture, the mainshock first motions should be representative of the (smaller) dip at depth. The theoretical seismograms produced here with a point-source model of the rupture can be expected (like the Choy et al. analysis) to be indicative of only the average dip of the rupture surface.

Figure 7c shows that the theoretical seismograms are not very sensitive to quite large variations in the rake angle. For λ near 140° , the relative amplitude of sP appears too large. For λ between 40° and 100° , the match with the observed seismogram is considered equally good. We have adopted $\lambda=90^\circ$ (i. e. pure thrust) but do not claim to have much resolution on this angle. [Wetmiller et al. (1984) estimated a rake of 120° ; Choy et al. (1983), a rake of 65° .] Figure 7d shows that the theoretical seismograms are not very sensitive to strike. The relative amplitude of sP is too large for strikes near 150° and too small near 210° . The match is considered equally good for strikes in the range 170° – 200° . Both Wetmiller et al. and Choy et al. found values of $\phi=195^\circ$. We have adopted a value of $\phi=180^\circ$ (i. e. north-south).

The final results for the mainshock are shown in Fig. 8 for the broad-band, WWSSN-SP and displacement passbands. The final match achieved with the broad-band and WWSSN-SP filters is considered very good. It was found during the experiments with the GRF sedimentary layer described earlier that the match of the theoretical and observed signals with the displacement passband could be improved from that shown if we included 2 km of GRF sediments, i. e. removed some of the high-frequency energy; but this worsened the match in the broad-band and WWSSN-SP passbands. This is an indication of the non-uniqueness of the overall model (source, attenuation and GRF crust) in introducing frequency content into the theoretical seismograms.

11 January aftershock

The principal difference from the mainshock seen in the observed seismograms of the 11 January aftershock is a

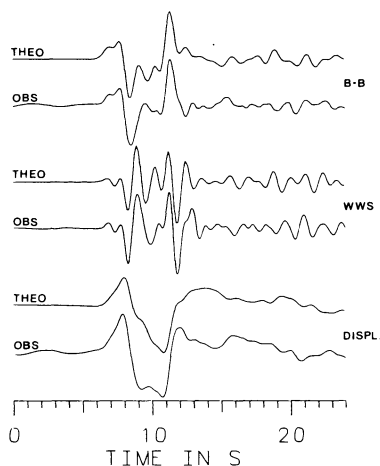


Fig. 8. Comparison of final mainshock theoretical seismograms (Theo.) with observed signals (Obs.) in the broad-band, WWSSN-SP and displacement passbands

“ringing”, or interference pattern, following the main P pulse, seen best in the WWSSN-SP seismograms (Fig. 6), and the absence of a clear depth phase. As indicated above, the theoretical seismograms cannot distinguish between complementary values of east and west dip angles. Therefore, we restrict the modelling to eastward dip on the basis of the convincing east-dipping trend of small aftershocks shown by Wetmiller et al. (1984). The goal of the modelling is to find appropriate values of focal depth and average dip angle for this aftershock.

Choy et al. studied the seismogram at one station (ZOBO) for this event, at an azimuth that showed a depth phase interpreted as pP indicating a focal depth of 6 km. Therefore, the starting model for the theoretical seismograms was an east-dipping pure thrust ($\phi=0^\circ$, $\lambda=90^\circ$) at a depth of 6 km. The theoretical seismograms are compared with the observed signals in Fig. 9. Figure 9a shows an effect of dip on the theoretical seismograms opposite to that seen for the mainshock in Fig. 7b. For the east-dipping rupture, pP is strong for large values of dip and sP strong for small values of dip. The first cycle of the observed signal is matched well by the theoretical seismograms with dip in the range 30° – 50° . The second part of the signal is matched best for dip in the range 45° – 55° , where the interference between pP and sP seems to be the strongest. We have adopted a dip of 50° and suggest a resolution of about 10° .

Figure 9b, computed for a dip of 50° , shows the effect of focal depth and confirms that a depth of 6 km is appropriate for this aftershock. However, with the lack of a clear depth phase among the ringing signal, there is no clear time delay on which to base a resolution on depth. Comparison of Figs. 9a and 9b shows that the characteristics of pP - sP interference change quite appreciably over small ranges of both dip and focal depth. Therefore, different combinations of the two could produce an equivalent match with the observed signals. As was found for the mainshock, the theoretical seismograms for this aftershock provide little resolution on rake or strike, and we have retained pure thrust with north strike.

This ringing, or interference phenomenon, now attributed to interference of pP and sP which have similar amplitudes for this dip, was seen most clearly in the WWSSN-SP

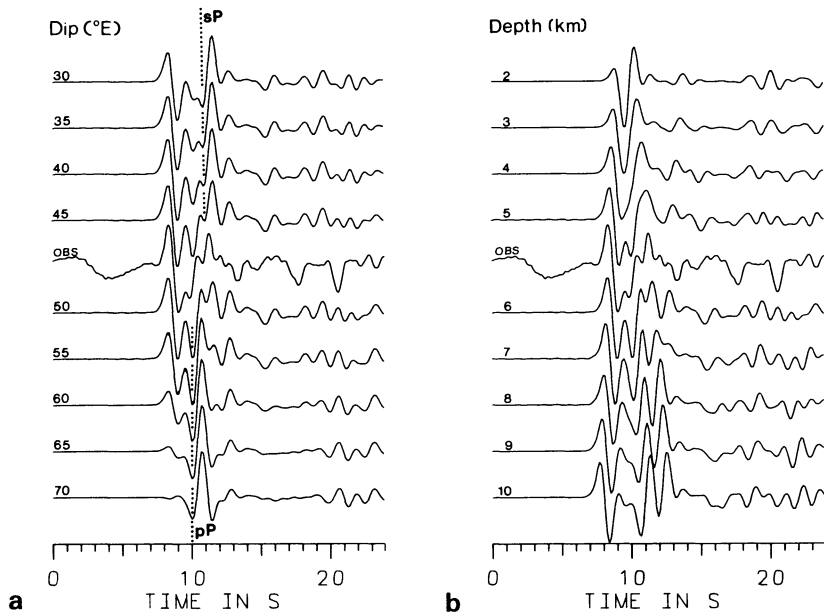


Fig. 9 a and b. Theoretical broad-band velocity seismograms for the 11 January aftershock: **a** with variable eastward dip for a depth of 6 km; **b** with variable depth for an eastward dip of 50°. The observed seismogram (obs.) is superimposed above the theoretical for dip = 50° and depth = 6 km

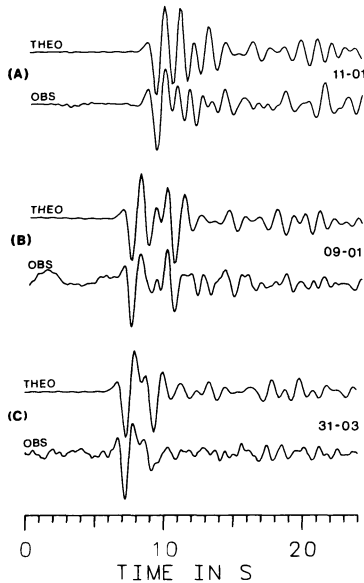


Fig. 10 a–c. Theoretical (*upper*) and observed (*lower*) WWSSN-SP filtered seismograms for the 11 January, 9 January and 31 March aftershocks. **a** The 11 January theoretical seismogram is computed for a focal depth of 6 km and eastward dip 50°, **b** the 9 January seismogram for depth 6 km and westward dip of 55° and **c** the 31 March seismogram for depth 3.5 km and westward dip 50°

filtered signal (Fig. 6). The WWSSN-SP filtered theoretical seismogram is compared with the observed signal in Fig. 10a. The match is reasonable, but the ringing phenomenon is too strong in the theoretical seismogram. In retrospect, this difference is apparent in the broad-band seismograms in Figs. 9a and b. The observed seismogram seems to have a low-amplitude ringing superimposed on a long-period signal, which may be a half cycle of the long-period noise seen in front of the *P* onset to be quite strong. In any case, with the model variations that we have tested, we cannot improve on this match of the short-period ringing phenomenon.

9 January and 31 March aftershocks

The general character of the signal of the 9 January aftershock is very similar to that of the mainshock, i. e. two simple velocity pulses representative of direct *P* and a depth phase (e. g. Fig. 6). This suggests a very similar mechanism, with a small difference in focal depth. The 31 March aftershock exhibits no clear depth phase. However, the spatial clustering of small aftershocks in the shallow region of the west-dipping rupture following this event, shown by Wetmiller et al., is sufficient evidence to also confine this aftershock to the shallow region of the west-dipping rupture. The modelling for these two events, therefore, becomes an attempt to independently determine focal depth and source orientation with west dip.

As was illustrated for the mainshock described above, the theoretical seismograms are not sensitive to quite large variations in rake and strike. Therefore, these two aftershocks are also assumed to be pure thrust on south-striking, west-dipping faults, and the model variations are made only for dip and focal depth. Dip controls the relative amplitudes of *P* and *sP* and depth the delay time of *sP*. Iterations of these two model parameters have produced the theoretical seismograms that are compared with the WWSSN-SP filtered signals in Fig. 10b and c. The agreement achieved for the 9 January aftershock with a dip of 55° and focal depth of 6 km is quite good. The resolution of dip is about 10° and of depth less than 1 km. Although in this study we cannot provide new information on the absolute locations of these aftershocks, this result confirms the speculation by Wetmiller et al. that the 9 January aftershock was located near the lower portion of the mainshock rupture surface.

The result for the 31 March aftershock with a depth of 3.5 km and dip of 50° is also quite good. The character of the theoretical seismograms following the first full cycle is very sensitive to small changes in depth and dip. And although there is a trade-off between these two parameters over small ranges, they cannot be significantly different from the adopted ones. The main difference between the two signals is the somewhat stronger negative depth phase

pulse in the theoretical seismogram. Therefore, even for this, the shallowest of the aftershocks, we suggest a depth resolution of less than 1 km and dip resolution of about 10°. The result is in good agreement with the results from smaller aftershocks shown in Fig. 15 of Wetmiller et al. (1984): the hypocentres are clustered at depths less than 3.5 km and their composite mechanism has a dip of 49°.

Conclusions

This analysis of the four principal Miramichi, New Brunswick, earthquakes using GRF broad-band data and reflectivity-method theoretical seismograms has produced results that are consistent with the conceptual model for these earthquakes developed by Wetmiller et al. (1984) and Choy et al. (1983). In a number of aspects the analysis has strengthened the previous suggestions. The prior knowledge of the thrust mechanisms due to east-west compressive stress has enabled us to converge on acceptable theoretical seismograms without sampling the entire parameter space of the four parameters depth, dip, rake and strike. Prior information on dip direction enabled estimates of focal depth and average dip angle from theoretical seismograms, which otherwise would be ambiguous with respect to complementary dip angles for opposite dip directions.

The general characteristics of the mainshock were not previously in doubt. The theoretical seismograms match the GRF recordings best for a focal depth of 7 km and average westward dip of 60°. Pure thrust with north-south strike has been adopted, but this single-station analysis provides little constraint on the source parameters (for all four events). In fact, the lack of influence of strike and rake (within reasonable bounds) on the theoretical seismograms gives us more confidence in the determination of average dip angles, to which the waveforms are quite sensitive. The suggestion by Choy et al. that the initial rupture was momentarily stopped by a fracture barrier is supported by modelling which indicates that a precursory rupture about 0.5 m_b units smaller preceded the main rupture by about 0.9 s.

The 9 January aftershock, the previously most uncertain of the four, is confirmed to have occurred in the region of the lower portion of the mainshock rupture. It has a well-constrained focal depth of 6 km and an average westward dip of about 55°. The 11 January aftershock, confined by other information to the east-dipping rupture surface, originated at a depth of about 6 km and had an average dip of about 50°. The 31 March aftershock, shown by previous work to be in the shallow region of the mainshock rupture, is matched best with a focal depth of about 3.5 km and westward dip of 50°.

This analysis, based on the data from a broad-band array station which recorded these four earthquakes with good signal-to-noise ratio, particularly in the short-period (WWSSN-SP) passband, has produced good focal depth (± 1 km) and average dip ($\pm 10^\circ$) resolution on moderate-magnitude shallow earthquakes. The availability of array data, rather than single-sensor data, has enabled improvements to signal-to-noise ratio for marginal signals and has improved confidence that observed signal characteristics are source-related and not due to path effects local to one or more stations. The results suggest that more information, particularly on the strike and rake angles of the four events, would be gained using this simple modelling and other types

of analysis on high-quality, teleseismic data at other azimuths.

Acknowledgements. This work was performed while the first author was a guest scientist at the Seismologisches Zentralobservatorium Gräfenberg in Erlangen, and he is grateful for the courtesy and assistance of the Observatory staff. We thank H. Hanka for computing assistance, and John Adams, George Choy, Sonja Faber, Henry Hasegawa, Bob North, Deiter Seidl and Max Wyss for comments and discussion. The GRF-array project is supported by the Deutsche Forschungsgemeinschaft and the Bundesanstalt für Geowissenschaften und Rohstoffe.

References

- Barbano, M.S., Kind, R., Zonno, G.: Focal parameters of some Friuli earthquakes (1976–1979) using complete theoretical seismograms. *J. Geophys.* **58**, 175–182, 1985
- Basham, P.W., Adams, J.: The Miramichi, New Brunswick, earthquakes: near-surface thrust faulting in the northern Appalachians. *Geoscience Canada* **11**, 115–121, 1984
- Brüstle, W.: Der Bruchvorgang im Erdbebenherd – Untersuchung ausgewählter Erdbeben mit beobachteten und synthetischen Seismogrammen. *Berichte des Instituts für Meteorologie und Geophysik der Universität Frankfurt/Main*, Nr. 63, 1–317, 1985
- Brüstle, W., Müller, G.: Moment and duration of shallow earthquakes from Love-wave modelling for regional distances. *Phys. Earth Planet. Inter.* **32**, 312–324, 1983
- Choy, G.L., Boatwright, J., Dewey, J.W., Sipkin, S.A.: A teleseismic analysis of the New Brunswick earthquake of January 9, 1982. *J. Geophys. Res.* **88**, 2199–2212, 1983
- Cranswick, E., Wetmiller, R., Boatwright, J.: High-frequency observations and source parameters of microearthquakes recorded at hardrock sites. *Bull. Seismol. Soc. Am.* **75**, 1535–1567, 1985
- Engdahl, E.R., Kind, R.: Interpretation of broadband seismograms from central Aleutian earthquakes. *Ann. Geophys.* **4**, B, 3, 233–240, 1986
- Faber, S., Bonjer, K.-P.: Phase recognition and interpretation at regional distances from the Liege event of November 8, 1983. In: *Seismic activity in western Europe*; P. Melchior, ed.: pp. 249–262, D. Reidel Publishing 1985
- Fuchs, K.: The reflection of spherical waves from transition zones with arbitrary depth-dependent elastic moduli and density. *J. Phys. Earth* **16** (Special Issue), 27–41, 1968
- Fuchs, K., Müller, G.: Computation of synthetic seismograms with the reflectivity method and comparison with observations. *Geophys. J.R. Astron. Soc.* **23**, 417–433, 1971
- Hanka, W.: Analysis of broad-band Rayleigh waves: a possibility for seismic discrimination. *J. Geophys.* **51**, 165–179, 1982
- Harjes, H.-P., Seidl, D.: Digital recording and analysis of broadband seismic data at the Gräfenberg (GRF)-array. *J. Geophys.* **44**, 511–523, 1978
- Kind, R.: The reflectivity method for a buried source. *J. Geophys.* **44**, 603–612, 1978
- Kind, R.: Observations of sP_n from Swabian Alb earthquakes at the GRF array. *J. Geophys.* **45**, 337–340, 1979a
- Kind, R.: Extensions of the reflectivity method. *J. Geophys.* **45**, 373–380, 1979b
- Kind, R.: Length of the rupture from the Swabian Alb event on 3 September 1978 derived from the P_n duration at GRF. *Geol. Jahrb.*, 13–25, Hannover, 1981
- Kind, R.: The reflectivity method for different source and receiver structures and comparison with GRF data. *J. Geophys.* **58**, 146–152, 1985
- Kind, R., Seidl, D.: Analysis of broadband seismograms from the Chile-Peru area. *Bull. Seismol. Soc. Am.* **72**, 2131–2145, 1982
- Mueller, C.S., Cranswick, E.: Source parameters of locally recorded aftershocks of the 9 January 1982 Miramichi, New

- Brunswick, earthquake. *Bull. Seismol. Soc. Am.* **75**, 337–360, 1985
- Räkers, E., Müller, G.: The Romanian earthquake of March 4, 1977: III Improved focal model and moment determination. *J. Geophys.* **50**, 143–150, 1982
- Saikia, C.K., Herrmann, R.B.: Applications of waveform modeling to determine focal mechanisms of four 1982 Miramichi aftershocks. *Bull. Seismol. Soc. Am.* **75**, 1021–1040, 1985
- Seidl, D.: The simulation problem for broad-band seismograms. *J. Geophys.* **48**, 84–93, 1980
- Seidl, D., Berckhemer, H.: Determination of source moment and radiated seismic energy from broadband recordings. *Phys. Earth Planet. Inter.* **30**, 209–213, 1982
- Seidl, D., Stammer, W.: Restoration of broad-band seismograms (Part I), *J. Geophys.* **54**, 114–122, 1984
- Upadhyay, S.K., Duda, S.J.: Source parameters of earthquakes from the Himalayan region. *J. Geophys.* **48**, 67–79, 1980
- Wetmiller, R.J., Adams, J., Anglin, F.M., Hasegawa, H.S., Stevens, A.E.: Aftershock sequences of the 1982 Miramichi, New Brunswick, earthquakes. *Bull. Seismol. Soc. Am.* **74**, 621–653, 1984
- Zonno, G., Kind, R.: Depth determination of North Italian earthquakes using Graefenberg data. *Bull. Seismol. Soc. Am.* **74**, 1645–1659, 1984

Received May 6, 1986; revised version July 20, 1986

Accepted August 4, 1986

Rockmagnetism and palaeomagnetism of an Early Cretaceous/Late Jurassic dike swarm in Rio Grande do Norte, Brazil

C. Bücker¹, A. Schult¹, W. Bloch², and S.D.C. Guerreiro³

¹ Institut für Allgemeine und Angewandte Geophysik, Theresienstraße 41/IV, D-8000 München 2, Federal Republic of Germany

² Institut für Geologie und Mineralogie, Schloßgarten 5, D-8520 Erlangen, Federal Republic of Germany

³ Núcleo de Ciências Geofísicas e Geológicas/UFPA, Caixa Postal 1611, 66000-Belém-Pará, Brasil

Abstract. Ten sites from a dike swarm of early Cretaceous/Late Jurassic age in northeast Brazil (5.7°S, 36.6°W) yielded a pole at 80.6°N, 95°E with $A_{95} = 9.5^\circ$, $K = 26.7$ after AF cleaning. Rock-magnetic investigations and chemical analyses revealed titanomagnetites and maghemites, both with low titanium content showing ilmenite exsolution lamellae (oxidation class III). These are due to an internal high-temperature oxidation during cooling of the large dikes, followed by low-temperature oxidation and/or hydrothermal alterations. There is evidence that with low-temperature oxidation the Ti-to-Fe ratio increases, a finding that is consistent with previous studies. Hysteresis parameters and susceptibility versus temperature curves can be interpreted in terms of pseudosingle-domain behavior with a trend toward multidomain behavior in accordance with moderate-to-weak stability of the remanence.

Key words: Rock magnetism – Palaeomagnetism – Basaltic dikes – South America

Introduction

Palaeomagnetic investigations in northeastern Brazil on Mesozoic volcanic rocks have been carried out by Schult and Guerreiro (1979, 1980) and by Guerreiro and Schult (1986). Preliminary palaeomagnetic results of a dike swarm in Rio Grande do Norte were published by Guerreiro and Schult (1983). In this paper, improved palaeomagnetic data and the rock magnetism of that dike swarm are presented.

Geological setting

The east-west-striking tholeiitic dike swarm in Rio Grande do Norte, northeast Brazil, extends over a distance of about 200 km (Fig. 1). The individual dikes are 5–50 m wide. The swarm can be divided into three subswarms (I, II, and III).

Radiometric determinations on three samples (whole rock) with the K/Ar method (cited in Sial, 1976) and on three samples with the fission track method (Sial, 1974) yielded ages between 125 and 131 m.y. with a mean of 128 m.y. (Early Cretaceous). New potassium-argon determinations were performed on samples from four sites (Fig. 1). Whole-rock isochrones yielded the following ap-

parent ages: site 43: 161 m.y.; site 44: 145 m.y.; site 46: 130 m.y.; site 47: 137 and 167 m.y. All rocks investigated were weathered and therefore not very suitable for age dating. The reported ages are probably minimum ages (the measurement details will be published elsewhere). These new data indicate that the age is Late Jurassic rather than Early Cretaceous. In recent publications (e.g., Mapa Geológico do Brasil, 1981) Early Cretaceous has been the age assigned to the dikes.

In the vicinity of the dikes, Tertiary necks and flows are also found (Fig. 1). K/Ar determinations on three samples from three necks yielded an age of about 18 m.y. (cited in Sial 1976). The best known of these necks, the Pico do Cabugi, is situated east of Lages on a dike.

Palaeomagnetism

The site locations selected are shown in Fig. 1. Samples (2.5 cm in diameter and 2.3 cm length) were taken with a portable drill. Some of details regarding the palaeomagnetic measurements and preliminary results have been published elsewhere (Guerreiro and Schult, 1983). For several sites, the palaeomagnetic data could be improved by more rigorous AF cleaning. The vector diagrams in Fig. 2 show that in some cases relatively high fields are necessary to erase secondary components. Such high fields were not applied in the first instance. The final results are summarized in Table 1. From 14 sites selected, 10 were used for the overall mean: For three sites (48, 53 and 54), no consistent results could be achieved (it is possible that from site 54 rolled blocks were sampled), and site B3 was discarded because it is not a dike but a basalt flow (of Tertiary age).

After AF cleaning, the mean direction of the characteristic remanent magnetization (CARM) was $D = 186.6^\circ$, $I = +20.8^\circ$ with $N = 10$, $\alpha_{95} = 14.1^\circ$, $k = 12.6$ yielding a pole at 80.6°N, 95°E with $A_{95} = 9.5^\circ$, and $K = 26.7$. Seven sites had reversed polarity (all from dike I and II) and three sites normal polarity (all from dike III). These results supersede the previous findings (Guerreiro and Schult 1983). However, there is little difference between results.

Figure 3 compares the new pole position with Early Cretaceous and Jurassic poles from stable South America (for compilation, see Schult et al., 1981; Guerreiro and Schult, 1986). The new (Early Cretaceous or Late Jurassic) pole is nearer to the Jurassic poles and lies at the edge of the Early Cretaceous pole distribution.

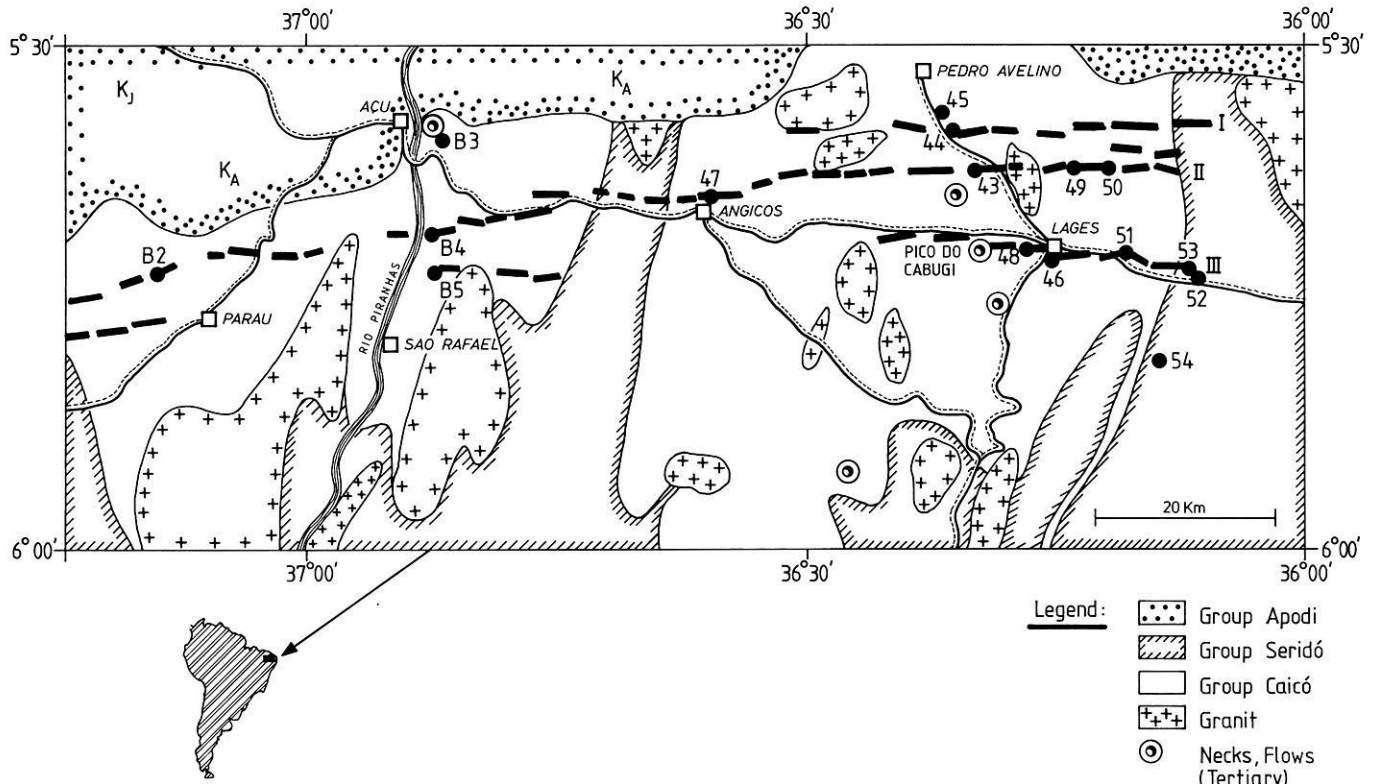


Fig. 1. Geological sketch map and sampling sites in Rio Grande do Norte, NE Brazil

Table 1. Palaeomagnetism of a dike swarm in Rio Grande do Norte (ca. 5.7°S, 36.6°W)

Site/dike	NRM						CARM					VGP	
	<i>N</i>	<i>D</i>	<i>I</i>	α_{95}	<i>k</i>	MDF (Oe)	<i>N</i>	<i>D</i>	<i>I</i>	α_{95}	<i>k</i>	°N	°E
43/II	9	231	+57.2	17.9	9	180	9	190.1	+51.6	3.9	174	61.8	125
44/I	11	196	-16.4	16.9	8	40	9	177.2	-5.3	2.6	387	81.2	305
46/III	10	357	-19.8	10.5	22	50	14	4.2	-3.3	4.1	91	84.2	10
47/II	7	223	+19.6	10.0	37	120	8	210.1	+33.5	4.2	169	58.0	79
48/III	15	No consistent results				50	15	No consistent results					
49/I	8	No consistent results				250	7	178.2	-2.3	6.1	97	82.9	309
50/II	5	304	+41.1	70	2	130	5	183.6	+38.6	15.8	25	73.6	132
51 a/III	8	No consistent results				60	8	No consistent results					
51 b/III	6	5	-10.5	19.0	13	180	8	1.9	-11.1	5.8	91	88.1	51
53/III		No consistent results				150		No consistent results					
54		No consistent results				50		No consistent results					
B2/II	5	204	+11.4	24.6	11	90	6	191.9	+40.1	3.2	436	69.4	110
B3	9	358	+17.4	30.8	9	240	9	(9.4	+18.0	5.2	97	72.4	355)
B4/II	4	227	+19.9	48.0	5	180	4	196.1	+34.5	8.3	125	69.5	95
B5/III	7	0	-5.5	3.5	239	130	7	0.9	-0.9	5.1	138	84.7	333
Mean of site means							10	186.6	+20.8	14.1	12.6	80.6	95.1
												$K=26.7$ $A_{95}=9.5$	

N, number of samples; *D*, declination; *I*, inclination; α_{95} and A_{95} , radius of 95% confidence circle; *k* and *K*, precision parameter; MDF, medium destructive peak field necessary to erase half of NRM intensity by alternating field demagnetization; 1 Oe \cong 79.58 Am⁻¹

Rock magnetism

The methods used to identify the magnetic minerals in basaltic rocks were X-ray investigations, microscopic investigations, chemical analyses, and measurements of magnetic

properties such as Curie temperature and temperature dependence of high-field magnetization and of susceptibility. The temperature dependence of specific high-field magnetization J_s and Curie temperature T_c were determined by means of an automatically recording balance in a field of

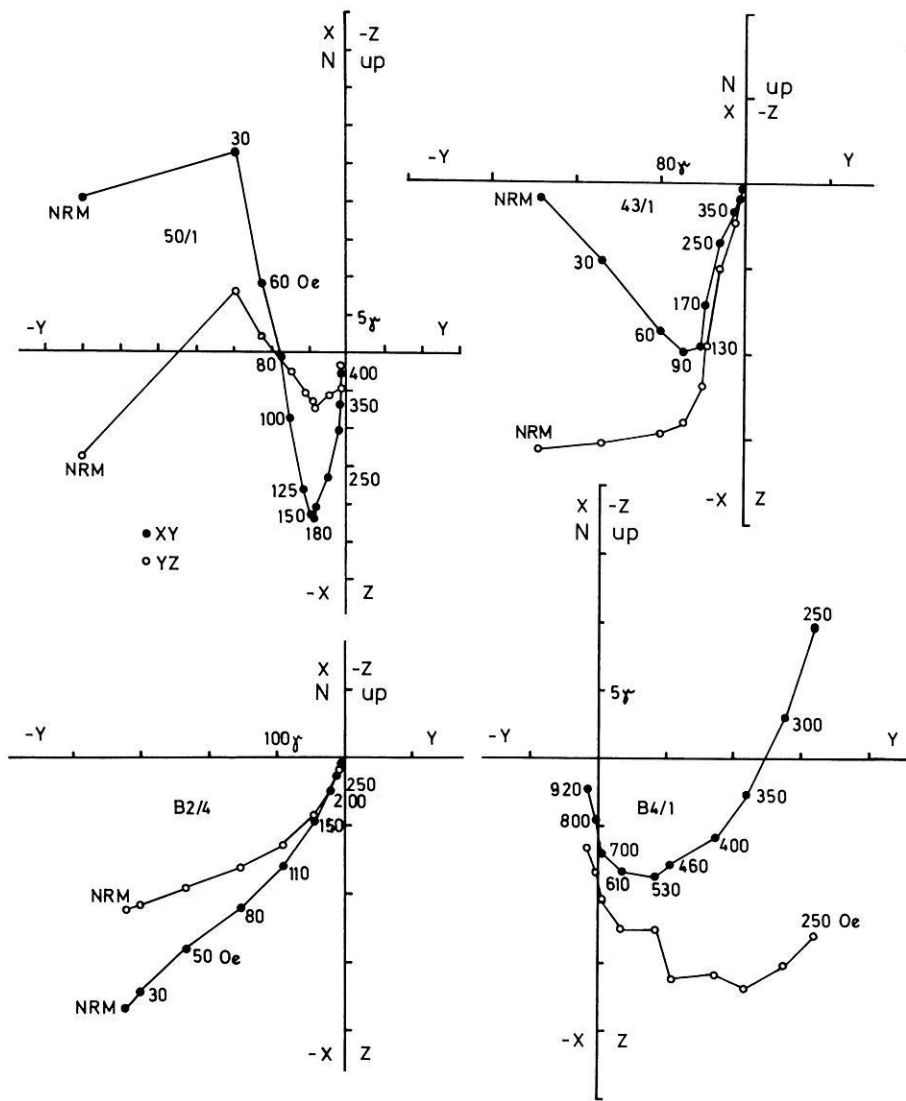


Fig. 2. Vector diagrams showing the variation of the remanence during progressive AF demagnetization. *Open* and *solid* symbols indicate components in the vertical EW and horizontal planes, respectively

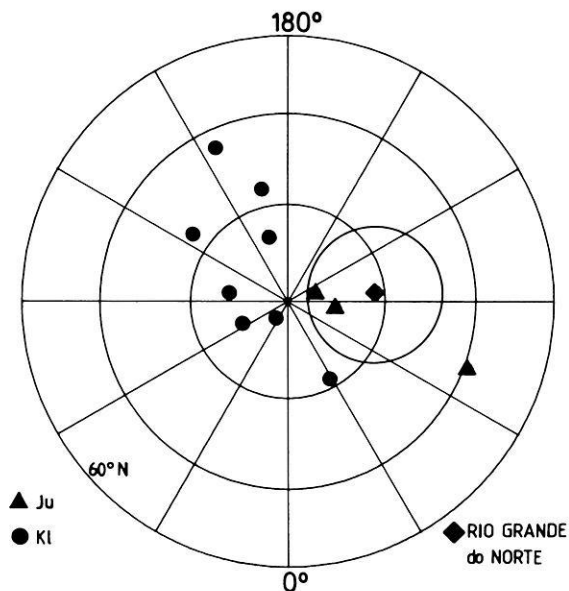


Fig. 3. Compilation of Early Cretaceous and Jurassic poles (this paper; Schult et al., 1981; Guerreiro and Schult, 1986)

about 1800 Oe ($1 \text{ Oe} = 79.58 \text{ Am}^{-1}$). The measurements were carried out in air on whole (moderately crushed) rock. Table 2 summarizes the results.

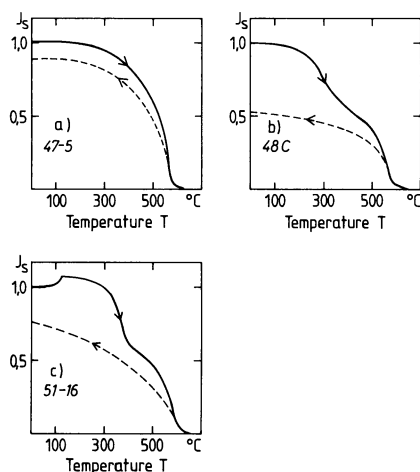
The typical $J_s(T)$ curves obtained are shown in Fig. 4; Fig. 4a indicates a composition near magnetite with low titanium content. The $J_s(T)$ curves of most samples are similar to Fig. 4b. This curve is symptomatic for the presence of some maghemite (with low titanium content), in addition to magnetite, and is characterized by the irreversible decrease of J_s between 350° and 480° C due to transformation of maghemite to hematite. The portion of (decomposing) maghemite was estimated from the irreversible decrease of J_s (see Table 2). Some samples showed a kink type $J_s(T)$ curve (Fig. 4c) (Ade-Hall et al., 1971). The kink (irreversible maximum near 150° C) was only observed in connection with maghemite decomposition at about 380° C . The shape of the kink depends on field strength: with decreasing field strength, the kink becomes more pronounced, which implies the presence of a magnetic phase with relative high coercivity that decreases strongly with increasing temperature.

For X-ray investigations, the samples were pulverised and the magnetic phase separated with a hand magnet. In

Table 2. Rockmagnetic data

Sample	a (Å)	T_c (°C)	J_s	T_{ph} (°C)	Other phases	x	z
B 2/3	(8.399)	550	b, Mt, Mgh (15%)		Ilm	0.11	0.25
B 3/7	8.395	575	a, Mt	+	Ilm, Hm	0.03	0.15
B 4/5	8.403	560	b, Mt, Mgh (15%)	+	Ilm	0.07	0.1
B 5/3	8.386	565	b, Mt, Mgh (15%)		Ilm	0.1	0.45
43/10	8.371	575	c, Mt, Mgh (35%), k		Ilm	0.15	0.75
44/3	8.399	560	a, Mt	+	Ilm, Hm	0.08	0.17
46/2	8.400	570	a, Mt	-150	Ilm	0.04	0.1
47/5	8.395	570	a, Mt	-165	Ilm	0.02	0.15
48/3	8.400	575	b, Mt, Mgh (20%)	-145	Ilm, Hm	0	0
48/F2	8.396	575	b, Mt, Mgh (25%)	-155	Ilm	0.03	0.2
49/2	8.387	575	b, Mt, Mgh (5%)		Ilm	0.08	0.5
50/4	8.354	570	c, Mt, Mgh (70%)		Ilm	0.26	0.9
51 a/3	8.403	580	a, Mt	-175	Ilm	0	0
51 b/16	(8.385)	580	c, Mt, Mgh (40%), k		Ilm, Hm	0.06	0.5
53/1	8.400	570	b, Mt, Mgh (20%)	-165	Ilm, Hm	0.05	0.1
54/4	8.398	575	b, Mt, Mgh (20%)	-155	Ilm, Hm	0.03	0.1

a , Lattice constant, error about 0.003 Å (in parentheses >0.003 Å); T_c Curie temperature; $J_s(T)$ curves are shown in Fig. 4; Mt, magnetite; Mgh, maghemite; parentheses, portion of maghemite estimated from irreversible decrease of J_s between 350° and 480° C; k , kink type $J_s(T)$ curve (Ade-Hall et al., 1971); T_{ph} low-temperature phase transition of magnetite according decrease of susceptibility (Fig. 6); +, transition indicated; other phases (detected by ore microscopy and X-ray investigation): Ilm, ilmenite; Hm, hematite; x , composition in $(1-x)\text{Fe}_3\text{O}_4 \times \text{Fe}_2\text{TiO}_4$ and z oxidation parameter estimated from T_c and a (after Readman and O'Reilly, 1972)

**Fig. 4.** Examples of thermomagnetic curves as described in the text

some cases, this procedure was repeated several times. A Debye-Scherrer camera with 114.83 mm diameter and cobalt radiation was used. The lattice constant of the titanomagnetites was determined and other iron titanium oxides were identified if sufficiently present. The titanium content x and the oxidation parameter z of the titanomagnetites derived from the lattice constants and the Curie temperatures (Readman and O'Reilly, 1972) are also listed in Table 2 and shown in Fig. 5.

For all samples, microscopic observations on polished sections showed ilmenite exsolution lamellae in magnetite grains that were consistent with the X-ray investigations. This finding can be classified with oxidation class III due to high-temperature oxidation according to Wilson and Watkins (1967). The occurrence of shrinkage gaps in the magnetite grains of several samples indicate low-temperature oxidation consistent with the presence of maghemite in the majority of samples.

The temperature dependence of the susceptibility was measured with a Highmoor susceptibility bridge between -196° and 700° C. Typical $\chi(T)$ curves are shown in Fig. 6. The Curie temperatures derived from these curves and also the presence of maghemite can be seen from the $\chi(T)$ curves. For magnetite, a decrease of susceptibility can be observed at about -150° C due to phase transition from cubic to orthorhombic and vanishing magnetocrystalline anisotropy constant K_1 . The transition temperature decreases with increasing titanium content (to about -220° C for $x=0.1$) (Collison et al., 1967). For several samples (Fig. 6 and Table 2), such a transition temperature (above -200° C) was detected, which indicated a relatively low titanium content that was qualitatively in agreement with the derived x values from the contour diagram or with the chemical analyses (see below).

The chemical analyses were carried out with a transmission electron microscope with energy dispersive equipment (Table 3). In all cases, a small amount of silicon was measured. As it is generally accepted that titanomagnetites and ilmenites contain practically no silicon, it is assumed that the silicon measured is due to contamination by adjacent silicates. The number of cations per formula unit was calculated, omitting silicon and assuming stoichiometry (see Table 3). In most cases, there was agreement between the titanium content obtained with the two methods (Tables 2 and 3), except for sample 50/4. This sample contained predominantly maghemite, which decomposed before its true Curie temperature was reached, yielding too low a Curie temperature and therefore too much titanium content in the contour diagram (Fig. 5). To a certain extent this was also valid for sample 43. The other metallic cations (Al, Mg, Mn, Cr, V) seemed to have relatively little influence on the contour diagram, so that the titanium content was essentially correct. At least for the lattice constant, some of these metallic cations have opposite effects: for magnetite it is increased by substitutions by Mn and V and decreased by Al, Mg, and Cr (Bleil and Petersen, 1982).

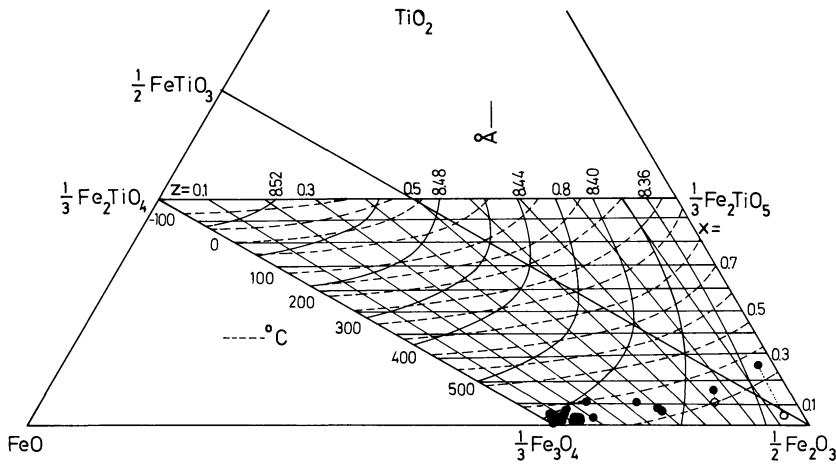


Fig. 5. Composition of titanomaghemites from the basaltic dike swarm using the contour diagram after Readman and O'Reilly (1972) and the Curie temperatures and lattice constants as listed in Table 2. The few open circles denote the deviating titanium content measured with a transmission electron microscope. Lines of equal oxidation parameter z are also given

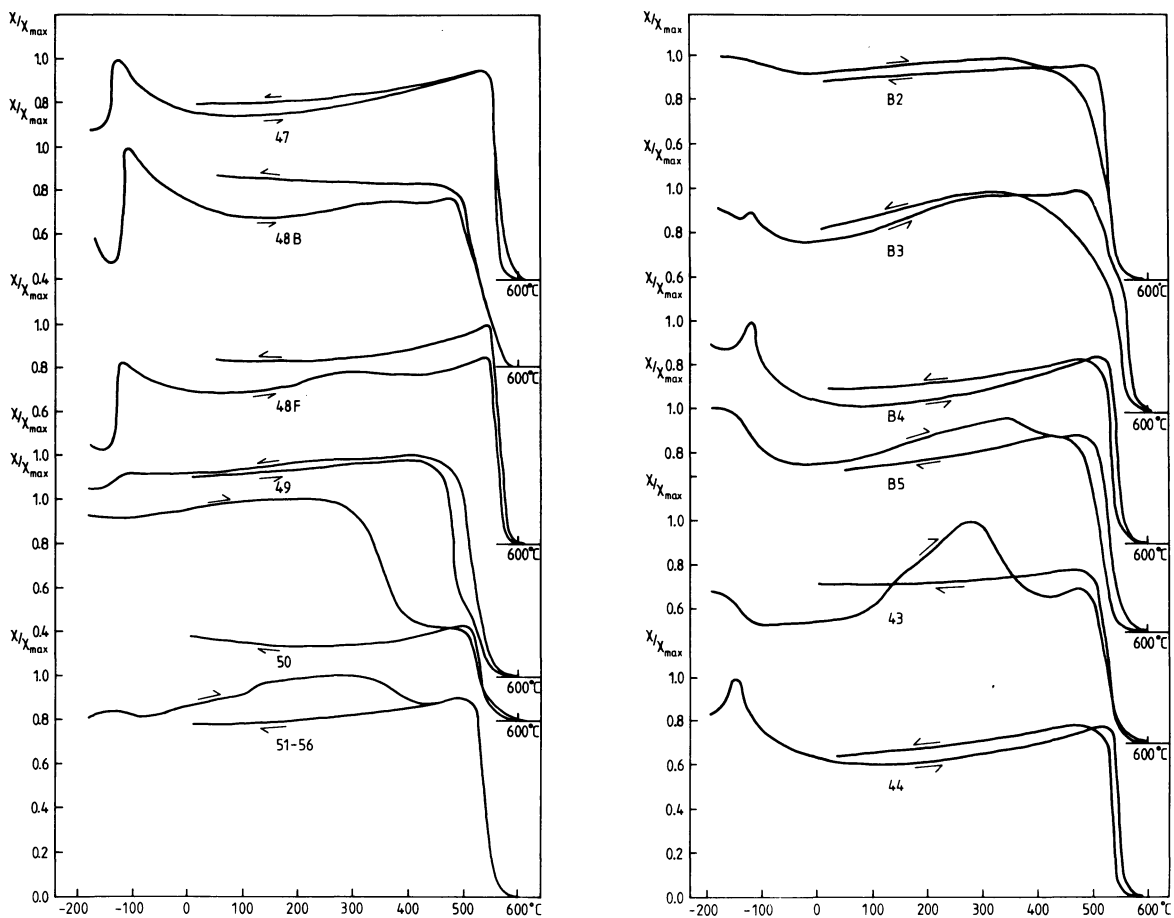


Fig. 6. Temperature dependence of susceptibility

The degree of the low-temperature oxidation of the titanomaghemites was generally not homogeneous. In several cases, the $J_s(T)$ curves indicated some amount of maghemite (i.e., z near unity) whereas the z value obtained from the contour diagram was small (e.g., samples B2, B4, 48, 53, 54). Despite this difficulty, it can be assumed that the z values represent mean values for the samples. Figure 5 is consistent with the finding in many studies that low-temperature oxidation of titanomagnetite involves the mi-

gration of iron away into the surrounding matrix, resulting in an increase in the Ti-to-Fe ratio of the remaining phase (e.g., Marshall and Cox, 1972; Petersen et al., 1979; Furuta et al., 1985). This behavior has been particularly supported by studies on basaltic rocks from the sea floor (titanomaghemites with x values of about 0.6). In our study, the titanomaghemites in the subaerial basaltic rocks had low x values (≈ 0.04) at the beginning of the low-temperature oxidation.

These (titano-) magnetites are probably the result of

Table 3. Chemical analyses of iron titanium oxides

Sample	<i>N</i>	Fe	Ti	Al	Mg	Mn	Cr	V	Si	Fe	Ti	Al	Mg	Mn	Cr	V	<i>x</i>
(atom percent)										(cations)							
B2																	
Tmt	15	93.4	3.6	0.7	—	0.3	0.7	—	0.6	2.84	0.11	0.02	—	0.01	0.02	—	0.11
Ilm	13	48.4	47.0	0.6	0.6	2.0	—	—	1.4	0.98	0.95	0.01	0.01	0.04	—	—	
B3																	
Tmt	12	95.9	1.7	0.7	0.3	0.7	—	—	0.7	2.90	0.05	0.02	0.01	0.02	—	—	0.03
Ilm	4	47.1	47.0	0.8	2.8	1.3	—	—	0.8	0.95	0.95	0.02	0.06	0.03	—	—	
B4																	
Tmt	10	94.5	2.3	0.6	0.4	0.4	—	1.1	0.6	2.85	0.07	0.02	0.01	0.01	—	0.03	0.07
Ilm	3	48.0	48.5	1.0	0.3	1.3	—	—	0.9	0.97	0.98	0.02	0.01	0.03	—	—	
Rt	2	3.7	93.5	1.2	0.2	0.2	—	—	1.1	0.04	0.95	0.01	0	0	—	—	
B5																	
Tmt	12	93.4	3.0	0.8	0.4	0.4	—	0.6	0.8	2.84	0.09	0.02	0.01	0.01	—	0.02	0.1
Ilm	3	48.8	46.4	0.9	1.3	1.4	—	—	1.2	0.99	0.94	0.02	0.03	0.03	—	—	
43/10																	
Tmt	11	92.1	3.5	1.0	0.3	0.4	—	1.2	1.5	2.81	0.11	0.03	0.01	0.01	—	0.03	0.15
Ilm	5	49.0	48.0	0.6	0.4	1.6	—	—	0.4	0.98	0.96	0.01	0.01	0.03	—	—	
Per	1	8.3	58.9	2.4	0.5	0.4	—Ca	27.4	2.8								
44																	
Tmt	9	93.9	1.9	1.5	0.5	—	—	—	1.2	2.88	0.06	0.05	0.02	—	—	—	0.08
Ilm	11	50.9	45.2	0.6	0.5	1.7	—	—	1.2	1.02	0.92	0.01	0.01	0.03	—	—	
Pyr	1	42.9	0.8	0.7	0.5	0.2	—S	52.3	2.0	0.95	0.02	0.02	0.01	0	—	S1.16	
46/2																	
Tmt	9	96.9	1.5	0.6	0.2	0.3	—	—	0.5	2.92	0.05	0.02	0.01	0.01	—	—	0.04
Ilm	3	47.7	48.0	0.7	—	2.8	—	—	0.7	0.96	0.97	0.01	—	0.06	—	—	
Rt	1	4.8	92.0	1.2	0.5	0.3	—	—	1.2	0.05	0.93	0.01	0.01	0	—	—	
47																	
Tmt	8	96.7	0.9	0.6	0.3	0.3	—	0.7	0.5	2.92	0.03	0.02	0.01	0.01	—	0.02	0.02
Ilm	3	48.2	48.0	1.0	—	1.4	—	—	1.3	0.98	0.97	0.02	—	0.03	—	—	
48/3																	
Tmt	7	96.0	0.7	0.6	0.8	0.1	—	—	1.6	2.93	0.02	0.02	0.02	0.01	—	—	0
Ilm	3	47.5	47.8	0.7	0.9	2.0	—	—	0.9	0.96	0.97	0.01	0.02	0.04	—	—	
48/F2																	
Tmt	8	97.0	1.0	0.6	0.3	0.1	—	—	1.0	2.94	0.03	0.02	0.01	0	—	—	0.03
Ilm	3	48.3	47.9	0.7	0.8	1.1	—	—	1.5	0.98	0.97	0.01	0.02	0.02	—	—	
49/2																	
Tmt	7	94.2	3.5	0.8	0.5	—	—	—	1.0	2.85	0.10	0.02	0.02	—	—	—	0.08
Ilm	3	48.2	47.9	0.7	0.7	1.4	—	—	1.0	0.97	0.97	0.01	0.01	0.03	—	—	
50/4																	
Tmt	10	97.2	1.3	0.5	0.2	0.3	—	—	0.5	2.93	0.04	0.02	0.01	0.01	—	—	(0.26)
Ilm	2	48.3	47.2	0.7	0.9	1.5	—	—	1.3	0.98	0.96	0.01	0.02	0.03	—	—	
51/16																	
Tmt	10	94.7	2.0	1.0	0.5	0.1	—	—	0.5	2.89	0.06	0.03	0.02	0	—	—	0.06
Ilm	9	51.5	43.0	0.8	0.7	1.7	—	—	1.5	1.05	0.88	0.02	0.01	0.03	—	—	
54/4																	
Tmt	7	95.8	1.8	0.5	—	—	—	1.3	0.5	2.89	0.05	0.02	—	—	—	0.04	0.03
Chr	4	47.5	1.0	0.3	—	—	50.0	0.6	0.8	1.43	0.03	0.01	—	—	1.51	0.02	

Analyses are given in atom percent (total 100%). Number of cations (per formula unit) was calculated assuming stoichiometry and omitting Si. *N*, number of analyses; *x* from Table 2, to compare with Ti or the sum of Ti and other metallic ions. Tmt, titanomagnetite; Ilm, ilmenite; Rt, rutile; Per, perovskite; Pyr, pyrrhotite; Chr, chromite

an “internal oxidation” during cooling of the (large) dikes, a special case of high-temperature oxidation. From the coexisting titanomagnetites and ilmenites, the temperature of their formation can be inferred (Buddington and Lindsley, 1964). The temperatures obtained are very low, ranging from 500° to 600° C. This would mean that the remanence

could be, in part, thermochemical remanent magnetization rather than thermal remanent magnetization. The low-temperature oxidation was evident for all samples. Also, hydrothermal alteration is possible. According to Ade-Hall et al. (1971), the kink type $J_s(T)$ curve is indicative for this alteration.

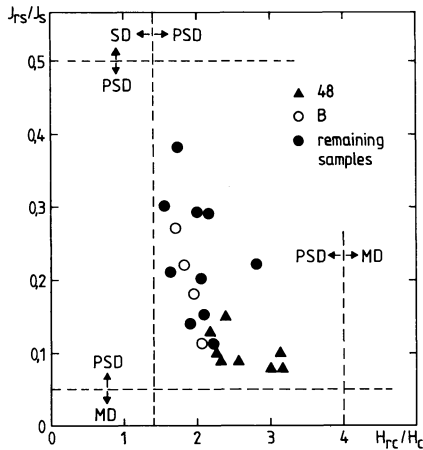


Fig. 7. J_{rs}/J_s versus H_{rc}/H_c . The horizontal and vertical lines indicate the single-domain (SD) pseudo single domain (PSD) transition and PSD multidomain (MD) transition, respectively (Day et al., 1977)

Hysteresis parameters

Relations between quotients H_{rc}/H_c (remanence coercivity, coercivity) and J_{rs}/J_s (saturation remanence, saturation magnetization) can be used to distinguish between different domain structure types (Day et al., 1977). Figure 7 shows PSD behavior for all samples with a trend to MD behavior. The weak Hopkinson peaks of the $\chi(T)$ curves (Fig. 6) indicate PSD with a trend toward MD behavior of the oxide grains as well (Dunlop, 1974). According to the microscopic observations, the magnetite grains are relatively large (several micrometers) despite the subdivision of the oxide grains by ilmenite lamellae. This is also in accordance with weak stability of the remanence in several cases (Table 1).

Conclusions

1. The mean pole position for the Lower Cretaceous or Late Jurassic dike swarm in Rio Grande do Norte compares favorably with other poles of South America.
2. The ferrimagnetic minerals are magnetites and maghemites with a low titanium content and still less of other metallic cations, such as Al, Mg, Mn, Cr, and V.
3. The magnetites have been affected by high-temperature oxidation during cooling of the large dikes. The magnetites show ilmenite exsolution lamellae (oxidation class III). The geothermometer (Buddington and Lindsley 1964) yields low temperatures (500°–600° C).
4. The magnetites have undergone low-temperature oxidation of varying degrees. Of the samples 70% also contain maghemite. There are indications of hydrothermal alterations.
5. There is evidence that, with low-temperature oxidation, the Ti-to-Fe ratio increases, which is consistent with previous studies on basaltic rocks from the ocean floor.
6. Hysteresis parameters can be interpreted in terms of PSD behavior with a trend approaching MD behavior. The stability of the remanence is moderate and in some cases weak.
7. The titanium content determined with the aid of the contour diagram according to Readman and O'Reilly (1972) is in agreement with microprobe chemical analysis.

Acknowledgements. We thank Prof. Dr. R. Schwab for his advice and help in the field work and Dr. P. Horn and Dr. D. Müller-

Sohnius (Institut für Mineralogie und Petrologie, München) for the potassium-argon determinations. This research was done within the bilateral agreement between Brazil and the Federal Republic of Germany within the Geochemistry Project. The financial support of Bundesministerium für Forschung und Technologie, Conselho Nacional de Desenvolvimento Científico e Tecnológico and Deutsche Forschungsgemeinschaft is gratefully acknowledged.

References

- Ade-Hall, J.M., Palmer, H.C., Hubbard, T.P.: The magnetic and opaque petrological response of basalts to regional hydrothermal alteration. *Geophys. J. R. Astron. Soc.* **24**, 137–174, 1971
- Bleil, U., Petersen, N.: Magnetic properties of natural minerals. In: Landolt-Börnstein, New Series, Group V, Vol. 1b, G. Angenheister ed.: pp. 308–365. Heidelberg, New York: Springer 1982
- Buddington, A.F., Lindsley, D.H.: Iron-titanium oxide minerals and synthetic equivalents. *J. Petrol.* **5**, 310–357, 1964
- Collinson, D.W., Creer, D.M., Runcorn, S.K.: *Methods in paleomagnetism*. Amsterdam: Elsevier 1967
- Day, R., Fuller, M., Schmidt, V.A.: Hysteresis properties of titanomagnetites: grain-size and compositional dependence. *Phys. Earth Planet. Interiors* **13**, 260–267, 1977
- Dunlop, D.J.: Thermal enhancement of magnetic susceptibility. *J. Geophys.* **40**, 439–451, 1974
- Furut, T., Otsuki, M., Akimoto, T.: Quantitative electron probe microanalysis of oxygen in titanomagnetites with implications for oxidation process. *J. Geophys. Res.* **90**, 3145–3150, 1985
- Guerreiro, S.D.C., Schult, A.: Palaeomagnetismo de um enxame de diques toleíticos de idade meso-cenozoica, localizados no Rio Grande do Norte. *Rev. Bras. Geofis.* **1**, 89–98, 1983
- Guerreiro, S.D.C., Schult, A.: Palaeomagnetism of Jurassic tholeiitic intrusions in the Amazon Basin. *Veröffentlichung des Geophysikalischen Observatoriums Fürstfeldbruck, Münchner Universitätsschriften, Serie B, Nr. 10*, 61–72, 1986
- Mapa Geológico do Brasil, Ministério das Minas e Energia, DNPM, 1981
- Marshall, M., Cox, A.: Magnetic changes in pillow basalt due to sea floor weathering. *J. Geophys. Res.* **77**, 6459–6469, 1972
- Petersen, N., Eisenach, P., Bleil, U.: Low temperature alteration of the magnetic minerals in ocean floor basalts. In: Maurice Ewing Series 2, M. Talwani, C.G. Harrison, D.E. Hayes (eds.), pp. 169–209. Washington O.C.: American Geophysical Union 1979
- Readman, P.W., O'Reilly, W.: Magnetic properties of oxidized (cation-deficient) titanomagnetites (Fe, Ti)₃O₄. *J. Geomagn. Geoelectr.* **24**, 69–90, 1972
- Schult, A., Guerreiro, S.D.C.: Palaeomagnetism of Mesozoic igneous rocks from the Maranhao Basin, Brazil and the time of opening the South Atlantic. *Earth Planet. Sci. Lett.* **42**, 427–436, 1979
- Schult, A., Guerreiro, S.D.C.: Palaeomagnetism of Upper Cretaceous volcanic rocks from Cabo de Sto. Agostinho, Brazil. *Earth Planet. Sci. Lett.* **50**, 311–315, 1980
- Schult, A., Hussain, A.G., Soffel, H.C.: Palaeomagnetism of Upper Cretaceous volcanics and Nubian sandstones of Wadi Natash, SE Egypt and implications for the polar wander path for Africa in the Mesozoic. *J. Geophys.* **50**, 16–22, 1981
- Sial, A.N.: Petrology and tectonic significance of the post-Palaeozoic basaltic rocks of northeast Brazil. Ph.D. Thesis, University of Columbia, 403 pp., 1974
- Sial, A.N.: The post-Palaeozoic volcanism of northeast Brazil and its tectonic significance. *Ann. Acad. Bras. Cienc. [Suppl.]*, **48**, 299–311, 1976
- Wilson, R.W., Watkins, N.D.: Correlation of petrology and natural magnetic polarity in Columbia Plateau basalts. *Geophys. J. R. Astron. Soc.* **12**, 405–424, 1967

Received April 21, 1986; revised version August 15, 1986
Accepted August 22, 1986

Conference

Second Conference on Scientific Ocean Drilling (COSOD II)

The future of ocean drilling will be discussed at the COSOD II meeting to be held in Strasbourg, France between 6–8 July 1987. This meeting will set up the scientific framework for ocean drilling until about 1996. A wide range of advice, from both within and outside the traditional oceanic community, will be sought. Five working groups will prepare prior position papers on Global Environmental Changes, Mantle-Crust Interactions, Fluid Circulation in Crust and Sediments and Global Chemical Budgets, Brittle and Ductile Deformation of the Lithosphere and Evolution and Extinction of Oceanic Biota. Since space at the conference will be limited, applications are invited from all interested scientists, which should be sent to Philippe Huchon, Executive Secretary, COSOD II, Département de Géologie, Ecole Normale Supérieure, 24 rue Lhomond 75231 Paris Cedex 05, France (Phone 33.1.43.31.84.88 – Telex 202 601 F NORM SUP). Please indicate in your letter the first and second working group topics with which you would wish to be associated, together with a short statement of the expertise that you can contribute to the discussion. Scientists from countries already members of JOIDES may obtain support from their national funding agencies. Closing date for applications is February 1st 1987.

Book reviews

De Bremaecker J.-C.: Geophysics: The Earth's Interior. John Wiley & Sons, 342 p., 1985

According to the intentions of the author, this small textbook is addressed to "nonspecialist" students to introduce the "academic" aspects of geophysics. It is based on the lecturer's notes of a one-semester course, slightly extended.

Thus, aiming at students of geology, the use of mathematics and physics is very basic. Under the scope of plate tectonics, the author intends to show that geology and physics of the earth's interior are inseparable, and that study of both is needed. Therefore, he presents a description of the methods as well as of some significant results. Explaining the geophysical concepts, he applies an inductive approach rather than the purely deductive one.

Thus it appears that this textbook can be used not only in courses for geologists, but also for introductory courses for students in geophysics. The problems mentioned at the end of each chapter may be used for a test of understanding as well as for a deeper discussion of the topics. On the other hand, the limited length of the text requires a selection of the material presented: whereas the fault plane method with its typical "football diagram" is well explained, the treatment of the earth's gravity field is much too short; e.g. the earth tides cover only some lines in order to mention tidal corrections to gravity exploration.

G. Jentzsch

Saltzman, B. (ed.): Satellite oceanic remote sensing. In: *Advances in Geophysics*, Vol. 27, Academic Press, 511 p., 1985

This special volume of "Advances in Geophysics" presents a review of the development and main results of the pioneering studies primarily conducted by the National Oceanic and Atmospheric Administration (NOAA), and which follows from the operation of three satellite systems launched by the NASA during 1978: Seasat, Nimbus-7 and TIROS-N.

The rapid refinement of satellite remote sensing techniques of the last decade caused a virtual step-function increase in the acquisition of oceanic data, which has opened a new era in oceanographic research. This volume is published exactly 200 years after the first marine chronometers were perfected to measure longitude as well as the traditional latitude. This allowed the birth of oceanology, wherein measurements could be located in time and space. Satellite observations of today allow the global description of the surface and the upper tens of metres of the ocean.

The purpose and scope of this volume is to summarize the results and accomplishments from these three satellite systems and to illustrate selected application of the operational use of satellites

for environmental monitoring of the global oceans. Thus, in more than ten different sections the satellite systems are described, as well as the analysis and interpretation of the data with respect to altimeter sea echo, oceanic surface winds, surface and internal ocean wave observations, Seasat microwave wind and rain observations in several tropical and midlatitude marine storms, sea surface temperature determinations, ocean colour measurements, observations of the polar regions, precipitation in tropical cyclones and application to living marine resources. Three appendices are dedicated to the instruments used, the Seasat validation program and the availability of data. The different sections are very comprehensive, including carefully drawn pictures and excellent photographs. Of special value are the colour-encoded images of the marine geoid, pigment concentrations and Arctic and Antarctic ice concentrations. Together with many up-to-date references, this volume is of special interest not only to the specialist but also to the interested reader.

G. Jentzsch

Stanley, Steven M.: Earth and life through time. Freeman, 690 p., 1986

This comprehensive textbook provides an integrated view on the physical and biological history of the earth. The description of our planet's evolution with respect to earth movements, climatic and oceanographic changes, and the transformation of life by evolution and extension, provides an exciting new concept of a text on the history of the earth.

The composition of the different chapters is well proved: The first eight chapters provide the facts and fundamentals on geology and ecology, a description of marine and non-marine environments, correlation and dating of the rock record, evolution and the fossil record, as well as plate tectonics and mountain building. Based on that, a chronological review of the earth and its biota is given in the following chapters (9 through 18).

Throughout the book, the author has relied heavily on many figures and comprehensive figure legends. The broad coverage of this book enables the teacher to concentrate on specific topics. Summaries, exercises and references for additional reading given at the end of each chapter make the text handy, and stimulate further discussion.

Thus, this textbook must be highly recommended to both teachers and students. In addition to the excellent textbook "Earth" by Press and Siever, we must appreciate that the publishers have now provided another text of the same quality and of a similar lay-out, which should not be missed in any library for geosciences.

G. Jentzsch

*Original investigations***Deep-seated lateral velocity variations beneath the GRF array inferred from mislocation patterns and P residuals**S. Faber¹, J. Plomerová², and V. Babuška²¹ Seismologisches Zentralobservatorium GRF, Krankenhausstraße 1–3, D-8500 Erlangen, Federal Republic of Germany² Geophysical Institute, Czechoslovak Academy of Sciences, 14131 Praha 4, Czechoslovakia

Abstract. The analysis of mislocation patterns and the three-dimensional inversion of travel-time residuals for *P* waves measured at the GRF array reveal the existence of strong lateral velocity variations beneath the array. The most expressive phenomenon consists of an increase of *P*-wave velocities in the upper mantle from north to south, in addition to a possible thickening of the lithosphere to the south; especially the Moldanubian part of the Bohemian massif located to the southeast of the GRF array is characterized by high *P*-wave velocities in the upper mantle. The systematic change of the magnitude of the residual variation across the array, depending on the incidence angle for *P* waves, leads to the conclusion that a low-velocity zone exists in the upper mantle to the northeast of subarray A. The appearance of low-velocity material in the vicinity of the border between the two tectonic units, namely the Saxothuringian zone to the north and the Moldanubian zone to the south, might be connected to the deep structure of the graben area which extends to the northeast into the Egergraben.

Key words: GRF array calibration – Mislocation vectors – *P*-wave travel-time residuals – 3-D inversion – Lateral velocity variations

Introduction

Since the installation of large-aperture seismic arrays within the last 20 years, numerous investigations have dealt with slowness and azimuth anomalies as well as with azimuthal variations of *P*-wave travel-time residuals observed at these arrays. These deviations of measured parameters from theoretical values calculated for standard earth models are due to lateral variations in structures located in most cases in the crust and upper mantle underneath these seismograph networks. This is shown, for example, in an investigation presented by Berteussen (1976), who refers to a number of publications concerning these problems at arrays such as LASA, NORSAR, YKA and others. Aki et al. (1976, 1977) applied a three-dimensional inversion technique to *P*-wave residuals observed at LASA and at NORSAR, respectively. In both cases the results show that strong small-scale inhomogeneities exist down to the bottom of the litho-

sphere. In a more recent paper, Christofferson and Husebye (1979) located such heterogeneities at NORSAR at even slightly greater depth. As a comparison to the relatively strong heterogeneous media beneath most of the seismic arrays, the Gauribidamur array in India should be mentioned because it seems to have an exceptionally homogeneous lithospheric structure underneath it (Berteussen et al., 1977; Ram and Yadav, 1980).

In our paper we present a study of the mislocation patterns and azimuthal variations in *P*-wave residuals at the broad-band seismic array Gräfenberg (GRF) in the Federal Republic of Germany. A detailed description of the GRF-array configuration is published by Harjes and Seidl (1978). The GRF array is located on a predominantly homogeneous geological surface structure, namely, the Franconian Jurassic limestone formation (Fig. 1). This area, which forms the eastern part of the South German block, is bordered by the Bohemian Massif to the east. The two blocks are separated by zones of fracturing which strike NW. The northern part of the Bohemian Massif is subdivided by ENE-striking zones with Cenozoic volcanism. The boundary between two Hercynian units, the Moldanubian zone in the south and the Saxothuringian zone in the north, crosses the GRF array approximately between subarray A and subarray B with a NE strike (Geologische Karte von Bayern 1:500,000, 1981; Jacobshagen, 1976).

According to the evaluation of seismic refraction data in the array siting area (Aichele, 1976; Giese, 1976a, b; Ströbenreuther, 1982), the crustal thickness beneath the GRF array has a constant value of approximately 28–30 km, while it increases to the east beneath the Bohemian Massif. While the crust-mantle boundary in the Moldanubian zone was found to be rather sharp, a change occurs to the NE of the array, entering the Saxothuringian zone where this boundary is less clearly developed and where the top of the upper mantle is characterized by a strongly reduced velocity (Giese, 1976b). Babuška et al. (1984, 1986) used *P* arrival times published in ISC bulletins for central European stations to study *P*-wave travel-time residuals at these stations. For GRF station A1 they calculated a representative average residual of 0.5 s and deduced a subcrustal lithospheric thickness of about 80 km. Raikes and Bonjer (1983), in their study of *P* residuals recorded in the Rhenish massif, included a small number of events recorded at the GRF array and inferred from these data a region of anoma-

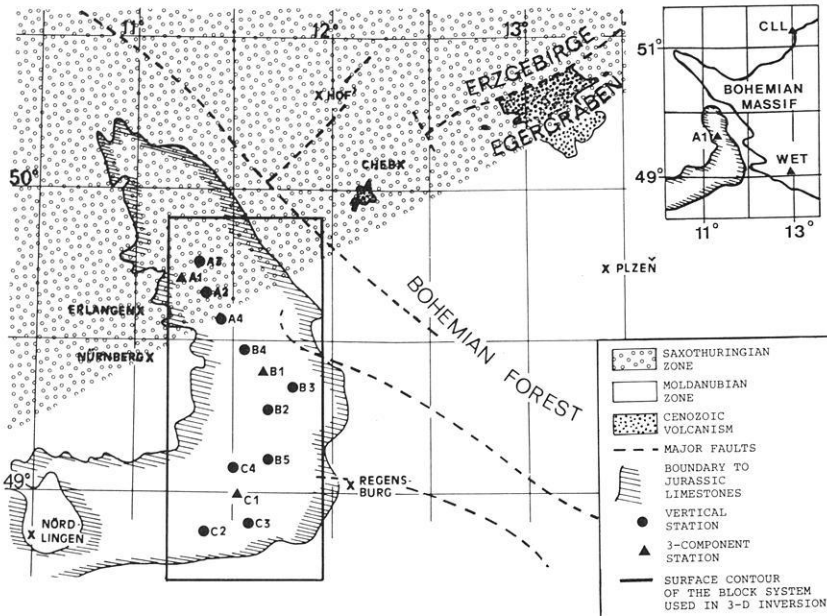


Fig. 1. Location of the GRF array with respect to the geotectonic surrounding. The contour of the block system used for the 3-D inversion is shown. *Upper right:* locations of the stations WET and CLL used as normalizing stations in the 3-D inversion

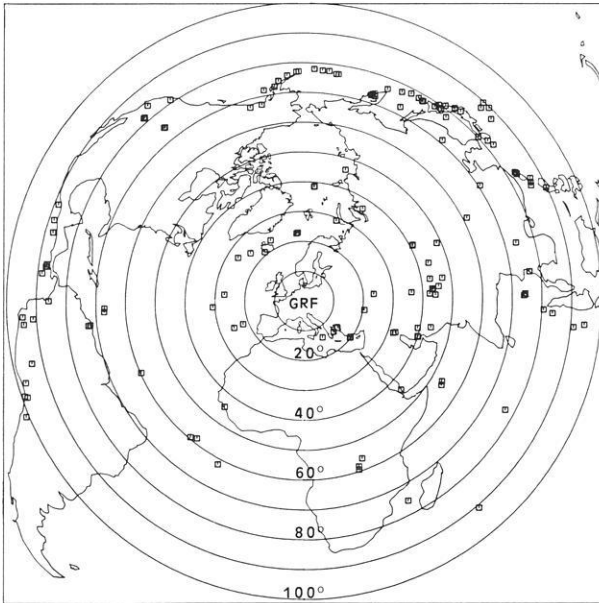


Fig. 2. Distribution of teleseismic events used in the analysis. Epicentral distances are given in degrees from GRF station A1

lously low velocity which extends to a depth of 200 km to the northeast of the array. The existence of deep-seated structures with relatively low velocities located in the north-eastern part of the GRF array is also required for the interpretation of the data used in our analysis.

GRF-array mislocations

Mislocation pattern

The most important task in compiling a data base for location calibration is to cover slowness space as densely as possible with mislocation vectors. Departure from an ideal coverage is of course unavoidable since seismic zones on the earth are not homogeneously distributed. Locations of epicentres used in this study are plotted in Fig. 2; epicentral

distances range from 20° to 100°. Due to the location of the GRF array relative to the zones of seismic activity, southern azimuths are poorly covered with data. By the term “azimuth”, we mean the station-to-source azimuth throughout this paper.

Figure 3 shows the GRF whole-array diagram which represents the mislocation vectors in slowness space. The theoretical and observed values of the slowness $dT/d\Delta$ versus azimuth are drawn as the heads and tails, respectively, of these vectors. Theoretical values have been determined from the USGS hypocentre parameters and a radially symmetric earth model (Jeffreys-Bullen tables). The observed values have been calculated by least-squares fitting of a plane wavefront to the time delays measured at the array stations. Relative onset times were determined by reading the first peak in the signal; this was found to be more accurate than picking first onset times, provided that the signal shape does not change across the array. This was ensured by imposing the restriction of high signal-to-noise ratio and high spatial coherency on the signals of the selected data. Before the relative onset times were determined, the digital broad-band data were filtered to simulate short-period WWNSS seismograms. This procedure produced narrow-band signals and hence sharp peaks such that the error in picking times did not exceed one digitization interval of 0.05 s.

The mislocation vectors are remarkably consistent in orientation and magnitude within large azimuthal ranges (Fig. 3). This observation leads to the assumption that mislocations are not caused by inhomogeneities near the focus or along the deep mantle path of the waves, but that they are due to lateral velocity variations in the array siting area. The variation in magnitude of the slowness and azimuth anomalies can not be correlated with the changes of slowness and azimuth resolution due to the array configuration. The slowness resolution is best at 165° and 345°, while the azimuth resolution is best at 75° and 255° (D. Seidl, personal communication). Generally, vectors point in the direction of lower velocity; for waves approaching from the west and from north to east, the vectors tend to point north-to-northeastward. This trend sometimes changes for larger

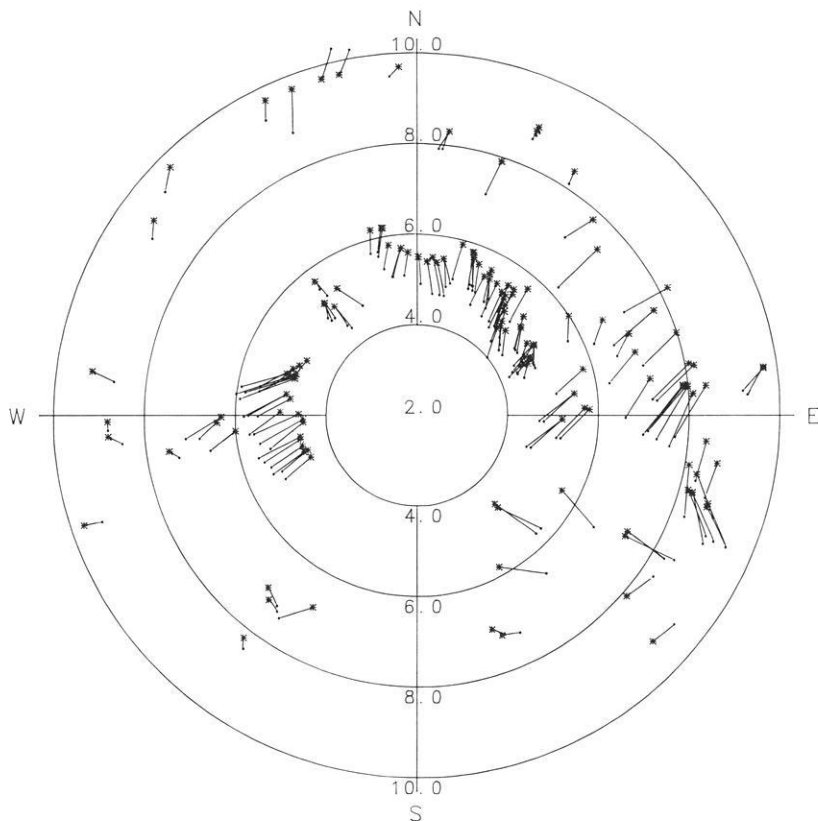


Fig. 3. GRF array diagram for all stations, including mislocation vectors plotted in slowness space. The radial component represents slowness in s/deg. The tail of each vector (●) gives the observed value, while the head (*) represents the PDE solution

incidence angles (high slowness values) as in the case of western azimuths, for instance. This particular change of magnitude and orientation of mislocation vectors, for higher slowness values at certain azimuths, indicates the presence of shallower local velocity perturbations which are sensed by waves depending on their angle of incidence and which are superimposed on the large-scale regional anomaly. Mislocation vectors for waves incident from the south-east and north-west show different behaviour when their orientation is compared to that at other azimuths, suggesting large-scale changes different from those in the north-eastern and south-western quadrants of the array diagram in Fig. 3.

Interpretation

A systematic change in structure (dipping layer or constant lateral velocity gradient) beneath an array will cause a deviation of observed slowness and azimuth from theoretical values which will usually be a periodic function of azimuth. This azimuthal dependence of the slowness and azimuthal anomalies shows up clearly in Fig. 4 which is another presentation of the parameters plotted in Fig. 3. The slowness anomaly is clearly negative for northern azimuths and positive for southern azimuths, with zero crossings close to east and approximately at WNW. For the azimuthal deviation, one zero crossing takes place near north, while the other one is less clear, especially since the data distribution is rather sparse for southern directions. Strong lateral variations of smaller dimension than the systematic change in structure, as they occur to the southeast for instance (Fig. 3), can produce a change of sign at other positions than that caused by the main anomaly. Neglecting for the moment the data points in the southeast and considering

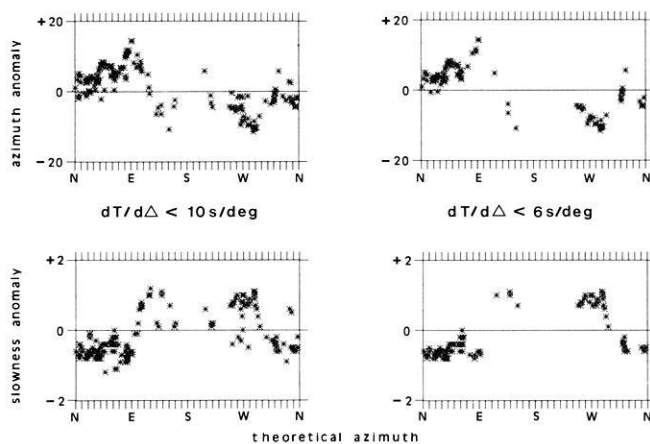


Fig. 4. Observed minus calculated (PDE) azimuth (*top*) and observed minus calculated slowness (*bottom*) as a function of calculated azimuth. The diagrams *on the left* include data for slowness values up to 10 s/deg, while *on the right* only data for slowness values below 6 s/deg are plotted

the fact that the main extrema of the azimuthal anomaly exist in the east (positive) and in the west (negative), a second zero crossing occurs close to south.

Similar azimuthal dependence of slowness and azimuth deviations have been modelled by dipping boundaries between layers of different velocities (Berteussen, 1974; Niazi, 1966; Otsuka, 1966). According to these investigations, the dipping angles and directions of inclined interfaces can be inferred from the position of zero crossings and extrema in azimuthal anomalies. Applying this to the azimuthal anomaly of the GRF array, a dipping interface beneath this area would strike in an east-west direction and dip

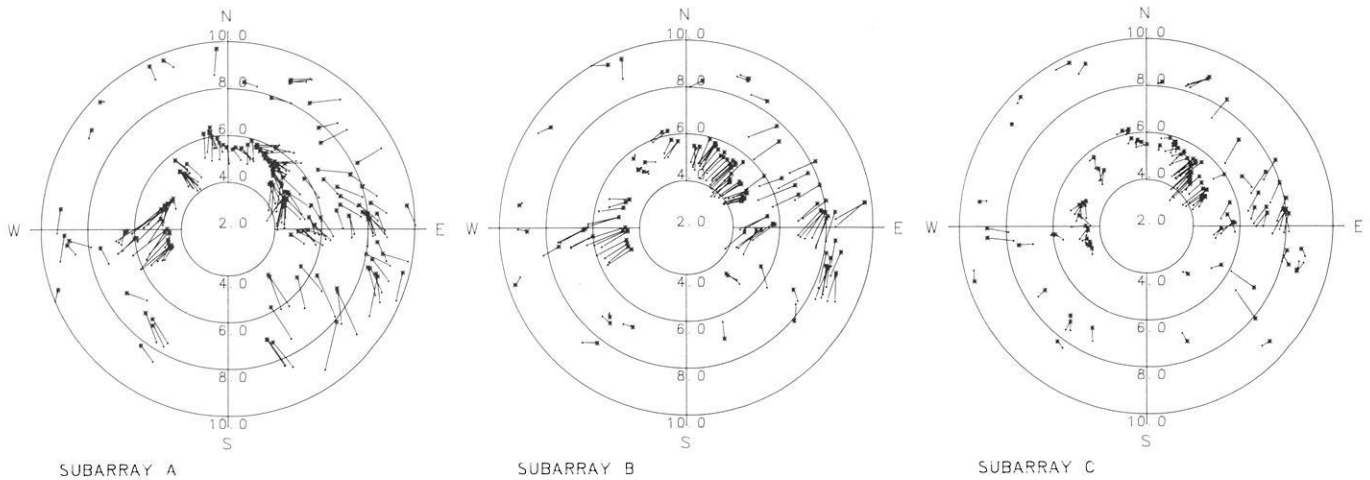


Fig. 5. Mislocation diagrams for single subarrays (for explanation of notations and symbols, see Fig. 3)

northwards in the case of a velocity increase downward across it, while it would dip southwards in the case of a velocity decrease. The dip angle can be approximated from the magnitude of the slowness anomaly, which depends on the angle of incidence under which the wavefront hits the dipping interface (Niazi, 1966). This is one reason for the reduction of scatter in the right part of Fig. 4 which only includes data for slowness values below 6 s/deg, corresponding to an incidence angle at the top of the upper mantle of about 24° . The mean magnitude of the slowness anomaly is approximately 0.8 s/deg. Regarding the relatively constant thickness of the crust beneath the GRF array deduced from refraction seismic measurements (Aichele, 1976; Giese, 1976a, b; Strößenreuther, 1982), the possibility of a strongly dipping crust-mantle boundary must be rejected; a northward dip with an angle of at least 13° would be required to explain the slowness anomaly.

Another possibly dipping interface to be taken into consideration is the lithosphere-asthenosphere boundary. The velocity decrease downwards across it requires a southward dip according to the azimuthal anomaly. The direction of dip would correspond to that deduced for this region from *P*-wave travel-time residuals by Babuška et al. (1986). Nevertheless, the magnitude of the slowness anomaly would require a dip angle of nearly 50° , assuming a velocity decrease from 8.3 km/s to 7.9 km/s at the lithosphere-asthenosphere boundary. Even if we accept a slightly dipping MOHO discontinuity with an angle of at most 2° – 3° , not to contradict previous investigations, the required remaining dip of the lithosphere-asthenosphere boundary would still be unrealistically large. From these approximations, it must be concluded that, in addition to a possible southward dip of the lithosphere-asthenosphere boundary, a lateral increase in upper-mantle velocities from north to south is required to explain the relatively large mislocations observed at the GRF array.

Another possibility to be considered is that these anomalies might be partially due to deep-seated abrupt lateral changes in structure, in contrast to the continuous variations across the array examined up to now. Mislocation vectors for the whole-array diagram (Fig. 3) represent average measurements of wavefront distortions across the whole array. Therefore, details in the anomaly pattern, e.g. local structural effects, could be hidden or smeared over all of

the array. As a matter of fact, the array diagrams for other station combinations, other than the whole array, reveal that mislocation patterns change with station configuration. Figure 5 shows the mislocation patterns for each subarray. The method and accuracy for the determination of the mislocation vectors has been discussed in connection with Fig. 3. Especially for waves incident from northeastern directions at subarray A, the orientations of mislocation vectors deviate largely from those at subarrays B and C; while for steep incidence from western directions at subarray C, mislocation vectors are substantially shorter than at subarrays A and B. At this point we would like to postpone the discussion on continuous and abrupt changes in velocity contrasts beneath the GRF array till later, since the *P*-wave travel-time residuals supply additional information concerning this problem.

P-wave travel-time residuals

Data

The events selected for the analysis of *P*-wave travel-time residuals were the same as those used for generating the mislocation vectors. The accuracy of the picked arrival times is the same as discussed above. As a first step, the *P* residuals for each station were determined by subtracting the *P* travel times through the Jeffreys-Bullen model from the observed *P* travel times using USGS hypocentral parameters. The effects on *P* residuals which arise from hypocentre mislocations and errors in origin time, as well as from lateral velocity variations in focal regions and along the deep mantle path of the waves, are largely eliminated by normalizing the data for each event. Normalizations are sometimes calculated with respect to the average residual of a station network. However, the interpretation of the mislocation patterns for the GRF array showed that large lateral velocity variations exist beneath the array which would affect the relative residuals considerably if the average is used as a normalization base. Therefore, we chose reference stations situated outside the station area. The location of these normalizing stations should not be too far from the territory under investigation in order to guarantee that the travel paths of the waves in the focal region and in the deeper mantle are about the same for the normalizing

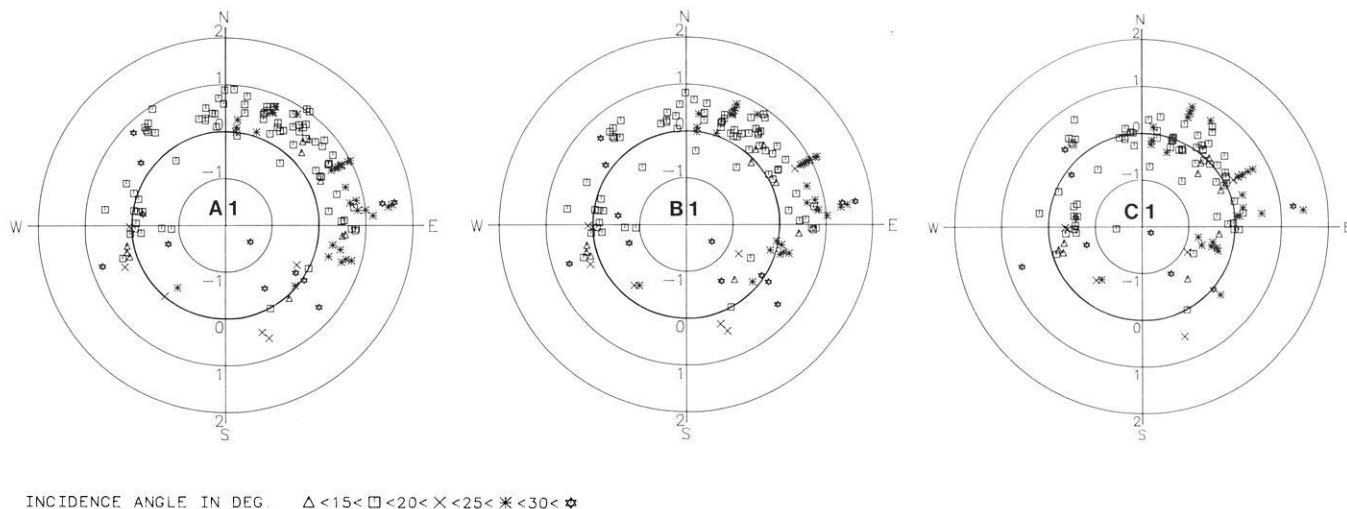


Fig. 6. P travel-time residuals for subarray-centre stations A1, B1, C1 calculated for each event relative to the respective mean residual of the normalizing stations WET and CLL. Symbols differ for different intervals of the theoretical incidence angle of P waves at the surface. The radial component represents the residuals from -2 s to $+2$ s

stations as for other stations. It is also important not to impose the effect of structure beneath the normalizing stations onto the data set to be investigated.

According to the patterns of azimuthal variations of P residuals at central European stations (Babuška et al., 1984), no single nearby station exists which would be ideal to use as a normalizing station. Therefore, we use the average residual of two stations with nearly opposite patterns in their azimuthal variation of residuals (Babuška et al., 1984) for the present normalization; expecting thus to cancel to a large extent, the structural effects under the normalizing stations. The two selected stations are Wettzell, (WET) located in the Moldanubian zone, and Collm (CLL) in the Saxothuringian zone (Fig. 1). We considered using an average of residuals from more than two stations to further minimize local structural influences, but this would have resulted in a considerable loss of data, since only such events from which onsets were reported at all of the normalizing stations could be used. The onsets at WET and CLL of the events selected in our study were read from station reports to ISC.

Figure 6 shows the P residuals for the GRF subarray-centre stations normalized to the average of the residuals of the corresponding events at WET and CLL. While the scatter in the P residuals due to errors in hypocentre determinations and in structural contrasts near the focus and in the deeper mantle should be largely eliminated by the applied normalization, we suppose that the scatter in the data of Fig. 6 is partially due to errors in reading onsets at normalizing stations which might sometimes be larger than those at the GRF stations, but also due to local structural variations beneath these stations. Since the onset times at normalizing stations were picked from bulletin reports it is difficult to estimate their accuracy, but we suppose that the errors in reading are not much larger than 0.1 s as we selected events with high-quality signals at the GRF stations. Despite the remaining scatter, the residual patterns (Fig. 6) reveal that a general shift of residuals of about 0.5 s takes place from north (station A1) to south (station C1) and for some azimuths, like ESE, it is even larger.

In order to demonstrate more clearly the change of re-

siduals as a result of lateral inhomogeneities beneath the GRF array and to perform a 3-D inversion, for stability comparisons, based only on the homogeneous data set of the GRF stations, we normalized the data set to one of the array stations, namely to A1. Since the error in picking onset times by doing this is not larger than 0.05 s also for the normalizing station A1, we end up with a minimum of scatter in Fig. 7 and the systematic changes in P residuals across the array show up clearly. Choosing A1 as the normalizing station in this case does not imply that the residuals at A1 are less affected by velocity perturbations due to structural inhomogeneities than at other stations of the array. Rather, since A1 is the most reliable station as regards operational time, we picked it in order to obtain as large a data set as possible. Looking at Fig. 7 one has to keep in mind the residual pattern at A1 with respect to the normalizing stations WET and CLL (Fig. 6), A1 being late by an average of 0.5 s from northwestern to eastern directions and just about “normal” for southeastern directions. Figure 7 demonstrates a strong shift in the residuals to negative values, from the northern station A3 to the southern station C2 (Fig. 1), and which is largest for eastern azimuths. For some directions the magnitude of the residual variation is strongly dependent on the incidence angle. From northern to northeastern azimuths, the shift for shallow incidence is small compared to steep incidence. Also, for waves arriving from the east at the southern stations B5 through C4, the shift is largest for angles of incidence between 25° and 30° , namely almost -1 s. A similar phenomenon occurs for southeastern azimuths where the residuals at the stations of subarray B differ by up to 0.5 s (at B3) for various angles of incidence.

3-D inversion of P residuals

Using the standard Aki three-dimensional velocity inversion scheme (Aki et al., 1976, 1977), an automatic inversion was applied to the P residuals presented earlier. In this procedure the region beneath the investigated area is divided into several layers, each layer consisting of a system of rectangular blocks. The linear 3-D inversion procedure

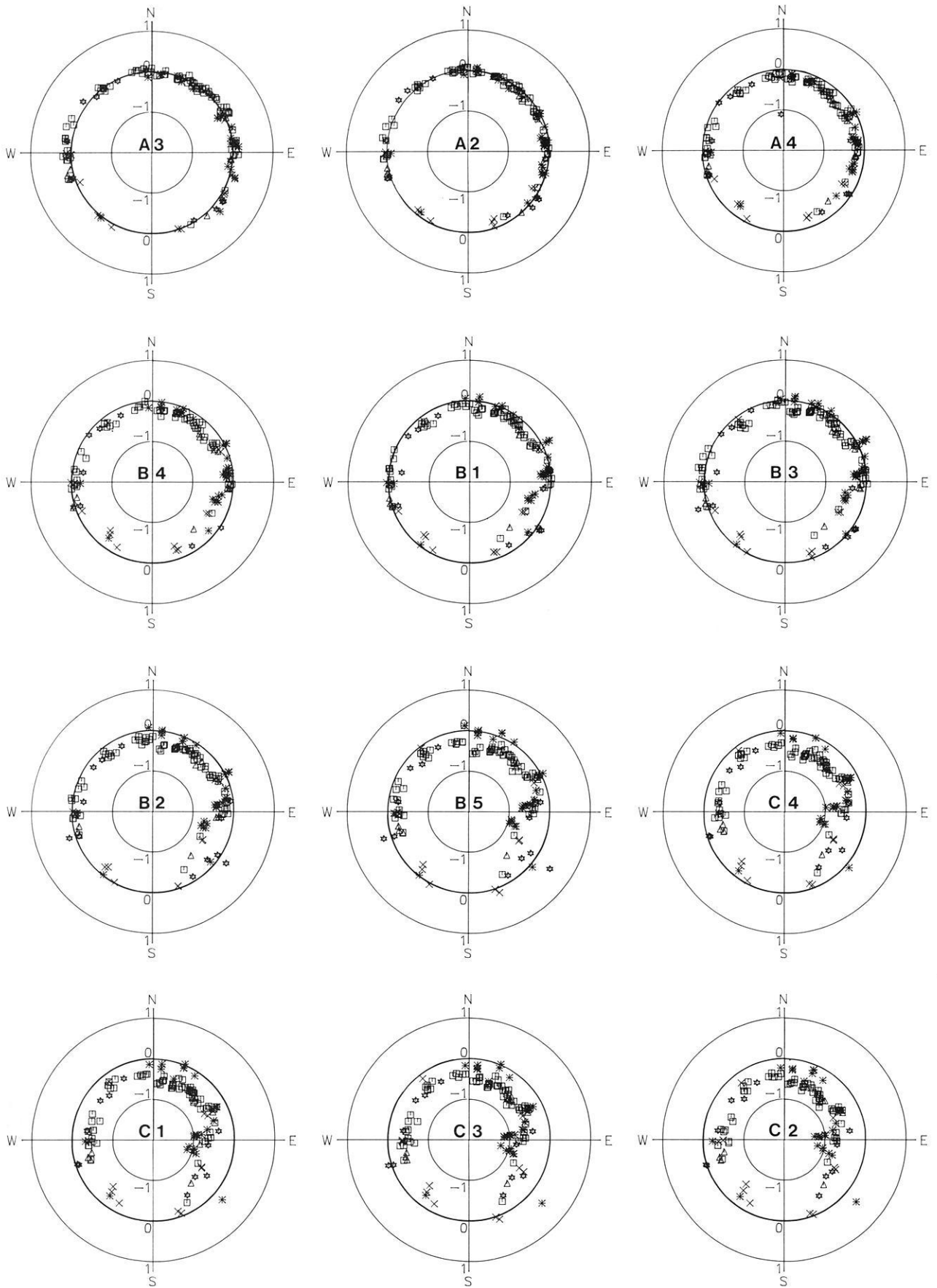


Fig. 7. *P* travel-time residuals for all of the GRF stations normalized to A1 for each event (for explanation of symbols, see Fig. 6). Stations are arranged from left to right and from top to bottom according to their geographic order from north to south

used in this study makes several approximations which severely bias the solution. The principal assumptions of the method are that in each layer a seismic ray propagates only in one single block, namely in that one in which the ray spends most of its time, and that refractions of the ray at the discontinuities between adjacent blocks are neglected. These approximations result in a degradation of the spatial resolution and in an underestimation of velocity perturbations (Koch, 1985). Moreover, the problem of the optimal choice of the block geometry and layer thickness for the reconstruction of an unknown model is difficult to solve without good knowledge of the tectonics and geology of the deep structure to be modelled.

In order to test the influence of the starting model and of the block size as well as of the normalization on the results, the inversion was performed for two different initial 5-layer models (Table 1) and for several block configurations using two sets of input data with different normalizations. The main differences between the two initial models exist in the lower lithosphere, where model 1 includes a velocity decrease from 8.4 km/s to 7.9 km/s at a depth of 79 km, while the velocity-depth function in the uppermost mantle of model 2 represents a gradual increase in velocity from 8.15 km/s at a depth of 30 km to 8.3 km/s at a depth of 130 km. A set of calculations with different damping parameters θ^2 was performed in order to find an acceptable trade-off between the resolution and the stability of the solution. The damping parameter θ^2 is conveniently expressed as $\theta^2 = F \cdot \max(A^T A)$, $\max(A^T A)$ being the largest diagonal element of the normal equation matrix and F the effective smoothing parameter (Hovland et al., 1981). Figure 8 represents the RMS velocity perturbations versus residual variance improvement for different parameters F ranging from 10 to 0.0001. The parameter 0.05 was adopted for further calculations, because the RMS velocity perturbations for lower values of F increases substantially without a considerable increase of the residual variance improvement.

Figure 9 shows the results of the 3-D inversion for the two initial models (Table 1) with layers being divided into 4×4 blocks. Each block is 33.2 km in the NS direction and 21.6 km in the EW direction. The contour of the block system is included in Fig. 1. The horizontal coordinates of the centre of the block system are: 49.31° N, 11.56° E. For good resolution, a minimum of ten rays with a homogeneous azimuthal distribution should pass through each block. When dealing with a real data set we must accept that the azimuthal coverage is far from ideal due to the irregular distribution of epicentres (Fig. 2). Due to the shape of the array, five blocks in the first layer of the models are not hit by rays and some of the blocks, namely those close to margins, are poorly resolved. In the deeper layers almost all of the blocks are crossed by rays; however, the resolution decreases because each block is sampled by fewer rays. Similar velocity perturbations were obtained for both models. The variance improvements of both inversions are the same: 36.1% and 36.8% for models 1 and 2, respectively. The same concerns the values of the diagonal elements of the resolution matrix of individual blocks in layers 1–3. The inversion with model 2 as the initial model results in higher values of the diagonal elements of the resolution matrix in layers 4 and 5 compared to the calculation with model 1. The inversion of the data set normalized with respect to the average residual at WET and CLL results

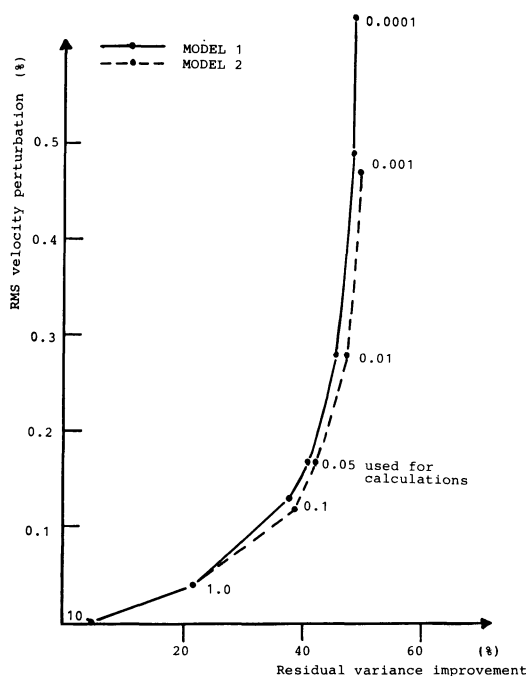


Fig. 8. RMS velocity perturbations versus residual variance improvement, calculated for various values of the effective smoothing parameter F . The computations were done for data normalized to the mean residuals at WET and CLL and for model 1 (dashed line) and model 2 (full line). The relation between F and the damping parameter θ^2 is given by $F = \theta^2 \cdot \max(\text{diagonal element of the normal equation matrix})$. The value $F = 0.05$ corresponding to $\theta^2 = 224 \text{ s}^2$ for model 1 and $\theta^2 = 242 \text{ s}^2$ for model 2 was adopted for further calculations

Table 1. Starting models for 3-D inversion

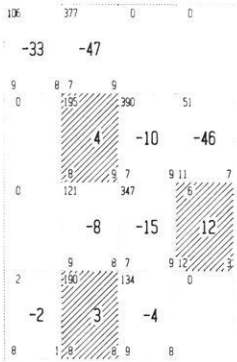
Layer	Thickness (km)		Velocity (km/s)	
	model 1	model 2	model 1	model 2
1	28	30	6.1	6.2
2	26	25	8.2	8.15
3	25	25	8.4	8.2
4	15	25	7.9	8.25
5	26	25	8.1	8.3

in a general increase of velocity from north to south (Fig. 9). The two layers of the uppermost mantle (model layers 2 and 3), especially, are characterized by relatively low-velocity blocks in the northeastern part and by relatively high-velocity blocks to the south, mainly to the southwest.

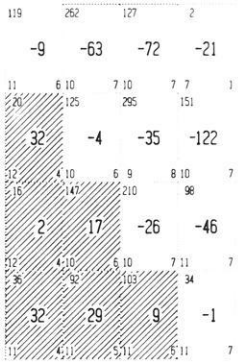
The 3-D inversion of the P residuals was also computed for the same initial models but for a system of 8×8 blocks. The horizontal dimensions of each block were half of those in the 4×4 block system. In this case, due to the smaller block dimensions, each block was sampled by a smaller number of rays and the solution became less stable, but the main tendency of the velocity changes across the array was preserved. In order to verify details in the velocity perturbation pattern, we shifted the block system relative to the station locations and recomputed the 3-D inversions; the perturbation pattern was preserved even in detail. These experiments demonstrate that the results of the 3-D inversion concerning the general pattern of velocity perturbations are reliable.

MODEL 1

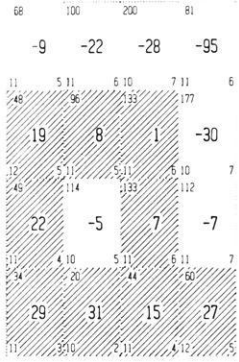
Layer 1 : 0 - 28



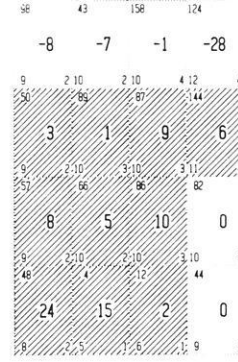
Layer 2 : 28 - 54



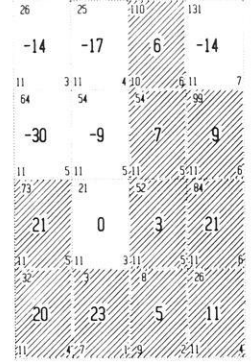
Layer 3 : 54 - 79



Layer 4 : 79 - 94

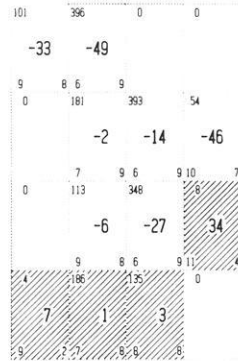


Layer 5 : 94 - 120

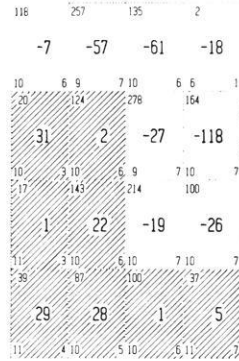


MODEL 2

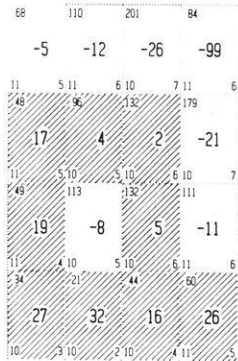
Layer 1 : 0 - 30



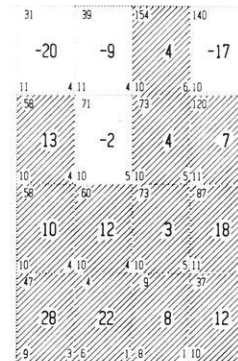
Layer 2 : 30 - 55



Layer 3 : 55 - 80



Layer 4 : 80 - 105



Layer 5 : 105 - 130

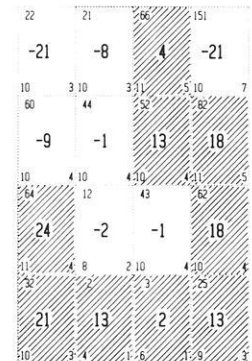
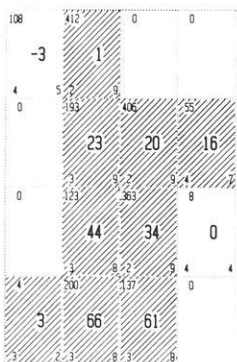


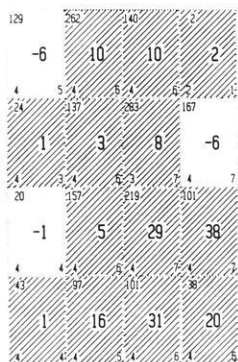
Fig. 9. Velocity perturbations (in tenths of percent of the respective layer velocity of the starting model) obtained by the 3-D inversion of the residuals normalized to WET and CLL. Variance improvements for models 1 and 2 are 36.1% and 36.8%, respectively. The number of rays passing through each block of the 4 x 4 block approximation of the area is given in the upper left corner of each block. The standard errors of the velocity perturbations (in tenths of a km/s) and the values (in tenths) of the diagonal elements of the resolution matrix are plotted in the left and right lower corners of each block, respectively. The blocks with positive velocity perturbations are hatched

MODEL 2

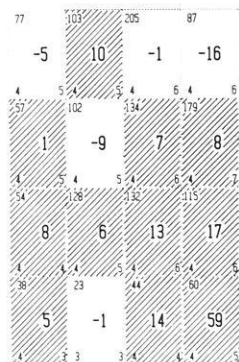
Layer 1 : 0 - 30



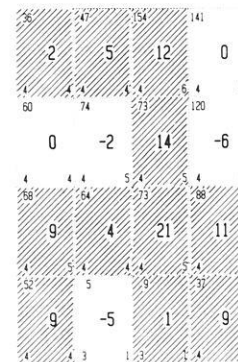
Layer 2 : 30 - 55



Layer 3 : 55 - 80



Layer 4 : 80 - 105



Layer 5 : 105 - 130

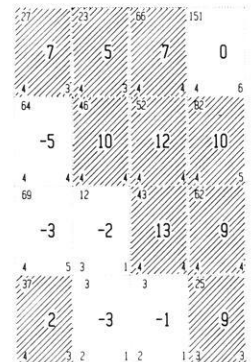


Fig. 10. Velocity perturbations resulting from the 3-D inversion of the residuals normalized to A1 computed for the 4 x 4 block approximation of the area. The variance improvement is 70% (for notations, see Fig. 9)

3-D inversions were also calculated for a data set normalized to A1 (Fig. 10) in order to check whether the stability of the solution increases if only the uniform data set of the GRF stations is used (Fig. 7). The relatively high value of 70% was obtained for the variance improvement from the inversion of the P residuals normalized to A1. Since P velocities beneath station A1 are predominantly low (negative velocity perturbations), the inversion of this data set is characterized by high-velocity blocks throughout most of the model. Nevertheless, the change in absolute magnitude of the velocity perturbations from north to south within the individual layers is comparable to that inferred from the data set normalized to the average residual at WET and CLL.

Discussion

The 3-D inversion of the P residuals observed at the stations of the GRF array resulted in an increase of velocity from north to south in the uppermost mantle. Considering the reliability of this result, it should, however, be kept in mind that several limitations to the method used for the inversion exist. One of these is that, due to the limited spread of the stations (Fig. 1), the area covered by the block system cannot be extended beyond its present lateral and depth dimensions. This means that the automatic inversion scheme would map velocity perturbations originating from inhomogeneities located outside the block system to the blocks within the system.

The 3-D inversion also produced a velocity decrease from south to north in the crustal layer. A delay of at most 0.1 s in P arrival times for the northernmost stations with respect to the southernmost can be explained by changes in sedimentary thicknesses, sedimentary layers being thicker by about 1.5 km in the northernmost part of the array than at the southernmost station sites (Emmert, 1981; Erläuterungen zur Geologischen Karte von Bayern 1:500,000, 1981). After stripping crustal influences, a mean residual variation across the array of about 0.5 s for steep incidence remains, which results in a general increase in velocities from north to south in the uppermost mantle using the 3-D inversion.

A similar effect on P residuals, as is produced by a velocity increase within a model with plane horizontal layers, could result from dipping layer boundaries and should therefore be considered. It has been concluded, in an earlier section, that the dipping angles of the crust-mantle or lithosphere-asthenosphere boundary, which would be required to explain the observed deviations in mislocations or the changes in residuals across the array by dipping layer boundaries only, are much too large to be realistic. Moreover, a southward dip of the lithosphere-asthenosphere boundary could not, by itself, produce as large a separation in residuals as a function of incidence angle as is observed across the GRF array, especially for northeastern azimuths. This observation points to another mechanism in addition to the gradual change in structure.

A deep-seated low-velocity region located to the northeast of the array would explain the differentiation of residuals as a function of incidence angle for northern to northeastern azimuths (Fig. 11). It is obvious that such a low-velocity zone cannot be located in the lithosphere directly beneath the stations, but has to be sought for at least at a distance from the array where the waves incident at

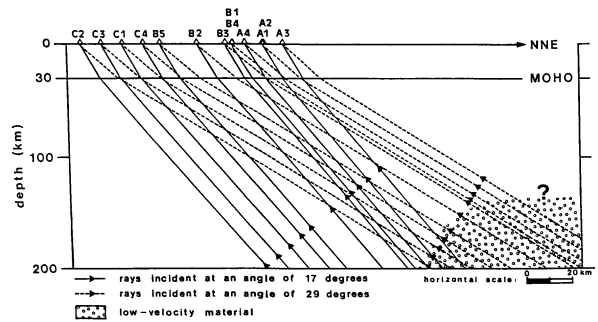


Fig. 11. Schematic ray tracing through a vertical crustal/upper mantle cross-section (simplified model) on a NNE-SSW profile through B1. The locations of the other GRF stations have been projected perpendicularly onto this line. The question mark denotes that the upper limit of the low-velocity region is undefined due to the non-existence of stations beyond A3 on this profile

steeper angles are separated enough from those with shallow incidence to produce the observed phenomenon (Fig. 7). In such a case the low-velocity region would be sensed across the whole array by rays incident at large angles from NNE, but would not influence the travel times of rays with steep incidence except at the northernmost stations. The location of this region is not, or only marginally, included in the block system set up for the inversion. Considered in terms of structural variations related to tectonic features, it must be kept in mind that the boundary between two geological units, the Saxothuringian zone in the north and the Moldanubian zone in the south, crosses the investigated region approximately between the subarrays A and B with an ENE strike (Fig. 1). A low-velocity material appearing as an asthenolith in the vicinity of this boundary between the two geological units and extending to the ENE, being less pronounced to the WSW, would explain the positive P residuals observed at subarray A as well as the differentiation of residuals as a function of incidence angle crossing the array from north to south. It has already been mentioned in an earlier section that the mislocation pattern of subarray A differs largely from those of the other two subarrays B and C, especially for northeastern azimuths, and this could also be explained by such a velocity anomaly. This supports the hypothesis that structures do not vary gradually from north to south across the array, but that the northeastern part is anomalously slow with a rather abrupt change to the south.

Besides the model specifications discussed up to now, the structures beneath the Moldanubian part of the Bohemian Massif seem to include very high velocities sensed by rays incident to subarrays B and C from eastern to southeastern directions. Mislocation vectors for these azimuths also indicate an increase in velocities. This pronounced velocity increase to the southeast of the array might be related to directional variations of velocities (anisotropy) within the lower lithosphere as well as to an increase in lithospheric thickness underneath the southern part of the Bohemian Massif. Refraction seismic studies in the southwestern part of the Bohemian Massif have shown a crust-mantle boundary dipping steeply from the SW to the NE underneath the Bohemian Massif (Ströbenreuther, 1982). As had been outlined before, the change in residuals discussed here is again coupled to a clear differentiation of their magnitude as a function of angle of inci-

dence, being strongest for subarray B from southeastern azimuths and for subarray C from eastern azimuths (Fig. 7). This dependence of the magnitude of the residuals on the angle of incidence leads to the conclusion that the velocity perturbations or lateral changes in structure causing this effect are located not directly beneath the stations but at some distance to the ESE in the upper mantle.

Summary

Strong lateral variations definitely exist in the uppermost mantle beneath the GRF array. The general feature is a deep-seated velocity increase from north to south, i.e. from the Saxothuringian zone into the Moldanubian zone, superimposed on the effect of a possible thickening of the lithosphere from north to south as has been derived by Babuška et al. (1986). This is inferred from the interpretation of the whole-array mislocation pattern as well as from the gradual decrease of *P* residuals from north to south across the array and from their differentiation as a function of incidence angle. A low-velocity zone located in the upper mantle to the NE of the array close to the transition region from the Saxothuringian into the Moldanubian zone might be connected to the deep structure of the Egergraben. This region is characterized by Cenozoic volcanism (Fig. 1) and by an increase in heat flow (Čermák and Hurtig, 1979) which might be coupled to the low-velocity material inferred from the *P* residuals. In contrast to these low-velocity structures in the north, the Moldanubian part of the Bohemian Massif which has been sampled by our data reveals very high velocities in the uppermost mantle.

Acknowledgements. We are indebted to U. Achauer and J. Šílený for providing programs and support in computing. We would like to thank U. Achauer, B. Buttkus and D. Seidl for critically reading the manuscript and for numerous helpful discussions. We appreciate very much the translation assistance and comments given by M. Hellweg. The present investigation was supported by the Deutsche Forschungsgemeinschaft (German Research Council) under contracts SZ32/6-1 and AI12/1-2 and partially by UNESCO under contract SC/RP 590992. The Gräfenberg array is part of the Bundesanstalt für Geowissenschaften und Rohstoffe (Federal Institute for Geosciences and Natural Resources) and is supported by the Deutsche Forschungsgemeinschaft.

References

- Aichele, H.: Interpretation refraktionsseismischer Messungen im Gebiet des fränkisch-schwäbischen Jura. Ph.D. thesis, University of Stuttgart, 1976
- Aki, K., Christofferson, A., Husebye, E.S.: Three-dimensional seismic structure of the lithosphere under Montana LASA. *Bull. Seismol. Soc. Am.* **66**, 501–524, 1976
- Aki, K., Christofferson, A., Husebye, E.S.: Determination of the three-dimensional seismic structure of the lithosphere. *J. Geophys. Res.* **82**, 277–296, 1977
- Babuška, V., Plomerová, J., Šílený, J.: Large-scale oriented structures in the subcrustal lithosphere of Central Europe. *Ann. Géophys.* **2**, 649–662, 1984
- Babuška, V., Plomerová, J., Šílený, J.: Structural model of the subcrustal lithosphere in Central Europe. In: The composition, structure and dynamics of the lithosphere-asthenosphere system, C. Froidevaux and K. Fuchs, eds. 1986 (in press)
- Berteussen, K.A.: NORSAR location calibrations and time delay corrections. Scientific Report No. 2-73/74, NTN/NORSAR, 1974
- Berteussen, K.A.: The origin of slowness and azimuth anomalies at large arrays. *Bull. Seismol. Soc. Am.* **66**, 719–741, 1976
- Berteussen, K.A., Husebye, E.S., Mereu, R.F., Ram, A.: Quantitative assessment of the crust – upper mantle heterogeneities beneath the Gauribidamur seismic array in southern India. *Earth Planet. Sci. Lett.* **37**, 326–332, 1977
- Čermák, V., Hurtig, E.: Heat flow map of Europe 1:5,000,000. In: Terrestrial heat flow in Europe, Čermák, V. and Rybach, L., eds. Berlin, Heidelberg, New York: Springer-Verlag 1979
- Christofferson, A., Husebye, E.S.: On three-dimensional inversion of *P* wave time residuals: option for geological modeling. *J. Geophys. Res.* **84**, 6168–6175, 1979
- Emmert, U.: Die Fichtelgebirgsschwelle an der Fränkischen Linie. *Jber. Mitt. oberrhein. geol. Ver.* **63**, 219–228, 1981
- Erläuterungen zur geologischen Karte von Bayern 1:500,000, (3. Auflage). Bayer. Geol. Landesamt, München, 1981
- Geologische Karte von Bayern 1:500,000, (3. Auflage). Bayer. Geol. Landesamt, München, 1981
- Giese, P.: Models of crustal structure and main wave groups. In: Explosion seismology in Central Europe, Giese P. et al., eds.: pp. 196–200, Berlin, Heidelberg, New York: Springer-Verlag 1976a
- Giese, P.: The basic features of crustal structure in relation to the main geological units. In: Explosion seismology in Central Europe, Giese P. et al., eds.: pp. 221–241, Berlin, Heidelberg, New York: Springer-Verlag 1976b
- Harjes, H.-P., Seidl, D.: Digital recording and analysis of broadband seismic data at the Graefenberg (GRF)-array. *J. Geophys.* **44**, 511–523, 1978
- Hovland, J., Gubbins, D., Husebye, E.S.: Upper mantle heterogeneities beneath Central Europe. *Geophys. J.R. Astron. Soc.* **66**, 261–284, 1981
- Jacobshagen, V.: Main geologic features of the Federal Republic of Germany. In: Explosion seismology in Central Europe, Giese P. et al., eds.: pp 3–17, Berlin, Heidelberg, New York: Springer-Verlag 1976
- Koch, M.: A numerical study on the determination of the 3-D structure of the lithosphere by linear and non-linear inversion of teleseismic travel times. *Geophys. J.R. Astron. Soc.* **80**, 73–93, 1985
- Niazi, M.: Corrections to apparent azimuths and travel-time gradients for a dipping MOHOROVICIC discontinuity. *Bull. Seismol. Soc. Am.* **56**, 491–509, 1966
- Otsuka, M.: Azimuth and slowness anomalies of seismic waves measured on the central California seismographic array. Part II. Interpretation. *Bull. Seismol. Soc. Am.* **56**, 655–675, 1966
- Raikes, S., Bonjer, K.-P.: Large-scale mantle heterogeneity beneath the Rhenish Massif and its vicinity from teleseismic *P*-residuals measurements. In: Plateau uplift, K. Fuchs et al., eds.: pp 313–331, Berlin, Heidelberg, New York: Springer-Verlag 1983
- Ram, A., Yadav, L.: Evidence for upper mantle heterogeneity around 650 km depth beneath the Indian subcontinent. *Tectonophysics* **68**, 17–23, 1980
- Strößenreuther, U.: Die Struktur der Erdkruste am Südwest-Rand der Böhmisches Masse, abgeleitet aus refraktionsseismischen Messungen der Jahre 1970 und 1978/79. Ph.D. thesis, University of Munich, 1982

Received January 3, 1986; revised version July 3, 1986
Accepted September 1, 1986

Lateral variations of the structure of the crust-mantle boundary from conversions of teleseismic *P* waves

Liu Qiyuan¹ and Rainer Kind²

¹ Institute of Geology, State Seismological Bureau, P.O. Box 634, Beijing, China

² Seismologisches Zentralobservatorium Gräfenberg, Krankenhausstraße 1, 8520 Erlangen, Federal Republic of Germany

Abstract. Clear *P*-to-*S* converted phases are observed in teleseismic seismograms recorded at the Gräfenberg array. The seismic events used are nuclear explosions from east Kasakh and deep-focus earthquakes from the region of Japan and central Asia. The identification of the converted phases has been improved by the rotation of the coordinate system. Theoretical seismograms have been computed to obtain the response of various velocity structures of the lithosphere under the receivers, using the reflectivity method of Kind (1985) for different source and receiver structures. The interpretation of the *P*-to-*S* conversions leads to a model of the crust-mantle transition zone with a first-order discontinuity and a normal velocity contrast in the north, an increased velocity contrast in the centre, and a reduced sharpness of the discontinuity in the south of the array. The sedimentary layers underneath the stations also cause strong converted phases, and they also influence strongly the waveform of the incoming *P* wave.

Key words: Lateral inhomogeneities – *P*-to-*S* conversions – Theoretical seismograms

Introduction

In recent years conversions of teleseismic body waves have been extensively used for exploring the structure of the earth (Bath and Stefansson, 1966; Polshkov et al., 1973; Vinnik, 1977; Vinnik et al., 1983; Burdick and Langston, 1977; Langston, 1979; Faber and Müller, 1980, 1984; Bock and Ha, 1984). Extensive experiments have been carried out in China, where *P*-to-*S* converted waves in the *P*-wave group of strong deep-focus events have been observed along profiles of about 3,000 km length (Shao et al., 1978, 1985). The results have been used for investigations of the common features of the deep structures in areas of strong earthquakes (Shao et al., 1985).

It has been shown that the converted phases can be used not only for determining the depth of discontinuities in the earth, but also for investigating their lateral fluctuations. This can be done because a specific converted phase within the body wave train is associated with a specific interface and its time delay and energy depends mainly on the depth and structure of the interface underneath the receiver.

The development of digital event recorders, particularly of digital broad-band arrays, will contribute to a more reliable and more convenient identification of converted phases because these new systems provide high-quality records and simplify data processing. In addition, the computation of theoretical seismograms is a powerful tool for the interpretation of seismic phases. The information about the fine structure of the lithosphere can be obtained from the broad-band or short-period seismograms.

Our purpose is to investigate the lateral inhomogeneities of the lithosphere under the Gräfenberg array (GRF) by using converted and multiply reflected waves which have been recorded by the three-component stations of the array. Our method is different from the method of Aki et al. (1976) or the method used by Faber et al. (1986) to determine the three-dimensional structure under arrays, which used *P*-wave travel-time delays. The observations of converted phases provide information about existence, location and sharpness of discontinuities and not about averaged velocities in block structures.

Method

The method is based on the identification of converted or multiply reflected phases within the first 10 s of the direct *P* wave. These phases are used to determine the interface depth and the velocity distribution within the lithosphere under a station. Lateral inhomogeneities of the lithosphere may then be derived by comparing these results at each station. It has been shown by observational and theoretical studies that, in China, there are several *PS* converted phases within the first 10 s of the direct teleseismic *P* wave train which can be identified on the rotated *SV* component of short-period records (Shao et al., 1978; Liu and Shao, 1985). The common features of the *PS* converted phases are described in these papers:

1) The time delays of phases converted at shallow structures depend mainly on the receiver structure and their variations are quite small with the epicentral distances.

2) The energy of *PS* conversions bears a close relation to the interface structure where the incoming wave is converted. *PS* conversions strong enough to be identified can be generated not only on sharp discontinuities, but also at other structures like gradients or stacks of thin layers.

3) The *PS* waveforms are generally quite similar to the ones of the original direct *P* wave, even if they are generated at stacks of thin layers.

Table 1. List of the events used (after PDE). *AZ* denotes back azimuth and i_0 denotes the experimentally determined best angle of incidence

No.	Date	Origin time	Latitude	Longitude	Depth (km)	m_b	Distance	<i>AZ</i> degrees	i_0
15	831008	07 45 26.6	44.2N	130.7E	558	5.7	72.6	41	1
14	840420	06 31 10.6	50.1N	148.7E	582	6.0	74.1	27	1
13	840415	07 34 12.0	42.9N	131.1E	538	5.0	73.8	42	1
12	810531	23 59 35.2	44.6N	137.3E	295	5.4	75.0	37	1
11	820714	10 42 13.5	45.6N	143.4E	325	5.3	76.3	32	1
10	830928	08 04 47.6	41.2N	132.5E	513	5.1	75.9	42	1
9	830928	07 59 13.9	41.2N	132.5E	522	5.1	75.9	42	1
8	830912	15 42 08.5	36.5N	71.1E	209	6.1	44.5	84	2
7	841027	01 50 10.6	50.0N	78.8E	0	6.2	44.7	69	4
6	840714	01 09 10.5	49.9N	79.0E	0	6.2	42.3	63	4
5	840526	03 13 12.4	50.0N	79.1E	0	6.0	42.4	62	4
4	840425	01 09 03.5	50.0N	78.9E	0	5.9	42.3	63	4
3	840329	05 19 08.2	49.9N	79.0E	0	5.9	42.4	63	4
2	840219	03 57 03.4	49.9N	78.8E	0	5.8	42.3	63	4
1	820704	01 17 14.4	50.0N	78.9E	0	6.1	42.2	63	4

4) A sedimentary layer with low velocity and high absorption is able to enhance the energy of *PS* conversions on the radial component.

A data processing procedure has been used in this paper to improve the identification of the *PS* conversions and the multiple reflections. The first step is to rotate the coordinate system in order to search for *PS* conversions (Vinnik 1977; Langston 1979). We denote

$$\begin{aligned} P(t) &= Z(t) \cdot \cos(i_0) + R(t) \cdot \sin(i_0) \\ Q(t) &= -R(t) \cdot \cos(i_0) + Z(t) \cdot \sin(i_0) \\ R(t) &= X(t) \cdot \cos(AZ) + Y(t) \cdot \sin(AZ) \\ T(t) &= Y(t) \cdot \cos(AZ) - X(t) \cdot \sin(AZ) \end{aligned}$$

where $Z(t)$, $X(t)$ and $Y(t)$ are the vertical, north and east components of a seismogram, respectively. AZ is the back azimuth; i_0 is the angle of incidence. In a laterally homogeneous and isotropic earth, *SH* waves should be recorded only on the T component. P and SV waves are recorded on the Z and R components, but the Q component should only have SV waves and the P component should only have P waves, provided the correct angle of incidence is chosen.

However, the uppermost part of the lithosphere is often laterally very inhomogeneous, therefore the separation of an incoming wave in its various wave types is not always easy. Experiments with varied back azimuths and angles of incidence must therefore be carried out in order to find the best signal enhancement of the converted phases. The first converted wave after the direct P wave often has such a short time delay that it interferes with the projection of the direct P wave on the horizontal components. Therefore, the choice of the proper angle of incidence is in this case especially critical. Plesinger et al. (1986) describe a method for the determination of azimuth and angle of incidence of incoming waves. This method has been used to determine the angle of incidence in this paper.

Another important step in the analysis method is the selection of events with simple source functions. Such events are very often deep-focus events. Nuclear explosions also have simple source functions. Therefore, we have restricted our data base to these two types of events.

The summation of the same components of events with the same epicentral distance increases the signal-to-noise ratio. This procedure greatly improves the reliability of the phase identification.

If converted phases are identified in the data, then a starting model of the structure under the station can be derived for the computation of theoretical seismograms. When the epicentral distance is greater than 40° , the depth h of the interface can be determined approximately by:

$$\begin{aligned} h &= (V_p \cdot \Delta T_{ps}) / (K - 1) \\ K &= V_p / V_s \end{aligned}$$

where V_p and V_s are the average P and S velocities, respectively, and ΔT_{ps} is the time delay of the PS wave relative to the direct P wave.

It has been shown that multiple reflections should be considered when theoretical seismograms of conversions are computed (Liu and Fan, 1985). Therefore, the new version of the reflectivity method by Kind (1985) has been used for calculating theoretical seismograms in order to infer the velocity distributions. This method can be used for different source and receiver structures and the multiple waves are automatically taken into account.

Data

The GRF array has been described in detail by Harjes and Seidl (1978). The 15 events used here are listed in Table 1. The seismograms recorded by the three-component GRF stations A1, B1, C1 are given in Figs. 1–3, respectively. A1 is located in the north, B1 in the centre, and C1 in the south of the array. Figures 1–3 show the seismograms after the rotations mentioned above. The back azimuths and the observed angles of incidence are also listed in Table 1. The angles of incidence in Table 1 are too small for the epicentral distances of the events. If horizontal layering is assumed, then only unrealistic low velocities of the sediments could explain these small angles. In order to show the correctness of these observations we show particle-motion diagrams of the stations A1, B1 and C1 in Fig. 4 for event 1 in Table 1. This figure shows clearly that the angle of incidence at the GRF stations is extremely small. For comparison, particle motions of the stations KHC (Kasperske Hory, Czechoslovakia) and KSP (Ksiaz, Poland) are also shown in Fig. 4. These two stations have more normal angles of incidence.

The reason for this anomaly at the GRF stations is

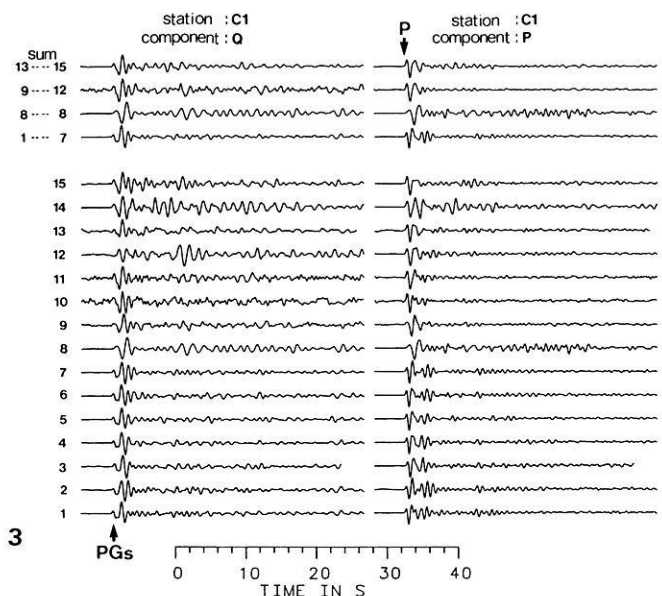
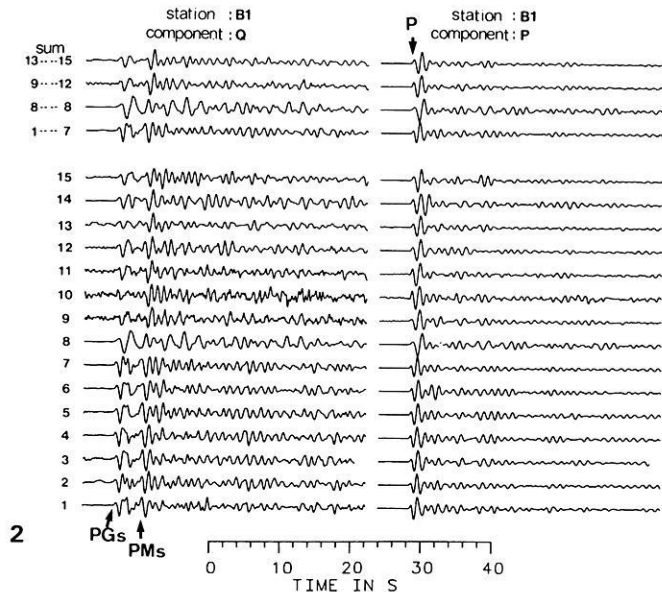
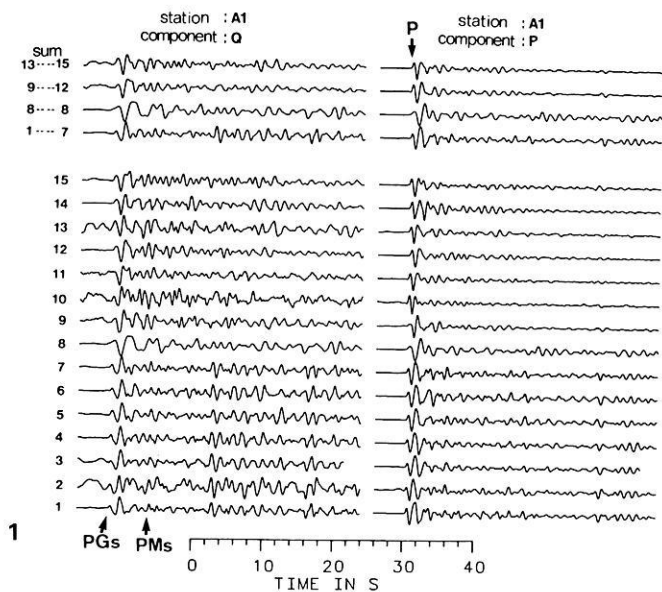


Fig. 1. Rotated Q and P components of WWSSN short-period simulations of events recorded at station A1. The numbers 1–15 refer to the event numbers in Table 1. Summation traces of groups of events are plotted at the top of the figure. The labelled phases are: PMs -converted S wave at the Moho, PGs -converted S wave at the bottom of the sediments, P -incoming P wave. All traces are independently normalized to the same size. The PMs conversion is much smaller than the PGs conversion. See Figs. 6 and 7 for a comparison of the amplitudes of the different traces

Fig. 2. Same as in Fig. 1, for station B1. The Moho conversion PMs is much stronger at station B1 than at A1

Fig. 3. Same as in Fig. 1, for station C1. The Moho conversion PMs is not visible at all

still unknown. Array slownesses of the same events, determined from P -wave arrival times of all vertical components, are not in agreement with such small angles of incidence. This could indicate that the anomaly is located at shallow depth. It should be kept in mind that this observation is made with short-period data. The anomaly underneath GRF makes the comparison with theoretical seismograms more difficult. We can at present only assume that the anomaly only rotates the angle of incidence without too many other complications. Another observation in Fig. 4 is also interesting: the particle motion at KHC and KSP is more linearly polarized than at GRF, where the polarization is more elliptical. This is an indication of the presence of more (delayed) shear waves in the P -wave group at GRF, due to conversions at the sediments. In spite of the small angle of incidence at GRF, the rotation into P and Q components has been performed. If the angle of incidence is, for example, 4° , then about 7% of the relatively large vertical component is added to the radial component in order to compute Q (see previous section).

Figures 1–3 show the WWSSN short-period simulations. Figure 5 shows the broad-band seismograms recorded at station B1. It can clearly be seen from broad-band data in Fig. 5 that all of the deep events and explosions used here have quite simple source time functions. The comparison of the WWSSN short-period simulations (Fig. 2) and the broad-band records (Fig. 5) at station B1 shows that all chosen events have mainly short-period energy and that the signal-to-noise ratio is much better for the WWSSN simulations. Therefore, we have used only the WWSSN short-period simulations in the following.

Figures 6 and 7 show the amplitude comparison of the energy on the three rotated components for some events. There is a clear phase shift between the P and the Q components in the first cycles; the Q component is delayed. This indicates that the energy on the Q component is converted shear wave energy, which arrives later and is not a projection from the P wave.

Each trace in Figs. 1–3 and 5 is normalized independently to its maximum amplitude. The correlation of weak

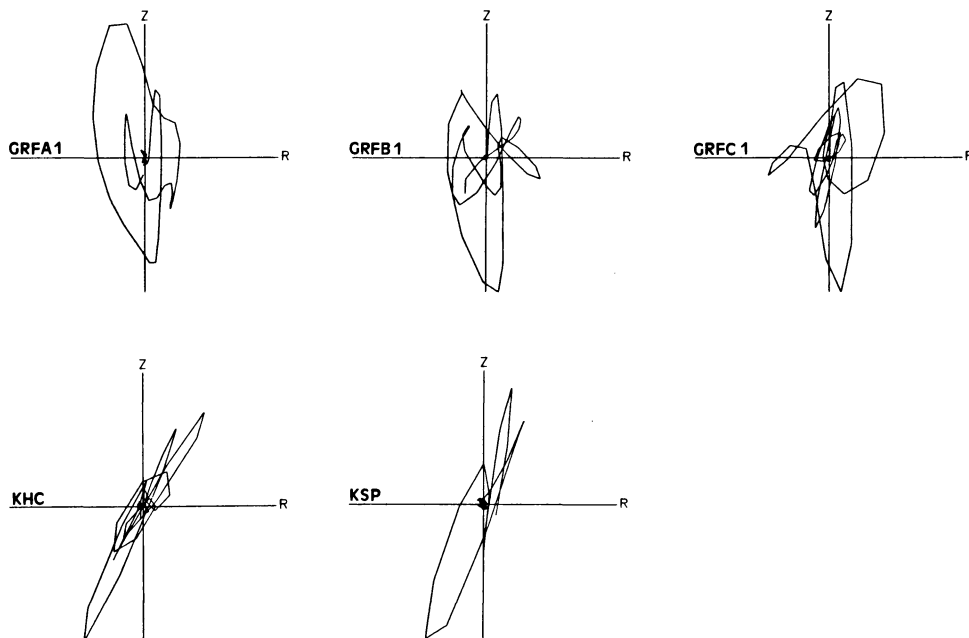


Fig. 4. Broad-band particle-motion diagrams of the first 5 s for event 1 in Table 1 at the GRF stations A1, B1 and C1, and at the stations KSP (Poland) and KHC (Czechoslovakia). The angle of incidence is abnormally small under the GRF array

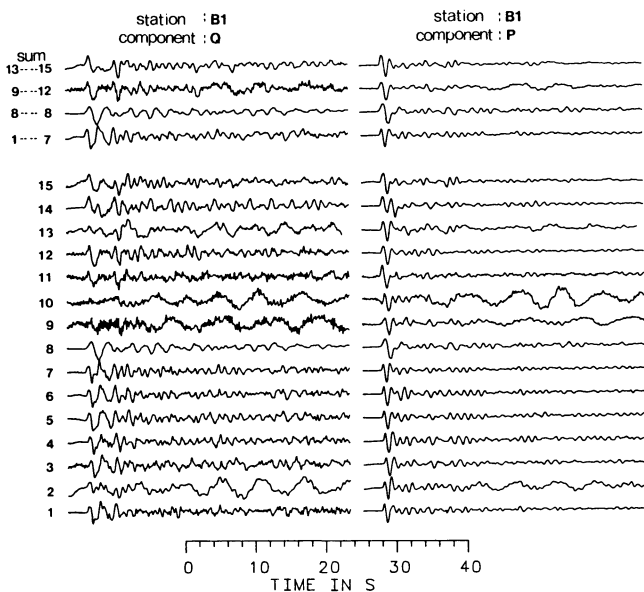


Fig. 5. Broad-band records at station B1 of the same data as in Fig. 2. The signal-to-noise ratio of the converted phases is better in the short-period data of Fig. 2 than here

phases, labelled *PGs* and *PMs* and interpreted as conversions at the bottom of the sediments or at the Moho, respectively, is made much clearer this way over a number of different events. But the relative amplitude information is lost in Figs. 1–3. In the *Q* component of Figs. 1 and 3 *PGs* is the strongest phase, and in Fig. 2 it is *PMs*. The amplitudes of these phases can be compared in Figs. 6 and 7 for some events. These figures show that *PGs* and *P* vary strongly across the array. *PGs* is largest at C1 and weakest at B1 and the *P* wave is often smallest at B1. The Moho conversion *PMs* is strongest at B1, weaker at A1 and not visible at C1. These observations indicate that their interpretation could lead to new information about the structure of the Moho underneath the GRF array. Travel-time variations

of the converted phases across the array are difficult to observe in our data. Therefore, no Moho depth variations can be derived. Summation traces of groups of events from one region have been computed (see Figs. 1–3 and 5) in an attempt to improve the signal-to-noise ratio. But it seems that more earthquakes from one region are required to obtain a significant improvement.

Theoretical seismograms

The most recent extension by Kind (1985) of the reflectivity method allows the computation of theoretical seismograms for models which have different structures at the sites of the stations and at the epicentre and a common model of the mantle underneath. The complete response in each of the three parts of the model is computed and only selected wave fields are permitted to penetrate through the boundaries between the different parts of the model. This method is very useful for comparisons with the type of data we are interpreting in this study, since the structure at the source can be kept fixed.

Since our data consist of records of nuclear explosions and deep-focus earthquakes with unknown source orientation, we have used a hypothetical explosive source at a depth of 80 km in our model, which allows a comparison of the theoretical seismograms with both types of data. The large depth was chosen in order to avoid complications due to crustal structure near the source. We think that the differences between the real situation and our model do not influence our results significantly, since we are using averaged observations of many different events. We used an epicentral distance of 50° and simulated the WWSSN short-period response in our theoretical seismograms, which was also simulated in most of the data.

At the beginning we investigated the influence of different structures of the crust-mantle boundary on the shear waves converted at this boundary. In Fig. 8 are shown theoretical seismograms of *Q* and *P* components for a number of different Moho structures. The models belonging to the seismograms in Fig. 8 are given in Table 2. All models in

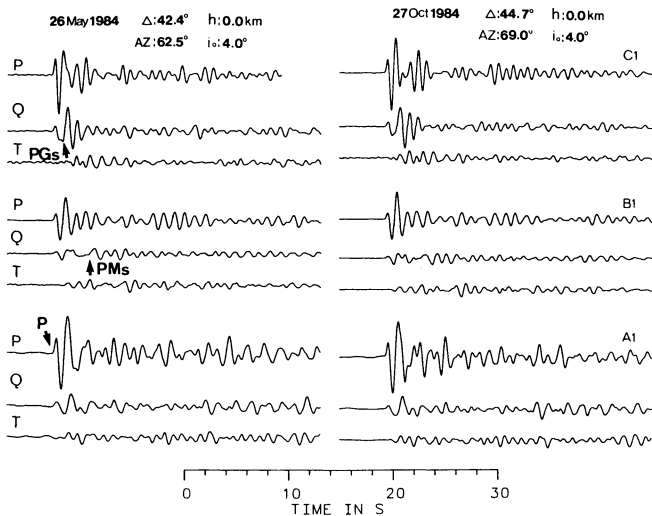


Fig. 6. *P*, *Q* and *T* components of the events 5 (left) and 7 (right). The amplitudes of one event are all on the same scale, so that they can be compared at the different components. There is a clear phase shift between the *P* and *Q* components in the first few cycles, indicating that we have delayed *S* energy on the *Q* component and not projected *P* energy. The transformation angles *AZ* and i_0 are experimentally determined by optimizing the energy at the appropriate component

Fig. 8 have no surficial sediments; the averaged crustal material extends to the free surface. The angle of incidence was chosen as 25° for the computation of the *Q* and *P* components from the *R* and *Z* components. This is not exactly the true angle of incidence for the model used, but it permits a small portion of the *P* wave to be seen on the *Q* component. The shear waves are not influenced significantly on the *Q* component by this manipulation and the relative position of the *P* waves remains visible.

The angles of incidence of the observed and theoretical data are very different. Since the reason for the unusually small observed angle of incidence is not yet certain, we have not attempted to model this with theoretical seismograms. We have rotated both types of data with their different angles of incidence, in order to obtain the optimum energy of the converted waves on the *Q* component. The amplitude of the *Q* component is enhanced 5 times in Fig. 8 relative to the *P* component. A comparison with Figs. 6 and 7 shows that the observed energy on the *Q* component is much larger relative to the *P* component than the theoretical ratio in Fig. 8. Therefore, the theoretical seismograms in Fig. 8 can be used only for a comparison of the converted waves at different Moho structures.

Trace 1 in Fig. 8 shows, for comparison, results from a model without a crustal layer. Trace 2 is for a first-order discontinuity and has a well-developed *PMs* conversion. Traces 3, 4 and 5 are for gradient zones with increasing thickness, which reduces the conversions gradually in size. The thickness of the transition zone has to be comparable to the wavelength to substantially reduce the conversion. A large reduction of the size of the converted phase is achieved by just one thin high-velocity layer above the Moho (trace 6). Since the main frequencies are near 1 Hz, the dominant wavelength is 8 km in the high-velocity material and 6 km in the crustal material. Several high- and low-velocity lamellas (see traces 7–11) increase the complex-

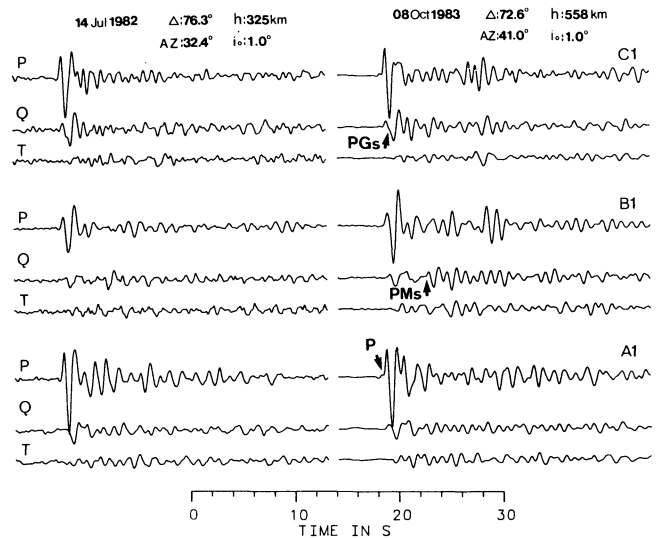


Fig. 7. Same as in Fig. 6, for the events 11 (left) and 15 (right)

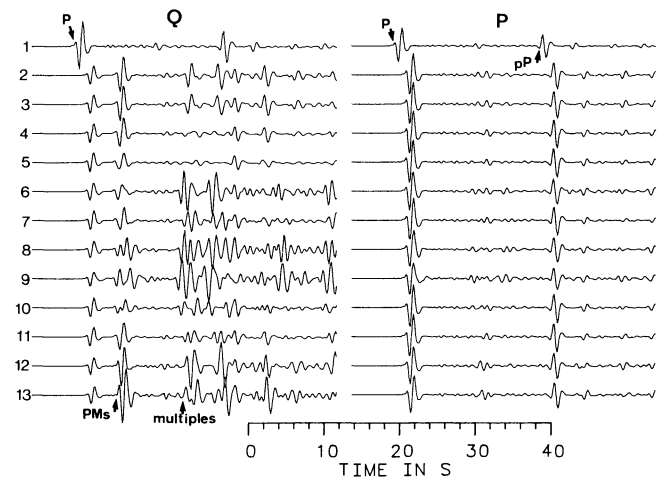


Fig. 8. *Q* and *P* components of theoretical seismograms for different Moho structures. The numbers refer to the Moho structures in Table 2. The amplitudes of the *Q* component are 5 times enlarged relative to those of the *P* component. All traces are rotated using an angle of incidence of 25°

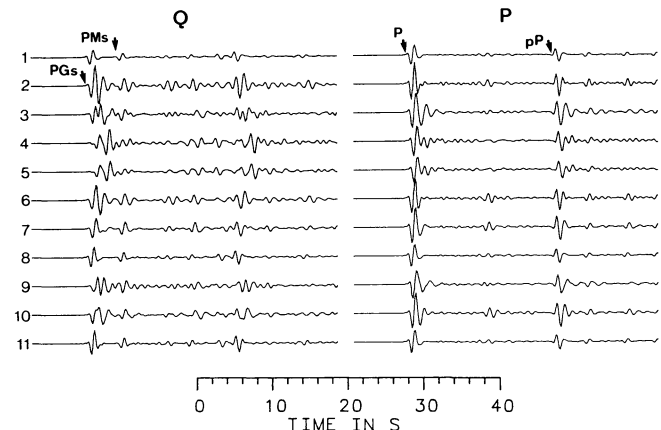


Fig. 9. *Q* and *P* components of theoretical seismograms for different structures of the sediments. The numbers refer to the sedimentary structures in Table 3. The amplitudes of the *Q* component are 2 times enlarged relative to those of the *P* component. All traces are rotated using an angle of incidence of 10°

Table 2. Model parameters of the crust-mantle transition zone used for the computation of theoretical seismograms in Fig. 8. The centre of the transition zone is always placed at 30 km depth. High-velocity lamellas have the velocity of the uppermost mantle (8 km/s); between the high-velocity layers are layers with 6 km/s and the same thickness; the low-velocity zones (Nos. 12 and 13) have a velocity of 5 km/s. *P* velocities are given. *S* velocities are obtained by dividing the *P* velocities by the square root of 3. The densities are obtained from Birch's law (density = 0.252 + 0.3788**P* velocity)

No.	Parameters of Moho transition zone
1	No crust, mantle with velocity 8 km/s extends to surface
2	First-order Moho at 30 km, crustal velocity 6 km/s
3	1 km linear gradient
4	3 km linear gradient
5	6 km linear gradient
6	1 high-velocity lamella 1.0 km thick
7	2 high-velocity lamellas 0.5 km thick
8	2 high-velocity lamellas 1.0 km thick
9	2 high-velocity lamellas 1.5 km thick
10	4 high-velocity lamellas 0.5 km thick
11	4 high-velocity lamellas 0.2 km thick
12	Low-velocity layer 1 km thick above Moho
13	Low-velocity layer 2 km thick above Moho

Table 3. Model parameters of sedimentary models used for the computation of theoretical seismograms in Fig. 9. *P* velocities are given, *S* velocities and densities are obtained as in Table 2

No.	Parameters of the sedimentary models
1	No sediments, crust with 6 km/s extends to surface
2	0.5 km sediments, 3.0 km/s
3	1.0 km sediments, 3.0 km/s
4	2.0 km sediments, 3.0 km/s
5	Like model 4, but upper 200 m replaced with 5 km/s
6	Like model 2, but upper 200 m replaced with 5 km/s
7	Linear gradient from surface (3 km/s) to 2.0 km depth
8	Linear gradient from surface (3 km/s) to 0.5 km depth
9	1.5 km sediments, 3.5 km/s (models sediments under A1)
10	0.9 km sediments, 3.5 km/s (models sediments under B1)
11	0.3 km sediments, 3.5 km/s (models sediments under C1)

ity of the converted wave. A large increase in the size of the converted phase is achieved by a low-velocity layer above the Moho (see traces 12 and 13).

Another observation in the *Q* component of Fig. 8 is that most traces have much energy beginning about 12 s after the *P* onset. This energy is due to incoming shear waves which have been multiply reflected within the crust. Traces 4 and 5 (belonging to 3- and 6-km-thick transition zones at the Moho) and traces 10 and 11 (belonging to transition zones with high-velocity lamellas) have significantly less multiples than all other models of the Moho.

The result from this study of *P*-to-*S* conversions at a number of Moho transition zones in Fig. 8 and Table 2 is that simple model perturbations can significantly alter the size of the converted phase. A thin (relative to the wavelength) high-velocity layer above the Moho, or a thick transition zone, reduces, and a thin low-velocity layer, also above the Moho, increases the size of the converted phase. The models discussed in Fig. 8 are not a complete or a very systematic search through all the possible models. Also, the relation between the frequency content of the

incoming signal and the layer thickness could be studied further. But we think that the theoretical seismograms shown in Fig. 8 indicate how the conversions at the Moho can be influenced by modifications of the structure of the crust-mantle boundary. The *P*-wave signal form or amplitude (Fig. 8) is not influenced very much by the different forms of the transition zone between the crust and the mantle.

The other significant structure which could influence the recorded wave fields are the sedimentary layers beneath the stations. Figure 9 shows *Q* and *P* components for a number of sedimentary models. The Moho is assumed to be a first-order discontinuity at 30 km depth, and a homogeneous crust with a velocity of 6 km/s extends up to the sediments. The *Q* and *P* components are computed from the *R* and *Z* components by assuming an angle of incidence of 10°. The different sedimentary models used for the theoretical seismograms in Fig. 9 are described in Table 3. The *P* component in Fig. 9 is multiplied by a factor 0.5 relative to the *Q* component in the same figure.

The presence of the sedimentary layers amplifies the amplitudes of both components, but the *Q* component, i.e. the converted phases, is much more amplified by the sediments beneath a station (trace 1 in Fig. 9 belongs to a model with no sediments for comparison). The conversion at the bottom of the sediments is labelled *PGs* in Fig. 9. Its size relative to the size of the *P* wave (Fig. 9) varies greatly as a function of the sedimentary model. The same large variation in the amplitude ratio can be seen in the observed data (Figs. 6 and 7). Within these wide limits there is agreement between the observed and computed data.

Traces 2, 3 and 4 have a sedimentary layer with a velocity of 3.0 km/s and increasing thickness from 0.5, 1.0 to 2.0 km. The conversion at the bottom of the sediments alters the signal very strongly. The reverberations within the sedimentary layer extend over the entire time interval to the Moho conversion *PMs*, which comes 4 s after *P* (see trace 4 especially). This means that realistic sedimentary layers underneath the GRF stations may interfere with possible conversion from the central or lower crust, which makes it very difficult to distinguish between such conversions and multiples within the sediments. The observed data in Figs. 1 and 2 seem to have more correlatable phases between *PGs* and *PMs*. But it is very likely that these phases are multiples in the sediments and not conversions from the middle crust.

Traces 5 and 6 are for models with high-velocity (5 km/s) Jurassic sediments at the surface (see Table 3), but these sediments have only very little influence on the converted waves (compare traces 4 and 5 and traces 2 and 6). Traces 7 and 8 belong to models which have linear gradients in the sediments instead of homogeneous layers. Such models preserve the incoming waveforms and generate only small multiples.

Traces 9, 10 and 11 model approximately the sedimentary layers under stations A1, B1 and C1 (Geologische Karte von Bayern, München, 1981). Although the models used to compute traces 9, 10 and 11 are very similar to those used to compute traces 4, 3 and 2, these traces themselves differ considerably. This means that small modifications of realistic sedimentary models under the GRF stations can have significant influences on the entire wave train between the first onset and the Moho conversion *PMs*. It should be noted that the *P* waves in Fig. 9 are also significantly

influenced by the sediments. The simple incoming signal is complicated by the reverberations within the sediments.

Results and conclusions

Refraction profiles near the GRF array have been interpreted by Aichele (1976). Reflections from the Moho have been observed but no details about the sharpness of the Moho have been obtained. We have observed, in the rotated short-period Q components of the GRF records, clear evidence for the existence of P -to- S converted phases at the crust-mantle boundary and at the bottom of the sediments. We have also computed theoretical seismograms of such converted phases for various models of the Moho transition zone and for models of the sediments. The clearest and most important observational result in the data is that the Moho conversion PMs differs significantly among the stations A1, B1 and C1. It is strongest at B1 (where it has about the same size as the conversion PGs at the bottom of the sediments); it is smaller at A1 (where it is about half the size of PGs); and it is not observable at C1 (see Figs. 1–3). But PGs , in contrast, is strongest at C1, weaker at A1 and weakest at B1 (see Figs. 6 and 7).

Theoretical seismograms of converted waves for different models of the sediments (Fig. 9) show that the PGs wave group may influence the entire time window to PMs . Even PMs may be influenced by PGs and multiples in the sediments. Therefore, it is difficult to identify additional conversions from other parts of the crust (this could be different for stations on different geological structures). For this reason it is also difficult to obtain a reliable estimate of the absolute amplitude of PMs (see Figs. 6 and 7). The Moho conversion PMs is least influenced by PGs at station B1 because PGs is relatively small there. Any interpretation of the size of PMs must relate this phase to another phase. As we have seen, PGs is not very useful for this purpose since it is very unstable across the array. The P wave is more useful since it is more stable than PGs , but it is also influenced by the sediments (see Fig. 9). Therefore, we try to discuss the amplitudes of PMs in relation to both PGs and P .

At station A1 the ratio of the observed P wave to the energy arriving at the time of PMs is roughly in agreement with the theoretical ratio in Fig. 7. In this figure the Moho was assumed to be a first-order discontinuity and the sedimentary model has been varied. In all considered cases, PGs is clearly larger than PMs . This is also in good agreement with the observations at station A1. For these reasons it seems that a first-order discontinuity and almost any sedimentary model can explain the observed data at station A1. Another observation at station A1, but not at B1 and C1, is that the nuclear explosions in Fig. 1 (traces 1–7) have a strong onset at about 15 s after P . This could be a multiple within the crust, similar to that produced by the laminated models belonging to traces 6–9 in Fig. 8. This could be an indication that such a lamination would also be a possibility for station A1.

At station B1 PMs is clearly stronger in relation to P and PGs than at A1. Such strong Moho conversions have only been obtained from models with thin low-velocity layers just above the Moho (see traces 12 and 13 in Fig. 8). We are not suggesting a velocity of 5 km/s in the lower crust, we have merely discussed the possibilities we have with laterally homogeneous models.

At station C1 we have observed practically no converted energy at the Moho. A comparison with the theoretical seismograms in Fig. 8 (trace 6) could lead to a model with a thin layer of high-velocity material just above the Moho. Such a model would be sufficient to suppress the converted energy. However, trace 6 in Fig. 8 has very strong multiples starting about 12 s after P , and there is no indication of that in the data. Trace 5 in Fig. 8 (belonging to a thick transition zone) also reduces PMs and does not generate such strong multiples. Therefore, a very thick transition zone seems to be the best model for the Moho underneath C1.

The conclusion from this comparison between observed and computed data is that the crust-mantle transition zone varies significantly across the array. At the northern part of the array a first-order discontinuity with normal velocity contrast or a lamination would explain the data; at the central part we need a transition zone with an increased velocity contrast; and in the southernmost part we need a reduced sharpness of the transition zone. A more quantitative analysis is not intended at this time, but this should be possible with a larger amount of data.

The second important conclusion is that the sediments have a strong influence on the entire wave train between the first onset and the Moho conversion about 4 s later. Correlatable phases certainly exist with time delays smaller than 4 s, but it is not possible to determine if these phases are multiples within the sediments or conversions from deeper parts of the crust.

Another conclusion from the theoretical P -wave seismograms in Fig. 9 is that sedimentary layers underneath a station can lead to severe disturbances of the signal form and the amplitude of the incoming P wave.

Acknowledgements. This research was supported by the Max-Planck-Gesellschaft and the Deutsche Forschungsgemeinschaft. We wish to thank S. Faber for contributing to the discussion, Frank Krüger for providing Fig. 4 and discussions, and Axel Plesinger for the data from KSP and KHC. We also thank M. Hellweg for help in our computations. The first author would also like to thank all his colleagues from the Seismologisches Zentralobservatorium for their help during his visit. We thank Peter Basham and Max Wyss for reading the manuscript.

References

- Aichele, H.: Interpretation refraktionsseismischer Messungen im Gebiet des Fränkisch-Schwäbischen Jura. Dissertation, Universität Stuttgart, 1976
- Aki, K., Christofferson, A., Husebye, E.S.: Three dimensional seismic structure of the lithosphere under Montana LASA. Bull. Seismol. Soc. Am. **66**, 501–524, 1976
- Bath, M., Stefansson, R.: S-P conversions at the base of the crust. Ann. Geofis. **19**, 119–130, 1966
- Bock, G., Ha, J.: Short-period S to P conversion in the mantle at a depth near 700 km. Geophys. J. R. Astron. Soc. **77**, 593–615, 1984
- Burdick, L.J., Langston, C.A.: Modeling crustal structure through the use of converted phases in teleseismic body waves. Bull. Seismol. Soc. Am. **67**, 677–691, 1977
- Faber, S., Müller, G.: Sp phases from the transition zone between the upper and lower mantle. Bull. Seismol. Soc. Am. **70**, 487–508, 1980
- Faber, S., Müller, G.: Converted phases from the mantle transition zone observed at European stations. J. Geophys. **54**, 183–194, 1984
- Faber, S., Plomerova, J., Babuska, V.: Deep seated lateral velocity

- variations beneath the GRF array inferred from mislocation patterns and P residuals. *J. Geophys.* 1986 (in press)
- Harjes, H.-P., Seidl, D.: Digital recordings and analysis of broadband seismic data at the Gräfenberg (GRF) array. *J. Geophys.* **44**, 511–523, 1978
- Kind, R.: The reflectivity method for different source and receiver structures and comparison with GRF data. *J. Geophys.* **58**, 146–152, 1985
- Langston, C.A.: Structure under Mount Rainier, Washington, inferred from teleseismic body waves. *J. Geophys. Res.* **84**, 4749–4762, 1979
- Liu Qiyuan, Fan Hueiji: Matrix-ray method for synthetic seismograms of body waves of earthquakes. *Acta Geophysica Sinica* 1986 (in press), (in Chinese with English abstract)
- Liu Qiyuan, Shao Xuezhong: A study of the dynamic characteristics of PS converted waves with synthetic seismograms. *Acta Geophysica Sinica* **28**, 291–302, 1985, (in Chinese with English abstract)
- Plesinger, A., Hellweg, M., Seidl, D.: Interactive high-resolution polarisation analysis of broadband seismograms. *J. Geophys.* **59**, 129–139, 1986
- Polshkov, M.K., Bulin, K.N., Sherbakova, B.E.: Crustal investigation of the U.S.S.R. by means of earthquake-generated converted waves. *Tectonophysics* **20**, 57–66, 1973
- Shao Xuezhong, Zhang Jiru, Yang Xiaofeng, Zhang Xiaohu, Lei Shengli, Wang Qiming, Gao Weian: An experimental study of the structure of the Earth's crust and upper mantle by converted waves. *Acta Geophysica Sinica* **21**, 89–100, 1978, (in Chinese with English abstract)
- Shao Xuezhong, Zhang Jiaru, Liu Qiyuan, Zhang Siya: The common features of deep structures in some large earthquake areas of North China plain and their meaning to the earthquake site prediction. *J. Phys. Earth* 1986 (in press)
- Vinnik, L.P.: Detection of waves converted from P to SV in the mantle. *Phys. Earth Planet. Inter.* **15**, 39–45, 1977
- Vinnik, L.P., Avetisjan, R.A., Mikhailova, N.G.: Heterogeneities in the mantle transition zone from observations of P-to-SV converted waves. *Phys. Earth Planet. Inter.* **33**, 149–163, 1983

Received April 22, 1986; revised version September 23, 1986
Accepted September 29, 1986

Cross spectral analysis of Swabian Jura (SW Germany) three-component microearthquake recordings

F. Scherbaum and J. Wendler

Institut für Geophysik der Universität Stuttgart, Richard-Wagner-Str. 44, D-7000 Stuttgart 1, Federal Republic of Germany

Abstract. Similar three-component microearthquake records have been observed in the Swabian Jura (SW Germany) seismic zone for different source-receiver geometries. This data set is used to study the resolution power of cross spectral analysis techniques for the estimation of relative differential times as well as the applicability to velocity monitoring. The differential times are estimated in the frequency domain by assuming a linear-phase cross spectrum with the slope indicating the individual time difference. All earthquakes have been relocated with respect to a master event, using the relative *P* and *S* delay times from the cross spectral analysis as a measure of source mislocation. The overall location error is strongly dependent on the initial distance between master and studied event. For earthquakes initially located farther apart than approximately 1.5 km, the relocation result in terms of total location error was poorer, whereas for events initially located closer than 1 km the precision of the relocation was improved. The remaining residuals are of the order of 10 ms, which is approximately 3 times the digitization interval.

In order to test the applicability of cross spectral analysis to velocity monitoring, synthetic data were used to model the influences of noise and source time function differences. The effect of additive white noise seems to be acceptable in cases where the S/N ratio is sufficiently high. Small changes in the shape of the source time function, however, were found to be of great influence to the differential time estimates. Variation of rise, sustain and decay times, which were negligible in the coherence spectrum, spuriously introduced phase differences which, in terms of delay times, easily reach the magnitude of the digitization interval. Thus, velocity monitoring using cross spectral analysis techniques seems to depend strongly on the equality – in contrast to similarity – of the source time functions of the events which are compared. The coherence spectrum is not a sufficient measure to detect all the significant differences.

Key words: Cross spectral analysis – Similar earthquakes – Earthquake doublets – Swabian Jura earthquake zone – Hypocenter relocation

Introduction

The application of cross spectral analysis (CSA) techniques has been recently demonstrated to provide relative travel-

time differences between the two events of an earthquake doublet with extraordinarily high accuracy (Poupinet et al., 1984; Frechet, 1985). If the two events are generated at essentially the same source location, this information can be used to resolve velocity changes in the crust (Poupinet et al., 1984; Fremont, 1984; Ito, 1985; Poupinet et al., 1985). For similar earthquakes, which do not necessarily have to originate at the *same* location, the information on the time differences can be exploited for precise relative relocation, thus offering a powerful method to investigate the fine structures of source regions (e.g. Evernden, 1969; Dewey, 1979; Ito, 1985). In the following, the term doublet is used for earthquakes occurring at an identical location, whereas similar earthquake is used as a more general term to describe events with waveform likeness.

For the Swabian Jura (SW Germany) earthquake zone, the observation of similar microearthquake recordings, including doublets from a relatively large area – approximately 10 km in diameter – (Scherbaum and Stoll, 1985; Scherbaum, 1986; Langer, 1986), offers the opportunity of studying the applicability range of the cross spectral analysis method. The purpose of the present paper is to investigate the resolution power of the CSA method using three-component records for relocation purposes as well as for velocity monitoring. Synthetic seismograms were used to test the influence of different source time signals on the resolution of onset times. Additionally, the influence of the source distances and the influence of noise will be demonstrated.

Figure 1 shows the location of the Swabian Jura earthquake zone within the Federal Republic of Germany. The local digital seismic network has been in operation since 1976. The area of investigation has shown three major earthquake sequences with main shock magnitudes of the order of $MWA = 5.5–6.0$ ($MWA = \text{Local Magnitude}$) since the beginning of this century. The last major event occurred in 1978 ($MWA = 5.7$) and was followed by a large number of aftershocks (Haessler et al., 1980; Turnovsky and Schneider, 1982; Scherbaum and Stoll, 1983). In 1982, the network was expanded to seven four-component stations, unified in its instrumental characteristics and rearranged to its present position (Table 1). The dataset used in this study consists of the microearthquake recordings obtained between October 1982 and the present. This time period is characterized by a comparably very low seismic activity. Only some 30 events have been detected. For the present study however, only events which were recorded by at least three stations were analysed. Thus, the dataset consists of six events. Table 2 lists the events which were used for the

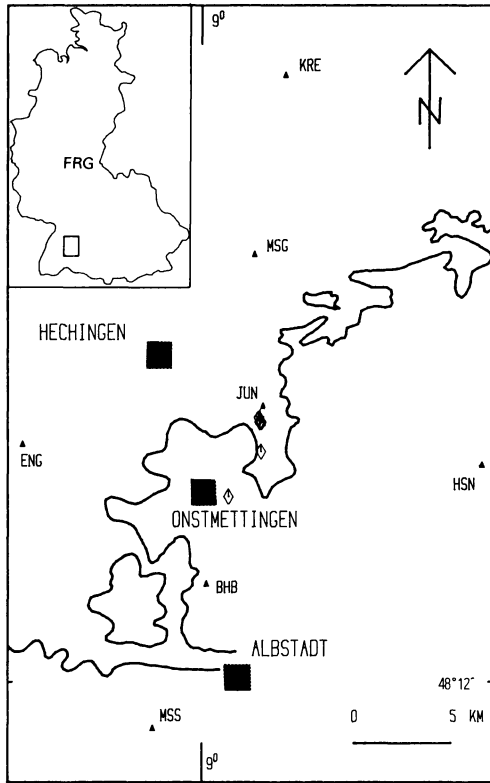


Fig. 1. Geographical location of the Swabian Jura, SW Germany, earthquake zone. The *inset* shows the position of the area under study with respect to the Federal Republic of Germany. The *solid triangles* indicate the recording stations of the Swabian Jura seismic network. *Diamonds* show the relocations of the earthquakes under study. The *solid line* indicates the outcrop of the Upper Jurassic limestone which is the most prominent topographic feature in the Swabian Jura region

present analysis. The locations and source parameters were taken from Langer (1986). As far as fault-plane solutions could be obtained, the focal mechanisms are consistent with a NNE-SSW-striking, left-lateral strike-slip fault (Langer, 1986). The distribution of epicenters is given in Fig. 2, in addition to the positions of the individual recording stations.

The cross spectral analysis method

The cross spectral analysis technique as applied by Poupinet et al. (1984) and Ito (1985) is based on the estimation of the travel-time differences in the frequency domain from the phase of the corresponding cross spectrum.

Provided that two time signals of identical shape s_1 and s_2 and a magnitude difference c are observed at a time difference τ , that is

$$s_2(t) = c \cdot s_1(t - \tau),$$

the corresponding Fourier spectra $S_1(\omega)$ and $S_2(\omega)$ are given by:

$$S_1(\omega) = |S_1(\omega)| \cdot e^{i\phi_1}, \quad (1)$$

$$S_2(\omega) = c \cdot |S_1(\omega)| \cdot e^{i\phi_2} \quad (2)$$

$$= c \cdot |S_1(\omega)| \cdot e^{i(\phi_1 - \omega\tau)} \quad (\text{shifting theorem}). \quad (3)$$

The corresponding cross spectrum is defined as (*denoting complex conjugate):

Table 1. Main characteristics of the Swabian Jura local network

Station coordinates				
Station	Longitude E	Latitude N	Altitude (m)	
BHB	9° 00' 07"	48° 14' 50"	890	
ENG	8° 52' 28"	48° 18' 38"	537	
HSN	9° 11' 38"	48° 18' 15"	710	
JUN	9° 02' 27"	48° 19' 49"	600	
KRE	9° 03' 22"	48° 28' 55"	458	
MSG	9° 02' 04"	48° 23' 57"	475	
MSS	8° 57' 56"	48° 10' 47"	915	
Instrumental characteristics				
Recording method	Digital PCM code on 1/4" magnetic tape			
Seismometer	Channel 1 (Z) Strobach	Channel 2 (N) Willmore MK III	Channel 3 (E) Willmore MK III	Channel 4 (E/N) Sundstrand Q-Flex
Eigen-frequency (HZ)	0.66	0.66	0.66	800
Sensor type	Displacement	Velocity	Velocity	Acceleration
A/D conversion 12 bit, 72 dB				

$$C(\omega) = |C(\omega)| \cdot e^{i\phi_c} \quad (4)$$

$$= S_1(\omega) \cdot S_2(\omega)^* \quad (5)$$

$$= c \cdot |S_1(\omega)| \cdot |S_1(\omega)| \cdot e^{i\phi_1} \cdot e^{-i(\phi_1 - \omega\tau)} \quad (6)$$

$$= c \cdot |S_1(\omega)|^2 \cdot e^{i\omega\tau}. \quad (7)$$

As can be seen from Eq. (7), in the case of identical signals, the cross spectrum is linear phase with the differential time τ being the slope of the phase spectrum, that is:

$$\Phi_c = \omega\tau. \quad (8)$$

In the case of additive uncorrelated noise, the slope of the phase is assumed not to be affected (Ito, 1985).

The likeness of real data, however, is never perfect. Similarity might be restricted to particular frequency bands or limited by noise. Thus, the degree of uniformity between the different signals has to be taken into account in the analysis. A well-established measure for the amount of association is given by the coherence spectrum COH (ω) (Kanasewich, 1981):

$$\text{COH}(\omega) = \frac{\text{CS}(\omega)^2}{\text{PS}_1(\omega) \cdot \text{PS}_2(\omega)}, \quad (9)$$

CS(ω) = smoothed cross spectrum C (ω),

PS₁(ω) = smoothed power spectrum of signal 1,

PS₂(ω) = smoothed power spectrum of signal 2.

Smoothing is required, otherwise the coherence will always be unity regardless of the nature of the process (Kanasewich, 1981).

The data analysis

The data analysis has been performed following the moving window procedure of Poupinet et al. (1984). In the first

Table 2. Earthquakes under study from the observation period October 1982–July 1985. Only events which have been recorded by at least three stations are displayed. Source parameters and locations from Langer (1986)

No.	Date	Time	Lat (°N)	Lon (°E)	Z (km)	MWA	M_0 (Nm)
03	1982 Nov 28	04:34	48° 18.2'	09° 02.2'	07.0	3.8	8.5×10^{13}
16	1983 Sep 11	11:48	48° 19.2'	09° 02.4'	05.5	3.6	4.0×10^{13}
18	1983 Sep 14	10:52	48° 18.9'	09° 02.4'	05.0	1.9	7.1×10^{11}
19	1983 Sep 14	18:25	48° 19.1'	09° 02.4'	05.5	2.3	1.9×10^{12}
20	1983 Sep 15	06:26	48° 19.1'	09° 02.4'	05.0	3.1	1.6×10^{13}
25	1984 Jan 03	15:28	48° 15.2'	09° 02.7'	09.4	2.5	2.8×10^{12}

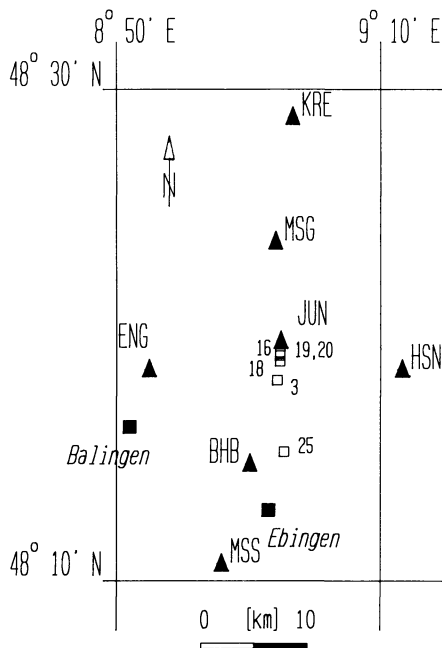


Fig. 2. Distribution of epicenters before relocations (*open squares*) of the earthquakes used for the cross spectral analysis. The *numbers* denote event numbers referred to in the text. The *solid triangles* indicate the recording stations of the Swabian Jura seismic network

step, the two records were aligned as closely as possible in order to avoid constant phase shifts in the cross spectra (e.g. Fig. 3a and b). A window of 0.96 s duration (256 samples), tapered with a cosine bell affecting 50% of the total window length, was moved along the seismograms in steps of 0.24 s (64 samples). This particular parameter set was obtained to yield an optimum time resolution for synthetic seismograms calculated for structural models resembling the geological situation in the studies area (Scherbaum, 1986) and sampled with the actual digitization frequency of 267 Hz.

For each time step, the cross spectrum, Eq. (5), and the coherence, Eq. (9), were calculated for the analysis window. The spectral smoothing required for the estimation of the coherence was carried out by weighted averaging over five neighbouring spectral estimates. The coherence has been scaled to give unity for identical, time-shifted signals. In Fig. 3d and e for example, the modulus of the cross spectrum and the coherence spectrum, respectively, for the first window of Fig. 3a and b are displayed. Finally, the relative time difference for an individual window was estimated by fitting a straight line to the slope of the cross

phase spectrum according to Eq. (8). Following Poupinet et al. (1984), the phase of the cross spectrum was weighted for the regression analysis. The product of the cross spectrum and the coherence was chosen as a weighting factor in order to concentrate on the strongest and most coherent signal components (Fig. 3e). Frequencies above the pass-band of the recording system (0.5–50 Hz) as well as contributions from spectral components with a weighting factor below a certain level were completely ignored (cf. Fig. 3f). The cutoff level for the weighting factor was chosen arbitrarily to be 0.4 in order to limit the regression analysis to that part of the phase spectra where the slope seemed to be essentially linear. The dotted line in the phase plots (e.g. Fig. 3f) gives the phase angle corresponding to a differential time of one sampling interval (3.75 ms). For each time step, the delay time was estimated following the same procedure and displayed as a function of lapse time along the seismogram (e.g. Fig. 3c).

Time differences from CSA were estimated for all the records with sufficient quality for the vertical (displacement) and the two horizontal components (velocity). The strong motion channel (acceleration) was not considered in the present analysis. Event 20 (1983 Sep 15, 06:26) was chosen as the master event, since it has been recorded and located by six out of seven stations.

In Figs. 3–5, the results of the CSA differential time measurements for events 19 and 20 at the recording station ENG (Engstlatt) are displayed. Cross amplitude spectra, coherences and cross phase spectra are displayed for those time windows containing either P_g or S_g . As a consequence of the small hypocentral distances (Fig. 2), these phases are in general easily identified in the observed seismograms. Figure 3a–c shows the aligned vertical seismogram components (Fig. 3a and b) together with the corresponding delay times as a function of lapse time along the seismogram (Fig. 3c). The squares in Fig. 3c indicate the centre times of the individual window positions (e.g. first window at 0.48 s). In Fig. 3d–f the cross amplitude spectrum, coherence and phase of the cross spectrum, respectively, for the first window – which is assumed to contain the P pulse – are displayed. Figures 4 and 5 show the result of the CSA analysis for the two horizontal components. For the display of the cross spectrum, coherence and phase of the cross spectrum for this trace, window 8 was assumed to contain the direct S pulse (cf. Figs. 4a and 5a). All the phase plots exhibit as sufficient linear slope in that frequency band where the phase weighting factor (cross spectrum \times coherence) is above the cutoff level. The coherence for events 19 and 20 is close to one for all frequencies, which might indicate that these earthquakes are doublets.

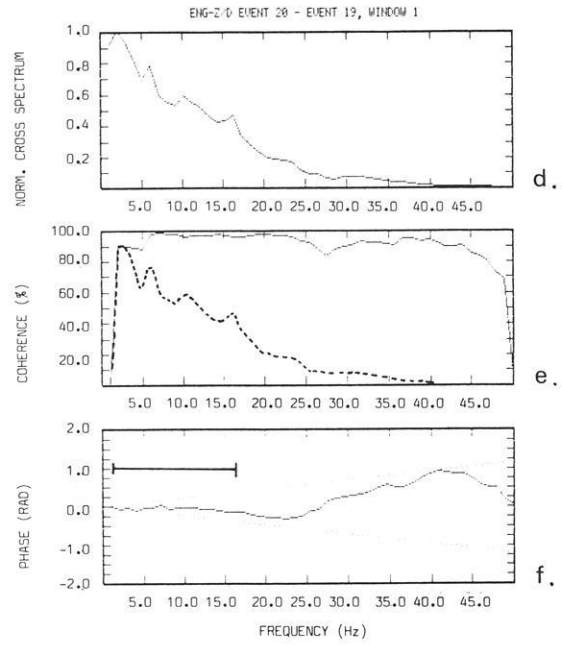
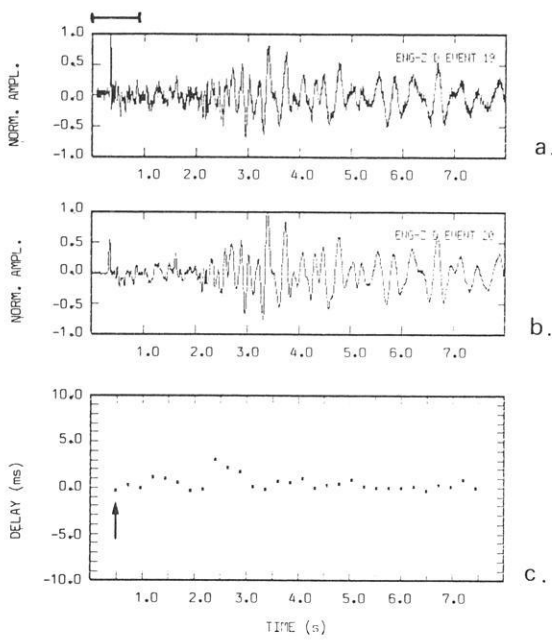


Fig. 3a-f. Cross spectral analysis of event 19 as compared with event 20. **a** and **b** show the aligned vertical component seismograms, **c** gives the delay times as a function of lapse time and **d** shows the cross amplitude spectrum for the window containing the *P* pulses. The window centre time and the corresponding window margins are indicated in Fig. 3c (arrow) and above Fig. 3a, respectively. **e** shows the coherence (solid line) and the weighting factor for the regression analysis (dashed line). **f** displays the corresponding phase spectrum. The frequency band used for regression analysis is indicated by the horizontal bar. The dotted line corresponds to the delay time equal to the sampling interval. Recording site is ENG

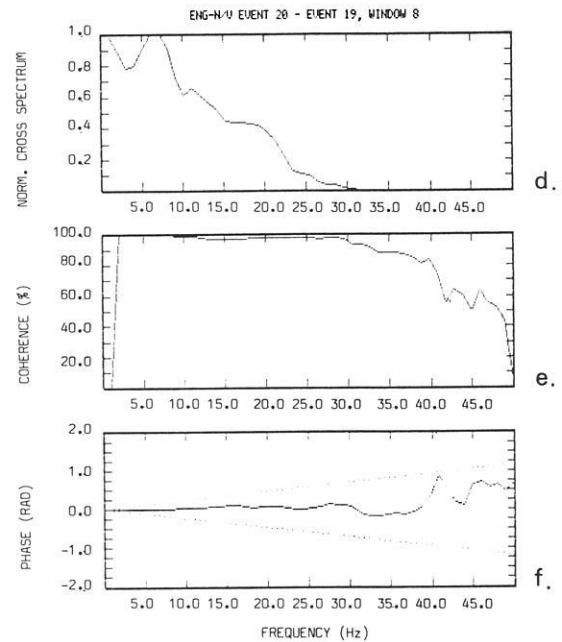
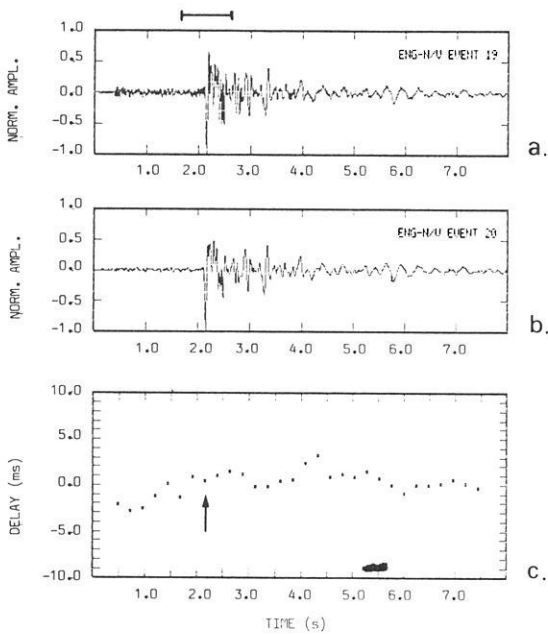


Fig. 4a-f. Cross spectral analysis of event 19 as compared with event 20. **a** and **b** show the aligned N-S component seismograms, **c** gives the delay times as a function of lapse time and **d** shows the cross amplitude spectrum for the window containing the *S* pulses. The window centre time and the corresponding window margins are indicated in Fig. 4c (arrow) and above Fig. 4a, respectively. The coherence is given in **e**. The corresponding phase spectrum is displayed in **f**. The dotted line corresponds to the delay time equal to the sampling interval. Recording site is ENG

The delay times (differential times) for all traces as a function of lapse time do not show oscillations. Thus, velocity changes between the occurrence time of these two events are not observable from this analysis.

Figures 6–8 give the seismograms, delay times, cross

spectra, coherences and phase plots for event 16 as compared with the master event, 20. The similarity of the dominant waveforms in terms of coherence (Figs. 6e, 7e, 8e) is still sufficient in the frequency band defined by the cutoff level of the weighting function, although it is clearly less

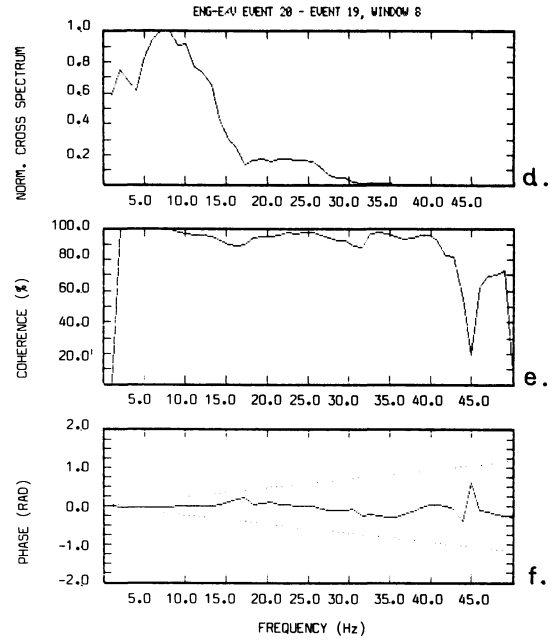
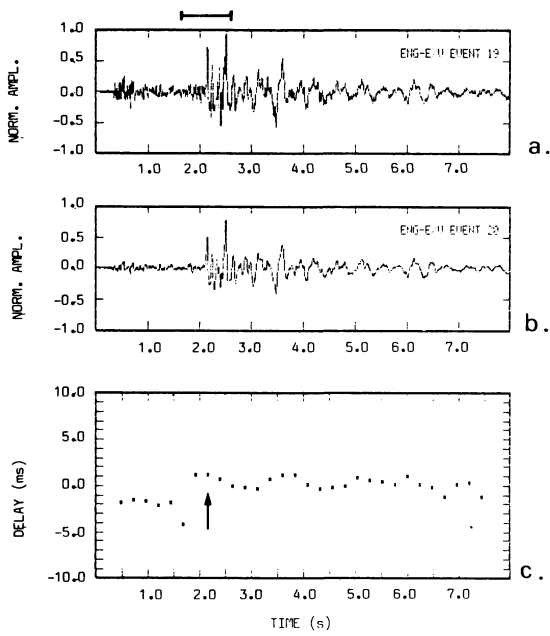


Fig. 5a–f. Cross spectral analysis of the E–W component seismograms for event 19 as compared with event 20. Recording site is ENG. For explanations, see Figs. 3 and 4

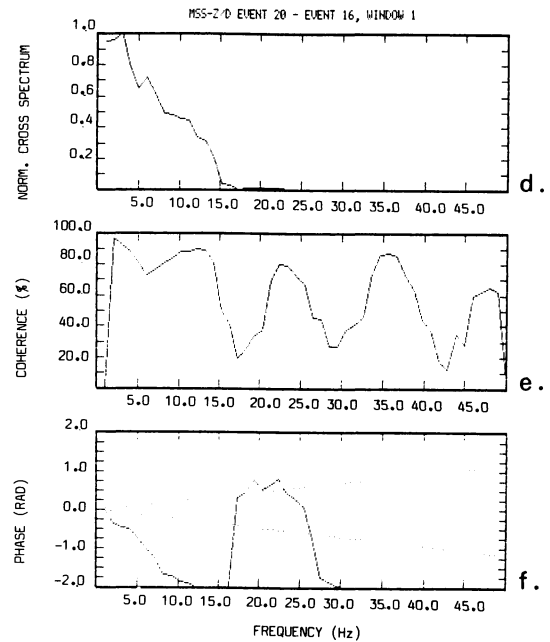
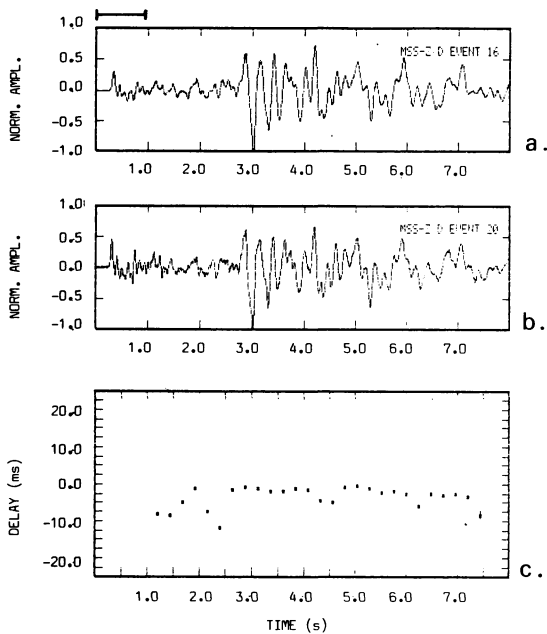


Fig. 6a–f. Cross spectral analysis of the vertical component seismograms for event 16 as compared with event 20. Recording site is MSS. For explanations, see Figs. 3 and 4. Differential time for the P pulses outside the plotting range

than for events 19 and 20. Additionally, the delay times vary more strongly as a function of lapse time. This might be due to a certain amount of noise in the records of event 20 at this station as well as a consequence of hypocentral differences.

All events were processed in a similar way in order to obtain the delay times as compared to the master event. For each two seismograms to be compared, the delay times for the windows containing the P_g and S_g arrivals were chosen from the individual delay time versus lapse time

plots (e.g. Fig. 3c). Finally, these values were corrected for the time differences introduced due to the different alignment of the individual traces in the first step of the analysis. The results are given in Table 3.

Relocation of hypocenters

The most obvious reason for the delay times to show differences for the individual stations is a difference in the location of the events under comparison. For this reason, a

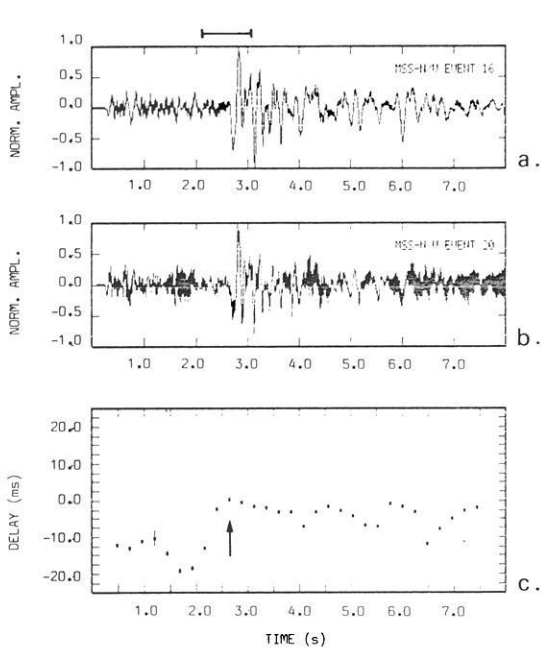


Fig. 7a-f. Cross spectral analysis of the N-S component seismograms for event 16 as compared with event 20. Recording site is MSS. For explanations, see Figs. 3 and 4

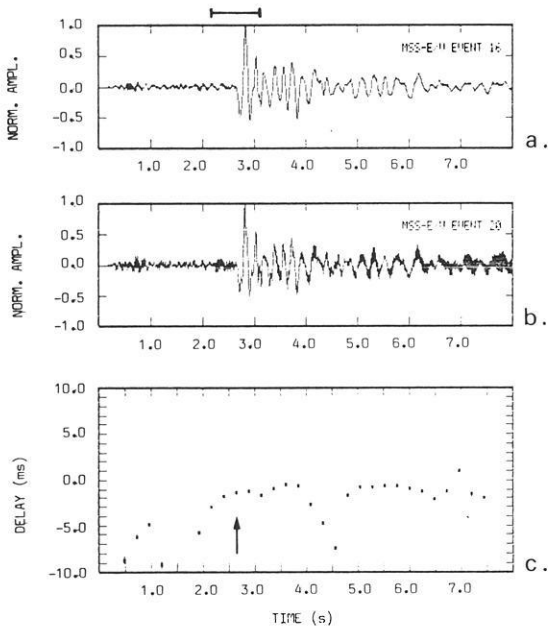
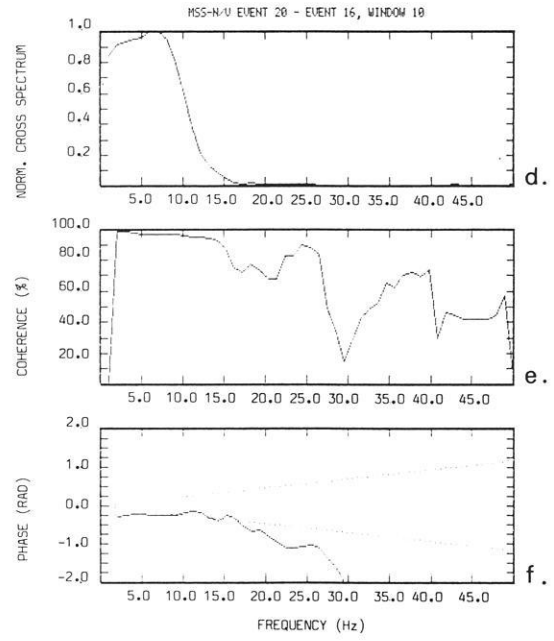
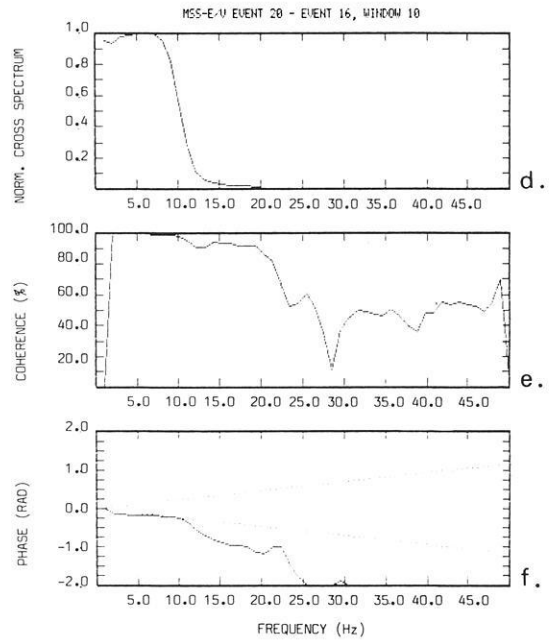


Fig. 8a-f. Cross spectral analysis of the E-W component seismograms for event 16 as compared with event 20. Recording site is MSS. For explanations, see Figs. 3 and 4



relocalization has been performed using a master event technique (e.g. Evernden, 1969; Dewey, 1979; Ito, 1985). For this purpose we calculated new individual arrival times using

$$\begin{aligned} P_{ik} &= P_{mk} - \tau_{pik} \\ S_{ik} &= S_{mk} - \bar{\tau}_{sik} \end{aligned} \quad (10)$$

Here, P_{ik} and S_{ik} are the new P and S onset times, respectively, for event i at station k . The index m denotes the master event index. τ_{pik} is the P -wave differential time ob-

tained from the vertical component, $\bar{\tau}_{sik}$ the averaged S -wave differential time obtained from the two horizontal components if possible. The localizations were obtained using a modified version of HYPO71 (Gelbke, 1977; Lee and Lahr, 1972).

As can be seen from Table 3, there are large differences in the delay times for the S phases estimated for different components, especially, if the event was located at some distance from the master event (e.g. event 25). Only for event 19, as compared with the master event, are the differ-

Table 3. Relative differential times (in ms) for the individual components. For the Z component, the differential times of the windows containing the *P* pulses are listed. For the N and E components, differential times for the *S*-pulse windows are given. All delay times are corrected for the different alignment of the individual traces prior to the cross spectral calculations

No.	Date	Time		Relative delay times in ms							
				BHB	ENG	HSN	JUN	KRE	MSG	MSS	
03	1982 Nov 28	04:34	Z	-94.3		-			-58.5	-85.8	
03	1982 Nov 28	04:34	N	28.0		-128.1			-258.2	61.5	
03	1982 Nov 28	04:34	E	-12.8		-			-364.7	60.2	
16	1983 Sep 11	11:48	Z	-44.9		26.1			-69.7	-31.5	
16	1983 Sep 11	11:48	N	-6.4		0.0			-84.8	0.0	
16	1983 Sep 11	11:48	E	-16.6		0.0			-96.0	1.0	
18	1983 Sep 14	10:52	Z	-215.2		-			-56.8		
18	1983 Sep 14	10:52	N	-176.2		-191.0			-172.9		
18	1983 Sep 14	10:52	E	-185.9		-206.3			-81.7		
19	1983 Sep 14	18:25	Z	62.1	78.4	-		-205.8	-18.8		
19	1983 Sep 14	18:25	N	-60.8	79.3	-		-	-17.3		
19	1983 Sep 14	18:25	E	-62.1	79.9	26.9		-202.9	-20.7		
20	1983 Sep 15	06:26		Master event							
25	1984 Jan 03	15:28	Z	37.0						-11.2	
25	1984 Jan 03	15:28	N	413.9	154.8					960.7	
25	1984 Jan 03	15:28	E	362.2	139.2					896.0	

Table 4. Relocation vector (*X*, *Y*, *Z* in m) pointing from the original location to the hypocenter from the relocation

No.	Date	Time	Relocation vector in m		
			<i>X</i>	<i>Y</i>	<i>Z</i>
03	1982 Nov 28	04:34	304	-33	2,730
16	1983 Sep 11	11:48	221	-95	-830
18	1983 Sep 14	10:52	161	-75	-900
19	1983 Sep 14	18:25	-32	86	-130
20	1983 Sep 15	06:26	Master event		
25	1984 Jan 03	15:28	-139	3,979	-1,190

ences in delay times for the two horizontal components below the duration of the digitization interval. Therefore, the average *S* delay times used for the relocations of events which were observed under different back azimuths might be in error. On the other hand, from data quality criteria, no preference could be given to any of the single components.

The differences between relocations and original locations are given in Table 4. The shift of the epicenters as a result of the relocation is shown in Fig. 9. The amount of shift is strongly related to the original hypocentral distance to the master event. The closest events were shifted by approximately 100 m, whereas the farthest event was moved by the relocation by approximately 4 km. In order to measure the improvement of the relocation, the total location error for the original location and for the relocation was calculated (Table 5). This quantity has been defined as the arithmetic mean of the standard deviations for the individual coordinate axes in the location procedure. It can be viewed as a measure of the size of the volume where the true hypocentre is located with a specific probability. In Fig. 10 the ratios of the total loca-

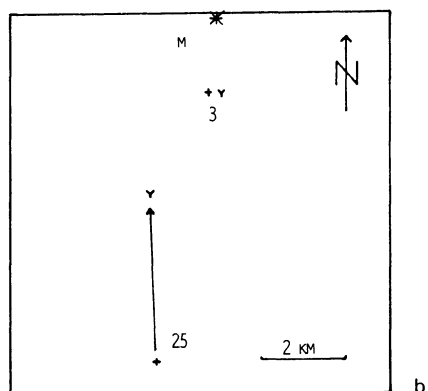
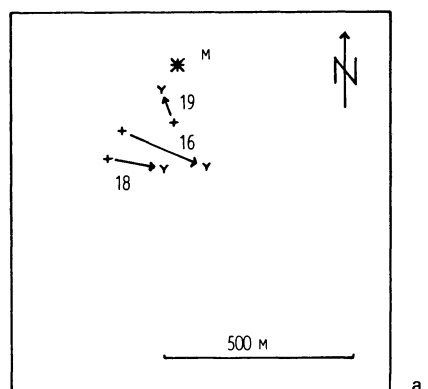


Fig. 9a and b. Difference vectors for the relocated epicenters as compared to the original locations. **a** shows the results for the events with small difference, whereas in **b** the difference vectors for the events with large epicentral shifts due to the relocation are displayed. Old epicentres are denoted by +, relocated epicentres by y

Table 5. Location errors for the original locations and relocations together with the error ratio. Location error was defined as the arithmetic mean of the localization standard deviation for the individual coordinate axes

No.	Date	Time	Location error in km		
			Original location	Relocation	Ratio
03	1982 Nov 28	04:34	0.316	1.451	0.218
16	1983 Sep 11	11:48	0.316	0.312	1.013
18	1983 Sep 14	10:52	0.106	0.045	2.356
19	1983 Sep 14	18:25	0.208	0.101	2.059
20	1983 Sep 15	06:26	0.316		
25	1984 Jan 03	15:28	0.277	4.295	0.064

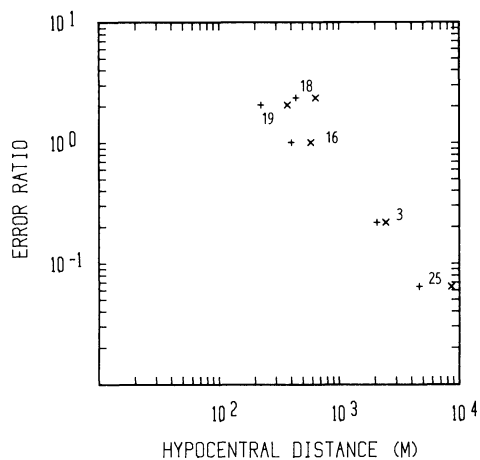


Fig. 10. Ratio of total location errors before and after relocation as a function of the individual event – master event distance. The x refer to the original distance, the $+$ to the relocated distances. For the explanation of the total location error, see text

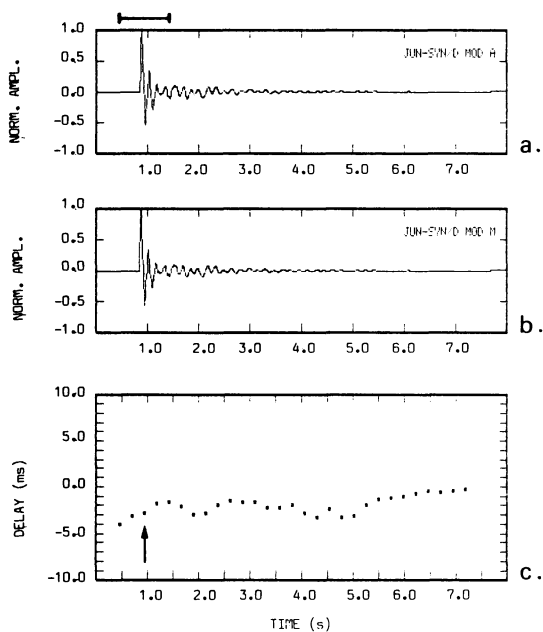


Fig. 11 a–f. Cross spectral analysis of noise-free synthetic seismograms from the same source location, but different source time functions. **a** and **b** show the aligned *SH* seismograms, **c** gives the differential times versus lapse time. **d** shows the cross amplitude spectrum for the window containing the *S* pulses. **e** and **f** give the corresponding coherence and cross phase spectrum, respectively. The dotted line in the phase plot corresponds to the delay time equal to the sampling interval

tion errors for the original localizations and the relocalizations are given as a function of the hypocentral distances to the master event. Only for events as close as 0.5 km from the master event could an improvement of the localization be obtained by the CSA method. This result is in agreement with the observation of increasing standard deviations with increasing distances from the master event shown by Ito (1985).

The influence of errors

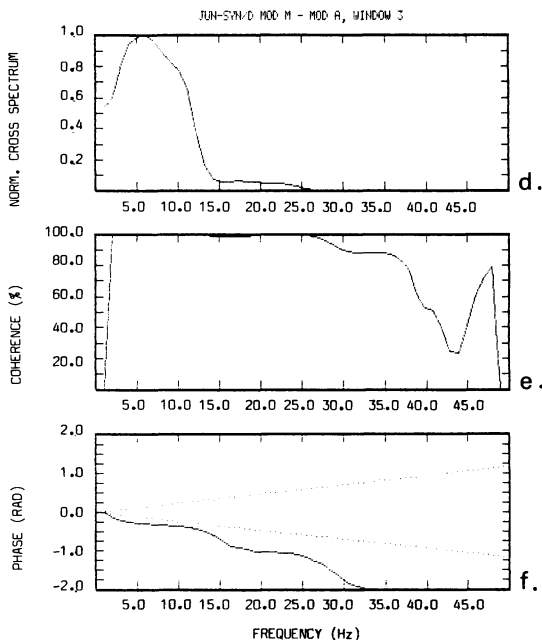
A) Instrumental errors

Systematic time shifts for the samples of neighbouring data channels are introduced during recording due to a multiplexed analog to digital conversion. Since this time difference is the same for the same channels at different stations, it has not been considered further.

After digitization, the time code is added to the data frame through a transmitter-synchronized time signal. The maximum tolerance is reported to be 1 ms (Lennartz electronic, personal communication, 1986). Since the data are digitized at the site, additional errors such as tape speed variations, telephone line delays, etc., are of no concern for the present analysis. Furthermore, errors due to instrumental differences are below the instrumental tolerance since all the recording systems are the same.

B) The influence of source pulse differences

In order to investigate the amount of error which might be introduced by source pulse differences, we performed the CSA method on a number of synthetic data with different source time functions. The geometry was chosen to resemble the actual situation in the present study using a well-established crustal model for the Swabian Jura earthquake zone (e.g. Langer, 1986). The seismograms were cal-



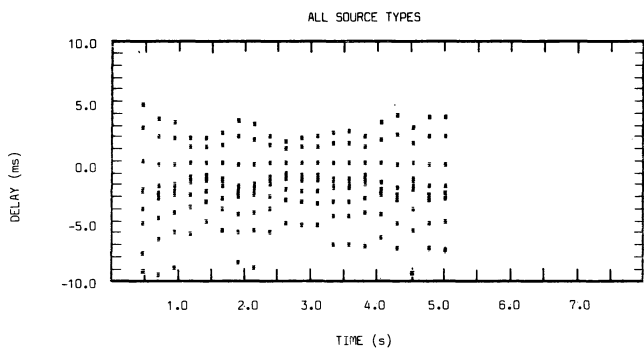


Fig. 12. Overall scatter of spurious times introduced by differences in the source functions. The amount of variation is explained in the text

culated for plane SH waves propagating in a stack of horizontal layers using the Haskell (1960) method. The source time functions consisted of trapezoidal pulses, defined by the three parameters: rise, sustain and decay time. These parameters were chosen for the synthetic master event to be 0.01, 0.02, 0.01 s in order to obtain a frequency content comparable to the observed signals. By variation of the individual source time parameters between 0.0 and 0.03 s with steps of 0.01 s, a number of slightly different individual events were simulated. The source locations were held fixed. An example is given in Fig. 11. As can be seen, the coherence of the different seismograms is close to one, not showing any significant difference in the signal shape. However, due to the phase differences of the source pulses, a spurious time difference is introduced (Fig. 11c and f). The amount of error introduced in the considered range can be seen in Fig. 12. Here the overall scatter of delay times for all the combinations – eight in total – in the source time para-

eters are displayed. The coherence in these examples did, in no case, suffer from the different source time functions. Thus, in practice this kind of error would be hard to detect. The absolute amount of spurious delay times easily reached the sampling interval (3.75 ms) in the present analysis.

C) The influence of additive noise

White noise was added to the seismograms presented in Fig. 11 in order to investigate the influence of noise. The results are given in Fig. 13. As can be seen from Fig. 13c in comparison with Fig. 11c, for regions where the signal-to-noise ratio is high, the delay times are not affected by additive noise. This agrees well with Ito's assumption (Ito, 1985).

Discussion and conclusions

Cross spectral analysis methods provide a powerful tool for a precise measurement of differential times between similar earthquakes. For the Swabian Jura seismic network, due to the precision of the internal clock synchronization, the maximum timing accuracy is limited to approximately 1 ms.

In terms of relocation precision, this corresponds to approximately 5 m. This offers an exciting possibility for high-resolution relative hypocentral determinations and the study of the fine structure of source regions (Ito, 1985). Prerequisite, however, are small original spatial differences for the events to be compared. The scatter of the delay times for the individual components increases strongly for the Swabian Jura earthquakes recorded from source locations further apart than 1.5 km. In these cases, S -wave delay times averaged over the individual components might, therefore, not be representative of the actual delay times. This effect can be understood from the observation geome-

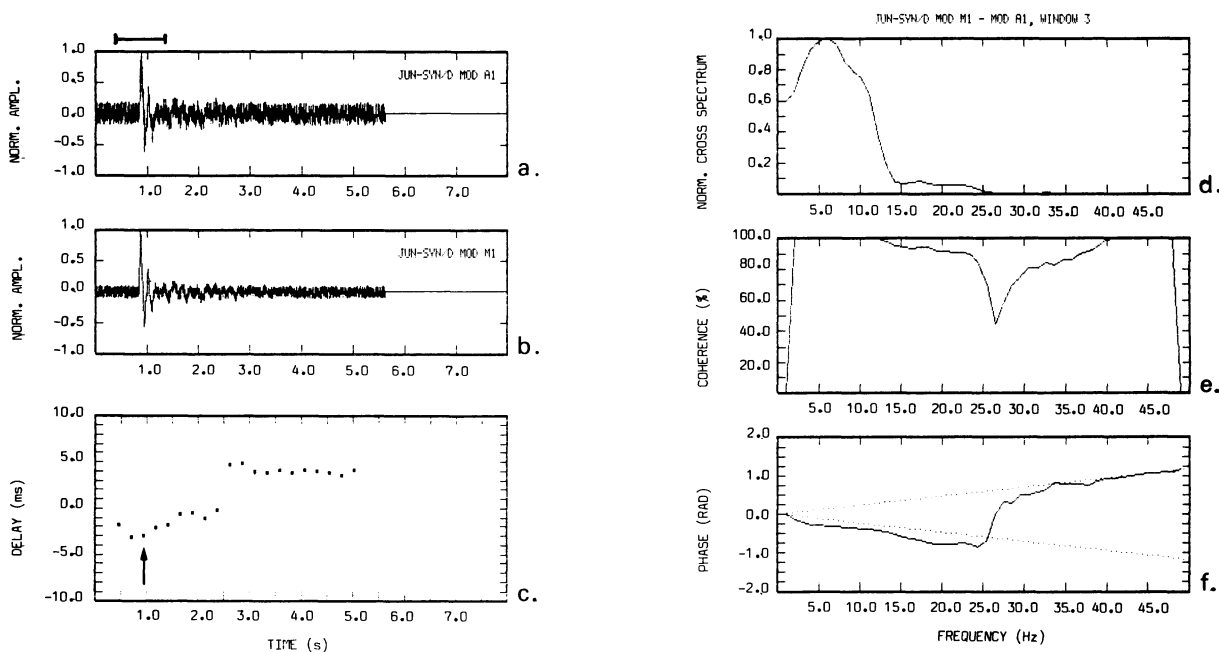


Fig. 13a-f. Cross spectral analysis of noisy synthetic seismograms. The seismograms are the same as in Fig. 11. **a** and **b** show the aligned SH seismograms, **c** gives the differential times versus lapse time. **d** shows the cross amplitude spectrum for the window containing the S pulses. **e** and **f** give the corresponding coherence and cross phase spectrum, respectively. The dotted line in the phase plot corresponds to the delay time equal to the sampling interval

try. Due to different back azimuths, the two events to be compared are observed in apparently different coordinate systems. With simultaneously sampled three-component records, this effect could possibly be reduced by simple coordinate rotation. In this context, multiplexed analog to digital conversion, as used in the Swabian Jura seismic network, shows severe disadvantages.

From the analysis of synthetic seismogram data, the influence of additive, uncorrelated white noise seems to be negligible as long as the signal/noise ratio is high, approximately $> 4-5$ in the considered cases.

No evidence for velocity variations in the Swabian Jura area could be detected from the present analysis. Provided two earthquakes were generated at the same location, a prerequisite for the applicability of the CSA method to monitor velocity variations is the equality of the shape of the source signal. Any differences in the phase spectra of the sources, which do not necessarily have to be a linear function of frequency, are subject to the regression analysis and will be treated as delay time differences. Even changes which do not show up significantly in the coherence (cf. Fig. 11c) might spuriously introduce delay times of the order of the digitization interval. Thus, the coherence spectrum does not seem to be a sufficient measure to detect source time function differences, which might spoil a velocity monitoring analysis using CSA.

For the purpose of relative localization, the influence of source shape differences might not be as severe in special cases, provided that directivity effects at the source are negligible. If the phase shift introduced from the source is identical in all azimuths and incidence angles, the relative location will be correct and the time delay will be considered only as an origin time difference.

In order to investigate these effects more thoroughly, the influence of complex sources producing anisotropic phase changes and their influence on the relocalization should to be modelled. This is, however, beyond the scope of this paper. Additionally, the observation of quarry blast signals, where differences in the source signals could actually be observed, would be of great interest. However, no adequate data for the Swabian Jura seismic network were at our disposal.

Acknowledgements. The comments of the reviewers are greatly appreciated.

References

Dewey, J.W.: A consumer's guide to instrumental methods for determination of hypocenters. *Geol. Soc. Am., Rev. in Eng. Geol.* **IV**, 109–117, 1979

- Evernden, J.F.: Identification of earthquakes and explosions by use of teleseismic data. *J. Geophys. Res.* **74**, 3828–3856, 1969
- Frechet, J.: Sismogenese et doublets sismiques. Ph. D. thesis, University of Grenoble, 206 pp., 1985
- Fremont, M.J.: Mesure de variations temporelles des paramètres de la croûte terrestre et d'effets de sources par traitement de doublets de séismes. Ph. D. thesis, University of Grenoble, 220 pp., 1984
- Gelbke, C.: Erweiterung des Erdbebenlokalisierungsprogramms HYPO71 (Lee and Lahr, 1972) um eine Laufzeitroutine fuer Mehrschichtenmodelle konstanter positiver und negativer Geschwindigkeitsgradienten. *Geophys. Inst. Univ. Karlsruhe*, 58 pp., 1977
- Haessler, H., Hoang-Trong, P., Schick, R., Schneider, G., Strobeck, K.: The September 3, 1978, Swabian Jura earthquake. *Tectonophysics* **68**, 1–14, 1980
- Haskell, N.A.: Crustal reflection of plane SH waves. *J. Geophys. Res.* **65**, 4147–4150, 1960
- Ito, A.: High resolution relative hypocenters of similar earthquakes by cross-spectral analysis method. *J. Phys. Earth* **33**, 279–294, 1985
- Kanasewich, E.R.: Time sequence analysis in geophysics. The University of Alberta Press, 480 pp., 1981
- Langer, H.: Seismotektonische Herdparameter und Ausbreitungseffekte bei Mikroerdbeben im Bereich der westlichen Schwabischen Alb. Ph. D. thesis, University of Stuttgart, 113 pp., 1986
- Lee, W.H.K., Lahr, L.C.: HYPO71: A computer program for determining hypocenter, magnitude and first motion pattern of local earthquakes. U. S. Geol. Survey, Open File Report, 113 pp., 1972
- Poupinet, G., Ellsworth, W.L., Frechet, J.: Monitoring velocity variations in the crust using earthquake doublets: An application to the Calaveras Fault, California. *J. Geophys. Res.* **89**, 5719–5731, 1984
- Poupinet, G., Frechet, J., Ellsworth, W.L., Fremont, M.J., Glangaud, F.: Doublet analysis: Improved accuracy for earthquake prediction studies. *Earthq. Predict. Res.* **3**, 147–159, 1985
- Scherbaum, F.: Die seimische Erkundung des Stationsuntergrundes mit Nahbebenseismogrammen. Habilitation thesis, University of Stuttgart, 209 pp., 1986
- Scherbaum, F., Stoll, D.: Source parameters and scaling laws of the 1978 Swabian Jura (Southwest Germany) aftershocks. *Bull. Seismol. Soc. Am.* **73**, 1321–1343, 1983
- Scherbaum, F., Stoll, D.: The estimation of Green's function from local earthquake recordings and the modelling of the site response. *Phys. Earth Planet. Inter.* **38**, 189–202, 1985
- Turnovsky, J., Schneider G.: The seismotectonic character of the September 3, 1978, Swabian Jura earthquake series. *Tectonophysics* **83**, 151–162, 1982

Received May 28, 1986; revised version September 8, 1986
Accepted September 19, 1986

The retrieval of the seismic moment tensor from first-order perturbation theory and generation of compatible models

X. Lana¹ and A.M. Correig^{1,2}

¹ Departament de Física de la Terra i del Cosmos, Facultat de Física, Universitat de Barcelona, Diagonal 645, Barcelona 08028

² Laboratori d'Estudis Geofísics Eduard Fontserè, Institut d'Estudis Catalans, Carme, 47, Barcelona 08008

Abstract. The first-order perturbation theory applied to the eigenvectors and eigenvalues of the recovered seismic moment tensor give rise to a more accurate determination of the whole scalar seismic moment and allows a quantification of a possible superposition of distinct focal mechanisms, such as the double couple and the compensated linear vector dipole. On the other hand, the elements of the seismic moment tensor recovered from spectral amplitudes of shallow earthquakes will be obtained with important uncertainties, especially the M_{xz} and M_{yz} elements, when the starting models of inversion are close to pure normal, reverse or strike-slip faults. By using properties associated with the Lanczos matrix decomposition of the system of equations that defines the linearized inversion, a solution is given to the uncertainties of the seismic moment tensor elements. In such a way, a set of focal mechanisms, all fitting the experimental data, are generated and discussed in terms of other geophysical evidence. The applicability of the perturbation theory is tested by means of numerical simulation and applied to two earthquakes. For each earthquake, a set of models fitting the data has been generated. The vertical component of the Rayleigh wave spectral amplitudes, with periods ranging from 30 to 90 s, has been used.

Key words: Seismic moment tensor – Perturbation theory – Focal mechanism – Focal depth

Introduction

Following the pioneering work of Gilbert (1970), it is nowadays usual to retrieve the elements of the seismic moment tensor from seismic records. If spectral amplitudes and phases are available, the inversion process is linear and does not present special problems (Patton and Aki, 1979). However, except for a few well-studied regions of the Earth, phases can not be used because phase velocities must be known with an accuracy better than 0.5%, and the inversion has to be carried out with the amplitudes only. Mendiguren (1977) showed that using spectral amplitudes only, the inversion, which is no longer linear, is not unique. Moreover, the lack of uniqueness may be increased due to ill-conditioned systems (that appear when the initial trial solution

is close to a reverse, normal or pure strike-slip fault) as well as errors in data (due to ambient noise, focusing, etc.) which may generate unrealistic spurious mechanisms.

In the present paper we study the problem of recovering the elements of the seismic moment tensor using only the amplitudes of the Rayleigh waves, vertical component, within a period range of 30–90 s. Periods shorter than 30 s have been avoided because of the difficulty of correction by attenuation as well as to avoid possible influences of directivity function (Correig and Mitchell, 1980), focusing and multipathing. Concretely, two problems are discussed: a quantification of the uncertainties of the seismic moment tensor and the influence of the lack of uniqueness on the focal mechanism obtained.

The uncertainties are quantified by applying first-order perturbation theory to the eigenvalues and eigenvectors of the seismic moment tensor. In order to carry out the process of inversion, the initial model is obtained by assuming a shear focal mechanism as deduced from the usual study of *P*-wave first motions. A first evaluation of the scalar seismic moment is made by dividing, at large periods, the recorded spectral amplitudes by the spectral amplitudes generated theoretically from the focal mechanism previously obtained with a unit scalar seismic moment.

We have found that perturbation theory is a useful instrument in recovering a correct scalar seismic moment. In addition, the existence of spurious focal mechanisms other than the double couple is also discussed through the study of the perturbed scalar seismic moment. The uncertainties associated with the focal mechanism are obtained from the perturbed eigenvectors and eigenvalues of the seismic moment tensor. The knowledge of the uncertainties of the focal mechanism is very important, for instance, when dealing with the orientation of the regional stress tensor (Angelier et al., 1982; Gephart and Forsyth, 1984). We show also that, in the case of moderate ambient noise, the correct focal depth corresponds to the depth for which the perturbation on the scalar seismic moment is a minimum.

The uniqueness is another parameter which we attempt to quantify. As a consequence of the lack of uniqueness, a badly constrained focal mechanism can be obtained. Using the properties of the matrix Lanczos decomposition applied to eigenvectors close to zero, a set of focal mechanisms that fit the observed data is analytically obtained as a function of the inversion residuals. This newly generated dataset is called “compatible models”.

Perturbation theory

Following Knopoff and Randall (1970) we assume that the eigenvalues of the seismic moment tensor, obtained from an inversion process, can be interpreted as the superposition of a double couple (DC) and a compensated linear vector dipole (CLVD) in the following way:

$$\begin{pmatrix} \beta_1 & 0 & 0 \\ 0 & \beta_2 & 0 \\ 0 & 0 & \beta_3 \end{pmatrix} = M_0(1-2f) \begin{pmatrix} 1 & 0 & 0 \\ 0 & -1 & 0 \\ 0 & 0 & 0 \end{pmatrix} + M_0 2f \begin{pmatrix} 1 & 0 & 0 \\ 0 & -\frac{1}{2} & 0 \\ 0 & 0 & -\frac{1}{2} \end{pmatrix} \quad (1)$$

where β_i are the eigenvalues of the retrieved seismic moment tensor, M_0 the (scalar) seismic moment, $M_0(1-2f)$ gives the amount of seismic moment due to a DC mechanism [with eigenvalues (1, -1, 0)] and $M_0 2f$ gives the amount of seismic moment due to a CLVD mechanism [with eigenvalues (1, $\frac{1}{2}$, $-\frac{1}{2}$)]. f is a parameter defined as (Dziewonski and Woodhouse, 1983):

$$f = |\beta_3/\beta_1| \quad (2)$$

with values ranging from 0 (pure DC) to $\frac{1}{2}$ (pure CLVD).

We apply first-order perturbation theory (Mathews and Walker, 1964) to eigenvectors and eigenvalues of the seismic moment tensor, in order to study the uncertainty associated with each mechanism. The method used to obtain the perturbed eigenvectors and eigenvalues is given in Appendix 1. The uncertainty in the mechanism is obtained as follows:

i) Let V'_i be the perturbed eigenvectors; following Mendiguren (1977) and Honda (1962), the perturbed principal axes of tension \tilde{T}' and pressure \tilde{P}' are given by:

$$\tilde{T}' = \pm V'_1 \quad \tilde{P}' = \pm V'_2. \quad (3)$$

ii) Equations (1) and (2) define the perturbed (scalar) seismic moments as:

$$M'_0 = \beta'_1 \quad M'_{DC} = \beta'_1 + 2\beta'_3 \quad M'_{CLVD} = -2\beta'_3. \quad (4)$$

Comparing the retrieved seismic moment with the computed perturbations, we can impose a criterion to decide which focal mechanism is representative and which is due to contaminating noise: the focal mechanism will be representative of a real physical process if the ratio M'/M is close to 1, where M is a (scalar) seismic moment (M_0 , M_{DC} or M_{CLVD}) and M' is its perturbed value. The term "close to 1" will be quantified in the numerical simulations and applications.

iii) Following Strelitz (1980), it is also possible to compute the angle between the eigenvector V_i and the perturbed eigenvector V'_j as:

$$C_{ij} = \cos(V_i \cdot V'_j). \quad (5)$$

This angle C_{ij} represents the confidence ellipse of pressure, tension and null vector axis, projected on the focal sphere.

Generation of compatible models of mechanisms

Let

$$\delta D = A \delta P + \varepsilon \quad (6)$$

be the system of equations from which we have computed the elements of the seismic moment tensor, where A is the matrix of partial derivatives of the spectral amplitudes with respect to the parameters of inversion (defined in Appendix 2) δD the difference vector between observations and predictions from an initial model P_0 , δP is the correction to P_0 and ε is the error vector associated with the observations. A solution of system (6), due to the existence of ε , will be one that minimizes:

$$E = \|D - AP'\| \quad (7)$$

where D are the observed spectral amplitudes and E the Euclidian norm of residuals of inversion. P' is the solution that minimizes Eq. (7).

The solution P' which minimizes Eq. (7) is not unique, because by solving Eq. (6) according to the decomposition of Lanczos (1961) of A in eigenvalues μ_i and eigenvectors (U_i , V_i), another possible solution is:

$$P^* = P' + P \quad (8)$$

where:

$$P = \sum_i \alpha_i U_i \quad (9)$$

is a linear combination of the eigenvectors U_i of A , associated with eigenvalues close to zero. Note that the complete set of eigenvectors U_i generates the parameter space. Taking this into account, our problem may now be formulated in a different way: finding a set of solutions P which satisfy:

$$\|AP' - AP^*\| \leq Q \quad (10)$$

where Q is a value to be determined as a function of the Euclidian norm E . Expression (10) can be interpreted in the following way: because the eigenvectors U_i are associated with eigenvalues close to zero, the set of models P that satisfy (10) will predict the observed amplitudes D with the same accuracy as model P' , solution of Eq. (7). This assessment is a consequence of the existence of the term ε in Eq. (6) and the residuals of the inversion.

To obtain maximized values of P^* , the coefficients α_i of Eq. (9) have to be computed. Using (8) and (9), expression (10) can be rewritten as:

$$\sum_i (\mu_i \alpha_i)^2 \leq Q. \quad (11)$$

From a geometrical point of view, expression (11) represents a hyperellipsoid with semiaxes $\mu_i Q^{\frac{1}{2}}$. The computation of the coefficients which maximize P is equivalent to searching the tangency point between the hyperellipsoid (11) and the hyperplane (9). Application of this concept gives rise to the expression:

$$(\alpha_i)_{\max} = \pm \frac{Q^{\frac{1}{2}}}{\left\{ \sum_j \left\{ \frac{V_{jk} \mu_j^2}{V_{ik} \mu_j} \right\}^2 \right\}^{\frac{1}{2}}} \quad (12)$$

where n is the number of parameters and $(\alpha_i)_{\max}$ is the coefficient that, substituted in (9), maximizes the component k of vector P that satisfies (10), and V_{jk} the component k of the eigenvector V_j . For a discussion on the parameter Q see the applications given below and a recent paper of

Table 1. Numerical simulation. Case S is an example of noise-free signal. Cases S1, S2 and S3 are signals contaminated with background noise. S4 is an example of signal contaminated by multiplicative noise. M_{DC}/M_0 gives the ratio of shear focal mechanism with respect to the whole focal mechanism. The percentage of perturbation in M_0 , M_{DC} and M_{CLVD} is given by $\%M_0$, $\%M_{DC}$ and $\%M_{CLVD}$, respectively. The scalar seismic moment tensor is given in units of $1.0 \text{ E} + 16 \text{ Nm}$. Focal depth is given in kilometers. The signal-to-noise ratio is also given

Focal depth	M_0	M_{DC}	M_{CLVD}	M_{DC}/M_0	$\%M_0$	$\%M_{DC}$	$\%M_{CLVD}$
Case S							
7.5	95.4	47.8	47.6	0.50	8.8	39.8	23.0
10.5	132.0	57.8	74.2	0.44	12.8	69.2	18.9
13.5	100.0	99.8	0.2	0.99	0.5	0.9	94.5
16.5	124.0	103.0	21.0	0.83	8.2	4.5	26.6
Case S1							
7.5	95.7	48.2	47.5	0.50	9.0	39.4	23.0
10.5	132.7	57.8	74.9	0.44	12.2	51.5	18.2
13.5	101.0	99.4	1.6	0.99	0.9	1.7	87.5
16.5	213.0	108.0	105.0	0.51	17.3	34.0	22.8
Case S2							
7.5	96.3	49.1	47.9	0.51	9.6	41.1	25.0
10.5	134.2	58.0	76.2	0.43	11.5	50.0	18.4
13.5	102.7	98.0	4.7	0.95	3.0	5.5	95.0
16.5	216.0	109.0	107.0	0.50	16.8	55.9	22.0
Case S3							
7.5	100.0	54.2	45.8	0.54	7.1	34.0	22.3
10.5	143.0	60.6	82.4	0.43	7.8	44.1	16.3
13.5	164.0	34.8	129.2	0.21	14.6	70.3	14.0
16.5	232.0	113.0	119.0	0.48	14.1	57.4	27.3
Case S4							
7.5	96.0	48.2	47.2	0.50	11.8	37.3	33.8
10.5	132.0	61.0	71.0	0.46	17.5	65.3	22.5
13.5	104.0	50.1	53.9	0.48	58.7	72.3	25.4
16.5	213.0	105.0	108.0	0.49	55.4	69.3	25.2

Period	Signal/noise ratio					
	60 s	50 s	40 s	35 s	30 s	25 s
Case S1	10	20	25	50	75	75
Case S2	2	4	5	10	25	25
Case S3	1	1	1	2	5	5

Pous et al. (1985). It is important to point out that, from Eq. (9), we will obtain as many maximized solutions P as parameters that define the model, five in our case. Moreover, in the computation of P , Eq. (12) gives stronger weight to the smaller eigenvalues; for this reason the addition that appears in (9) can be extended to the total number of parameters.

Numerical simulation

In order to study the uncertainty in the M_0 , M_{DC} , M_{CLVD} scalar seismic moments, and focal depth determination due to ambient noise, some numerical simulations have been carried out. Synthetic spectral seismograms, with periods ranging from 25 to 60 s, have been generated (case S) for a pure double couple shear fault, located at a depth of

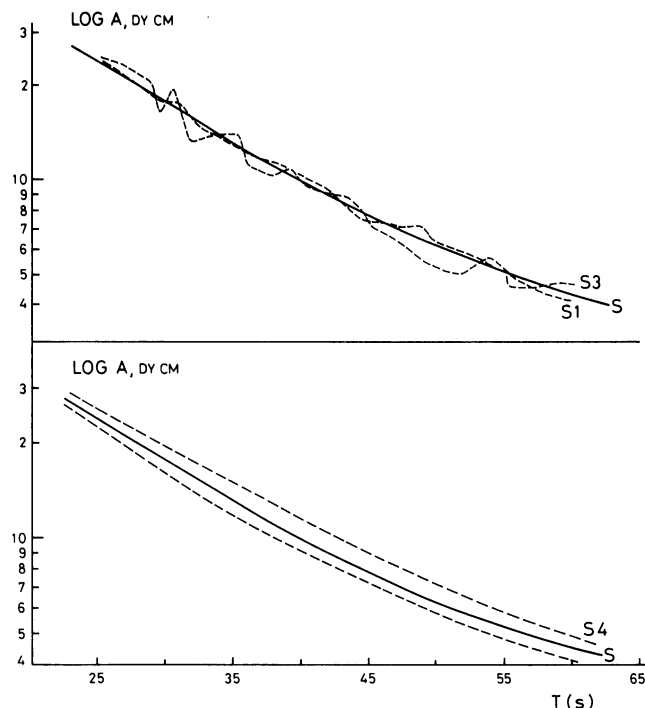


Fig. 1. Synthetic spectral amplitudes of the vertical component reduced to the seismic source for an arbitrary azimuth. Case S corresponds to signal without noise. Case S1 corresponds to signal contaminated with the first level of noise in Table 1. Case S3 corresponds to signal contaminated with the third level of noise in Table 1. *Dashed lines* (cases S4) correspond to maximum variations in the spectral amplitude when multiplicative noise is present

13.5 km with the following parameters: dip = 45° , slip = 45° , strike = 80° (clockwise from north) and a scalar seismic moment of $1.0 \text{ E} + 18 \text{ Nm}$. As a propagating medium, we use the model of Dziewonski and Anderson (1981). The ambient noise of the seismograms pretend to be randomly distributed values ranging from -1 to $+1$, added to the real and to the imaginary parts of the spectra and multiplied by three increasing levels of signal-to-noise ratio. These levels of signal-to-noise ratio are similar to those used in Patton and Aki (1979), which were obtained by studying the spectral components of several sets of background noise recorded at WWSSN stations. Corresponding results have been named cases S1, S2 and S3. The signal-to-noise ratios for periods within 25–60 s are given in Table 1. Besides this, possible existing lateral inhomogeneities have been simulated by random multiplications or divisions of the spectral amplitudes by a factor of 0.7; (case S4). The focusing and multipathing effects can be generated by random multiplications or divisions of spectral amplitudes by a factor dependent on frequency for periods lower than 30 s. This possibility will not be taken into consideration because the process of inversion has been applied to periods greater than 30 s. In doing so, we have avoided the influence of multipathing focusing, attenuation and finite extension of the seismic source. As a counterweight to this situation, there will exist some loss of resolution in the focal depth determination, especially when there is very important seismic noise. In Fig. 1, logarithms of some spectral amplitudes in dyne cm reduced to the source with an arbitrary azimuth are shown, corresponding to cases S1, S3 and S4.

The process of retrieving focal mechanisms for a noise-free spectrum (case S) and contaminated spectra (cases S1, S2, S3 and S4) was carried out in a previous work (Lana and Correig, 1985), minimizing the residual of the inversion and the standard deviation of the first parameter of inversion (defined in Appendix 2). For cases S, S1 and S2 the correct focal depth of 13.5 km was obtained, whereas the retrieved focal depth for cases S3 and S4, obtained from the minimum standard deviation of P_1 , was 7.5 km.

In the present study the numerical simulation has been carried out by applying only the perturbation theory. The algorithm of mechanism generation in perturbation theory will be applied, later on, to two real events. The inversion process is repeated for several depths and perturbation theory is applied to each one. In Table 1 the retrieved seismic moments (M_0 , M_{DC} and M_{CLVD}) are summarized, as well as the percentage of perturbation for every seismic moment ($\%M_0$, $\%M_{DC}$, $\%M_{CLVD}$) and the ratio M_{DC}/M_0 for the five cases S to S4. It is stated for cases S, S1 and S2 that not only the residuals and standard deviations are minimal, but the ratio M_{DC}/M_0 is a maximum for this focal depth, the percentage associated with perturbation of M_0 and M_{DC} is a minimum and the component M_{CLVD} of the mechanism makes no sense because the associated perturbation is too large. For cases S3 and S4, the ratio M_{DC}/M_0 is a maximum for a focal depth of 7.5 km and the perturbation percentage of M_0 and M_{DC} are minimum. We can conclude that for a poor signal-to-noise ratio, such as in case S3, and for relatively high multiplicative noise, case S4, the scalar seismic moment M_0 is retrieved with enough accuracy and a spurious focal depth, with an error of approximately 6 km, is recovered. We also obtain the CLVD component of the focal mechanism with moderate uncertainties. In short, in cases S3 and S4 there are some uncertainties concerning the correct focal depths and focal mechanism components, but the whole scalar seismic moment M_0 , which gives information about the strength of the seismic event, is well recovered.

Applications

Perturbation theory and the computation of compatible mechanisms has been applied to two earthquakes: event January 1, 1965 (MED) and event November 18, 1970 (PAC). Focal mechanisms for both earthquakes were previously studied by Lana and Correig (1985) by means of the retrieval of the elements of the seismic moment tensor. Table 2a shows information obtained from NEIS agency; azimuthal distribution and epicentral distances of the WWSSN stations used. Due to the moderate magnitude of both earthquakes, the seismic signal is poorly recorded at some WWSSN stations and the azimuthal distribution is not entirely fulfilled. Figure 2 shows several vertical-component seismograms for event PAC. Table 2b shows the focal parameters, elements of the seismic moment tensor, focal mechanism and focal depth for both earthquakes as reported by Lana and Correig (1985).

In the study of residuals, focal depth showed some uncertainty which could be resolved for event MED by searching for a minimum of the standard deviations of parameter P_1 associated with the real part of the spectra. The study of the P_1 standard deviations for several depths is entirely coherent because P_1 is the only parameter depending explicitly on the focal depth according to the functions G_1 and

Table 2a. Information available from NEIS agency (approximate focal depth, location, origin time and magnitude) WWSSN stations, epicentral distances in km, and azimuth clockwise from north

Event:	MED (35.7°N, 4.4°E)	PAC (28.7°S, 112.7°W)
Date:	January 1, 1965	November 18, 1970
Focal depth:	10 km	5 km
Magnitude:	5.2 (<i>mb</i>)	5.6 (<i>mb</i>)

WWSSN stations	Epicentral distance	azimuth
Event MED		
PTO	1,284.3	301.9
AKU	3,560.6	343.0
COP	2,305.2	12.9
ESK	2,257.8	347.4
KEV	4,033.9	13.1
STU	1,506.9	13.9
TOL	876.5	304.5
VAL	2,146.7	331.7
AQU	1,073.6	43.8
ATH	1,738.4	75.9
PDA	2,476.1	285.6
Event PAC		
BKS	7,430.6	352.1
LON	8,400.1	353.5
QUI	3,983.3	69.9
NNA	4,148.5	71.0
TUC	6,742.0	1.8
COR	8,180.5	352.1
LPS	5,384.4	31.2
ARE	4,421.4	81.2
PEL	4,018.7	107.8
LEM	14,176.8	234.1
MAT	13,451.3	297.4

Table 2b. Elements of the seismic moment tensor, focal depth, dip, slip, strike and scalar seismic moment (M_{DC}) for the double couple focal mechanism (Lana and Correig, 1985)

Event PAC		
$M_{XX} = -0.86 \text{ E} + 18$	$M_{XY} = 0.21 \text{ E} + 18$	$M_{XZ} = -0.10 \text{ E} + 14$
$M_{YY} = 1.10 \text{ E} + 18$	$M_{YZ} = 0.10 \text{ E} + 14$	$M_{ZZ} = -0.24 \text{ E} + 18$
Dip = 90°	Slip = 0°	Strike = N 51° E
$M_{DC} = 0.65 \text{ E} + 18 \text{ Nm}$		Depth: 0–30 km
Event MED		
$M_{XX} = -0.38 \text{ E} + 18$	$M_{XY} = 0.13 \text{ E} + 18$	$M_{XZ} = -0.11 \text{ E} + 17$
$M_{YY} = 0.95 \text{ E} + 17$	$M_{YZ} = 0.51 \text{ E} + 18$	$M_{ZZ} = 0.29 \text{ E} + 18$
Dip = 48.9°	Slip = 70.1°	Strike = N 29° E
$M_{DC} = 0.54 \text{ E} + 18 \text{ Nm}$		Depth: 10.5 km

G_2 . However, an uncertainty in the focal depth was obtained (Lana and Correig, 1985) for event PAC, studying the residuals and the standard deviation of parameter P_1 . This situation could be associated with the ill-conditioned system result of an initial model for event PAC close to a pure strike-slip fault. The poor dependence on the focal depth of the standard deviation of P_1 remains unexplained because a better resolution of the focal depth is expected by studying the parameters associated with the real part of the spectral amplitudes.

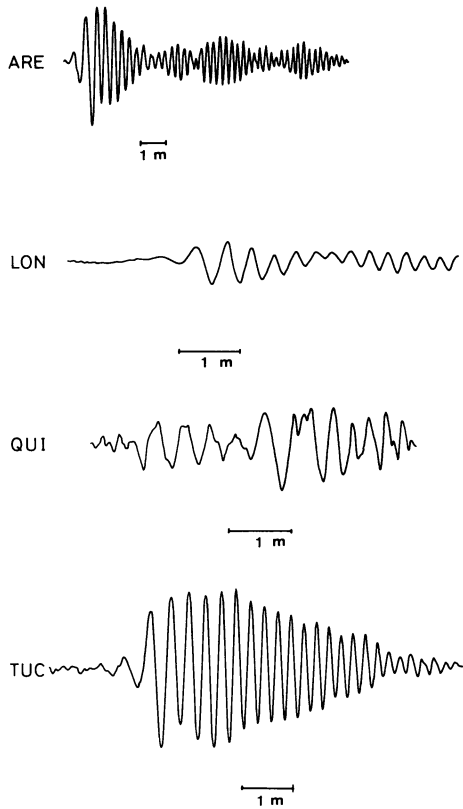


Fig. 2. Long-period vertical-component records of event PAC at WWSSN stations LON, TUC, QUI, ARE

In Table 3 there is a summary of results obtained from perturbation theory; a focal depth of 10.5 km for event MED is confirmed. For event PAC, the uncertainty is less than in the previous results, and we conclude a focal depth of 4.5 km. Although the percentage of shear mechanism for event PAC is practically the same for a focal depth of 4.5 km as for 7.5 km, the perturbation in the M_{DC} seismic moment is smaller at a focal depth of 4.5 km. The focal depth obtained for the two events were very similar to those reported by NEIS agency. It is important to note that in both events the possible CLVD mechanism for the assumed focal depth is obtained with a very large perturbation in their seismic moment; for this reason we conclude that it is not representative of the physical process at the seismic source.

Angles C_{ij} formed by perturbed and unperturbed eigenvectors of the mechanism are listed in Table 4 for both events. It can be seen that the uncertainty in the orientation of the null, compressional and tensional axes ranges between 0° and 5° . We can conclude that the uncertainty in the orientation of the principal axes is small and, consequently, the strike, dip and slip of the DC mechanisms will be accurately obtained.

The algorithm of generation of compatible models has been applied to events MED and PAC when the elements of the seismic moment tensor, the scalar seismic moment and the focal depth have been well delimited. The criterion we have considered, for deciding whether a model is compatible with that obtained by generalized inversion or not, imposes that the square error between the amplitudes used in the inversion and those given by compatible models generated by Eq. (11) should be, in the worst case, as large

Table 3. Results obtained by applying perturbation theory. M_{DC}/M_0 gives the ratio of shear mechanism with respect to the whole mechanism. The percentage of perturbation in the scalar seismic moments is given by $\%M_0$, $\%M_{DC}$ and $\%M_{CLVD}$. The scalar seismic moment is given in units of $1.0 \text{ E} + 16 \text{ Nm}$. The focal depth is given in kilometers

Focal depth	M_0	$\%M_0$	M_{DC}	$\%M_{DC}$	M_{CLVD}	$\%M_{CLVD}$	M_{DC}/M_0
Event PAC							
4.5	1.12	8.2	0.65	5.9	0.47	20.1	0.58
7.5	1.23	12.2	0.67	8.3	0.56	23.2	0.54
10.5	1.35	15.3	0.70	13.5	0.65	28.4	0.52
13.5	1.49	27.2	0.72	18.4	0.77	32.3	0.48
16.5	1.64	32.5	0.81	22.6	0.83	37.9	0.49
19.5	1.85	35.1	0.84	28.0	1.01	42.1	0.45
Event MED							
7.5	0.34	26.5	0.08	3.8	0.26	38.5	0.23
10.5	0.62	10.1	0.54	17.0	0.08	72.3	0.88
13.5	0.42	13.3	0.19	22.1	0.23	44.8	0.46
16.5	0.47	46.0	0.31	25.5	0.16	46.6	0.66
19.5	0.41	53.4	0.35	30.2	0.06	85.3	0.85

Table 4. Angles between perturbed and unperturbed principal axes of the two earthquakes. In the absence of perturbation, the angles will be equal to 90° . C_{ij} is the angle between the unperturbed vector i and the perturbed vector j , with i different to j

	Event PAC	Event MED
C_{12}	89.95°	95.17°
C_{21}	90.50°	90.18°
C_{13}	89.96°	85.03°
C_{31}	89.95°	93.97°
C_{23}	89.32°	88.92°
C_{32}	89.95°	88.40°

as the residual E of the inversion. The first approximate value of Q may be assumed to be the residual E of the inversion. We will have to reduce the assumed value of Q until the condition of linearity, implicit in the derivation of (11), is satisfied, because our system is not linear, although it has been linearized in (6).

Since P is obtained as a linear combination of eigenvectors associated with very small eigenvalues of the Lanczos (1961) decomposition, it is reasonable to expect important deviations in models generated from event PAC for which two eigenvalues close to zero have been obtained in all steps of the inversion process. For event MED none of the obtained eigenvectors is too small, so the obtained compatible models will not really differ from that obtained by inversion.

A similar situation to that obtained for event PAC has been reported by Kanamori and Given (1981) in an inversion study of the real and imaginary parts of the spectra corresponding to very superficial earthquakes. To avoid an ill-conditioned system, those authors impose the condition that parameters P_4 and P_5 (see Appendix 2) are zero. Once the inversion is performed, they try to determine the values of parameters P_4 and P_5 from geological or geophysical information. From the point of view of the present study, we solve this problem by first generating the maximized

Table 5. Increments of P parameters (see Appendix 2) that maximize the five compatible models for events PAC and MED

Components	(1)	(2)	(3)	(4)	(5)
Event PAC					
Model 1	0.160 E+08	-0.942 E+09	-0.123 E+09	-0.393 E+12	-0.685 E+18
Model 2	-0.101 E+08	0.149 E+10	-0.154 E+09	-0.729 E+12	0.631 E+18
Model 3	-0.246 E+07	-0.287 E+09	0.799 E+09	-0.142 E+12	0.130 E+16
Model 4	-0.907 E+04	-0.157 E+09	-0.164 E+06	0.693 E+15	-0.124 E+15
Model 5	-0.139 E+08	0.119 E+09	0.132 E+07	-0.109 E+12	0.787 E+18
Event MED					
Model 1	0.418 E+14	0.192 E+16	0.659 E+15	0.300 E+15	-0.414 E+15
Model 2	0.224 E+14	0.357 E+16	0.419 E+15	0.997 E+14	-0.346 E+15
Model 3	0.133 E+14	0.720 E+15	0.206 E+15	-0.669 E+15	0.185 E+16
Model 4	0.352 E+13	0.998 E+15	-0.387 E+15	0.357 E+16	-0.149 E+16
Model 5	-0.294 E+13	-0.210 E+15	0.649 E+15	-0.904 E+15	0.589 E+16

Table 6. Shear focal mechanism and whole scalar seismic moment for the five maximized compatible models obtained for event PAC. Models 1, 2 and 5 correspond to a normal fault. Models 3 and 4 correspond to a pure strike-slip fault. Strike is given clockwise from north

	M_0 (Nm)	M_{DC} (Nm)	Dip	Slip	Strike
Event PAC					
Model 1	1.31 E+18	0.94 E+18	64.9°	-21.6°	56.1°
Model 2	1.26 E+18	0.98 E+18	65.9°	-21.9°	57.8°
Model 3	1.12 E+18	0.65 E+18	89.9°	0.0°	51.0°
Model 4	1.12 E+18	0.64 E+18	89.9°	0.0°	51.4°
Model 5	1.40 E+18	0.85 E+18	63.4°	-22.2°	56.8°

models compatible with observations and, in a second step, we select the model that fits other geophysical and geological data best. Note that there is no need to make parameters P_4 and P_5 zero, although in the case of an ill-conditioned system no variation of those parameters are allowed.

In Table 5 there is a list of the five series of increments in P that generate the maximized compatible models for both events. We can clearly see that only for event PAC are compatible models, well differentiated from that of inversion, obtained; especially for parameters P_4 and P_5 , the values of which zero at the initial model P_0 . Table 6 shows the maximized generated compatible models for event PAC. We can clearly see that two solutions are possible. Models 3 and 4 represent a strike-slip fault, whereas models 1, 2 and 5 represent a normal fault. On the other hand, the strike angle is practically the same for all the models. The strike-slip solution agrees with that obtained by Forsyth (1972), who locates this event on a transform fault. If this is the case, the strike-slip solution is the correct one. However, the percentage of DC mechanism with respect to total mechanism is higher for the normal fault solution. Because there is no evidence of a CLVD mechanism, the normal fault solution could be favoured.

The maximized compatible models for event MED are not included in Table 6 because the increments of P in Table 5 are very small with respect to the parameters P obtained in the inversion. Consequently, the compatible strike, dip, slip and seismic moments are very close to those shown in Table 2a.

Conclusions

Perturbation theory has been applied to the retrieval of the scalar seismic moment of earthquakes. Through numerical examples and applications to two previously studied earthquakes, perturbation theory appears to be a powerful method in improving the scalar seismic moment M_0 and in discussing the physical meaning of focal mechanisms different to the DC model. The focal depth determination is also improved in some cases. When different kinds of noise contaminate the seismic signals, the applicability of the perturbation theory to the recovery of very exact focal depths is restricted.

The generation of compatible models is especially useful in solutions where the lack of resolution affects some inversion parameters. These solutions will appear when the initial models are close to pure normal, reverse and strike-slip faults, generating ill-conditioned systems. By applying this algorithm of generation, we are able to obtain a large set of models. These models fit the observations as well as models obtained by inversion, although they represent different focal solutions. Once this large set of possible models has been obtained, it is straightforward to incorporate data from other sources to delimit realistic seismic source models.

Appendix 1

Let M be the seismic moment tensor obtained by inversion of spectral amplitudes of Rayleigh waves, and let δM be the tensor whose elements are a function of the standard deviations $\sigma(M_{ij})$ associated with each element M_{ij} .

Let us define the perturbed seismic moment as:

$$M' = M + \delta M \quad (13)$$

where

$$\delta M_{ij} = \sigma(M_{ij}) g_{ij} \quad (14)$$

and g_{ij} is a gaussian variable with zero mean and unit standard deviation.

Following Mathews and Walker (1964), the perturbed eigenvalues β'_i and eigenvectors V'_i , assuming that the eigenvalues are not degenerated, are given by:

$$V'_j = V_j + \sum_k a_{kj} V_k, \quad (15)$$

$$\beta'_j = \beta_j + V_j \delta M V_j \quad (16)$$

where:

$$a_{kj} = V_k \delta M V_j / (\beta_k - \beta_j), \quad j \neq k \quad (17)$$

and V_j and β_j are the unperturbed eigenvectors and eigenvalues, respectively.

From a statistical point of view, we are interested in computing the expected value of $\|a_{kj}\|$ that can be expressed as:

$$E(\|a_{kj}\|) = \left\{ \sum_{s,t,l,m} V_{ks} V_{jt} V_{lj} V_{mn} E(\delta M_{lm} \delta M_{st}) / (\beta_k - \beta_j)^2 \right\}^c \quad (18)$$

where V_{ij} means the component j of vector V_i . $\delta M_{lm} \delta M_{st}$ may be interpreted as a fourth-order tensor which, if $st = lm$, give us the covariance of M_{lm} and, if $st \neq lm$, give us the correlation between M_{lm} and M_{st} .

Assuming that the correlation between M_{lm} and M_{st} is small, implying that $E(\delta M_{lm} \delta M_{st})$ are close to zero, we get:

$$E(\|a_{kj}\|) = \left\{ \sum_{l,t} (V_{lk} V_{lj} \delta M_{lt})^2 / (\beta_k - \beta_j)^2 \right\}^{\frac{1}{2}} \quad (19)$$

and the expected value of the perturbed eigenvalue is given by:

$$E(\beta'_j) = \beta_j + \left\{ \sum_{l,t} (V_{lj} V_{lj} \delta M_{lt})^2 \right\}^{\frac{1}{2}} \quad (20)$$

Similarly, the expected value of the perturbed eigenvector can be expressed as:

$$E(V'_j) = V_j + \sum_k V_k E(\|a_{kj}\|), \quad k \neq j. \quad (21)$$

Appendix 2

Let

$$U_n = M_{pq}(w) G_{np,q}(w) \quad (22)$$

be the spectral displacement field, expressed as a product of the seismic moment tensor by the derivative of the Green's function of the medium with respect to spatial coordinates (Aki and Richards, 1980).

Following Mendiguren and Aki (1978), if we develop Eq. (22) with as many equations as different azimuths for which we have observations, we can resolve the following five parameters:

$$P_1 = (M_{xx} + M_{yy}) G_1 + M_{zz} G_2$$

$$P_2 = M_{yy} - M_{xx}$$

$$P_3 = M_{xy} \quad (23)$$

$$P_4 = M_{yz}$$

$$P_5 = M_{xz}$$

where G_1 and G_2 are functions that depend of the medium structure, stress and displacement functions and focal depth (Takeuchi and Saito, 1972).

The covariance matrix of the parameters of inversion is:

$$\text{Cov}(P) = A^{-1} \phi (A^{-1})^T \quad (24)$$

where A^{-1} is the generalized inverse of matrix A of Eq. (6) (Lanczos, 1961) and ϕ is the covariance matrix of associated errors of Eq. (6). From Eq. (23) it can be seen that only the covariances of M_{xy} , M_{yz} and M_{xz} can be computed. The following process can be devised to compute the remaining terms. By imposing that the trace of the tensor be zero, and using the definitions of P_1 and P_2 [Eq. (23)], the following system can be written down:

$$\begin{pmatrix} P_1 \\ P_2 \\ 0 \end{pmatrix} = \begin{pmatrix} G_1 & G_1 & G_2 \\ -1 & 1 & 0 \\ 1 & 1 & 1 \end{pmatrix} + \begin{pmatrix} M_{xx} \\ M_{yy} \\ M_{zz} \end{pmatrix} + \varepsilon \quad (25)$$

where ε are the uncertainties associated with P_1 and P_2 . By writing the covariance matrix of ε as:

$$\text{Cov}(\varepsilon) = \begin{pmatrix} C_{11} & C_{12} & 0 \\ C_{21} & C_{22} & 0 \\ 0 & 0 & 0 \end{pmatrix} \quad (26)$$

where C_{ij} is the covariance matrix of P_1 and P_2 , and using (24), one gets the following expression for the covariance of M_{xx} , M_{yy} , M_{zz} :

$$\text{Cov}(M_{xx}, M_{xx}) = (C_{11} - 2C_{12}G + C_{22}G^2)G'$$

$$\text{Cov}(M_{yy}, M_{yy}) = (C_{11} + 2C_{12}G + C_{22}G^2)G'$$

$$\text{Cov}(M_{zz}, M_{zz}) = 4C_{11}G'$$

$$\text{Cov}(M_{xx}, M_{yy}) = \text{Cov}(M_{yy}, M_{xx}) = (C_{11} - C_{22}G^2)G' \quad (27)$$

$$\text{Cov}(M_{zz}, M_{xx}) = \text{Cov}(M_{xx}, M_{zz}) = (-2C_{11} + 2C_{12}G^2)G'$$

$$\text{Cov}(M_{yy}, M_{zz}) = \text{Cov}(M_{zz}, M_{yy}) = (-2C_{11} - 2C_{12}G^2)G'$$

where $G = (G_1 - G_2)$ and $G' = G^{-2}/4$.

Acknowledgements. Enric Banda read the manuscript and made valuable suggestions.

References

- Aki, K., Richards, P.G.: Quantitative seismology. Theory and methods, vol. I. San Francisco: Freeman, E.W. 1980
- Angelier, J., Tarantola, A., Valette, B., Manoussis, S.: Inversion of field data in fault tectonics to obtain the regional stress. I. Single phase populations: a new method of computing the stress tensor. *Geophys. J.R. Astron. Soc.* **69**, 607–621, 1982
- Correig, A.M., Mitchell, B.: Regional variation of Rayleigh wave attenuation coefficients in the Eastern Pacific. *Pure Appl. Geophys.* **118**(3), 831–845, 1980
- Dziewonski, A.M., Anderson, D.L.: Preliminary reference Earth model. *Phys. Earth Planet. Inter.* **25**, 297–356, 1981
- Dziewonski, A.M., Woodhouse, H.: An experiment in systematic global seismicity: centroid moment tensor solutions for 201 moderate and large earthquakes of 1981. *J. Geophys. Res.* **88**, 3247–3272, 1983
- Forsyth, D.W.: Mechanisms of earthquakes and plate motions in the East Pacific. *Earth Planet. Sci. Lett.* **17**, 189–193, 1972
- Gephart, J.W., Forsyth, D.W.: An improved method for determining the regional stress tensors using earthquake focal mechanism data: application to the San Fernando earthquake sequence. *J. Geophys. Res.* **89**, 9305–9320, 1984
- Gilbert, F.: Excitation of normal modes of the Earth by earthquakes sources. *Geophys. J. R. Astron. Soc.* **22**, 223–226, 1970
- Honda, H.: Earthquake mechanism and seismic waves. *J. Phys. Earth* **10**(2), 1–98, 1962
- Kanamori, H., Given, J.W.: Use of long period surface waves for rapid determination of earthquake source parameters. *Phys. Earth Planet. Inter.* **27**, 8–31, 1981
- Knopoff, L., Randall, M.J.: The compensated linear vector dipole: a possible mechanism for deep earthquakes. *J. Geophys. Res.* **75**, 4957–4963, 1970
- Lana, X., Correig, A.M.: Determinación de mecanismos focales y profundidades focales mediante la inversion linealizada del tensor de momento sísmico. *Rev. de Geofísica* **41**(1), 37–51, 1985

- Lanczos, C.: Linear differential operators. London: Van Nostrand Co. 1961
- Mathews, J., Walker, R.: Mathematical methods of physics. Menlo Park (California): Benjamin 1964
- Mendiguren, J.A.: Inversion of surface wave data in source mechanism studies. *J. Geophys. Res.* **82**, 889–894, 1977
- Mendiguren, J.A., Aki, K.: Source mechanism of deep Colombian earthquake of July 31, 1970 from free oscillation data. *Geophys. J. R. Astron. Soc.* **55**, 539–556, 1978
- Patton, H., Aki, K.: Bias in the estimate of the seismic moment tensor by the linear inversion method. *Geophys. J. R. Astron. Soc.* **59**, 479–495, 1979
- Pous, J., Lana, X., Correig, A.M.: Generation of Earth stratified models compatible with both ellipticity and phase velocity observations of Rayleigh waves. *Pure Appl. Geophys.* **123**, 1985 (in press)
- Strelitz, R.A.: The fate of the downgoing slab: a study of the moment tensor from body waves of complex deep focus earthquakes. *Phys. Earth Planet. Inter.* **21**, 83–96, 1980
- Takeuchi, H., Saito, M.: Seismic surface waves. *Methods in computational physics* (11), 217–303, Academic Press 1972

Received April 2, 1985; revised version July 20, 1986

Accepted October 19, 1986

Impulsive processes in the magnetotail during substorm expansion

V.A. Sergeev¹, T. Bösinger² and A.T.Y. Lui³

¹ Institute of Physics, University of Leningrad, Leningrad 198904, USSR

² Department of Physics, University of Oulu, SF-90570 Oulu 57, Finland

³ Applied Physics Laboratory, The Johns Hopkins University, Laurel, MD 20707, USA

Abstract. Anisotropy and intensity variations of high-energy particles and magnetic variations detected by IMP-J at 37 R_e in the central part of the magnetotail within 2 R_e of the neutral sheet were studied during a few consecutive substorms on March 3, 1976, and related to a large body of ground observations. A close correlation is usually found between bursts observed in Pi pulsations on the ground (having a duration of ~ 1 min and usually being repeated in 1–3 min) and high-energy particle bursts observed in the far tail. The magnetic field response is examined relative to the onsets of high-energy particle bursts. A three-dimensional current system RIPD (Reconnection Induced Propagating Disturbance) is constructed which can, in principle, produce the magnetic field variations observed in the boundary part of the plasma sheet (PS). Previously reported properties of high-energy particle bursts (inverse energy dispersion, preferential acceleration of alpha particles, dawn-dusk asymmetry in the acceleration of electrons and protons and transient PS expansions) are found to be typical of these impulsive processes. Together with earlier results, these observations show that the expansion process (identified here as a transient reconnection or explosive tearing mode) clearly operates in an impulsive fashion. The superposition of impulse-induced propagating disturbances necessarily results in complex, variable patterns of magnetic field and thermal plasma behaviour, such as are frequently found in the PS during substorms.

Key words: Substorm expansion – Magnetotail-ground correlation – Plasma sheet boundary – High-energy particle bursts – Propagating magnetic field disturbance

Introduction

The substorm expansion process includes a change in the gross structure of the magnetotail magnetic field and plasma configuration accompanied by strongly enhanced energy dissipation in the magnetosphere-ionosphere system. Detailed synthesis of plasma sheet (PS) phenomena observed to date (such as plasma flow and energization, magnetic and electric field variations, etc.) is still a subject giving rise to many controversies, and consequently there are not yet any well-developed theoretical models available.

The authors of numerous papers on substorm morphology in the PS nevertheless seem to agree on certain major findings. These include:

a) A source at 10–15 R_e distance in the night-time magnetotail is turned on and later displaced tailward in some way (stepwise and/or continuously) during the substorm expansion phase (Pytte et al., 1976; Nishida and Fujii, 1976; Hones et al., 1973).

b) Earthward of this source strong plasma flows tend to exist, mainly in an earthward direction, and the magnetic field relaxes somewhat towards a more dipole-like configuration in conjunction with the PS expansion (Pytte et al., 1976; Lui et al., 1976; Hones, 1979 and others).

c) Tailward of the source the direction of strong plasma flows and the polarity of the B_z component of the magnetic field are variable and complex, but tailward plasma flows and southward turnings of B_z are quite common (Lui et al., 1977; Hones and Schindler, 1979; Nishida et al. 1981; Caan et al., 1979 and others).

d) A strongly enhanced, newly accelerated, high-energy (HE) particle population up to MeV energies is found, which propagates from the source both tailwards and earthwards (Krimigis and Sarris, 1979; Baker et al., 1982).

The characteristics mentioned above depict only a type of average behaviour, and the numerous discrepancies in the details of PS observations indicate a complex space-time evolution of the substorm process in the tail (Coroniti et al., 1980). This seems to operate in a sporadic manner (time scales from 10 s to several minutes have been distinguished) in localized parts of the PS (Pytte et al., 1976, 1978; Sergeev, 1977, 1981; Krimigis and Sarris, 1979; Belian et al. 1984), and there are even indications of the simultaneous presence of several sources (Sarris et al., 1976 b).

The interpretation of PS observations is particularly problematical because temporal and spatial variations are difficult to separate on the basis of single-satellite measurements. The situation is further complicated because of the different propagation speeds involved (e.g. MHD, plasma drift and HE particle speeds). Williams (1981) has demonstrated that, due to dispersion, a wealth of energy and pitch-angle distributions of energetic ions exists (after the step-like process of ion acceleration) even in the relatively simple case of non-interacting particles. Possibly the most serious difficulty in the interpretation of PS observations arises when large-scale effects of the source are masked by disturbances of local origin (e.g. strong turbulence, as apparently identified by Coroniti et al., 1980). These difficulties are

well known, but to our knowledge they have not yet been explicitly taken into account.

It seems possible, however, to isolate large-scale effects from small-scale ones, namely when the source acts in an impulsive fashion, provided we are looking at the phenomena on a time-scale which is small in comparison with the duration of the impulse. There are indeed facts which speak in favour of an impulsively operating source. First there are the observations of large impulsive electric fields (Aggson et al., 1977; Pedersen et al.; 1978; Cattell et al., 1982), and then there are reports on multiple short HE particle bursts and injections (Krimigis and Sarris, 1979; Lui and Meng, 1979; Kirsch et al., 1981; Baker et al. 1982; Belian et al., 1984). Impulsive or step-like behaviour in the sub-storm expansion process has been inferred from ground-based observations (here the temporal and spatial effects can be clearly separated). In this way Sergeev et al. (1978) were able to elucidate the fine structure of auroral expansion. Practically all studies based on high time resolution ground observations, including auroras, currents, HE electron precipitations and ULF-waves, have confirmed that the expansion process operates in an impulsive manner characterized by a time-constant typically of 1–3 min (e.g. Sergeev and Yahnin, 1979; Bösinger et al., 1981; Yahnin et al., 1983). This holds for expansions of different strength and different spatial extent (Yahnin et al., 1983). Impulsive HE particle injections with similar temporal characteristics were found to be common at geosynchronous distance (Belian et al. 1984).

As will be seen below, HE particle bursts often show a remarkable correspondence with impulsive modulation of the expansion process as observed on the ground. This is true even in cases of very weak, small-scale expansions (Yahnin et al., 1984).

The aim of this paper is two-fold: firstly, to provide a detailed ground – satellite comparison to show once again the impulsive behaviour of the expansion process and, secondly, to monitor changes in the PS magnetic field and HE particles after the switching on of the source in order to construct a phenomenological scheme of manifestations of the expansion process in the far PS.

Since the behaviour of HE particles in the 0.3–2.0 MeV energy range (i.e. energies 2–3 orders of magnitude larger than the thermal energy of PS particles) is considered here to be of crucial importance, we recall below some of their properties as given in the literature (Buck et al., 1973; Krimigis and Sarris, 1979; Williams, 1981; Andrews et al., 1981; Belian et al. 1981 and others):

1. At IMP-J distance ($37 R_e$ in the magnetotail, in our case) the gyroradius of the HE protons ($1 R_e$) is comparable to both the PS thickness and – in our case – the distance of the satellite from the PS centre. This allows the HE protons to be seen almost all the time during expansion, and also allows the spatial and temporal effects to be distinguished and the configurational changes of the PS to be investigated to some extent (N–S displacements of its boundary).

2. Since the protons in the bursts are highly anisotropic and are collimated mainly along the magnetic field lines, we have information on the source location (tailward or earthward with respect to the satellite). Due to the high speeds of the HE particles (tens of R_e/s for electrons), their arrival time forms a reference time for the study of the concurrent thermal plasma and magnetic field behaviour.

Instruments, data and observations

General correspondence between HE particle bursts and ground activity, characteristics of the period studied

The most important PS parameters studied here were obtained from the GSFC magnetometer and two energetic-particle detectors on board the IMP-J satellite. We use the 15.36-s averages of the magnetic field vector expressed either in the GSE or GSM coordinate system, and the standard deviation (σ) of individual 1.28-s measurements. This quantity characterizes the field variability or magnetic fluctuations below 1 Hz. The particle detectors (the APL/JHU experiment CPME, for details see Sarris et al., 1976a) provide information on the HE proton and electron fluxes in a few energy channels above 0.3 MeV. Alpha-particle fluxes are measured above 2 MeV. A complete cycle comprises measurements made during a 5.12-s interval repeated every 10.24 s and provides information on the particle fluxes in eight angular sectors of the ecliptic plane. We also use data on 50–200-keV protons from the EPD experiment (for details, see Roelof et al., 1976), which yields better angular resolution (data from 16 sectors of the ecliptic plane) but only every 20.48 s.

During the period of interest the IMP-J satellite made measurements in the central part of the magnetotail, moving from dusk towards midnight. Its GSM coordinates in R_e early and late on March 3, 1976 read $-34.8, 16.3, 0.1$ and $-36.7, 0.5, 3.1$, respectively. Because of fortunate details of both the satellite orbital motion and the diurnal movement of the neutral sheet, the satellite stayed within $2-3 R_e$ of the PS centre throughout the day (see the bottom curve in Fig. 1). This extremely rare and fortunate circumstance permits us to consider the association between HE particle bursts and different ground-based observations during various kinds of magnetospheric activity. The second fortunate circumstance is the large number of available ground-based observations obtained from the world-wide networks of magnetometers, all-sky cameras, photometers, riometers, induction magnetometers, etc.. The data were collected and analysed in an informal workshop devoted to the global and local relationship between different ground phenomena during substorms. Much of the data collected has been published (Sergeev et al., 1981; Mishin et al., 1982), and the results of the analysis are collected in a special issue (Pudovkin and Sergeev, 1984). We will refer extensively to these publications below. Information on the ground-based instrumentation can be found in Sergeev (1981).

As can be seen from the upper panel of Fig. 1, the day concerned is characterized by various types of magnetic activity. It contains an 8-h period of intense and prolonged activity, well-pronounced substorms – both isolated and superimposed – and also a 3-h long quiet period between 13 and 16 UT. It also shows significant HE particle activity, the intensity of which generally reflects the behaviour of the AE index. These time intervals, based on 5.5-min averages, are marked by black spaces in Fig. 1, sequences which contain strong fluxes of 0.5-MeV electrons (HEE) and 3-MeV protons (HEP). Threshold fluxes of $1 \cdot (\text{cm}^2 \cdot \text{s} \cdot \text{ster})^{-1}$ for HEE and $3 \cdot 10^3 (\text{cm}^2 \cdot \text{s} \cdot \text{ster} \cdot \text{MeV}/\text{nucl})^{-1}$ for HEP are chosen, which are a factor of three higher than the maximum values during the quiet interval of 15–16 UT, when the satellite stayed within the PS. HE particles were pre-

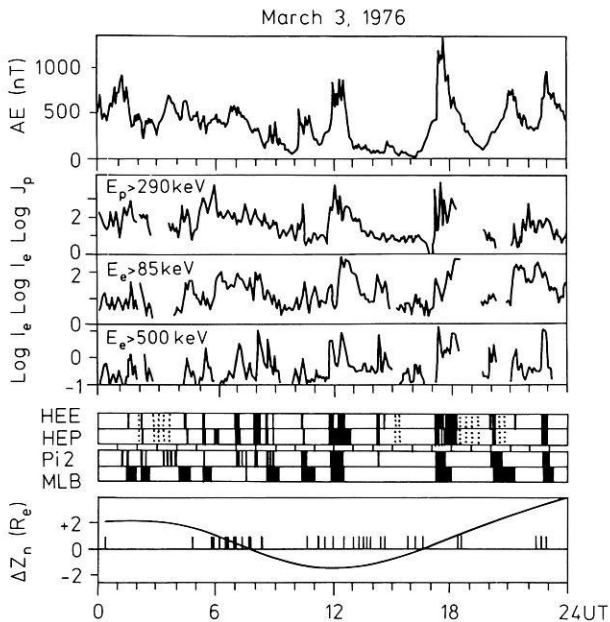


Fig. 1. Magnetic and particle activity on March 3, 1976. From top to bottom: AE(7) index; 5.5-min averages of differential proton (J_p) and integral electron (I_e) flux intensities measured by the EPD and CPME experiment on board the IMP-J satellite; intervals (indicated by *black space*) of most intense electron (HEE) and proton (HEP) particle bursts (for details, see text); intervals (*black space*) of Pi-2 activity (Pi2) and magnetic bays (MLB) as observed at nightside mid-latitude observatories; the distance (ΔZ_n) of IMP-J from the calculated position of the neutral sheet (the vertical bars indicate times of neutral sheet crossings, i.e. changing polarity of the B_x component), is from IMS/SSC report N 5, 1975

ferred as tracers, since these particles exit faster from the acceleration region (due to their higher drift speeds). Consequently, the time intervals of peak HE particle flux indicate the time intervals of particle acceleration more accurately and reliably. Note also that the gyroradius of a 3-MeV proton in the lobe field (2–3 R_e) is larger than the distance of the satellite from the neutral sheet during the whole period of observation. The dotted lines indicate gaps in the IMP-J data. One can see that the time intervals of the strong fluxes in the highest energy channels are, in general, the same for particles of both types.

Let us first compare the appearance of these HE particle bursts with the ground signatures of substorm expansion. The two lower panels of Fig. 1 (marked Pi2 and MLB) indicate the time intervals during which expansion-related Pi2 pulsations and magnetic bays are seen at mid-latitudes (standard, rapid-run and induction magnetometer data from the world-wide networks are used). As already known for HE particle bursts (Murayama, 1970) and for other expansion-related signatures of the magnetotail (Pytte et al., 1976, 1978), the bursts tend to appear in close association with Pi2s and mid-latitude bays whenever the activity is continuously high (as before 08 UT) or low. One remarkable example of this association is the very strong HE particle burst detected around 14:15 UT during conditions of magnetic calm (AE \sim 100 nT). The few exceptions from this close temporal correlation may be consequences of the known screening effect (Pi2 intensity is strongly damped at mid-latitudes when the expansion proceeds beyond 70° corrected geomagnetic latitude (CG Lat); see examples in

Wolcott et al., 1976; Pytte et al., 1978 and also Sergeev, 1981).

The typical pattern of the proton flux and its anisotropy during substorm expansion is best depicted by an isointensity-contourline presentation, as used earlier by Roelof et al. (1976). Figure 2 contains such presentations for the two clearest and most intense substorms observed on March 3, 1976, (onsets at 11.51 and at 17.16 UT, cf. Sergeev, 1981). The gross features of these substorm expansions are similar in terms of the HE particle characteristics, although IMP-J spent most of the time within the PS during the first event and outside it during the second, as evidenced by the magnetic field and thermal plasma data (E.W. Hones, personal communication). These common features include strong tailward anisotropy during the first stage (the first 20 min in these cases), and strong earthward anisotropy during the second stage up to the final PS expansion. The spot-like appearance (intense, collimated particle bursts) during the first 40 min in each case in Fig. 2 deserves special attention, since it reflects a burst-like particle behaviour (more pronounced in the higher energy proton channels). The HE particle bursts during the interval 17:32–17:34 UT were examined in detail by Lui and Krimigis (1983) and were found to be hot beams with low densities and high drift speeds. With reference to Fig. 2 and similar presentations by Roelof et al. (1976), Carbary and Krimigis (1979) and similar findings by Lui and Meng (1979), we can say that series of repetitive HE particle bursts with repetition periods of 1–3 min form a typical feature of the expansion phase.

In Fig. 2 another interesting feature can be noted. There are sporadically occurring signatures of counterstreaming HE proton flows (flux contours are centred at both 180° and 360°). These signatures are particularly clear from 17.29 to 17.32 UT and 17.42 to 17.49 UT. The observation of counterstreaming HE protons is not unusual (see e.g. Williams, 1981). It should be noted, however, that the parent beam (tailward between 17.10 and 17.35 and earthward between 17.42 and 17.50 UT) exceeds the oppositely directed flux by more than one order of magnitude. This kind of counterstreaming may be understood in terms of return fluxes caused by magnetic mirroring or magnetic loops.

In all the substorm cases of March 3, 1976 the series of particle bursts appear synchronously with enhanced Pi activity (Pi2 at mid and auroral latitudes, Pi1B in the nightside auroral zone). Often, however, it is hard to recognize unambiguously the overlapping effects of individual bursts and to identify the intensifications observed on the ground with these individual HE particle bursts. For the purpose of ground-satellite comparison we will therefore present a case below in which the HE particle bursts are well separated in time.

An example of detailed PS – ground correlation

As evidenced by ground-based observations, the substorm which initiated at 19:59:00 UT developed mostly within the Scandinavian sector. Because of this the temporal variation and the relationships between phenomena such as auroral structures, brightness and heights, cosmic noise absorption, equivalent currents and Pi2/Pi1B type magnetic pulsations could be studied in great detail and with high temporal and spatial resolution. Readers are referred to the companion paper by Sergeev et al. (1986, referred to as paper II

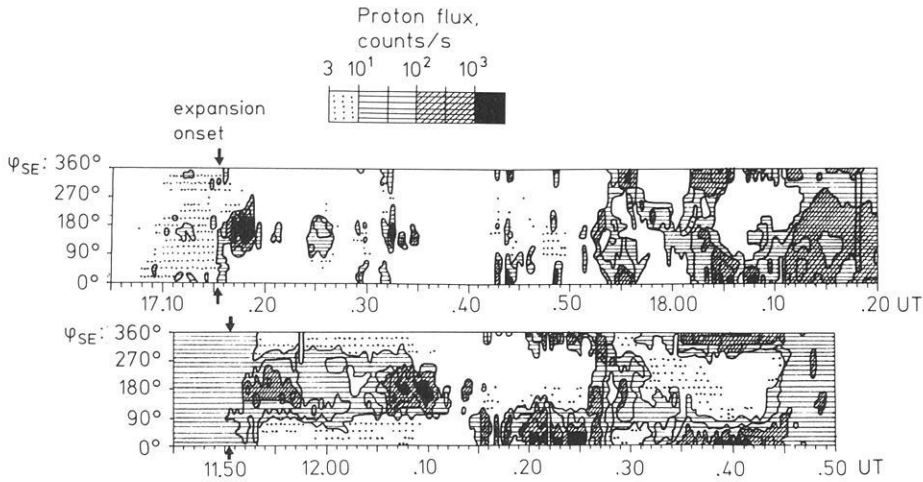


Fig. 2. Azimuthal proton fluxes ($E_p = 50\text{--}200$ keV) in isocontourline presentation as measured by the EPD detector of IMP-J in the ecliptic plane during the two most intense substorms of March 3, 1976 ($\psi_{SE} = 0^\circ, 90^\circ, 180^\circ$ correspond to earthward, dawn-to-dusk and tailward directions, respectively)

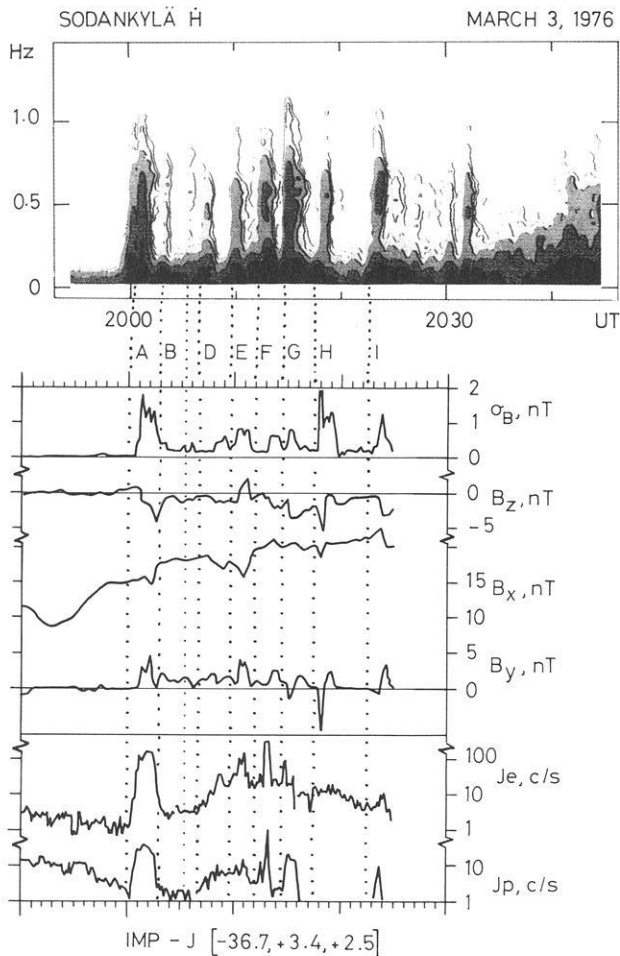


Fig. 3. Sonogram showing successive Pi1 bursts as recorded at Sodankylä ($\phi = 63.8^\circ$, MLT = 22.5 h) during the expansion phase of the substorm commencing at 19:59 UT on March 3, 1976 (top). Summary of IMP-J magnetic field and particle data ($E = 0.3\text{--}0.5$ MeV) as measured in the boundary part of the plasma sheet up to the data gap of 20:25 UT (bottom). The magnetic field components are displayed in the GSM coordinate system. The IMP-J projection into the ionosphere lies at 23.1 MLT meridian. Dotted lines indicate times of onset of Pi1 burst. To convert count rates into fluxes, use a geometry factor of $1.51 \text{ cm}^2 \text{ ster}$

in the following). We reproduce here, in the upper part of Fig. 3, a sonogram of the induction magnetometer record from Sodankylä, which gives the onsets and relative intensities of a dozen well-defined impulsive activations which occurred during the first half-hour of the substorm expansion.

This time the IMP-J was gradually leaving the thinning PS, as evidenced by a gradually increasing B_x component (Fig. 3) and a decreasing energy density in the thermal plasma (E.W. Hones, personal communication). Shortly after the first ground signatures of the expansion onset (19:59–20:00 UT, see paper II) the substorm manifests itself at a distance of $37 R_e$ in the central magnetotail by a significant increase in HE particle fluxes and by the onset of magnetic field fluctuations σ and variations in all three components (Fig. 3). The onsets of all the impulsive activations, as detected on the ground, are given in Fig. 3 by dotted lines labelled A, B, D, E, F, G, H and I. The activation C (between B and D) is very weak but nevertheless included (dotted line, but not labelled) here because it is dealt with in paper II. Almost simultaneous impulsive changes in the magnetic field and the HE particle fluxes at IMP-J can be recognized. There is not only a temporal correspondence between the ground and IMP-J observations, but there is also a similar intensity response of the Pi1Bs to spikes in the particle fluxes. The most prominent HE particle bursts are associated with the activations A, E, F and H, which appear to be the strongest ones in terms of their other ground signatures as well (see paper II).

In order to obtain information on the time delays between phenomena observed on the ground and at the boundary of the PS, we restrict our analysis to the most intensive particle bursts (in which the concurrent magnetic field variations can be expected to be well above the background noise). The broken lines in Fig. 4 denote onsets of HE bursts, which are distinct in the protons and the electrons. Both the superimposed (F, G) and isolated impulses (A, I), are followed by a distinct rise in σ and an impulsive negative excursion of B_z (dotted lines). The time delay ranges from 0 s (I) to 50 s (A). Similarly, the appearance of the HE bursts seems to be delayed relative to the onsets of Pi bursts observed on the ground. Both the delays and their tendency to decrease in the course of the expansion can be explained by the relative position of the satellite with respect to the source region. As in the first stage of the cases shown in Fig. 2, the proton flow in the ecliptic

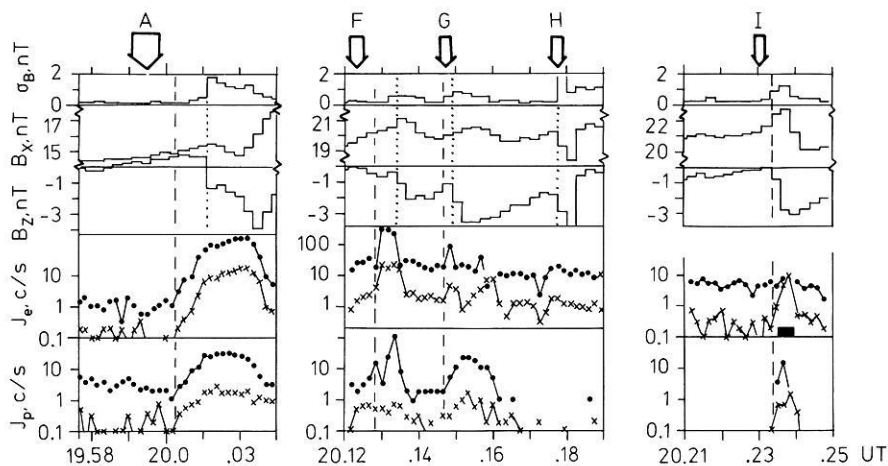


Fig. 4. High-resolution data of the magnetic field (15.36 s) and spin-averaged (10.24 s) particle count rates for the periods of intense particle bursts in Fig. 3. Onsets of the particle bursts and impulsive negative B_z excursions are indicated by broken and dotted lines, respectively. The arrows at the top of the figure mark the Pi1 burst onset (cf. Fig. 3)

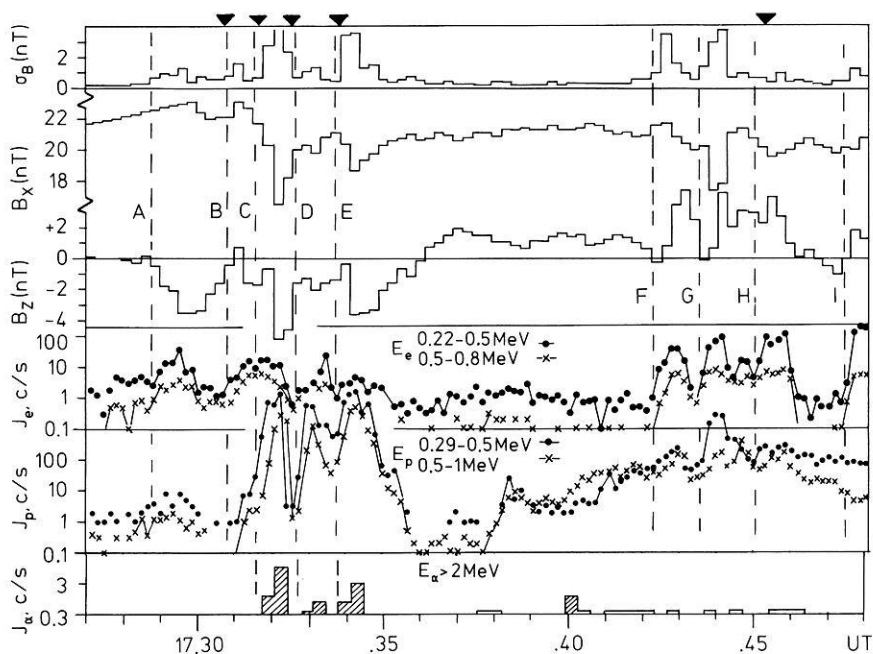


Fig. 5. Data as in Fig. 4, but for the most intense substorm observed on March 3, 1976. The count rates of alpha particles are added in the bottom panel. Distinct impulsive changes in Pi2 signals are marked by triangles at the top of the figure. Lines with dots or crosses denote the 0.29–0.50 MeV and 0.5–1.0 MeV energy channels, respectively. Note that the proton fluxes are highly anisotropic during this interval and are directed tailwards before 17:36 UT and earthwards after 17:42 UT (cf. Fig. 2)

plane was found to be highly anisotropic and oriented in a tailward direction (almost) along the magnetic field lines. From this we can conclude that the source during this period is located somewhere between the Earth (behind $10 R_e$, to be exact) and the satellite ($37 R_e$). From the auroral-zone data we know that the auroral expansion started at 66° CG Lat and expanded polewards in a stepwise fashion, reaching 71° CG Lat at 20:23 UT (paper II). Correspondingly, we can assume that in the course of the successive activations the source region is displaced tailward (towards the satellite), which gives a natural explanation for the decreasing time delay. If so, we can further argue that the observed negative excursion of B_z , which is largest in the first activation, is caused by some current system which propagates in the PS with a speed lower than that of the HE particles.

Returning to the magnetic variations in the PS shown in Fig. 3, we can note the following. First of all, there is no simple correlation between the magnetic field variation amplitude and the intensities of the HE and/or Pi1 bursts. The event G, for example, shows a very intense magnetic

field variation (possibly of local origin) with no significant HE particle response. Then, by comparing the variations in B_z and B_y relative to their levels both before the onset of the substorm and a few minutes prior to the isolated activation I, we can conclude that their response to the impulsive activations constitutes mainly a negative excursion for B_z and a positive one for B_y . Exceptions, however, are evident, particularly the positive B_z variation after activation E. Variations in the largest component, namely B_x , are less distinct, probably because of the continuous growth of the tail current at IMP-J position. For the most intense HE particle bursts seen in Fig. 4, a rise in B_x in the first 30 s (after the onset of the burst) and then a drop below the previous level seems to be typical.

Intense HE proton bursts in both channels (>0.3 and >0.5 MeV) are observed only during three activations (A, G, I). Indications of inverse energy dispersion (0.3-MeV protons arrive and/or reach the maximum flux first) show impulse G and impulse I in Fig. 4. A brief appearance of HE alpha particles above 2 MeV is detected at the maximum phase of activation A (20:00:53 UT).

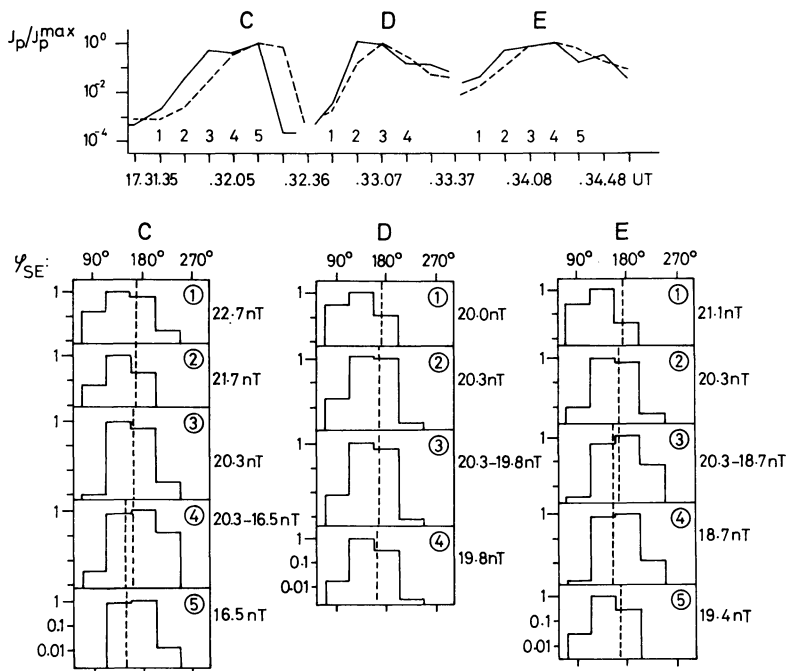


Fig. 6. Energy dispersion and pitch-angle distribution of the intense bursts C–E in Fig. 5. *Top*: relative changes in spin-averaged fluxes for 0.29–0.50 MeV (solid line) and 0.5–1.0 MeV (broken line) protons (the fluxes of each channel are normalized to the maximum flux of each burst). *Bottom*: evolution of the flux distribution of 0.29–0.50 MeV protons in the ecliptic plane in the course of each burst. The encircled numbers ①–⑤ indicate the time sector for which the distributions are shown. The fluxes are normalized to the maximum count rate of each time sector. The 15.36-s averages of magnetic field strength are also given for each time sector (two values, if the particle measurement falls between two neighbouring intervals of the magnetic field measurement). The vertical broken line indicates the GSE longitude

HE particle and magnetic field response tailward and earthward of the source region

The expansion of the most intense substorm on March 3, 1976, started at 17:16 UT. Figure 5 contains the strongest HE proton bursts (for almost all periods of IMP-7 and IMP-8 observations). The ground data published by Sergeev (1981) for this interval show a very rapid and extensive auroral expansion towards 75° CG Lat with clear impulsive substructures. Due to the tailward motion (or jump) of the source region passing over the satellite at 17:36–17:40 UT, the source in this period is first earthward and then tailward of the satellite (see Fig. 2). This may indicate that the source is not so far from the observation site during the 10-min period considered as during other activations of this substorm. Consequently, differences in timing due to different propagation speeds are expected to be smaller. The onsets of the HE particle bursts, therefore, serve well as reference times for the concurrent magnetic variations.

As in Fig. 4, the onsets of the HE particle bursts are indicated in Fig. 5 by broken lines. Once again one can notice the excellent time correlation between these HE particle bursts and those in σ . Again, however, there is no exact intensity correlation between them. The striking difference in the impulse response of B_z before and after 17:38 UT calls for special attention. Before 17:38 UT (tailward proton flow, source earthward of satellite) the onsets of bursts A–E are followed by a mainly negative B_z excursion, whereas the B_z response to the onsets of bursts F–I (source tailward of satellite) is primarily positive. One remarkable additional detail should be noted. The main B_z excursion is advanced by a short (~ 15 s) pulse of reverse polarity, and the B_y component (not shown here, cf. Fig. 5 in Sergeev, 1981) also displays coherent impulsive variations of similar magnitude, being negative before 17:38 and positive after 17:42 UT. It also becomes evident from Fig. 5 that the σ and B_x responses from both sides of the source region do not differ significantly.

It is of great importance here to ensure the temporal nature of the observed variations (responses). First there is the simultaneity of the onsets of the impulsive rises in both the HE electron and proton fluxes (this is clear for bursts A, D, E, F, G and H). Taking into account the large differences in the gyroradii of both species, this gives the first evidence of the temporal nature of the observed variations. Secondly, we show in the upper part of Fig. 6 the fluxes of 0.3–0.5 MeV and 0.5–1.0 MeV protons (normalized to the maximum flux of each impulse) for the three most intense (superimposed) bursts, C, D and E. The inverse energy dispersion effect is clearly visible. The same effect can also be verified for the bursts F, G and H in Fig. 5. This is further evidence of the temporal nature of the observed variations. Additional evidence comes from the ground-satellite correlation, as will be shown later.

Normalized azimuthal flux distributions of 0.3–0.5 MeV protons are shown in successive frames for each burst in the lower part of Fig. 6. The fluxes are strongly collimated, so that only a portion of the full azimuthal range is displayed. A persistent feature of all three cases of an intense particle burst is that the initial rise in proton counts starts at an $\sim 45^\circ$ pitch angle. The distribution then shifts towards the field-aligned direction at the time of the burst intensity maximum and turns back to an $\sim 45^\circ$ pitch angle at the end of the burst. Dawn-to-dusk-directed anisotropy is a common feature of HE protons, and finds its explanation in the N–S gradient of the HE proton number density (Sarris et al., 1976a). This being so, the shift in flux distribution demonstrated here is consistent with the spatial movement of the flux tube containing the highly collimated proton beam, which approaches the satellite and then moves back again. This is also supported by the observations of phases C-4, C-5, E-3 and E-4, when the distributions are obviously shifted towards dawn relative to the local magnetic field direction (broken vertical line). Only at these moments is the satellite embedded in the PS, as evidenced by the lowest values for the magnetic field magnitude (B_x component),

also presented in Fig. 6, and by the brief spikes in the thermal electron energy density (data kindly provided by E.W. Hones). This “N–S gradient interpretation” thus enables us to see HE field-aligned proton beams whose gyrocentres are contained in the narrow outer boundary part of the PS and which experience local N–S displacements (possible expansion – contraction or flapping motions of the PS) in association with each impulsive activation.

In contrast to the substorm commencing at ~ 20 UT, the HE electrons are found in this case to be highly anisotropic. First, before 17:36 UT, they exhibit a persistent strong tailward anisotropy and then, during the bursts F–H, they occasionally show significant earthward anisotropy (with front-to-back ratio > 2). In summary, we can say that the proton and electron data, and also the change in the sign of B_z at 17:36 UT (Fig. 5), are consistent with a tailward movement of the source region beyond the satellite (for $T > 17:40$ UT the source is certainly tailward of the satellite).

One of the strongest alpha-particle events in the IMP-J observations is detected in coincidence with the strong proton bursts C–D (cf. Fig. 5), showing that the acceleration mechanism was effective in accelerating charged particles up to a few MeV energy in the same, short (impulsive) process. It is important to note that the proton fluxes in the corresponding energy channel (> 2 MeV) are at least one order of magnitude smaller.

The small time difference (~ 1 min) between the particle bursts themselves within the first (B–E) and second sequence (F–H) makes it difficult to establish a one-to-one correspondence between them and the individual impulsive activations seen on the ground. In this event, the main information from the ground observations is obtained from an analysis of the Pi-2 signals recorded at auroral and mid-latitudes. The Pi-2 pulsations serve the same purpose here as the earlier Pi1B pulsations shown in Fig. 3. As shown by Sergeev (1981) and supported by an additional data survey, an intense Pi-2 wavetrain starts coherently at widely displaced stations at 17:30:45 UT (± 5 s) in coincidence with Pi1Bs, after which an extended, rapid auroral expansion takes place until 17:36 UT. The trains observed at all sites at mid-latitudes display coherent, abrupt phase or amplitude changes, two of which occur at 17:32:30 and 17:34:00 UT, respectively (see Fig. 6 in Sergeev, 1981). A repeated survey including additional data revealed one more coherent change at 17:31:40 UT. These times (triangles at the top of Fig. 5) give an almost exact coincidence of impulsive changes in Pi-2 trains with the onsets of the HE particle bursts B, C, D and E seen at $37 R_e$.

The situation after 17:40 UT is not so well suited for a ground-tail comparison, because the various ground observations do not correlate with each other. In particular, the signature of an auroral expansion at very high latitudes (CG Lat $> 74^\circ$) after 17:43–44 UT (see Fig. 2 in Sergeev, 1981) does not correlate with the Pi-2 activity at mid-latitudes, where it is weak and irregular, with the exception of a 2-min pulsation train starting at 17:45:05 UT. Since very high latitude auroral activations are not usually accompanied by clear mid-latitude pulsations in the Pi-2 range (Pytte et al., 1978), and since auroral-zone data alone do not provide sufficient accuracy over the period studied, we cannot support or reject the presence of ground counterparts for bursts F–I in Fig. 5. All that can be said is that the auroral expansion onset and the onset of the mid-lati-

tude Pi-2s seem to be delayed by 1–3 min with respect to the onset of a series of strong HE proton particle bursts. Note that in this case the source region is very much further down the tail than $37 R_e$.

Discussion and conclusions

The observations presented in this paper support the finding of an impulsive energy dissipation process in the substorm expansion phase (Sergeev, 1981; Yahnin et al., 1983). Among the wealth of different variations (temporal and spatial, small- and large-scale), we can apparently distinguish the properties of an “elementary” impulsive process, seen at some distance from the source region. The essential PS features inherent to such an elementary process are summarized below and its physical relevance is discussed.

HE particle bursts

Many impulsive HE particle bursts of short duration were seen at IMP-I or J satellite distances, according to Sarris et al. (1976a, b), Carbary and Krimigis (1979), Lui and Meng (1979), Kirsch et al. (1981); see also the review by Krimigis and Sarris (1979). Bursts of HE electron precipitation (clearly temporal in origin) were often found within the expanding auroral bulge in close association with impulsive Pi activity (Sergeev et al., 1978; Yahnin et al., 1983). Recently, Belian et al. (1984) have reported impulsive structures frequently observed (in more than 75% of all studied cases) in the 0.5-MeV proton injections at geosynchronous orbit. This stresses the generality of the impulsive phenomena with which we are dealing here, and lends further support to the temporal origin of the impulses. In our observations (cf. Figs. 3–5), no significant modulation was found in the individual bursts (at least within the available time resolution of 10 s). The duration of the flux rise is 20–50 s and that of the whole burst ~ 1 min, figures which are in agreement with earlier results (Lui and Meng, 1979). Typically there are intervals of 1–3 min between consecutive bursts. These temporal characteristics agree well with the properties of impulsive structures observed on the ground and at a geosynchronous distance.

Some intense HE proton bursts clearly exhibit the inverse energy dispersion characteristics pointed out earlier for many similar cases by Sarris et al. (1976a) and Kirsch et al. (1981). Strong flux enhancements (up to three orders of magnitude) are seen during some HE particle bursts (e.g. C–E in Figs. 5 and 6), these being practically coherent for electrons and protons having gyroradii of a few hundredths to several R_e , respectively. Simultaneous impulsive phenomena were recorded on the ground. Taking all these facts together, we may argue that the inverse dispersion effect is due to temporal changes in the efficiency of the acceleration mechanism. Any explanation of the inverse dispersion by spatial effects (velocity filtering), as described by Sarris and Axford (1979) for example, cannot be satisfactory in our case. Firstly it has to be noted that inverse dispersion was observed during a PS boundary which was approaching the satellite, for which Sarris and Axford’s model predicts direct (as opposed to inverse) dispersion (assuming a duskward electric field, as is normal) and, secondly, in the case of Figs. 5 and 6, the source is not very far from the spacecraft (clearly less than $20 R_e$). In this situation an explana-

tion in terms of velocity filtering would require unrealistically large electric fields.

The impulsive acceleration of alpha particles up to 2 MeV in the absence of a similar acceleration of 2-MeV protons was first reported by Kirsch et al. (1981). Similar intense alpha-particle bursts without bursts of protons of corresponding energies were observed on March 3, 1976 in three cases (12:07, 17:18, 22:02 UT) in addition to those presented in Fig. 5, each taking place simultaneously with a strong substorm intensification observed on the ground. The charge dependency of the acceleration process is, therefore, to be regarded as a characteristic of impulsive processes in substorm expansions, which provide particle accelerations up to MeV in tens of seconds.

Dawn-dusk asymmetries in the intensity of HE proton (maximum at dusk) and HE electron fluxes (maximum in the dawn sector of the PS) is known to be a characteristic of HE particle bursts (Krimigis and Sarris, 1979). As shown in paper II, such asymmetries may be a consequence of different longitudinal positions of the satellite (duskwards or dawnwards) relative to the localized active region (auroral bulge). This asymmetry can be very pronounced over a distance less than 10 R_e across the tail (tail width some 45 R_e) during the initial phase of strong, isolated substorms. Let us compare the ratio of electron to proton fluxes for the studied bursts in relation to the positions of the active region with respect to the satellite as defined from the ground-based data.

In the case of the first substorm presented here (Figs. 3 and 4), the auroral expansion developed mainly to the west of the satellite's meridian before 20:20 UT (paper II). During this period, IMP-J detected the HE electron fluxes well above the level prior to the expansion, which is quite in contrast to the HE proton flux behaviour. Also, the enhancements of the HE fluxes of the bursts are somewhat higher for electrons than for protons during this period. In the case of the second substorm, the expansion region is further west during 17:42–45 UT (bursts F–I) than during 17:30–35 UT (bursts B–E); cf. Fig. 2 of Sergeev (1981). Correspondingly, a pronounced difference is found in the electron/proton content of the bursts between the series C–E and the series F–I in Fig. 5. Thus the acceleration regions seem rather to be localized across the tail and their momentary position apparently defines a demarcation line between the areas of high HE proton and high HE electron flux intensities in the bursts. All these findings are compatible with an acceleration of particles in a localized region in the tail by strong impulsive electric fields.

Due to the limited angular resolution of the CPME experiment and the very large proton gyroradii (in comparison to the thickness of the PS), the ability of this instrument to track movements of HE proton structures within the PS is limited. Nevertheless, we found that in the case where the fluxes are collimated in the direction of the magnetic field lines (e.g. in the cases of Fig. 6) the gyrocentres of protons in HE bursts are contained in a relatively narrow flux tube at the outer boundary of the PS. A similar conclusion was drawn on the basis of the IMP-J measurements for initial phase of substorm expansion (Sergeev, 1983). The presence of a thin layer of energetic protons and alpha particles during both transient and final (recovery) PS expansion was also found by ISEE-1,2 observations made at shorter distances from the earth (Spjeldvik and Fritz, 1981; Möbius et al., 1980; Andrews et al., 1981). This find-

ing can therefore be considered a characteristic feature of the expansion-associated acceleration process, since it is found both earthward and tailward of the source region and since it holds for multiple impulsive bursts (Spjeldvik and Fritz, 1981; Parks et al., 1979 and our results) as well as for the first burst at the expansion onset (Sergeev, 1983).

Propagating magnetic field disturbances and configurational changes of the PS

The impulsive, discrete, short-lived nature of the expansion process was demonstrated in great detail above. This nature was already suggested by earlier findings (Sergeev and Yahnin, 1979; Sergeev, 1981; Bösinger et al., 1981; Yahnin et al., 1983; Belian et al., 1984). In many previous studies, however, one was looking only for long-lived, large-scale patterns of magnetic field disturbances in the PS presumably caused by reconnection. This pattern is nevertheless strongly contaminated by dynamic small-scale processes, in agreement with the findings of Lui et al. (1977), Coroniti et al. (1980), Kirsch et al. (1981) and Sergeev (1981). Here, therefore, we are looking for an elementary process of explosive dissipation which occurs somewhere in a localized region within the PS.

Around the onset of substorm expansion, the onset of the southward excursion of B_z in the outer part of the PS at 37 R_e was delayed by about 1 min relative to the arrival of the HE particles. This gives an apparent propagation speed for the magnetic field disturbance relative to the HE particles (see Sergeev, 1983 for other examples) of about 18 R_e /min, given that the source is at a distance of 20 R_e from the satellite (i.e. at 15 R_e in the nightside PS). This speed is comparable to the speed of sound, 1,000 km/s (for $T_i \sim 6$ keV), or with the Alfvén speed $V_A = 0.21 B(\text{nT})/\sqrt{n(\text{cm}^{-3})} R_e/\text{min}$ (for $B = 20$ nT with $n = 0.05 \text{ cm}^{-3}$) in the PS. We have noted a shortening of this delay for successive activations occurring at progressively higher latitudes in the auroral zone. Finally, there was no delay when the expansion developed at $\phi = 73^\circ\text{--}75^\circ$ (the source was apparently situated close to the satellite).

The typical patterns of magnetic field variation observed in the outermost part of the PS after an impulsive activation can be produced by a propagating current system of the type shown in the upper part of Fig. 7 (here called the Reconnection Induced Propagating Disturbance – RIPD). The propagation of some kind of current system producing these variations could explain such findings. At least two spacecraft would be needed to verify this, however. This current system must always cause a pronounced southward excursion of the magnetic field within the propagating loop tailward of the source and a short, weak northward excursion ahead of it. A rise in field strength as its front passes by may be expected at the satellite outside or at the outer boundary of the PS. This magnetic field behaviour can be found in the data of Fig. 4 and during the intense bursts A–E displayed in Fig. 5. Earthward of the source the sign of the B_z variation is reversed, as is in fact observed during bursts F–I shown in Fig. 5. The tail-aligned closure of this current system must exist because of the localization of the source region across the tail.

Such patterns of magnetic field variations are compatible with the recent results of Hones et al. (1982), who studied B_y variation during substorm onsets. It can be said, however, that the B_z variations must be more distinct, since

the B_x and B_y variations depend in a more complicated way on the position (z -coordinate) of the satellite with respect to the RIPD. In addition, it can be emphasized that the earthward-propagating part of the RIPD (as discussed by Hill and Reiff, 1980) corresponds well with the three-dimensional system of the substorm current wedge (Akasofu, 1977), which is a well-known phenomenon in the substorm expansion phase. Such a propagating current system (Alfvén wave) must be launched in each act of a localized current disruption which initiates the reconnection process. Similar characteristics of current distribution in the boundary part of the PS were indeed obtained in computer simulation of a three-dimensionally driven reconnection by Sato et al. (1984). It is worthwhile mentioning that the RIPD is qualitatively similar to the meander system introduced by Pellinen and Heikkilä (1984).

As a result of our study, in the lower part of Fig. 7 a schematic and – in view of the complex reality – certainly oversimplified picture is given of what may happen in the tail during successive elementary substorm expansion processes and how this may be embedded into the large-scale “neutral-line-plasmoid” configuration. Several important additions to this scenario should be considered: firstly, the simultaneous presence of several sources, as suggested by the results of Sarris et al. (1976b) and Sergeev and Yahnin (1979), and secondly, an unsystematic change in the source location during successive impulses. The study of auroral arc expansion by Sergeev and Yahnin (1979) and model computations by Forbes and Priest (1983) indeed suggests that new neutral lines may appear at different places in the PS. Note, in Fig. 2, the changes in the directions of arriving HE protons from tailward to earthward and then again to tailward, so that the source may apparently move back and forth.

Mechanism of explosive (impulsive) dissipation

The short-lasting impulsive phenomenon of substorm expansion studied here represents the essential (and presumably elementary) part of the whole substorm expansion process, since it provides the significant inputs for auroral expansion, formation of the three-dimensional current system and particle energization and injection. Many of the essential observational signatures of the impulsive process are already known. Most of them have been described in earlier studies (Krimigis and Sarris, 1979; Sergeev, 1981; Kirsch et al., 1981) and are summarized and expanded on in this paper (the first objective). These signatures include:

- a) the time scale – a few tens of seconds
- b) acceleration of HE particles in a localized part of the PS up to MeV energies
- c) indications of acceleration by a strong impulsive electric field (inverse energy dispersion, preferential acceleration of particles with a higher charge, dawn-dusk asymmetry in the acceleration of HE protons and electrons)
- d) the launching of a three-dimensional current system (like the RIPD) propagating from the source within the Y -sector of the source location.

Note that the strong impulsive electric field reaching a few tens of mV/m has certainly been detected (Aggson and Heppner, 1977; Pedersen et al., 1978; Cattell et al., 1982). At the present time most of these signatures can be explained by only one mechanism: the non-linear (explosive), collisionless tearing mode (Galeev, 1979). This pro-

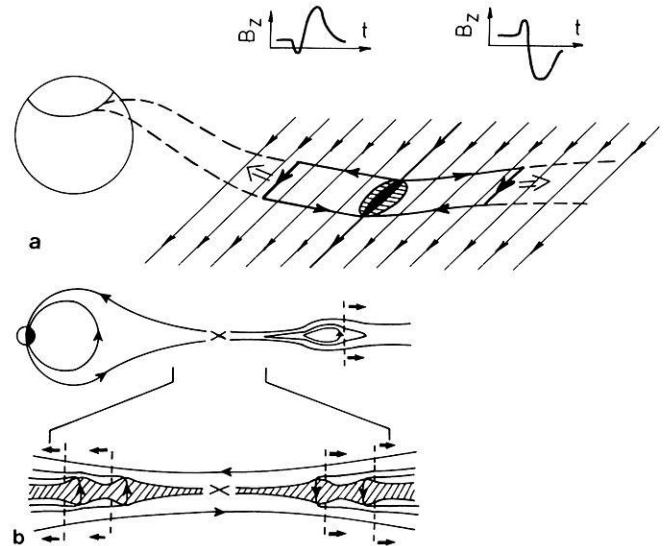


Fig. 7. a Current system (Reconnection Induced Propagating Disturbance – RIPD) launched by each impulse in the explosive expansion process. b Simplified scheme showing the small-scale configurational change in the plasma sheet caused by the inferred impulsive expansion process

vides a consistent explanation for signatures a) – c) and a good description of the spectrum of accelerated ions in the thermal and nonthermal part (Zeleny et al., 1984). This theory has not been completely developed to model the propagation of the magnetic disturbance induced in the PS, but a MHD model describing the latter aspect has recently been developed by Semenov et al. (1983) including, as a particular case, the well-known stationary model of H. Petschek. In spite of inherent simplifications, the model simulates some of the experimental findings of our paper such as a current system of the RIPD type and the swelling of the PS following the propagating RIPD. The model also demonstrates that a transient reconnection is an effective mechanism of energy dissipation.

Both theoretical models are, nevertheless, not yet capable of modelling a real space-time development of the process in a three-dimensional configuration and, in particular, they are not able to produce the repetitive impulsive process. In this respect, the results of a recent numerical MHD modelling within the framework of the line-tied reconnection by Forbes and Priest (1983) deserves special attention. These authors have found very complex behaviour in the system, namely the sporadic growth of a few magnetic islands, corresponding impulsive behaviour of the electric field associated with the growth of each island and a complex movement of active regions back and forth along the tail. Although a collision-dominated process of the tearing mode is not completely realistic in the PS, we find here a time history of the process qualitatively similar to that of the observed expansion process. We conclude that the theoretical attempts yield results basically in agreement with experimental findings, but we must admit that we are still far from achieving a complete insight into the problem.

Our results show how important it is to consider the impulsive, small-scale structures in the PS. At the same time, the large-scale “neutral-line-plasmoid” concept is not excluded by this. On the contrary, many features of our observations are well in tune with the “neutral-line-plas-

moid" concept. Among these features are: the formation of a neutral line in the near-earth region at the substorm onset with preferential tailward anisotropy of HE protons and southward-directed magnetic field deflections at the initial state of substorm expansion (cf. Figs. 2, 4 and 5), the tailward retreat of the main neutral line at the second stage of the expansion with preferential earthward anisotropy of the HE proton and mainly northward-directed magnetic field deflections and, after this, the final PS expansion. One has to be aware that any mode of the reconnection process (impulsive or steady, driven or spontaneous) ends up with the same large-scale configuration and time-averaged properties. In this paper we have looked for, and found, details which can give some insight into the elementary process by which the whole substorm expansion (presumably reconnection) operates in the earth's magnetotail.

Acknowledgements. We are indebted to V.S. Semenov and L.M. Zeleny for useful and stimulating discussions. Data on the magnetic field measurements (N. Ness and R. Lepping, principal investigators) and the EPD experiment (D. Williams, principal investigator) onboard the IMP-J satellite were made available through World Data Center A (Rockets and Satellites) by courtesy of J.J. Vette. The data from the LASL thermal plasma experiment were kindly provided by Dr. E.W. Hones. The authors are grateful to A. Yahnin, R. Rachmatulin, E. Barkova, L. Natsvalyan and other colleagues who took part in the collection and preliminary analysis of the ground observations. The work of two of the authors (V.S. and T.B.) is supported by the Finnish-Soviet Committee on Cooperation in Science and Technology, and that of the third author (A.T.Y.L.) by the Atmospheric Sciences section of the National Science Foundation, grant ATM 83-05537 to the Johns Hopkins University.

References

- Aggson, T.L., Heppner, J.P.: Observations of large transient magnetospheric electric fields. *J. Geophys. Res.* **82**, 5155–5164, 1977
- Akasofu, S.-I.: Physics of magnetospheric substorms. Dordrecht, Holland: D. Reidel 1977
- Andrews, M.K., Keppler, E., Daly, P.W.: Plasma sheet motions inferred from medium-energy ion measurements. *J. Geophys. Res.* **86**, 7543–7556, 1981
- Baker, D.N., Fritz, T.A., Wilken, B., Higbie, P.R., Kaye, S.M., Kivelson, M.G., Moore, T.E., Stüdemann, W., Masley, A.J., Smith, P.H., Vampola, A.L.: Observation and modeling of energetic particles at geosynchronous orbit on July 29, 1977. *J. Geophys. Res.* **87**, 5917–5932, 1982
- Belian, R.D., Baker, D.N., Hones, E.W., Higbie, P.R., Bame, S.J., Asbridge, J.R.: Timing of energetic proton enhancements relative to magnetospheric substorm activity and its implication for substorm theories. *J. Geophys. Res.* **86**, 1415–1421, 1981
- Belian, R.D., Baker, D.N., Hones, E.W., Higbie, P.R.: High-energy proton drift echoes: Multiple peak structure. *J. Geophys. Res.* **89**, 9101–9106, 1984
- Bösinger, T., Alanko, K., Kangas, J., Opgenoorth, H., Baumjohann, W. Correlations between PiB type magnetic micropulsation, auroras, and equivalent current structures during two isolated substorms. *J. Atmos. Terr. Phys.* **43**, 933–945, 1981
- Buck, R.M., West, H.I., D'Arcy, R.G.: Satellite studies of magnetospheric substorms on August 15, 1968. 7. Ogo 5 energetic proton observations – spatial boundaries. *J. Geophys. Res.* **78**, 3103–3118, 1973
- Caan, M.N., Fairfield, D.H., Hones, E.W.: Magnetic fields in flowing magnetotail plasmas and their significance for magnetic reconnection. *J. Geophys. Res.* **84**, 1971–1976, 1979
- Carbary, J.F., Krimigis, S.M.: Energetic particle activity at 5-min and 10-s time resolution in the magnetotail and its relation to auroral activity. *J. Geophys. Res.* **84**, 7123–7137, 1979
- Cattell, C.A., Kim, M., Lin, R.P., Mozer, F.S.: Observations of large electric fields near the plasmasheet boundary by ISEE-1. *Geophys. Res. Lett.* **9**, 539–542, 1982
- Coroniti, F.V., Frank, L.A., Williams, D.J., Lepping, R.P., Scarf, F.L., Krimigis, S.M., Gloeckler, G.: Variability of plasma sheet dynamics. *J. Geophys. Res.* **85**, 2957–2977, 1980
- Forbes, T.G., Priest, E.R.: On reconnection and plasmoids in the geomagnetic tail. *J. Geophys. Res.* **88**, 863–870, 1983
- Galeev, A.A.: Reconnection in the magnetotail. *Space Sci. Rev.* **23**, 411–435, 1979
- Hill, T.W., Reiff, P.H.: Plasma-sheet dynamics and magnetospheric substorms. *Planet. Space Sci.* **28**, 363–374, 1980
- Hones, E.W.: Plasma flow in the magnetotail and its implications for substorm theories. In: Dynamics of the magnetosphere, S.-I. Akasofu, ed.: pp. 545–562. Dordrecht: D. Reidel 1979
- Hones, E.W., Schindler, K.: Magnetotail plasma flow during substorms: a survey with IMP 6 and IMP 8 satellites. *J. Geophys. Res.* **84**, 7155–7169, 1979
- Hones, E.W., Asbridge, J.R., Bame, S.J., Singer, S.: Substorm variations of the magnetotail plasma sheet from $X \approx -6 R_E$ to $X \approx -60 R_E$. *J. Geophys. Res.* **78**, 109–132, 1973
- Hones, E.W., Birn, J., Bame, S.J., Paschmann, G., Russell, C.T.: On the three-dimensional magnetic structure of the plasmoid created in the magnetotail at substorm onset. *Geophys. Res. Lett.* **9**, 203–206, 1982
- Krimigis, S.M., Sarris, E.T.: Energetic particle bursts in the Earth's magnetotail. In: Dynamics of the magnetosphere S.-I. Akasofu, ed.: pp. 599–630. Dordrecht: D. Reidel 1979
- Kirsch, E., Krimigis, S.M., Sarris, E.T., Lepping, R.P.: Detailed study on acceleration and propagation of energetic protons and electrons in the magnetotail during substorm activity. *J. Geophys. Res.* **86**, 6727–6738, 1981
- Lui, A.T.Y., Krimigis, S.M.: Energetic ion beam in the earth's magnetotail lobe. *Geophys. Res. Lett.* **10**, 13–16, 1983
- Lui, A.T.Y., Meng, C.-I.: Relevance of southward magnetic fields in the neutral sheet to anisotropic distribution of energetic electrons and substorm activity. *J. Geophys. Res.* **84**, 5817–5827, 1979
- Lui, A.T.Y., Akasofu, S.-I., Hones, E.W., Bame, S.J., McIlwain, C.E.: Observation of the plasma sheet during a contracted oval substorm in a prolonged quiet period. *J. Geophys. Res.* **81**, 1415–1419, 1976
- Lui, A.T.Y., Meng, C.-I., Akasofu, S.-I.: Search for the magnetic neutral line in the near-earth plasma sheet. 2. Systematic study of IMP 6 magnetic field observations. *J. Geophys. Res.* **82**, 1547–1565, 1977
- Mishin, V.M., Nemtsova, E.I., Saifudinova, T.I., Urbanovich, V.D., Loginov, G.A., Sergeev, V.A., Danilov, A.A., Sobolev, A.V., Solov'ev, S.I., Zaitsev, A.N., Lyubimova, N.P., Shevnina, N.F., Baumjohann, W.: Results of observations during substorms on March 3, 1976. 2. Data of geomagnetic observations. Siberian Institute of Terrestrial Magnetism, Ionosphere and Radio Wave Propagation Preprint Sib-1-82, Irkutsk 1982
- Möbius, E., Ipavich, F.M., Scholer, M., Gloeckler, G., Hovestadt, D., Klecker, B.: Observations of a nonthermal ion layer at the plasma sheet boundary during substorm recovery. *J. Geophys. Res.* **85**, 5143–5148, 1980
- Murayama, T.: Correlated occurrence of energetic electron bursts in the magnetotail and geomagnetic impulsive micropulsation. *Rept. Ionos. Space Res.* **24**, 135–147, 1970
- Nishida, A., Fujii, K.: Thinning of the near-earth (10–15 R_E) plasma sheet preceding the substorm expansion phase. *Planet. Space Sci.* **24**, 849–853, 1976
- Nishida, A., Hayakawa, H., Hones, E.W.: Observed signatures of reconnection in the magnetotail. *J. Geophys. Res.* **86**, 1422–1436, 1981
- Parks, G.K., Lin, C.S., Anderson, K.A., Lin, R.P., Reme, H.: ISEE 1 and 2 particle observations of outer plasma sheet boundary. *J. Geophys. Res.* **84**, 6471–6476, 1979
- Pedersen, A., Grard, R., Knott, K., Jones, D., Gonfalone, A., Fahlson, U.: Measurements of quasi-static electric fields be-

- tween 3 and 7 earth radii on Geos-1. *Space Sci. Rev.* **22**, 333–346, 1978
- Pellinen, R., Heikkilä, W.J.: Inductive electric fields in the magnetotail and their relation to auroral and substorm phenomena. *Space Sci. Rev.* **37**, 1–61, 1984
- Pudovkin, M.I., Sergeev, V.A. (eds): Results of substorm studies on March 3, 1976. In: *Magnetospheric Res.* (in Russian) **5**, 1984
- Pytte, T., McPherron, R.L., Kivelson, M.G., West, H.I., Hones, E.W.: Multiple-satellite studies of magnetospheric substorms: radial dynamics of the plasma sheet. *J. Geophys. Res.* **81**, 5921–5933, 1976
- Pytte, T., McPherron, R.L., Kivelson, M.G., West, H.I., Hones, E.W.: Multiple-satellite studies of magnetospheric substorms: Plasma sheet recovery and the poleward leap of auroral zone activity. *J. Geophys. Res.* **83**, 5256–5268, 1978
- Roelof, E.C., Keath, E.P., Bostrom, C.O., Williams, D.J.: Fluxes of 50-keV protons and 30-keV electrons at 35 R_e . 1. Velocity anisotropies and plasma flow in the magnetotail. *J. Geophys. Res.* **81**, 2304–2314, 1976
- Sarris, E.T., Axford, W.I.: Energetic protons near the plasma sheet boundary. *Nature* **277**, 460–462, 1979
- Sarris, E.T., Krimigis, S.M., Armstrong, T.P.: Observations of magnetospheric bursts of high-energy protons and electrons at 35 R_e with Imp 7. *J. Geophys. Res.* **81**, 2341–2355, 1976a
- Sarris, E.T., Krimigis, S.M., Iijima, T., Bostrom, C.O., Armstrong, T.P.: Location of the source of magnetospheric energetic particle bursts by multispacecraft observations. *Geophys. Res. Lett.* **3**, 437–440, 1976b
- Sato, T., Walker, R.J., Ashour-Abdalla, M.: Driven magnetic reconnection in three dimensions: Energy conversion and field-aligned current generation. *J. Geophys. Res.* **89**, 9761–9769, 1984
- Semenov, V.S., Heyn, M., Kubyshev, I.V.: Magnetic field line reconnection in nonstationary case. *Astron. J.* (in Russian) **69**, 1138–1147, 1983
- Sergeev, V.A.: On the microstructure of the magnetospheric substorm. *Geomagn. Researches* (in Russian) **21**, 5–15, 1977
- Sergeev, V.A.: High-time resolution correlation between the magnetic field behaviour at 37 R_e distance in the magnetotail plasma sheet and ground phenomena during substorm expansion phase. *J. Geophys. Res.* **49**, 176–185, 1981
- Sergeev, V.A.: Changes in the far plasma sheet at substorm expansion onset. *Geomagn. Aeron.* (in Russian) **23**, 822–828, 1983
- Sergeev, V.A., Yahnin, A.G.: The features of auroral bulge expansion. *Planet. Space Sci.* **27**, 1429–1440, 1979
- Sergeev, V.A., Yahnin, A.G., Raspopov, O.M.: On the spatial-temporal structure of the expansion phase of microsubstorm. In: *Dynamical processes of the auroral magnetosphere* (in Russian), O.M. Raspopov, L.L. Lazutin, eds.: pp. 42–54, Apatity 1978
- Sergeev, V.A., Yahnin, A.G., Gorely, K.I., Danielsen, C., Pellinen, R.I., Samsonov, V.P., Urbanovich, V.D., Latov, Y.O., Ranta, H., Stauning, P., Armstrong, T.P., Hones, E.W., Krimigis, S.M., Lepping, R.R., Ness, N.F.: Results of observations during substorms on March 3, 1976. 1. Auroral precipitation data and measurements in the magnetotail. Polar Geophysical Institute preprint PGI-81-1, Apatity 1981
- Sergeev, V.A., Pellinen, R.J., Bösinger, T., Baumjohann, W., Stauning, P., Lui, A.T.Y.: Spatial and temporal characteristics of impulsive structure of magnetospheric substorm. *J. Geophys. Res.* **60**, 186–198, 1986
- Spjeldvik, W.N., Fritz, T.A.: Energetic ion and electron observations of the geomagnetic plasma sheet boundary layer: Three-dimensional results from ISEE 1. *J. Geophys. Res.* **86**, 2480–2486, 1981
- Williams, D.J.: Energetic ion beams at the edge of the plasma sheet: ISEE 1 observations plus a simple explanatory model. *J. Geophys. Res.* **66**, 5507–5518, 1981
- Wolcott, J.H., Pongratz, M.B., Hones, E.W., Peterson, R.W.: Correlated observations of two auroral substorms from an aircraft and from a Vela satellite. *J. Geophys. Res.* **81**, 2709–2718, 1976
- Yahnin, A.G., Sergeev, V.A., Pellinen, R.J., Baumjohann, W., Kaila, K.U., Ranta, H., Kangas, J., Raspopov, O.M.: Substorm time sequence and microstructure on 11 November 1976. *J. Geophys. Res.* **53**, 182–197, 1983
- Yahnin, A.G., Sergeev, V.A., Ievenko, I.B., Solovjev, S.I., Rakhmatulin, R.: Characteristics of phenomena accompanied by the local flares of discrete auroras. In: *Magnetospheric Res.* (in Russian) **5**, 93–110, 1984
- Zeleny, L.M., Lipatov, A.S., Lominadze, D.G., Taktakishvili, A.L.: The dynamics of the energetic proton bursts in the course of the magnetic field topology reconstruction in the Earth's magnetotail. *Planet. Space Sci.* **32**, 313–324, 1984

Received August 22, 1984;
 revised July 23, 1985 and June 2, 1986
 Accepted July 21, 1986

Spatial and temporal characteristics of impulsive structure of magnetospheric substorm

V.A. Sergeev¹, R.J. Pellinen², T. Bösinger³, W. Baumjohann⁴, P. Stauning⁵, A.T.Y. Lui⁶

¹ University of Leningrad, Institute of Physics, 198904 Leningrad, USSR

² Finnish Meteorological Institute, Department of Geophysics, Box 503, SF-00101 Helsinki 10, Finland

³ University of Oulu, Department of Physics, SF-90570 Oulu 57, Finland

⁴ Max-Planck-Institut für Physik und Astrophysik, Institut für Extraterrestrische Physik, D-8046 Garching, Federal Republic of Germany

⁵ Danish Meteorological Institute, Division of Geophysics, DK-2800 Lyngby, Denmark

⁶ Johns Hopkins University, Applied Physics Laboratory, Laurel, MD 20707, USA

Abstract. At least a dozen well-defined activations were recorded with high spatial resolution during the first 25 min of a substorm commencing at 1959 UT on 3 March 1976. The activations were determined by Pi1 and 2-type magnetic pulsations, magnetic variations and cosmic noise absorption. The activations exhibited differences in intensity, spatial extent and the accompanied auroral behaviour. In all cases but one an impulsive counterclockwise differential equivalent current vortex was observed superimposed on the continuously growing westward electrojet. The high-energy particle precipitation reached its maximum in these vortex regions. In cases where the activations observed on the ground occurred close to the footpoint of the IMP-J satellite, it registered simultaneously (within 2 min) burst-like enhancements of the high-energy particle fluxes. The satellite was at these times $37 R_E$ away from the earth in the plasma sheet boundary layer.

Large, practically isotropic high-energy electron fluxes detected at the satellite during the substorm expansion suggested the existence of a large-scale magnetic loop structure in the far magnetotail. The results give evidence of a time-varying dissipation process operating in an impulsive manner in separate regions of the plasma sheet (within a few R_E). According to the magnetic variations at mid-latitude, the intensity of the cross-tail current disruption (or the substorm current wedge) does not respond to these activations in the same impulsive manner, but seems to integrate their effects.

Key words: Magnetospheric substorm – Microsubstorm – Substorm current wedge – Pi2 and Pi1B pulsation – Auroral behaviour – Plasmoid – Magnetotail acceleration

Introduction

It is commonly known that the development of a magnetospheric substorm process can occur in several different ways. Concepts such as the “classical” substorm (Akasofu, 1968), the convection bay (Sergeev, 1977; Pytte et al., 1978), the multiple onset substorm (Wiens and Rostoker, 1975; Pytte et al., 1976b) and the microsubstorm (Sergeev, 1974) have been introduced to classify the different modes of sub-

storm-related processes. In order to understand the basic physics involved in the dissipation mechanisms, it has turned out to be necessary to introduce one more concept; an “elementary event”, i.e. one which does not contain any further temporal or spatial fine structure. It is assumed that all impulsive magnetospheric dissipation processes, even if they show extreme complexity and variability, are made up of a series of these elementary events. It is the main task of this paper to investigate, both on the ground and in space, the temporal and spatial scales of these elementary events and to compare the present results with existing theoretical models.

In the past, two different time-scales have been identified in the fine structure of ground-based substorm data. The first, 5–15 min, represents the interval between substorm intensifications (or microsubstorms). The second, 1 min, characterizes details in the temporal fine structure of substorm intensifications. What is meant by substorm intensification is well documented in literature (Sergeev, 1974; Wiens and Rostoker, 1975; Vorobjev and Rezhnev, 1973; Pytte et al., 1976a, b and c). If the duration of the Pi2 train and/or deflection in mid-latitude and auroral-zone magnetic bays are taken as a time measure of the substorm intensification, one can say that a substorm intensification lasts typically some 5 min. Within this time interval burst-like enhancements can usually be noticed. They represent a fine structure of the substorm intensification. It was discovered and described first by Sergeev et al. (1978), Sergeev and Yahnin (1979), and Yahnin et al. (1983). It can be added that the substorm analyses underlying the document of the Victoria Workshop (Rostoker et al., 1980) were not detailed enough in the temporal and spatial evolution of substorm intensifications for a description of a substructure of the intensification. This substructure constitutes – what we have called – elementary events. In other words, a sequence of elementary events forms a substorm intensification (microsubstorm). This paper demonstrates (once again) the coexistence of the different time scales characterizing the substorm development.

Short-lived, localized features have been reported to occur in the plasma sheet (PS) during substorm processes (cf. Aggson et al., 1977; Krimigis and Sarris, 1979; Coroniti et al., 1980), although it is impossible to separate temporal and spatial effects by means of single-satellite measurements. Multiple-satellite observations may be useful in this

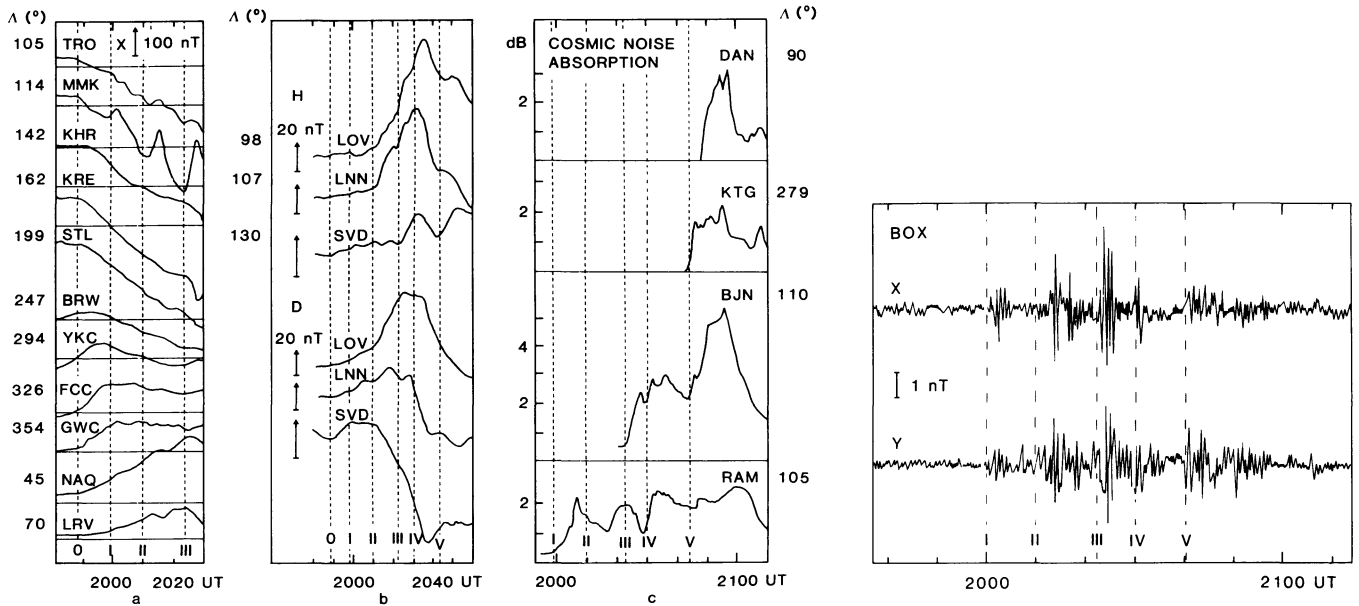


Fig. 1 a–d. General characteristics of the substorm event starting at 1959 UT on 3 March 1976. **a** H -component variations at auroral-zone stations around the northern hemisphere; **b** Mid-latitude magnetic variations; **c** Cosmic noise absorption; **d** Pi2 recordings at Borok. Five microsubstorms (I–V) are indicated by broken vertical lines

respect, but have until now only rarely been reported. The problem of spatial and temporal separation may partially be overcome by forming a global picture of substorm development by means of ground-based data and by comparing the spatial and temporal details on the ground with satellite recordings.

A correlation study of irregular pulsations on the ground and processes in the PS is carried out in an accompanying paper (Sergeev et al., 1986, referred to in the following as paper I). One important conclusion of paper I is that the time scale of 1–3 min represents an “elementary” length for an impulsive substorm process in the PS. In this paper we deal mainly with the spatial aspects of the elementary events, studying their localized character on the ground and impulsive response near the upper boundary of the remote PS.

The present investigation concerns a substorm that was unusually well suited for such detailed treatment. The expansion phase commenced at 1959 UT on 3 March 1976, and the region of impulsive expansion processes in the ionosphere was within the field of view of the Scandinavian geophysical network for the next 25 min. The IMP-J satellite was located in the far PS on the field line mapping into the same magnetic local time (MLT) sector where the ground-based recordings were made. A dozen impulsive elementary events were detected within the first 25 min, most of them with a clear ground-PS correlation.

Description of the event

The event under consideration is one of the substorm periods of 3 March 1976 which have already been investigated by a working group of scientists. An extensive set of data has been gathered from both permanent and temporary ground observatories and from the IMP-J satellite. Corresponding data reviews have been published by Sergeev et al. (1981) and Mishin et al. (1982). Figure 1 presents results of ground-based observations of various types. According

to all the data obtained both on the ground and in the magnetotail, the substorm onset took place at 1959 UT over Kevo (see Fig. 5), approximately at 66° corrected geomagnetic latitude (CG Lat, Tsyganenko, 1979) within the sector 110° – 115° CG Long (~ 23.0 MLT). We are primarily interested in the 25-min period after the onset, since the auroral expansion subsequently moved outside the field of view of the Scandinavian network and there is a gap in the satellite data after 2025 UT.

The substorm started at the end of the recovery phase of a preceding strong substorm that commenced at 1715 UT. Both the polar-cap (data not shown here) and auroral-zone magnetic data show an intensification in the convection-driven twin-vortex DP2 current system after 1948 UT (Fig. 1a). According to these data and those from other stations published in Mishin et al. (1982), a monotonous increase in convection-related auroral electrojets (AEJ) and their equatorward expansion continued at least during the period under investigation. Both the oval expansion and the increase in magnetic-field magnitude at IMP-J in the magnetotail are evidence of a growing tail current.

According to the mid-latitude pulsation data in Fig. 1d, at least five well-defined Pi2 trains occurred during the expansion phase. As usual, these five microsubstorms are pronounced both in the mid-latitude magnetic variations (Fig. 1b) and in the cosmic noise absorption (CNA) data from the auroral zone (Fig. 1c). Only the first three lie within the period under consideration.

No significant Pi activity or CNA enhancement was observed during the entire event at two Antarctic stations, Molodeznaya and Syowa (approximately at 67° CG Lat and 70° CG Long). The riometer data from this longitude sector (Sergeev et al., 1981) suggest that expansion-associated increases in CNA appeared at higher latitudes only after 2045 UT (Fig. 1c). Hence, the western edge of the substorm expansion is estimated to have been at 80° – 90° CG Long (~ 21.5 MLT) until 2030 UT.

To the east, at 145° – 160° CG Long, both magnetic and

Table 1. Geographic and corrected geomagnetic coordinates (Tsyganenko, 1979) of the permanent or temporary stations from which data are used

Station	Symbol	Geographic coordinates		Corrected geomagnetic	
		Latitude	Longitude	Latitude	Longitude
Barrow	BRW	71°	203°	70°	247°
Bjørnøya (Bear Island)	BJN	75	19	71	110
Borok	BOX	58	39	54	114
Danmarkshavn	DAN	77	341	77	90
Fort Churchill	FCC	59	266	70	326
Great Whale River	GWC	55	282	67	354
Kaliningrad	KNG	55	21	50	98
Kap Tobin	KTG	70	238	76	279
Kerguelen	KGL	−49	70	−59	121
Kevo	KEV	70	27	66	111
Kharasovey	KHR	65	72	66	142
Kiruna	KIR	68	20	64	107
Kresty	KRE	72	88	66	162
Leirvogur	LRV	64	338	66	70
Leningrad	LNN	60	31	55	107
Loparskaya	MMK	68	33	65	114
Lovozero	LOZ	68	35	64	116
Lovö	LOV	59	18	56	98
Muonio	MUO	68	24	64	108
Narssarsuaq	NAQ	61	315	67	45
Port Alfred	CZT	−46	52	−53	105
Ramfjord	RAM	70	19	66	105
Sokankylä	SOD	67	27	63	109
Stolbovoy	STL	74	133	68	199
Sverdlovsk	SVD	57	61	52	134
Tbilisi	TFS	42	45	36	117
Tromsø	TRO	70	19	67	105
Yellowknife	YKC	62	245	70	294

photometric data (not shown here) fail to show any expansion-associated signatures during the period concerned (Sergeev et al., 1981; Mishin et al., 1982). The mid-latitude data in Fig. 1b lead us to infer that before 2023 UT the eastern edge of the substorm current wedge (SCW) was located west of 130° CG Long. Only during the third microsubstorm (III) did the H -component at SVD start to rise, indicating that the SCW had extended beyond 130° CG Long (~ 00.0 MLT).

It was only at 2023 UT that the CNA started to increase at BJN (Fig. 1c). Thus before this time the active region was restricted in both latitude (within 65°–69° CG Lat) and longitude (between 21.5–00.0 MLT), causing the auroral activity to remain in the field of view of the Scandinavian observatories during most of the period 1959–2025 UT.

The observation sites are listed in Table 1. Auroras were recorded by all-sky cameras (ASC) at KEV, MUO, SOD and MMK (Loparskaya) at a speed of 1 frame/min. CNA was monitored by a riometer network (described in Ranta et al., 1981) with a time resolution of about 0.5 min (chart speeds 60 or 76 mm/h). Pulsation recordings (frequency range 0.1–2 Hz) were made at Sodankylä and Nurmijärvi (details in Böisinger et al., 1981). Only two chains ($\sim 104^\circ$ and 107° CG Long) of the Scandinavian Magnetometer Array (SMA, Küppers et al., 1979) were in operation; time resolution, 10 s. In addition, sensitive rapid-run magneto-

grams (90 mm/h) were available from LOZ. Mid-latitude magnetic data (resolution ≤ 1 min) were collected from a longitudinal chain of observatories (105° – 133° CG Long). Mid-latitude induction magnetometer data (0.01–0.2 Hz) were obtained from a meridional chain of stations (36° – 64° CG Lat).

The IMP-J satellite performed measurements near the upper boundary of the plasma sheet at a distance of $37 R_E$ from the earth. Its ionospheric projection along the magnetic field line is estimated to be at 117° CG Long, just at the eastern border of the Scandinavian network (details in later section).

Temporal development of the impulsive events

Burst-like Pi1 pulsations (Pi1B) recorded at auroral and subauroral latitudes show a clear response to strong or weak, wide or localized substorm activations, if the recordings are carried out in the MLT sector of the activation (Böisinger et al., 1981; Yahnin et al., 1983). In the present study, Pi1Bs provide the most accurate definition of the temporal sequence of the impulsive activations.

Intensity variations of Pi1 pulsations in a few frequency bands (Fig. 2a) synchronously display a large number of bursts. Bursts that are well separated and distinct through all frequency bands are indicated by dotted vertical lines and letters. Similar impulsive Pi1B structures appear both at Sodankylä (Fig. 2a) and at Nurmijärvi (located 800 km further south).

According to the results reported in Sergeev et al. (1978) and its supporting verifications in Sergeev (1981) and Yahnin et al. (1983), similar impulsive activations are seen even at mid-latitudes in the form of sudden changes in the characteristics of Pi2 pulsations (intensity and phase).

In Fig. 2b 1-min time intervals are marked by a shaded vertical band laid across the Pi2 registrations of one auroral-zone (LOZ) and three mid-latitude (BOX, KNG and TFS) stations. Within these time intervals at least four instances of Pi2 onsets and/or sudden changes in the Pi2 waveform indicating activations can be recognized in the seven Pi2 registrations displayed. A length of 1 min for the time intervals was chosen because it is representative of the time accuracy of the method in question (average period of Pi2s, some 60 s).

The Pi2 data of Fig. 2b reveal some additional activations of which the most significant ones are marked as A', F', G' and I'. At least two of these (A' and G') correspond to additional strong spikes within the Pi1Bs in Fig. 2a.

Response of other ground-based phenomena to the impulses

Energetic electron precipitation and equivalent currents in the ionosphere

Figure 3 (upper panel) demonstrates well both the impulsive variations and the spatial changes in the high-energy electron precipitation patterns. The auroral break-up at 1959 UT (A) started at $\sim 66^\circ$ CG Lat and significant auroral activity was confined between 65° and 69° CG Lat until 2023 UT (I). Most of the active auroras throughout the period were within the riometer beams of KEV and RAM, which are located 270 km apart on the same 66.6° CG Lat. Hence the data from these two stations

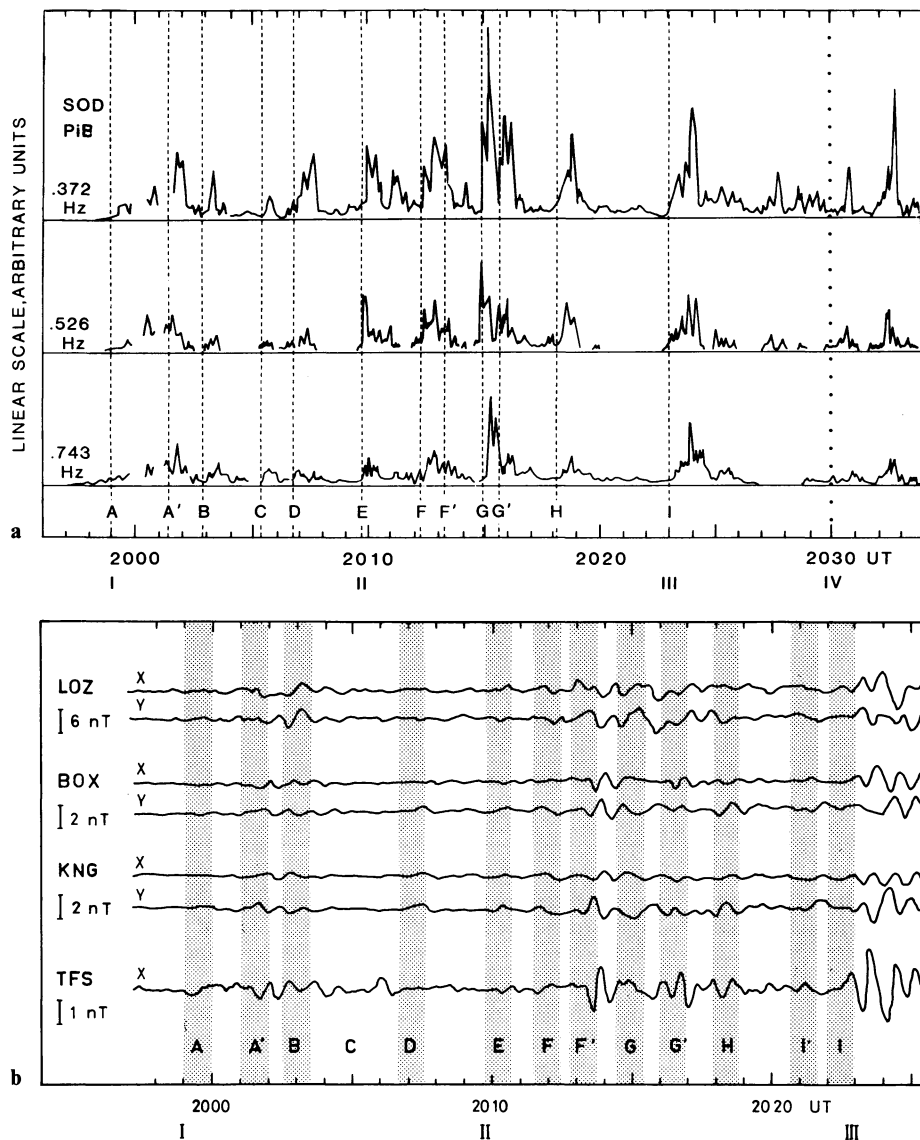


Fig. 2. a PiB amplitudes in different frequency channels at Sodankylä; b Pi2 recordings from the auroral zone (LOZ) to mid-latitude (TFS) in the longitudinal sector of the auroral expansion. The vertical shaded bands (A–I) indicate impulsive activations

(Fig. 3) demonstrate the changes in energetic precipitation pattern during the time interval under consideration.

There is a striking difference in CNA behaviour between KEV and RAM. In the east (KEV), distinct rises in CNA are seen in response to impulses A and G' (with less confidence for F'); while in the west (RAM), the responses to the same impulses are absent or negligible. Conversely, responses to impulses B, C, D and H are only observed in the west. Thus, most of the impulses A–H are associated with an enhancement in the energetic electron precipitation in very localized MLT sectors. Impulse I gives no immediate response at these locations, but results in a sharp onset of CNA at BJN (71° CG Lat, Fig. 1c).

Data from three magnetometer stations (Fig. 3, lower panels), aligned along 64° CG Lat within the 104°–114° CG Long sector, demonstrate the response of equivalent currents. At 1950 UT the magnetic *A* and *B* components (directed approximately northwards and eastwards; for an exact definition, see Küppers et al., 1979) are almost at the quiet-time level (within 10–20 nT) before the onset, the *A* components decreasing monotonically until 1959 UT, this being most effective at the easternmost station, LOZ. The

substorm started at 1959 UT in the sector 108°–115° CG Long, eastwards of MUO, obviously in the region of a westward auroral electrojet (AEJ). We can infer from Fig. 1a that during the period concerned here the monotonical growth of the convection-associated westward AEJ continued in the morning sector of the oval, and apparently also within the expansion sector. The latter tendency is indicated by the broken lines in Fig. 3, which also serve (at least in a qualitative sense) as reference lines for the impulse-associated responses.

Figure 3 shows that the clearest responses appear in the *A* component, in the form of sudden increases associated with most of the impulses A–I. The significance of this observation is underlined by the similarity of the magnetic field behaviour at MUO and LOZ to the CNA development at KEV (located approximately at the mid-point between the two magnetometer sites). The details of the magnetic-field trends at KIR, MUO and LOZ differ, however, suggesting spatial changes in the active region between the impulses. Hence, information from the entire SMA seems to be of utmost importance for this purpose.

It may be concluded from the discussion above that

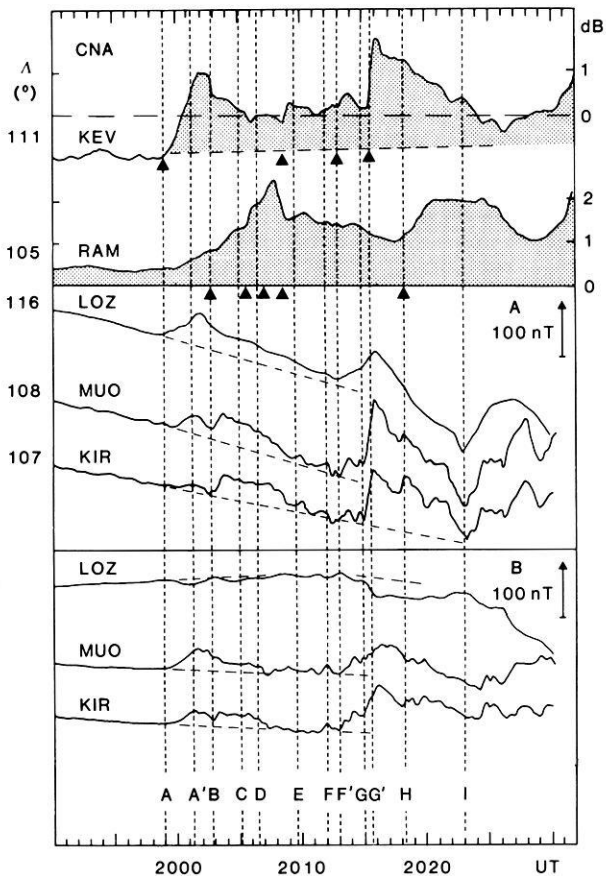


Fig. 3. Changes in cosmic noise absorption (*top panel*) and magnetic field variations (*middle and bottom panel*) at a longitudinal chain of stations. The *vertical broken lines* are the same as in Fig. 2, *triangles* denote onsets of CNA enhancements

the magnetic variations superimposed on the monotonically growing convection background are in accordance with the sequence of impulses reported in Fig. 2. Hence the method of differential equivalent current (DEC) analysis introduced by Untiedt et al. (1978) and Opgenoorth et al. (1980), showing the relative changes in current patterns after each impulse, seems to be fairly convenient here.

As shown above, the impulses can be separated roughly into two different groups (the western and eastern ones), depending on the appearance of the CNA increases at RAM or KEV. Figure 4 clearly demonstrates that the DEC patterns are similar within each group, while there are differences between the groups. Assuming that the DEC patterns for each impulse are similar within the observation site covering the active region, we can combine the DEC patterns of both groups. This results in a counterclockwise equivalent current vortex for each case centred at the peak precipitation area for high-energy electrons.

Our results exhibit a clear response of both equivalent currents and CNA behaviour to individual impulses. The impulse-induced patterns seem to be short-lived. After a rapid formation phase (~ 1 min), the vortex tends to fade within 2–3 min. Similar features are reported in Yahnin et al. (1983). There are also some similarities in the time and amplitude structures of the vortices and mid-latitude Pi2s (cf. Fig. 2b), in that a good correlation can be found in the case of B, D, F', G and H, suggesting a close relationship between their source mechanisms.

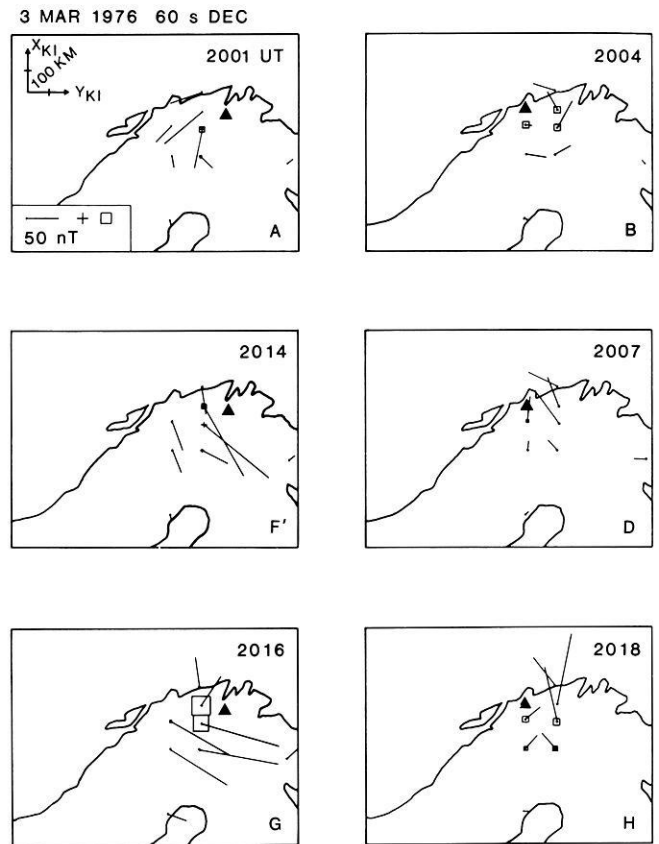


Fig. 4. Differential equivalent current patterns building up during 1 min around the activations A, B, D, F', G and H. CNA enhancement occurs at Kevo (*triangle*) in the left-hand column, and at Ramfjord (*triangle*) in the right-hand column

Intensity, structure and height of the auroras

The main information on auroral characteristics was obtained from the ASC films recorded at KEV and MUO. Both cameras are in a favourable position for estimating auroral altitudes and for locating the spatial distribution of the auroral structures within the field of view of the geophysical network. The method is described in detail in Kaila (1981). ASC information from MMK (Loparskaya) is used to obtain auroral data from the eastern sector (113° – 125° CG Long), where the footpoint of the IMP-J satellite was located. Unfortunately, the temporal resolution of the ASC data (1 frame/min) is not high enough to study details of the auroral responses to the impulses. Hence the main interest will lie in comparing the location of the bright, active auroras with that of the vortices. The original ASC pictures from KEV in Fig. 5 give an impression of the variations in auroral brightness and structures while more quantitative information on auroral location and lower-border altitude is given in Fig. 6.

The auroral activity in Fig. 5 can be divided into four stages:

1959–2002 UT: The first sign of the auroral break-up was observed at 1959:03 UT as an inhomogeneous brightening (ripples) of the most equatorward arc within the 108° – 115° CG longitudinal sector. This observation is confirmed by the SMA magnetometer data with a 10-s time resolution. Thereafter the auroras brighten rapidly and the

KEVO
3 MAR 1976

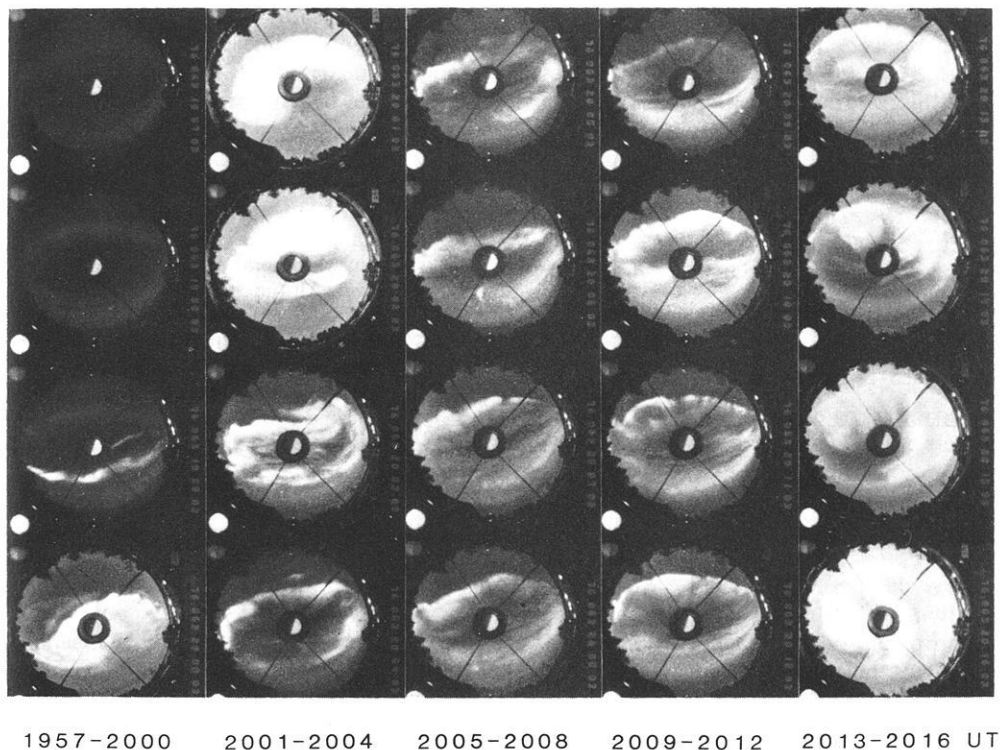


Fig. 5. All-sky camera data recorded at Muonio from 1957 to 2016 UT

bulge is formed at 2000 UT within the sector 110° – 118° CG Long. The westward-travelling surge (WTS) on the western edge of the bulge coincides in space with the vortex structure A in Fig. 4. One more important detail is the thin bright structure appearing at 2002 UT in the eastern poleward half of the bulge (Fig. 5). According to the simultaneous ASC data from Loparskaya, the active structure expanded eastwards as far as 120° – 125° CG Long. This eastward expansion, taking place after A', agrees well with the increase in the magnetic A component observed only at LOZ in Fig. 3.

2003–2008 UT: The most significant difference compared with the previous interval is the fading of auroral activity over Kevo, while the activity seems to continue in the west (data not shown). This is in good agreement with the location of the vortices and CNA peaks at the moments B and D in Figs. 3 and 4. The westward expansion continues at an average speed $\sim 2^{\circ}/\text{min}$.

The magnetic A component at MUO (Fig. 3) shows an impulsive rise starting at 2003 (B) and leading to the formation of vortex B in Fig. 4. At the same time the ASC picture from MUO (data not shown) reveals a rippled structure (inhomogeneous brightening) ahead of the WTS, in a place where the WTS is located 1 min later. This development closely resembles that observed at the initial break-up. The rippled structure appearing abruptly in a previously undisturbed region may be regarded as a sign of auroral response to the onset of impulse.

2009–2012 UT: No clear impulsive signs in CNA (the CNA onset at KEVO marked by a triangle in Fig. 3 occurred well before 2009 UT), Pi2 or equivalent currents are evident during this period. The brightening of the bulge at 2010 (Fig. 5) is associated with a spike (E) in the Pi1B data (Fig. 2a). No significant changes in auroral structure, location or height are recorded (Fig. 6). Some weak continuous poleward expansion is observed along the western meridian.

2013–2016 UT: The auroras brighten rapidly and expand both equatorwards and polewards, as seen at Kevo (Fig. 5). The most effective poleward movement, associated with impulse G, takes place along 113° CG Long between 2014 and 2017 UT (Fig. 6). After 2017 the edge of the bulge is seen at such low elevation angles (10° – 15°) that only limited information on auroral variations can be obtained. A sudden intensification at 2023 UT (data not shown) can be detected within 105° – 115° CG Long and $\sim 70^{\circ}$ – 71° CG Lat, obviously associated with impulse I (Fig. 3) and the CNA enhancement at BJJ (Fig. 1).

The auroral observations presented above seem to agree with the material presented in the previous sections. A close correlation both in strength and location was found between auroral activity and impulsive vortex formation. When the response in vortex formation was extremely weak (cf. impulse E) no deformation in auroral structures or changes in height were observed during a clear auroral brightening. Still, this comparison must nevertheless be considered incomplete due to inadequate time resolution.

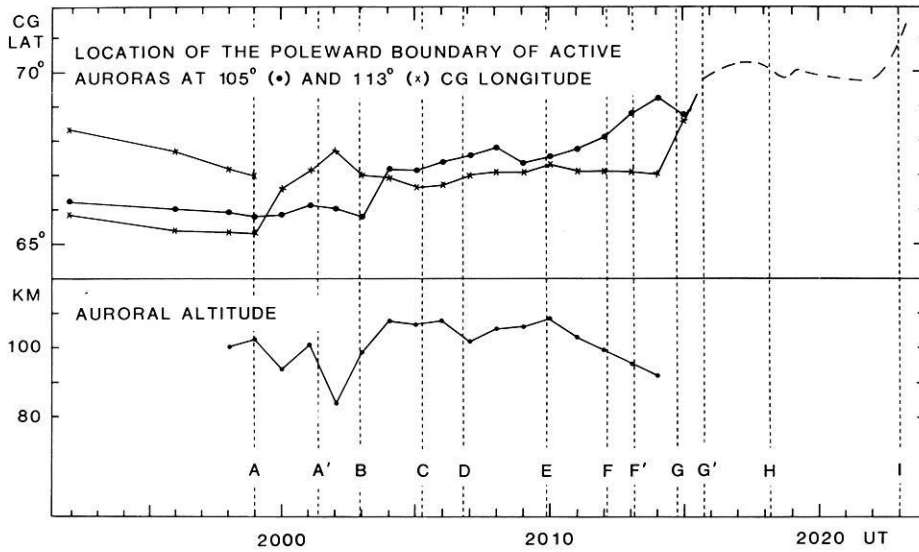


Fig. 6. Position of the poleward boundary of active auroral structures (bright edge of the auroral bulge after break-up) obtained from digitized ASC films from Muonio and Kevo (*top panel*). Altitude variations of the bulge edge obtained by triangulation (*bottom panel*). A rough estimate of the auroral development after 2016 UT is indicated by the *broken line*

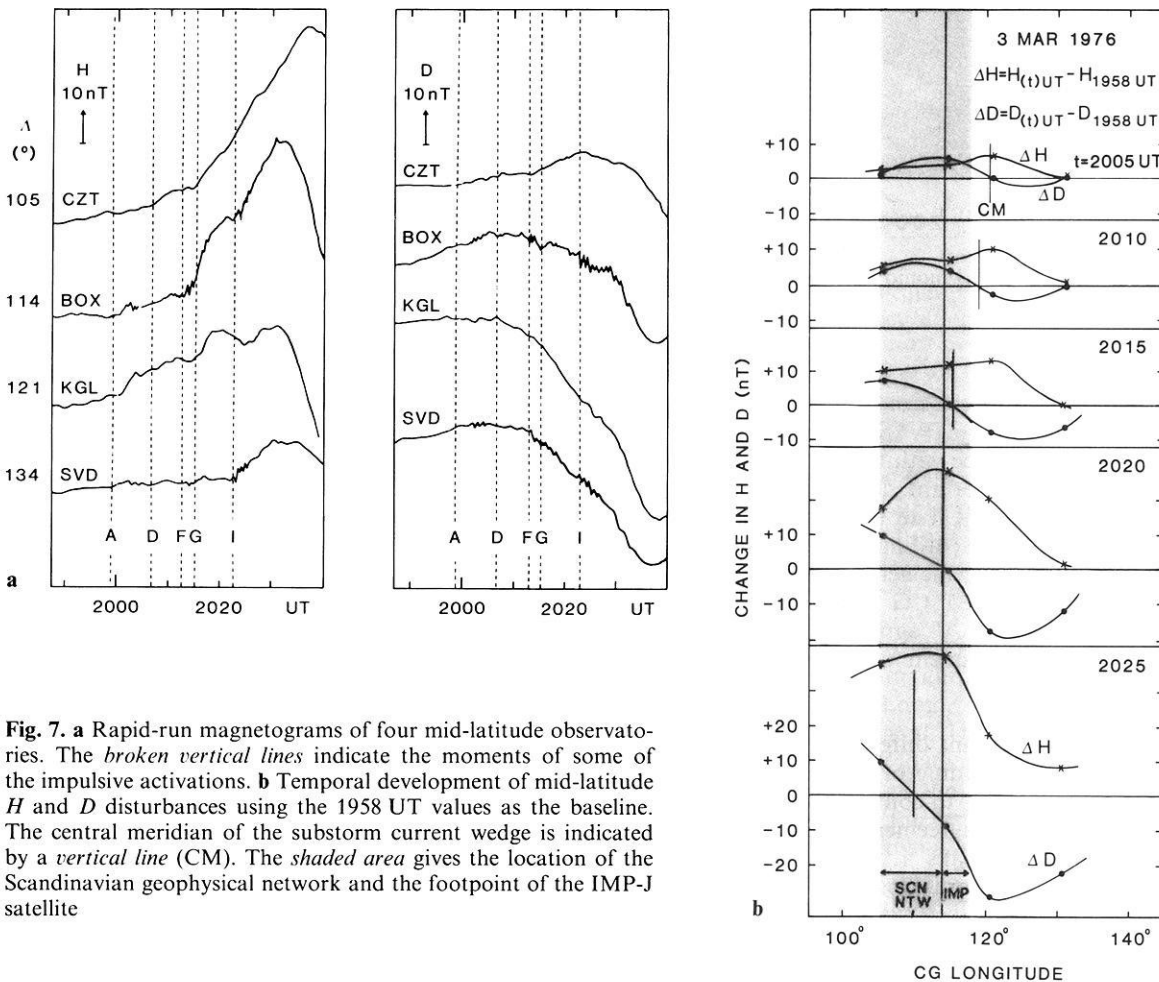


Fig. 7. **a** Rapid-run magnetograms of four mid-latitude observatories. The *broken vertical lines* indicate the moments of some of the impulsive activations. **b** Temporal development of mid-latitude H and D disturbances using the 1958 UT values as the baseline. The central meridian of the substorm current wedge is indicated by a *vertical line* (CM). The *shaded area* gives the location of the Scandinavian geophysical network and the footprint of the IMP-J satellite

Three-dimensional substorm current wedge

Variations in the intensity and position of the expansion-related three-dimensional substorm current wedge (SCW) system were monitored by four stations located along 52°–58° CG Lat within 105°–134° CG Long (Fig. 7a). Two

of these, CZT and KGL, located in the southern hemisphere, provided digital data with 1-min time resolution, while rapid-run (90 mm/h) sensitive magnetograms were available from BOX and SVD in the northern hemisphere. No significant qualitative differences in SCW behaviour were found between hemispheres. The effects in terms of

both auroral electrojet and field-aligned currents (FAC) are larger at KGL, located at 58.5° CG Lat, 5°–6° poleward of the other stations than at the lower-latitude stations. This has to be taken into account in the data analysis, especially when presenting longitudinal profiles (Fig. 7b).

The changes in the horizontal magnetic field after the onset of the substorm at mid-latitudes (Fig. 7b) are typical of a SCW system. The ΔD profile resembles a sinusoidal wave in which D changes its sign at the variation maximum ΔH . This point may be regarded as the central meridian of the SCW system. According to McPherron et al. (1973), the maximum and minimum for ΔD should be located at meridians in which the FACs are directed into the ionosphere or out of it, respectively.

At the onset (A), the H -component increase at BOX and KGL and the D -component increase at BOX and CZT indicate the appearance of the SCW around 115°–120° CG Long, in good agreement with other data. At 2007 (D) H starts to increase more rapidly at CZT and D decreases at KGL, indicating a westward expansion of the SCW. The whole pattern shifts westwards and intensifies during impulses F, G and H, and finally, at impulse I, a new intensification of the SCW starts, expanding eastwards (rise in H at SVD) and westwards (decrease in D at CZT). Comparison of the pattern of the SCW system with the vortex positions in Fig. 4 leads us to conclude that all the vortices appear in the western part of the SCW and are highly localized compared with the total size of the SCW (Fig. 7b).

The intensity of the SCW increases throughout the period studied here, but the rate of increase and the spatial configuration clearly change in response to major intensifications in currents and precipitation in the auroral zone. There also seems to be a close relationship between SCW intensifications and the poleward expansion of auroras (Fig. 6). Hence, the SCW system seems to integrate the effects of individual impulses, leading to long time constants (up to 20–30 min).

IMP-J observations and their relation to ground phenomena

In the following we will refer to the magnetic field and energetic particle data presented in Fig. 3 of paper I. As can be seen from this figure, the magnetic field increased up to the data gap, which started at 2025 UT. The thermal electron energy density decreased during this time interval with the exception of a brief partial recovery between 2007 and 2015 UT (E.W. Hones, personal communication). After the onset at 1959 UT, high fluxes of accelerated HE particles (especially electrons) appeared. The proton fluxes were highly anisotropic with a pronounced tailward flow component until the end of the interval considered. The HE electrons had practically isotropic pitch-angle distributions, and it was only during two brief intervals (at 2018 and 2023 UT) that the 30-keV electron fluxes showed any pronounced tailward anisotropy (ratio >2). The significance of these observations will be discussed later.

In order to compare the IMP-J satellite data with ground recordings, the ionospheric projection of the magnetic field line passing through the satellite has been estimated using different variants of the magnetospheric model of Tsyganenko (1979), which takes into account the tilt of the dipole axis and the shift in the position of the neutral sheet. The different variants give large variations in pro-

jected latitude, but the longitude remains fairly constant (within a few degrees) around 117° CG Long. Hence it seems safe to pay principal attention to the longitudinal effects when comparing satellite recordings with ground data. It is evident that even the longitude can be severely distorted by the SCW system, but not in our case since the projection point is close to the SCW central meridian (Fig. 7b), where longitudinal distortions are minimal (Vasyliov et al., 1986).

As can be seen in Fig. 3 of paper I, short-lived HE particle spikes with an enhancement of more than an order of magnitude are recorded in both the e^- and p^+ components during activation A–A', F–F', G–G' and J (the primed letters are taken from the corresponding figures of this paper, paper II). The rise in particle fluxes after 2007 UT looks different and may be associated with the partial recovery of the PS seen in the thermal plasma data. One more spike appears at 2010 UT (E), which is recorded most clearly in the electron channel.

A detailed comparison of ground and satellite recordings reveals that spikes A, F' and G appear in conjunction with short-lived vortex structures (Fig. 4) developing near the satellite conjugate point in the eastern part of the ground-based network. There was no vortex formation during impulse E, but the aurora was also activated in this sector. Both the auroral and CNA observations at moment I indicate that this event was centred over Bear Island, at 110° CG Long. HE particle spikes do not appear at moments B, C, D and H, when there was intense vortex formation only 5°–10° to the west of the easternmost vortices. The vortex formations were associated with local enhancements in CNA, indicating peak precipitation of HE particles at their centres, as in the case of the easternmost vortices. It may be concluded from these observations that the main acceleration region in the PS was shifted with respect to the IMP-J position. A shift of 5°–10° in the peak precipitation region in the ionosphere corresponds to only about 2 R_E shift across the tail at $x \approx 20$ –40 R_E . In practice, this means that the acceleration region is fairly localized and very small in size.

Discussion

Impulsive structure as a common feature of substorms and their relationship to microsubstorms

We shall discuss initially to what extent this event is a representative example of substorm expansion. At first glance, there seem to be some uncommon features: the continuously growing, large (compared with the expansion-related disturbances in Figs. 1 and 3) convection-related auroral electrojet, the spatially confined active region and the unusually rich impulsive fine structure (it is quite rare to find more than ten distinct Pi1B impulses in a single-station sonagram).

A detailed study of the literature reveals, however, that these features are not so uncommon. Strong (or growing) twin-vortex current systems appear in practice during all substorms that occur in conjunction with continuously southward-directed IMF. This has been clearly demonstrated in studies where the global twin-vortex current system and the expansion-related current pattern have been separated (Troshichev et al., 1974; Baumjohann et al.,

1981). According to these authors (see also Pellinen et al., 1982; Yahnin et al., 1983; Kamide and Baumjohann, 1985), the relative strength of these two current systems varies in a wide range from case to case, the twin-vortex current system being mainly controlled by the IMF variations. A similar type of control is also evident for changes in the magnetic field of the tail lobes (Fairfield et al., 1981).

In most substorm studies so far the authors have preferred to select well-isolated cases associated with an abrupt, strong negative magnetic bay in the nightside auroral zone. Such cases are more rare than those characterized by the magnetograms in Fig. 1. The choice of such uncommon cases also predetermines the properties of substorms to be observed. In such cases it is typical for the active part of the auroral bulge to move quickly away from the initial break-up region, thus preventing one-site observations of a large number of impulsive activations associated with bulge formation. Such activations have been well-documented in cases having a small-scale, moderate-intensity auroral bulge (Bösinger et al., 1981; Yahnin et al., 1983, 1984). Hence the relatively small dimension of the active region in our case and the consequent rich impulsive activity are due to the relatively weak expansion-related three-dimensional current system.

Microsubstorms are a common feature of substorm development and can be detected in magnetograms with ordinary time resolution, as in Fig. 1. The results presented here show the microsubstorms (I, II and III in Fig. 1) to consist of groups of distinct impulses. The first started within 110°–120° CG Long (A, A') with the vortices associated with the following impulses (B, C, D) observed further west. A similar spatial development in vortex position was found in the second microsubstorm (F, G, H) and possibly in the third one, where the activity was again initiated in the same sector, shifting westwards later. It may be speculated that a microsubstorm is not a simple superposition of impulses, but also includes some rules controlling their spatial development. It is possible that control of the repetition rate, strength and position of the impulses is due to some (unknown) feedback in the magnetosphere-ionosphere system.

Impulsive activations have been found in all recordings made with appropriate time resolution under the active part of an auroral bulge. Balloon-borne X-ray recordings were the first to be reported in the literature (Hones et al., 1971; Pytte et al., 1976b; Melnikov et al., 1976). A close relationship between X-ray bursts, Pi1 bursts and the appearance of short-lived current vortices has been demonstrated by Yahnin et al. (1983) and the coincidence of current vortex and Pi1B appearance by Bösinger et al. (1981). It has been shown that all these impulsive features can be recorded simultaneously only in an extremely limited area of the auroral zone, under the active part of the expanding auroral bulge. A similar type of restriction is also valid for observations made in the magnetotail. The changes of recording impulsive bursts are strongly dependent on the shift of the small-sized source in a cross-tail direction (see later) and on the position of the satellite in relation to the outer boundary of the PS, which changes rapidly in the course of a substorm. In our case and in those presented by Sergeev et al. (1978, 1981) multiple bursts seem to appear near the dynamic boundary of the PS.

The sudden changes in the characteristics of Pi2 pulsations observed at mid-latitudes (Fig. 2b) are closely related

to the impulsive phenomena observed in the auroral zone and magnetotail (Sergeev et al., 1978; Sergeev, 1981; Yahnin et al., 1983). Use of the mid-latitude Pi2 *alone* as a (quantitative) indicator of impulsive activity in the auroral zone is somewhat dangerous, however, as in most cases it permits one to infer the number of impulsive activations regardless of their strength and size in the auroral zone (see also Yahnin et al., 1983). This strongly supports the idea that all substorms develop through brief impulsive activations of a common nature.

Three-dimensional substorm current wedge

The formation of a substorm current wedge is due to an interaction between the ionosphere and the magnetosphere. We have demonstrated here that the growth in its intensity and spatial extent is intimately related to the strongest impulses associated with spikes in HE electron precipitation, rapid auroral expansions and the formation of current vortices. In addition to the impulsive changes, there is a continuous increase in the SCW intensity during the entire period studied. The smooth character of the mid-latitude magnetic bays (Pi2s subtracted) is an indicator of a long time constant (of the order of 20–30 min) for the SCW system, probably due to the high inductance of such an electric circuit (Boström, 1974).

How do the impulsive activations produce or control the SCW? The answer is not clear. An impulsive dissipative process in the plasma sheet launches Alfvén waves propagating both earthwards and tailwards, away from the source region. The earthward wavefront carries a westward current closed by field-aligned currents directed into (out of) the ionosphere at the eastern (western) edge of the disturbance (paper I; Hill and Reiff, 1980). Similar current configurations have been found in a numerical simulation study of tail reconnection by Sato et al. (1983).

Enhanced precipitation into the ionosphere will produce a similar FAC configuration (Baker et al., 1984) and will launch a corresponding Alfvén wave into the magnetosphere (Maltsev et al., 1974). The relative importance and interaction of the two mutually acting processes in generating the SCW are unexplored at present.

The existence of a SCW can influence both the PS and auroral-zone dynamics. A continuous growth in SCW intensity leads to an enhanced electric field in the PS ($\sim 1 \text{ mVm}^{-1}$; Semenov and Sergeev, 1981). A SCW creates magnetic-field deformation, which moves the auroras poleward (Akasofu, 1977) and apparently forms the auroral bulge (Vasyliiev et al., 1986). Hence, both poleward and westward expansions superimposed on the impulse-related changes are to be expected during continuous growth of the SCW. In our case, westward motion was observed until 2010 UT, when the structure moved beyond the field of view of our all-sky cameras.

Impulse-induced phenomena: spatial extent and intensity correlation

A counterclockwise differential equivalent current vortex seems to be a common feature of substorm expansion. The vortices are typically short-lived (~ 5 min) and appear at different places during different stages of expansion. They

are superimposed on a smooth, large-scale (convective) current system, as shown by Baumjohann et al. (1981). Yahnin et al. (1983) demonstrate that Pi1Bs, X-ray bursts, CNA impulses in the auroral zone and Pi2s at mid-latitudes appear simultaneously with current vortices. The results presented here are similar, but extend the observations to a later stage, beyond the first few minutes of the expansion phase.

Magnetic-field topology in the boundary-layer plasma sheet, as inferred from the dawn-dusk asymmetry of the high-energy particle fluxes

A few striking features can be observed in the long-term development of the thermal PS population and the HE particle fluxes (Fig. 3, paper I). Fluxes of thermal plasma decrease significantly, except for the short partial recovery between 2007 and 2015 UT, and the HE proton fluxes show similar behaviour. The HE electron fluxes are surprisingly steady and high (well above their pre-onset values), especially at higher energies. In order to understand the high flux of very hot electrons in the PS boundary layer, the following has to be pointed out:

There is an almost isotropic pitch-angle distribution of high-energy electrons between the short bursts, which suggests magnetic trapping. Hence, the magnetic field lines penetrating the PS boundary layer must be closed (connected to the ionosphere or closed field line loops). The observed proton-electron asymmetry can be explained as being due to the spatial separation between the satellite and the acceleration region in the cross-tail direction (cf. paper I). When this region is west of IMP-J, accelerated electrons that drift eastwards in the PS magnetic field appear at the satellite. This is in agreement with our ground observations, since the vortex structure always appeared westwards of the satellite footprint. These observations support the conclusion that the cross-tail extent of the acceleration region is very limited and that the magnetic flux tube connected to the vortex structure passes near the acceleration region in the far PS.

Figure 8 presents some limited statistics to support the above conclusion. The IMP-J made observations of strong substorm expansions ($AE > 500$ nT) in the PS on six occasions. The first five are from 3 March 1976, 1000 to 2400 UT, and the last one from 20 February 1976, as studied earlier by Krimigis and Sarris (1979). Data from two proton and electron channels in the CPME experiment are plotted. The arrows on the top indicate onset times of mid-latitude Pi2s and Pi1Bs in the auroral zone in the 2200–0000 MLT time sector. The onsets of irregular pulsations seem to occur simultaneously with HE particle spikes (within 1 min). Some differences between the Pi1B and Pi2 moments exist, but these cannot be studied due to the limited station coverage in the active sector of the auroral zone. The events in Fig. 8 are ordered according to the Y_{GSM} coordinate of IMP-J. In the westernmost position (a) the protons develop a spike, while in the easternmost location (e, f) the electrons show the most distinct increases. This demonstrates that over a relatively limited cross-tail distance ($\sim 8 R_E$) there is a significant electron-proton asymmetry in the response to substorm onsets. Also, the acceleration region seems to be displaced into the duskward half of the PS. This observation is in agreement with the results of Krimigis and Sarris (1979), where the frequency

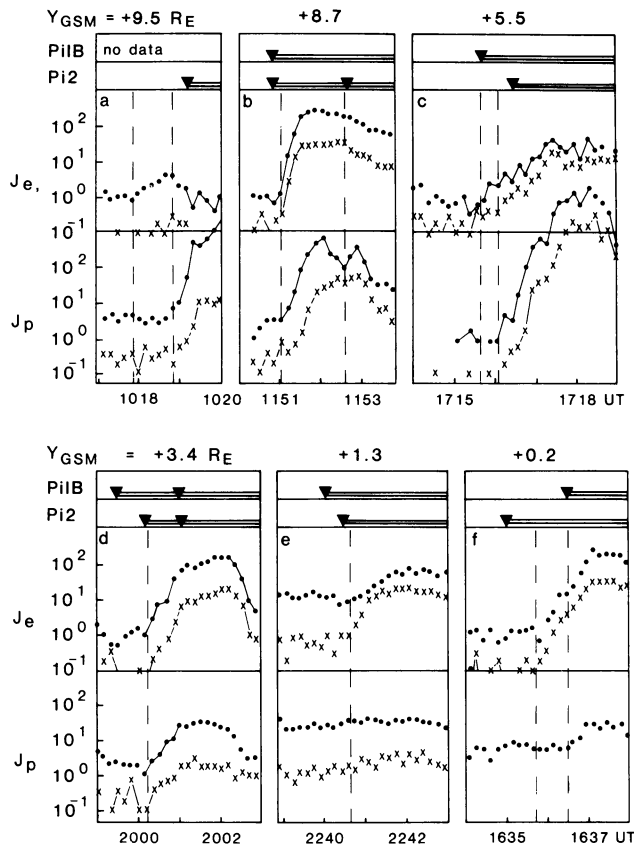


Fig. 8. Electron and proton count rates from two high-energy channels recorded by IMP-J during six strong substorm expansions ($AE > 500$ nT). The Y position of the satellite is given on the top ($x < -35 R_E$). The onset times of mid-latitude Pi2s and Pi1Bs in the auroral zone are indicated by the arrows and broken vertical lines

of occurrence of HE particle bursts was studied under similar conditions.

The proposed loop-type configuration of magnetic field lines tailward of the particle acceleration region is consistent with the “neutral line model” of Hones (1979), where the field lines beyond the neutral line are stretched into the far tail and closed across the equator tailward of the escaping plasmoid. According to recent ISEE-3 observations reported by Hones et al. (1984), a plasmoid reaches $x \sim -200 R_E$ some 20–30 min after the onset of a substorm, which means in our case that the length of the magnetic loop will be a few hundred R_E after an expansion phase of 25 min. Such a length partially explains both the almost isotropic pitch-angle distribution of the HE electrons between the brief bursts and the strong tailward anisotropy during some bursts. HE electrons travelling with a speed of $> 10 R_E/s$ take about 1 min to travel around the loop. Hence, during the first half-minute interval (when the acceleration power is increasing impulsively) the electrons are streaming mainly tailward, while during the second half (when the acceleration ceases) the anisotropy fades due to the returning electrons and their pitch-angle diffusion. The length of the magnetic loop depends on many parameters: e.g. the stage of expansion (i.e. the position of the plasmoid) and the amount of magnetic flux developed in the PS region during the pre-substorm condition.

Cross-tail extent of the acceleration region

HE particle observations made simultaneously by two spacecraft led Krimigis and Sarris (1979) to suggest that the extent of the acceleration region in the Y direction is only a few R_E ($<10 R_E$). As far as we know, there are no other published results dealing with this important parameter. Moreover, the same authors claim that observed HE particle bursts are sensitive to the Z coordinate of the spacecraft. This means that their conclusions should be approached with a certain degree of care, although our results are in compliance with their view.

The asymmetry of the HE protons and electrons in the dawn-dusk direction in Fig. 8 suggests an extent of $<8 R_E$ for the acceleration region (i.e. $<20\%$ of the total tail width). According to the various magnetospheric models (e.g. Tsyganenko, 1979) 1 h in MLT (15° in longitude) in the nightside auroral oval corresponds to a width of $3\text{--}4 R_E$ at $x \sim -15 R_E$. At 2001–2002 (i.e. towards the end of the first HE particle burst) the active auroras were confined between 108° and 120° CG Long, but a few minutes later at 2005 UT the width of the SCW was between 10° and 20° CG Long. In any case, the longitudinal width of the active region at the onset of the substorm was $<30^\circ$ ($=2$ h MLT), which means that the value $\Delta Y = 8 R_E$ serves well to characterize the upper limit of the dawn-dusk extent of the active region in the magnetotail.

Errors in magnetic projection between the equatorial magnetotail and the ionosphere are to be expected, due to deformation of the magnetic field in the PS during substorms. The relative displacement of the active regions in the ionosphere and its influence on the appearance of HE particle bursts at the satellite nevertheless allow us to draw some conclusions on the size of the active region in the Y direction. HE particle bursts are recorded at the satellite during the “eastern” cases in Fig. 4 (vortex centre within 10° CG Long of the estimated satellite projection meridian), while a $5^\circ\text{--}10^\circ$ CG Long westward shift of the vortex seems to prevent these observations. This sets the lower limit of the size of the acceleration region at $\Delta Y \sim 2\text{--}3 R_E$.

Impulse-related disturbances in the magnetic field and thermal plasma may appear more widely in the magnetotail due to different propagation modes, e.g. magnetosonic and magnetohydrodynamic waves. Long-term enhancements in HE particle fluxes due to drift and diffusion (like the observations after 2007 UT in our case) are also observed. Hence, brief field-aligned HE particle bursts are the most important tracers of the source region, since particles accelerated at source appear immediately on the magnetic field lines connected to the source.

According to the theoretical model of Pellinen and Heikila (1984), and more recently that of Zeleny et al. (1984), the inductive electric field in the proximity of the X-type neutral line and within the magnetic loop produces the observed characteristics of the HE particle bursts. The mechanism may be a non-linear (explosive) tearing process (Galeev, 1982), an assumption which would predict both the duration of the HE particle burst and the ΔY size of the acceleration region ($5\text{--}10 R_E$).

Conclusions

1. The present study of a dozen impulsive activations occurring during the first 25 min of a substorm in an approxi-

mately constant MLT sector enables us to extract information on the ground-based patterns associated with both short-lived (1–3 min) and longer-term variations.

2. The short-lived patterns appearing in the auroral zone during the impulsive activations are counterclockwise rotating differential equivalent current (vortex), enhancement in the CNA within the vortex and brightening and/or deformation of auroral structures in the same area. The appearance of the vortex is associated with Pi1B-type pulsations in the auroral zone and a change in Pi2 characteristics at mid-latitudes. The time constant of the vortex is 2–3 min and its diameter about 400 km.

3. Impulsive spikes of HE protons and electrons ($E > 0.2$ MeV) are observed in the far magnetotail ($37 R_E$) only in cases where the meridional projection of the satellite is near the vortex. Asymmetry in the occurrence of HE protons and electrons is observed within only $8 R_E$ across the tail. Our estimates give 2–8 R_E for the ΔY dimension of the acceleration region.

4. Stable signatures of closed magnetic field lines are observed within 25 min of the onset of the substorm in the plasma sheet boundary layer at $37 R_E$, well beyond the major acceleration region (X-type neutral line).

5. The substorm current wedge seems to integrate the effects of the elementary impulses. This leads to a longer time constant for the SCW (>10 min). The vortex formation and HE particle precipitation events jump between locations within the western part of the SCW.

6. A microsubstorm consists of several elementary impulses and is modulated by their intensity and spatial displacement.

Acknowledgements. IMP-J recordings of magnetic fields (Drs. N.F. Ness and R.P. Lepping, principal investigators) and energetic particles (Dr. D.J. Williams, principal investigator of the EPD experiment) were obtained through WDC-A (Rockets and Satellites) by courtesy of Dr. J.I. Vette. Digital magnetic field data from the Port Alfred and Kerguelen observatories were provided by WDC-A (geomagnetism). Other ground magnetic field data were obtained through WDC-B in Moscow. The riometer data from Finland were provided by the Sodankylä Geophysical Observatory. We are grateful to Drs. G.A. Loginov, Ya.M. Gogatishwili, B.I. Klain and L.N. Ivanova for allowing us to use their rapid-run and induction magnetometer recordings, and to all the colleagues who participated in the collection of the data for 3 March 1976. The SMA observations and the work of W. Baumjohann were supported financially by grants from the Deutsche Forschungsgemeinschaft. The work by V. Sergeev, R. Pellinen and T. Böisinger was supported by the Finnish-Soviet Committee on co-operation in science and technology.

References

- Aggson, T.L., Heppner, J.P.: Observations of large transient magnetospheric electric fields. *J. Geophys. Res.* **82**, 5155–5164, 1977
- Akasofu, S.-I.: Polar and magnetospheric substorms. Dordrecht: D. Reidel, 1968
- Akasofu, S.-I.: Physics of magnetospheric substorms. Dordrecht: D. Reidel 1977
- Baker, D.N., Akasofu, S.-I., Baumjohann, W., Bieber, J.M., Fairfield, D.H., Hones, E.W., McPherron, R.L., Moore, T.E.: Substorms in the magnetosphere. Chapter 8, Solar-terrestrial physics – present and future. K. Papadopoulos and D. Butler, eds. NASA, Washington, D.C., 1984
- Baumjohann, W., Mishin, V.M., Saifudinova, T.I., Shpynev, G.B., Bazarzhapov, A.D.: Substorms, microsubstorms and disruption of currents in the magnetospheric plasma sheet. *Issled. Geomagn. Aeron. Fys. Sol.* (in Russian), **53**, 182–191, 1981

- Boström, R.: Ionosphere-magnetosphere coupling. In: *Magnetospheric physics*, M. McCormack, ed.: pp. 45–59. Dordrecht: D. Reidel 1974
- Bösinger, T., Alanko, K., Kangas, J., Opgenoorth, H.I., Baumjohann, W.: Correlations between PiB type magnetic micropulsations, auroras and equivalent current structures during two isolated substorms. *J. Atmos. Terr. Phys.* **43**, 933–945, 1981
- Coroniti, F.V., Frank, L.A., Williams, D.J., Lepping, R.P., Scarf, F.L., Krimigis, S.M., Gloeckler, G.: Variability of plasma sheet dynamics. *J. Geophys. Res.* **85**, 2957–2977, 1980
- Fairfield, D.H., Lepping, R.P., Hones, E.W., Bame, S.I., Asbridge, J.R.: Simultaneous measurements of magnetotail dynamics by IMP spacecrafts. *J. Geophys. Res.* **86**, 1396–1414, 1981
- Galeev, A.A.: Magnetospheric tail dynamics. In: *Magnetospheric plasma physics*. A. Nishida, ed.: p. 143. Center for Academic Publ. Japan, 1982
- Hill, T.W., Reiff, P.H.: Plasma sheet dynamics and magnetospheric substorms. *Planet. Space Sci.* **28**, 363–374, 1980
- Hones, E.W.: Plasma flow in the magnetotail and its implications for substorm theories. In: *Dynamics of the magnetosphere*. S.-I. Akasofu, ed.: pp. 545–562. Dordrecht: D. Reidel 1979
- Hones, E.W., Karas, R.H., Lanzerotti, L.I., Akasofu, S.-I.: Magnetospheric substorms on September 14, 1968. *J. Geophys. Res.* **76**, 6765–6780, 1971
- Hones, E.W., Baker, D.N., Bame, S.J., Feldman, W.C., Gosling, J.T., McComas, D.J., Zwickl, R.D., Slavin, J.A., Smith, E.J., Tsurutani, B.T.: Structure of the magnetotail at 220 R_E and its response to geomagnetic activity. *Geophys. Res. Lett.* **11**, 5–7, 1984
- Kaila, K.U.: Three-dimensional mapping of the aurora from digitized all-sky pictures. *Finn. Met. Inst., Technical Report No. 25*, 38, 1981
- Kamide, Y., Baumjohann, W.: Estimation of electric fields and currents from IMS magnetometer data for the CDAW-6 intervals: Implications for substorm dynamics. *J. Geophys. Res.* **90**, 1305–1317, 1985
- Krimigis, S.M., Sarris, F.T.: Energetic particle bursts in the Earth's magnetotail. In: *Dynamics of the magnetosphere*, S.-I. Akasofu, ed.: pp. 599–630. Dordrecht: D. Reidel 1979
- Küppers, F., Untiedt, J., Baumjohann, W., Lange, K., Jones, A.G.: A two-dimensional magnetometer array for ground-based observations of auroral zone currents during IMS. *J. Geophys. Res.* **46**, 429–450, 1979
- Maltsev, Yu.P., Leontyev, S.V., Lyatsky, W.B.: Pi2 pulsations as a result of evolution of an Alfvén impulse originated in the ionosphere during a brightening of aurora. *Planet. Space Sci.* **22**, 1519–1533, 1974
- McPherron, R.L., Russel, C.T., Aubry, M.P.: Satellite studies of magnetospheric substorms on August 15, 1968 (9). *J. Geophys. Res.* **78**, 3131–3147, 1973
- Melnikov, A.O., Khrushinsky, A.A., Zhulin, I.A., Kornilov, I.A., Lazutin, L.L., Raspopov, O.M., Riedler, V.K., Sakharov, Ya.A., Tagirov, V.R., Treilhou, T.P.: X-ray burst structure of break-up and Pi2 geomagnetic pulsations. In: *Dynamical processes and structure of auroral magnetosphere (SAMBO experiment)* (in Russian). Ed. Kola Branch Acad. Sci. USSR, pp. 28–42. Apatity 1976
- Mishin, V.M., Nemtsova, E.I., Saifudinova, T.I., Urbanovich, V.D., Loginov, G.A., Sergeev, V.A., Danilov, A.A., Sobolev, A.V., Solovjev, S.I., Zaitsev, A.N., Lyubimova, N.P., Shevnina, N.F., Baumjohann, W.: Results of observations during substorms on March 3, 1976. 2. Data of geomagnetic observations. Preprint SibIZMIR N1–82, Irkutsk, 1982
- Opgenoorth, H.I., Pellinen, R.J., Maurer, H., Küppers, F., Heikkila, W.J., Kaila, K.U., Tanskanen, P.: Ground-based observations of an onset of localized field-aligned currents during auroral break-up around magnetic midnight. *J. Geophys. Res.* **48**, 101–115, 1980
- Pellinen, R., Heikkila, W.J.: Inductive electric fields in the magnetotail and their relation to auroral and substorm phenomena. *Space Sci. Rev.* **37**, 1–61, 1984
- Pellinen, R.J., Baumjohann, W., Heikkila, W.J., Sergeev, V.A., Yahnin, A.G., Marklund, G., Melnikov, A.O.: Event study on pre-substorm phases and their relation to the energy coupling between solar wind and magnetosphere. *Planet. Space Sci.* **30**, 371–388, 1982
- Pytte, T., McPherron, R.L., Kivelson, M.G., West, H.I., Hones, E.W.: Multiple-satellite studies of magnetospheric substorm. Radial dynamics of the plasma sheet. *J. Geophys. Res.* **81**, 5921–5933, 1976a
- Pytte, T., Trefall, H., Kremser, G., Tanskanen, P., Riedler, W.: On the morphology of energetic (> 30 keV) electron precipitation at the onset of negative magnetic bays. *J. Atmos. Terr. Phys.* **38**, 757–773, 1976b
- Pytte, T., McPherron, R.L., Kokubun, S.: The ground signatures of the expansion phase during multiple-onset substorms. *Planet. Space Sci.* **24**, 1115–1132, 1976c
- Pytte, T., McPherron, R.L., Kivelson, M.G., West, H.I., Hones, E.W.: Multiple-satellite studies of magnetospheric substorms: Plasma sheet recovery and the poleward leap of auroral activity. *J. Geophys. Res.* **83**, 5256–5268, 1978
- Ranta, H., Ranta, A., Collis, P.N., Hargreaves, J.K.: Development of the auroral absorption substorm: Studies of pre-onset phase and sharp onset using an extensive riometer network. *Planet. Space Sci.* **29**, 1287–1313, 1981
- Rostoker, G., Akasofu, S.-I., Foster, J., Greenwald, R.A., Kamide, Y., Kawasaki, K., Lui, A.T.Y., McPherron, R.L., Russell, C.T.: Magnetospheric Substorms-Definition and Signatures. *J. Geophys. Res.* **85**, 1663–1668, 1980
- Sato, T., Hayashi, T., Walker, R.J., Ashour-Abdalla, M.: Neutral sheet current interruption and field-aligned current generation by three-dimensional driven reconnection. *Geophys. Res. Lett.* **10**, 221–224, 1983
- Semenov, V.S., Sergeev, V.A.: A simple semi-empirical model for magnetospheric substorm. *Planet. Space Sci.* **29**, 271–281, 1981
- Sergeev, V.A.: On the longitudinal localization of substorm active region and its changes during the substorm. *Planet. Space Sci.* **22**, 1341–1343, 1974
- Sergeev, V.A.: On the state of magnetosphere during prolonged periods of southward oriented IMF. *Phys. Solariterr., Potsdam N 5*, 39–50, 1977
- Sergeev, V.A.: High-time resolution correlation between the magnetic field behaviour at 37 R_E distance in the magnetotail plasma sheet and ground phenomena during substorm expansion phase. *J. Geophys. Res.* **49**, 176–185, 1981
- Sergeev, V.A., Yahnin, A.G.: The features of auroral bulge expansion. *Planet. Space Sci.* **27**, 1429–1444, 1979
- Sergeev, V.A., Yahnin, A.G., Raspopov, O.M.: On the spatial-temporal structure of the expansive phase of microsubstorm. In: *Dynamical processes and structure of auroral magnetosphere* (in Russian). O.M. Raspopov, L.L. Lazutin, eds.: pp. 42–54. Apatity 1978
- Sergeev, V.A., Yahnin, A.G., Gorely, K.I., Danielson, C., Pellinen, R.J., Samsonov, V.P., Urbanovich, V.D., Latov, Yu.O., Ranta, H., Stauning, P., Armstrong, T.P., Hones, E.W., Krimigis, S.M., Lepping, R.P., Ness, N.F.: Results of observations during substorms on March 3, 1976. 1. Auroral precipitation data and measurements in the magnetotail. Polar Geophysical Institute preprint PGI-81-1, Apatity 1981
- Sergeev, V.A., Bösinger, T., Lui, A.T.Y.: Impulsive processes in the magnetotail during substorm expansion. *J. Geophys.*, 1986 this issue.
- Troshichev, O.A., Kuznetsov, B.M., Pudovkin, M.I.: The current systems of the magnetic substorm growth and expansion phases. *Planet. Space Sci.* **22**, 1403–1412, 1974
- Tsyganenko, N.A.: The subroutines and tables for calculation of geomagnetic field. WDC-B report, Moscow 1979
- Untiedt, J., Pellinen, R., Küppers, F., Opgenoorth, H.J., Pelster, W.D., Baumjohann, W., Ranta, H., Kangas, J., Chechowsky, P., Heikkila, W.J.: Observations of the initial development of an auroral and magnetic substorm at magnetic midnight. *J. Geophys. Res.* **45**, 41–65, 1978

- Vasyliiev, E.P., Malkov, M.V., Sergeev, V.A.: Three-dimensional effects of substorm current wedge. *Geomagn. Aeronomy (in Russian)* **26**, 114–119, 1986
- Vorobjev, V.G., Rezhenov, B.V.: Progressive westward displacements of the region of the auroral substorm localization in conjunction with impulsive variations of the magnetic field. *Inst. Ass. Geomag. Aeron. Bull.* **34**, 441–449, 1973
- Wiens, R.G., Rostoker, G.: Characteristics of the development of the westward electrojet during the expansive phase of the magnetospheric substorm. *J. Geophys. Res.* **30**, 2109–2128, 1975
- Yahnin, A.G., Sergeev, V.A., Pellinen, R.J., Baumjohann, W., Kaila, K., Ranta, H., Kangas, J., Raspopov, O.M.: Substorm time sequence and microstructure on November 11, 1976. *J. Geophys.* **53**, 182–197, 1983
- Yahnin, A.G., Sergeev, V.A., Ievenko, I.B., Solovjev, S.I., Rakhmatulin, R.: Characteristics of phenomena, accompanied by the local flares of discrete auroras. In: *Magnetospheric Res. (in Russian)* **5**, 93–110, 1984
- Zeleny, L.M., Lipatov, A.S., Lominadze, D.G., Taktakishvili, A.L.: The dynamics of the energetic proton bursts in the course of the magnetic field topology reconstruction in the Earth's magnetotail. *Planet. Space Sci.* **32**, 313–324, 1984

Received July 23, 1985 / Revised June 5, 1986

Accepted July 21, 1986

Short communication

Seismic signal velocity in absorbing media

T. Schmidt and G. Müller

Institute of Meteorology and Geophysics, University of Frankfurt, Feldbergstr. 47, 6000 Frankfurt, Federal Republic of Germany

Abstract. One-dimensional synthetic-seismogram calculations are reported for homogeneous media with a quality factor which depends on frequency according to a power law. The purpose is to find out with which signal velocity, i.e. onset velocity, the weakly dispersed body-wave pulses propagate. Three types of seismic waves are simulated: (1) long-period teleseismic P and S waves, (2) short-period regional S waves, (3) P_g waves in explosion seismology. In all cases the signal velocity is close to the group velocity at the dominant period of the source pulse. Phase velocity describes the onsets less accurately. The difference between group and phase velocity becomes significant when the dissipation time t^* exceeds the dominant period. This is the case when the propagation distance exceeds Q times the dominant wavelength.

Key words: Absorption – Group velocity – Phase velocity – Signal velocity

Introduction

Absorption of seismic waves is connected with weak dispersion. Even in a homogeneous medium plane-wave propagation (or far-field propagation from a point source) is characterized by pulse-form changes, and it is not clear with which velocity a special feature of the pulse, e.g. the onset, an extremum or a zero crossing propagates. For seismological applications the most interesting question is with which velocity the wave onset travels. Our definition of the wave onset refers to the time at which about 1% of the maximum amplitude is reached; this definition is plausible for noise-free and unclipped seismic body-wave pulses, as the seismogram examples given later show. The onset velocity will be called signal velocity, in agreement with the definition by Brillouin (1960). The specific question that we will attempt to answer is the following: is signal velocity closer to phase velocity or to group velocity at a representative frequency of the wave, or can neither of these velocities be preferred? The usual stationary-phase argument by which group velocity is favoured works only in cases with well-developed dispersion, where a particular frequency can be assigned to a particular time, but not in cases of weak

dispersion, where a wave pulse experiences broadening and amplitude decay, but remains a pulse.

The literature on the dispersion of seismic body waves offers quite different answers to the question posed. For instance, Futterman (1962, p. 5281) states: "For sufficiently small absorption group velocity can be identified with the velocity with which a measured signal propagates ...". Similarly, Brennan and Stacey (1977) remark on group velocity: "This is the observed velocity in the case of a body wave ...". A less definitive statement is from Carpenter (1981, p. 422f): "Neither the phase velocity ... nor the group velocity ... are appropriate ...". Similarly, Minster (1980, p. 180) writes: "This implies that the average signal velocity from the origin decreases as time and distance increase". In another paper this author calculates travel times in an earth model from phase velocities (Minster, 1978). Finally, Strick (1970), Kjartansson (1979) and Chin (1980) in papers on one-dimensional waves in viscoelastic media discuss travel-time aspects, partly at great length, without mentioning group velocity at all. This brief survey of some of the literature illustrates that the question of seismic signal velocity in absorbing media needs more study. It is shown below that accurate numerical calculations can settle the problem for absorptive conditions as they exist in the earth.

Before presenting these results we discuss briefly a theoretical argument, and its limitations, in favour of group velocity as the essential velocity for body-wave travel times. For the sake of simplicity we consider a plane wave in a weakly dispersive elastic medium. The Fourier representation of this wave is

$$S(z, t) = \frac{1}{\pi} \operatorname{Re} \int_0^{\infty} \bar{S}(0, \omega) e^{j(\omega t - kz)} d\omega, \quad (1)$$

where $\bar{S}(0, \omega)$ is the wave spectrum at $z=0$. In the case of weak dispersion, the real wavenumber $k(\omega)$ can be approximated linearly:

$$k(\omega) = k(\omega_0) + k'(\omega_0)(\omega - \omega_0) \\ = \left(\frac{1}{c_0} - \frac{1}{U_0} \right) \omega_0 + \frac{\omega}{U_0}. \quad (2)$$

Here $c_0 = c(\omega_0) = \omega_0/k(\omega_0)$ is the phase velocity and $U_0 = U(\omega_0) = 1/k'(\omega_0)$ the group velocity at the frequency ω_0 which is taken in the frequency band of the input. Inserting

Eq. (2) into Eq. (1) yields the following exact result:

$$S(z, t) = \cos \chi \cdot S \left(0, t - \frac{z}{U_0} \right) - \sin \chi \cdot S_H \left(0, t - \frac{z}{U_0} \right), \quad (3)$$

$$\chi = \left(\frac{1}{c_0} - \frac{1}{U_0} \right) \omega_0 z.$$

$S_H(0, t)$ is the Hilbert transform of the waveform $S(0, t)$ at $z=0$. The dispersed wave at coordinate z , therefore, is a linear combination of the source pulse and its Hilbert transform, delayed by the *group* travel time z/U_0 . This result can be considered as giving some support to the statement that it is group velocity, and not phase velocity, which determines onset times. Brillouin (1960), in a discussion of mainly electromagnetic waves which includes contributions by Sommerfeld and others from the early twentieth century, presents analytical calculations with a similar result. However, the weights $\cos \chi$ and $\sin \chi$ in Eq. (3) depend on z such that, as expected, the pulse form changes with z and hence also the character of the onset. Moreover, it is not immediately evident which frequency ω_0 should be chosen; it is plausible, but not necessary, to take the dominant frequency. More definitive conclusions can only be derived from numerical experiments.

Synthetic seismograms

We have investigated one-dimensional wave propagation in a homogeneous medium whose anelastic quality factor has power-law dependence on frequency:

$$Q(\omega) = Q(\omega_r) \left(\frac{\omega}{\omega_r} \right)^\gamma, \quad 0 \leq \gamma < 1. \quad (4)$$

Here ω_r is a reference frequency at which Q is known. Equation (4) represents cases with practical relevance for seismology: $\gamma=0$ is the often-used case of constant Q , and positive γ values have been suggested on the basis of seismological observations (Anderson and Minster, 1979; Ulug and Berckhemer, 1984; Schmidt, 1986) and laboratory experiments (Berckhemer et al., 1982; Kampfmann, 1984).

The velocity dispersion of a medium with Q according to Eq. (4) has been investigated, among others, by Brennan (1980) and Müller (1983). The phase velocity $c(\omega)$, the group velocity $U(\omega)$ and the dissipation operator $A(\omega, z)$ are ($0 < \gamma < 1$):

$$c(\omega) = c(\omega_r) \left\{ 1 + \frac{1}{2Q(\omega_r)} \cot \frac{\gamma\pi}{2} \left[1 - \left(\frac{\omega_r}{\omega} \right)^\gamma \right] \right\}, \quad (5)$$

$$U(\omega) = c(\omega) / \left(1 - \frac{\gamma}{2Q(\omega)} \cot \frac{\gamma\pi}{2} \right), \quad (6)$$

$$A(\omega, z) = \exp \left\{ - \frac{\omega z}{2c(\omega_r)Q(\omega_r)} \left(\left(\frac{\omega_r}{\omega} \right)^\gamma - j \cot \frac{\gamma\pi}{2} \left[1 - \left(\frac{\omega_r}{\omega} \right)^\gamma \right] \right) \right\}. \quad (7)$$

The results for frequency-independent Q ($\gamma=0$) are:

$$c(\omega) = c(\omega_r) \left(1 + \frac{1}{\pi Q} \ln \frac{\omega}{\omega_r} \right), \quad (8)$$

Table 1. Parameters of the wave-propagation cases studied

Case	T (s)	$\omega_r/2\pi$ (Hz)	$c(\omega_r)$ (km/s)	$Q(\omega_r)$	γ	z (km)
Long-period $\begin{matrix} P \\ S \end{matrix}$	10	1	10 6	600 300	0, 0.3	0–10,000
Short-period S	1	1	6	300	0.3	0–4,000
Explosion seismology (P_g phase)	0.1	1	5	200	0.3	0–100

$$U(\omega) = c(\omega) / \left(1 - \frac{1}{\pi Q} \right), \quad (9)$$

$$A(\omega, z) = \exp \left\{ - \frac{\omega z}{2c(\omega_r)Q} \left(1 - \frac{2j}{\pi} \ln \frac{\omega}{\omega_r} \right) \right\}. \quad (10)$$

The dispersion implied by Eqs. (5) and (6) or by Eqs. (8) and (9) is anomalous ($U > c$) and inverse (U increases with frequency). A few numerical results for c and U can be found in Müller (1983).

The meaning of the dissipation operators (7) and (10) is the following. The wave spectrum at the coordinate z in an anelastic medium is obtained from the elastic spectrum, corresponding to propagation with the known phase velocity $c(\omega_r)$ at the reference frequency, through multiplication by $A(\omega, z)$:

$$\bar{S}(z, \omega) = \bar{S}(0, \omega) e^{-j\omega z/c(\omega_r)} A(\omega, z). \quad (11)$$

Equations (5)–(11) are practically exact for frequencies for which dissipation is slight [$Q(\omega) \gg 1$]; at least several frequency decades above and below ω_r can be considered, if $Q(\omega_r) \gg 1$ and γ is not too close to 1. In the cases studied below, the condition $Q(\omega) \gg 1$ is always satisfied.

Equation (11) has been used to calculate synthetic seismograms $S(z, t)$ for the source pulse $S(0, t) = \sin(2\pi t/T) - 0.5 \sin(4\pi t/T)$, normalized to unit amplitude ($0 \leq t \leq T$). T is the dominant period of the input, and the spectrum is effectively confined to frequencies from 0 to $3/T$. Three different cases have been studied: the first simulates propagation of long-period body waves to teleseismic distances, the second corresponds to the propagation of short-period S waves to regional distances and the third simulates the P_g wave of explosion seismology. Table 1 summarizes the parameters of the three cases. The numerical calculation of synthetic seismograms in the frequency domain via Eq. (11) poses no problems; in order to avoid time-domain aliasing, which can be severe for larger propagation distances, we used the standard method of complex frequencies. The seismograms calculated in this way can be considered as exact and thus well suited for inferences on travel times and signal velocity.

The synthetic record sections in Figs. 1–3 have been reduced with the velocity $c(\omega_r)$. Each seismogram is normalized by its maximum amplitude. This is the adequate procedure for a theoretical study of signal velocity; it agrees also with the routine practice of seismograms display in explosion seismology. The tick marks in the seismograms correspond to the time when the amplitude has reached 1% of the maximum amplitude. This is approximately the time where an observer would place the onset in a noise-free and unclipped trace. The straight travel-time lines in the

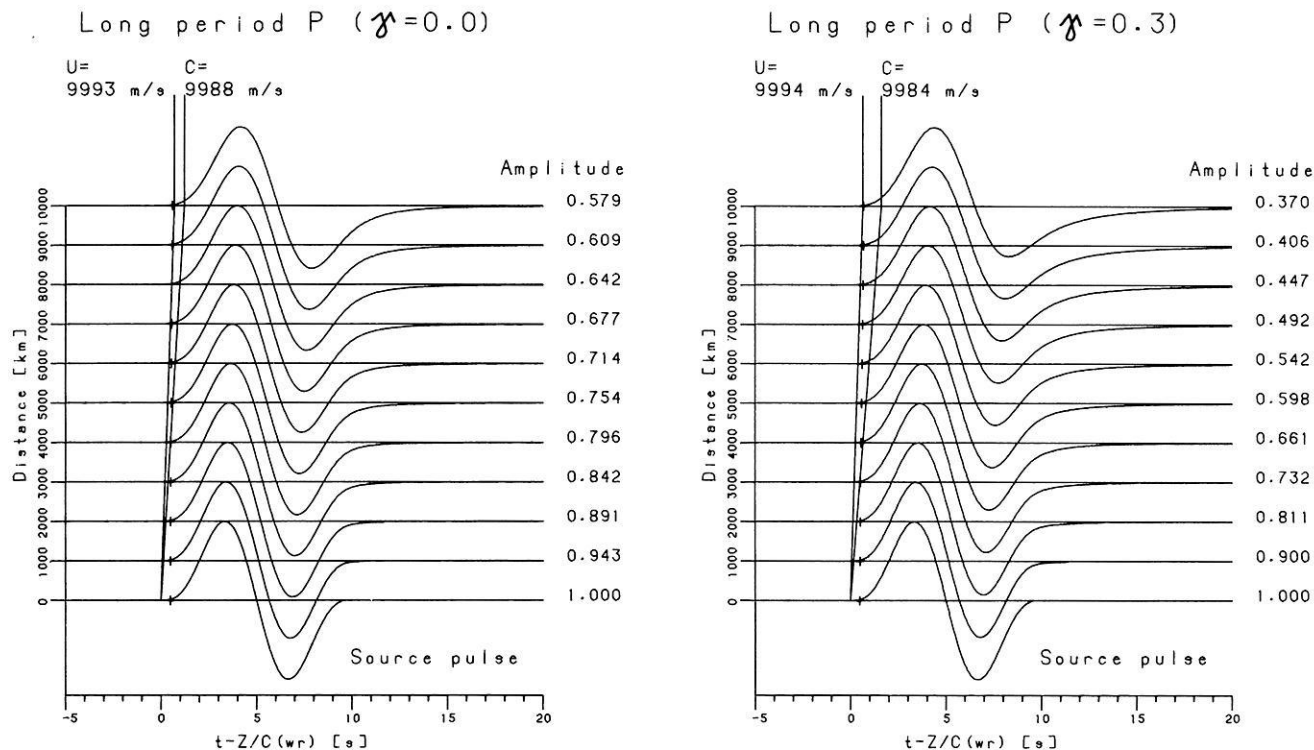


Fig. 1. Synthetic seismograms for the long-period P -wave case of Table 1; $\gamma=0$ (left) and $\gamma=0.3$ (right). The seismograms are normalized, with peak amplitudes given at the end of the traces. The tick marks corresponds to 1% of the peak amplitudes. The travel-time lines follow from group velocity U and phase velocity c , respectively, at the dominant frequency of the source pulse

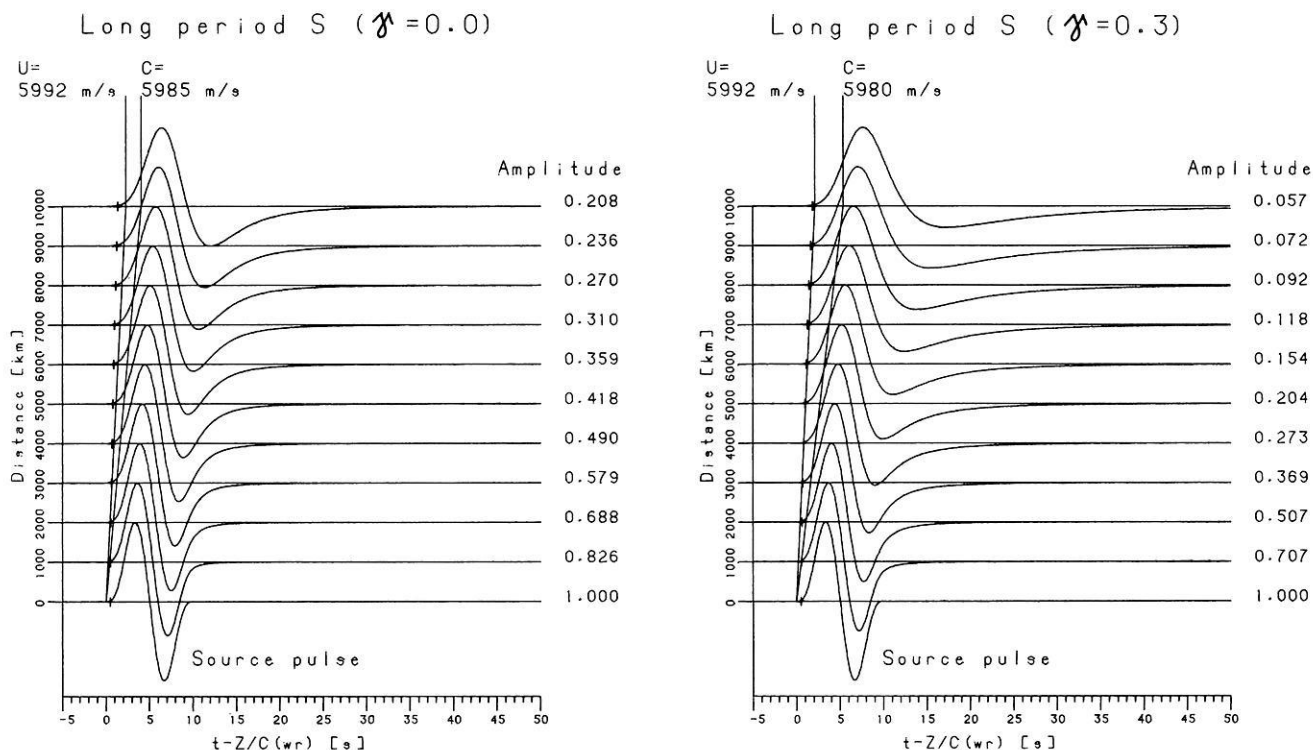


Fig. 2. The same as Fig. 1 for the long-period S -wave case

record sections start at $z=0$ and correspond to the phase and the group velocity, respectively, taken at the dominant frequency $1/T$ of the source pulse. It is obvious that in all sections group velocity explains the onsets at larger distances considerably better than phase velocity. Only at short

distances is phase velocity sometimes better suited, in particular in the case of Fig. 1. However, at these distances the difference between group-velocity travel time and phase-velocity travel time is so small, compared with the pulse duration, that it is of no interest to discriminate the two.

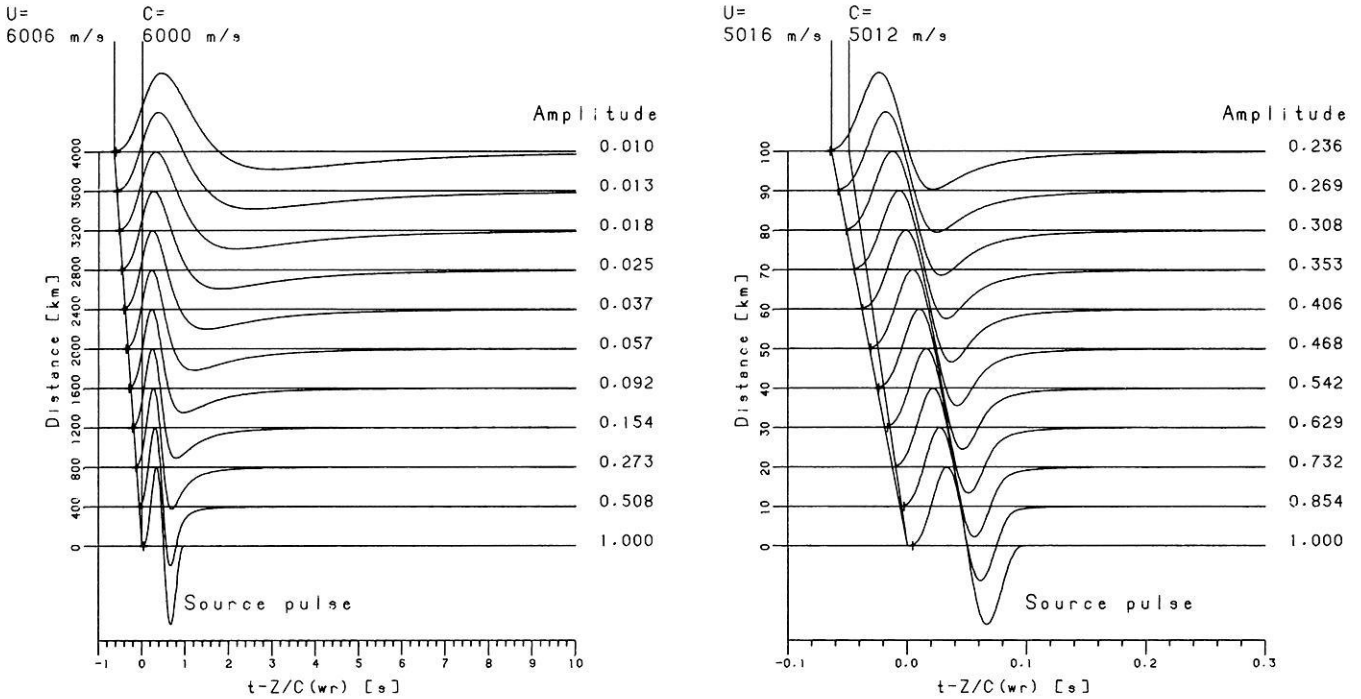
Short period S ($\gamma=0.3$)Pg phase ($\gamma=0.3$)

Fig. 3. The same as Fig. 1 for the short-period S-wave case (left) and the explosion-seismology case (right)

Thus, the conclusion from all three cases investigated is that the signal velocity is well represented by group velocity at the dominant frequency of the wave at the source; phase velocity usually is less accurate in explaining onset times.

Discussion and conclusions

Our results are numerical and apply, strictly speaking, only in the particular case studied, characterized by the Q law (4) and the source pulse chosen above. However, these results certainly are typical and apply also in other cases where the source spectrum is bandlimited with a relatively well-defined dominant frequency, and where significant absorption exists in this frequency band.

It is of interest to have a rule of thumb, by which one can approximately decide when it is advisable to work with group rather than phase velocity. Group velocity should be chosen when the travel-time difference $z/c(\omega) - z/U(\omega)$ at the dominant frequency $\omega = 2\pi/T$ exceeds a significant fraction of the dominant period T , say T/π . Inserting Eqs. (5) and (6) gives a simple condition in terms of the dissipation time $t^* = z/[c(\omega)Q(\omega)]$ at the dominant frequency:

$$\frac{t^*}{T} > \frac{1}{\frac{\gamma\pi}{2} \cot \frac{\gamma\pi}{2}}. \quad (12)$$

The function on the right side of Eq. (12) is 1 for $\gamma \rightarrow 0$, 1.05 for $\gamma = 0.25$ and 1.27 for $\gamma = 0.5$. Thus, for a relatively broad range of γ values the right side of Eq. (12) is about 1. The conclusion, then, is that the difference between group and phase velocity becomes significant if the dissipation time t^* exceeds the dominant wave period T . In this case,

one should use the group velocity for travel-time calculations. The condition $t^* > T$ can be translated into the condition $z > \lambda Q$ for the propagation distance z , where λ is the dominant wavelength and Q corresponds to the dominant frequency.

A conclusion from our investigations, with perhaps some practical relevance, concerns the Preliminary Reference Earth Model (PREM) of Dziewonski and Anderson (1981). In the construction of PREM, velocity dispersion was assumed to follow the laws for frequency-independent Q , but body-wave travel times were calculated with the phase velocity (8) rather than the group velocity (9). According to our results, the joint inversion of free-oscillation periods and travel times should, in principle, incorporate the distinction of phase and group velocity. In practice, this distinction may be marginally relevant for S waves. Should PREM be revised in the future, it may be reasonable to calculate body-wave travel times with group velocity.

Finally, we want to emphasize the approximate nature of the statement that signal velocity agrees with group velocity at about the dominant frequency of the source pulse. This agreement is valid when the shift of the dominant frequency with increasing propagation distance is moderate, such that the dominant frequency of the source pulse is present also at large distances. If this frequency is completely lost, either due to strong absorption or due to extremely long propagation distances, group velocity at this frequency also loses its significance. Signal velocity then becomes distance-dependent, and the group velocity at about the local dominant frequency may well be a good approximation. We have not tested this idea numerically since in the earth extremely strong absorption, connected with amplitude decay by orders of magnitude, normally does not occur.

Acknowledgements. We obtained several stimulating and helpful comments on the first draft of this paper by Hans Berckhemer, Dieter Seidl, Erhard Wielandt and Walter Zürn. We also thank Ingrid Hörnchen for typing the manuscript.

References

- Anderson, D.L., Minster, J.B.: The frequency dependence of Q in the earth and implications for mantle rheology and Chandler wobble. *Geophys. J.R. Astron. Soc.* **58**, 431–440, 1979
- Berckhemer, H., Kampfmann, W., Aulbach, E., Schmeling, H.: Shear modulus and Q for forsterite and dunite near partial melting from forced oscillation experiments. *Phys. Earth Planet. Inter.* **29**, 30–41, 1982
- Brennan, B.J.: Pulse propagation in media with frequency-dependent Q . *Geophys. Res. Lett.* **7**, 211–213, 1980
- Brennan, B.J., Stacey, F.D.: Frequency dependence of elasticity of rock – test of seismic velocity dispersion. *Nature* **268**, 220–222, 1977
- Brillouin, L.: Wave propagation and group velocity. New York: Academic Press 1960
- Carpenter, E.W.: Absorption of elastic waves – an operator for a constant Q mechanism. In: *Seismic wave attenuation*. M.N. Toksöz, D.H. Johnston, eds.: pp. 418–430. Tulsa: Society of Exploration Geophysicists 1981 (original publication 1966)
- Chin, R.C.Y.: Wave propagation in viscoelastic media. In: *Physics of the earth's interior*. A. Dziewonski, E. Boschi, eds.: pp. 213–246. Amsterdam: North-Holland 1980
- Dziewonski, A.M., Anderson, D.L.: Preliminary reference earth model. *Phys. Earth Planet. Inter.* **25**, 297–356, 1981
- Futterman, W.I.: Dispersive body waves. *J. Geophys. Res.* **67**, 5279–5291, 1962
- Kampfmann, W.: Laborexperimente zum elastischen und anelastischen Verhalten hochtemperierter magmatischer Gesteine im Frequenzbereich seismischer Wellen. Ph.D. thesis, University of Frankfurt, 1984
- Kjartansson, E.: Constant Q -wave propagation and attenuation. *J. Geophys. Res.* **84**, 4737–4748, 1979
- Minster, J.B.: Transient and impulse responses of a one-dimensional linearly attenuating medium – II. A parametric study. *Geophys. J.R. Astron. Soc.* **52**, 503–524, 1978
- Minster, J.B.: Anelasticity and attenuation. In: *Physics of the earth's interior*. A. Dziewonski, E. Boschi, eds.: pp. 152–212. Amsterdam: North-Holland 1980
- Müller, G.: Rheological properties and velocity dispersion of a medium with power-law dependence of Q on frequency. *J. Geophys.* **54**, 20–29, 1983
- Schmidt, T.: Untersuchungen zur Absorption und Dispersion von Raumwellen. Diploma thesis, University of Frankfurt, 1986
- Strick, E.: A predicted pedestal effect for pulse propagation in constant- Q solids. *Geophysics* **35**, 387–403, 1970
- Ulug, A., Berckhemer, H.: Frequency dependence of Q for seismic body waves in the Earth's mantle. *J. Geophys.* **56**, 9–19, 1984

Received August 15, 1986; revised October 24, 1986

Accepted October 28, 1986

In memoriam

Nachruf Professor Ludwig Biermann



Ludwig Biermann wurde am 13. 3. 1907 als Sohn eines Richters in Hamm geboren. Das juristisch orientierte, geistig rege Elternhaus prägte ihn. Den Stil der juristischen Argumentation, die sich in erster Linie auf Zitate stützt, hat er nie ganz abgelegt. Nach einem Studium an verschiedenen Universitäten kam er nach Göttingen zu Hans Kienle, wo er 1932 mit einer Arbeit über „Konvektionszonen im Innern der Sterne“ promovierte. Dieses Thema war insofern besonders aktuell, da einerseits Atkinson und Houtermans gezeigt hatten, wie die Sterne durch Kernreaktionen ihre Strahlungsenergie gewinnen können, andererseits Ludwig Prandtl in seiner Mischungswegtheorie eine brauchbare Methode zur Behandlung des Energietransports durch turbulente Konvektion bereitgestellt hatte. Sternstruktur und Sternentwicklung zusammen mit turbulenter Konvektion sind deshalb auch die Themen, die Ludwig Biermann in der Folge beschäftigen. Von Göttingen aus geht er nach Jena und von da 1937 an die Babelsberger Sternwarte. Hier greift er ein weiteres Arbeitsgebiet auf, das durch die neuen großen Teleskope akut geworden war, nämlich die Berechnung zuverlässiger atomarer Daten als Grundlage für die Deutung von Sternspektren. Während des Krieges finden

wir ihn teils in Babelsberg, teils in Hamburg, wo er nach dem Zusammenbruch noch weitere zwei Jahre als Diäten-dozent tätig ist. Dankbar vermerkt er die Hilfe, die er in dieser schwierigen Zeit bei den ausgedehnten numerischen Rechnungen zur Bestimmung von atomaren Übergangswahrscheinlichkeiten erfährt. Aufschwung erhielten diese Arbeiten aber besonders, als er 1947 in Göttingen eine Rechengruppe übernehmen konnte, die wegen des Verbots aerodynamischer Forschung arbeitslos war. So entscheidet er sich zwischen einem Ruf an die Universität Hamburg und einem an das Max-Planck-Institut für Physik in Göttingen für letzteres. Hier baute er die Abteilung für Astrophysik auf. Sein breit gestreutes Interesse fand und gab Anregung im Zusammenwirken mit Werner Heisenberg, Carl-Friedrich von Weizsäcker und Karl Wirtz. Schon 1948, als menschliche Arbeit billig und Technik teuer war, erkannte Ludwig Biermann, daß zur Bewältigung größerer numerischer Rechnungen auf die Dauer die Beschäftigung einer Rechengruppe nicht genügt. Er sorgte dafür, daß Heinz Billing, der zur Verwirklichung seiner Vorstellung von einem automatischen Rechner nach Australien gegangen war, an das Max-Planck-Institut für Instrumentenkunde zurückberufen wurde.

Vier Jahre nach seiner Berufung durch Heisenberg wird Biermann 1951 auch formal wissenschaftliches Mitglied des Max-Planck-Instituts für Physik. Ein Jahr später, im Herbst 1952 lief die erste in Göttingen entworfene und gebaute Rechenmaschine G1, eine lochbandgesteuerte Relaismaschine mit 26 Speicherplätzen, davon 4×4 zyklisch vertauschbaren. Wir haben damit unsere Atomfunktionen (Hartree-Fock mit „Konfigurationsmischung“) und „Störmerbahnen“ (Bahnen geladener Teilchen im Erdmagnetfeld) gerechnet. Sogar partielle Differentialgleichungen wurden damit gelöst. Zwei weitere größere Maschinen sollten in der Folge noch gebaut werden, bevor diese Aktivitäten endgültig der Industrie überlassen wurden.

Die Beschäftigung mit der Physik der Sonnenatmosphäre – Konvektionszone, Magnetfelder – zusammen mit Kometenbeobachtungen – die ionisierten Gasschweife zeigen eine Beschleunigung, die weit über den Strahlungsdruck des Sonnenlichts hinausgeht – führten Anfang der 50er Jahre Biermann dazu, einen ständigen von der Sonne emittierten Teilchenstrom anzunehmen, den „Sonnenwind“. Nachdem dieser Sonnenwind zunächst bei vielen Kollegen auf Skepsis gestoßen war, konnte er rund 10 Jahre später

im Oktober 1962 von der Raumsonde Mariner 2 gemessen werden. Heute prägt der Sonnenwind und seine Wechselwirkung mit dem Erdmagnetfeld unsere Vorstellung von der magnetischen Umgebung der Erde. Er dient der Erklärung der erdmagnetischen Aktivität und ist damit auch für die Geophysik von grundlegender Bedeutung.

Ein Zentralthema in Prof. Biermanns Abteilung wurde nun die Entwicklung der Magnetohydrodynamik, mit deren Hilfe man die kontrollierte Kernverschmelzung in den Griff zu bekommen hoffte. Wieder war es Ludwig Biermann, der schon frühzeitig darauf drang, daß auch bei uns die Fusionsforschung im nötigen institutionellen Rahmen aufgegriffen wurde. 1960 wurde das Institut für Plasmaphysik gegründet. Als Leiter der theoretischen Abteilung wurde Biermanns langjähriger Mitarbeiter Arnulf Schlüter berufen.

Das Jahr 1958 bringt eine Umorganisation des Instituts. Ein Teil unter Karl Wirtz geht nach Karlsruhe an das neugegründete Kernforschungszentrum. Der Rest siedelt nach München über. In Anbetracht ihres großen Forschungspotentials wird die Abteilung Astrophysik zum Teilinstitut erhoben. Zu ihm gehört auch die Abteilung Numerische Rechenmaschinen unter Heinz Billing. Der Name des Gesamtinstituts ist nun Max-Planck-Institut für Physik und Astrophysik.

Die Bewegung ionisierter Gase im interplanetaren Raum, wofür die Kometenschweife ein Beispiel sind, beschäftigte Biermann auch weiterhin. So entstand der Plan, leicht ionisierbares Material mittels Raketen in großen Höhen zu verdampfen und seine Bewegung zu beobachten. Dies nahm Biermann zum Anlaß, in der Max-Planck-Gesellschaft für die Gründung eines Instituts für extraterrestrische Physik einzutreten. Es wurde 1963 als weiteres Teilinstitut des Max-Planck-Institut für Physik und Astrophysik gegründet unter der Leitung von Reimar Lüst, bis dahin Abteilungsleiter der Astrophysik.

Seinen Namen als Kometenphysiker bekräftigte Biermann Anfang der 60er Jahre, als er aus dem Auftreten der verbotenen Sauerstofflinien in Kometen – Swings und Greenstein hatten sie 1958 entdeckt – auf die Gesamtanzahl der vom Kometenkern abgedampften Moleküle schloß, eine Zahl, die um den Faktor 100 bis 1000 über der Anzahl der sichtbaren Moleküle lag. Bestätigt wurden seine Abschätzungen durch thermodynamische Überlegungen von Walter Huebner. Biermann folgerte daraus, daß die Kometen eine Wasserstoff-Koma haben müßten, die weit über die Ausmaße der sichtbaren Koma hinausginge. Im Jahre 1970 gelang es Code, Lillie und Mitarbeitern, die Wasserstoff-Koma des Kometen Tago-Sato-Kosaka in Lyman α vom US Orbiting Astronomical Observatory (OAO 2) aus nachzuweisen. Dem folgten weitere Beobachtungen anderer Kometen.

Als 1975 Biermanns Emeritierung anstand, war es wieder einer seiner langjährigen Mitarbeiter, Rudolf Kippenhahn, der mit der Leitung des Instituts betraut wurde. Auch nach seiner Emeritierung beschäftigte Biermann die Physik der Kometen, ihre Herkunft und ihr Erscheinen im inneren Sonnensystem. Fast jeden Sommer reiste er für einige Wochen in die USA, wo er in Boulder und Los Alamos Freunde gefunden hatte, die seine Interessen teilten. Mit großer Anteilnahme verfolgte er die Vorbereitungen zur Giotto Mission. Den Vorbeiflug der Sonde am Kometen Halley an seinem Geburtstag, dem 13. 3. 1986, sollte er nicht mehr erleben.

Nach längerer Krankheit, während der er – dank der Fürsorge seiner Frau – immer noch wissenschaftlich tätig war, erlag Ludwig Biermann am 12. Januar 1986 seinem Leiden.

Betrachtet man rückblickend Ludwig Biermanns Lebenswerk, so fällt zunächst sein Ideenreichtum und sein sicheres Gefühl für das physikalisch Wesentliche ins Auge. Diese Gaben waren es jedoch nicht allein, die den Erfolg seiner Arbeit begründeten. Schon von Anbeginn an verstand er es, Ergebnisse für seine Arbeit nutzbar zu machen, die in völlig anderem Zusammenhang gewonnen waren. Die Freude an über sein Fach hinausgreifenden Kombinationen begleitete ihn bis zuletzt, wenn er Spekulationen nachsann über Zusammenhänge zwischen der Entwicklung der Erde und des Lebens auf ihr und dem Durchgang eines Sterns durch die äußersten Bereiche des Sonnensystems, wo man sich den Ursprungsort der Kometen, die Oort'sche Wolke, zu denken hat. Was Ludwig Biermann aber in erster Linie ausgezeichnet hat, war sein Mut, sowohl wissenschaftlich wie organisatorisch, dort, wo er sich wissenschaftlichen Fortschritt versprach. Der flüchtige Beobachter hätte ihn diesem distanzierten, eher schüchternen Menschen nicht zutraut. Biermann griff Probleme auf, die andere für hoffnungslos hielten. Der Erfolg gab ihm Recht. Bezeichnend schon war meine Anstellung vier Wochen nach der Währungsreform, als keiner wußte, wo überhaupt Geld herkommen sollte. Er initiierte den Rechenmaschinenbau, als menschliche Arbeit noch viel billiger war – erst 1971 wurde die letzte selbstgebaute Maschine, die G3, außer Betrieb gesetzt. Er regte die Fusionsforschung an, er sorgte für die Gründung des Instituts für extraterrestrische Physik. Dabei ging er durchaus vorsichtig vor und holte gründlich die Meinung der Kollegen ein, die er für kompetent hielt. Er hätte nie etwas angefangen, ohne sich nicht auf breiter Basis mit anderen zu beraten. Von dem Problem, das ihn gerade beschäftigte, war er stets ganz erfüllt und suchte, dafür seine Mitarbeiter zu motivieren. Das kam dem Arbeitsklima außerordentlich zugute. Die Diskussionen waren sehr frei. Es fiel Biermann nicht auf, wenn die Formulierungen wenig respektvoll waren, sie mußten nur wissenschaftlich engagiert sein. Schmeicheleien nahm er nicht wahr, sie gingen ins Leere. Auf einen gewissen Grundkonsens im Umgang miteinander, der dem entsprach, was er von Haus aus gewöhnt war, war er allerdings angewiesen.

Biermanns wissenschaftliche Produktivität blieb nicht ohne Resonanz. 1943 erhielt er den Copernicus-Preis. Ihm folgten 1967 die Catherine-Wolfe-Bruce-Goldmedaille der Astronomical Society of the Pacific, 1973 die Emil-Wiechert-Medaille der Deutschen Geophysikalischen Gesellschaft und 1974 die Goldmedaille der Royal Astronomical Society London. 1969 erhielt er den Ehrendoktor der University of Colorado, Boulder. Er war Mitglied der Bayerischen Akademie der Wissenschaften, der Internationalen Academy of Astronautics, Associate of the Royal Astronomical Society, London, Korresp. Mitglied der Société Royal des Sciences, Lüttich, Mitglied der Astron. Society of the Pacific, der Deutschen Akademie der Naturforscher Leopoldina, Halle, und Foreign Associate der National Academy of Sciences, Washington.

Ich möchte den Artikel nicht schließen, ohne seiner Familie zu gedenken. Die Fürsorge seiner Gattin machte ihn frei für seine Wissenschaft. Mit Humor und tiefem menschlichen Verständnis freute er sich seiner drei Kinder. Die Vitalität seiner Frau brachte ihm Schwung. Daß er

so ganz in seiner Wissenschaft lebte, war für sie eine Lebens-
tatsache, die sie kürzlich etwa folgendermaßen beschrieb:
„Als ich bemerkte, daß man meinen Mann und seine Wis-
senschaft nicht trennen kann, habe ich beschlossen, die
Astrophysik in die Familie zu integrieren.“ Wie gut ihr das
gelungen ist, haben wir besonders in den letzten Monaten

seines Lebens gemerkt, wenn wir Ludwig Biermann, der
schon sehr schwach und sehr anfällig für Infekte war, besu-
chen durften, im gemütlichen Wohnzimmer beim Tee saßen
und natürlich über Astrophysik sprachen.

Eleonore Trefftz

Book Reviews

Brekhovskikh, L., Goncharov, V.: Mechanics of continua and wave dynamics. Springer series on wave phenomena, vol. 1, 342 p., Springer-Verlag, Berlin, Heidelberg, New York, Tokyo 1985.

This volume is a simple introduction to the mechanics of continua which has emerged from lectures given by the authors at the Physico-Technical Institute at Moscow. It is divided into two main parts:

The first part (consisting of 5 chapters) deals with the theory of elasticity in the limit of the linear theory and of isothermic or adiabatic strain. The first two chapters contain the basic laws of the deformation of an elastic body and an analysis of waves and vibrations in rods. Chapter 3 and 4 then proceed with the general theory of stress and strain and wave propagation in simple media. Chapter 5 gives a treatment of waves in plates, which is of special interest for model seismic experiments.

The second part on fluid dynamics, which comprises 9 chapters, is by far the more extensive and comprehensive part of this volume. Again it starts with the simplest case of ideal fluids and potential flow. In chapter 8 viscosity is introduced and chapter 9 gives the basic theory of turbulent flows. The remainder of the volume is devoted to waves in fluids. Gravity waves and sound waves are studied in chapters 10 to 12. In chapter 13 some aspects of magnetohydrodynamics are discussed, and chapter 14 finally gives an introduction to nonlinear effects in wave propagation.

An appendix on tensors, a bibliographical sketch with proposals for further reading and a subject index are included.

The intention of this volume is to present the main features of continuum mechanics and wave propagation in a simple and self-contained manner without using much sophisticated mathematics. This goal is achieved by the authors: all the material is presented step by step, starting with simple questions and proceeding to more complicated ones.

A very important part of this volume are the numerous exercises (including solutions) which conclude every chapter. By trying to solve at least some of them the reader can immediately check his understanding. Some of the exercises also give additional information which is excluded from the main text.

The only criticism I have is that the part on elastic waves in solid materials is too short. Therefore many topics of special relevance to seismology had to be omitted. For example, nothing is said about seismic sources and the propagation of spherical waves. Ray theory and viscoelasticity are other topics which have been excluded.

In spite of this shortcoming the volume can be strongly recommended as a textbook for students in the field of physics and geophysics. It requires only the knowledge of basic mathematics as given in undergraduate courses, and it provides the background for the study of other monographs on this subject. **M. Korn**